THE EFFECTS OF NUTRIENT DEPRIVATION ON MACROAUTOPHAGIC FLUX AND CHAPERONE-MEDIATED AUTOPHAGY IN A MODEL OF ALZHEIMER'S DISEASE

By

MATLAKALA CLAUDIA NTSAPI

Thesis presented in fulfillment of the requirements
for the degree of Doctor of Philosophy (Physiological Sciences)
in Faculty of Science at Stellenbosch University

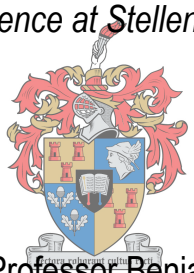

Promotor: Professor Benjamin Loos

December 2018

DECLARATION

I, the undersigned, hereby declare that the work contained in this dissertation is my own original work and that I have not previously in its entirety or in part submitted it at any university for a degree.

Date: December 2018

ABSTRACT

Introduction: Alzheimer's disease (AD) is a devastating neurodegenerative disease characterized by progressive cognitive impairment, particularly in brain regions crucial for learning and memory. These symptoms are caused by neuronal death resulting from two pathological features: extracellular senile plaques composed of aggregated amyloid-beta (Aβ) peptides, and intracellular neurofibrillary tangles generated by the hyperphosphorylation of tau protein. Although AD is a multifactorial disease, much of the AD research continues to be guided by the amyloid cascade hypothesis, which posits that Aβ aggregation is the key initiate in AD pathogenesis. Aβ is generated from the proteolytic cleavage of the amyloid precursor protein (APP) by β - and γ-secretase. Accordingly, research efforts to modulate APP processing, and better clarify the mechanisms that regulate intracellular Aβ metabolism and clearance during AD progression have been explored in the treatment of AD. Autophagy, a lysosome-based proteolytic pathway that plays a crucial role in intracellular protein quality control, has been implicated in both the production and clearance of Aβ peptide. Cumulative evidence shows that AD-related autophagic dysfunction coincides with the detection of Aβ within autophagic vacuoles (AVs) that accumulate within dystrophic neurites with the initial increase in Aβ neurotoxicity. Therefore, autophagy dysfunction may exacerbate Aβ pathology and further augment disease progression; however, when in this context autophagy becomes dysfunctional remains unclear. Moreover, although it is known that Aβ levels themselves may induce autophagy, how long autophagy remains upregulated and functional in this process is unclear. It also remains unclear whether autophagy plays a causative, or protective role in Aβ neurotoxicity; or whether autophagy dysfunction is a consequence of the disease process itself. Therefore, the aims of this study were (i) to characterize the expression profile of key amyloidogenic pathway proteins, both macroautophagy and chaperone-mediated autophagy (CMA) proteins as well as the extent of neuronal toxicity using a unique APP overexpression model, (ii) to dissect the interplay between proteolytic pathways and cell death markers in the context of APP overexpression using a proteomics approach, (iii) to assess macroautophagic flux in the context of APP overexpression and to unravel the extent of autophagy dysfunction, (iv) to assess the contribution of macroautophagy and CMA in Aβ clearance and neuronal toxicity by modulating each pathway, and (v) to assess the effects of prolonged intermittent fasting (IF) on the modulation of macroautophagy and CMA in a paraquat (PQ)-induced *in vivo* brain injury model.

Methods: A unique AD overexpression model, the N2a mouse neuroblastoma cell line stably overexpressing the human Swedish double mutation was utilized. APP overexpression was characterized, and the induction of macroautophagy, CMA, and apoptosis was assessed over time using a combination of cell viability assays, western blot analysis, fluorescence microscopy, transmission electron microscopy (TEM), and correlative light and electron microscopy techniques. Moreover, the effect of APP overexpression on a global proteome level was quantified using high resolution liquid-chromatography coupled to tandem mass spectrometry. Finally, a PQ – induced brain injury model was established and utilized to assess the effects of prolonged IF on macroautophagy and CMA using GFP–LC3 transgenic mice. Mice were injected twice weekly with 10 mg/kg PQ for a duration of 3 weeks. A prolonged IF protocol of 48 hrs fasting, followed by 24 hrs refeeding was implemented for a duration of 3 weeks. Modulation of macroautophagy and CMA following chronic oxidative stress exposure, and prolonged IF was evaluated in selected brain regions by western blot analysis, fluorescence microscopy, comparative haematoxylin and eosin staining, and TEM analysis.

Results: The results indicate that APP overexpression leads to prominent apoptosis induction after 48 hrs and activates the autophagy machinery in a time-dependent manner. To our surprise, macroautophagic flux analysis reveals that autophagy is upregulated upon APP overexpression but remains elevated in the presence of apoptosis induction. Our CMA analysis indicates that APP overexpression activates the CMA machinery, particularly during the 48 hrs time point. However, induction of apoptosis proceeded despite elevated levels of CMA activity. Next, our proteome analysis reveals a time-dependent increase in APP protein-protein interaction partners over time. Cumulatively, the *in vitro* results suggest that the modulation of macroautophagy and CMA augments Aβ clearance and mitigates neuronal toxicity. *In vivo*, a significant decrease in cytochrome c, and 4HNE expression were observed with prolonged IF intervention in selective brain regions. These changes were associated with elevated levels of macroautophagy and CMA induction, as evidenced by the significant increase in LC3II and LAMP2A protein expression. Therefore, suggesting that protection was brought about by the prolonged IF intervention through the modulation of macroautophagy and CMA.

Conclusion: Our findings indicate that autophagy is upregulated in the presence of high levels of APP and Aβ, and to our surprise, remains upregulated even in the presence of apoptosis induction, suggesting an insufficient autophagy response in the mitigation of Aβ neurotoxicity. However, enhanced Aβ clearance was observed with a sufficiently high autophagy response even during 48 hrs APP overexpression, suggesting that autophagy modulation may be a viable treatment approach long into disease progression. These findings were also confirmed with prolonged IF intervention, where markers of apoptosis, and lipid peroxidation were notably decreased in brain regions associated with neurodegeneration. Further studies, specifically using *in vivo* APP overexpression models are warranted to further verify the clinical use of autophagy control.

OPSOMMING

Inleiding: Alzheimer se siekte (AS) is ‘n vernietigende neuro-degeneratiewe siekte wat gekenmerk word deur ‘n progressiewe verlies in kognitiewe funksie in dele van die brein wat ‘n rol speel in geheue en leervermoë. Hierdie simptome word toegeskryf aan die doodgaan van neurone as gevolg van twee patologiese kenmerke: ekstrasellulêre seniele plake wat bestaan uit geaggregeerde beta-amiloïed (Aβ) peptiede en intrasellulêre neurofibrillêre knope wat ontaard danksê te hiperfosforilasie van die tau proteïen. Alhoewel AS vele oorsake het, volg die meerderheid van huidige navorsing die amiloïed kaskade hipotese waarin Aβ aggregasie as die hoof oorsaak van AS beskou word. Proteolitiese skeiding van die amiloïed voorloper proteïen (AVP) by β - en γ-sekretase veroorsaak die produksie van Aβ. Daar is tans vele navorsing veldtogte geloods wat poog om AVP prosessering te moduleer asook om die regulerende meganismes van intrasellulêre Aβ metabolisme en verwydering te ontbloot, met die hoop dat dit kan bydra tot beter behandeling van AS. Autofagie is ‘n lisosoom gebaseerde proteolitiese sisteem wat ‘n belangrike rol speel in die beheer van intrasellulêre proteïen kwaliteit en is gevind om betrokke te wees in beide die produksie en verwydering van die Aβ peptied. Kumulatiewe bewyse dui aan dat tydens AS verwante autofagiese disfunksie kan Aβ binne autofagiese vakuole (AV) gevind word en dat hierdie AV akkumuleer binne distrofiese neuriete tydens die aanvanklike vermeerdering in Aβ neurotoksisiteit. Daarom kan autofagiese disfunksie die Aβ patologie vererger en bydra tot die vorming van AS. Merendeels, alhoewel dit bewys is dat autofagie aangeskakel kan word namate die Aβ konsentrasie verhoog, is dit nog nie bekend vir hoe lank autofagie aangeskakel en funksioneel bly tydens hierdie proses nie. Dit is ook onduidelik of autofagie ‘n veroorsakende of beskermende rol in Aβ neurotoksisiteit speel en of autofagiese disfunksie nie net ‘n na gevolg van die siektetoestand self is nie. Dus was die doelwitte van hierdie studie om (i) ‘n proteïen uitdrukkings profiel van belangrike amiloïed reguleeringsproteïne te skep, (ii) die wisselwerking tussen proteolitiese prosesse en sel dood reguleerders in die konteks van AVP ooruitdrukking te verduidelik deur gebruik te maak van *proteomics*, (iii) die spoed van autofagie verwante proteïen degenerasie te assesseer in die konteks van APP ooruitdrukking asook die mate van autofagiese disfunksie, (iv) die bydrae van makroautofagie asook gemedieërde autofagie (GA) in Aβ verwydering en neuron toksisiteit te assesseer deur modulering van elke proses en (v) om die effek van langdurige afwisselende vas tydperke op die modulering van makroautofagie en GA te assesseer in ‘n paraquat (PQ)-geïnduseerde *in vivo* brein beskadiging model.

Metodes: ‘n Unieke AS ooruitdrukking model was geskep deur gebruik te maak van die N2a muis neuroblastoma sellyn wat ‘n dubbele Sweedse mutasie stabiel ooruitgedruk het. AVP ooruitdrukking was sodoende gekarakteriseer en die induksie van makroautofagie, GA en apoptose was met verloop van tyd geassesseer deur gebruik te maak van lewensvatbaarheid stoetse, Westerse blottering tegnieke, fluoressensie mikroskopie, transmissie elektron mikroskopie (TEM) en korrelatiewe lig en elektron mikroskopie (KLEM). Merendeels was die effek van AVP ooruitdrukking op globale proteoom vlakke gekwantifiseer deur gebruik te maak van hoë resolusie vloeistof chromatografie gekoppel aan tandem massa spektrometrie. Laastens, ‘n PQ geïnduseerde breinbeskadigingsmodel was opgestel en gebruik om die effek van langdurige afwisselende vas tydperke op makroautofagie en GA te toets in GFP-LC3 transgeniese muise. Die muise was twee maal per week ingespuit met 10mg/kg PQ vir ‘n tydperk van 3 weke. Die langdurige afwisselende vas protokol was ook oor 3 weke toegepas en het bestaan uit 48 ure se vas, gevolg deur 24 ure van voeding. Evaluering van makroautofagiese en GA modulasie na blootstelling aan kroniese oksidatiewe stres en langdurige afwisselende vas in geselekteerde brein areas het geskied deur middel van Westerse blottering, fluoressensie mikroskopie, vergelykende haematoxylin en eosien kleuring asook TEM analise.

Resultate: Die resultate dui aan dat AVP ooruitdrukking tot prominente apoptose lei na 48 ure en dat die autofagie in ‘n tyd verwante manier aktiveer. ‘n Onverwagte bevinding was dat die spoed van autofagie nie net verhoog het tydens AVP ooruitdrukking nie, maar dat hierdie hoë vlakke behou was selfs tydens apoptose. Dit was ook gevind dat AVP ooruitdrukking GA reguleerders aanskakel, veral tydens die 48ste uur. Desnieteenstaande, die induksie van apoptose het voortgegaan ongeag die verhoogde GA aktiwiteit. Ons proteoom analise dui ook ‘n tydafhanklike verhoging in AVP proteïen tot proteïen interaksies. Gesamentlik dui die *in vitro* resultate aan dat die modulasie van makroautofagie en GA ‘n rol speel in Aβ verwydering en neuron toksisiteit verlaag. *In vivo* was daar ‘n beduidende vermindering van sitokroom c en 4HNE uitdrukking was gevind tydens langdurige afwisselende vas intervensies en selektiewe dele van die brein. Dus dui dit aan dat hierdie vas tydperke meegebring was deur modulasie van beide makroautofagie en GA.

Gevolgtrekkings: Ons bevindinge dui aan dat autofagie aangeskakel word in die aanwesigheid van hoë hoeveelhede AVP en Aβ, en merkwaardig hierdie toestand behou selfs

tydens apoptose aktivering, moontlik as gevolg van ‘n onvoldoende autofagiese reaksie om Aβ neurotoksisiteit teen te werk. Desnieteenstaande, verhoogde Aβ verwydering was gevind met ‘n voldoende autofagiese reaksie selfs tydens 48 ure van AVP ooruitdrukking, wat aandui dat autofagie modulasie ‘n lewensvatbare behandelings alternatief kan wees lank na die siektetoestand bevestig is. Hierdie resultate was ook bevestig deur langdurige afwisselende vas intervensies, waar aanduiders van apoptose en lipied peroksidasie beduidend verlaag was in die areas van die brein wat geassosieer word met neurodegenerasie. Verdere studies, spesifiek dié wat gebruik maak van *in vivo* AVP ooruitdrukking modelle, word dus benodig om die kliniese belang van autofagie regulering te bevestig.

ACKNOWLEDGEMENTS

First and foremost, thank you Almighty GOD, for saying “yes” to the fulfilment of a lifelong dream!

This thesis is the result of the cumulative effects of a phenomenal group of people, who generously contributed their knowledge, and experience.

Words cannot express how extremely grateful and very fortunate I am to have been able to complete my PhD project under the supervision of Professor Ben loos. The last 3 years as part of the Neuro Research Group have been the most transformative years of my life, both scientifically and on a personal level. Thank you, Ben for all the support and encouragement, I know without a doubt that the successful completion of this project is in no small part due to you, and for this I am eternally grateful. Your work ethic is beyond commendable and I am immensely grateful to have had the privilege of being a student under your tutorage. Your patience, and constant encouragement have truly gotten me through the hardest of times, and because of your contribution to both my PhD and to me personally, I have developed critical skills that I will take with me to wherever life should take me. Above all, I wish you continued success being the phenomenal researcher and supervisor you are.

I would also like to thank Prof. Anna-Mart Engelbrecht, for the constant words of encouragement and to Prof. Resia Pretorius for allowing me to make the Physiological Sciences Department my “home away from home”.

Thank you to Stellenbosch University’s Central Analytical Facility (CAF) staff, Lize Engelbrecht, Dumisile Lumkwana, and Rozanne Adams for assistance with the acquisition of confocal micrographs. Thank you to Dr Maré Vlok for proteomic data acquisition, Nolan Muller for the acquisition of the TEM micrographs, Reggie Williams for assisting with the brain tissue sections, and Noel Markgraff for the invaluable assistance with the GFP-LC3 mice.

Thank you to the staff members at the Department of Physiological Sciences, including Judy, Grazelda, Jonnifer, Annadie, Lydia and Ashwin for ensuring the labs run smoothly.

I would also like to thank Chrisna, Andre, and Dumi for your contribution to a number of successful publications over the past 3 years. We made a phenomenal team and accomplished more together than I could ever have hoped to accomplish on my own.

I would also like to thank the many students in Department of Physiological Sciences, especially the NRG group of students both past and present, for their friendships, camaraderie and critical discussions. I would like to extend a special thank you to Yigael for the much-needed hugs during those tough times, and for allowing me to frequently hijack your time. To Jurgen, thank you for all your help, and the occasional dosage of dry humour. To Bianca, thank you for always being my sounding board through the tears, and the laughter, I am truly blessed to count you amongst my closest friends. To Andre, my gratitude for everything you have patiently assisted me with cannot be captured with words. I am truly in awe of your quiet brilliance and have no doubt that you will be great in whatever you choose to do in the future. To Zanobuhle, thank you for trusting me to co-supervise your Honours project, it truly was one of the most fulfilling experiences of my PhD journey. To Akile, for all the inspiring messages, thank you.

I would like to thank the National Research Foundation (NRF), the Medical Research Council (MRC) and the Oppenheimer Trust for financial support. I would also like to thank the University of Stellenbosch, WhitSci- Scientific and the EMBO Conference travel grant awards for the opportunity provided to attend the “Autophagy: From molecular principles to human disease” in Cavtat-Dubrovnik, Croatia.

To my family, thank you for the unwavering support, and prayers. Most importantly, I would like to thank my mother, who never once questioned or vetoed my never-ending study ambitions, I am who I am because of the sacrifices you made for me. You are the reason I continue to push forward, so that I may one day give you the life you deserve. This thesis is dedicated to you.

LIST OF CONFERENCE CONTRIBUTIONS AND PUBLICATIONS

Talks and poster presentations

International:

Claudia Ntsapi and Ben Loos. The time-dependent pro-survival role of autophagy in the face of amyloid beta-induced cytotoxicity in an *in vitro* model of Alzheimer's disease. EMBO Conference on: Autophagy - From molecular principles to human disease. 24-30 September 2017. Cavtat-Dubrovnik, Croatia.

National:

Claudia Ntsapi and Ben Loos. The link between autophagy dysfunction and amyloid beta-induced neurotoxicity in an *in vitro* model of Alzheimer's disease. South African Medical Research Council Young Researchers Forum. Parow Valley, Cape, South Africa 11-13 October 2017. Oral presentation.

Claudia Ntsapi and Ben Loos. Cells in stress/Cell death: The face of autophagy in response to amyloid-β induced neurotoxicity. Cell and Development Biology Mini Symposium. 22nd April 2017. New learning Centre, Faculty of Health Sciences, University of Cape Town, Anzio Road, Observatory. Oral presentation.

Claudia Ntsapi, and Ben Loos. Differential increase in macroautophagy and chaperone-mediated autophagy attenuates amyloid precursor protein-induced neurotoxicity in an *in vitro* model of Alzheimer's disease. 44thConference of the Physiology Society of Southern Africa. University of Cape Town, 28-31 August 2016. Poster presentation.

Publications:

- Claudia Ntsapi, Dumisile Lumkwana, Chrisna Swart, Andre du Toit and Ben Loos. New Insights into Autophagy Dysfunction Related to Amyloid Beta Toxicity and Neuropathology in Alzheimer's Disease. International Review of Cell and Molecular Biology. Volume 336, 2018.

- Claudia Ntsapi, Chrisna Swart, Dumisile Lumkwana and Ben Loos. Autophagic Flux Failure in Neurodegeneration: Identifying the Defect and Compensating Flux Offset. Biochemistry, Genetics and Molecular Biology. Autophagy in Current Trends in Cellular Physiology and Pathology. 2016.

- Claudia Ntsapi, and Ben Loos. Caloric restriction and the precision-control of autophagy: A strategy for delaying neurodegenerative disease progression. Experimental Gerontology. Volume 83. 2016.

- Claudia Ntsapi, and Ben Loos. Caloric restriction regulates autophagic flux to modulate the proteostasis of APP in Alzheimer's disease. Article in preparation, to be submitted shortly to the Journal of Molecular Neurodegeneration.

- Claudia Ntsapi, and Ben Loos. Enhanced APP processing and autophagy: new insights into the mechanism of Aβ neurotoxicity in Alzheimer's disease. Article in preparation, to be submitted shortly to the Journal of Neuroscience.

- Claudia Ntsapi, and Ben Loos. Prolonged intermittent fasting stimulates macroautophagy and chaperone-mediated autophagy in an *in vivo* model of paraquat-induced brain injury. Article in preparation, to be submitted shortly to the Journal of Experimental Neurobiology.

INDEX
LIST OF FIGURES
LIST OF TABLES
LIST OF ABBREVIATIONS

CHAPTER 1: LITERATURE DISCUSSION

CHAPTER 2: MATERIALS AND METHODS

LIST OF FIGURES

CHAPTER 1

CHAPTER 2

CHAPTER 3

CHAPTER 4

CHAPTER 5

CHAPTER 6

ADDENDUM B

LIST OF TABLES

CHAPTER 1

CHAPTER 2

ADDENDUM A

ADDENDUM B

LIST OF ABBREVIATIONS

2DG	2-deoxy-D-glucose
4HNE	4-Hydroxynonenal
3MA	3-methyladenine
Ab	Antibody
AD	Alzheimer's disease
ADAM	A disintegrin and metalloproteinase
ADP	Adenosine diphosphate
AICD	Amino-terminal APP intracellular domain
AKT	Gene Name (Synonymous with Protein Kinase B)
AMPK	AMP-activated protein kinase
APLP	APP-like proteins
APOE	Apolipoprotein E
APP	Amyloid precursor protein
sAPPα	Soluble APP generated by α-secretase cleavage
sAPPβ	Soluble APP generated by β-secretase cleavage
APP-CTFα/CTFβ	APP C-terminal fragment generated by α-/β-secretase cleavage
Aβ	Amyloid beta
ATG/atg	Autophagy-related genes or proteins
ATP	Adenosine triphosphate
AVs	Autophagy vacuoles
BACE1	β-site amyloid precursor protein cleaving enzyme 1
BA	Butyric acid
BafA1	Bafilomycin A1
BBB	Blood brain barrier
BECN1	Beclin 1
BSA	Bovine Serum Albumin
CMA	Chaperone-mediated autophagy
CNS	Central Nervous System
CSF	Cerebrospinal fluid
C83	83 amino-acid long Amyloid precursor protein C-terminal fragment
C99	99 amino-acid long Amyloid precursor protein C-terminal fragment
CTF	C-terminal fragment
CR	Caloric restriction
CRM	Caloric restriction mimetic
DAPI	4',6-Diamidino-2-phenylindole
DMSO	Dimethyl sulfoxide
DMEM	Dulbecco's Modified Eagle's Medium
DNA	Deoxyribonucleic acid
EE	Early endosomes
ER	Endoplasmic reticulum
ESCRT	Endosomal sorting complex required for transport
FBS	Fetal bovine serum
FAD	Familial Alzheimer's disease
FDA	Food and drug administration
FITC	Fluorescein isothiocyanate
GFP	Green fluorescent protein
GFAP	Glial fibrillary acidic protein
GTPase	Guanosine triphosphate hydrolase
HSC70	heat shock cognate 70
HD	Huntington's disease
IGF-1	Insulin-like Growth Factor-1
IF	Intermittent fasting
LAMP2A	Lysosome-associated membrane protein type 2a

LC-MS	Liquid chromatography–mass spectrometry
MA	Macroautophagy
mRNA	Messenger ribonucleic acid
MVB	Multivesicular bodies
MAP1-LC3	Microtubule Associated Protein 1-Light Chain 3
mTOR	Mammalian target of rapamycin
mTORC1	Mammalian target of rapamycin complex 1
N2a	Neuroblastoma cells/cell line
NCT	Nicastrin
NFT	Neurofibrillary tangles
n	number of experiments
PD	Parkinson's disease
PARP	Poly (ADP-ribose) polymerase
PBS	Phosphate-buffered saline
PE	Phosphatidylethanolamine
PEN1/2	Presenilin 1 and 2
PI3K	Phosphatidylinositol 3-kinase
PI3KC3	phosphatidylinositol-3-kinase class III
PIP3	Phosphatidylinositol 3-phosphate
PKB	Protein kinase B
PSM	Plasma membrane
RT	Room temperature
PTM	Post-translational modification
PQ	Paraquat
ROS	Reactive oxygen species
sAPP	Soluble amyloid precursor protein
SIRT1	Sirtuin 1 class III histone deacetylase;
p62/SQSTM1	Sequestosome 1
SWE	Swedish
TBST	Tris Buffered Saline with Tween 20
TGN	Trans Golgi network
UPS	ubiquitin–proteasome system
VEC	Vector
WT/wt	Wild type

AMINO ACID ABBREVIATIONS

Amino acid	3-letter	1-letter
Alanine	Ala	A
Arginine	Arg	R
Asparagine	Asn	N
Aspartic acid	Asp	D
Cysteine	Cys	C
Glutamine	Gln	Q
Glutamic acid	Glu	E
Glycine	Gly	G
Histidine	His	H
Isoleucine	Ile	I
Leucine	Leu	L
Lysine	Lys	K
Methionine	Met	M
Phenylalanine	Phe	F
Proline	Pro	P
Serine	Ser	S
Threonine	Thr	T
Tryptophan	Trp	W
Tyrosine	Tyr	Y
Valine	Val	V

UNITS OF MEASUREMENT

A	Ampere
%	Percentage
ºC	degrees Celsius
µl	Microliter
µg	Microgram
µm	Micrometer
µM	Micromolar
g	Gram
mg	Milligram
h/hrs	Hours
kDa	Kilodalton
l	Liter
M	Molar
min	Minutes
mM	Millimolar
nM	Nanomolar
V	Volt

CHAPTER 1: LITERATURE DISCUSSION

1.1. Introduction

Alzheimer's disease (AD) is a neurodegenerative disease associated with aging and is currently the most common form of dementia, impacting more than 35 million people worldwide (Alzheimer's Association, 2016). The incidence of this disease doubles every 5 years after 65 years of age, with the diagnosis of 1.275 new cases per year per 100.000 persons older than 65 years of age (Wimo et al., 2017). Paradoxically, AD is an unexpected consequence of increasing lifespan, which is the result of medical advances and research efforts that have curtailed the effects of communicable diseases, malnutrition and other health problems. Recent estimates indicate that by 2050 the proportion of people aged 60 years and older will account for nearly 22% of the global population, with the majority living in developing countries such as sub-Saharan Africa, where the effects of AD are further aggravated by limited medical resources (de Jager et al., 2017). Recent epidemiological studies have suggested that developed countries, perhaps due to better medical care, would have in the future a limited increase in AD cases, whereas developing countries are expected to be most significantly affected by the increasing AD epidemic (Ferri and Jacob, 2017). To date, 66% of the global elderly population resides in developing countries, and in the continued absence of effective therapeutic strategies to either delay or prevent disease progression, 79% of the global elderly population is predicted to reside in developing countries by 2050 (Wimo et al., 2017). Hence, the magnitude of the AD crisis is set to pose an even greater burden on society and public health systems.

The preclinical stage of AD is inconspicuous and there are no reliable or consistent symptoms which would allow for early diagnosis before the manifestation of irreversible cognitive deficits. This disease involves a progressive loss of synapses in the cerebral cortex and hippocampus leading to impaired memory and deterioration of cognitive functions (DeKosky and Scheff, 1990; Robinson et al., 2014). For a clinical diagnosis of dementia, cognitive impairment must be severe enough to compromise daily living activities. In the mild dementia stage, difficulties with declarative memory become prominent; as evidenced by increasingly frequent symptoms of depression,

hallucination, the increasing need for constant supervision. In the moderate dementia stage, cognitive function becomes more apparent, with obvious indications of cognitive impairments, including skewed perception and behaviour, as the patient gradually transitions into the late stage of disease progression, becoming completely dependent on caregivers (Dickerson et al., 2016, 2017). AD remains an unmet clinical challenge, the life expectancy of patients with a clinical diagnosis of AD is therefore significantly reduced. Despite the plethora of therapeutic agents currently being investigated in phase II and phase III clinical trials (https://clinicaltrials.gov/), currently approved medications, including acetylcholinesterase inhibitors (e.g. tacrine) and *N*-methyl-D-aspartate (NMDA) receptor AD antagonist (memantine), only treat the disease symptoms without targeting the underlying causative molecular mechanism, or altering the natural course of the disease (Blanco-Silvente et al., 2017; Hyde et al., 2013; Tan et al., 2014).

The anatomical distribution of pathological changes in AD, although highly selective for only certain brain areas, can be widespread at the end stage of the disease and can affect many neural systems. Neuroanatomical studies reveal prominent brain atrophy, particularly of the hippocampal area, temporal lobes and parieto-temporal cortices (Ringman, 2017). The destruction of these brain regions plays a prominent role in the memory deficits that herald the onset of AD and characterize the disease throughout its course (**Fig. 1.1**).

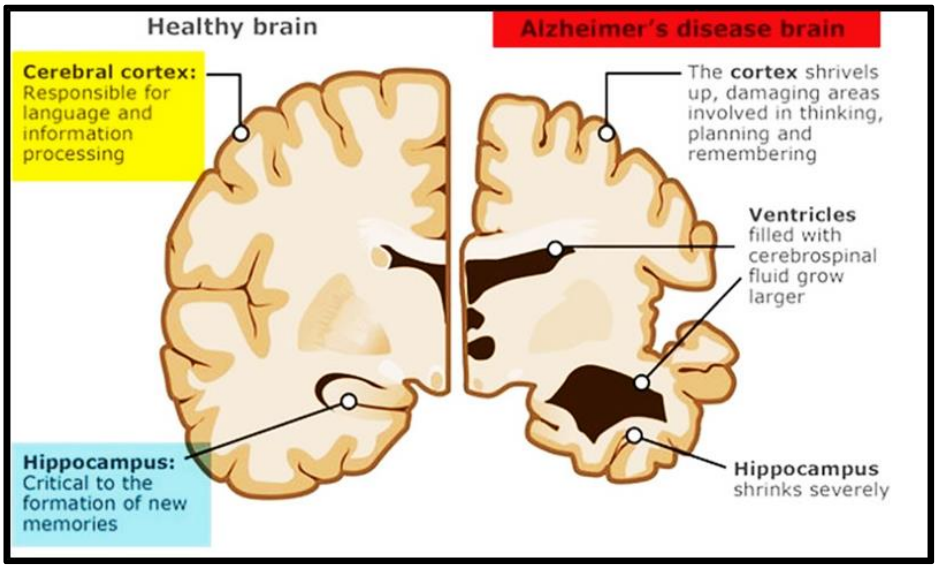

Figure 1.1: The anatomical distribution of AD pathological changes. Neuronal cell loss leads to extensive brain atrophy in the AD brain (**right**), compared to the healthy brain (**left**) [adapted from (Jin, 2015)].

At a molecular level, AD diagnosis is based on two hallmark features (**Fig. 1.2**): neuritic plaques, which are abnormal extracellular clusters of β-amyloid peptides (Aβ), and intraneuronal neurofibrillary tangles (NFTs), which are somatic inclusions of hyperphosphorylated microtubule-associated protein tau (Bateman et al., 2012). Neuritic plaques play a critical role in blocking communication among nerve cells and disrupting processes that cells need to survive, while NFTs impair vital transport systems involved in the transportation of key molecules (Dickerson et al., 2016).

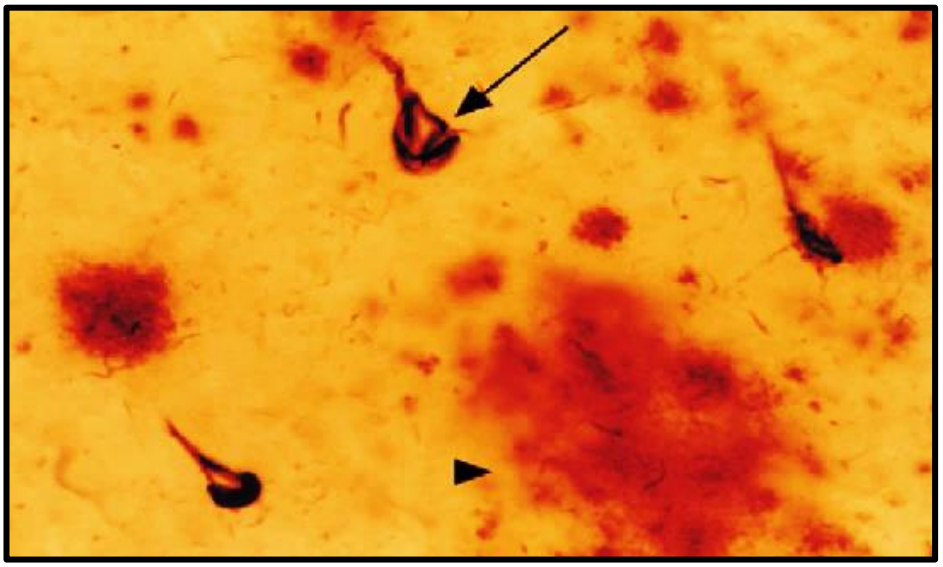

Figure 1.2: Neuropathological hallmarks of AD. Microscopic view of AD brain demonstrating Aβ plaque deposition (**arrowhead**), and the presence of NFTs (**arrow**) (Karch and Goate, 2015).

AD is classified according to the age of onset, the aetiology, the pathophysiology, and the biochemical and genetic alterations associated with disease progression. Familial AD (FAD) is a rare (~3 to 5% of all diagnosed cases) form of dementia affecting individuals younger than the age 65 and is usually associated with genetic mutations (Alzheimer's Association, 2016). While the overwhelming majority of AD cases are classified as late-onset/sporadic, occurring in individuals 65 years of age and older, and is usually associated with multifactorial aetiology (Hondius et al., 2016). FAD cases have a strong genetic correlation associated with mutations in genes coding for amyloid precursor protein (APP; chromosome 21), presenilin 1 (PSEN1; chromosome 14) and presenilin 2 (PSEN2; chromosome 1), which skew the production of Aβ, to favour production of the more neurotoxic Aβ species (Jarrett et al., 1993). In the case of sporadic AD, multiple genetic and environmental risk factors have been implicated, with the overall impairment of Aβ clearance considered to be a major contributor to disease progression (Mawuenyega et al., 2010). Although age is considered to be the principal risk factor for sporadic AD development, studies also suggest that the ε4 allele of the ApoE gene (apolipoprotein E; chromosome 19), a lipid transport protein that supports brain injury repair, may contribute to the risk of AD by initiating and accelerating Aβ production, and deposition in the brain (Head et al., 2012; Reiman et al., 2009). Neurotoxic forms of Aβ have been shown to be abundant in both sporadic (Kuo et al., 1996) and FAD cases (Scheuner et al., 1996), suggesting that the accumulation of Aβ is a common pathological mechanism underlying both forms of AD, therefore making the balance between Aβ production and clearance crucial to understanding the pathogenesis of AD.

Although extracellular aggregates of Aβ plaques and intraneuronal accumulations of NFTs define AD, it is clear that the aggregation, and conformational changes in Aβ play a more central role in initiating AD pathogenesis, while the contribution of NFT pathology has been shown to be more pronounced with late disease progression (Huynh and Mohan, 2017) (**Fig. 1.3**).

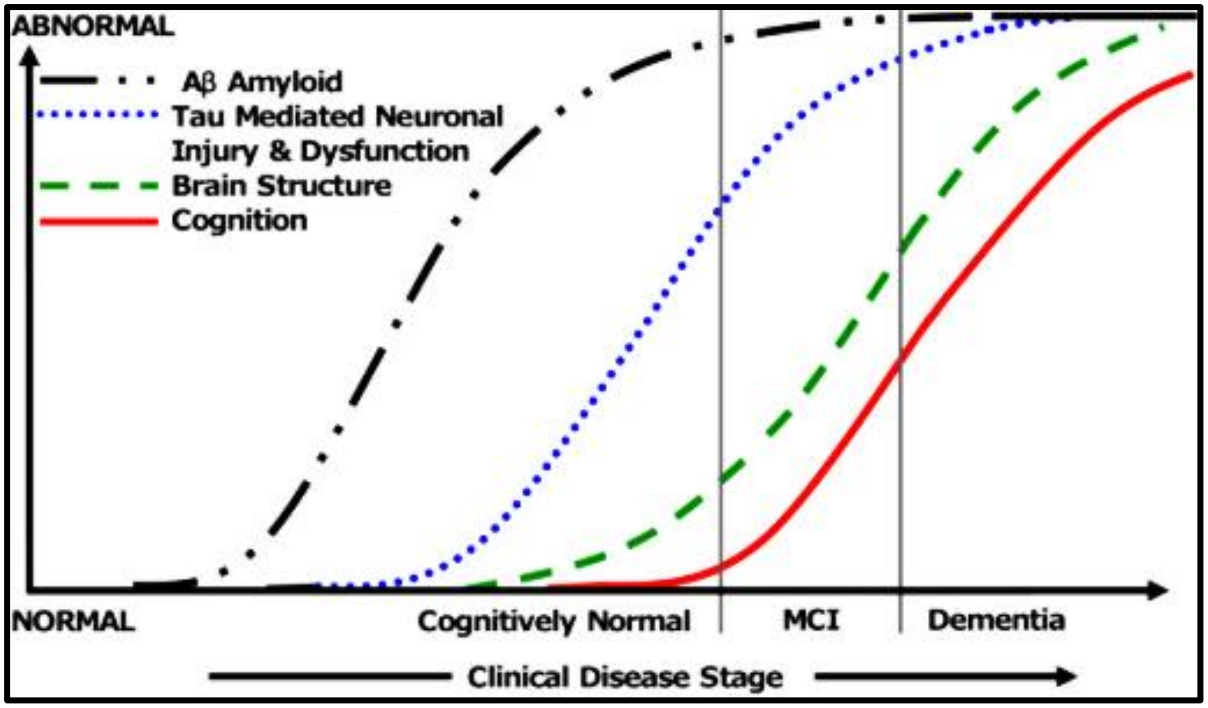

Figure 1.3: A hypothetical temporal model integrating AD biomarkers in relation to cognitive capacities, and brain structure. Elevated Aβ levels are the initial trigger in AD, while tau mediated neuronal injury only manifests years later in disease progression, ultimately leading to neuronal loss. MCI, mild cognitive impairment (Vemuri and Jack, 2010).

Several hypotheses have been put forward to better understand the multifactorial pathophysiology of AD, including the amyloid cascade hypothesis (ACH), the cholinergic and tau hypothesis, as well as inflammation (Karch and Goate, 2015). However, the underlying molecular alterations, and their dynamic changes during disease progression remain unclear. The ACH has been the central dogma in AD pathogenesis for the past 25 years and continues to guide the development of current disease modifying therapeutics used in the symptomatic treatment of AD (**Fig. 1.4**) (Selkoe and Hardy, 2016).

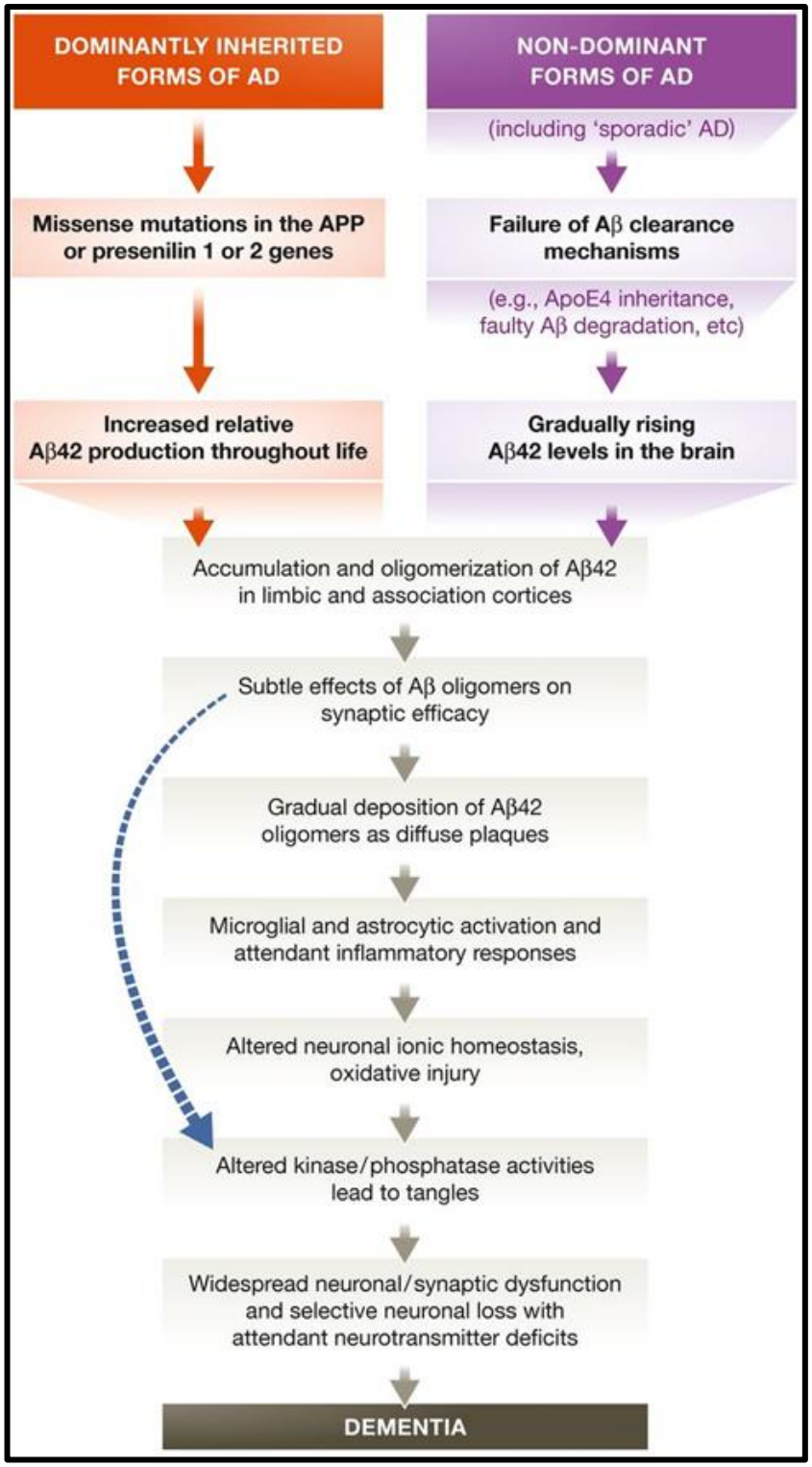

Figure 1.4: The amyloid cascade hypothesis (ACH). The ACH posits that the imbalance between Aβ production and clearance may be the central event in AD pathogenesis, with increased Aβ production in FAD and decreased Aβ clearance in sporadic AD. The common denominator in the pathogenesis of both AD forms is the conformational change in Aβ, which makes the peptide aggregate-prone. NFT formation is regarded as a downstream event that contributes to cognitive impairment. APP, amyloid precursor protein; PSEN1/2, presenilin genes 1 and 2; *ApoE*ε4, apolipoprotein E ε4 allele. The curved blue arrow indicates that Aβ oligomers may directly injure the synapses and neurites of brain neurons, in addition to activating microglia and astrocytes (Selkoe and Hardy, 2016).

As the most widely accepted mechanistic hypothesis for AD, the ACH suggests that the accumulation of the neurotoxic Aβ isoform triggers a cascade of events leading to increased inflammation, tau pathology, synaptic and neuronal loss which ultimately culminate in disease progression (Hardy and Higgins, 1992). The basis of the ACH stems from the following lines of evidence: (1) the identification of Aβ as the primary proteinaceous constituent in neuritic plaques (Glenner and Wong, 1984); and (2), the identification of several FAD mutations that occur within the Aβ region of APP and have been reported to increase the ratio of nontoxic to neurotoxic Aβ species, increase the aggregation potential of the mutant neurotoxic Aβ variant to further promote the peptides propensity to aggregate into more complex toxic conformations, such as oligomeric structural formation (Giasson et al., 2003). The most notable of these mutations include the Swedish APP (KM670/671NL), London APP (V717I), and Indiana APP (V717F) which have been demonstrated to exert their pathogenic effects by inducing the formation of Aβ oligomers and protofibrils (**Fig. 1.5**) (Goate et al., 1991; Mullan et al., 1992). These mutations confirm the relevance of the Aβ in the fundamental mechanism of AD pathogenesis. Thus, intense efforts have been made in the search for anti - Aβ directed targets which may enhance Aβ degradation or prevent its aggregation.

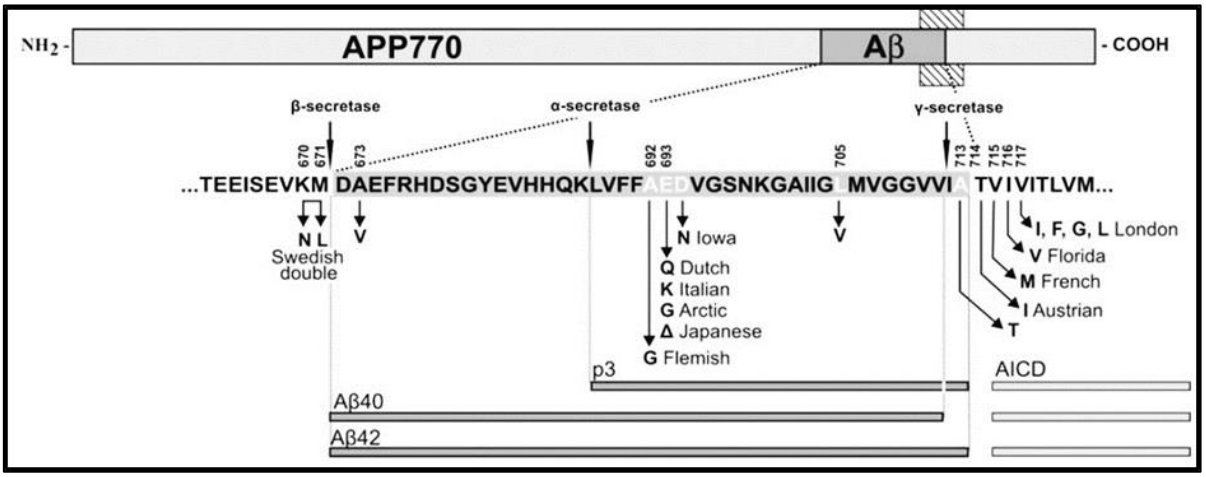

Figure 1.5: Schematic representation of amyloid precursor protein (APP). Positions of the Aβ sequence, APP transmembrane domain of (Tm), and sites of α-, β- and γ-secretase cleavage are illustrated with the Aβ sequence enlarged below. The constitutive proteolytic cleavage by α- and γ-secretases leads to the formation of the short p3 peptide and processing by β- and γ-secretases leads to the production of $Aβ_{40}$ and $Aβ_{42}$ peptides, along with a consecutive release of a C-terminal APP intracytoplasmic domain (AICD). Also shown are AD causing pathogenic mutations within APP (Kumar-Singh, 2009).

1.2. Biology and pathophysiology of APP

1.2.1. APP localization, subcellular trafficking and processing

APP is the only type I transmembrane protein unequivocally linked to AD pathogenesis, as the unique source of Aβ neurotoxicity (Rajendran and Annaert, 2012). During early development, APP is highly enriched at the growth cones of developing neurites (O'Brien and Wong, 2011). In more mature neurons, APP localizes to focal adhesion sites and within pre - and postsynaptic structures of the central and peripheral nervous tissue, suggesting a functional role in neuritic growth and synaptic plasticity (Makioka et al., 2009).

APP is synthesized in the endoplasmic reticulum (ER) and is transported to the plasma membrane (PM) via the secretory pathway. Studies suggest that APP may be transported through the secretory pathway in the following order: rough ER → ER-to-Golgi transport vesicles → Golgi cisternae → secretory or transport vesicles → PM (Lodish et al., 2000). At the PM, APP undergoes the following: (1) proteolytic cleavage via α-secretases following the non-amyloidogenic (constitutive) pathway, releasing soluble APPα (sAPPα) in the extracellular environment (α-secretases cleavage occurs within the Aβ domain of APP, thus preventing Aβ generation) (Sisodia, 1992), (2) APP may be recycled back to the trans-Golgi network (TGN) for further packing and trafficking or, (3) APP may be reinternalized from the PM via endocytosis into the endosomal - lysosomal system pathway for proteolytic cleavage via β-secretases following the amyloidogenic pathway (**Fig. 1. 6**) (Audrain et al., 2016; O'Brien and Wong, 2011). APP has been shown to be cleaved by β-secretases in early endosomes (EEs), with the activity of these enzymes being dependent on the acidification of these organelles (Rajendran and Annaert, 2012; Sannerud et al., 2011). APP and β-secretases only interact when both are endocytosed in common EEs (Sannerud et al., 2011), subsequently β-secretases cleave APP at the N-terminus of the Aβ sequence, generating soluble APPβ in the endosomal lumen before being targeted for degradation in lysosomes (Castello and Soriano, 2014). In this regard, studies have shown a limited amount of Aβ immunoreactivity in lysosomes, suggesting that cells are able to perform rapid proteolytic digestion of this peptide under normal

physiological conditions (Baranello et al., 2015). In support of this notion, work by Zheng et al. (2006) revealed that inhibition of lysosomal enzymes further exacerbate Aβ accumulation within the lysosomal compartment. Moreover, Aβ has been shown to accumulate within lysosomes in AD model systems, where Aβ production has been found to promote neuronal cell death through lysosomal destabilization (Nixon et al., 2000; Yang et al., 1998).

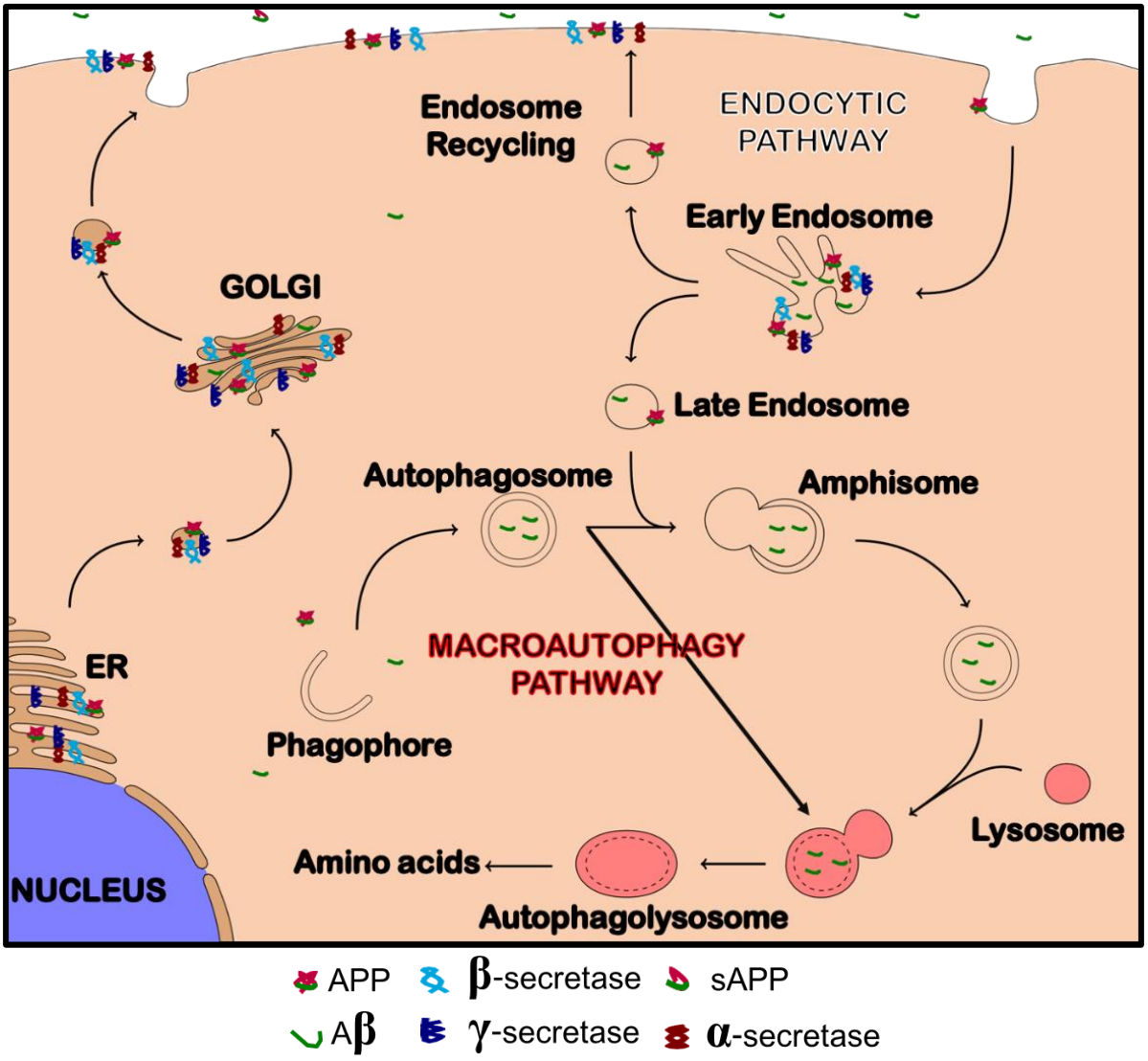

Figure 1.6: The trafficking, localization and processing of APP in cell vesicles. APP is transcribed in the ER, modified in the Golgi, shuttled to the cell surface and delivered to the plasma membrane for α-secretase mediated cleavage via the non-amyloidogenic pathway. Non-processed APP is internalized from the cell surface through endocytosis. From early endosomes, APP is transported to the late endosomes, and can be degraded via the autophagy pathway following the fusion of amphisomes and autophagosomes for subsequent degradation in autophagolysosomes. Alternatively, APP can be recycled via recycling endosomes and enter the cycle again. Amyloidogenic processing of internalized APP by β- and γ-secretases is primarily thought to occur in endosomes, and autophagosomes [adapted from (Nixon, 2007)].

After α- and β-secretase cleavage (non-amyloidogenic versus amyloidogenic), the resulting membrane associated C-terminal fragments, αCTF/C83 or βCTF/C99 respectively, are generated. Subsequently C99 and C83 are cleaved by γ-secretase within the transmembrane domain, resulting in the release of a nontoxic p3 fragment, APP intracellular domain (AICD), and Aβ species of different lengths (**Fig. 1.7**) (Sisodia and St George-Hyslop, 2002). The amyloidogenic or pathogenic pathway has been shown to be the more favoured pathway for APP processing in neurons, whereas the non-amyloidogenic pathway is predominant in all other cell types (Haass et al., 1992, 2012). Accordingly, β-secretase continues to be the target of intense therapeutic efforts, as genetic knockdown of this enzyme has been found to completely block Aβ generation (Cai et al., 2015; Luo et al., 2003). β-secretase is ubiquitously expressed, with the highest expression levels being documented in the brain and pancreas (Cai et al., 2001). The physiological relevance of enhanced β-secretase expression in the pancreas remains unclear. However, APP is also expressed at very high levels in the brain, making this tissue one of the primary locations for increased Aβ generation.

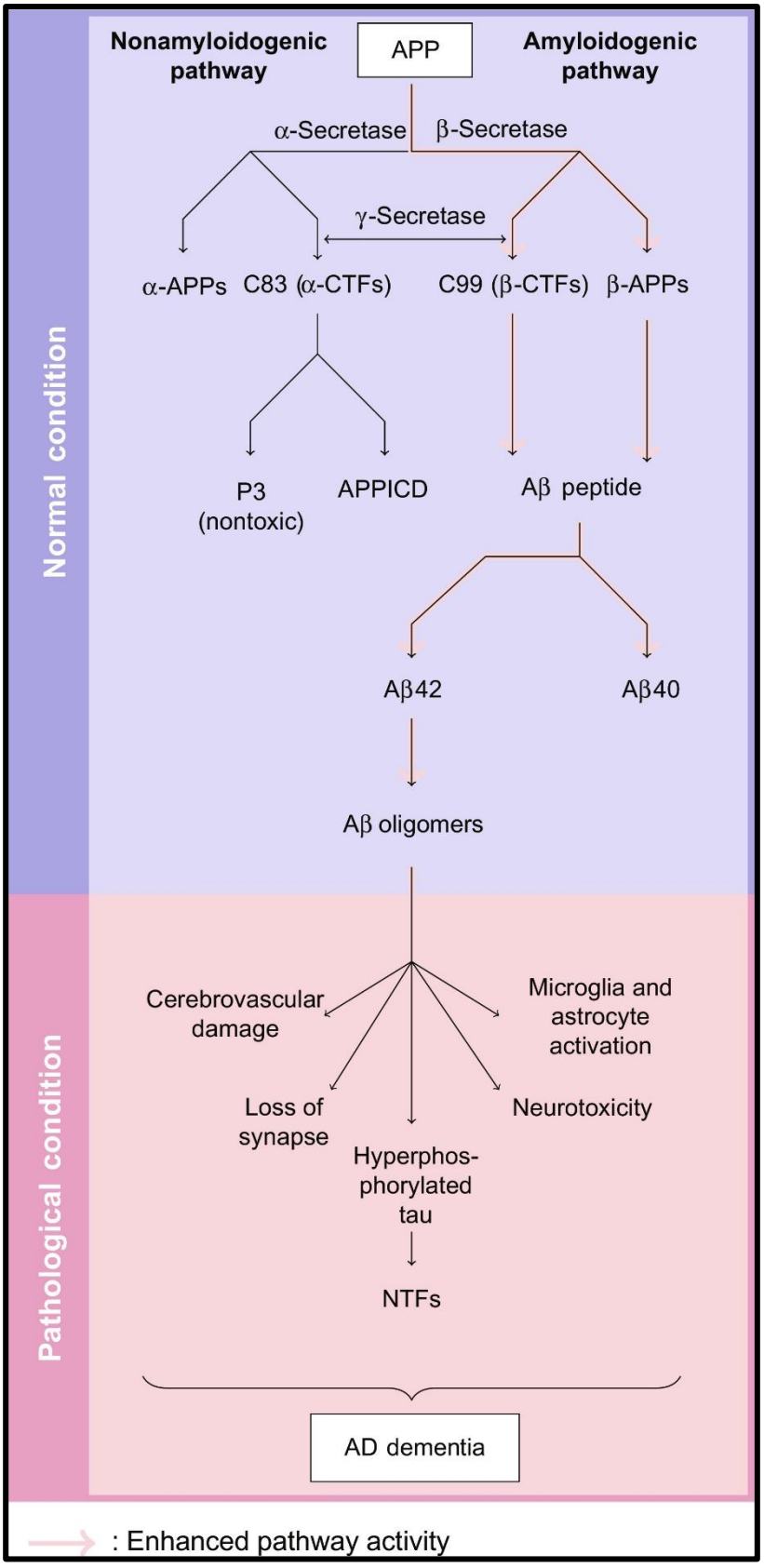

Figure 1.7: The non-amyloidogenic and amyloidogenic pathway. Enhanced amyloidogenic pathway activity increases neuronal synthesis of aggregate prone toxic Aβ oligomers, which in turn triggers a downstream pathogenic cascade, ultimately driving neurofibrillary tangle (NFT) formation and AD progression (Ntsapi et al., 2018).

1.2.2. The role Aβ oligomers in neurotoxicity and disease propagation

Aβ is naturally present in the brain and cerebrospinal fluid (CSF) throughout life, indicating that its mere presence does not cause neurodegeneration (Sun et al., 2015). Rather, it is the dysfunctional clearance of selective Aβ isoforms, in concert with an elevated concentration thereof, that appears sufficient to cause both sporadic and FAD (Greener, 2014; Murphy and LeVine, 2010). APP cleavage by α-secretase is protective in the context of AD, given that the enzyme cleaves within the Aβ sequence, thereby preventing the production of Aβ (Marr and Masliah, 2015). In contrast, the activity of β-secretase is significantly elevated in both FAD and sporadic AD (Leissring, 2014), giving rise to an admixture of Aβ peptides composed of 39–43 amino acid long peptides, with $A\beta_{40}$ (90%) and $A\beta_{42}$ (10%) being the two major Aβ species (Gouras et al., 2000). Although the role of $A\beta_{40}$ remains unclear, studies suggests a role in the modulation of synaptic function (O'Brien and Wong, 2011). On the other hand, $A\beta_{42}$ has a higher tendency to self-aggregate and form higher order structures, including toxic Aβ dimers, trimers, and oligomers. These structures then coalesce to form Aβ fibrils, which is an insoluble beta-sheet conformation that eventually deposits into neuritic plaques (Burdick et al., 1992; Gravina et al., 1995). Prior to Aβ plaque deposition, $A\beta_{42}$ oligomers have been shown to induce oxidative stress, promote tau hyperphosphorylation, and lead to synaptic and mitochondria dysfunction (Lustbader et al., 2004). Studies have also shown that elevated $A\beta_{42}$ levels impair the functionality of the cells principle proteolytic system, by impeding clearance of other cytotoxic proteins, such as α-synuclein, through the autophagy-lysosomal pathway (Lin et al., 2016; Silva et al., 2011). Moreover, during late disease progression, $A\beta_{42}$ neuritic plaques have been found to activate microglia, resulting in the release of proinflammatory cytokines, which in turn stimulate nearby astrocytes to further exacerbate $A\beta_{42}$ production (Heurtaux et al., 2010). In agreement, immunohistochemical analysis reveals significantly higher $A\beta_{42}$ levels in AD brains compared to controls (Huynh and Mohan, 2017). Additionally, the extent of $A\beta_{42}$ deposition is much greater in AD brains, while $A\beta_{40}$ shows no apparent age-dependent accumulation. Although many factors contribute to AD pathogenesis, the imbalance in Aβ production, particularly in favour of $A\beta_{42}$, is increasingly being recognized as a common theme in both FAD and sporadic AD (Selkoe and Hardy, 2016).

1.2.3. Aβ clearance systems in the brain: implications for AD progression

The mechanisms of Aβ clearance and degradation include the activity of Aβ proteases, which are enzymes that degrade or cleave Aβ into smaller peptide fragments. Other proteins with a crucial role in Aβ clearance are ApoE and α2-macroglobulin (α2-M); which interact with transporters such as low-density lipoprotein receptor-related protein 1 (LRP1) receptors, very low-density lipoprotein receptor (VLDLR), and P-glycoprotein, and localized in astrocytes on the luminal side of the cerebral endothelium, where they facilitate the transportation of Aβ across the blood brain barrier (BBB) (Deane et al., 2009; Miller et al., 2008). Genetic mutations resulting in loss of function of these proteins have been documented during disease progression, particularly in sporadic AD, where LRP1 dysfunction has been shown to result in the reduced efflux of Aβ from the brain, thus leading to increased Aβ accumulation (Kang et al., 2000; Van Uden et al., 2002). In normal brain plasma, a soluble form of LRP1 (sLRP1) has been found to sequester approximately 70-90% of plasma Aβ peptides, but in AD the levels of sLRP1 and its capacity to bind Aβ are markedly reduced, thereby increasing the concentration of free Aβ in blood plasma (Deane et al., 2003). This in turn may lead to enhanced Aβ accumulation in brain, and the gradual oligomerization of this peptide (Kayed et al., 2003; Walsh et al., 2005).

The autophagy pathway is critical for the turnover of cell organelles and degradation of aggregated proteins in cells under stress conditions. It has been suggested that the inefficient clearance of Aβ-generating autophagic vacuoles (AVs) creates conditions favourable for Aβ accumulation in AD, and this notion is supported by findings indicating that enhancing autophagy activity using rapamycin treatment (a macrolide compound known to induce autophagy) drastically reduces Aβ burden *in vivo* (Nixon, 2007). Therefore, failure of autophagy-mediated Aβ clearance is increasingly being recognized as a central theme in the pathogenesis of AD (Cai et al., 2015), and accumulating evidence suggests that localized defects in the autophagy pathway, are likely to precede the neurotoxic aggregation of Aβ oligomers (Nixon and Yang, 2011; Zare-shahabadi et al., 2015). An understanding of autophagic function with AD progression, and Aβ clearance through this pathway, may reveal novel strategies to reduce excess Aβ deposition and mitigate AD pathogenesis.

1.3. Intracellular proteolytic systems

Eukaryotic cells are equipped with two major protein quality control mechanisms known to impact cell survival, the ubiquitin–proteasome system (UPS) and the autophagy-lysosome pathway. While the UPS is primarily responsible for the degradation of short-lived proteins, autophagy is capable of degrading a much wider spectrum of substrates, which on average tend to be longer-lived proteins, and often organized into oligomeric complexes or aggregate structures (Mizushima, 2007; Rubinsztein, 2006). Autophagy is particularly necessary for the clearance of aggregate-prone proteins that are especially detrimental to post-mitotic cells (Rubinsztein, 2006). The post-mitotic nature of neuronal cells is thought to further predispose these cells to cytotoxic protein accumulation, as these cells cannot replicate, making neuronal integrity more vulnerable to alterations in basal autophagy than any other cell types (Nikoletopoulou et al., 2015). Protein and damaged organelle turnover, e.g. mitochondria, and peroxisomes, is essential to maintain cellular homeostasis and survival. Autophagy has been implicated in various physiological processes, including adaptive immune responses, cellular homeostasis, development, differentiation, longevity, the elimination of invading pathogens, and intracellular protein turnover to counteract the onset of diseases characterized by the accumulation of protein aggregates (Mizushima and Komatsu, 2011). Although autophagy has previously been defined as a form of non-apoptotic, programmed cell death (Liu and Levine, 2015), recent findings suggest that autophagy functions primarily to sustain cell survival, and only localized defects in the autophagy pathway have been suggested to result in cell death onset (Kroemer and Levine, 2008). In agreement, the induction of autophagy has been shown to have compelling anti-aging effects, while inhibition of this process accelerates aging and compromises the longevity effects of caloric restriction (CR) (Rajawat et al., 2009; Rubinsztein et al., 2015).

1.3.1. The role of autophagy in stress response and neurodegeneration

Autophagy is an essential pro-survival pathway induced by a variety of cellular stressors which have been found to contribute to the aetiology of various pathology, these include nutrient deprivation, growth factor withdrawal, oxidative stress, infection, and hypoxia (Murrow and Debnath, 2013). Although basal autophagy exists in all eukaryotic cells (Mizushima et al., 2008), a landmark study using a green fluorescent protein tagged microtubule-associated protein 1A/1B-light chain 3 (GFP-LC3) transgenic mouse model demonstrated that autophagy is distinctly regulated in neurons (Mizushima, 2004). Work by Mitra and colleagues demonstrated significant differences in basal autophagy between neuronal and non-neuronal cells (Mitra et al., 2009), and pioneering loss-of function studies further support a critical role for basal autophagy in the brain (Hara et al., 2006; Komatsu et al., 2006, 2007a). For instance, tissue specific deletion of key autophagy genes in murine muscle, heart or the central nervous system have been shown to result in neurodegeneration, muscular atrophy, and cardiac hypertrophy (Hara et al., 2006; Nakai et al., 2007). Additionally, genetic knockout of the essential autophagy gene ATG5 in mice, has been shown to cause lethality soon after birth, suggesting a crucial role for autophagy during the early neonatal period in the maintenance of energy homeostasis (Kuma et al., 2004). Moreover, cells deficient in autophagy show diffuse abnormal protein accumulation and mitochondrial disorganization (Nishiyama et al., 2007), suggesting that autophagy is necessary to maintain cellular homeostasis, through the removal of protein aggregates and damaged organelles. In contrast, enhanced autophagy has been shown to extend lifespan (Rubinsztein et al., 2011). More recently, a study highlighted the pivotal role of dysregulated autophagy in neurodegenerative diseases, where toxic protein aggregates were shown to accumulate within specific types of neurons and lead to neuronal dysfunction and ultimately, cell death onset (Caballero and Coto-Montes, 2012). In contrast, enhanced autophagy has been shown to improve clearance of aggregated proteins and reduce the symptoms of neurodegeneration in various animal model systems (Ravikumar et al., 2004; Spilman et al., 2010). Autophagy induction may therefore serve as a therapeutic target for several neurodegenerative diseases in which cytotoxic protein aggregation has been shown to be a pathological hallmark of the disease progression (Douglas and Dillin, 2010).

1.3.2. Autophagy and its machinery

Depending on the delivery route of the cytoplasmic material to the lysosomal lumen, three different autophagy pathway subtypes have been classified: (i) macroautophagy, or simply autophagy, (ii) microautophagy, which is further subdivided into endosomal microautophagy, and (iii) chaperone-mediated autophagy (CMA) (Wang and Mandelkow, 2012). Macroautophagy (hereafter referred to as autophagy) is the most extensively characterized, and quantitatively the most important proteolytic pathway, whereby a portion of cytoplasm targeted for degradation is first wrapped inside a specialized organelle, the autophagosome, which then fuses with lysosomal vesicles and delivers the engulfed cytoplasmic material for lysosomal degradation (Weidberg et al., 2011). While a continuous and dynamic process, the precision-controlled autophagy process is mechanistically organized into five separate steps that comprise (1) initiation, the formation of the phagophore structure; (2) nucleation, the expansion of the phagophore to engulf entire cytoplasmic regions; (3) elongation and enclosure of the phagophore membrane to form the autophagosome; (4) maturation, the fusion of the mature autophagosome with the lysosome to form the autolysosome/autophagolysosome, and (5) degradation of luminal contents, with the resultant biomolecules being released back into the cytosol for reuse by the cell (Galluzzi et al., 2017) (**Fig. 1.8**).

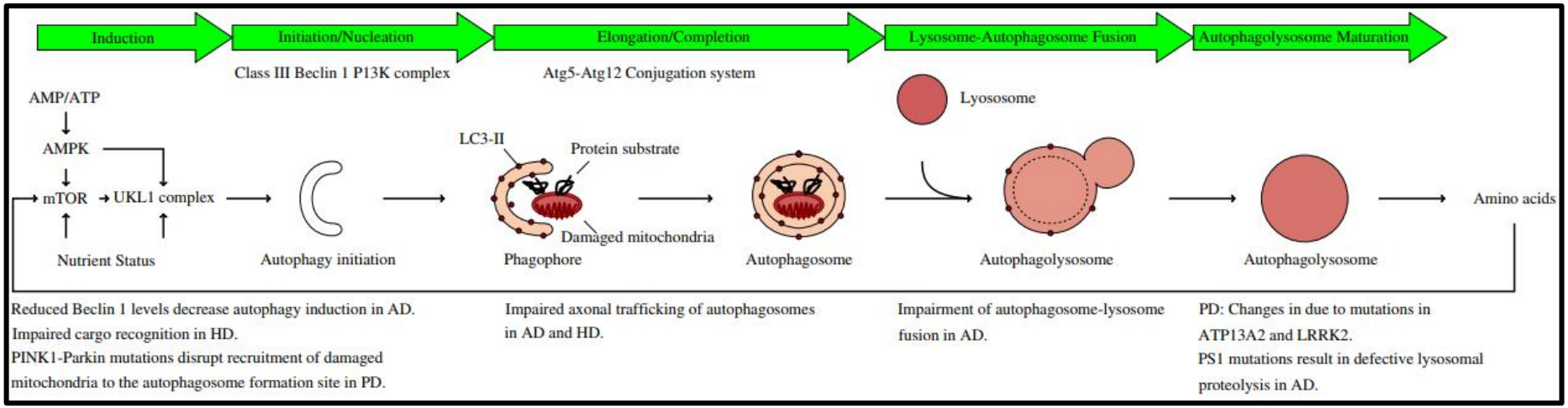

Figure 1.8: The process of macroautophagy (MA) and the major functional complexes involved in its regulation during nutritional stress. Distinctly localized autophagy defects have been shown to result in autophagic flux changes during the progression of Alzheimer's disease (AD), Parkinson's disease (PD), and Huntington's disease (HD). The multistep pathway of macroautophagy forms an energetic feedback loop from energetic sensing to cargo degradation and amino acid release. The rate of flow through this pathway is termed autophagic/macroautophagic flux and contributes to proteostasis, quality control and metabolite substrate generation (Ntsapi and Loos, 2016).

1.3.3. The precision control of the autophagy machinery

Given the important roles played by the autophagy pathway, it is not surprising that this process requires to be finely regulated to avoid both excessive, and insufficient activity. Over 50 years have passed since Nobel laureate Christian de Duve first coined the term autophagy, or “self-eating’, through identification of the lysosome (Deter and de Duve, 1967). Years later, pioneering genetic studies in yeast by Nobel laureate, Yoshinori Ohsumi ushered in the era of molecular autophagy research, allowing for the identification of several ATG genes, i.e. ATG1-ATG35, conserved from yeast to mammals, with ATG or atg referring to “autophagy related” (Ohsumi, 1997, 2014). Each step in the autophagy process is mediated by the tight regulation of several indispensable ATG proteins.

1.3.3.1. Autophagy regulation by nutrient signalling pathways

The regulation of autophagy tightly interconnects multiple nutrient sensing pathways, to ensure that during conditions of nutrient deprivation, or nutrient excess, cellular homeostasis can still be maintained. Starvation is the classic stimulus for autophagy, allowing cells to respond to nutrient scarcity through increased allocation of amino acids from cytoplasmic material sequestered as autophagic cargo (Hosokawa et al., 2009). The classical pathway regulating mammalian autophagy involves the serine/threonine kinase, mammalian target of rapamycin (mTOR), that receives and merges input from various signalling pathways, such as adenosine monophosphate-activated protein kinase (AMPK), phosphatidylinositol 3-kinases (PI3K), and the serine/threonine kinase Akt (also known as protein kinase B or PKB), to trigger or halt the synthesis of proteins in response to a shift in nutrient availability and energy status (Kim and Guan, 2015). mTOR forms two functionally distinct complexes in mammals, mTOR complex 1 (mTORC1) and mTOR complex 2 (mTORC2), distinguished by their partner proteins and differing sensitivities to rapamycin. Autophagy is negatively regulated by mTORC1 (**Fig. 1.9**) (Guertin and Sabatini, 2007; Noda and Ohsumi, 1998), while mTORC2 is implicated in the regulation of CMA in response to nutrient starvation (Arias et al., 2015; Ebner et al., 2017).

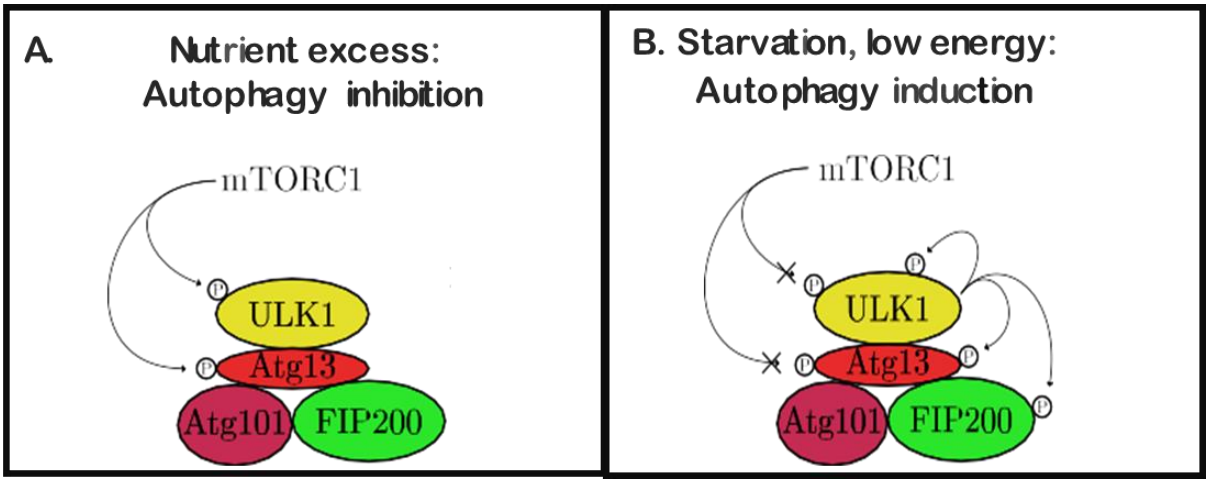

Figure 1.9: Nutrient-dependent regulation of the autophagy pathway. A. Under conditions of nutrient excess, mTORC1 binds the Ulk1 kinase complex and inhibits autophagy by phosphorylating ULK1 and Atg13. **B**. When cells are starved or depleted of energy, mTORC1 dissociates from the complex, ULK1 autophosphorylation increases and the kinase phosphorylates Atg13 and FIP200, resulting in autophagy induction [adapted from (Ntsapi and Loos, 2016)].

In brief, during conditions of nutrient availability, activated mTORC1 is sequestered into a complex with the Unc-51 Like Autophagy Activating Kinase 1 (ULK1), consisting of Atg13, and focal adhesion kinase family interacting protein of 200 kDa (FIP200), and phosphorylates Atg13 and ULK1, thereby inhibiting the initiation of autophagy (Ganley et al., 2009; Mercer et al., 2009). During conditions of nutrient starvation, amino acid deprivation, growth factor withdrawal, or treatment with rapamycin, mTORC1 dissociates from the ULK1 complex, which frees ULK1 to auto-phosphorylate, and trans- phosphorylate its binding partners Atg13 and FIP200 to induce autophagy (**Fig. 1.9**) (Jung et al., 2010). Subsequently, activated ULK1 phosphorylates and activates the Beclin1-vacuolar protein sorting 34 (VPS34) complex, which contains Beclin1 (BECN1), VPS34, and Atg14L (Itakura et al., 2012). The activated Beclin1 complex functions as a class III phosphatidylinositol 3-kinase (PI3KCIII), to produce phosphatidylinositol 3-phosphate (PI3P), which in turn provides a platform to recruit PI3P-binding proteins during the nucleation process (Kim et al., 2011; Sarkar, 2013). The PI3P-binding proteins label and recruit binding proteins, termed WD repeat domain phosphoinositide interacting (WIPI) and double FYVE domain-containing protein 1 (DFCP1), which serve as a docking platform (Neer et al., 1994). Atg14L targets the Beclin1/PI3KCIII complex to the specialized subdomain of the ER, called the omegasome, which consequently triggers phagophore formation (Matsunaga et al., 2010). Although the Golgi apparatus, mitochondria and

PM may also act as membrane sources for phagophore formation under certain conditions (Axe et al., 2008; Mizushima et al., 2011), a growing number of studies have revealed that phagophores locate between two cisterns of rough ER in starved cells (Hayashi-Nishino et al., 2009). In support of this finding, the omegasome marker protein DFCP1 has also been reported to be localized within delicate membrane tubules extending from the ER, thus making the ER the most likely membrane source for the phagophore formation (Uemura et al., 2014). Two ubiquitin-like conjugation systems are involved in the elongation and expansion of the phagophore membrane. Firstly, Atg12 is conjugated to Atg5, which then interacts with Atg16L to form the Atg12-Atg5-Atg16L complex, which is necessary for autophagosome formation (Mizushima et al., 2003). This is followed by the conjugation of LC3 to the lipid phosphatidylethanolamine (PE). LC3 is cleaved at its C-terminus by Atg4 to form the cytosolic LC3I, which is conjugated with PE to generate LC3II (Tanida et al., 2004). LC3II specifically associates with both the internal and external surfaces of the autophagosome membrane, where it plays a role in selecting cargo for degradation (Tanida et al., 2002). The synthesis and processing of LC3 is increased in response to autophagy induction, making it a key readout of autophagosome abundance present in cells (Kuma et al., 2007; Tanida et al., 2004). However, it must be noted that the appearance of LC3II represents the abundance of autophagosomes rather than a true reflection of the dynamic nature of the autophagy process. Autophagic activity can be affected by either the formation, or the degradation of selective structures; hence, the concept of “autophagic/macroautophagic flux” was coined to represent the sum total of autophagy, from the induction to autophagosome formation, to subsequent degradation thereof (Klionsky et al., 2016; Loos et al., 2014). To assess flux, the conversion of LC3I to LC3II is measured using a turnover assay involving autophagy inhibitors. Following their formation, autophagosomes undergo a maturation process that may include fusion with endosomal and lysosomal vesicles (Eskelinen, 2005). Studies show that undisturbed macroautophagic flux requires a tight cooperation between the endosomal compartments, including early and late endosomal sorting, and autophagosomes (Eskelinen, 2005). For example, before fusing with lysosomes to form autophagolysosomes, autophagosomes can also directly fuse with early and/or late endosomes to form hybrid structures called amphisomes, which then fuse with lysosomes, to form autophagolysosomes in which

cytosolic contents are degraded (Gutierrez et al., 2004; Saftig et al., 2008). Fusion of autophagosomes, or amphisomes with lysosomes is mediated by Rab7 and the lysosomal transmembrane protein LAMP2 (Filimonenko et al., 2010). Degradation products, such as amino acids, are released back into the cytoplasm to replenish cellular energy reserves, and to sustain growth during starvation conditions (Mindell, 2012). mTORC1 signalling is reactivated in response to prolonged starvation, as increased mTORC1 activity functions as a negative feedback mechanism to avoid excessive autophagy induction. Subsequently, the lysosomal pool is renewed through a process called autophagic lysosome reformation (ALR), to maintain lysosome homeostasis at the terminal stage of autophagy (Chen and Yu, 2017; Yu et al., 2010).

While starvation-induced autophagy leads to the indiscriminate engulfment and degradation of cytoplasmic material for anabolic reactions, selective autophagy accepts preferentially ubiquitinylated cargo. A number of autophagy receptors, such as scaffold protein sequestosome 1 (SQSTM1/p62) (Pankiv et al., 2007), and p62-related proteins such as Neighbor of BRCA1 gene 1 (NBR1), and Optineurin are involved in selective autophagy degradation (Birgisdottir et al., 2013). These receptor proteins share similar domain architecture containing an N-terminal Phox/Bem1p (PB1) domain which plays a critical role in mediating protein–protein interactions, a LC3-interacting region (LIR) domain for direct incorporation of cargo into autophagosomes, and a C-terminal ubiquitin binding domain (UBD) for the selective targeting of ubiquitinated proteins (Stolz et al., 2014; Zaffagnini and Martens, 2016).

1.3.4. Chaperone-mediated autophagy: the exclusive degradative machinery

In sharp contrast to the above pathway, CMA involves the selective recognition and unfolding of substrate proteins bearing a KFERQ amino acid motif by a complex of cytosolic chaperones, with heat shock cognate chaperone of 70 kDa (HSC70) being the most prominent. This substrate/chaperone complex is targeted to the lysosomal membrane for docking at the cytosolic tail of CMA-specific lysosome-associated membrane protein type-2A (LAMP2A), and then translocated across the lysosomal

membrane for subsequent degradation (Kaushik and Cuervo, 2012). The KFERQ targeting motif is found in nearly 30% of all cytosolic proteins (Dice, 1990). However, even more proteins could potentially be degraded via CMA, as proteins that do not carry the KFERQ motif can also be degraded via CMA after posttranslational modifications, e.g. phosphorylation or acetylation (Dice, 2007). Although the presence of the KFERQ motif is a requirement for all CMA substrates, validation of a protein as a CMA substrate requires more than the mere identification of the KFERQ targeting motif, as this motif has also been shown to be utilized for targeting of proteins to late endosomes for endosomal microautophagy (Sahu et al., 2011). A set of criteria (**Table 1.1**) must be met to validate that a protein is in fact a CMA substrate; but ultimately, it is recommended that the best way to confirm that a protein is a CMA substrate is to reproduce its binding and translocation across the membrane of isolated lysosomes(Arias, 2017; Kaushik and Cuervo, 2018).

Protein degradation via CMA is characterized by four distinct stages (**Fig. 1.10**): (1) substrate proteins bearing the KFERQ motif are recognized by HSC70, and translocated to the lysosomal surface; (2) the HSC70-substrate complex binds to the CMA specific substrate receptor, LAMP2A, leading to its multimerization; (3) the substrate protein unfolds and is translocated across the lysosomal membrane aided by a luminal form of HSC70 (lys-HSC70); and (4) degradation of substrate proteins by lysosomal hydrolases (Kaushik and Cuervo, 2018). Importantly, CMA is maximally activated in response to nutritional stress, oxidative stress and hypoxia, while its activity has been shown to decline with age (Bejarano and Cuervo, 2010).

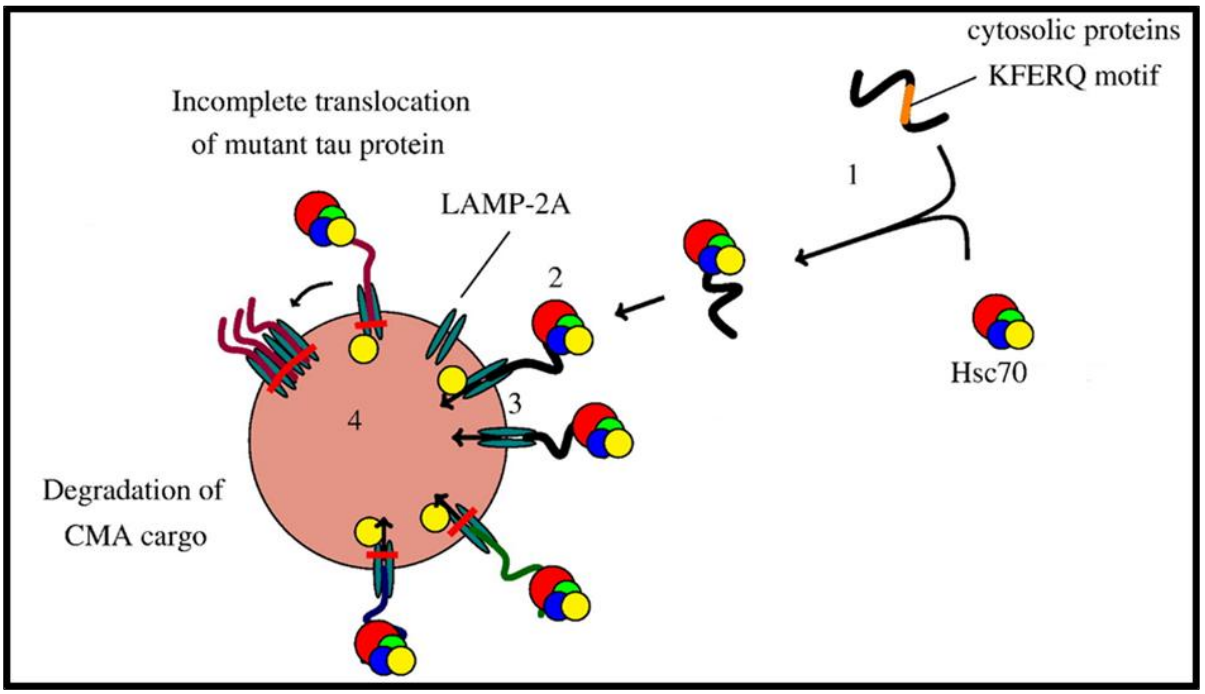

Figure 1.10: Stepwise characterisation of protein degradation through the chaperone-mediated autophagy (CMA) pathway. The sequential steps involved in the preferential degradation of substrate proteins via CMA are as follows: **(1)** recognition of substrate proteins by HSC70; **(2)** binding of the substrate–chaperone complex to LAMP2A; **(3)** unfolding of the substrate-chaperone complex; **(4)** LAMP2A multimerization resulting in substrate translocation across the lysosomal membrane for subsequent degradation. With disease progression, LAMP2A levels are diminished at the lysosomal membrane, and increasing levels of selective mutated proteins, such as mutant tau protein in AD, inhibit LAMP2A receptor function and thereby impair CMA activity. Abbreviations: CMA, chaperone-mediated autophagy; HSC70/Hsc70, heat shock cognate protein of 70 kDa; LAMP2A, lysosome-associated membrane protein type 2A [adapted from (Ntsapi and Loos, 2016)].

Table 1.1. Prerequisite criteria for a CMA substrate.

Requirements	Validation assays	References
KFERQ motif bearing proteins.	Sequence analysis.	(Dice, 1990)
CMA-targeting motif that is accessible for chaperone binding.	A decrease in substrate levels upon LAMP2A overexpression.	(Kaushik and Cuervo, 2012)
Association with CMA-active lysosomes (positive for HSC70 and LAMP2A).	Co-immunofluorescence substrate/lysosomal markers.	(Terlecky and Dice, 1993)
Long half-life (> 10 hrs to several days).	Metabolic labelling and immunoprecipitation.	(Cuervo et al., 2004)
Substrate protein must increase with CMA blockage and decrease with CMA activation.	Metabolic immunoprecipitation.	(Cuervo et al., 1995a)
Must be compatible for binding with cytosolic HSC70.	Co-immunoprecipitation using cytosol fractions.	(Cuervo et al., 1998)
Interaction with LAMP2A through its cytosolic tail.	Co-immunoprecipitation using isolated lysosome fractions.	(Cuervo et al., 2004)
ATP- and HSC70-dependent translocation into isolated lysosomes.	*In vitro* binding and uptake by immunoblotting. Degradation by intact lysosomes	(Cuervo et al., 1995a)

1.3.4.1. CMA regulation

Pioneering studies, mostly through the work of the laboratories of Erwin Knecht, Fred Dice and, more recently, Ana Maria Cuervo led to the discovery of the CMA pathway, as well as the elucidation of the molecular mechanisms underlying this process. Although multiple factors may regulate the assembly and disassembly of the HSC70-substrate complex, the rate of CMA depends largely on the levels of LAMP2A at the lysosomal membrane (Arias, 2017; Kaushik and Cuervo, 2018). Although the signalling pathways which regulate starvation-induced CMA activation have not been fully clarified, recent findings have revealed a putative CMA regulatory axis comprised of the Pleckstrin homology (PH) domain and leucine-rich repeat protein phosphatase

1 (PHLPP1), mTORC2 and their common downstream target Akt (mTORC2/PHLPP1/Akt) (Arias et al., 2015). The mTORC2/PHLPP1/Akt axis has been shown to modulate basal CMA activity in response to starvation, or during nutrient limitation. Using isolated lysosomes *in vitro*, Arias and colleagues observed that signalling through mTORC2 under basal conditions was relatively lower than constitutive CMA activity in most cells. The cause of this repressed CMA activity was associated with the phosphorylation of lysosome associated Akt by mTORC2. This kinase transiently repressed CMA activation by negatively regulating the assembly of LAMP2A into the CMA translocation complex (Arias et al., 2015). However, following enhanced CMA activity in response to starvation-conditions, the transient inhibition by mTORC2/Akt was released, and phosphatase PHLPP1 (that dephosphorylates and inactivates Akt) and the GTPase Rac1 (that stabilizes PHLPP1 at the lysosomal membrane) was recruited to CMA-active lysosomes where it altered the kinetics of assembly and disassembly of the CMA translocation complex (Arias et al., 2015).

Microautophagy is the least characterized autophagic pathway, involving the engulfment of cytosolic material through the formation of multivesicular bodies (MVBs) which are either degraded in late endosomes, or upon their fusion with lysosomes (Mukherjee et al., 2016).

Autophagy forms the primary focus of this review discussion, given that this pathway is distinctively associated with Aβ toxicity, and autophagic dysfunction has been shown to be extensively impaired during AD progression (Boland et al., 2008; Nixon et al., 2005). Moreover, given the association of autophagy as part of a compensatory cell survival response with CMA (Kaushik et al., 2008; Massey et al., 2006a), the role of CMA will also be shortly discussed where appropriate. Notably, autophagy is henceforth referred to as macroautophagy, to better distinguish between the two autophagic pathways.

1.4. Aging: insufficient proteostasis, or dysfunctional proteolytic function?

1.4.1. Macroautophagy declines with age

Advancing age is a major risk factor for AD, and macroautophagy is thought to dictate normal and pathological aging through its intricate regulation of toxic protein accumulation (Rubinsztein et al., 2011). Age is a cumulative process characterized by the accumulation of detrimental molecular, cellular and functional changes in various organisms (Rubinsztein et al., 2011). Age is associated with a gradual deterioration in cellular fitness and viability which is thought to begin when the rate of cell damage exceeds the rate of continual repair and protein turnover (Kaushik and Cuervo, 2015). Dysfunction of macroautophagy has been shown to increase with aging (Rubinsztein et al., 2011), contributing both directly and indirectly to cellular damage, through the accumulation of toxic protein aggregates as seem in neurodegenerative diseases such as AD, Parkinson's disease (PD), and Huntington's disease (HD), thus compounding the overall functional decline associated with aging. These diseases are characterized by the formation, and deleterious aggregation of selective protein deposits which are composed of ubiquitin conjugates, suggesting a failure in the principal protein degradation machinery (Nixon, 2013). Constitutive macroautophagy activity is essential for neuronal homeostasis; thus, malfunction in the quality control function of this process results in the cytotoxic build-up of defective proteins and organelles (Caballero and Coto-Montes, 2012).

The notion that functional macroautophagy increases longevity is well illustrated by experiments in which the induction of macroautophagy by either pharmacological methods, such as the administration of rapamycin (which is the best characterized pharmacological inducer of macroautophagy), or CR (which is best characterized physiological inducer of macroautophagy), has been found to extend the lifespan of the nematode *Caenorhabditis elegans* (*C. elegans*) only when the autophagic machinery was intact (Jia and Levine, 2007; Mariño et al., 2014). Indeed, macroautophagy mediated protein clearance becomes increasingly impaired with age (Martinez-Vicente et al., 2005; Ward, 2002), as evidenced by a decrease in

autophagosome formation with age (Taneike et al., 2010; Terman, 1995). Moreover, macroautophagy has been found to be transcriptionally down-regulated during normal aging in the human brain (Lipinski et al., 2010). Declining autophagic function with age has been shown to result from the following factors: (1) impaired autophagosome-lysosome fusion, (2) variable autophagic response to insulin and glucagon levels; and (3) insufficient turnover of damaged mitochondria (Donati, 2006; Donati et al., 2013). Using liver from aging rodents, impaired lysosomal hydrolase activity was revealed to be the cause of impaired autophagosome-lysosome fusion, and reduced AV clearance (Vittorini et al., 1999). This defect was attributed to a change in lysosomal pH, and the accumulation of lipofuscin (an age-associated pigment that accumulates in the lysosomal compartment of post-mitotic cells) (Brunk and Terman, 2002). The first experimental study examining the role of ATG protein in lifespan regulation was performed using *C. elegans* (Meléndez et al., 2003), where inhibition of Tor kinase (whose activity inhibits macroautophagy) was found to double the lifespan of this nematode, thus supporting the notion that macroautophagy dysfunction may induce premature aging (Vellai, 2009; Vellai et al., 2003). Knockdown of Beclin1 by RNA interference (RNAi) has been shown to shorten the lifespan of wildtype nematodes (Meléndez et al., 2003). Results in aged *Drosophila melanogaster* (*D. melanogaste*r) brains demonstrate that enhanced ATG8 expression in the nervous system extends the average adult lifespan by 56%, promotes resistance to oxidative stress, and prevents the accumulation of ubiquitinated proteins in the brain (Simonsen et al., 2008; Vellai, 2009). These findings indicate that genetic or age-dependent suppression of macroautophagy is closely associated with the increased manifestation of cellular damage and reduced lifespan, while enhancing macroautophagic activity has been shown to reverse these effects, promote longevity, and is confer protection in various animal models of neurodegeneration (Hara et al., 2006; Ravikumar et al., 2004). Therefore, diminishing macroautophagic activity with age may contribute to the age-dependent development of chronic neurodegenerative diseases, suggesting that upregulation of the macroautophagy pathway may be beneficial in maintaining neuronal function with age.

1.4.2. CMA declines with age

A decrease in the lysosomal levels of LAMP2A has been shown to be the primary cause of diminishing CMA activity with age (Cuervo and Dice, 2000a, 2000b). Although the synthesis and lysosomal targeting of LAMP2A has been found to remain consistent during middle age, at advanced age, LAMP2A levels have been found to be drastically reduced (Cuervo and Dice, 2000b). Consequently, the binding and translocation of CMA substrates into the lysosome is progressively compromised with age (Bandyopadhyay and Cuervo, 2008). Indeed, the stability and expression of LAMP2A at the lysosomal membrane has been shown to be significantly reduced in aged rats, compared to their younger counterparts (Kiffin et al., 2007). Compelling evidence of the detrimental role of reduced LAMP2A levels with age was demonstrated using aged transgenic mouse models in which CMA function was preserved by exogenously expressing an extra copy of LAMP2A in the liver (Zhang and Cuervo, 2008). The restoration of CMA activity resulted in improved cellular homeostasis, enhanced stress resistance, and led to an overall improvement in liver function comparable to that observed in younger mouse models (Zhang and Cuervo, 2008). Although further studies are required to elucidate the mechanisms underlying these altered LAMP2A dynamics with age, ongoing studies support the notion that primary changes in the lipid composition of the lysosomal membrane with age may contribute to the LAMP2A alterations (Koga and Cuervo, 2011).

1.5. Macroautophagy, CMA and AD pathogenesis

1.5.1. Autophagosome/lysosomal dysfunction in AD

Although extracellular Aβ plaques and intraneuronal NFTs are the defining hallmarks of AD neuropathology, a growing body of literature suggests that localized deficits in the macroautophagy pathway are likely to precede the formation of these pathological features (Nixon and Yang, 2011; Zare-shahabadi et al., 2015). The extensive involvement of macroautophagy in AD pathology was first demonstrated in an electron microscopy-based study of the AD brain, where prominent accumulation of immature

AVs was observed in dystrophic neurites, suggesting that the transport of these AVs and their fusion with lysosomes may be impaired (Nixon et al., 2005). In a separate study, Yu et al. (2004) revealed that purified AVs found in the AD brain were a major reservoir of intracellular Aβ production, and other AD-associated proteins including full-length APP, sAPPβ, and the γ-secretase complex subunits presenilin 1 (PS1) and nicastrin, suggesting that AVs may serve as Aβ production sites. Lysosomal intracellular aspartyl proteases, cathepsin D and E, have been found to influence Aβ peptide generation within the macroautophagy machinery as these proteases exhibit both β- and γ-secretase-like activity (Ingegni et al., 2003; Mo et al., 2014). Accordingly, macroautophagy has been shown to facilitate the degradation of APP, and Aβ (Tian et al., 2014b; Zhou et al., 2011a), whereas inhibition of cathepsin activity has been shown to result in a rapid and pronounced build-up of these proteins (Bahr et al., 1994; Butler et al., 2011). The deletion of cathepsin B, a lysosomal cysteine protease that primarily degrades the aggregation-prone $A\beta_{42}$ species, has been shown to result in increased $A\beta_{42}$ levels and robust Aβ plaque deposition in an APP mouse model (Mueller-Steiner et al., 2006). The underlying mechanism of Aβ accumulation and neuronal cell death in AD is thought to, at least in part, result from a combination of increased autophagic induction, impaired clearance of Aβ-containing AVs, and defective lysosomal proteolysis (Boland et al., 2008; Lee et al., 2010, 2011a). The role of macroautophagy in the secretion of Aβ is further supported by recent findings in which the measurement of extracellular Aβ in macroautophagy-deficient mice revealed that the Aβ secretion was reduced by 90%, while restoration of macroautophagy enhanced Aβ secretion to control conditions (Nilsson and Saido, 2014). In separate work, Nilsson et al. (2015) revealed that the secretion of Aβ was significantly reduced in ATG7 knockdown mice, and this reduction was accompanied by the profound intracellular accumulation of Aβ. The macroautophagy inducer trehalose (a natural disaccharide that block glucose transporters), was shown to rescue the AD-like phenotype in APP/PS1 transgenic mice. In this sense, trehalose treatment significantly improved cognitive function; and more notably, Aβ deposits were significantly reduced in the hippocampus region following macroautophagy pathway induction (Rami, 2009). This suggests that insufficient macroautophagic activity can be reversed through pharmacological stimulation to promote Aβ degradation, translating to cell protection. Indeed, several studies have shown that rapamycin reduces the

accumulation of Aβ fibrillar aggregates approximately 40 to 50% in AD mouse models (Yu et al., 2005). Using an AD mouse model overexpressing Aβ, Pickford et al. (2008) revealed that BECN1 haploinsufficiency reduced macroautophagic activity and exacerbated AD pathology, as evidenced by increased Aβ deposition and neurodegeneration. Morphological evidence from Yu et al. (2004) demonstrates that APP and Aβ peptide are colocalized with LC3II-positive autophagosomes, showing greater colocalization of Aβ with AVs. Intervention strategies targeting macroautophagy induction have been shown to enhance the clearance of Aβ and APP-derived fragments *in vitro* and *in vivo* models of AD (Caccamo et al., 2010, 2011; Majumder et al., 2011). The degradation of extracellular Aβ through microglia has been shown to involve at the first step endocytosis; once Aβ peptide is in the cytosol, it is then recognized by LC3II via optineurin, which has been shown to promote Aβ degradation through the autophagic pathway (Du et al., 2013). These results provide compelling evidence for the efficacy of macroautophagy induction in AD model systems. On the other hand, Aβ has also been shown to regulate macroautophagic activity. For example, $A\beta_{40}$ has been found to induce macroautophagy in endothelial cells and impair neurovascular regeneration (Hayashi et al., 2009). Taken together, it is evident that enhancing autophagic degradation ameliorates Aβ neurotoxicity and, in some cases, even prevents cytotoxicity and cognitive decline *in vivo* (Yang et al., 2011a). To date, rapamycin remains the most widely used pharmaceutical inducer of macroautophagy (Miller et al., 2014; Wu et al., 2013a). However, the side effects of rapamycin make it unsuitable for clinical use due to the side-effects associated with long-term usage. Primary amongst these are the immune suppressive effects, and metabolic defects including hyperglycaemia, hyperlipidaemia, insulin resistance and increased incidence of type 2 diabetes (Fischer et al., 2015; Salmon, 2015). In healthy rodents, dose-dependent rapamycin treatment has been shown to impair glucose homeostasis (Miller et al., 2014). Hence, physiological induction of macroautophagy may represent a more practical strategy for the enhancement of Aβ degradation.

1.5.2. The putative role of CMA in AD

Similar to macroautophagy, CMA has been found to play an important role in both the formation of tau protein NFT formation and, to a lesser extent, Aβ aggregate formation (Koga and Cuervo, 2011). The role of CMA in AD pathogenesis, although poorly understood, is thought to modulate the extent of NFT formation resulting from the aggregation of mutant tau tangles (Wang et al., 2009). Tau protein contains two CMA-targeting motifs, thus making it amiable for efficient degradation via the CMA pathway (Wang et al., 2009), or as recently shown, endosomal microautophagy (Tekirdag and Cuervo, 2018). In contrast, mutant tau protein has been shown to be partially internalized once bound to LAMP2A, and while the portion of the protein that enters the lysosomal lumen is enzymatically cleaved, the portion at the lysosomal membrane has been shown to form smaller tau fragments that oligomerize directly at the lysosomal surface, thereby disrupting the integrity of the lysosomal membrane and blocking LAMP2A receptor (**Fig. 1.10**). Indeed, studies using an inducible neuronal tauopathy model have shown that mutant tau protein fragmentation is initiated in the cytosol and is completed at the lysosomal surface upon binding to LAMP2A (Wang et al., 2009). Although the mechanism of tau mediated CMA blockage is not fully understood, inefficient translocation of mutant tau fragments across the lysosomal membrane has been shown to promote the formation of tau oligomers at the lysosomal surface, and these oligomers are then thought to act as precursors of aggregation (Wang et al., 2009), thereby blocking CMA activity. In the case of APP, a direct connection with CMA is not easily inferred, as membrane proteins have generally not been shown to be amenable to CMA degradation (Koga and Cuervo, 2011). However, the cytoplasmic tail of APP, has recently been discovered to bear a CMA-targeting motif which is recognized by HSC70 (Park et al., 2016). It is thus conceivable that CMA, or endosomal microautophagy, could aid in APP clearance under basal conditions, and that alteration of either of these pathways may impair APP clearance and contribute to Aβ toxicity. Interestingly, deletion of APP's KFERQ motif has not been found to abolish its interaction with HSC70 (Park et al., 2016), suggesting that the KFERQ motif may not be crucial for CMA degradation in this context. However, further studies are warranted to better unravel the putative role of CMA in APP processing.

Given the increasing evidence in support of the essential role of macroautophagy in the generation, secretion and clearance of Aβ, modulators of macroautophagy offer great potential for the treatment of AD. To this end, a number of macroautophagy modulators have been demonstrated to have positive effects in various AD animal models, but adverse effects in patients (Ross et al., 2015; Salmon, 2015). This scenario makes it clear that non-pharmaceutical interventions, such as CR, that can robustly modulate macroautophagy, positively impact lifespan in various organisms, and consistently favour neuronal protection in neurodegeneration, may hold therapeutic promise.

1.6. Doubling up: CR impacts longevity through macroautophagy and CMA

1.6.1. CR and macroautophagy

CR, also called the “longevity diet” refers to the restriction of energy (food) intake, beginning early or in mid-life and sustained over the life span, without causing malnutrition (Bales and Kraus, 2013). CR is to date been shown to be the most robust physiological inducer of the macroautophagy pathway, to confer neuroprotection with increasing age in diverse species, ranging from yeast to mammals (Fontana et al., 2010). Increased generation of ROS has been postulated to be one of the major hallmarks of increasing age, and CR has been found to reduce the levels of oxidative stress in mammals (Sohal and Forster, 2014). Similarly, rodents subjected to CR show a decreased incidence of age-associated mitochondrial dysfunction, and oxidative damage resulting from increased oxidative stress (Forster et al., 2000; Sohal and Weindruch, 1996). The compelling role for CR in delaying the onset of age-associated pathologies appears to have emerged in the early 20th century (Osborne et al., 1917), when McCay and colleagues published the first manuscript on the beneficial effects of CR on life extension in rats (McCay et al., 1989). Since then, CR-induced life extension has been documented in species from the following kingdoms: Animalia (mammals), Protista (single-celled eukaryotes), and fungi (fungus and related organisms) (Lee and Longo, 2016; Li et al., 2017a). CR enhances macroautophagic activity to promote the rapid turnover of macromolecules and

organelles in aging mice kidneys. This enhanced macroautophagic activity under CR conditions suggests a protective role for macroautophagy pathway induction with age. In the kingdom of Animalia, the anti-aging benefits of CR have been extensively studied in mice, hamsters, dogs (Masoro, 2006, 2009); and more recently in long-lived non-human primates, the rhesus monkey (Colman et al., 2014; Mattison et al., 2017). The rhesus monkey serves as an ideal model for human physiology as it shares approximately 93% sequence identity with the human genome (Gradnigo et al., 2016), as well as numerous aspects related to endocrinology, anatomy, neurology, immunology, and behaviour (Zimin et al., 2014). Accordingly, a plethora of data supporting the role of CR in improving health has been generated using the rhesus monkey as an experimental model over the past 20 years. The first report on increased lifespan emanated from work by Bodkin and colleagues where a 2.6-fold increased risk of death was reported in control animals compared with animals subjected to CR (Bodkin et al., 2003). In agreement, work by Colman and colleagues reported a 2.9-fold increased risk of disease and 3.0-fold increased risk death for control animals compared with CR animals (Colman et al., 2009). In a more recent study, these researchers further cemented the role of CR in longevity, reporting a significant improvement in age-related pathology and overall survival in rhesus monkeys on a long-term (~30%) CR diet since young adulthood (Colman et al., 2014). If, and to what extent the health benefits of CR can be translated to human ageing remains to be determined, although there is evidence to suggest that CR provides at least some benefits to humans consistent with delayed aging (Lefevre et al., 2009). Although compelling data from *in vivo* animal models clearly support the view that CR dietary regimes decrease the incidence of various diseases, including AD and PD (Lee and Longo, 2016; Mattison et al., 2017). The absence of adequate information on the effects of CR in humans reflects the difficulties involved in conducting long-term CR studies, including ethical and methodologic considerations. However, there are a limited number of ongoing clinical trials funded by the National Institute of Aging, to bring about insight into the question of whether the observed health benefits of CR in nonhuman primates can be translated to humans. One of these trials, entitled the Comprehensive Assessment of Long-Term Effects of Reducing Intake of Energy (CALERIE), is evaluating the effects of a 2-year long CR regimen (25% less calories than controls) in healthy, non-obese individuals. Preliminary data of this study

indicates that similar metabolic and endocrine changes previously observed in rodents and rhesus monkeys subjected to CR, are also evident in humans (Heilbronn et al., 2006; Redman and Ravussin, 2009). The biological outcomes of CR include, but are not be limited to, the reduction and clearance of damaged protein, and the decrease in chronic inflammation associated with increased circulating free fatty acids, cytokines, and chemokines (Balasubramanian et al., 2017; Li et al., 2017a). A more recent report stemming from a 2-year randomized controlled trial in non-obese humans subjected to CR, provided the first evidence that sustained CR is both feasible and without adverse effects on quality of life (Ravussin et al., 2015). The feasibility, safety, and effects of sustained CR can be better elucidated from epidemiological and cross-sectional observations in longer-lived humans, i.e. centenarians, and individuals who self-impose CR. Perhaps the most compelling epidemiological support in favour of the anti-aging effects of CR in humans is represented by the population of Okinawa (Japan) where the mean number of centenarians is generally 4 to 5 times that of most industrialized countries (Suzuki et al., 2001; Willcox et al., 2007, 2009). Here, it was revealed that these individuals had undergone a mild form of prolonged CR (~20% CR) for about half their adult lives (Willcox et al., 2009). The composition of a traditional Okinawan diet was shown to be similar to a Mediterranean diet, which is known to be beneficial to human health with age (Rosenbaum et al., 2010; Willcox et al., 2009). Indeed, elderly Okinawans have been found to have the lowest mortality emanating from age-related diseases (Rosenbaum et al., 2010; Willcox et al., 2009). Although these reports have provided valuable insight regarding the translatability CR-induced benefits to humans, studies of longer duration are required to better understand the causative factors in age-related disease susceptibility, and to quantify the impact of CR in attenuating the deleterious effects associated with advanced age in humans.

1.6.2. CR and CMA

Activation of CMA in response to CR is associated with higher levels HSC70 and LAMP2A at the lysosomal membrane (Agarraberes et al., 1997; Cuervo et al., 1995a). Studies have shown a drastic increase in the percentage of HSC70-containing

lysosomes from 40% under basal conditions, to 80% under conditions of prolonged starvation or mild oxidative stress in liver (Cuervo et al., 1995a, 1997). In rat liver, CMA activity has been found to plateau after 36 hrs of CR, remaining active for 72 hrs (Cuervo et al., 1995a). Although basal level of CMA activity can be detected in most cell types, maximal activation of this pathway has been demonstrated during prolonged starvation *in vivo* (Cuervo et al., 1995), or serum removal *in vitro* (Dice, 1987). While the initial cellular response to starvation has been shown to be the activation of macroautophagy, CMA is induced much later (Cuervo et al., 1995a). However, for reasons yet unknown, the time course activation of CMA in response to starvation is tissue and cell type specific (Wing et al., 1991). The effects CR on lifespan have been extensively documented by Nikolai et al. (2015), but the key effectors of CR-activated pathways remain largely unknown. Further research is warranted in this regard.

1.6.3. Two pathways are better than one

1.6.3.1. The compensatory response to prolonged CR or starvation conditions

The macroautophagic pathway is extensively interconnected through various crosstalk mechanisms which facilitate controlled and well-balanced cellular responses to specific stress signals. For example, crosstalk exists between macroautophagy and apoptosis (Delgado et al., 2014), macroautophagy and the UPS (Zhan et al., 2016), and macroautophagy and CMA (Kaushik et al., 2008; Massey et al., 2006b). The focus of this section is on the latter, as there is evidence for a clearly dynamic and temporal balance between the two processes (Wu et al., 2015a). Under physiological conditions, macroautophagy and CMA both occur at basal levels, but can be maximally induced when cells are subjected to starvation conditions (Boya et al., 2013). Under these conditions, macroautophagy has been found to be rapidly upregulated as early as 30 minutes following nutrient deprivation and reaches a plateau of maximal activation around 4 to 6 hrs post-starvation (Backer and Dice, 1986; Massey et al., 2006b). However, macroautophagy is progressively downregulated thereafter, and CMA is consequently upregulated in response to prolonged starvation

following 10 hrs onwards (Arias et al., 2015). It has been proposed that differences in the levels and time frames of activation may be due to CMA's higher selectivity, which enables this pathway to tightly control the choice of proteins degraded (Kaushik and Cuervo, 2018). Moreover, maintaining high levels of the less selective macroautophagic pathway could quickly tip towards pathologically enhanced activity, and become detrimental to cell survival (Kiffin et al., 2004; Zhang and Cuervo, 2008). Compensatory activation of macroautophagy has been shown to confer protection in CMA-defective cells by maintaining basal levels of protein degradation (Massey et al., 2006b). Consistent with these findings, further studies by Massey et al. (2008) demonstrated that CMA inactivation, mediated through RNAi against LAMP2A, increased macroautophagy levels *in vitro*. However, macroautophagy could only partially compensate for CMA function, suggesting that the continuous activation of macroautophagy could be detrimental to cell viability (Massey et al., 2008). Therefore, there is a need to identify the conditions when this compensatory macroautophagy-CMA activation can maintain cellular viability, and for how long. Additionally, whether neuronal protection can be conferred through the compensatory activation of macroautophagy-CMA in neurodegenerative diseases remains unknown.

1.6.3.2. Compensatory macroautophagy-CMA response in neurodegeneration

Individual proteins were previously thought to follow a particular autophagic pathway for their degradation. However, it is now known that macroautophagy and CMA can simultaneously, or in a compensatory fashion dynamically contribute to protein degradation, depending on the cellular conditions and presence of specific aggregate-prone protein species (**Fig. 1.11**).

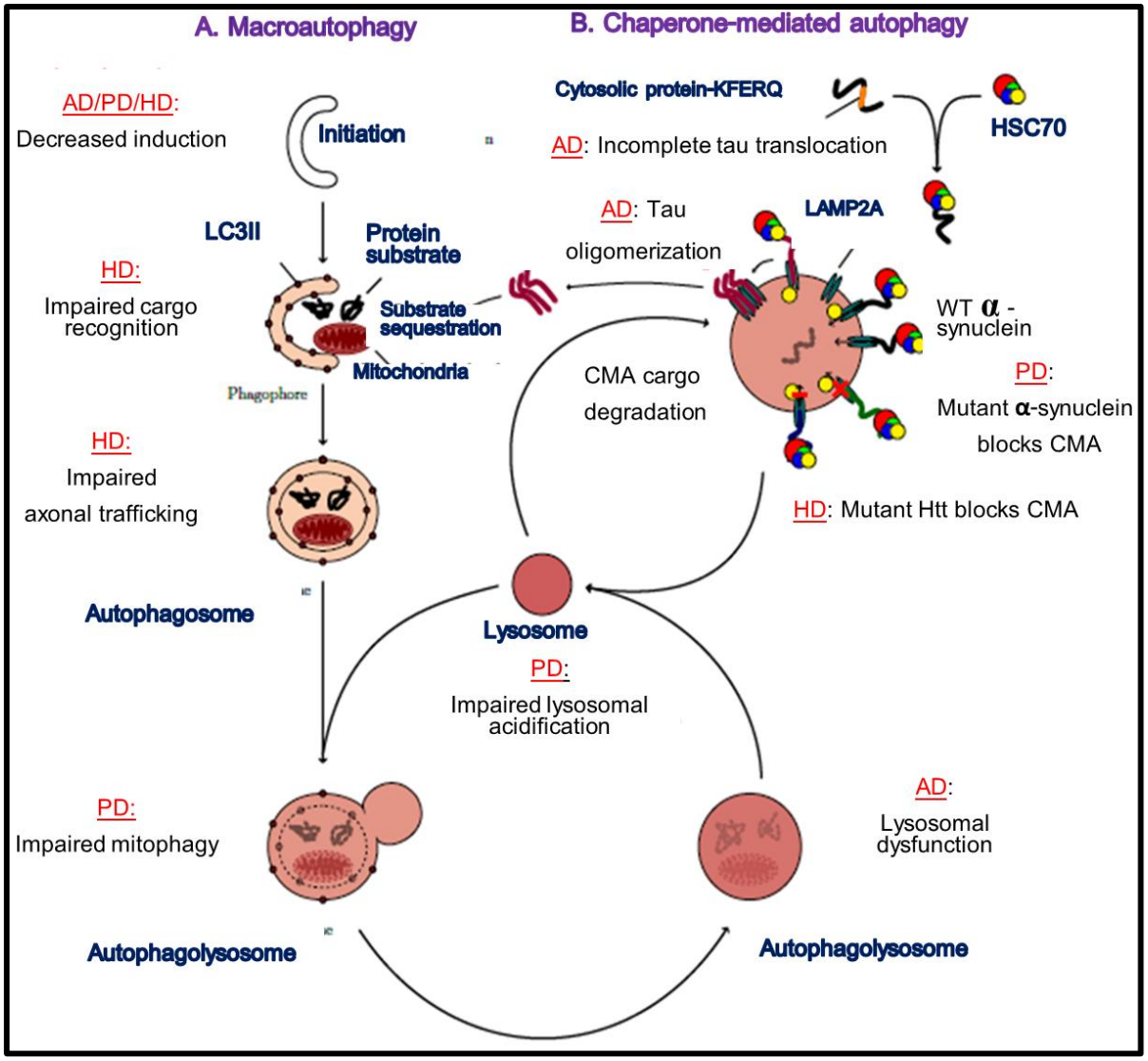

Figure 1.11: Substantial crosstalk exists between (A) macroautophagy, and (B) chaperone-mediated autophagy (CMA), with precision defect localization. This calls for the need to precisely map and quantify both macroautophagic and CMA fluxes, to correct localized impairments in either pathway, and re-establish proteostasis [adapted from (Ntsapi et al., 2016)].

This demands for a crosstalk-based assessment that is inclusive in assessing both macroautophagy and CMA fluxes. For example, in an *in vitro* model of taupathology, mutant tau protein was shown to impair CMA function by blocking the LAMP2A receptor (Wang et al., 2010). However, CMA impairment was alleviated through the compensatory upregulation of macroautophagy which attenuated the aggregation of tau fragments, thus providing compelling evidence of a functional interplay between macroautophagy and CMA in neurodegeneration (Wang et al., 2010). Using a PC12 cell model, CMA blockage by mutant α- synuclein, implicated in PD neuropathology,

was shown to be partially alleviated by macroautophagy upregulation (Cuervo et al., 2004). Similar findings were reported in cortical neurons and differentiated SHSY5Y cells, where CMA activity was found to be ameliorated by increased levels of macroautophagic activity (Xilouri et al., 2009). Further evidence for the interaction of both autophagic pathways in the degradation of wildtype α-synuclein was observed through the simultaneous inhibition of macroautophagy and CMA which resulted in α-synuclein accumulation (Vogiatzi et al., 2008; Webb et al., 2003). These results suggest that both pathways are important for the degradation of wildtype α-synuclein. Importantly, this compensatory upregulation has been found to be compromised with age (Schneider et al., 2015). Therefore, it is crucial to fully elucidate the molecular machinery that enables macroautophagy-CMA compensatory mechanisms. The relationship between macroautophagy and various neurodegenerative diseases has been extensively documented in literature (Nixon et al., 2008). Only recently; however, it became clear that defined localized defects are present in the onset of AD, PD and HD. These defects are defined as: 1) insufficient macroautophagy induction, 2) impaired lysosomal hydrolase activity, and 3) macroautophagic dysfunction related to dysregulated excessive activation (Cherra and Chu, 2008). Knowing the location of the autophagic pathway impairment in each disease is important when designing appropriate strategies to overcome the defect. This requires careful dissection of the macroautophagy and CMA pathway under physiological conditions, and their dysfunction in the context of the protein species driving various pathology.

1.7. The integration of macroautophagy signalling pathways during CR

The physiological changes induced by CR have been extensively characterized with the hope of better understanding the basis of the beneficial effects of CR. However, have not been clearly defined. This disparity in knowledge is due to, at least in part, the complexity of these mechanisms, and the fact that multiple regulatory pathways are likely activated to mediate the full range of CR benefits (Masoro, 2009). The consensus is that the beneficial effects of CR on longevity are associated with nutrient-triggered signalling cascades, including the insulin/insulin-like growth factor-1 (IGF1) signalling, and the mTORC1 pathway (Balasubramanian et al., 2017). The

convergence of CR-triggered pathways on macroautophagy has attracted increased attention, as CR is a robust inducer of this process (Bergamini and Gori, 2013). In this regard, three highly conserved nutrient and energy sensing signalling pathways are thought to converge on mTOR to regulate the lifespan of many species (Rabinowitz and White, 2010; Zoncu et al., 2011). The integral role of the Insulin-IGF1/PI3K/Akt/mTORC1 signalling pathways in CR- mediated longevity is underscored by the following lines of evidence: (1) prolonged lifespan has been described in response to the Akt deletion in yeast (Fontana et al., 2010), (2) mTORC1 inhibition results in overall health improvement in yeast, flies, worms and mice (Kaeberlein et al., 2005); and (3), genetic manipulation of *daf-2* (encoding an insulin receptor-like protein) demonstrated that reduced Insulin-IGF1 signalling could increase lifespan in invertebrate models (Anisimov and Bartke, 2013). Briefly, under nutrient rich conditions, such as excess amino acids, Insulin/IGF1 activates the PI3K/Akt signalling pathway, Akt then phosphorylates the tuberous sclerosis complex (TSC) and thereby inhibits TSCs GTPase activity. TSC in turn activates Rheb and mTORC1, thereby inhibiting macroautophagy induction (Inoki et al., 2002, 2003). Inhibition of Insulin-IGF1/PI3K/Akt/mTORC1 pathway during CR plays a central role in the induction of macroautophagy, which has been shown to lead to lifespan extension in various organisms (Feng, 2010). Apart from decreased signalling through the Insulin-IGF1/PI3K/Akt/mTORC1 pathway, the increased signalling through the AMPK/SIRT1-FOXO (1/3) pathway has also been shown to be an integral effector of CRs beneficial effects (**Fig 1.12**). Sirtuin 1 (SIRT1, silent information regulator 2 Sir2 homolog), and AMPK are well established sensors of cellular energy status (Gomes et al., 2013). Notably, due to their cross-activation, AMPK and SIRT1 are targets of common activators and produce overlapping outcomes, one of which is the stimulation of peroxisome proliferator- activated receptor γ co-activator α (PGC1 α), which regulates mitochondrial biogenesis and energy expenditure (Brenmoehl and Hoeflich, 2013). SIRT1 is an evolutionally conserved nicotine amide (NAD^+)-dependent deacetylase whose transgenic overexpression has been found to prolong lifespan in *C. elegans*, and *D. melanogaster* (Rogina and Helfand, 2004). SIRT1 can be activated by CR, through fluctuations in the NAD^+/NADH concentration, or through activators such as CR mimetic resveratrol (Nisoli et al., 2005). When nutrients, especially glucose, decrease because of CR, NAD^+ accumulates and SIRT1 is activated and

directly induces macroautophagy, or indirectly activates macroautophagy through deacetylation of Forkhead box class O (FoxO) family members 1 and 3, which in turn coordinate the induction of macroautophagy (López-Lluch and Navas, 2016). SIRT1 deacetylates FOXO1 and FOXO3, which are required for the transcriptional activation of genes that are involved in autophagosome formation, such as PIK3C3, ATG12, ATG4L, BECLIN1, and ULK1 and through direct protein-protein interaction with Atg7 (Bánréti et al., 2013; Eisenberg et al., 2009). This interplay between protein acetylation and deacetylation appears to underlie the role of SIRT1 in CR.

AMPK is also integral to CR's longevity benefits, as this kinase is activated in response to decreased energy or glucose levels, which are consequences of CR (Kahn et al., 2005). Under CR conditions, AMPK initiates the signalling cascade that stimulates the processes to generate ATP through mTORC1 inhibition and subsequent macroautophagy induction through phosphorylation of the ULK1 complex as previously described (Alers et al., 2012; Kim et al., 2011). Evidence in support of this role has been extensively provided using *C. elegans*, where nematodes overexpressing AMPK (*aak-2*) were found to live longer compared to controls (Greer et al., 2007; Schulz et al., 2007). Additionally, glucose restriction increased *aak-2* activity, further prolonging lifespan, thus suggesting that the benefits of CR were dependent on *aak-2* in the nematode model (Schulz et al., 2007). Based on these and other findings, it is plausible to conclude that macroautophagy is universally required for the benefits of CR.

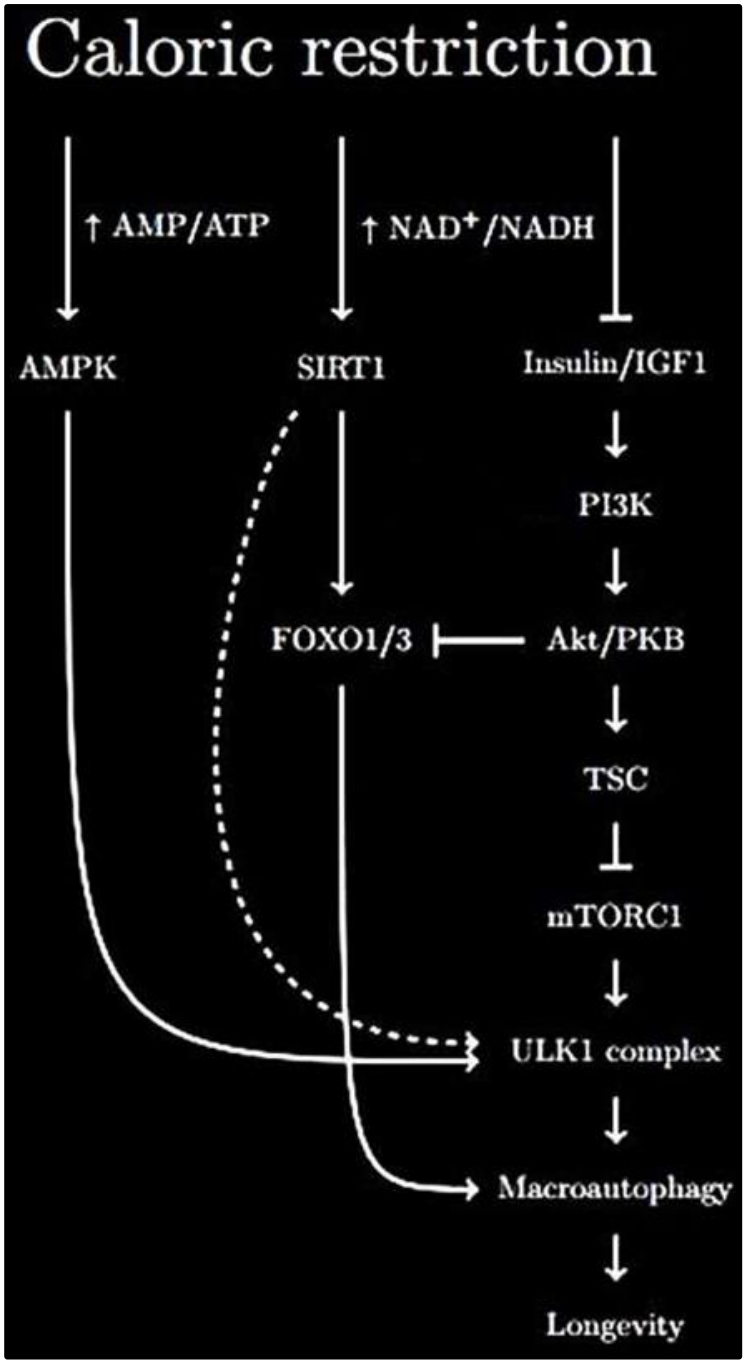

Figure 1.12: Potential role of macroautophagy in caloric restriction (CR)-mediated longevity. CR causes reduced levels of insulin, IGF and amino acids, and increased levels of NAD^+ and AMP as a result of diminished energy production and decreased nutrient availability. These changes result in the inhibition of the insulin-IGF1/PI3K/AKT/mTOR pathway, and activation of the AMPK/SIRT1-FOXO (1/3) pathway. As a consequence of diminished mTORC1 activity, protein translation, and overall cell growth would be limited and the dynamics of decreased mTORC1 would favour increased macroautophagy to sustain cell survival translating in neuronal protection, and ultimately, longevity. TSC, Tuberous sclerosis complex [adapted from (Schultz and Sinclair, 2016)].

1.7.1. CR mimetics: targeting macroautophagy induction

Studies of CR in rhesus monkeys have reported beneficial effects of CR on health and aging. Specifically, prolonged CR (approximately 30% CR) since young adulthood has been found to extend lifespan in rhesus monkeys, which exhibited overall improved health; lower incidence of neurodegeneration, cardiovascular disease, type 2 diabetes mellitus, and cancer (Colman et al., 2012, 2014). However, recent findings have demonstrated that although some of the beneficial effects of CR persist for 2 weeks after subsequent *ad libitum* refeeding in mice, the entirety of CR-mediated effects is reversed within 6 months of re-feeding (Giller et al., 2013). This finding suggests that long term CR is necessary to continuously maintain its beneficial effects, and that the magnitude of maximal lifespan extension is determined by the degree, duration and age at which this regime is initiated (Rosenbaum et al., 2010). An alternative approach to long-term CR is intermittent fasting (IF) (Goodrick et al., 1990), a dietary regimen that alternates between 24 hrs *ad libitum* food consumption, with 24 hrs of total or partial CR (Varady and Hellerstein, 2007). Indeed, studies have shown that IF can increase lifespan to an extent similar to that of CR, even when there is little or no overall decrease in calorie intake (Bhutani et al., 2010). Although the health and longevity benefits of a CR regimen are numerous, it is not without its potential adverse effects (Redman and Ravussin, 2011). These include lowered body temperature (Soare et al., 2011), slowed wound healing (Hunt et al., 2012), a reduction in resting energy expenditure (Blanc et al., 2003), hypotension (Cava and Fontana, 2013), and indications of osteoporosis in post-menopausal women (Michaëlsson et al., 1996). Nevertheless, emerging evidence indicates that dietary therapies, in which the nutritional composition of the restricted diet is carefully monitored, can be safely executed in children and adults, and are effective in the attenuation of a variety of neurodegenerative diseases (Cervenka et al., 2013). Moreover, there is considerable evidence suggesting the role of CR in ‘therapeutic fasting’ to improve general health, manage a broad range of chronic diseases, and delay the onset of age associated pathologies (Balasubramanian et al., 2017; Lee and Longo, 2016). For these reasons, increasing interest is now being shown to determine the efficacy of natural or pharmacological alternatives to classical CR, such as the use of CR mimetics (CRM). These are compounds that mimic the biochemical and functional effects of CR. These

compounds mimic the biological effects of a rigorous CR regimen by reproducing CR-like beneficial effects on mortality and age-related ailments through the activation of selective stress responsive pathways, while circumventing the need to drastically reduce food and calorie intake (Mariño et al., 2014; Roth and Ingram, 2015). Such compounds, including resveratrol SIRT1 supplementation, 2-deoxyglucose, and metformin (Lee and Min, 2013; Selman, 2014), may be of more practical use in humans as the implementation of long-term CR regimes may be difficult for most to maintain. It is expected that IF regimens or the use of CRM can trigger similar biological pathways as CR, and thereby impact the clearance of aggregate toxic protein species in neurodegenerative diseases such as AD, PD and HD.

1.8. Treatment strategies

To date, only four compounds have been approved by the FDA for the symptomatic treatment of AD (**Table 1.2**). While these compounds have been shown to improve the disease symptoms and may positively impact on the rate of cognitive decline, they do not reverse neuronal damage, or prevent cognitive decline in AD (Berk and Sabbagh, 2013). Hence, a large body of evidence supporting the ACH has led to robust efforts dedicated to the development of disease-modifying strategies that either disrupt aggregation, promote removal or prevent formation of Aβ (Gao et al., 2016; Sanabria-Castro et al., 2017). To this end, the feasibility β-secretase inhibitors has been considered to be an important therapeutic target. The β-secretase enzyme complex participates in the initial stages of the amyloidogenic pathway, and its inhibition has been shown to reduce Aβ levels, preventing the accumulation of βCTFs which contain the entire Aβ domain and serve as the final substrate for Aβ production (Citron, 2004). Indeed, several pharmaceutical inhibitors of this enzyme, such as MK- 8931 (clinical trial ID# NCT01739348), E2609 (clinical trial ID# NCT01600859), and LY2886721 (clinical trial ID# NCT01807026 and NCT01561430) have all shown efficacy in reducing Aβ production by 80–90% in the CSF in humans (Folch et al., 2016, 2017). Towards the end of 2012, Merck initiated the phase II/III studies of MK-8931 for the treatment of AD (Dobrowolska et al., 2014). The safety and efficacy of MK-8931 versus a placebo was determined in patients with mild and moderate AD, and published findings thus far indicate that this drug reduced $A\beta_{40}$ and $A\beta_{42}$ CSF levels

up to 84%, and was well tolerated by patients (Dobrowolska et al., 2014), but further clinical validation of MK-8931 efficacy is still required. One notable challenge that continues to impact several β-secretase inhibitors during clinical trials has been their propensity to induce off-target toxicity (Vassar, 2014). This is likely due to the role of β-secretase in a number of functions including myelination, synaptic plasticity, axon targeting, maintaining spine density, neurogenesis, as well as processing of non-APP substrates such as neuregulin-1 (Hu et al., 2013; Vassar, 2014). Moreover, findings suggest that the use of β-secretase inhibitors may be better suited early in disease onset, before the deposition of Aβ plaques, as inhibition of enzyme has been found to have no impact on already existing Aβ aggregates (Menting and Claassen, 2014).

Table 1.2: Current symptomatic treatments for AD.

Drug	AD stages	Target	Mechanism of action	Side effects
Donepezil	Mild to severe	Cholinesterase Inhibitor	Prevents acetylcholine breakdown in the brain	Nausea, diarrhoea, muscle cramps, fatigue, weight loss
Galantamine®	Mild to moderate	Cholinesterase Inhibitor	Prevents acetylcholine breakdown and stimulates nicotinic receptors to release more in the brain	Nausea, diarrhoea, decreased appetite
Memantine	Moderate to severe	NMDA receptor Antagonist	Blocks the toxic effects associated with excess glutamate, and regulates glutamate activation	Dizziness, headache, diarrhoea, constipation, confusion
Rivastigmine	Mild to moderate	Cholinesterase Inhibitor	Prevents acetylcholine breakdown in the brain	Nausea, diarrhoea, weight loss, decreased appetite, muscle weakness

[adapted from (Folch et al., 2017)

1.8.1. CR-induced macroautophagy and Aβ neurotoxicity

The neurotoxic accumulation of Aβ peptides and subsequent deposition into plaques has been shown to be the result of an imbalance between Aβ production and clearance. Thus, pharmaceutical targeting of Aβ production through modulation of the amyloidogenic pathway has been the overarching focus of AD research efforts for more than two decades (Li et al., 2013). However, the failure rate of these amyloidocentric agents since 2002, excluding agents currently in Phase 3, is 99.6% (Cummings and Fox, 2017). It has been suggested that use of anti-Aβ agents may be optimized by intervening earlier in the disease process before neurodegeneration begins (Aisen et al., 2013; Vellas et al., 2012). Alternatively, identifying new disease pathways more amenable to pharmacologic or physiological manipulation, may increase the likelihood of developing effective AD therapies in the future. Increasing evidence has demonstrated the neuroprotective role of macroautophagy in mediating the degradation of aggregated proteins implicated in AD pathology (Baranello et al., 2015; Folch et al., 2017). Thus, macroautophagy is thought to be a potential therapeutic target to mitigate the effects of Aβ aggregation in neurons, and alleviate neurotoxicity (Rubinsztein et al., 2015). Accordingly, targeting Aβ degradation, through enhanced macroautophagic activity, instead of targeting its production via the amyloidogenic pathway may represent a more viable disease-modifying strategy. Indeed, inhibition of macroautophagy activity through Beclin1 deletion has been shown to increase Aβ accumulation, extracellular Aβ deposition, and neurodegeneration in mice (Pickford et al., 2008). In contrast, enhanced Aβ clearance has been observed in response to resveratrol treatment, which has been shown to impact Aβ levels through macroautophagy induction *in vitro* (Marambaud et al., 2005). Importantly, studies reveal that the underlying mechanism of CRM-induced macroautophagy is mediated, at least in part, through inhibition of the insulin-IGF1/PI3K/AKT/mTOR pathway, and activation of the AMPK/SIRT1-FOXO (1/3) pathway (Heras-Sandoval et al., 2014), the same pathways previously implicated in the macroautophagy mediated longevity benefits of CR.

1.9. Methods for measuring macroautophagy and CMA activity

1.9.1. Methods for measuring macroautophagic flux

Taking the above information into account, it becomes clear that the ability to measure the macroautophagy process accurately is a critical to understand the degree of macroautophagy dysfunction in neurodegeneration. Methodologies used to quantify macroautophagy in both *in vitro* and *in vivo* experimental systems are continuously being developed given the intense medical interest in the role of macroautophagy in various diseases. Macroautophagy maintains a basal flux of substrates to lysosomes that accelerates during stress or starvation; thus, analysing static levels of autophagosome markers does not provide information on macroautophagy activity. In contrast, measuring macroautophagic flux that reveals the net amount of substrate delivered to lysosomes per unit time, provides information to what extent macroautophagy is active or inhibited (Loos et al., 2014). Recent developments focusing on molecular tools that measure macroautophagic flux are continually being updated, suggesting new ideas for linking proteostasis and the loss thereof with cell death onset (Klionsky et al., 2016; Loos et al., 2014). Updated overviews on how to more precisely measure the macroautophagic flux *in vitro* and *in vivo* have been extensively described (Klionsky et al., 2016; Yoshii and Mizushima, 2017). Here, we only shortly summarize the markers and inhibitors that are most commonly used for fundamental macroautophagic flux measurements (**Table 1.3**).

Measurement of macroautophagic flux depends on the ability to distinguish between autophagosome formation and the completion of macroautophagy through lysosome fusion and degradation. To distinguish between these processes, one can block either the synthesis or degradation of autophagosomes using common autophagic inhibitors, such as bafilomycin A1, hydroxychloroquine and NH_4Cl, all of which alter lysosomal pH, thereby blocking autophagosome-lysosome fusion, resulting in the accumulation of autophagosomes which are unable to fuse with lysosomes. Other lysosomal inhibitors include leupeptin, pepstatin A, and E64d, which can be used in combination to inhibit lysosomal proteases for longer periods of time (Yang et al., 2013). The

lipidation of LC3 can be demonstrated by western blot analysis, upon an increase in autophagosomes, the LC3 band will shift from LC3I (18kDa) to LC3II (16kDa) on SDS-PAGE (Tanida et al., 2005). Compounds such as 3-methyl adenine (3MA), Wortmannin and LY294002 can inhibit autophagosome synthesis through inhibition of the PI3KC3 complex, which activates the macroautophagy machinery (Pasquier, 2016). In this scenario, if LC3 is still lipidated by the experimental condition in the presence of these inhibitors, this would imply that autophagosome-lysosomal fusion is impaired, as inhibition of synthesis should result in a decrease in LC3II/autophagosome formation (Mizushima and Yoshimori, 2007). Caution should however be applied when using 3MA, as it has a time-dependent dual effect on macroautophagy, whereby class 1 PI3K, a kinase which triggers mTORC1 signalling, is persistently blocked while 3MA's inhibition of class III PI3K is transient (Wu et al., 2010). Levels of p62 can also be used as an indirect measure of functional macroautophagy since p62 accumulates when macroautophagy is defective. However, macroautophagy-independent regulation of p62 makes this a less robust readout of macroautophagic flux (Barth et al., 2010). In addition to measuring macroautophagic flux by western blot analysis, it is recommended to routinely perform intracellular staining for endogenous LC3. In unstressed cells, LC3 is expressed ubiquitously and is detected in a diffuse pattern in the cytoplasm of cells by immunofluorescence. As a result of elevated macroautophagy, this staining pattern changes from largely diffuse to predominantly punctate structures (Mizushima, 2004). Quantification of LC3- positive puncta is thus also used to measure increases in macroautophagy flux when experiments are performed in the presence and absence of bafilomycin A1 or hydroxychloroquine. Co-staining with other antibodies can also be performed to determine whether a putative macroautophagic substrate colocalizes with LC3-positive autophagosomes to examine the maturation state of autophagosomes in cells. For example, LC3 can be co-stained with LAMP2A to examine when autophagosomes overlap with lysosomes as a measure of functional macroautophagy. Similar approaches can be utilized to examine the fusion process of endosomes, e.g. using Rab5, or Rab7 as endosomal markers, with LC3-positive autophagosomes to characterize pathways that interact with macroautophagy.

Expression of exogenously introduced green fluorescent protein (GFP)-fused LC3 provides a convenient method for measuring macroautophagy both qualitatively and quantitatively by measuring the punctate green fluorescence structures in stably transfected cells (Loos et al., 2014; Sharifi et al., 2015), and in transgenic mice expressing GFP–LC3 under the constitutive CAG promoter to aid macroautophagy studies *in vivo* (Mizushima, 2004). In transfected cells, GFP-LC3 is expressed as punctate signals, observed by fluorescence microscopy as ring-shaped structures or dots. It should however be noted that while GFP is a stably folded protein in the cytosol and lumen of early autophagosomes, its fluorescence is quenched by the low pH inside the lysosome and LC3 degradation inside autophagolysosomes. To overcome this limitation, Kaizuka et al. (2016) recently developed a fluorescence probe, GFP-LC3-RFP-LC3ΔG, to directly demonstrate macroautophagic flux without being combined with lysosomal inhibitors. When expressed in transfected cells the probe is cleaved into a degradable/quenchable part, i.e.GFP-LC3, and stable/cytosolic part, i.e. RFP-LC3ΔG. The latter serves as an internal control and a decrease of the GFP: RFP ratio indicates the occurrence of macroautophagy flux (Kaizuka et al., 2016). The degradation of GFP-LC3 can also be used to measure the cumulative effect of basal macroautophagy. Using the transgenic GFP–LC3 mouse model, occurrence of macroautophagy can be directly monitored by creating tissue cryosections and analysing these by fluorescence microscopy. Overexpression of GFP-LC3 is found in all tissues where the level of GFP-LC3 is comparable to the endogenous LC3 expression (Alirezaei et al., 2010), with low expression thereof suggesting a rapid turnover of autophagosomes (Boland et al., 2008). However, caution should be taken when interpreting the GFP signal, because GFP-LC3 overexpression can generate protein aggregates, and cells possess autofluorescent punctate structures such as lipofuscin that are also detectable in the green spectrum. To avoid these artefacts, GFP-LC3 transgenic mice cryosections are compared with non-transgenic control littermates, with GFP fluorescence only detected using FITC filter sets (Mizushima, 2009). A list of other transgenic mice models has been described for more targeted macroautophagy flux measurement *in vivo* (Moulis and Vindis, 2017).

Aside from measuring LC3II and p62 using biochemical methods, macroautophagy can also be semi-quantitatively analysed using transmission electron microscopy (TEM). TEM facilitates the numerical quantification of the number of autophagosomes formed and measures the surface area of each autophagolysosome structure (Eskelinen and Kovács, 2011). These structures, including the sequestration of specific substrates by autophagosomes, such as mitochondria, and AVs structures, can be distinctly analysed and quantified for macroautophagic flux if cells are incubated with lysosomal inhibitors (Eskelinen et al., 2011). Upon macroautophagy induction, the number of degradative compartments increases and the quantification of the number of autophagolysosomes, lysosomes and amphisomes per cell section, provides a simple morphological readout (Klionsky et al., 2016). However, it can be difficult to distinguish between autophagolysosomes, lysosomes and amphisomes, and the consensus in such cases is to classify all these organelles together, as AVs structures (Klionsky et al., 2016). It is thus critical that more than one experimental approach is used in parallel to obtain a firm conclusion whether there is a change in macroautophagic flux. Moreover, the choice of experimental model system is key for the achievement of a successful outcome, as different mammalian cell lines and tissues exhibit varying degrees of basal macroautophagy and show distinct capacities to increase their rates of macroautophagic flux in response to various stressors (Mizushima, 2010).

Table 1.3: Current methods for monitoring macroautophagic flux.

			Expected Results			
	Assays	Methods	Basal	Induction	Inhibition of synthesis	Inhibition of degradation
Autophagosomes	Number of LC3 positive puncta	IHC	→	↑	↓	↑
	LC3II level	WB	→	↑	↓	↑
Morphology	AP/AL detection	TEM	**AP** →	**AP** ↑	**AP** ↓	**AP** ↑
			AL →	**AL** ↑	**AL** ↓	**AL** ↓
Macroautophagic flux	LC3II turnover	WB	→	↑	↓	↓
	p62 level	IHC/WB	→	↓	↑	↑
	mCherry-GFP-LC3	IHC/FM	**Red** →	**Red** ↑	**Red** ↓	**Red** ↓
			Yellow →	**Yellow** ↑	**Yellow** ↓	**Yellow** ↑

mCherry-GFP-LC3, tandem fusion of LC3 to the acid-insensitive mCherry (Red) and the acid-sensitive GFP (Green). At first, both GFP and mCherry are detected in autophagosomes, which appear as yellow puncta. Once autophagosomes fuse with lysosomes, the green fluorescence is quenched because of the degradation of GFP by acid lysosomal proteases, resulting in LC3 emitting only red fluorescence. The dynamic switch from yellow to red fluorescence indicates a functional macroautophagic flux. AP, autophagosome; AL, autolysosome; IHC, immunohistochemistry; FM, flow cytometry; TEM, transmission electron microscopy; WB, western blotting. Inhibition of synthesis refers to early step macroautophagy suppression, and inhibition of degradation refers to late step macroautophagy suppression. ↑ indicate an increase, ↓indicates a decrease, → indicates no change [adapted from (Zhang et al., 2013)].

1.9.2. Methods for measuring CMA activity

Most cells have a basal level of CMA activity, and cellular stressors such as oxidative stress (Kiffin et al., 2004), lipotoxicity (Rodriguez-Navarro et al., 2012), nutrient-limitation (Cuervo et al., 1995a), and proteotoxicity (Koga et al., 2011a) have been shown to upregulate CMA. The connection between CMA and different human diseases has seen a growing interest to finely quantify CMA flux in different model systems and manipulate its activity for therapeutic purposes. For example, reduced CMA activity has been described in several age-related neurodegenerative diseases (Cuervo and Dice, 2000a), diet-induced obesity (Rodriguez-Navarro et al., 2012), and diabetes (Sooparb et al., 2004). In contrast abnormal upregulation of CMA activity is common in many types of cancer (Kon et al., 2011). However, unlike macroautophagic flux measurement, the study of CMA flux measurement is still in its infancy, and most of the current assays have been developed and optimized by Cuervo and colleagues (Arias, 2017; Kaushik and Cuervo, 2018). Commonly used assays include the following: (1) steady-state readout of CMA using western blot and immunofluorescence analysis to assess the expression and distribution of key CMA proteins, using antibodies that can specifically recognize the cytosolic tail of LAMP2A, and lysosomal-HSC70 (Agarraberes et al., 1997). CMA activity can also be tracked over time using photoconvertible fluorescent reporters, including photoswitchable KFERQ-ps-CFP reporter in which fluorescence switches from CFP to GFP upon exposure to 405nm light, and the photoactivatable KFERQ-PA-mCherry1 reporter which becomes fluorescent upon exposure to 405nm light (Koga et al., 2011b). Changes in the number of fluorescent puncta per cell represent a readout of CMA activation and may vary depending on the cell type and their level of basal CMA activity. CMA can finely be measured when working with isolated lysosomes from cells or tissues, in the presence and absence of inhibitors of lysosomal proteases such as leupeptin (Schneider et al., 2014). CMA-substrate flux can be quantified using [^{14}C]-radiolabelled CMA substrates, e.g. GAPDH, or even a pool of long-lived radiolabelled cytosolic proteins (common CMA substrates) which can be incubated with purified isolated lysosomes, and their association and degradation in the lysosome can be monitored by free [^{14}C]-radiolabelled amino acids released in the incubation media as proteolysis occurs (Terlecky et al., 1992). By comparing degradation of these

substrates, it is possible to distinguish substrate uptake and degradation through CMA pathway induction (Cuervo et al., 1997). However, such assays are both labour and resource intensive and require a high level of expertise as a large number of cultured cells or tissue is required to isolate and purify a sufficient number of CMA-active lysosomes (lysosomes containing both LAMP2A and HSC70).

1.10. Thesis outline

Although much has been learnt about the role of macroautophagy dysfunction in AD, the relationship between APP pathology and macroautophagy remains unclear. In particular, how macroautophagy activity changes in the disease progression, and whether both macroautophagy and CMA are equally implicated, remains unknown.

Using an *in vitro* and *in vivo* model of AD, the overarching aims of this project are therefore:

i. To characterize the expression profile of key proteins in amyloidogenesis, macroautophagy, CMA, and proteins implicated in the execution of apoptosis using a unique APP overexpression model system.
ii. To characterise the impact of early and late APP overexpression on the proteome.
iii. To assess macroautophagic flux in the context of APP overexpression and to unravel the extent of macroautophagy dysfunction with disease progression.
iv. To assess the contribution of macroautophagy and CMA in Aβ clearance and neuronal toxicity by modulating each pathway.
v. To assess the effects of intermittent fasting on the modulation of macroautophagy and CMA activity in a paraquat-induced *in vivo* brain injury model.

It is hypothesized that increased Aβ production, as a consequence of APP overexpression, will decrease macroautophagy activity and cell viability over time. Conversely, implementation of CR will induce a compensatory macroautophagy-CMA response which mitigates Aβ neurotoxicity, translating to neuronal protection.

CHAPTER 2: MATERIALS AND METHODS

2.1. Reagents and consumables

Nunc ™ Lab-Tek™ II Chamber Slide™ 8-chamber dishes (#154534) were purchased from ThermoFisher Scientific (TFS). Sterile T175 (175 cm^2, #431080), T75 (75 cm2, #708003), and T25 (25 cm^2, #707003) cell culture flasks were purchased from Whitehead Scientific (Winelands, Stikland). Tissue culture falcon tubes, including 15 ml (#50015) and 50 ml (#50050), and cell culture plates (96 (#30096), 48 (#30048), 24 (#30024), 6 (#30006) well – plates; flat and round bottom) were all purchased from Bio-Smart Scientific (Edgemead, Cape Town). Sterile serological pipettes, including 5 ml (#326001), 10 ml (#327001) and 25 ml (#328001) were purchased from B&M Scientific (Parow, Cape Town). Pipette tips and Eppendorf tubes were also purchased from B&M Scientific. Other consumables are listed in **Table 2.1**, and the formulations of routinely used solutions is described in **Table A.1**.

Table 2.1. List of reagents and consumables used in the study.

Reagents/products	Company	Catnr#
APS	Sigma Aldrich	A3678-25G
Bromophenol Blue	Sigma Aldrich	SAAR1437500CB
2-Mercaptoethanol	Sigma Aldrich	M6250
n-Pentane	Merck	1.07177.1000
Potassium chloride	Merck	SAAR5042020EM
Sodium hydroxide	Sigma Aldrich	S5881-500G
Sodium chloride	Merck	1.06404
SDS	Sigma Aldrich	L3771
Temed	Merck	1.10732.0100
TGX Stain-Free™ Fast Cast™ Acrylamide Kit, 12%	Bio-Rad Laboratories	1610185
Trans-Blot® Turbo Midi PVDF Transfer Packs	Bio-Rad Laboratories	1704157
Clarity™ ECL Western Blotting Substrate	Bio-Rad Laboratories	1705061
Triton X-100	Sigma Aldrich	T8787
Glycerol	Merck	SAAR2676520
Hoechst 33342 Stain solution	Sigma Aldrich	H6024
Mounting media	Diagnostech	S302380
Spar Fat Free Long-Life Milk	Local Spar	-

Running buffer	Bio-Rad	161-0772
Prestained Protein Ladder	Biocom Biotech	PM007-0500
cOmplete™ Protease Inhibitor	Sigma Aldrich	11873580001
NP40	Sigma Aldrich	74385-1L
NaF	Merck	193270
Na3VO4	Sigma Aldrich	S6508
PMSF	Sigma Aldrich	93482-50ml -F
Tween-20	Sigma Aldrich	P1379
BSA	Sigma Aldrich	10735078001
Cell scrapers	Whitehead Scientific	710001
Microscope slides	Sigma Aldrich	BR474701
Coverslips	Sigma Aldrich	Z692263
Cryovials	Scientific Group	430658
DMSO	Whitehead Scientific	D2650
Opti-MEM Reduced Serum Media	ThermoFisher Scientific	31985047
DMEM	LifeTechnolgies	41965-062
Fetal Bovine Serum (FBS)	Biocom Biotech	FBS-G1-12A
PenStrep	LifeTechnolgies	15140-122
Trypsin-EDTA	LifeTechnolgies	25200072
Syringe Insulin 29 g needle 1 ml	Lasec	LLSCIS-1ML

2.1.1. Antibodies

A list of primary antibodies used for western blotting, and immunofluorescence analysis is presented in **Table 2.2**. All primary antibodies were purchased either from Cell Signalling Technology Inc. (Danvers, Massachusetts), or Abcam Inc. (Pretoria, South Africa). All primary antibodies were used at a 1:1000 dilution in a 5% BSA in 1x TBS-T solution, and 1:200 dilution in a 5% BSA in 1x PBS-T solution for western blot and immunofluorescence analysis, respectively.

Table 2.2. Primary antibodies.

Antibody	Company/Catnr#	Host species	Size (kDa)
APP (NAB228)	Cell Signalling #2450	Mouse monoclonal IgG2a	100-140
APP	Cell signalling #2452	Rabbit polyclonal IgG	100-140
Amyloid beta (Aβ)	Cell signalling #2454	Rabbit polyclonal IgG	5
LC3B	Cell Signalling #2775	Rabbit polyclonal IgG	16, 18
SQSTM1/p62	Abcam #ab155686	Rabbit polyclonal IgG	62

Lamp2a *CMA selective*	Abcam #ab18528	Rabbit polyclonal IgG	140
HSC70 *CMA selective*	Abcam #ab2788	Mouse monoclonal IgM	70
Cleaved-PARP Asp 214	Cell Signalling #9541	Rabbit polyclonal IgG	89
Total Capase-3 (Asp175)	Cell Signalling #9661	Rabbit polyclonal IgG	35
Ubiquitin (P4D1)	Cell Signalling #3936	Mouse monoclonal IgG1	40-200
4-hydroxy-2-nonenal	Abcam #ab46545	Rabbit polyclonal IgG	52-76
cytochrome c (136F3)	Cell Signalling #4280	Rabbit polyclonal IgG	14

A list of Horse Radish Peroxidase (HRP)- and Fluorophore-conjugated secondary antibodies used for western blotting, and immunofluorescence analysis, respectively, is presented in **Table 2.3**. HRP, and Fluorophore-conjugated secondary antibodies were purchased from Cell Signalling and ThermoFisher Scientific (Pittsburgh, Pennsylvania), respectively.

Table 2.3. Secondary antibodies.

HRP-conjugated			
Antibody	Company/Catnr#	Western Blotting dilution	
Anti-mouse IgG	Cell Signalling # CST7076S	1:10 000 in 1x TBS-T	
Anti-rabbit IgG	Cell Signalling # CST7074S	1:10 000 in 1x TBS-T	
Fluorophore-conjugated			
Antibody	Fluorophore	Company/Catnr#	Immunofluorescence dilution
Donkey anti-Rabbit FITC	Alexa 568	ThermoFisher Scientific # A-10042	1:200 in 5% BSA
Donkey anti-Goat FITC	Alexa 647	ThermoFisher Scientific # A-21447	1:200 in 5% BSA
Mouse anti–GFAP FITC	Alexa 594 conjugate	ThermoFisher Scientific # A-21295	1:200 in 5% BSA
Donkey anti-Mouse FITC	Alexa 568	ThermoFisher Scientific #A-10037	1:200 in 5% BSA
Donkey anti-Rabbit FITC	Alexa 488	ThermoFisher Scientific #F-2761	1:200 in 5% BSA
Routinely used fluorophores for immunofluorescence labelling			
Fluorophore Dye	Absorbance wavelength	Emission wavelength	Visible colour
Alexa Fluor 488	494	517	Green
Alexa Fluor 568	578	603	Red
Alexa Fluor 594	590	617	Red
Alexa Fluor 647	650	670	Red

2.2. Cell culture and treatments

2.2.1. Cell culture propagation

Three stably transfected mouse neuroblastoma cell lines, N2a wild-type cells stably transfected with the wild-type human APP695 plasmid (N2awt/APPwt); Swedish mutant form of the APP695 plasmid (N2aswe/APPswe); and N2a cells transfected with an empty vector-(N2avec/APPvec) (Sisodia et al., 1990), were kindly provided by Professor Sangram Sisodia (Department of Neurobiology, University of Chicago, USA). The generation of these cell lines has been extensively described by Lo et al. (1994). Briefly, the APPwt plasmid was generated by subcloning a DNA fragment encoding wild-type human APP695 with a carboxyl (COOH)-terminal epitope tag of 12 amino acids from the c-Myc oncoprotein at the COOH terminus of APP downstream of a cytomegalovirus (CMV) promoter in plasmid pCB6 (ATCC, #37274). The N2aswe plasmid was generated by subcloning a DNA fragment encoding Myc epitope- tagged human APP695 containing the Swedish Familial AD-specific amino acid substitutions (K595N→M596L) downstream of a butyrate-inducible CMV in pCB6 for finer transcriptional control of the APP transgene induction. The pCB6 vector contains a gene encoding resistance to the neomycin analogue, stable pAPPwt and pAPPswe transfectants were therefore selected in medium containing 0.4 mg/ml G418 (Chen and Okayama, 1987).

The N2aswe cell line has been extensively used in the characterization of various disease pathology related to Aβ neurotoxicity, revealing valuable clues towards the elucidation of AD-related neuropathogenesis (Lee et al., 2015; Salto et al., 2015; Schlachetzki et al., 2013). In accordance with the manufacturer's instructions, these cells were optimally cultured in growth media containing an equal volume of Dulbecco's modified Eagle's medium (DMEM, Gibco®) and OptiMEM Reduced Serum Media (Gibco®) supplemented with 5% fetal bovine serum (FBS, Gibco®), and 1% Penicillin-Streptomycin (solution stabilized with 10,000 U penicillin, and 10 mg streptomycin/ml; PenStrep). To induce the butyrate-inducible CMV promoter-driven APP transgene expression, N2aswe cells were treated with 1 mM to 10 mM butyric

acid (sodium salt, BA), with 5 mM BA showing a significant increase in APP expression following 12 and 24 hr treatment with minimal cytotoxic effects (Lo et al., 1994, 1995; Ramalho et al., 2006). Experiments were performed at a cell passage of 6 to 12.

2.2.2. Thawing of cryopreserved cells

Cryovials containing ~1x10^6 N2a cells were rapidly thawed in 37°C pre-warmed water, and the cell suspension was gently added to 12 ml pre-warmed growth media in a T75 cell culture flask which was stored in a humidified incubator with 5% CO_2 at 37°C. After 2 hrs, the growth media was aspirated to remove dimethyl sulfoxide (DMSO) from the media, as DMSO is toxic to growing cells. The adhering cells were then replenished with 12 ml pre-warmed growth prior to being placed in the incubator under the described conditions. Cells were passaged twice weekly through trypsinization with 0.25% Trypsin-EDTA (Gibco®) at a 1:5 ratio in a T75 flask, or once weekly at a 1:20 ratio in a T25 flask.

2.2.3. Passaging of cells

For passaging of cells grown in T75 flasks, growth media was aspirated from the flask and the cell monolayer was briefly rinsed with 5 ml pre-warmed 1x phosphate buffered saline (PBS) (**ADDENDUM A Table A.1**) to remove residual media. Subsequently, cells were briefly detached by adding 4 ml pre-warmed 0.25% Trypsin-EDTA to the flask, which was then allowed to incubate for ~5 min at 37°C with gentle agitation. Cells were then visualized under an Olympus CKX41 light microscope (Olympus) to ensure visible cell detachment from the flask surface area. The trypsin reaction was immediately neutralized by adding pre-warmed growth media to the dissociated cells (2x the volume relative to trypsin used), and this cell suspension was then transferred to a 15 ml falcon tube, which was then spun in a centrifuge for 5 min at 1500 RPM at room temperature (RT). The cell supernatant was removed, and the pellet was resuspended in 1 ml pre-warmed growth media and the cells were counted using a Neubauer-improved haemocytometer coverslip (Sigma Aldrich) with 0.1 mm sample depth. The Neubauer chamber was prepared by placing a sterile coverslip in the

middle of the chamber. A 10 µl volume of homogenous cell suspension was transferred to the edge of the Neubauer counting chamber, and this suspension was then drawn by capillary action under the cover slip. The chamber was then placed under the Olympus CKX4 inverted light microscope, and cells were individually counted in all 4 quadrants using the 40x objective lens. The volume of cells was determined using the following calculation: cells/ml = (number of cells counted/4) x dilution factor x 10^4

After counting, cells were seeded at the desired volume into appropriate pre-labelled experimental plates and/or flasks containing pre-warmed growth media. Throughout this study, cells were cultured in a humidified incubator, with a CO_2 concentration held at 5%, and a temperature of 37˚C.

2.2.4. Cryopreservation of cell lines

Cryopreservation of cells was routinely performed to ensure long term maintenance of N2a cell lines. Confluent cells were detached from the culture plate/flask following the procedure for cell passaging. After centrifugation, the cell pellet was resuspended in a predetermined volume of pre- chilled, freshly prepared freezing mixture consisting of 90% fetal bovine serum (FBS), 10% DMSO (Sigma Aldrich). A volume of 1 ml cell suspension, containing $1x10^6$ cells, was transferred into a pre-labelled 1.2 ml cryovial using a sterile pipette tip (P1000 micropipette). These cryovials were stored at -80˚C overnight to for allow slow cooling and avoid crystal formation. The following day, the cryovials were transferred to a liquid nitrogen tank for long-term storage.

2.3. Categorisation of N2a cell treatment groups

N2avec cells were used to validate the level of APP expression, expected for the N2awt cells, and the N2aswe APP overexpression model. N2awt cells were used as a control for N2aswe cells in selective experiments. Given that the N2awt Myc expression vector is not driven by the butyric acid (BA)-inducible CMV promoter, N2aswe BA untreated cells, i.e. control, was thought to be a more appropriate control for the BA induced N2aswe-myc expression vector as performed previously by others

(Sinha et al., 1999; Yan et al., 2012). Pure BA is a carboxylic acid, shown to play several beneficial roles in the treatment of gastrointestinal infections (den Besten et al., 2013). Sigma Aldrich supplies pure BA for research purposes owing to its stimulatory effects on CMV driven transgene expression, as shown for the N2aswe Myc expression vector following BA treatment (Lo et al., 1994, 1995). For experimental purposes, cells were passaged when ~80% confluent as described in section 2.2.3. After counting, $5x10^5$ N2aswe and N2awt cells were seeded into pre-labelled T75 flasks, or culture plates and allowed to adhere overnight.

2.3.1. Treatment groups for macroautophagy and CMA modulation

Cells were treated with the following treatment compounds in accordance with the study aims.

Table 2.4. Treatment compounds.

Treatment compounds	Company	Catnr#	Working concentration
Butyric acid (BA)	Sigma Aldrich	B103500	5 mM
2-Deoxy-D-glucose (2DG)	Sigma Aldrich	407248	5 mM
3-Methyladenine (3MA)	Sigma Aldrich	M9281	5 mM
Bafilomycin A1 (BafA1)	Lkt® Laboratories	B0025	400 nM

Treatment groups were defined as follows:

1. Control
2. 12, 24, 36, or 48 hrs BA treated groups
3. 6 or 12 hrs 2-DG treated groups
4. 6, 12, 18, 24, or 30 hrs 3MA treated groups
5. 2 hrs BafA1 treated group

Combination groups were selected as described in appropriate results chapter.

2.4. Cell viability

A ready-to-use cell proliferation reagent (#11644807001), containing WST-1 {4- [3-(4-iodophenyl)-2-(4-nitrophenyl)-2H-5-tetrazolio]-1,3-benzene disulphonate} and an electronic coupling reagent, diluted in phosphate buffered saline (Roche Diagnostics) was used to measure cell viability. This calorimetric assay is based on the cleavage of the tetrazolium salt WST-1 (slightly red) to formazan (dark red) by various mitochondrial dehydrogenase enzyme. An increase in metabolically healthy cells is accompanied by increased absorbance signal detected at the wavelength of 450 nm, while a decrease in signal can indicate a decrease in metabolically healthy cells in response to the cytotoxic effects of treatment compounds. To perform WST-1 assays, $2x10^5$ N2aswe and N2awt cells were seeded into 48-well plates containing 200 ul pre-warmed growth media and allowed to adhere overnight. Culture media was aspirated the following day, and cells were treated as described in section 2.3.1. Following completion of the various treatment protocols, 10 µl pre-warmed WST-1 reagent was added directly to each 200 µl test-compound containing well, and the cells were incubated at a temperature of 37°C for 2 hrs. Subsequently, the culture plates were gently shaken for ~5 min and the colorimetric readings were recorded using the EL800 universal microplate reader (BioTek Instruments Inc), at a wavelength of 595 nm. The calorimetric readings were then exported using the KC Junior software (Bio-Tek Instruments Inc.). The treated versus untreated control readings were subtracted from the background control. The results were expressed as a percentage of the optical density of treated versus untreated controls. The optical density values corresponding to the control cells were recorded as 100%.

2.5. Western blot analysis of cells

2.5.1. Protein extraction and cell lysis preparation

After completion of the appropriate incubation period, growth media was aspirated from T75 culture flasks and cells were harvested by trypsinization method as previously described. Resuspended cells were transferred to 15 ml tubes and centrifuged at 1500

RPM for 5 min at room temperature (RT). After centrifugation, the 15 ml tubes were placed on ice, the supernatant was removed, and the cell pellet was resuspended in 500 µl cold 1x PBS. The cell suspension was then transferred to pre-chilled 1.5 ml Eppendorf tubes and centrifuged at 1500 revolutions per minute (RPM) for 5 min at 4°C. The cell pellet was washed in 1x cold PBS and centrifuged 3x prior to being resuspended in pre-chilled radio immunoprecipitation assay (RIPA) buffer supplemented with phosphatase inhibitors (**ADDENDUM A Table A.1**), and EDTA-free protease inhibitors (1x Complete protease inhibitor mixture, Sigma-Aldrich) (as per manufacturers protocol). Depending on the size of the cell pellet, 50-200 µl cold RIPA lysis buffer was added, and the cells were gently resuspended in this buffer to achieve a homogenous suspension of cells and lysis buffer. The cell suspension was then allowed to incubate for 15 min on ice. The cell suspension was sonicated on ice at an amplitude of 5 for 2-3 sec bursts followed by a 30 min cooling interval. To pellet the cell debris, cell lysates were centrifuged at 8000 RPM for 10 min at 4°C. The supernatant containing total protein lysates was then collected and transferred to a fresh pre-chilled microcentrifuge tube and stored at -80°C for future utilization.

2.5.2. Determination of protein concentration

Stored at -80ºC, cell lysates were placed on ice to slowly thaw. For measuring cell concentration, the lysates were diluted 1:10 in distilled water (dH_2O) to avoid the sample being too concentrated for accurate measurement. To determine protein concentration, each sample was gently vortexed, and the concentration was determined using the Direct Detect™ system (EMD Millipore). This is an infrared (IR)-based spectrometry system used to determine the quantity of protein (0.25–5 mg/ml), and lipid content present in biological samples based on their separable IR spectra (Strug et al., 2014). The IR - based spectrometer employs an innovative hydrophilic polytetrafluoroethylene (PTFE) membrane card technology that is transparent in most of the infrared spectral region. The protein concentration is determined by loading 2 µl of cell lysate solution and blank buffer solution, which is usually fully supplemented RIPA lysis buffer, directly onto a blank PTFE card according to manufacturer's protocol. Briefly, the card content is measured by inserting the card into the sampling accessory slot of the Direct Detect™ spectrometry system. The instrument then dries

the loaded sample card and proceeds to measure each sample for its respective lipid, detergent and protein concentration. The results of these measurements are then graphically represented using the Direct Detect Data Export Software™.

2.5.3. Protein separation

During western blotting, proteins are immobilized on a membrane and labelled by complexing with primary antibodies followed by incubation with horseradish peroxidase conjugated secondary antibodies. To this end, proteins were fractionated by sodium dodecyl sulphate polyacrylamide gel electrophoresis (SDS-PAGE; Mini-PROTEAN® Tetra cell, Bio-Rad) at a voltage of 100-120 V and current of 200 mA (Bio-Rad Power Pac 1000) until the migration front reached the bottom of the gel. Resolved proteins were then electro-transferred onto polyvinylidene fluoride membrane (PVDF; Immobilon, Millipore, USA) using a horizontal semi-dry electrotransfer system (Bio-Rad Trans-blot® SD, USA) at voltage of 15 V and constant current of 0.5 A (Bio-Rad Power Pac 1000). Alternatively, a vertical wet transfer system (Mini- Trans blot cell, Italy) was used when electrotransfer was performed using a voltage of 200 V and constant current of 200 mA (Bio-Rad Power Pac™ HC). Briefly, after determining the exact concentration of each lysate sample, a cell lysate volume containing 50 µg/ul of protein was diluted in Laemaelli's loading buffer (**ADDENDUM A Table A.1**) at a ratio of 2:1. The addition of the anionic detergent sodium dodecyl sulphate (SDS) in Laemaelli's loading buffer causes denaturation of the tertiary structure of the protein, hence, all the proteins become negatively charged by their attachment to the SDS anions. Glycerol is added to the loading buffer to increase the density of the sample to be loaded, thereby maintaining the sample at the bottom of the well, restricting overflow and uneven gel loading. Bromophenol blue is added to the loading buffer to enable visualization of the migrating proteins and the separation progress.

2.5.3.1. Western blotting procedure

After brief vortexing, cell lysates were boiled for 5 min at 95^{o}C and resolved using a

12% TGX Stain-Free Fast Cast SDS–PAGE gel (Bio-Rad). After polymerization, the fast cast gels were placed in a Mini-PROTEAN Tetra System (Bio-Rad Laboratories Inc., USA) and filled with running buffer (**ADDENDUM A Table A.1**). The first lane position on each gel was loaded with 4 µl of BLUeye® Prestained Protein Ladder (Biocom Biotech) to aid with molecular weight determination for specific protein bands. The second lane was loaded with a control sample, and subsequent lanes contained samples from treated groups. Proteins were separated for 10 mins at 100 V, followed by 1 hr at 120 V until the Laemaelli's loading buffer reached the bottom of the gel.

2.5.3.2. Protein probing and signal detection

Following protein separation, the SDS–PAGE gel was carefully removed from the electrophoresis chamber and placed on the ChemiDoc™ Imaging System (Bio-Rad Laboratories Inc., USA) for stain-free gel activation. Subsequently, resolved proteins were electro-transferred onto PVDF membranes using the semi-dry electrotransfer system for 7 mins at voltage of 15 V and constant current of 0.5 A. The membrane was then visualized using the ChemiDoc™ Imaging System to ensure proper electrotransfer, and thereafter soaked in methanol for 60 secs to allow the membrane to tightly interact with the transferred proteins. After washing the membrane 3x in 1x TBS-T (**ADDENDUM A Table A.1**) for 5 min, the membrane was blocked in 5% fat-free milk in 1x TBS-T to prevent nonspecific antibody binding, blocking was performed with gentle agitation for 1 hr at RT. Following the 1 hr blocking period, the membrane was then washed 3x in 1x TBS-T for 5 min, followed by overnight incubation on a rotor at 4^{o}C in a 1:1000 dilution of various primary antibodies made up in a 5% BSA/1x TBS-T solution. The following day, the membranes were washed 3x with 1x TBS-T for 5 mins each, followed by 1 hr incubation with a HRP-conjugated secondary antibody in a 1:10 000 1x TBS-T solution gentle rotation at RT. After incubation in secondary antibody, the membranes were then washed 3x with 1x TBS-T for 5 mins, and thereafter exposed to Enhanced chemiluminescence Clarity™ Western ECL Substrate Chemiluminescence Reagents (Bio-Rad Laboratories Inc) utilizing the Bio-Rad ChemiDoc™ imaging system to activate the protein signal. In the chemiluminescence reaction, HRP catalyses the oxidation of luminol to a light emitting reagent, which releases light during its decay. Since the oxidation of luminol is

catalysed by HRP, which is complexed with the membrane bound protein of interest, the amount and location of light that HRP catalyses the emission of is directly correlated with the location and amount of the protein on the membrane. In accordance with the manufacturers protocol, an equal volume of ECL solution A and B were prepared away from light, and thoroughly mixed together. A volume of 200 µl of the ECL mixture was evenly added onto the membrane, and the proteins of interest were visualized using the Bio-Rad ChemiDoc™ imaging software.

2.5.3.3. Membrane stripping and re-probing

Membranes were generally probed for several proteins at a time by incubating the membrane in stripping buffer (**ADDENDUM A Table A.1**) for 30 min followed by a wash step of 5 min in 1x TBS-T with gentle agitation, to remove bound antibodies. The membranes were then blocked in 3% fat milk/1x TBS-T buffer for 1hr at RT. The membrane was then washed 3x with 1x TBS-T for 5 mins each and probed for different target proteins as previously described.

2.5.3.4. Quantification of protein densitometric measurements

To control for protein loading, all blots were probed for the representative β-actin protein. The images were refined in terms of their display using the Image Lab™ Software (version 4.0 build 17). Target protein bands were quantified and normalized to their respective β-actin loading control using Image J v1.43 (NIH) software (http://lukemiller.org/index.php/2010/11/analyzing-gels-and-western-blots-with-image-j/). The intensity values (measured in arbitrary units (A.U) of various proteins of interest were expressed as a ratio of the intensity value of their respective β-actin loading control, and these values were then exported to Microsoft Excel software for further processing, prior to statistical analysis with the appropriate tests. A minimum of three independent experiments were performed.

2.6. Caspase-Glo® 3/7 Assay

The Caspase 3/7 Assay is a sensitive, luminescent assay that qualitatively measures the activity of caspase 3 and 7 in response to various stressors. Caspase-3 and caspase 7 are activated universally to coordinate the execution of apoptosis by cleaving multiple structural and repair proteins and are therefore primarily responsible for the majority of proteolytic reactions that take place during apoptosis (Brentnall et al., 2013). The Caspase 3/7 assay is based on the reaction of a caspase substrate that is conjugated with an enzyme luciferase. Caspase substrate lyses and enters the cell to interact with caspase 3/7, which causes the cleavage and activation of luciferase enzyme, resulting in the emission of light, which is then measured in relative light units (RLU) using a luminometer.

To measure caspase-3 and 7 activities in response to APP overexpression over time, 15,000 N2aswe cells were seeded into 96-well luminometer plates and allowed to adhere overnight. The following day, cells were treated with 5 mM BA to induce APP transgene overexpression for 12, 24, 36, or 48 hrs. Following completion of the treatment protocol, an equal volume of Caspase-Glo® 3/7 reagent was added to the media in each well (70 µl), and cells were incubated for 3 hrs at 37°C due to RT fluctuations. Luminescence was measured using the GloMax® 96 Microplate Luminometer (Promega), and the luminescence values were recorded using the GloMax® software (Promega) using optimised pre- installed settings for the Caspase-Glo® 3/7 Assay. Caspase 3/7 activity was reported as a mean of RLU by subtracting the blank (measured luminescence) from the corresponding sample luminescence value.

2.7. Immunofluorescence microscopy

2.7.1. Transfection

2DG was used to elucidate its effects in AD-related Aβ-pathology, using N2aswe cells, to assess chaperone-mediated autophagic activity. To this end, N2aswe cells were

transiently transfected with the KFERQ-mCherry plasmid. The KFERQ-mCherry plasmid is a CMA reporter which preferentially recruits CMA substrates to the lysosomal membrane for subsequent degradation via this pathway (Koga et al., 2011b). The plasmid was a kind gift from Professor Ana Maria Cuervo (Department of Developmental and Molecular Biology, Albert Einstein College of Medicine, NY). N2aswe ells were transfected using the Lipofectamine 3000 Transfection Reagent (Invitrogen, #L3000008) according to manufactures instructions. Briefly, N2aswe cells were seeded into 6-well plates at a high density of $8x10^5$ and allowed to adhere overnight. The following day cells were transfected at a confluency of ~90% to ensure a high transfection efficiency. A total of 1.5 µg plasmid DNA was transfected per well at a ratio of 1:3 to Lipofectamine™ 3000 transfection reagent, prepared in 200 µl OptiMEM reduced serum media. Diluted pDNA: lipofectamine 300 reagent complexes were incubated for 15 to 20 min at RT, and subsequently added to each well in a dropwise manner. The transfection efficiency was determined through live-cell imaging of the KFERQ-mCherry construct using the 40x objective lens on the Olympus Cell® system attached to an Ix 81 Inverted fluorescence microscope, equipped with a F-view-II cooled CCD camera (Soft Imaging Systems). When the cells were determined to have ~50% transfection efficiency, cells were treated with BA and 2DG combination treatment, or BA only as previously described, and allowed to incubate for 12, 24, and 48 hrs under these treatment conditions. After completion of the treatment protocol, transfected cells were imaged per group at a 100x magnification. Three excitation filters were used to capture images: the TxRed excitation filter was used to capture images of lysosomal puncta and the DAPI excitation filter for the acquisition of nuclei. Images were processed, and the background was subtracted using the Olympus Cell® software (Hamburg, Germany), and presented in a maximum intensity projection.

2.7.2. Cell fixation

N2aswe cells were seeded at a density of $3x10^4$ into 6-well plates containing round 22x22 mm coverslips (No 1.5H High precision cover slips, Zeiss, #474030-9020-000) and 2 ml growth media and allowed to adhere at a temperature of 37°C, and a 5% CO_2 concentration. Following BA treatment for 12, 24, or 48 hrs, with untreated cells serving as the control, the media was aspirated, and the cells were fixed for 10 min in

a 1:1 ratio of 4% paraformaldehyde (PFA) (w/v): Opti-MEM/DMEM (Sigma Aldrich, #158127) and incubated at 37°C for 15 min to maintain cell integrity. The fixative solution was then aspirated, and the coverslips were washed 3x for 5 min with cold 1x PBS-T, after which cells were permeabilized by adding 0.2% Triton-X-100 and incubation for 2 min at RT. The coverslips were then washed 3x for 5 min with cold 1x PBS-T, and cells were incubated for 30 min a blocking buffer solution, containing 5% donkey serum (Sigma Aldrich, #D9663) in 1x PBS-T. After blocking, coverslips were washed 3x for 5 min with cold 1x PBS-T, before incubation in various primary antibodies, which were diluted in 5% BSA/1x PBS-T (**see Table 2.2** for list of antibodies). Each coverslip was incubated with 50 µl primary antibody solution overnight at 4°C. The following day the coverslips were washed 3x for 5 min with cold 1x PBS-T, and incubated in fluorophore-conjugated secondary antibodies against the appropriate species (**see Table 2.3** for list of antibodies) for 50 min. Following this, a 50 µl volume of Hoechst 33342 nuclear dye (diluted 1:200 in 1x PBS-T) was added to the coverslips for 10 min. Coverslips were then washed 3x for 5 min with 1x PBS-T, and mounted in an inverted manner onto microscope slides containing Dako® fluorescent mounting media (Diagnostech), sealed with clear nail varnish and left to dry for 60 min at RT protected from light. Slides were wrapped in foil paper to prevent bleaching of fluorescent molecules and stored at -20°C until further analysis.

2.7.3. Confocal microscopy

Cells were imaged at the Central Analytical Facility (CAF, Stellenbosch University) with a laser scanning confocal microscope, LSM780 ELYRA PS1 confocal microscope (Carl Zeiss, Germany) using the 60x oil immersion objective lens. Hoechst was excited with the 405 nm laser, with the MBS405 beam splitter and detection in the range 415-499 nm, and the appropriate lasers, primarily 488 and 561, were used to excite the corresponding fluorophore-conjugated proteins of interest. Images were acquired with the Zen Imaging software, and further processed using the Zeiss Zen Lite Black Edition Imaging Software v.2.3 (Carl Zeiss, Germany). Cells incubated without primary antibody served as negative controls.

2.7.4. APP localization: correlative light and scanning electron microscopy

Correlative light and electron microscopy (CLEM) is a microscopy technique that combines the capabilities of two typically separate microscopy platforms: fluorescently labelled proteins localized by fluorescence microscopy (FM), and the visualization of subcellular ultrastructure by electron microscopy (EM). While FM enables the user to retrieve information from fluorescently labelled structures, EM provides detailed information about the biological ultrastructure (Russell et al., 2017). By combining these two techniques, CLEM makes it possible to image dynamic biological events for structural analysis at high resolution. EM micrographs were acquired using a scanning electron microscope (SEM), which uses a focused electron beam to form an image with information pertaining to the surface topography and composition, captured at a high imaging magnification and resolution.

2.7.4.1. Sample preparation

A total of $3x10^4$ N2aswe cells were seeded into 6-well plates containing round 22x22 mm coverslips, grown overnight and treated for 12, 24, or 48 hrs BA, including an untreated control. Upon completion of the treatment protocol, coverslips were prepared for confocal microscopy analysis as previously described. Notably, for this experiment, cells in each experimental group were only incubated in APP (#2452) primary antibody overnight at 4°C, and its corresponding secondary antibody, Alexa Fluor 488 Donkey anti-rabbit for 50 min, followed by 10 min Hoechst staining. Coverslips were then rinsed and immersed in 1x PBS-T overnight in a 6-well plate prior to CLEM/SEM analysis.

2.7.4.2. CLEM image acquisition

Each cover slip was separately placed in the CLEM sample holder for Life Science Cover Glass (Zeiss, Germany) to be imaged. Confocal imaging was performed as previously described in section 2.7.3. The marker coordinates of the sample holder were saved using the Shuttle and Find mode of ZEN 2012 software using transmitted

light with the 10x objective. After calibration, a 3 x 3 tile scan of the area of interest was imaged using the EC “Plan-Neofluar”10x/0.3 objective, followed by a 1x image of identified regions with the same objective. This was then followed by Z-stack imaging with both the LD “Plan-Nuofluar” 40x/0.6 Corr M27 objective and the LCI “Plan-Apochromat”63x/1.4 Oil DIC M27 objective. For all samples, the 488 nm Argon laser was used for excitation of Alexa Fluor 488, with the MBS488 beam splitter and emission was detected with the GaAsP detector in the range 499- 588 nm. Hoechst was excited with the 405 nm laser, with the MBS405 beam splitter and detection in the range 415-499 nm.

After confocal imaging, each sample was washed with dH_2O, without removing it from the sample holder. The assembly was coated with a thin (~5 nm thick) layer of carbon prior to analysis, using a Quorum Q150T coater by performing carbon rod evaporation. Once the samples were coated, the coating cannot be removed without damaging the sample, therefore electron analysis must succeed fluorescence analysis as coating diminishes the fluorescent signals. Secondary electron (SE2) In Lens micrographs were acquired using a Field Emission Gun Scanning Electron Microscope (FEG-SEM) and SmartSEM® software (Zeiss MERLIN, Germany) at the Electron Microbeam Unit (CAF). First the coordinates of the sample holder were saved again in ZEN 2012 Imaging Software (Carl Zeiss, Germany), after which the areas of interest were automatically located by the Shuttle and Find mode. The precision of superposition of the FM images on the SEM micrographs is important for accurately localizing the labelled proteins within the SEM micrographs. Beam conditions during the analysis on the Zeiss MERLIN were 5 kV accelerating voltage, with a working distance of 9.1 mm and a beam current of 250 pA. Final images were acquired with the Zeiss SmartSEM® software.

2.7.5. Colocalization analysis and immunofluorescence microscopy

Colocalization analysis is typically used to determine if two different proteins of interest cluster to the same subcellular location. The quantification of colocalization between two fluorescence channels is performed on a pixel by pixel basis which can be split into two categories: (1) co-occurrence and (2), correlation (Adler and Parmryd, 2010). The

former measure, quantifies the presence of both fluorophores in individual pixels, while the latter quantifies the extent overlap between the signals from each fluorophore (Adler and Parmryd, 2010). Two measures of correlation are used to quantify the degree of colocalization between fluorophores, the Pearson correlation coefficient (PCC) and the Mander's overlap coefficient (MOC) (Manders et al., 1993). The formulae for the PCC and MOC, respectively, are presented below for a quantification of two fluorophore channels.

$$\mathrm{PCC} = \frac{\sum_i (\mathrm{Ch1_i Ch1_{avg}}) * (\mathrm{Ch2_i Ch2_{avg}})}{\sqrt{\sum_i (\mathrm{Ch1_i Ch1_{avg}})^2 * \sum_i (\mathrm{Ch2_i Ch2_{avg}})^2}}$$

Ch1*i* and Ch2*i* refer to the pixel intensity values of two different colour channels of the same image, and $\mathrm{Ch1_{avg}}$ and $\mathrm{Ch2_{avg}}$ indicate the mean intensities of the colour channels across the entire image. The PCC values range from 1 to -1, with the former indicating perfect correlation, the latter indicating a negative correlation, i.e. every pixel that contains green does not contain red and vice versa, and a PCC value of 0, signifying the total absence of a relationship (Adler et al., 2008).

$$\mathrm{MOC} = \frac{\sum_i Ch1_i * Ch2_i}{\sqrt{\sum_i (Ch1_i)^2 * \sum_i (Ch2_i)^2}}$$

The MOC provides a highly sensitive measure of co-occurrence and correlation (Zinchuk and Grossenbacher-Zinchuk, 2009). MOC values range from 0 to 1, with the former corresponding to non-overlapping images, i.e. no overlap of pixels from either of two or more channels, while the latter signifies 100% colocalization between all pixels. The Mander's colocalization coefficients (MCC), M1 and M2 metrices are an extension of the MOC analysis (Manders et al., 1993), and defined mathematically as follows:

$$\mathrm{M_1} = \frac{\mathrm{pixels_{Ch1.coloc}}}{\mathrm{pixels_{Ch1.total}}} \qquad \mathrm{M_2} = \frac{\mathrm{pixels_{Ch2.coloc}}}{\mathrm{pixels_{Ch2.total}}}$$

Pixels Ch1.coloc is the intensity of the fluorophore 1 in pixels where fluorophore 2 is present. Similarly, pixels Ch2.coloc is the intensity of the fluorophore 2 in pixels where fluorophore 1 is present. Pixels Ch1.total, and Ch2.total represent the ratio of the "summed intensities of pixels from each co-localizing fluorophore for which the intensity is above zero".

Although the PCC and MOC coefficients are mathematically similar, differing only in the use of either the absolute intensities (MOC), or the deviation from the mean (PCC), MOC is more widely used, partly due to its interpretative ease, while the negative values generated using the PCC may be difficult to interpret when the degree of overlap is being measured (Churchman and Spudich, 2012). A threshold value for each channel is also required to define the cut-off value for colocalization.

2.7.5.1. Colocalization sample preparation and imaging

For colocalization analysis, N2aswe cells adherent coverslips were treated with BA and prepared for microscopy analysis as previously described. To avoid bleed-through, i.e. when the red fluorochrome emits into the green channel and/or the green fluorochrome emits into the red channel, fluorophore-linked secondary antibodies that do not have cross-reactivity, and with well- separated excitation and narrow band emission spectra were selected for dual channel colocalization. Single stained controls were used for evaluating any bleed-through and unstained negative controls were used to determine the degree of background autofluorescence. Dual-stained images were obtained using the LSM780 ELYRA PS1 confocal microscope (Zeiss, Germany) oil immersion 100x objective lens.

2.7.5.2. Quantification of colocalized proteins

Quantitative analysis of colocalization was performed on randomly selected images using the Zeiss Zen Lite Black Edition Software v.2.3. To improve the quality of images before analysis of colocalization, deconvolution methods, filtering, and background noise was reduced using the Zeiss Software Colocalization threshold and

Colocalization Test plug-ins, prior to overlap quantification. For each image, the region of interest (ROI) was selected using the Overlay tool, thereby reducing the number of pixels outside the region of colocalization to improve the accuracy of colocalization measurements. Every pixel in the image was plotted in a scatterplot diagram based on its intensity level from each channel. The colour in the scatterplot represents the number of pixels that are plotted in that region. Using the Colocalization test plug-ins, four software quadrants were designated for each image, with only quadrants 1 and 2 being selected for colocalization analysis. Colocalized pixels were viewed by selecting quadrant 3 and setting to white for easier visualization of the pixels exhibiting colocalization. The Zeiss Software then automatically generates a table with denoting different measurements extrapolated from the scatterplot. These measurements include values signifying the PCC, MOC, and MCC for each selected ROI. To identify statistically significant differences in colocalization of BA treated groups relative to a control sample, the colocalization coefficients were exported into an appropriate statistical program for further quantification.

2.7.6. Detection of cellular ultrastructure using transmission electron microscopy

In transmission electron microscopy (TEM), electrons are transmitted through a plastic-embedded specimen, allowing for the resolution and visualization of ultrastructural detail not possible via confocal microscopy. Accordingly, TEM is a widely utilized approach when investigating the changes in cellular morphology in response to various treatment conditions.

2.7.6.1. TEM sample preparation

A total of $5x10^6$ N2aswe and N2awt cells were seeded into T75 flasks in duplicate. Cells were grown to approximately 90% confluency prior to being treated as follows: control, control + BafA1, 12 hrs BA, 12 hrs BA + BafA1, 24 hrs BA, 24 hrs BA + BafA1, 48 hrs BA, or 48 hrs BA + BafA1. Following treatment, 4 ml trypsin was added to each flask and incubated for 5 min prior to being supplemented with 8 ml media and

transferred into 15 ml falcon tubes. Tubes were centrifuged at 1500 RPM for 5 min at RT, the supernatant was removed, and the remaining cell pellet was resuspended in pre-warmed 1x PBS to remove residual trypsin and media. Cells were rinsed twice with 1x PBS with repeat of the centrifugation step. Primary fixation was performed by resuspending the cell pellet in 1 ml pre-warmed 2.5% glutaraldehyde. The cell suspension was then transferred to new 15 ml falcon tubes and centrifuged as before, but for an additional 10 min to ensure tight pellet formation. The fixative solution was carefully removed, and the pellet was resuspended in 1 ml fresh fixative solution and stored overnight at 4°C to slow down autolytic processes and reduce cell shrinkage. TEM processing of samples was performed by Stellenbosch University's National Health Laboratory Services at Tygerberg Medical Campus.

2.7.6.2. Processing of TEM samples

Briefly, the primary fixative solution was carefully aspirated, and the cells were washed 3x in 0.1 M sodium phosphate buffer for 5 min, with centrifugation at 1500 RPM between each successive wash step. The cells were then washed 5x in dH_20 to remove residual phosphate ions, and post-fixed with 1% osmium tetroxide in 0.1 M sodium phosphate buffer at 4°C for 1 hr. Subsequently, cell samples were washed 5x in dH_20, transferred to an automated tissue processer, where they immersed in a sequence of dehydration solutions as described below:

i. 10% uranyl acetate for 15min
ii. 30% Ethanol for 10 min
iii. 50% Ethanol for 10 min
iv. 70% Ethanol for 10 min
v. 90% Ethanol for 10 min
vi. 95% Ethanol for 10 min
vii. 100% Ethanol for 10 min
viii. 100% Ethanol for 10 min

Following dehydration, the cells were infiltrated by progressive incubations with ethanol and Spurr's resin (Low viscosity embedding kit, Electron Microscopy Sciences) at a

ratio of 1:1 for 90 min, followed by incubation with 100% Spurr's resin. After 120 min infiltration in Spurr's resin, the cell samples were embedded and polymerized in 100% Spurr's resin using the BEEM® Embedding Capsules (Electron Microscopy Sciences) by heating for 72 hrs in a 60°C oven. Subsequently, the BEEM® Embedding Capsules were removed from the hardened resin block and dipped into liquid nitrogen, where the difference in the shrinkage of the resin and the capsule allowed for separation of the capsule from the resin, thereby leaving the cells attached to the resin. The resin-embedded samples were then trimmed and sectioned with a Leica EM UC7 ultramicrotome (Leica Microsystems, Wetzlar, Germany) to obtain 200 nm thick sections. These sections were then fully stretched through exposure to chloroform vapor prior to being placed onto 200 mesh copper grids (G200-Cu, Electron Microscopy Sciences).

2.7.6.3. TEM image acquisition

Images were examined using the JEOL JEM 1011 transmission electron microscope (JEOL, Inc., Peabody, MA) operated at 100 kV, and the iTEM Olympus Soft Imaging Solutions' imaging platform. Ten to thirty random areas were selected from each treatment group and captured at magnifications of 1000×, 2000×, 3000 and 5000×, as 8-bit grey-level images at a minimum TIFF resolution of 300 pixels/inch required for RGB images (24-bit with 8-bits for each of the red, green and blue channels).

2.7.6.4. TEM morphometric analysis

Quantitative morphometric analysis of TEM micrographs was performed as described by Asikainen et al. (2014), using the semi-automatic open source image processing program, ImageJ v1.41 (Schneider et al., 2012), as illustrated in **Fig. 2.1**. Briefly, an automated image grayscale binarization tool, "thresholding", in ImageJ was used to process TIFF images into black-and-white image maps as follows: Image>adjust>threshold. Accordingly, pixels with grey levels falling under a specified threshold were turned into black pixels, and those with grey levels above the specified threshold were turned into white pixels, thereby separating the structures of interest from the background. After thresholding, the images were segmented using the

"watershed analysis plug-in" as follows: process>binary>watershed. The number of structures, i.e. autophagic vacuoles (AVs), and the area measurements thereof were calculated using the "Particle analysis plug-in" as follows: analyse>analyse Particles, and the "Wand Auto measure tool" was used to select individual AVs to obtain the area measurements (in μm^2), and to quantify the number of AVs present per cell analysed. The data was then exported to Statistica® 13 software for statistical analysis.

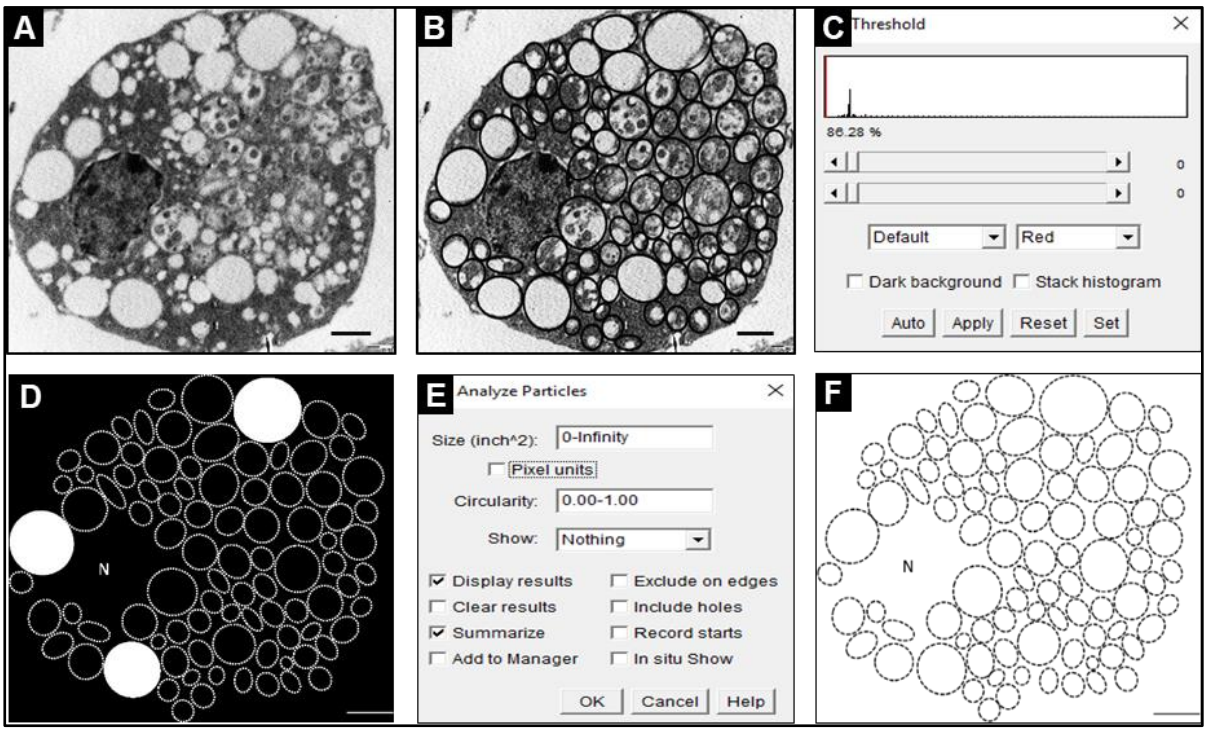

Figure 2.1: Quantitative morphometric analysis of TEM micrographs. A. Representative micrograph of an N2aswe cell captured at low magnification. **B.** Particle outline and segmentation of vacuolar bodies. **C, D.** Setting of threshold range to distinguish vacuolar bodies apart from the background. **E, F.** Automated estimation of the surface area (μm^2) using the empirical parameters (spherical body estimate, density of the body radii, recognition threshold, and calculation range).

2.8. Global proteome analysis

2.8.1. Liquid chromatography-mass spectrometry-based proteome analysis

Liquid chromatography coupled with mass spectrometry (LC-MS) based proteomics consists of two powerful separation techniques that allow the sample (s) of interest in highly complex mixtures to be isolated and interrogated for their global proteolytic

profile (Mesaros and Blair, 2016). LC-MS is a robust technique that combines the dual selectivity, and physical separation capabilities of liquid chromatography with the mass analysis capabilities of mass spectrometry. The basic LC-MS processes is performed as follows: (1) introduction of sample onto a mass spectrometry device for subsequent vaporization, (2) ionization; sample components are ionized by an electron ionization source which exposes the analyte, under a vacuum, to a stream of electrons produced from a heated filament to create ions, (3) analyser sorting; the ions are sorted in an analyser according to their m/z ratios through the use of electromagnetic fields, (4) detector; the ions are then passed through a detector in which the ion flux is converted into electrical current and (5) data conversion; the magnitude of the ion/electrical signals is converted into a mass spectrum (Chatfield and Fitzgerald, 2004). A schematic workflow of LC-MS experiment is illustrated in **Fig. 2.2**.

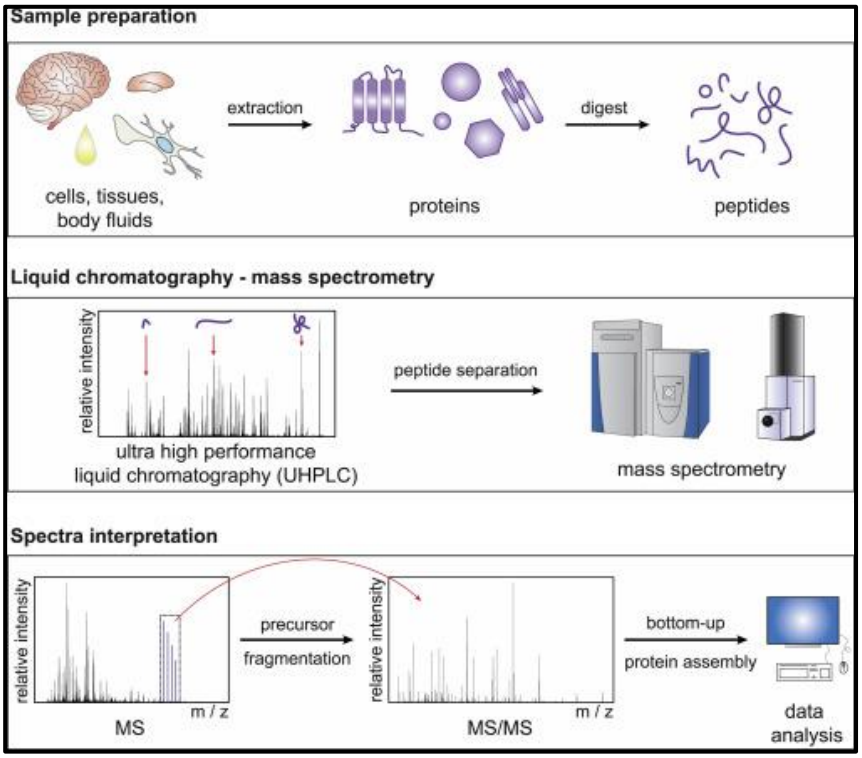

<u>Figure 2.2</u>: LC-MS schematic workflow of sample preparation. Proteins can be extracted from any biological source, e.g. whole tissues, cells, or body fluids. Peptides are separated by liquid chromatography systems to reduce the complexity of the sample. MS analysis is performed by selecting individual peptides, which are then fragmented by collisions, generating tandem mass spectra (MS/MS) containing peptide sequence information. In the final step, organism-specific databases are searched to identify proteins from the peptide sequence information (Hosp and Mann, 2017).

2.8.2. LC–MS sample preparation

N2aswe and N2awt cells were seeded in T75 flasks at a density of $5x10^6$ cells per flask in triplicate, allowed to adhere overnight, and then treated with BA. The former cell line consisted of a control, 24 hrs BA, and 48 hrs BA treatment group. The latter cell line only consisted of a control and 48 hrs BA treated group. Following treatment, cellular protein extraction was carried out according to standard procedures as previously described. After centrifugation of the cell lysates at 8000 RPM for 30 min at 4°C, protein concentrations were determined as previously described, and the supernatant was stored at -80°C for a maximum of 1 week prior to LC-MS analysis. Using a minimal concentration of 70 µg/µl, LC-MS was performed at the CAF Proteomics Unit (Stellenbosch University) using the Thermo Scientific™ UltiMate™ 3000 Rapid Separation systems for high-performance liquid chromatography (HPLC) separations, linked to the Thermo Scientific Orbitrap Fusion™ mass spectrometer. LC-MS was performed as follows:

2.8.2.1. In-solution protein digestion

In-solution digestion was performed to yield shorter peptides with suitable m/z range for MS analysis, as most MS systems require that the analysed particle is not too large and contains adequate number of charges. Several different enzymes, were used for protein digestion. Samples were reduced by adding 50 mM tris carboxyethyl phosphine (TCEP; Fluka) in 100 mM triethylammonium bicarbonate (TEAB) [final concentration 5 mM (tris(2-carboxyethyl)phosphine) (TCEP)] for 30 min at 37°C. Following reduction, cysteine residues were modified to methylthio using 200mM methane methylthiosulphonate (MMTS; Sigma Aldrich) in 100 mM TEAB (final concentration 20 mM) for 30 min at 37°C. After modification, the samples were diluted to 98 µl with 100 mM TEAB. To allow the identification of peptides participating in sulphur bridges, proteins were digested by adding 5 µl trypsin (Promega) (1 µg/µl) to the samples, which were then allowed to incubate for 18 hrs at 37°C. Trypsin adds a secondary ionization site at the C-terminus of peptides, thereby increasing the coverage of MS fragmentation (Olsen et al., 2004). The samples were then dried down

and resuspended in 100 µl 2% acetonitrile (Fluka): water; 0.1% formic acid (formic acid; Sigma Aldrich).

2.8.2.2. On-column desalting

Given that the mixture of peptides generated by an enzymatic digest can vary in complexity, LC based separation of peptides is required to reduce the complexity of the analyte before entering the MS instrument. Hence, residual digest reagents were removed using an in-house manufactured C_{18} stage tip (Empore Octadecyl C_{18} extraction discs; Supelco). A total of 20 µl of the sample analyte was loaded onto the stage tip after activating the C_{18} membrane with 30 µl methanol (Sigma Aldrich) and equilibrating with 30 µl 2% acetonitrile: water; 0.05% trifluoroacetic acid (TFA). The bound sample was then washed with 30 µl 2% acetonitrile: water; 0.1% formic acid (FA), before elution with 30 µl 50% acetonitrile: water; 0.1% FA. The eluate was evaporated to dryness, and the dried peptides were dissolved in 20 µl 2% acetonitrile: water; 0.1% FA for LC-MS analysis.

2.8.2.3. Liquid chromatography

LC nano-LC-MS was performed on a Dionex™ Ultimate 3000 RSLCnano system (Ultimate 3000, Thermo Scientific) equipped with a 0.5 cm x 300 µm C_{18} trap column and a 35 cm x75 µm in-house manufactured C_{18} (Luna C_{18}, 3.6 µm; Phenomenex) analytical column. The following solvent system was employed for loading: 2% acetonitrile: water; 0.1% FA; solvent A: 2% acetonitrile: water; 0.1% FA and solvent B: 100% acetonitrile: water. Samples were loaded onto the trap column using loading solvent at a flow rate of 15 nl/min from a temperature controlled autosampler set at 7^0C. Loading was performed for 5 min before the sample was eluted onto the analytical column. Flow rate was set to 500 nl/min and the gradient was generated as follows: 2.0% - 10% B over 5 min; 5%-25% B from 5-50 min using Chromeleon non-linear gradient 6 (Chromeleon™ Chromatography Data System), 25%-45% from 50-65 min, using Chromeleon non-linear gradient 6. Chromatography was performed at 50°C and the outflow delivered to the mass spectrometer through a stainless steel

nano-bore emitter.

2.8.2.4. Mass spectrometry

Mass spectrometry (MS) was performed using a Thermo Scientific Fusion mass spectrometer equipped with a Nanospray Flex ionization source. The sample was introduced through the stainless steel nano-bore emitter. Data was collected in positive mode using the Nanospray Flex (Thermo Scientific) nano-ESI source with spray voltage set to 2 kV and ion transfer capillary set to 275°C. Spectra were internally calibrated using polysiloxane ions at m/z = 445.12003 and 371.10024. MS1 scans were recorded in the Orbitrap mass analyser set to 12 000 resolutions over the scan range m/z = 350-1650 with a maximum injection time of 40 ms, or until adaptive gain control (AGC) target of 3e5 was reached. Generated MS data was acquired in profile mode (**Fig. 2.3**). MS2 acquisitions were performed using monoisotopic precursor selection for ion with charges +2 to +6 with error tolerance set to ± 0.02 ppm. Precursor ions were excluded from fragmentation once for a period of 30 sec. Precursor ions were selected for fragmentation in HCD mode using the quadrupole mass analyser with HCD energy set to 32.5%. Fragment ions were detected in the orbitrap mass analyser set to 15 000 resolutions. The AGC target was set to 1e4 and the maximum injection time to 45 ms. The data was acquired in centroid mode. MS data is usually presented as either profile or centroid mode (**Fig. 2.3**. In profile mode, a peak is represented by a collection of signals over several scans, while centroid mode displays the peaks as discrete m/z value weighted by the intensity, thereby generating a significantly smaller file size for faster processing (Murray et al., 2013).

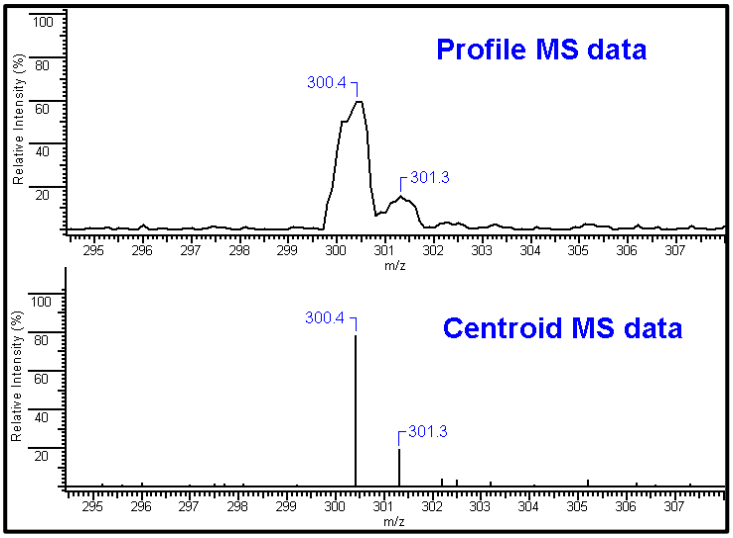

Figure 2.3: Representative mass spectrometry data presentation (Dutta et al., 2015).

2.8.2.5. Data analysis

The raw files generated by the mass spectrometer were imported into Proteome Discoverer™ v1.4 (Thermo Scientific) and processed using the SequestHT algorithm included in Proteome Discoverer. Data analysis was structured to allow for methylthio as fixed modification as well as NQ deamidation (NQ), oxidation (M). Precursor tolerance was set to 10 ppm and fragment ion tolerance to 0.02 Da. The database used was the murine taxonomy database, obtained from UniProt (http://www.uniprot.org/) with the FASTA sequence for amyloid beta A4 P05067 downloaded from the UniProt Knowledgebase, UniProtKB/Swiss-Prot. The results files were important into Scaffold v1.4.7.5 (http://www.proteomesoftware.com) (Proteome Software Inc., Portland, OR) and identified peptides validated using Sequest and X! Tandem (http://thegpm.org/TANDEM/index.html) search algorithms included in Scaffold. Peptide and Protein validation were performed using the Peptide and Protein Prophet algorithms, which automatically validate peptides assignments to MS/MS spectra.

2.8.2.5.1. Bioinformatics analysis: blast search

The basic local alignment search tool (BLAST) was used to compare sequences of

interest against various gene and genome databases, such as the Ensemble Genomes Release 36 (as of May 2017) (http://www.ensembl.org/index.html), which includes the new, updated *Mus musculus* genome assemblies and gene annotation, including updated variation data and comparative genomics analyses from the European Nucleotide Archive (http://www.ebi.ac.uk/ena) and NCBI's reference sequence (RefSeq) database (http://www.ncbi.nlm.nih.gov/RefSeq/).

2.8.2.5.2. Bioinformatics analysis: protein validation strategy

The proteins expressed in the different treatment groups were differentiated using spectral counting, which represents the total number of spectra (peak areas in label free proteomics) identified for a protein satisfying a specified quality threshold (Lundgren et al., 2010; Milac et al., 2012). The data was first normalized prior to standard statistical analyses, using a mathematical normalization technique referred to as the normalized spectral abundance factor (NSAF). Changes in protein expression were compared using *t*-tests. Post hoc analyses were performed with the Benjamini and Hochberg false discovery rate correction. All values were expressed as the mean ± SEM. Significance was accepted at $p<0.05$.

2.8.2.5.3. Bioinformatics analysis: false discovery rate

The false discovery rate (FDR) test is the most widely accepted LC-MS proteomic validation approach, ensuring the accurate and precise estimation of both protein identifications and quantifications (Colquhoun, 2014; Yang et al., 2016). Using this approach, decoy/false versions of the murine taxonomy database was constructed by reversing each protein sequence from the normal murine databases (He et al., 2015). This strategy is based on the premise that decoy protein sequences added to the search space would correspond with incorrect search results that might otherwise be deemed to be correct. With this knowledge, it is possible to estimate how many incorrect results are in a final data set and design a filtering criterion that sensitively separates the data set into correct and incorrect identifications using the decoy hits as a guide.

2.8.2.5.4. Bioinformatics analysis: protein quantification strategy

Peptide hits were accepted if they could be established at greater than 95% probability by the Scaffold Local FDR algorithm. Protein hits were accepted if they could be established at greater than 99.0% probability and contained at least two identified peptides. Protein probabilities were assigned by the Protein Prophet algorithm (Serang and Noble, 2012). Proteins sharing significant peptide evidence were grouped into clusters. Proteins found to be statically different were automatically marked for fold change calculations. These proteins were then further analysed using the STRING v10 functional protein association networks database (https://string-db.org/). The basic interaction unit in STRING is the functional association, i.e. a specific and productive functional relationship between two proteins. Interactions are derived from multiple sources including: (i) known experimental interactions, (ii) pathway knowledge from curated databases, (iii) automated text-mining which is applied to uncover statistical links between proteins, based on Medline abstracts and a large collection of full-text articles, (iv) *de novo* interactions which are predicted by a number of algorithms using genomic information and co-expression analysis (Chiva and Sabidó, 2017; Mei, 2018). All sources of protein-protein interactions are benchmarked and calibrated against previous knowledge, using the high-level functional groupings provided by the Kyoto Encyclopaedia of Genes and Genomes (KEGG) pathway maps (Szklarczyk et al., 2015).

2.9. Animal study: GFP-LC3 transgenic mice

2.9.1. Experimental animals

The generation of green fluorescent protein (GFP)–LC3 expressing transgenic C57BL/6 mice (GFP-LC3) has been extensively described (Mizushima, 2004, 2009b). The expression of the green fluorescent protein (GFP)-linked microtubule-associated protein 1 light chain 3 alpha (LC3) protein is the most widely used marker for autophagosome formation, used in this context, to analyse autophagy in whole animals (Mizushima, 2009b). A GFP-LC3 mouse breeding pair was purchased from the RIKEN Bio- Resource Centre in Japan (http://www.brc.riken.jp/lab/animal/en/dist.shtml #BRC00806). The mice were acclimatized for one week prior to experimentation and maintained at constant ambient temperature (21 ± 1°C) with 12 hrs light/dark cycle and humidity (55 ± 9%) at the Stellenbosch University's animal breeding facility. During this period, mice were provided with water and standard chow *ad libitum*. All procedures were carried out in accordance with the recommendations set forth in the South African national standard for the care and use of laboratory animals for scientific purpose (ISBN 978-0-626-22296-3, SANS 10386:2008) as outlined in the 8th Edition of the South African Veterinary Foundation (http://www.savf.org.za/). All experiments were performed following the protocols approved by Stellenbosch University's Ethical Committee guidelines (ethics approval no. SU- ACUD16-00175). Expression of the GFP-LC3 marker in the whole animal was confirmed using 360 nm goggle instrument in the dark. Green fluorescence could typically be seen on the snout, ears and tail.

2.9.2. Experimental design

A total of 48 GFP-LC3 mice were randomly y assigned into 4 groups of 12, as illustrated in **Fig. 2.4**. Group 1, control group, had *ad libitum* access to a standard chow diet, group 2 was subjected to 48 hrs intermittent fasting (IF), group 3 was subjected to a two-weekly intraperitoneal (i.p.) injection with nonselective herbicide, paraquat (PQ) (Ali et al., 1996; Chen et al., 2012) to mimic the elevated oxidative stress condition observed in the brains of AD patients, and group 4 was the combination treatment group, subjected to 48 hrs alternate day IF, and twice-weekly

PQ i.p. injection. All groups had *ad libitum* access to fresh water throughout the study.

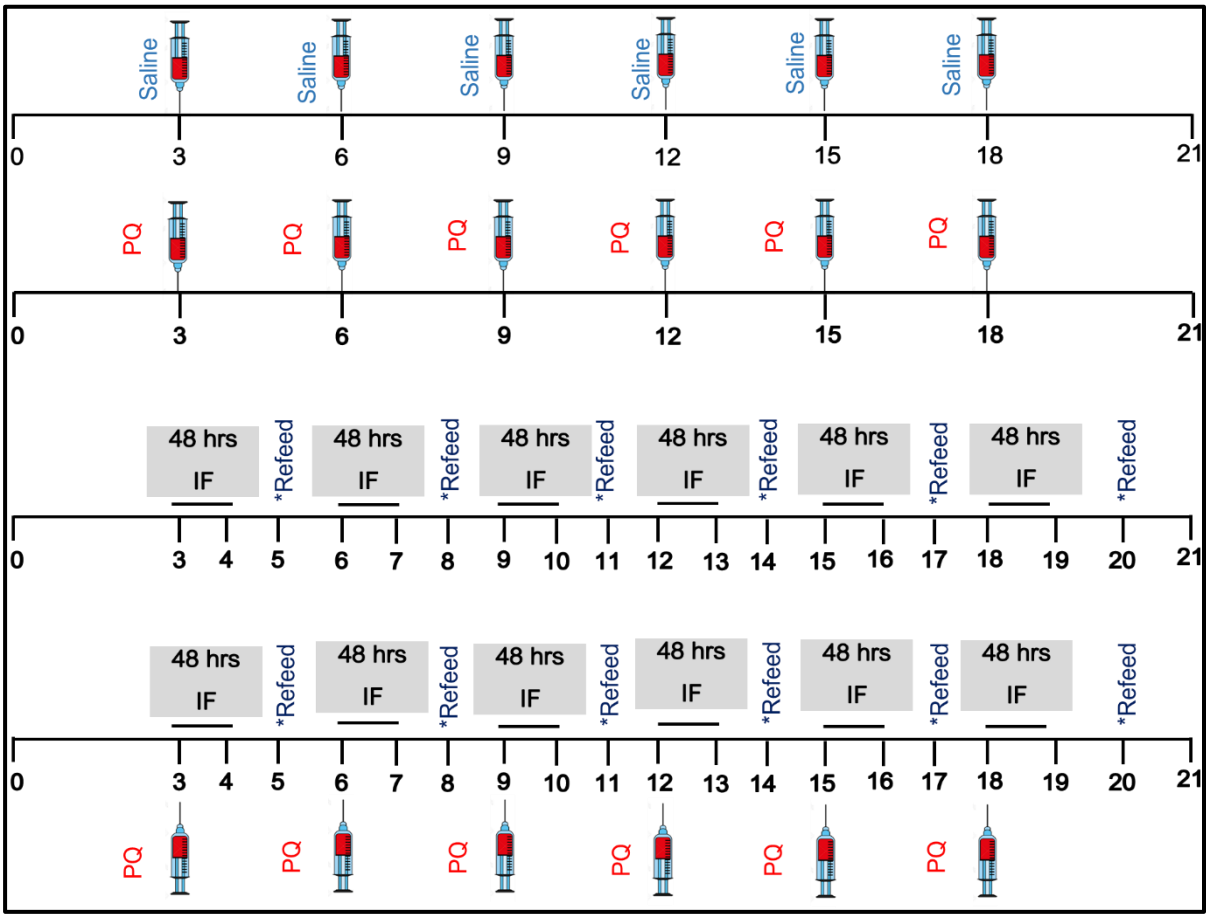

Figure 2.4: *In vivo* study design. (1) Control group, (2) PQ exposed group, (3) 48 hrs IF group, and (4) [(48 hrs IF) + PQ] group.

2.9.2.1. Intermittent fasting treatment intervention

To investigate the effects of IF on the functionality of macroautophagy and CMA in the event of increased ROS in vulnerable neuronal populations from selective brain regions which are crucial to sustained cognition function, eight-week-old male GFP-LC3 mice were deprived of the standard chow diet for 48 hrs, i.e. from 10:00 am on day 1 until 10:00 am on day 3. The mice were then permitted to 24 hrs *ad libitum* access to standard chow following the 48 hrs IF period.

2.9.2.2. PQ treatment protocol

To investigate the effects of PQ in selective brain regions, GFP-LC3 mice were treated with either saline or PQ using a well-established PQ-induced brain injury protocol (Chen et al., 2012). PQ (Sigma-Aldrich, #36541) was reconstituted in sterile saline solution and administered at a dosage of 10 mg/kg for 3 weeks (60 mg/kg total in 6 injections). Mice were weighed immediately prior to PQ administration by i.p. injection using a 26 g needle twice weekly. Control mice were i.p. injected with saline using the same volume as that in the PQ exposed and [(48 hrs IF) + PQ] groups.

2.9.2.3. Animal welfare monitoring

Each animal was closely monitored daily, including weekends, and various observations were recorded [**ADDENDUM B (Table B1-B2)**].

2.9.2.4. Animal sacrifice and whole brain extraction

Two mice per group were sequentially euthanized by cervical dislocation from 10 am to 10 pm. Whole brain tissue was carefully excised by inserting sterile surgical scissors and cutting first laterally and then anteriorly through each skull, and then cutting toward the midline. The skull was carefully lifted upward and peeled back to expose the hindbrain. The intact brain was extracted using curved forceps, and subsequently placed on a pre-chilled petri dish filled covered with wet filter paper. Whole brain tissues were then rapidly sectioned into two equal parts by cutting in the sagittal plane using a surgical scalpel. One part, was rapidly dissected into the cortex, cerebellum, and the hippocampus using a dissecting microscope, transferred to a pre-labelled 2 ml Eppendorf tube, snap-frozen in liquid nitrogen, and stored at -80°C for western blotting analysis. The second part, to be used for immunofluorescence analysis, was completely immersed in isopentane at -30°C for less than 5 secs to preserve the shape of the brain, transferred to a pre-labelled 2 ml Eppendorf tube and snap-frozen in liquid nitrogen within 30 secs to avoid expansion or cracking.

2.9.3. Tissue preparation for immunofluorescence analysis

After snap freezing, the second part of the whole brain section was secured to a cryostat pedestal using Jung Tissue Freezing Medium™ (Leica Microsystems). The brain cryomold was left to equilibrate in the Leica CM1100 cryostat (Leica-Microsystems) at -20°C for ~10 to 15 min to prevent cracking of the tissue block wile sectioning. Subsequently, three 5-15 µm thick tissue sections were sectioned using the freezing microtome, the tissue sections were then allowed to attach onto glass microscope slides by air drying for 30 min at RT. Using a hydrophobic barrier pen (Dako), tissue sections were outlined on the microscope slide to ensure optimal coverage of the reagents followed by fixation with 4% PFA for 15 min. The slides were then washed 3x with 1x PBS-T for 5 mins each, and permeabilized using 0.2% Triton X-100 for 2 min at RT. Non-specific binding between the primary antibodies and the tissue was prevented by incubating slides in blocking buffer (5% donkey serum in 1x PBS-T) for 60 min. Subsequently, slides were incubated with various primary and secondary antibodies as previously described. Immunofluorescent images of each brain section were acquired using the LSM780 Confocal microscope (Carl Zeiss, Germany) with a 10x and 40x objective lens.

To determine the extent of brain tissue damage caused by an inflammatory stress response to the treatment intervention, blocked tissue sections were probed for Alexa Fluor conjugated glial fibrillary acidic protein (GFAP, **Table 2.3**) for 4 hrs at 4^{o}C. GFAP is highly expressed in numerous cell types of the central nervous system, particularly in astrocytes where GFAP is generally highly expressed in response to brain injury (Kamphuis et al., 2012; Li et al., 2017b). PQ is a prolific inducer of oxidative stress; therefore, blocked tissue sections were also probed for 4-hydroxynonenal (4HNE, **Table 2.3**). It is well recognized that excessive production of reactive oxygen species (ROS) can lead to oxidative stress and tissue damage (Flora, 2007; Sinclair et al., 1990). ROS reacts with many cellular components including lipids, which can initiate lipid peroxidation (Bergamini et al., 2004). One of the products of lipid peroxidation, 4HNE, is a relatively abundant reactive aldehyde derived from the peroxidation of omega-6-polyunsaturated fatty acids (Poli et al., 2008), and is formed in biological tissues under physiological and pathological conditions (Maniti et al., 2015). Its

concentration increases with oxidative stress and induces deleterious modifications of proteins and membranes (Majima et al., 2002). Moreover, elevated 4HNE expression has been identified in the plasma and brain of AD patients (Ma et al., 2018; Markesbery and Lovell, 1998), and in colocalization with Aβ deposits (Huang et al., 2016). To assess the effects of increased oxidation on 4HNE production, blocked tissue sections were incubated in 4HNE primary antibody overnight at 4°C and prepared for confocal microscopy analysis as described previously.

2.9.3.1. H & E staining of brain tissue

As previously described, H & E stains were used the detailed assessment of cellular structures including the cytoplasm, nuclei and selective extracellular components.

2.9.3.1.1. Preparation of tissue sections for H & E staining

Stored at -80°C, 5 to 15 µm tissue sections were air dried for ~15-20 min to remove moisture, and processed as follows:

1. Tissue sections were stained with filtered 0.1% Mayer's Haematoxylin (Sigma; MHS-16) for 10 min in a 50 ml conical tube.
2. Using a Coplin jar, tissue sections were rinsed in cool running dH_2O for 5 min.
3. Tissue sections were dipped in 0.5% Eosin (1.5 g dissolved in 300 ml of 95% EtOH) 12x.
4. Tissue sections were dipped in dH_2O until the eosin stopped streaking.
5. Tissue sections were dipped in 50% EtOH 10x.
6. Tissue sections were dipped in 70% EtOH 10x.
7. Staining was equilibrated in 95% EtOH for 30 secs followed by equilibration in 100% EtOH for 1 min.
8. Tissue sections were then dipped in Xylene 5x, and the slide was gently wiped off using a Kim wipe before using Cytoseal XYL (Stephens Scientific; cat# 8312-4) to mount the coverslip, which was then allowed to dry at RT for 1 hr prior to confocal microscopy imaging.

2.9.3.1.2. H & E image acquisition

H & E stained sections were imaged using the Nikon Eclipse E400 phase contrast microscope (Nikon, USA) equipped with a RT Colour Spot Camera (Diagnostics Instruments Inc., USA). Spot Analysis v4.0.9 software (Diagnostics Instruments Inc., USA) was employed for optimization of image quality and image acquisition.

2.9.4. Western blot analysis: brain tissue

2.9.4.1. Sample preparation for western blot analysis

Frozen brain tissue sections including the cerebellum, cortex and hippocampus region, were dissected into smaller pieces using aseptically treated surgical scissors while on ice. For a ~10 mg piece of brain tissue, 500 µl ice cold RIPA buffer supplemented with protease and phosphatase inhibitors was added to the Eppendorf tube and the tissue was rapidly homogenized by sonication on ice, using 3 bursts of 5 secs in the Kine Matica Polytron PT2100 homogenizer (ThermoFisher Scientific). The tissue homogenates were t briefly allowed to settle on ice before being centrifuged at 8000 RPM for 10 min at 4^{o}C. The supernatant was then aspirated from the pellet and transferred to a new pre-chilled Eppendorf tube. After using the Direct Detect™ System (EMD Millipore) to determine the protein concentration of each sample, tissue lysates were prepared for SDS gel loading, and assessed for various proteins according to previously described standard procedures.

2.10. Statistical analyses

All statistical analysis was performed in Statistica 64 v.13 (Dell Inc.). All data sets were assessed for normality and the appropriate tests were performed, including paired Student's t-tests, one-and two-way ANOVA with Fisher's least significance difference test as post hoc test. Bonferroni correction for multiple comparisons was applied where appropriate. Mean values ± standard error of the mean (SEM) are reported. Results were considered statistically significant when $p<0.05$.

CHAPTER 3 RESULTS. *IN VITRO* CHRACTERISATION OF APP OVEREXPRESSION MODEL

3.1. Introduction to results

Neurotoxic deposition of Aβ peptides, owing to increased APP cleavage or decreased Aβ degradation, has been shown to be an early event in AD progression (Selkoe and Hardy, 2016). Elevated Aβ levels have been found in cells from both patients with pre-symptomatic and clinical AD (Citron et al., 1994; Selkoe, 2001), supporting the notion that Aβ overproduction may occur many years prior to the onset of clinical symptoms. Increased Aβ levels have been shown to correlate with the level of cognitive decline observed in AD patients, supporting the hypothesis that failure to regulate the production and clearance of Aβ, leads to neurotoxicity and contributes to AD pathogenesis (Bharadwaj et al., 2009). Moreover, studies comparing Aβ levels in young (3 months old) and old (12 to 15 months old) mice found that the half-life of Aβ within the brain interstitial fluid is doubled in older animals (Herukka et al., 2015). This data indicates that AD progression may be primarily associated with diminished Aβ clearance from the brain, in part, due to a diminished protein clearance capacity, with age. In order to assess the role of macroautophagy (MA) and CMA in this context, mouse neuroblastoma (N2a) cells stably expressing: (i) the APP Swedish double mutation K670N/M671L shown to augment Aβ production (N2aswe); (ii) human wild-type APP695 (N2awt); and (iii) N2a cells transfected with an empty vector (N2avec) were utilized as a means to mimic *in vitro* APP processing that may be associated with that observed in the human condition in AD. N2aswe cells were incubated in BA-containing medium for 12, 24, 36, and 48 hrs to simulate the effects of early and late amyloidogenesis. Notably, BA treatment is specific for the induction APP transgene CMV promoter (Lo et al., 1994). To rule out the potential influence of BA treatment on the APP expression levels observed in N2awt, and N2avec cells, these cells were treated with BA to validate the null-effect of this compound.

3.2. Results

3.2.1. Validation of APP overexpression model: western blot analysis of APP, Aβ, and LC3II in N2avec/N2awt/N2aswe cells

As shown in **Fig. 3.1.A**, APP protein expression is significantly increased in the 24 hrs BA treated N2aswe cells [1.65 ± 0.05 ($p<0.05$)] compared to control N2aswe cells [1.16 ± 0.08]. Similarly, APP expression is significantly increased in the 24 hrs BA treated N2awt cells [1.11 ± 0.07 ($p<0.05$)] compared to control N2awt cells [0.76 ± 0.1], with no difference in APP expression in the 24 hrs BA treated N2avec cells [0.14 ± 0.03] compared to control N2avec cells [0.11 ± 0.003] (**Fig. 3.1.B**).

Figure 3.1.C reveals that Aβ protein expression is significantly increased in the 24 hrs BA treated N2aswe cells [0.19 ± 0.02 ($p<0.05$)] compared to control N2aswe cells [0.32 ± 0.03]. No significant difference in Aβ expression is indicated in the 24 hrs BA treated N2awt cells [0.15 ± 0.02] compared to control N2awt cells [0.14 ± 0.03], or in the 24 hrs BA treated N2avec cells [0.04 ± 0.0] compared to control N2avec cells [0.04 ± 0.0] (**Fig. 3.1.D**).

As shown in **Fig. 3.1.E**, LC3II protein expression is significantly increased in the 24 hrs BA treated N2aswe cells [1.38 ± 0.14 ($p<0.05$)] compared to control N2aswe cells [0.8 ± 0.14]. No significant difference in LC3II expression is indicated in the 24 hrs BA treated N2awt cells [0.39 ± 0.1] compared to control N2awt cells [0.36 ± 0.06], or in the 24 hrs BA treated N2avec cells [0.15 ± 0.1] compared to control N2avec cells [0.15 ± 0.0] (**Fig. 3.1.F**).

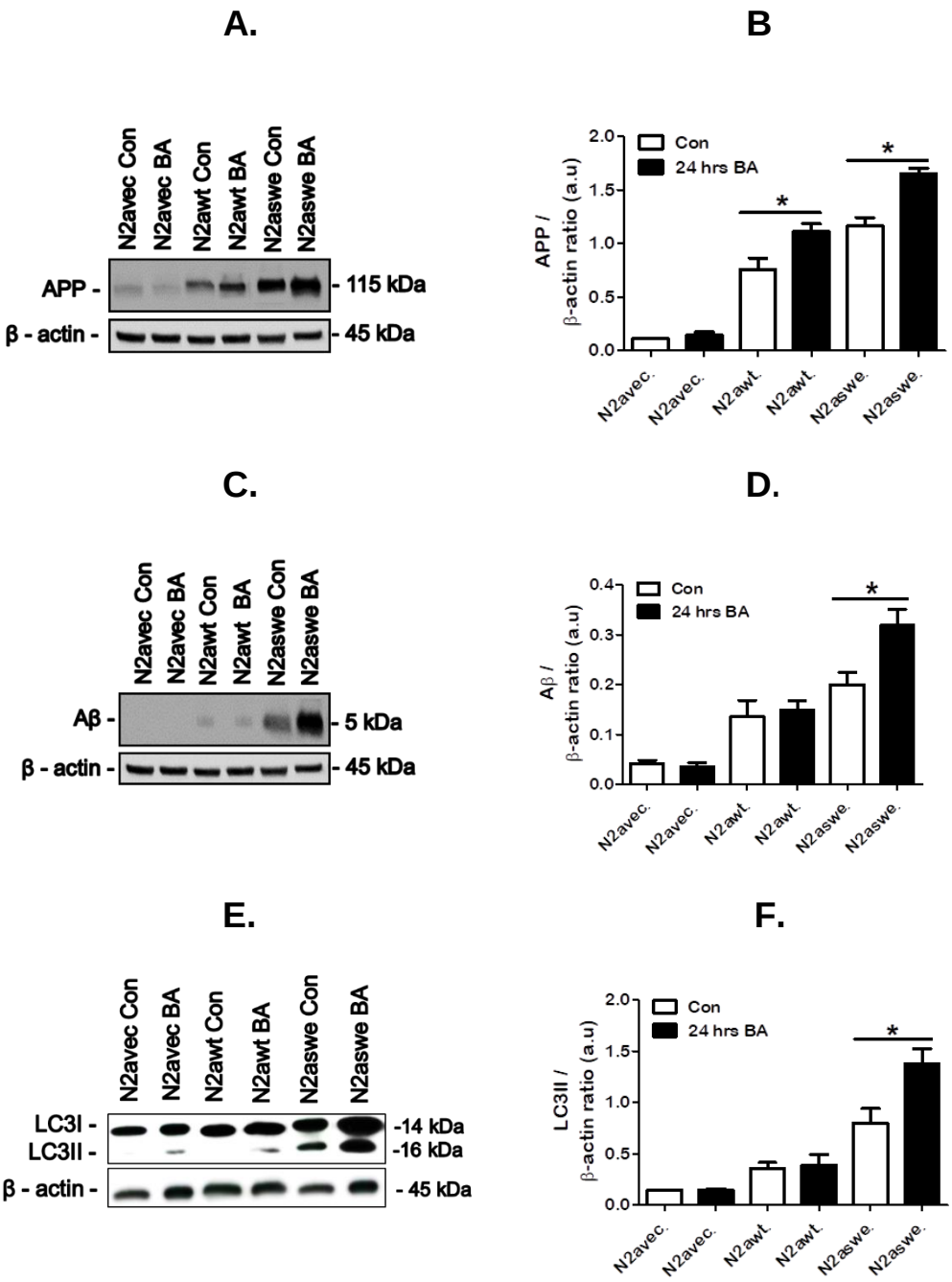

<u>Figure 3.1:</u> Amyloidogenic processing and MA activity in N2avec, N2awt and N2aswe cells in response to 24 hrs APP overexpression. Representative western blot and densitometric analysis for (**A**, **B**) APP, (**C, D**) Aβ, and (**E**, **F**) LC3II protein expression is shown. Data expressed as mean ± SEM, statistical analysis: ANOVA and Bonferroni correction, *p<0.05 vs. cell line specific control, n = 6, arbitrary units (a.u).

3.3. Time-dependent characterization of APP overexpression model

3.3.1. Effect of APP overexpression on cell viability

In order to assess the effects of BA treatment on cell viability, the WST-1 tetrazolium reduction assay was utilized. The results indicate that viability (indicated by the WST-1 tetrazolium product that is directly proportional to the number of viable cells) measured in N2aswe cells is significantly decreased in the 24 hrs BA treated group [0.065 ± 0.005 ($p<0.05$)], 48 hrs BA treated group [0.046 ± 0.002 ($p<0.05$)], 72 hrs BA treated group [0.036 ± 0.002 ($p<0.05$)], 96 hrs BA treated group [0.016 ± 0.004 ($p<0.05$)], 120 hrs BA treated group [0.009 ± 0.002 ($p<0.05$)], and 144 hrs BA treated group [0.006 ± 0.002 ($p<0.05$)] compared to control cells [0.087 ± 0.002] (**Fig. 3.2**). BA treatment time points of 12, 24, 36, and 48 hrs BA exposure were selected for subsequent experiments.

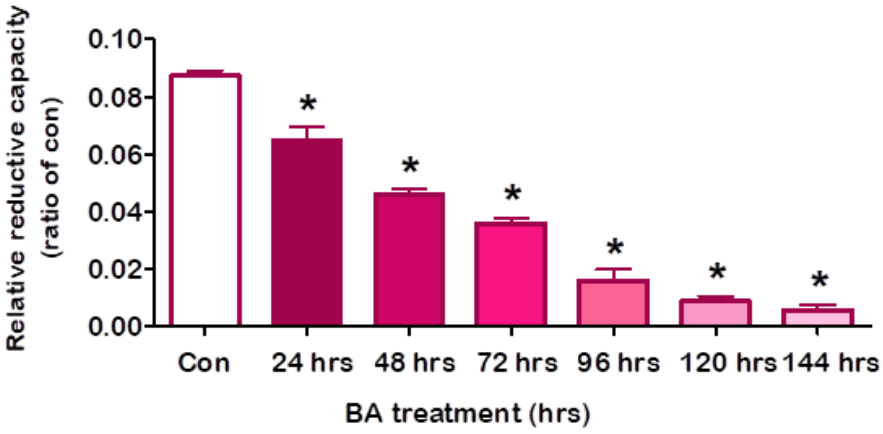

Figure 3.2: Effect of APP overexpression on reductive capacity in N2aswe cells. Data expressed as mean ± SEM, statistical analysis: ANOVA and Bonferroni correction, *$p<0.05$ vs. control.

3.3.2. Western blot analysis of amyloidogenic processing in response to APP overexpression

APP protein expression is significantly increased in the 12 hrs BA treated group [1.69 ± 0.12 ($p<0.05$)], 24 hrs BA treated group [2.79 ± 0.13 ($p<0.05$)], 36 hrs BA treated group [3.17 ± 0.24 ($p<0.05$)], and 48 hrs BA treated group [4.32 ± 0.14 ($p<0.05$)] compared to control cells [0.31 ± 0.03]. Additionally, APP expression is significantly increased in the 48 hrs BA treated group compared to the 24 hrs BA treated group and 36 hrs BA treated group (**Fig. 3.3.B**).

As shown in **Fig. 3.3.C**, β-secretase protein expression is significantly increased in the 24 hrs BA treated group [2.23 ± 0.33 ($p<0.05$)], 36 hrs BA treated group [3.51 ± 0.18 ($p<0.05$)], and 48 hrs BA treated group [4.04 ± 0.19 ($p<0.05$)] compared to control cells [0.5 ± 0.12], with no significant difference in the 12 hrs BA treated group [1.35 ± 0.17] compared to control cells. Additionally, β-secretase expression is significantly increased in both the 36 hrs BA treated group and 48 hrs BA treated group compared to the 24 hrs BA treated group (**Fig. 3.3.D**).

Figure 3.3.E reveals that Aβ protein expression is significantly increased in the 24 hrs BA treated group [1.25 ± 0.07 ($p<0.05$)], 36 hrs BA treated group [1.33 ± 0.08 ($p<0.05$)], and 48 hrs BA treated group [1.52 ± 0.12 ($p<0.05$)] compared to control cells [0.04 ± 0.01], with no significant difference in the 12 hrs BA treated group [0.08 ± 0.01] compared to control cells (**Fig. 3.3.F**).

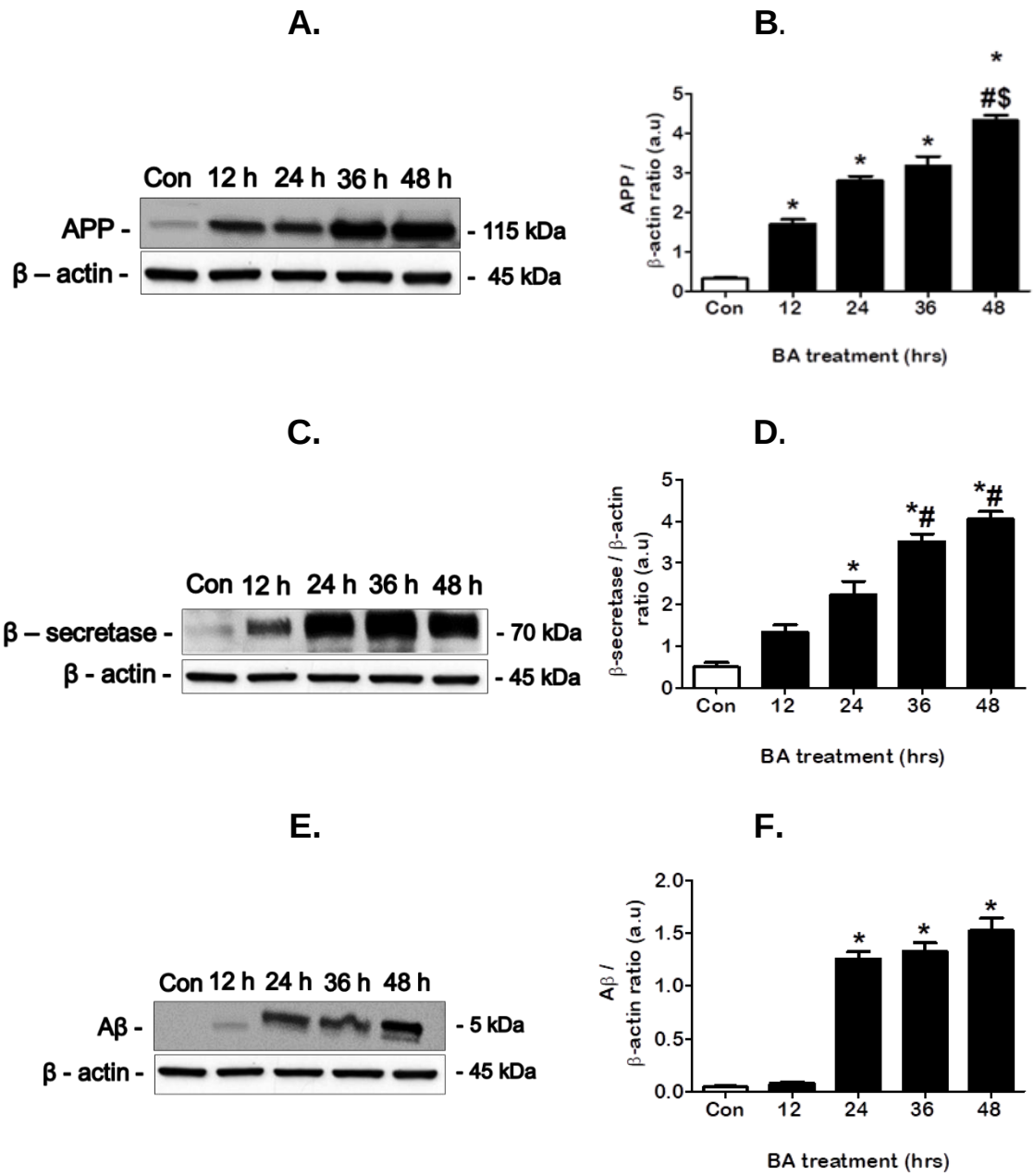

Figure 3.3: Effect of APP overexpression on amyloidogenic processing in N2aswe cells. Representative western blot and densitometric analysis for **(A, B)** APP, **(C, D)** β-secretase, and **(E, F)** Aβ protein expression is shown. Data expressed as mean ± SEM, statistical analysis: ANOVA and Bonferroni correction, *p<0.05 vs. control, #p<0.05 vs. 24 hrs BA, $p<0.05 vs. 36 hrs BA, n = 3, arbitrary units (a.u).

3.3.3. Correlative Light and Electron Microscopy (CLEM) of APP localization in response to APP overexpression

CLEM analysis indicates that APP positive membrane structures (**green**) are increasing shed in a time-dependent manner into the extracellular environment in response to increasing APP expression (**Fig. 3.4**).

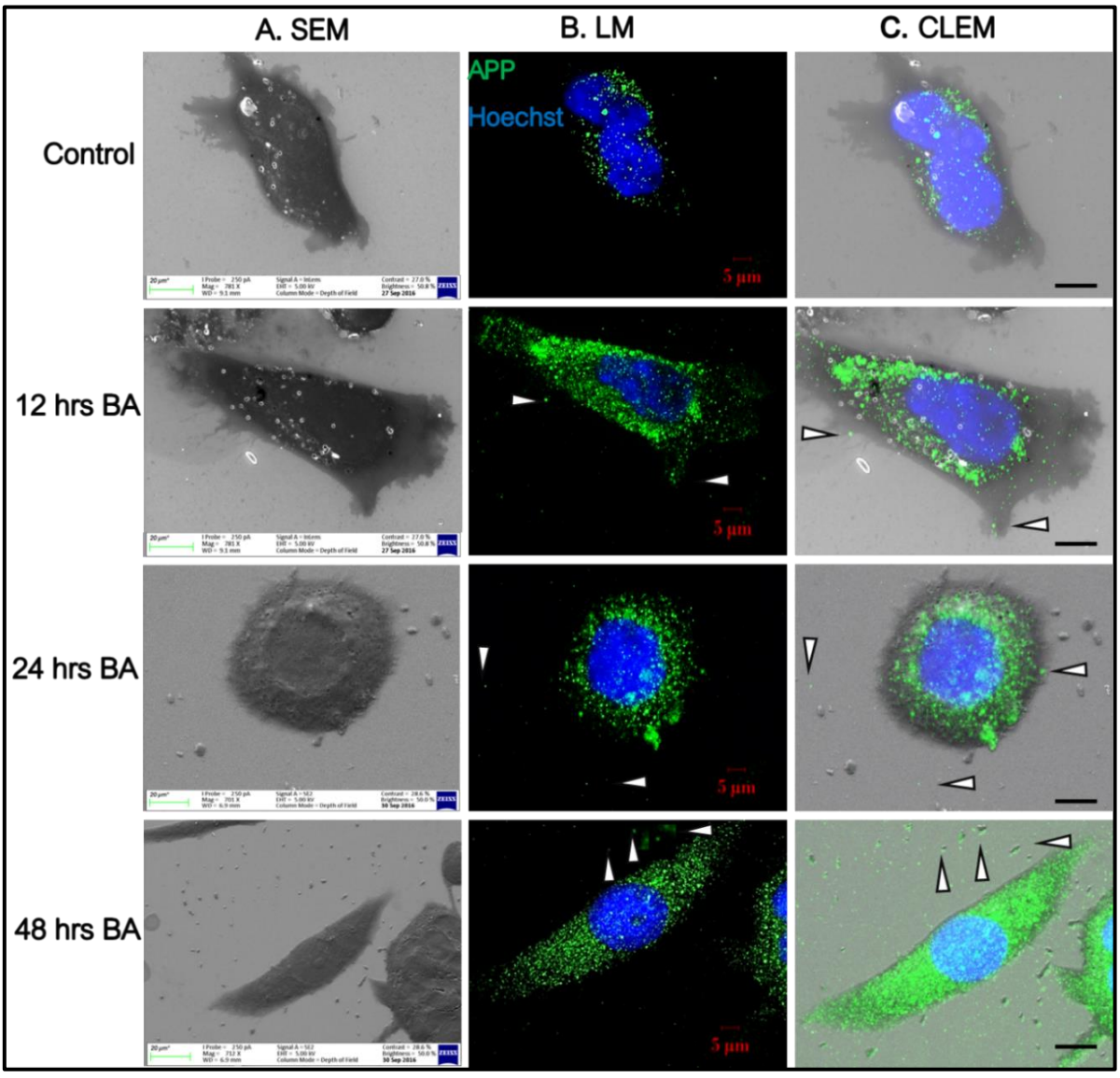

Figure 3.4: CLEM characterization of APP localization in response to APP overexpression. Left panel. Scanning electron microscopy (SEM) micrographs indicating surface topography and composition. **Middle panel.** Light microscopy (LM) micrographs indicating the localization of APP (**green**). **Right panel**. CLEM micrographs of APP localization at different time points. Nuclei are counterstained with Hoechst 33342 (**blue**). SEM and CLEM scale bars indicate 20 µm, LM scale bars indicate 5 µm. Arrowheads indicate APP membrane shedding.

3.3.4. Western blot analysis of key macroautophagy (MA) proteins in response to APP overexpression

As shown in **Fig 3.5.A**, LC3II protein expression is significantly increased in the 24 hrs BA treated group [2.77 ± 0.28 ($p<0.05$)], 36 hrs BA treated group [4.73 ± 0.42 ($p<0.05$)], and 48 hrs BA treated group [6.17 ± 0.53 ($p<0.05$)] compared to control cells [0.09 ± 0.0]. Moreover, LC3II expression is further enhanced in the 36 hrs BA treated group, and 48 hrs BA treated group compared to the 24 hrs BA treated group (**Fig. 3.5.B**).

Figure. 3.5.C reveals that MA cargo protein p62, is significantly increased in the 12 hrs BA treated group [2.79 ± 0.22 ($p<0.05$)], and the 24 hrs BA treated group [2.58 ± 0.28 ($p<0.05$)] compared to both the control cells [0.62 ± 0.12] and 48 hrs BA treated group [6.17 ± 0.53] (**Fig. 3.5.D).**

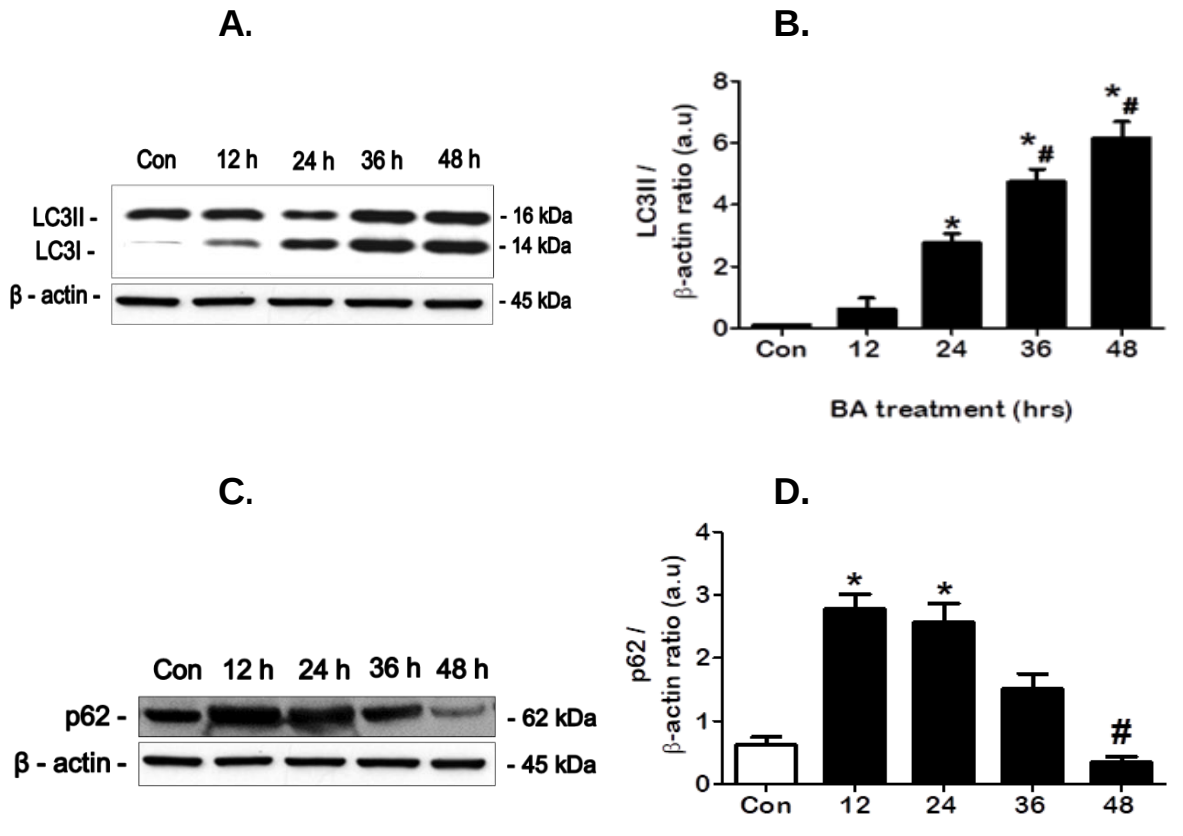

Figure 3.5: Effect of APP overexpression on key MA proteins in N2aswe cells. Representative western blot and densitometric analysis for **(A, B)** LC3II, and **(C, D)** p62 protein expression is shown. Data expressed as mean ± SEM, statistical analysis: ANOVA and Bonferroni correction, *$p<0.05$ vs. control, #$p<0.05$ vs. 24 hrs BA, n = 3, arbitrary units (a.u).

APP localizes in distinct protein clusters that increase in abundance over time. Similarly, Aβ is indicated as cytoplasmic clusters that increase in abundance, particularly in the 24 hrs BA treated group and 48 hrs BA treated group. Similarly, LC3II positive structures are most abundant in the 24 hrs BA treated group, and the 48 hrs BA treated group (**Fig. 3.6**). These data suggest a concomitant increase in MA activity with increasing APP and Aβ protein expression, particularly at later time-points.

3.3.5. Immunofluorescence characterization of APP, Aβ and LC3II localization in response to APP overexpression

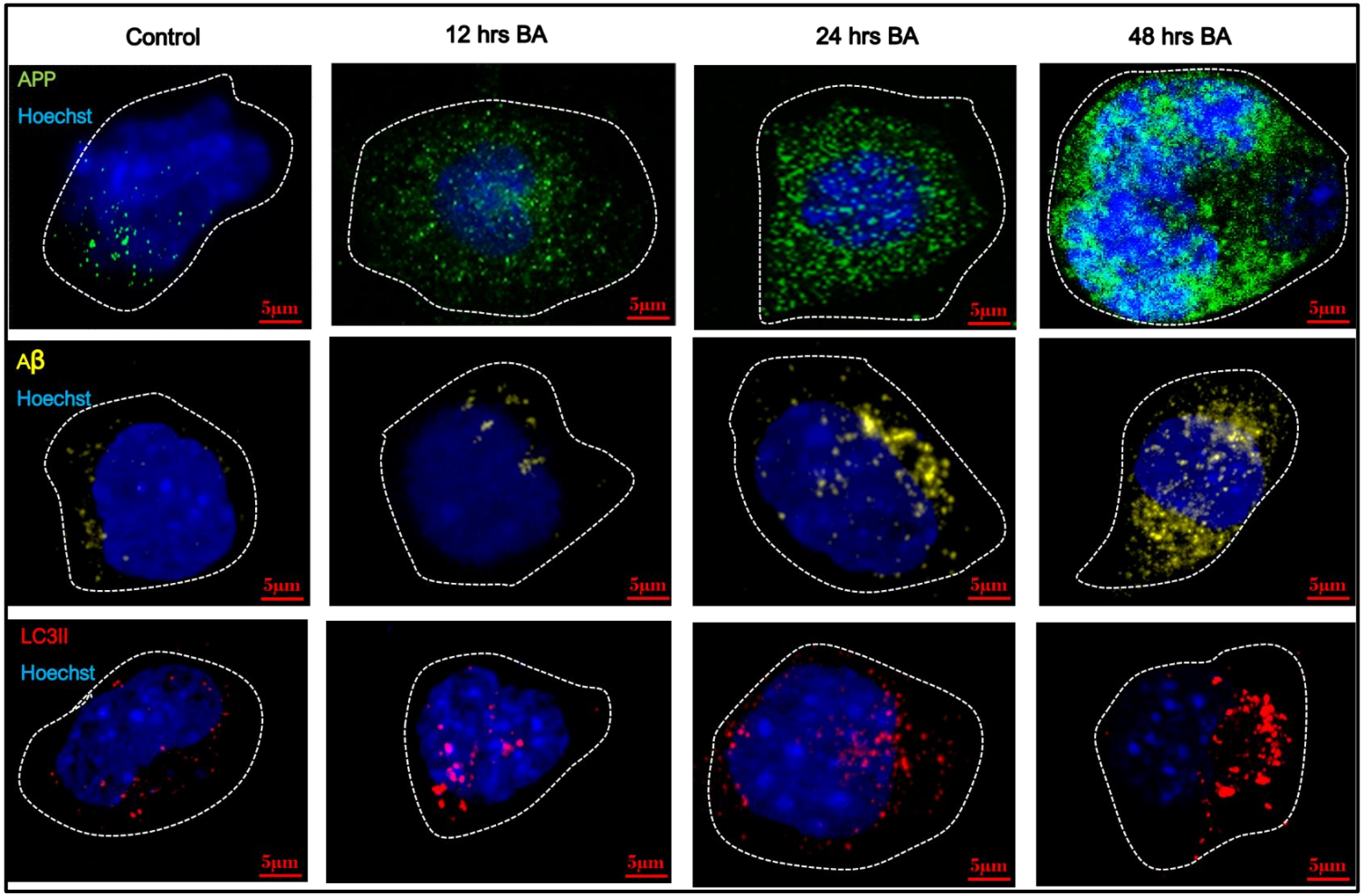

Figure 3.6: Immunofluorescence micrographs indicating a time-dependent increase in APP, Aβ, and LC3II localization in N2aswe cells in response to APP overexpression in time. Representative micrographs of APP **(green),** Aβ (**yellow**), and LC3II (**red**) are displayed. Nuclei are counterstained with Hoechst 33342 (**blue**). Scale bars indicate 5µm. Individual cells are demarcated.

3.3.6. Western blot analysis of key chaperone-mediated autophagy (CMA) proteins in response to APP overexpression

As shown in **Fig. 3.7.A,** LAMP2A protein expression is significantly increased in the 36 hrs BA treated group [2.46 ± 0.19 ($p<0.05$)], and the 48 hrs BA treated group [3.06 ± 0.24 ($p<0.05$)] compared to control cells [1.17 ± 0.08]. Additionally, LAMP2A expression is significantly increased in the 48 hrs BA treated group compared to the 24 hrs BA treated group (**Fig. 3.7.B**).

No significant difference in HSC70 protein expression following BA treatment is indicated for all the treatment groups (**Fig. 3.7.D**).

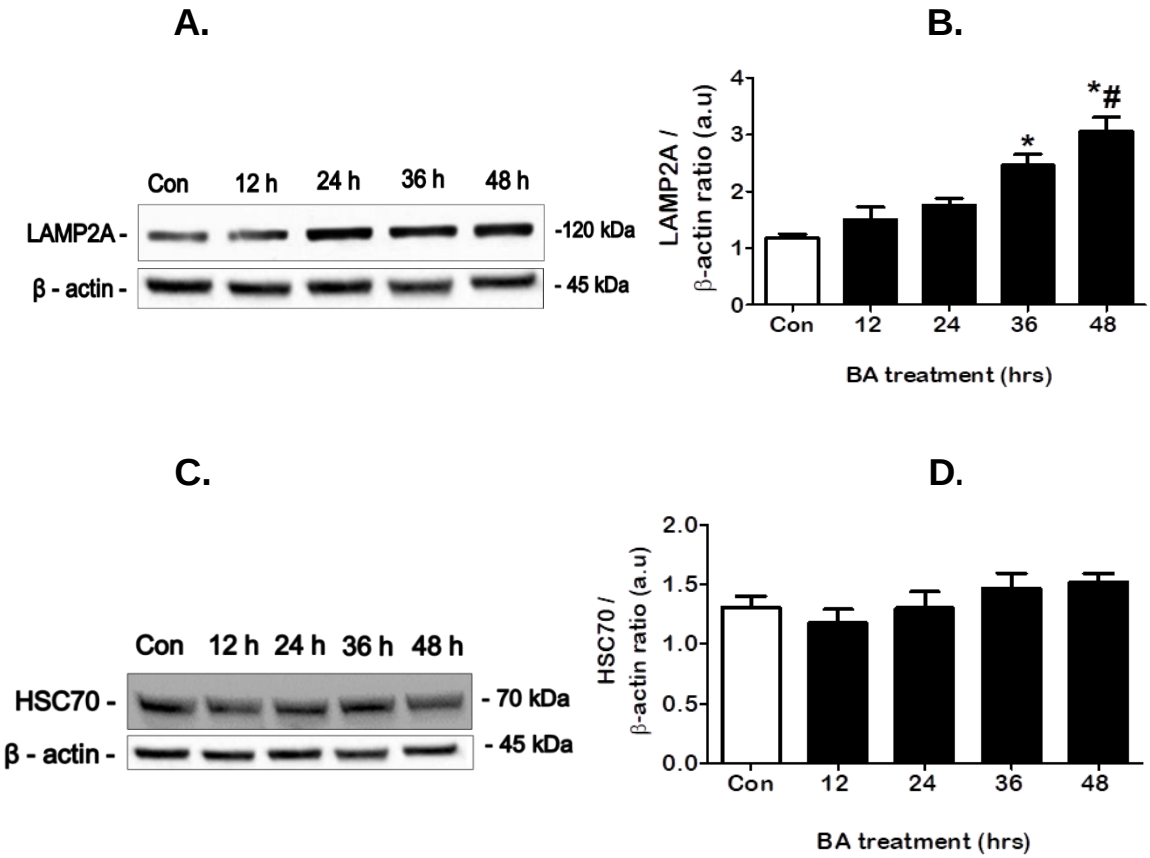

Figure 3.7: Effect of APP overexpression on key CMA proteins in N2aswe cells. Representative western blot and densitometric analysis for **(A, B)** LAMP2A, and **(C, D)** HSC70 protein expression is shown. Data expressed as mean ± SEM, statistical analysis: ANOVA and Bonferroni correction, *$p<0.05$ vs. control, #$p<0.05$ vs. 24 hrs BA, n = 3, arbitrary units (a.u).

3.3.7. Immunofluorescence and colocalization analysis of CMA markers following APP overexpression

Colocalization of HSC70 with LAMP2A is often used to identify the subset of CMA active lysosomes, with the level of colocalization being used as a reliable steady-state indication of the CMA status (Kiffin et al., 2004). Colocalization analysis of key CMA proteins **LAMP2A/HSC70** was performed (**Fig. 3.8.A)**. A significant increase in LAMP2A/HSC70 colocalization is indicated in the 12 hrs BA treated group [0.32 ± 0.02 ($p<0.05$)], 24 hrs BA treated group [0.47 ± 0.02 ($p<0.05$)], and in the 48 hrs BA treated group [0.56 ± 0.03 ($p<0.05$)] compared to control cells [0.23 ± 0.0]. Colocalization is significantly increased in the 48 hrs BA treated group compared to the 24 hrs BA treated group (**Fig. 3.8.B**).

A.

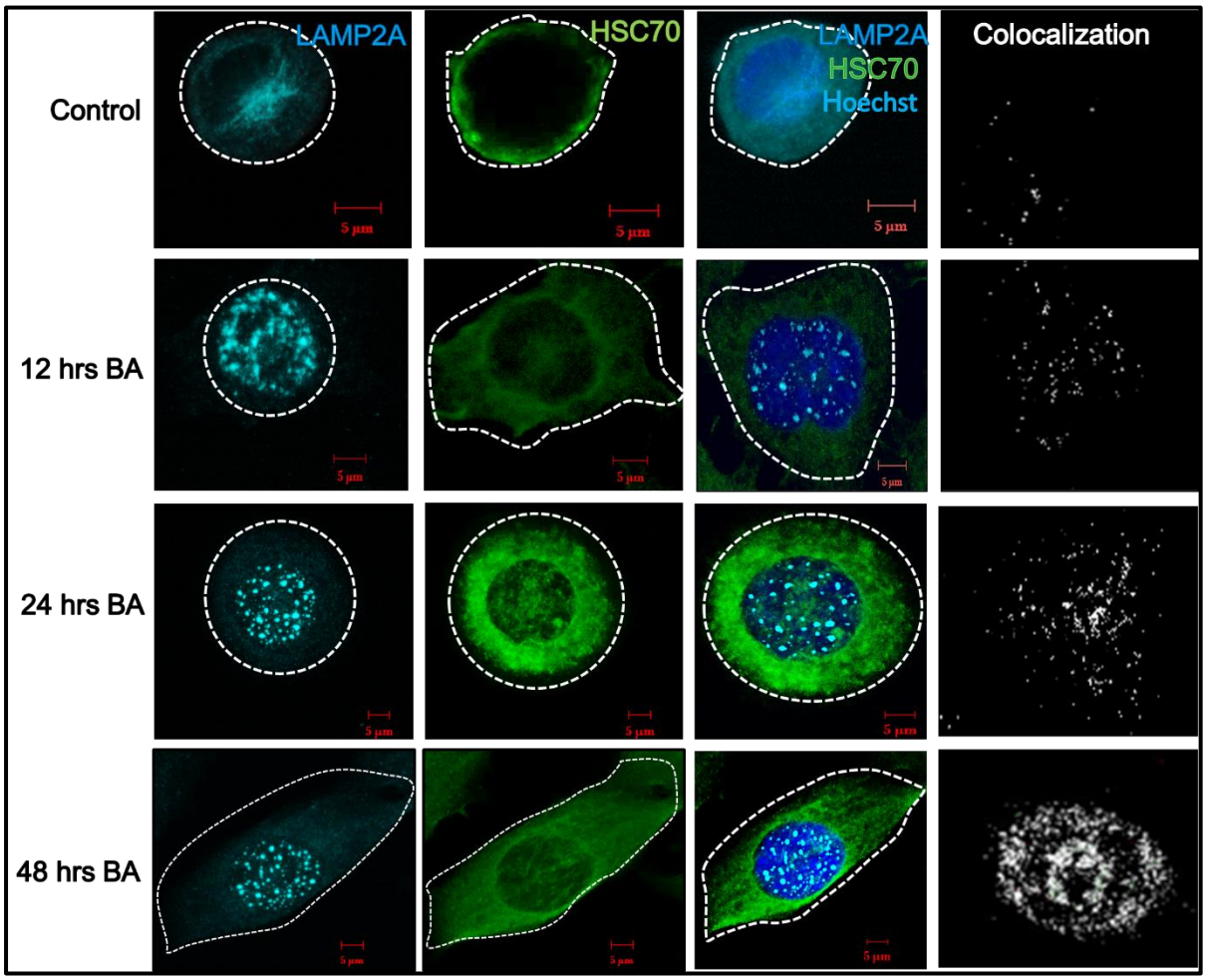

B.

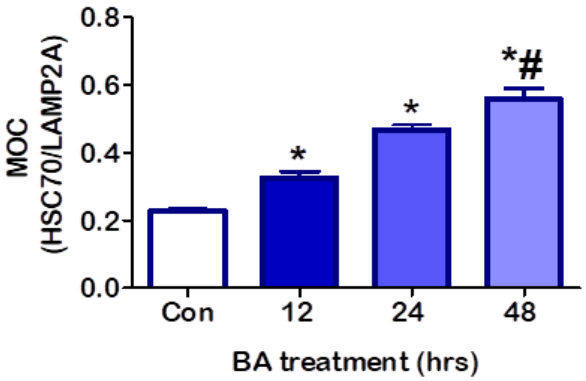

Figure 3.8: Immunofluorescence micrographs indicating colocalization of LAMP2A and HSC70 in N2aswe cells in response to APP overexpression. A. Colocalization of LAMP2A (**cyan**) and HSC70 (**green**) puncta. **B.** Colocalization is quantified using *Mander's Overlap Coefficient* (MOC). Data expressed as mean ± SEM, statistical analysis: ANOVA and Bonferroni correction, *p<0.05 vs. control, #p<0.05 vs. 24 hrs BA, n = 3, a total of 18 cells were analysed, scale bar indicates 5 µm.

3.3.8. Western blot and Caspase-Glo analysis of both expression and activity of key apoptosis proteins in response to APP overexpression

A luminescent assay was utilized to measure the activity of caspase-3 and caspase-7, proteases involved in the execution of apoptosis. The results indicate a significant increase in caspase 3/7 activity in the 24 hrs BA treated group [154.4 ± 10.9 ($p<0.05$)], 36 hrs BA treated group [168.4 ± 15.0 ($p<0.05$)], and 48 hrs BA treated group [208.0 ± 17.6 ($p<0.05$)] compared to control cells [100.0 ± 0.0]. Additionally, the activity of caspase 3/7 is significantly increased in the 48 hrs BA treated group compared to the 24 hrs BA treated group (**Fig. 3.9.A**).

Cleaved-PARP expression is significantly increased in the 24 hrs BA treated group [1.49 ± 0.24 ($p<0.05$)], 36 hrs BA treated group [2.61 ± 0.17 ($p<0.05$)], and 48 hrs BA treated group [2.76 ± 0.24 ($p<0.05$)] compared to control cells [0.04 ± 0.0]. Cleaved-PARP expression remains significantly increased in the 36 hrs BA treated group and the 48 hrs BA treated group compared to the 24 hrs BA treated group (**Fig. 3.9.C**).

Total Caspase-3 protein expression is significantly increased in the 36 hrs BA treated group [1.46 ± 0.12 ($p<0.05$)], and in the 48 hrs BA treated group [1.45 ± 0.1 ($p<0.05$)] compared to control cells [0.59 ± 0.14] (**Fig. 3.9.E**).

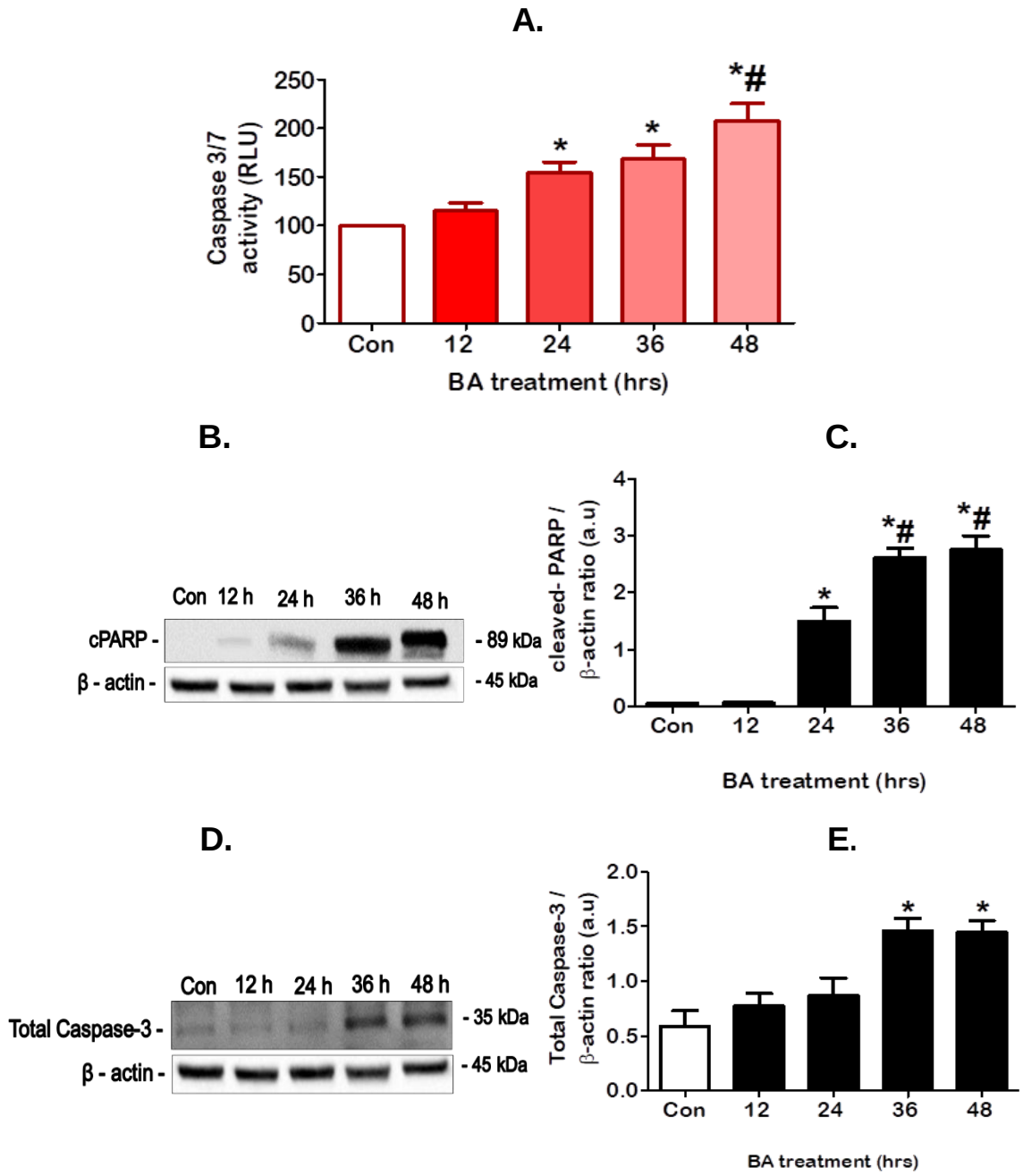

Figure 3.9: Effect of APP overexpression on key apoptosis proteins. **A**. Caspase-3/7 activity in response to APP overexpression. The luminescnt intensity produced is directly proportional to caspase 3/7 activity. Values are expressed as a percentage of the control (100%) in relative luminescence units (RLU). **B**. Representative western blot and densitometric analysis for **(B, C)** cleaved-PARP, and **(D, E)** Total Caspase-3 protein expression is shown. Data expressed as mean ± SEM, statistical analysis: ANOVA and Bonferroni correction, *$p<0.05$ vs. control, #$p<0.05$ vs. 24 hrs BA, n = 3, arbitrary units (a.u).

3.3.9. Immunofluorescence and colocalization analysis following APP overexpression

The cytosolic cargo p62 binds directly to LC3 for co-degradation by MA (Pankiv et al., 2007), and is often used to assess protein turnover through MA. In order to assess the role of APP as a proteinaceous MA cargo, **APP/p62** colocalization analysis was performed (**Fig. 3.10.A)**. A significant increase in APP/p62 colocalization is indicated in the 24 hrs BA treated group [0.63 ± 0.04 ($p<0.05$)], and 48 hrs BA treated group [0.64 ± 0.04 ($p<0.05$)] compared to control cells [0.43 ± 0.03] (**Fig. 3.10.B**).

Studies indicate that LAMP2A antibodies that specifically recognize the amino acid residues that constitute the cytosolic tail of LAMP2A are specific for LAMP2A levels present at the lysosomal membrane, which are limiting on substrate binding and degradation through CMA (Cuervo and Dice, 1996; Kaushik and Cuervo, 2012). In order to assess the role of APP as a proteinaceous CMA cargo, **APP/LAMP2A** colocalization was performed (**Fig. 3.11.A)**. A significant decrease in APP/LAMP2A colocalization is indicated in the 12 hrs BA treated group [0.59 ± 0.02 ($p<0.05$)], 24 hrs BA treated group [0.69 ± 0.03 ($p<0.05$)], and in the 48 hrs BA treated group [0.57 ± 0.03 ($p<0.05$)] compared to control cells [0.41 ± 0.02]. Moreover, APP/LAMP2A colocalization is significantly decreased in the 48 hrs BA treated group compared to the 24 hrs BA treated group (**Fig. 3.11.B**).

A.

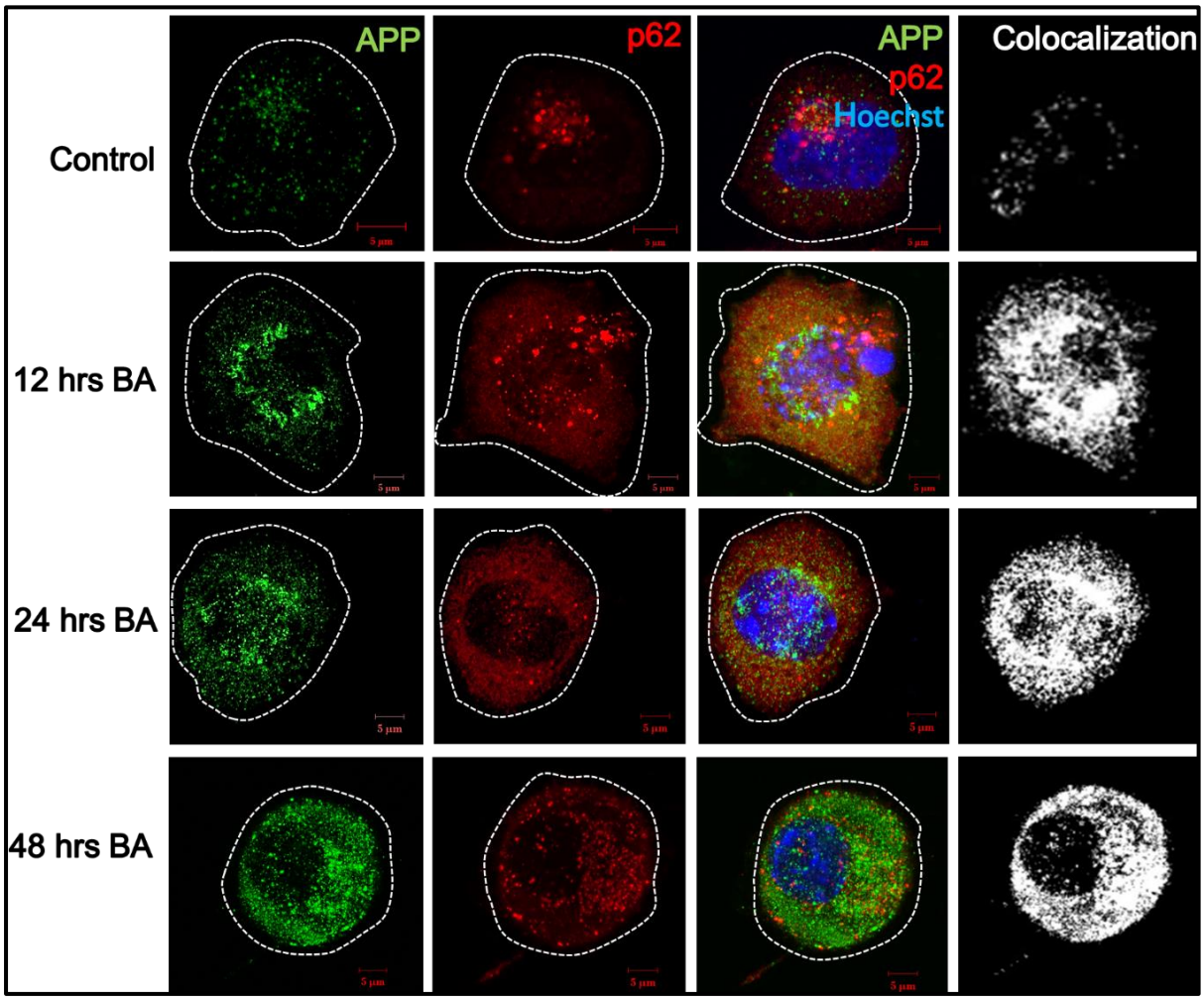

B.

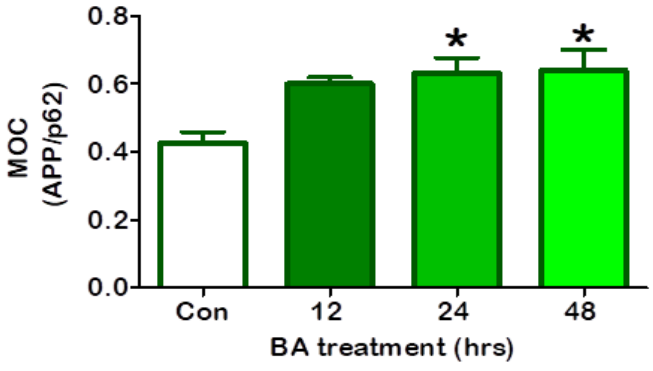

Figure 3.10: Immunofluorescence micrographs indicating colocalization of APP and p62 in N2aswe cells in response to APP overexpression. **A.** Colocalization of APP (**green**) and p62 (**red**). **B.** Colocalization is quantified using *Mander's Overlap Coefficient* (MOC). Data expressed as mean ± SEM, statistical analysis: ANOVA and Bonferroni correction, *p<0.05 vs. control, n = 3, a total of 18 cells were analysed, scale bar indicates 5 µm.

A.

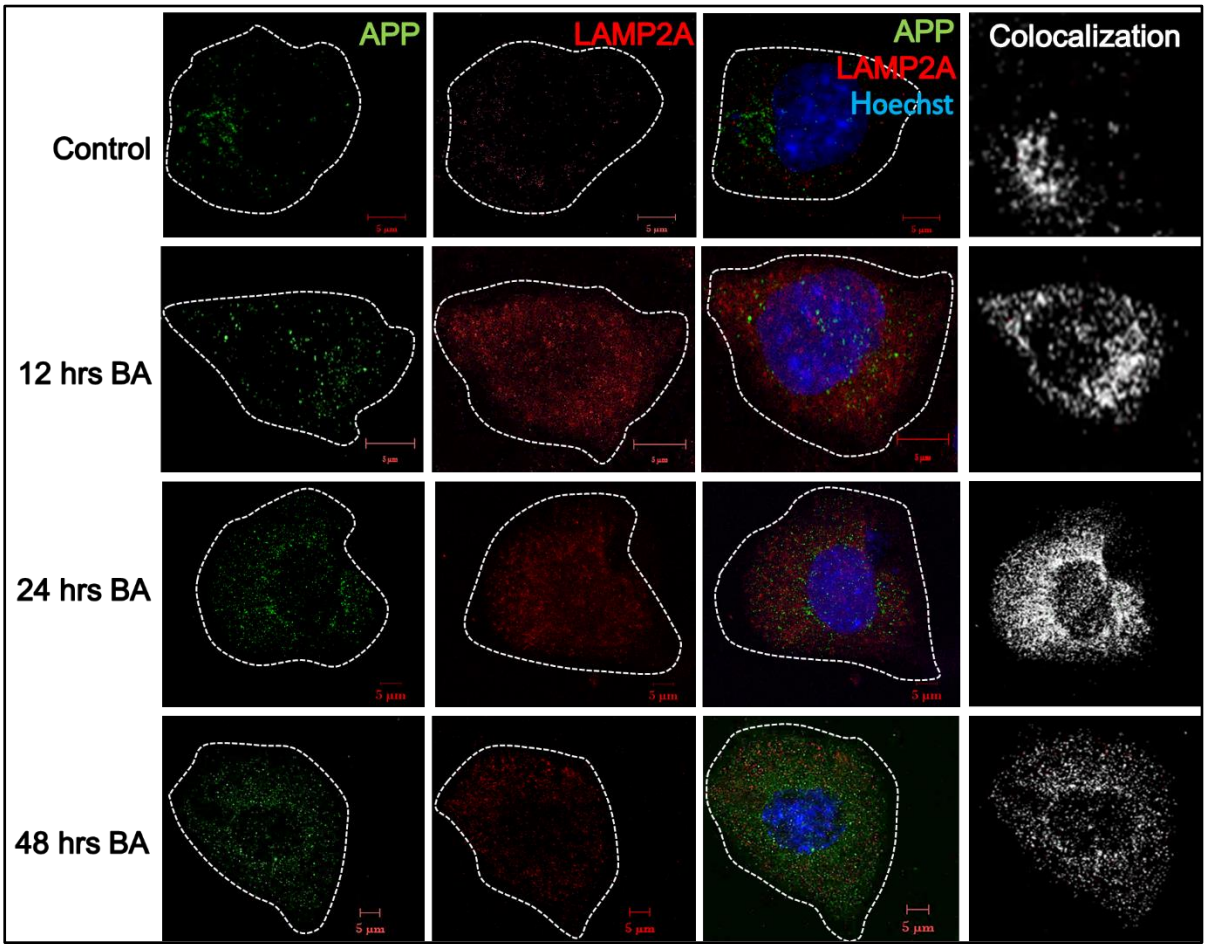

B.

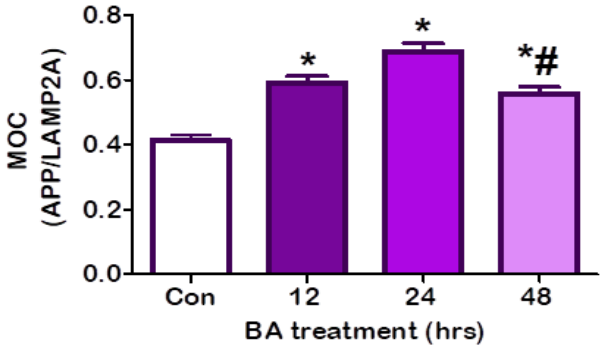

Figure 3.11: Immunofluorescence micrographs indicating colocalization of APP and LAMP2A in N2aswe cells in response to APP overexpression. A. Colocalization of APP (**green**) and LAMP2A (**red**) puncta. **B.** Colocalization is quantified using *Mander's Overlap Coefficient* (MOC). Data expressed as mean ± SEM, statistical analysis: ANOVA and Bonferroni correction, *p<0.05 vs. control, #p<0.05 vs. 24 hrs BA, n = 3, a total of 18 cells were analysed, scale bar indicates 5 µm.

3.4. APP and proteomics

Having determined whether or not MA and CMA are both implicated during APP overexpression, next the proteome signature profile of N2aswe cells was characterised to assess the effects of APP overexpression on the global proteome. A LC-MS based quantitative proteomics approach was utilized to perform a comprehensive large-scale assessment of protein abundance following APP overexpression. Notably, 24 hrs BA treatment and 48 hrs BA treatment is hereafter referred to as early and late APP overexpression.

Venn diagrams, graphs represented as either overlapping or non-overlapping circles, were employed to depict how groups of proteins relate to each other in response to early, and late APP overexpression. As shown in **Fig. 3.12**, the Venn diagram indicates that the largest set of proteins are shared and unique in response to early APP overexpression compared to control cells (**Fig. 3.12.A**). Further analysis was performed using volcano plots, scatter-plots with the − log10 (p-value) from the t-test as shown on the y-axis, and log2 fold change as shown on the x-axis. As shown in **Fig. 3.13**, preliminary analysis reveals that MA associated protein BECN1, CMA associated protein HSP7c, and apoptosis associated protein CASP3 are upregulated upon early APP overexpression, indicated as a 1.6 FC compared to control. Preliminary analysis of **Fig. 3.14** reveals that MA associated protein BECN1, endocytosis protein RAB7a, and amyloidogenic protein APBA1 are upregulated upon late APP overexpression, indicated as a 3.0 FC compared to control. Lastly, preliminary analysis between early and late APP overexpression reveals that CMA protein HSP7c, anti-apoptotic protein BCL6 are upregulated, with APP overexpression indicated as a 2.28 FC when late APP overexpression is compared to early APP overexpression (**Fig. 3.15**).

3.4.1. Assessment of N2aswe cell proteome in response to early and late APP overexpression

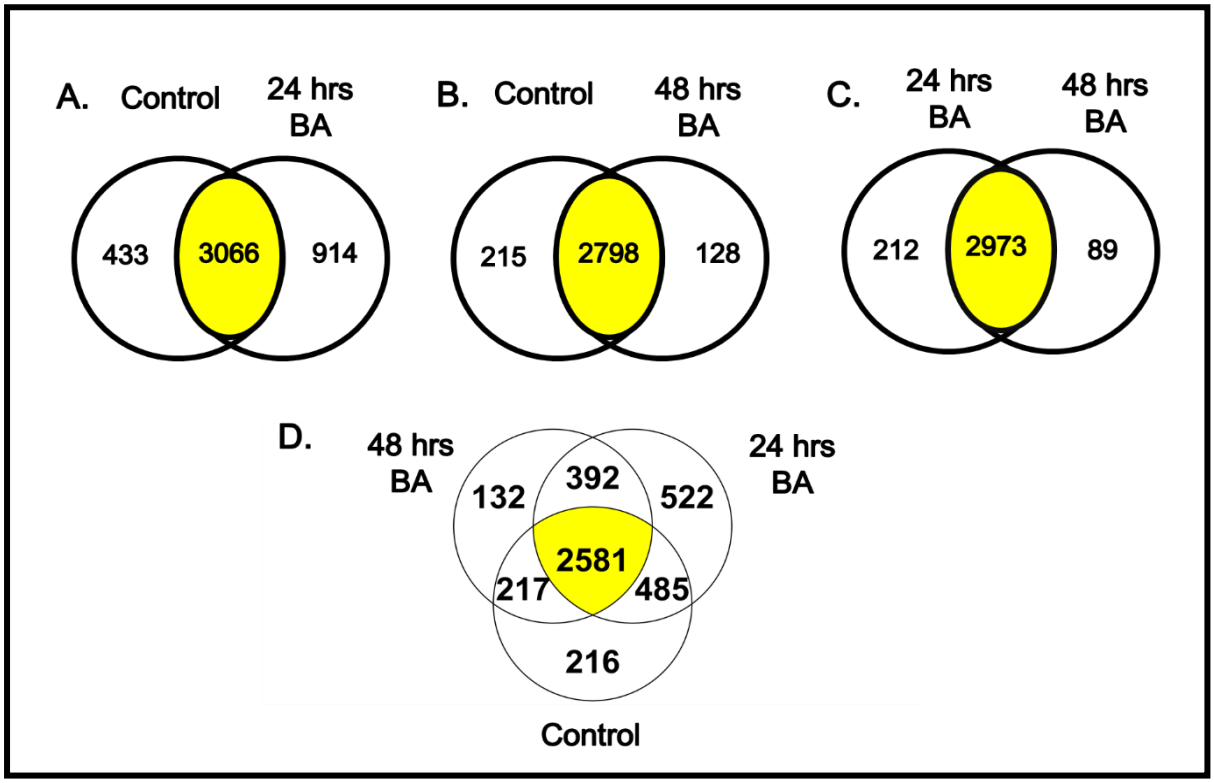

Figure 3.12: Venn diagram indicating shared (yellow), and unique proteins expressed in response to early and late APP overexpression in N2aswe cells. A. Shared and unique proteins expressed between the control and early APP overexpressing group. **B.** Shared and unique proteins expressed between the control and late APP overexpressing group. **C.** Shared and unique proteins expressed between the early and late APP overexpressing group. **D.** The total number of shared and unique proteins expressed between the control, early APP overexpressing group, and late APP overexpressing group.

3.4.2. Volcano plot analysis of early APP proteome signature

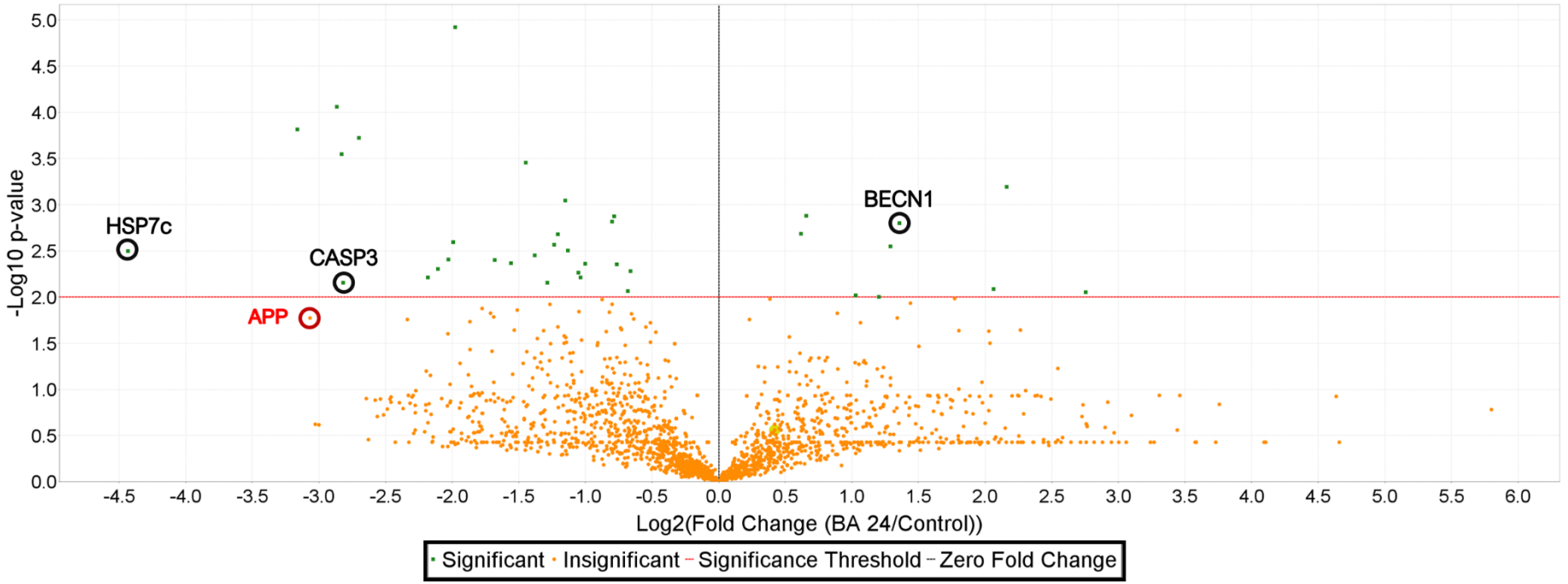

Figure 3.13: Volcano plot indicating changes in the level of protein expression in response to early APP overexpression in N2aswe cells. Differentially expressed proteins are displayed, red dashed line demarcates proteins with a 2.0-fold increase and above ($p<0.05$). Each protein is represented as a dot and is mapped according to its fold change, represented as the − log10 (p-value) from the t-test as shown on the y-axis, and log2 fold change as shown on the x-axis.

3.4.3. Volcano plot analysis of late APP proteome signature

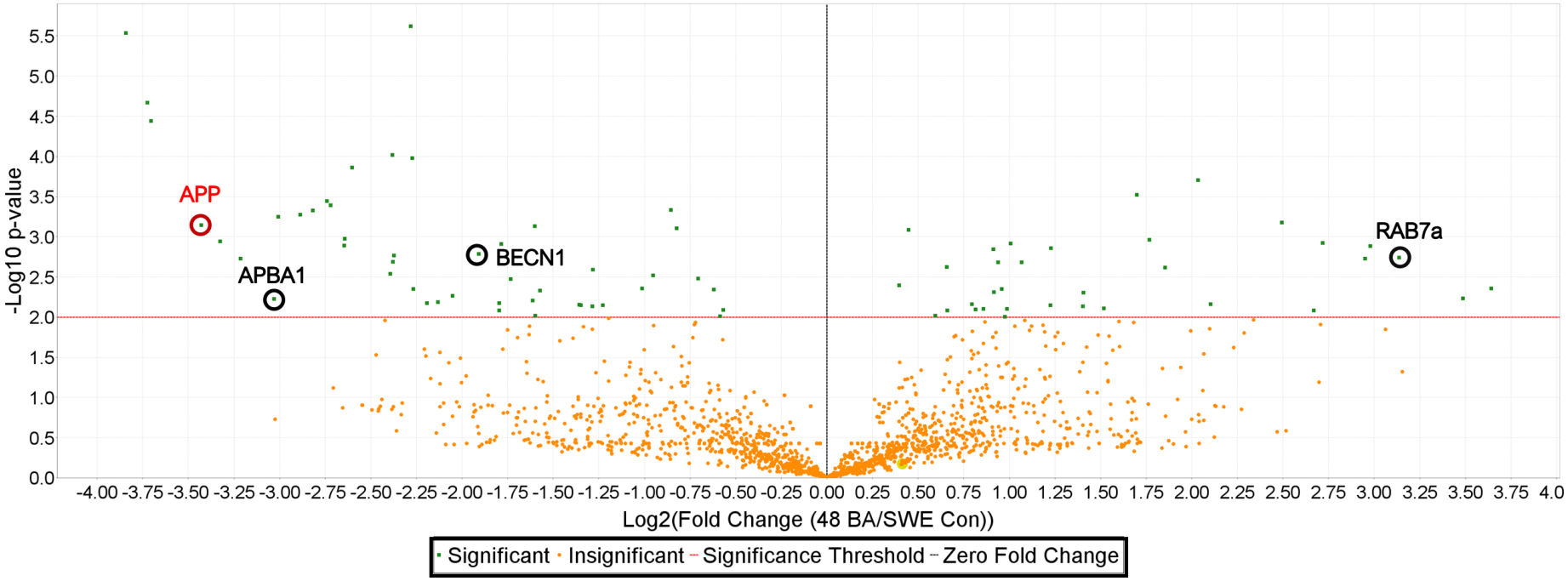

Figure 3.14: Volcano plot indicating changes in the level of protein expression in response to late APP overexpression in N2aswe cells. Differentially expressed proteins are displayed, red dashed line demarcates proteins with a 2.0-fold increase and above ($p<0.05$). Each protein is represented as a dot and is mapped according to its fold change, represented as the − log10 (p-value) from the t-test as shown on the y-axis, and log2 fold change as shown on the x-axis.

3.4.4. Volcano plot analysis of early versus late APP proteome signature

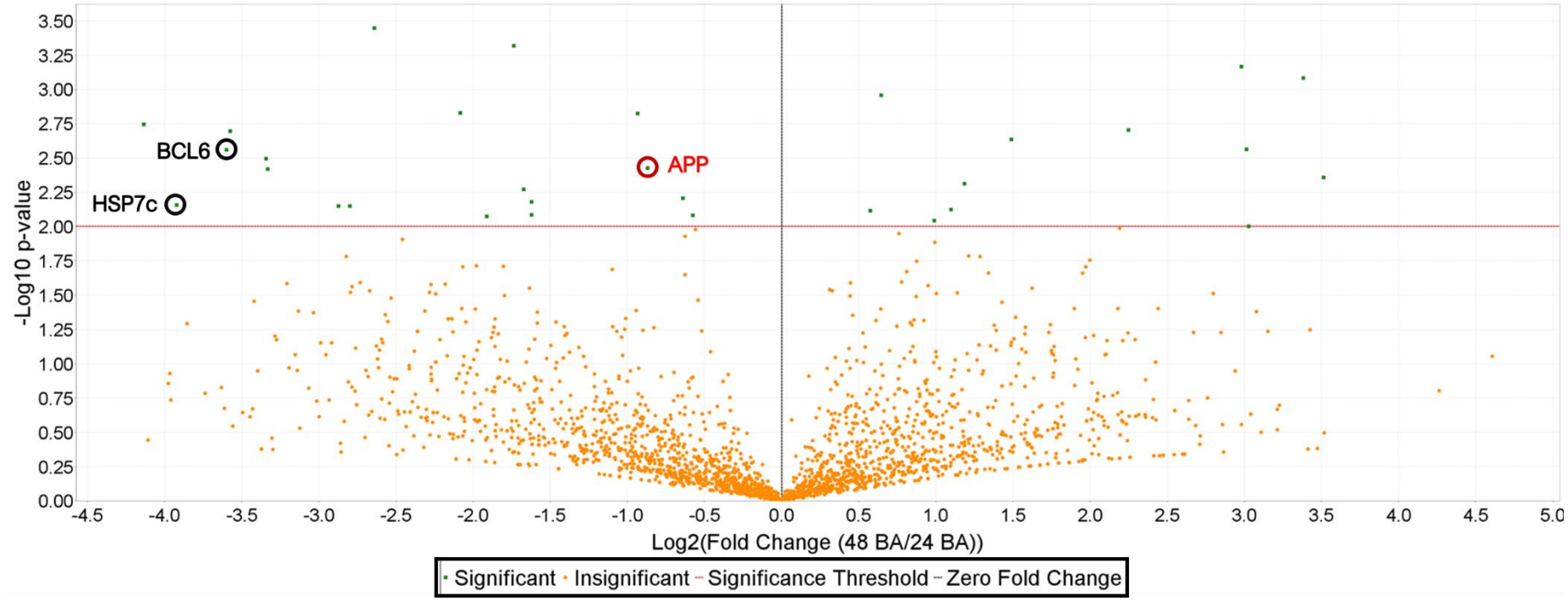

Figure 3.15: Volcano plot indicating changes in the level of protein expression between early and late APP overexpression in N2aswe cells. Differentially expressed proteins are displayed, red dashed line demarcates proteins with a 2.0-fold increase and above ($p<0.05$). Each protein is represented as a dot and is mapped according to its fold change, represented as the − log10 (p-value) from the t-test as shown on the y-axis, and log2 fold change as shown on the x-axis.

To provide a critical assessment of the protein–protein interactions, including direct (physical) and indirect (functional) associations in response to APP overexpression, the STRING (Search Tool for the Retrieval of Interacting Genes/Proteins) database which displays functional associations between proteins on a global scale was employed. As shown in **Fig. 3.16**, the STRING analysis reveals a preliminary direct functional association between early APP overexpression and the following key proteins: MA protein **BECN1**, lysosomal membrane protein **LAMP1**, apoptosis protein **CASP3**, oxidative stress protein **CAT**, glycolytic and CMA cargo protein **GAPDH,** and APP cleaving enzyme **BACE1,** when control cells are set as the reference group.

Figure 3.17 reveals a preliminary direct functional association between late APP overexpression and the following key proteins: amyloidogenic protein **APBA**, and APP cleaving enzyme **BACE1**, apoptosis protein **CASP3**, glycolytic and CMA cargo protein **GAPDH**, and the major blood plasma protein **ALB**, when control cells are set as the reference group.

When the formed protein–protein interactions between early versus late APP overexpression was assessed, the STRING analysis reveals a preliminary direct functional association between the following key proteins: lysosomal aspartyl protease **CATD**, APP cleaving enzyme **BACE1,** and glycolytic and CMA cargo protein **GAPDH** (**Fig. 3.18**)**,** when the early APP overexpressing group is set as the reference group.

3.4.5. The STRING network analysis of early APP proteome signature

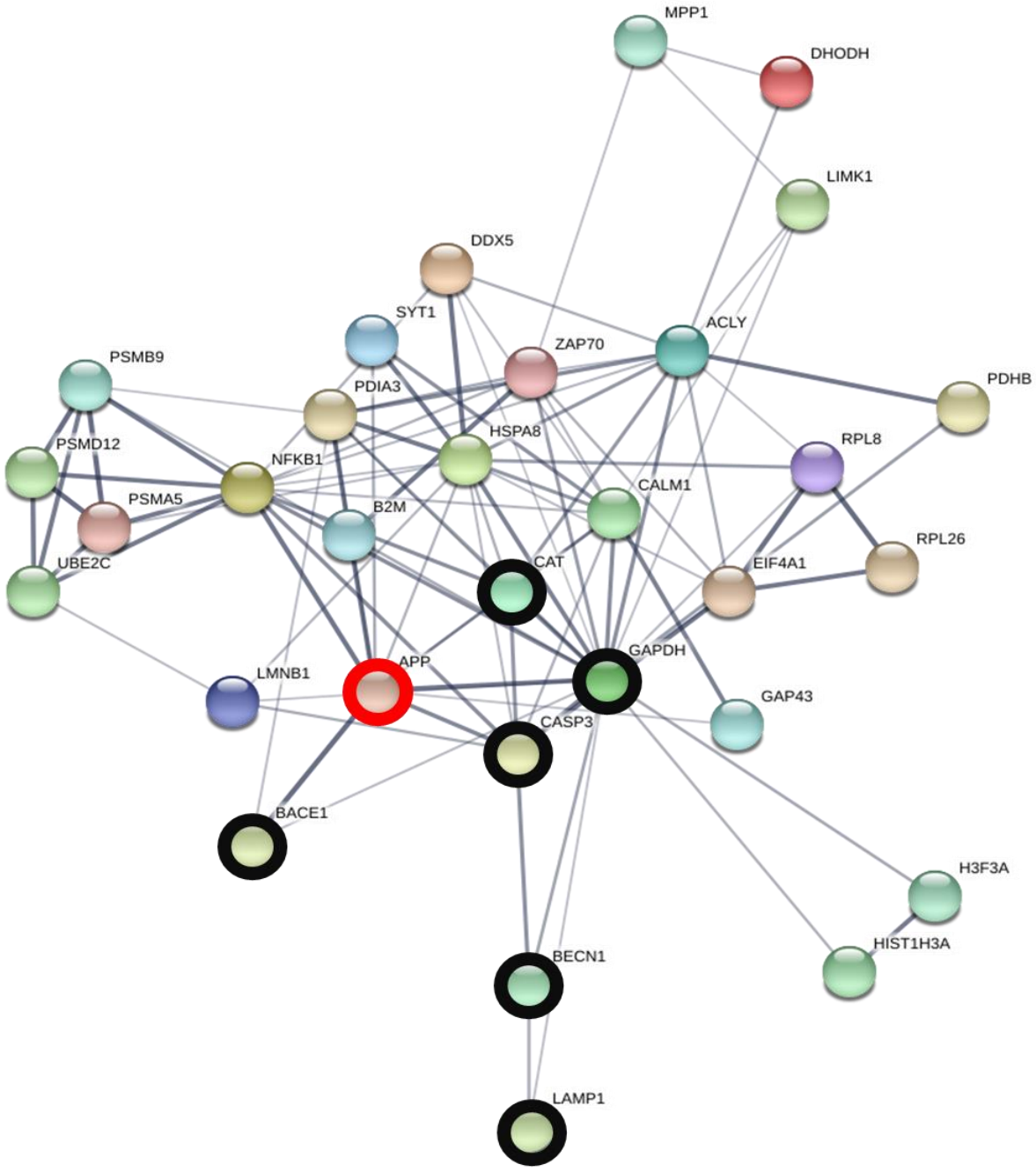

Figure 3.16: Proteome interaction network in N2aswe cells upon early APP overexpression. The STRING proteome network indicates direct protein-protein interactions between proteins with similar coloured nodes. The thicker the connecting line, the greater the strength of evidence for direct association. Red encircled indicates APP; black encircled nodes represent proteins of interest.

3.4.6. The STRING network analysis of late APP proteome signature

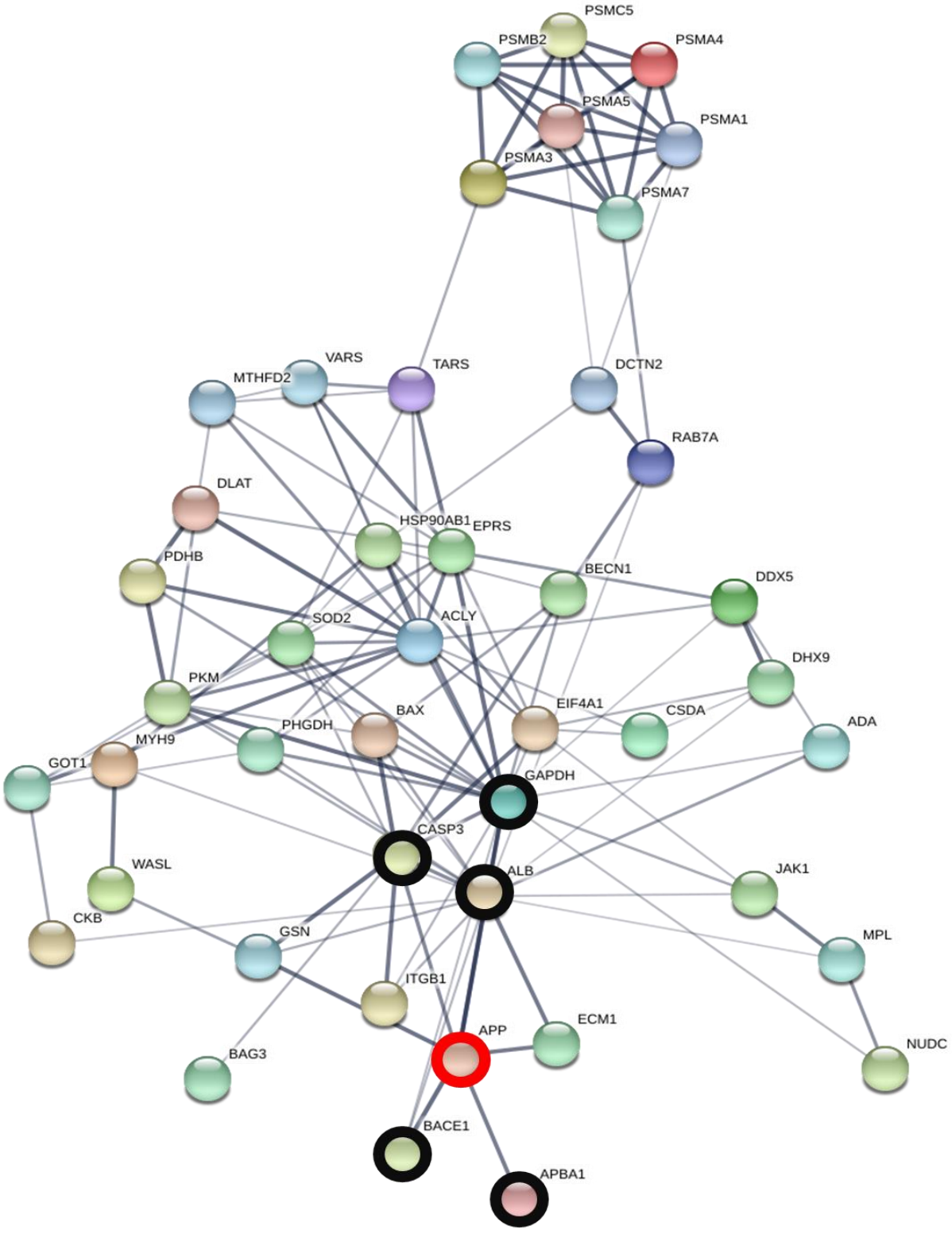

Figure 3.17: Proteome interaction network in N2aswe cells upon late APP overexpression. The STRING proteome network indicates direct protein-protein interactions between proteins with similar coloured nodes. The thicker the connecting line, the greater the strength of evidence for direct association. Red encircled node indicates APP; black encircled nodes represent proteins of interest.

3.4.7. The STRING network analysis of early versus late APP proteome signature

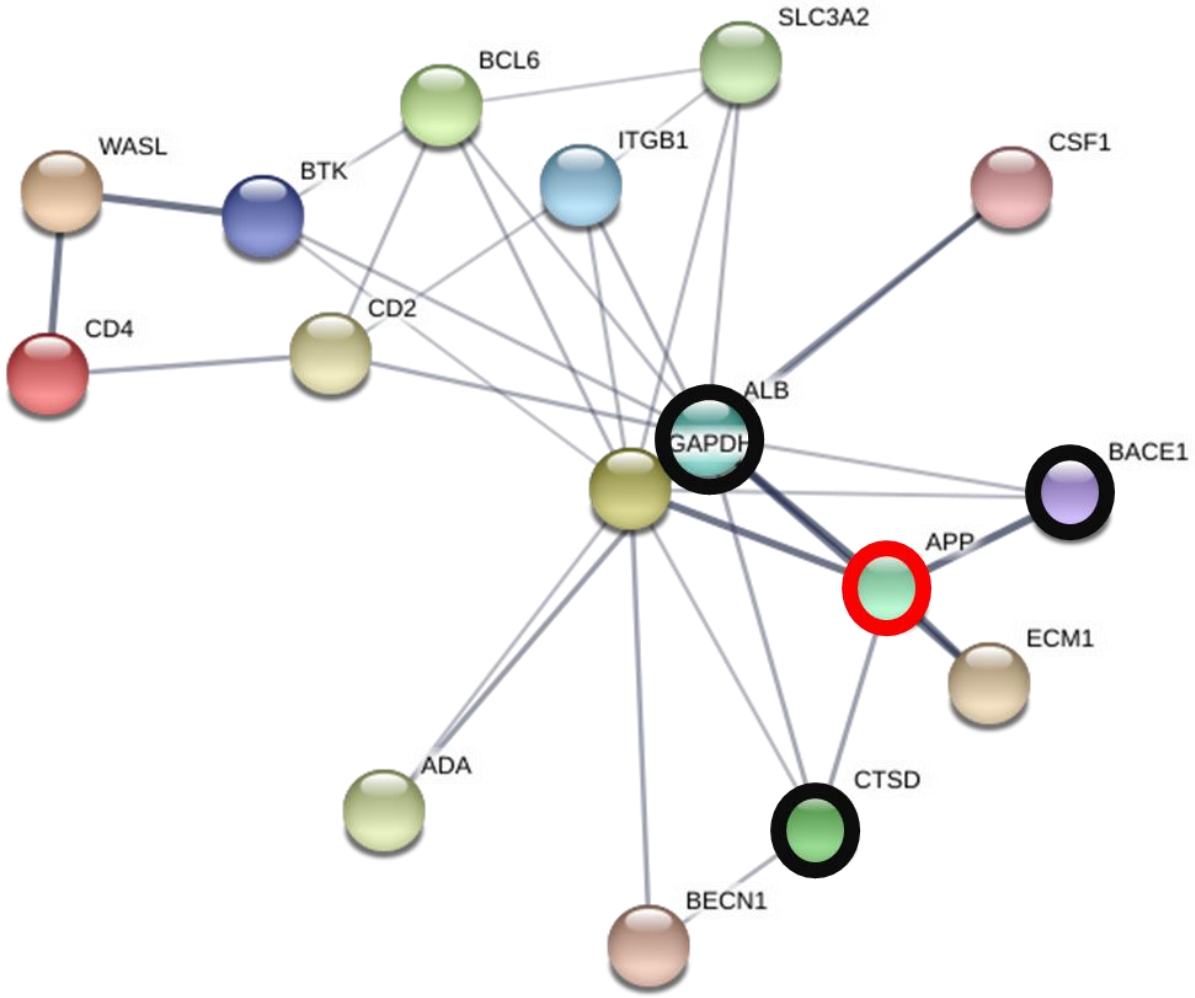

Figure 3.18: Proteome interaction network of early versus late APP expression in N2aswe cells. The STRING proteome network indicates direct protein-protein interactions between proteins with similar coloured nodes. The thicker the connecting line, the greater the strength of evidence for direct association. Red encircled node indicates APP; black encircled nodes represent proteins of interest.

3.4.8. Western blot analysis of samples utilized for proteome analysis

3.4.8.1. Western blot analysis of APP and Aβ expression in early versus late APP overexpression

APP protein expression is significantly increased in the 24 hrs BA treated group [1.85 ± 0.17 ($p<0.05$)], and in the 48 hrs BA treated group [2.03 ± 0.12 ($p<0.05$)] compared to control cells [0.19 ± 0.05] (**Fig. 3.19.B**).

Similarly, Aβ protein expression is significantly increased in the 24 hrs BA treated group [0.09 ± 0.005 ($p<0.05$)], and in the 48 hrs BA treated group [0.13 ± 0.01 ($p<0.05$)] compared to control cells [0.01 ± 0.003] (**Fig. 3.19.C**).

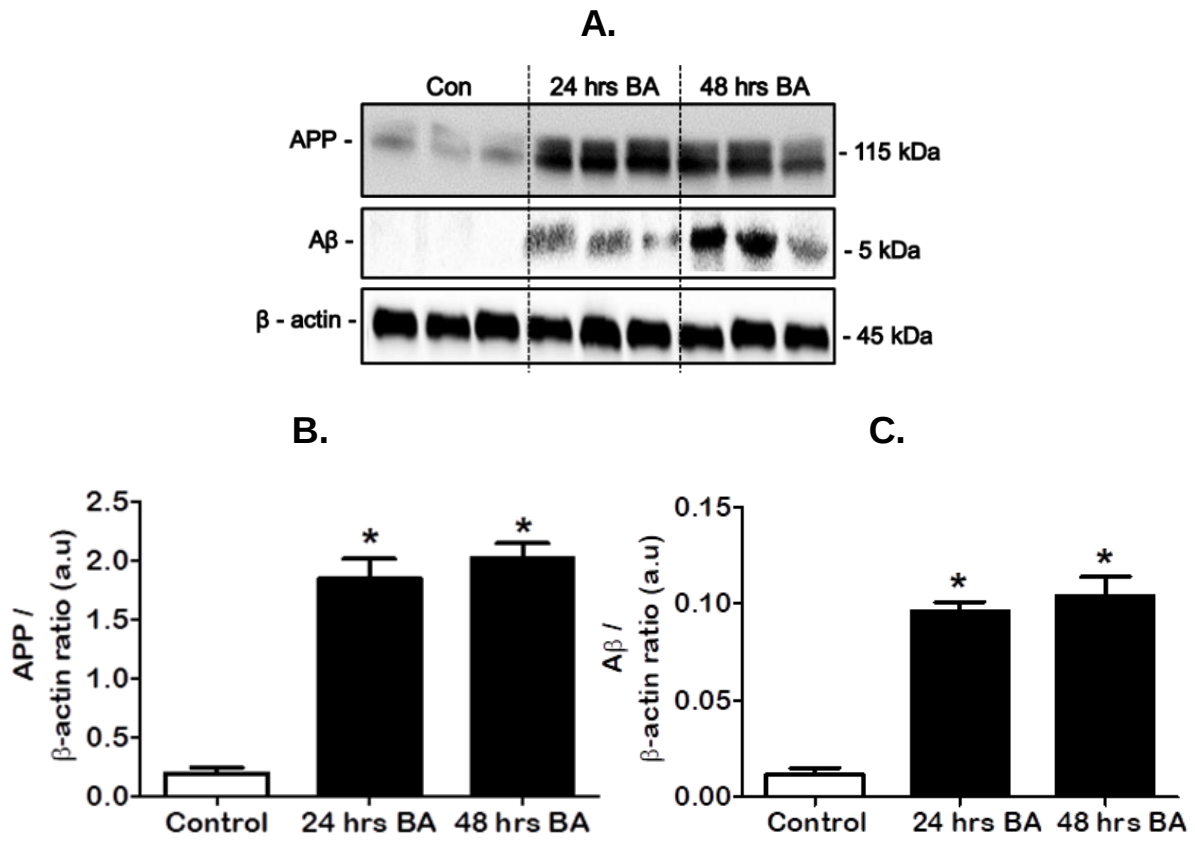

Figure 3.19: Effect of early and late APP overexpression on amyloidogenic processing proteins in N2aswe cells. Representative western blot and densitometric analysis for **(A, B)** APP, and **(A, C)** Aβ protein expression is shown. Data expressed as mean ± SEM, statistical analysis: ANOVA and Bonferroni correction, *$p<0.05$ vs. control, n = 3, arbitrary units (a.u).

3.4.8.2. Western blot analysis of LC3II and ATG5 expression in early versus late APP overexpression

As shown in **Fig. 3.20.A**, LC3II protein expression is significantly increased in the 24 hrs BA treated group [1.31 ± 0.08 ($p<0.05$)], and the 48 hrs BA treated group [2.08 ± 0.06 ($p<0.05$)] compared to control cells [0.57 ± 0.05]. Moreover, 48 hrs BA treatment led to a significant increase in LC3II protein levels compared to 24 hrs BA treatment (**Fig. 3.20.B**).

ATG protein expression is significantly increased in the 24 hrs BA treated group [1.35 ± 0.08 ($p<0.05$)], and the 48 hrs BA treated group [1.58 ± 0.05 ($p<0.05$)] compared to control cells [0.39 ± 0.0] (**Fig. 3.20.C**).

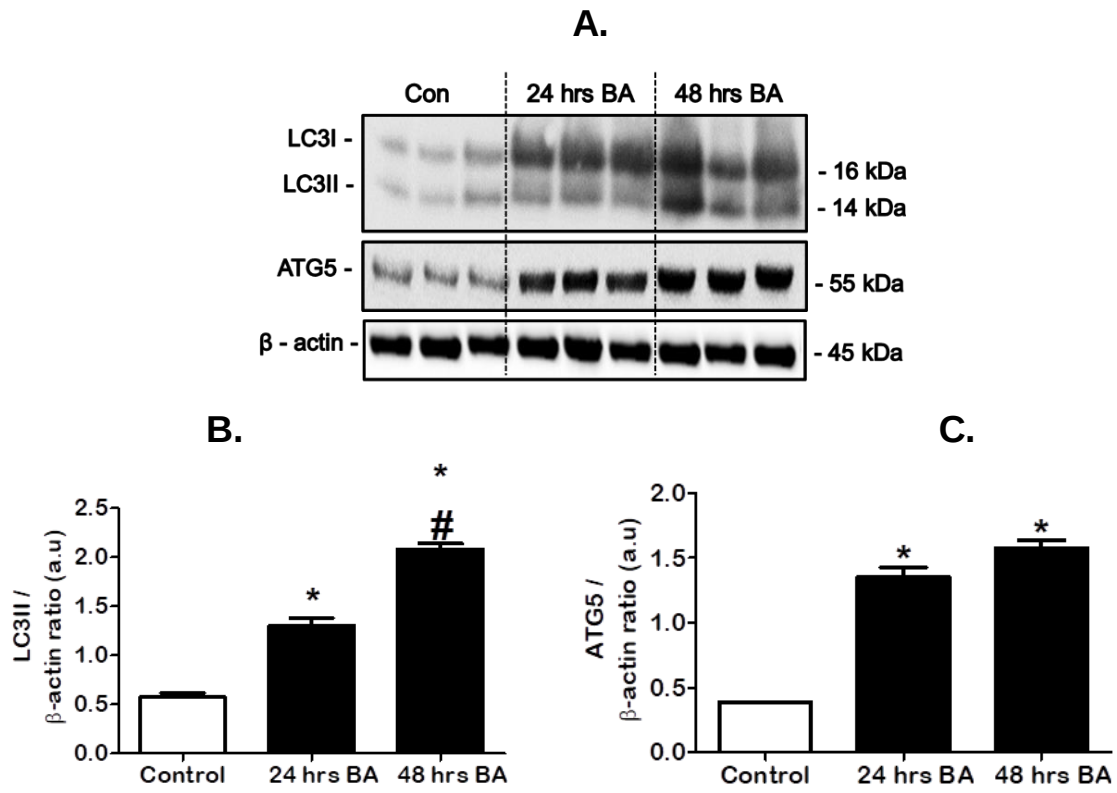

Figure 3.20: Effect of early and late APP overexpression on key MA proteins in N2aswe cells. Representative western blot and densitometric analysis for **(A, B)** LC3II, and **(A, C)** ATG5 protein expression is shown. Data expressed as mean ± SEM, statistical analysis: ANOVA and Bonferroni correction, *$p<0.05$ vs. control, #$p<0.05$ vs. 24 hrs BA, n = 3, arbitrary units (a.u).

3.4.8.3. Western blot analysis of key CMA proteins in early versus late APP overexpression

As shown in **Fig. 3.21.A**, LAMP2A protein expression is significantly increased in the 48 hrs BA treated group [0.55 ± 0.03 ($p<0.05$)] compared to control cells [0.37 ± 0.01], with no significant difference indicated in the 24 hrs BA treated group [0.42 ± 0.03] compared to control cells. Moreover, 48 hrs BA treatment led to a significant increase in LAMP2A expression compared to 24 hrs BA treatment (**Fig. 3.21.B**).

No significant differences in HSC70 protein expression are indicated in the 24 hrs BA treated group [1.04 ± 0.05], or the 48 hrs BA treated group [1.11 ± 0.1] compared to control cells [0.83 ± 0.2] (**Fig. 3.21.C**).

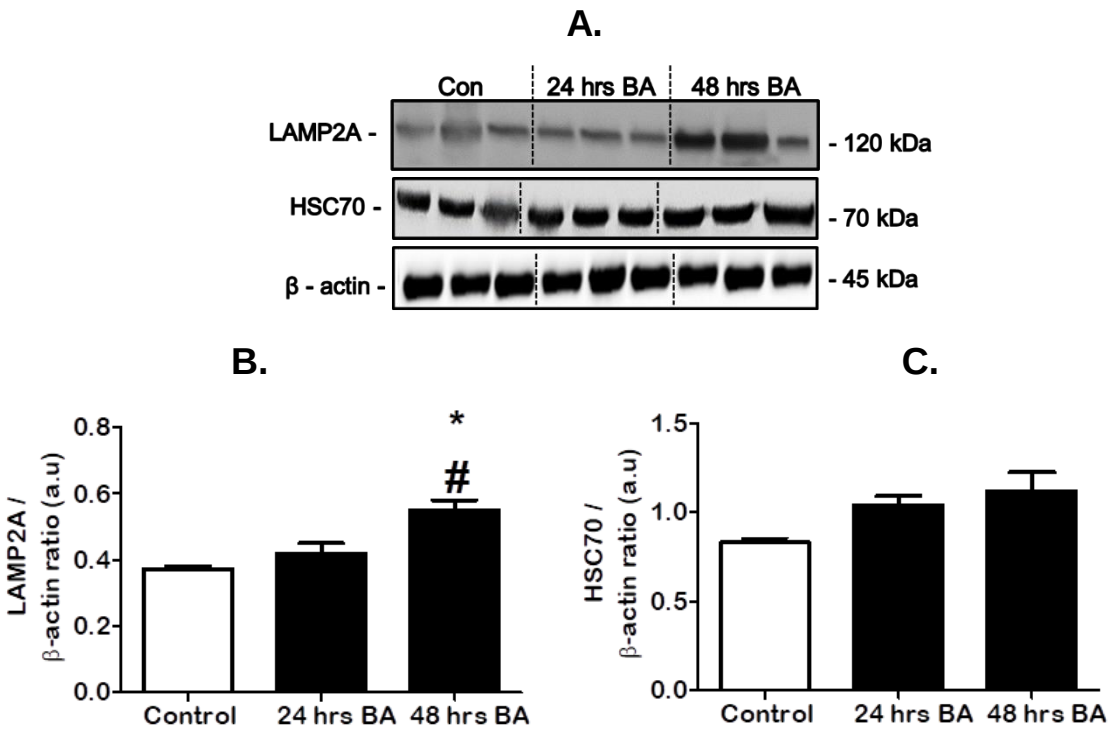

Figure 3.21: Effect of early and late APP overexpression on key CMA proteins in N2aswe cells. Representative western blot and densitometric analysis for **(A, B)** LAMP2A, and **(A, C)** HSC70 protein expression is shown. Data expressed as mean ± SEM, statistical analysis: ANOVA and Bonferroni correction, *$p<0.05$ vs. control, #$p<0.05$ vs. 24 hrs BA, n = 3, arbitrary units (a.u).

3.4.8.4. Western blot analysis of cytochrome c expression in early versus late APP overexpression

As shown in **Fig. 3.22.A**, cytochrome c expression is significantly increased in the 48 hrs BA treated group [0.96 ± 0.06 ($p<0.05$)] compared to control cells [0.29 ± 0.05], with no significant difference indicated in the 24 hrs BA treated group [0.48 ± 0.03] compared to control cells. Moreover, 48 hrs BA treatment led to a significant increase in cytochrome c expression compared to 24 hrs BA treatment (**Fig. 3.22.B**).

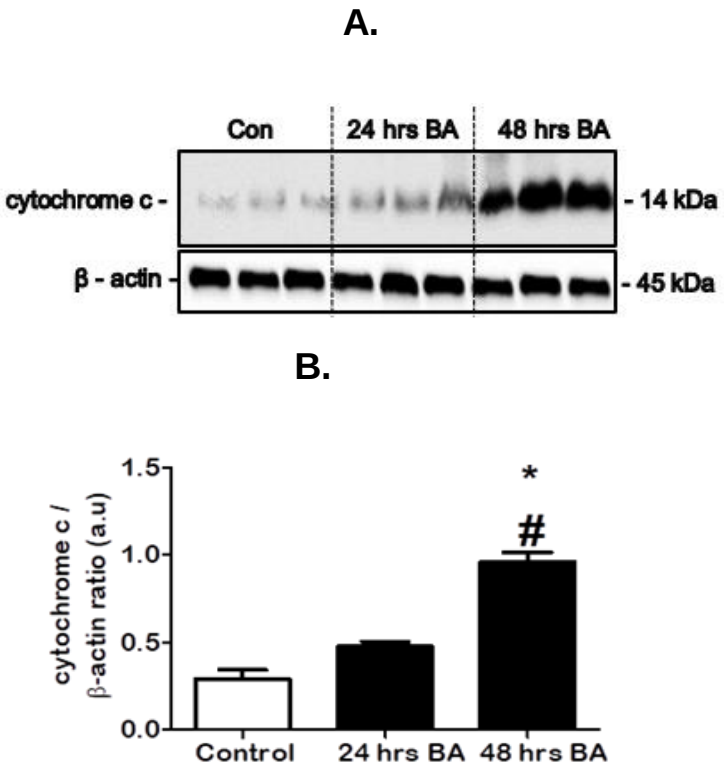

Figure 3.22: Effect of early and late APP overexpression on apoptosis in N2aswe cells. Representative western blot and densitometric analysis for **(A, B)** cytochrome c protein expression is shown. Data expressed as mean ± SEM, statistical analysis: ANOVA and Bonferroni correction, *$p<0.05$ vs. control, #$p<0.05$ vs. 24 hrs BA, n = 3, arbitrary units (a.u).

CHAPTER 3 DISCUSSION: *IN VITRO* CHRACTERISATION OF APP OVEREXPRESSION MODEL

Despite the significant advancement in our understanding of the mechanisms that contribute to AD progression, the aetiology of this complex disease remains unclear. The prevailing dogma provides compelling support for the prominent role of increased Aβ generation and/or accumulation in AD pathogenesis (Selkoe and Hardy, 2016). Moreover, as evidenced in initial studies by Glenner and Wong (1984), Aβ is present in its soluble form in the healthy brain, while only found in its aggregated form in the AD brain. Two primary mechanisms have been implicated in the clearance of Aβ peptides: firstly, degradation facilitated by various Aβ-degrading proteases, including β-secretase and cathepsin D (Saido and Leissring, 2012), and secondly, Aβ-laden autophagosomes have been shown to accumulate in dystrophic neurites (i.e. main constituents of neuritic plaques in AD), due to impaired MA function (Nixon et al., 2005; Yu et al., 2005). The is especially prevalent in the brains of AD patients, as evidenced by the accumulation of intracellular Aβ with neuronal degeneration in AD (Nilsson and Saido, 2014; Nilsson et al., 2013). Although the link between MA dysfunction and Aβ generation and/or clearance is increasingly being recognized as a unifying theme in AD pathology (Nixon, 2007; Nixon and Yang, 2011), the changes in macroautophagic activity during AD progression are poorly understood. In particular, the relationship between MA activity and Aβ clearance remains unclear, and to what extent a failing macroautophagic activity or increased proteotoxicity contributes to neuronal cell death.

We demonstrate a clear relationship between increased APP overexpression with concomitant Aβ generation, resulting in increased neurotoxicity with time (**Fig. 3.3**). In line with these findings, several studies have shown that increased APP expression is proportionately associated with increased Aβ generation and may contribute to neurotoxicity through activation of the apoptotic pathway in both sporadic and FAD patients (Matsui et al., 2007; Wu et al., 2015). We also demonstrate that MA activity

is increased, even with APP overexpression at later time points (**Fig. 3.5**). Conversely, work by Nixon et al. (2005) indicates that MA is dysregulated in AD brains, and others have shown that the end stage of autophagosomal clearance is impaired in AD mouse models (Cataldo et al., 1991; Yang et al., 2011a).

3.5. APP in vitro model validation – assessed by western blot analysis

The mouse N2aswe cell line is one of the most frequently utilized *in vitro* AD models, and its use has advanced the understanding of both AD pathology and neurodegeneration over the past decades (Netzer et al., 2017; Thinakaran et al., 1996). One of the most important lessons learned from genetic cases of AD, is that the neuropathology of FAD is very similar to sporadic AD, most notably, that Aβ deposition is also the primary event in sporadic AD (Shepherd et al., 2009). Moreover, the changes in biomarker expression observed in sporadic and FAD cases appears similar in many, but not all cases, thus making the N2aswe cell model informative for both disease subtypes (Dorszewska et al., 2016). Using western blot analysis, our results consistently demonstrate a marked increase in APP expression, with subsequent Aβ expression following the induction of APP overexpression in the 24 hrs BA treated N2aswe cells compared to the untreated N2aswe cells (**Fig. 3.1.B,D**). Although the level of APP expression is also significantly increased in the 24 hrs BA treated N2awt cells compared to the untreated N2awt cells (**Fig. 3.1.B**), no differences in Aβ expression are demonstrated (**Fig. 3.1.D**). In line with these findings, Netzer et al., (2017) demonstrate that the ratio of $A\beta_{42}/A\beta_{40}$, i.e. increased production of the more toxic $A\beta_{42}$ relative to $A\beta_{40}$, is enhanced following APP overexpression in 5 hrs BA treated N2aswe cells compared to both the untreated N2aswe cells and 5 hrs BA treated N2a 695 cells (same as N2awt cells) using an enzyme-linked immunosorbent assay (ELISA). Similarly, Lo et al. (1994) revealed that relative to the steady-state levels of APP and Aβ in N2aswe cells, the levels of these proteins were significantly diminished following 3 hrs BA treatment, demonstrated using surface biotinylation and release approaches. Importantly, our results indicate that the level of MA activity is

notably increased upon APP overexpression in the 24 hrs BA treated N2aswe cells compared to untreated N2aswe cells, while no differences are observed in the N2awt cells (**Fig. 3.1.F**). Consistent with these findings, others have shown that MA is a key regulator of Aβ generation and clearance (Nilsson and Saido, 2014), thus reinforcing the significance of APP, Aβ and the MA pathway in the pathophysiology of AD (Colacurcio and Nixon, 2016). Our results validate the use of the N2aswe cell line in this context, as evidenced by the profound increase in APP expression and Aβ generation, which is consistent with the cell line specifications outlined by Lo et al. (1994). Moreover, indications of markedly increased MA activity in the BA treated N2aswe cells suggests that the MA machinery is engaged during APP overexpression and requires further investigation to determine how functional the MA system remains in this context. The validity of our results was further confirmed by our comparison of the levels of APP, Aβ, and LC3II in the 24 hrs BA treated N2avec cells. As expected, the expression of these proteins was consistently negligible in the N2avec cells compared to the 24 hrs BA treated N2aswe cells (**Fig. 3.1.B,D,F**).

3.6. Time-dependent effects of APP overexpression on cell viability - assessed by WST-1 analysis

The importance of APP in AD pathogenesis relates to its role in the increased generation of toxic Aβ (Butterfield, 2002; Chen et al., 2000). However, when this toxicity becomes detectable, and what levels APP expression causes the loss of cell viability is less clear. The results of the WST-1 assay indicate that the cytotoxic effects of APP overexpression are time-dependent, with a profound decrease in cell viability revealed as early as 24 hrs BA treatment (**Fig. 3.2**). In agreement, initial *in vitro* studies by Yankner et al. (1989) demonstrates that increased Aβ production is acutely toxic, resulting in complete cell death within 24 hrs of APP overexpression in APPswe transfected PC12, and fibroblast (NIH 3T3) cells. More recent studies have also shown that the effects of increased APP expression as early as 24 hrs, results in the augmentation of neuronal cell death by favouring increased Aβ production in human

neuroblastoma medium spiny neuronal cells (MSN) (Quiroz-Baez et al., 2009) and APPswe transfected PC12 cells (Tong et al., 2005). Therefore, therapeutic interventions that mitigate APP overexpression with disease progression may translate in neuronal protection.

3.7. Time-dependent assessment of APP, Aβ, and LC3II protein expression - assessed by western blot and immunofluorescence analysis

Based on our WST-1 results (**Fig. 3.2**), it was concluded that BA treatment time points of 12, 24, 36, and 48 hrs would be most suitable to assess the progression of mild to more sever cell injury for subsequent experimental in N2aswe cells.

Studies reveal that APP is continuously produced in large quantities in neurons, and rapidly metabolized to Aβ in the brain (Bateman et al., 2006; Lee et al., 2008b). Under physiological conditions, the amyloidogenic and non-amyloidogenic pathway are thought to exist in dynamic equilibrium in all cells (Haass et al., 1992; Mohamed and Posse de Chaves, 2011). Conversely, robust correlation has been demonstrated between the altered processing of APP, the increased production Aβ, and the extent of synaptic loss and cognitive decline in AD (Lue et al., 1999; McLean et al., 1999), suggesting that amyloidogenic processing is favoured in AD. It is however less clear, to what extent the MA machinery would be engaged during APP overexpression over time. To this end, the extent of amyloidogenic processing in N2aswe cells was assessed by western blot analysis. Our results reveal no APP, β-secretase, or Aβ expression under control conditions (**Fig. 3.3**). The results indicate a significant time-dependent increase in APP levels as early as 12 hrs BA exposure, with APP expression further increasing upon 24, 36, and 48 hrs APP overexpression compared to control cells (**Fig. 3.3.B**). Moreover, our results indicate a similar pattern in β-secretase levels, with its expression being significantly indicted upon 12 hrs BA exposure, and further increasing upon 24, 36, and 48 APP overexpression compared

to control cells (**Fig. 3.3.D**), indicating the very close relation between APP levels and β-secretase activity. In line with these findings, others have shown that the Swedish APP mutation, causes increased proteolysis of APP by β-secretase to generate elevated levels of total Aβ or $A\beta_{42}$, as this mutation clusters near the β-secretase cleavage site (Di Fede et al., 2009; Kuhn et al., 2010). The levels of Aβ expression is significantly enhanced already at 24 hrs APP overexpression, and is further increased upon 36, and 48 hrs APP overexpression compared to control cells, while no expression is observed upon 12 hrs BA exposure (**Fig. 3.3.F**). This observation suggests that even though APP levels are already significantly elevated upon 12 hrs, a time-dependent effect is required for enhanced APP availability to translate into the generation of enhanced Aβ levels. To this effect, MRI-based studies in AD patients suggests that either Aβ continues to be sufficiently cleared, or not sufficiently generated early in disease progression (Butterfield, 2002; Holtzman et al., 2011). Alternatively, as suggested by Walsh and Selkoe (2007), the total levels of Aβ may only be detected when the abundance of $A\beta_{42}$ is elevated above a certain threshold, and the abundance of $A\beta_{40}$ is severely decreased. Although speculative, our results may suggest that the ratio of $A\beta_{42}$ to $A\beta_{40}$ is gradually elevated with time, and only becomes apparent upon 24 hrs APP overexpression and onward. In line with this idea, *in vivo* microdialysis (measurement of the levels of Aβ in the extracellular interstitial fluid (ISF) of the brain) comparing Aβ clearance in young (3 months old) and old (12 to 15 months old) APP mouse models, demonstrated that the half-life of Aβ within the ISF is doubled in older animals, even when Aβ production is prevented (Cirrito et al., 2003; Wildsmith et al., 2013), suggesting impaired/reduced Aβ clearance with age as also revealed by microdialysis analysis of ISF of the human brain (Mawuenyega et al., 2010; Ramanathan et al., 2015). Interestingly, work by Yan et al. (2009) reveals that a small reduction in Aβ production is sufficient to reduce Aβ load in 6-month-old, but not in 10-month-old mice, suggesting that the brain's ability to clear Aβ diminishes with age/time, and that APP and Aβ homeostasis may be impacted by both production and clearance mechanisms. Overall, our results demonstrate a significant increase in β-secretase only after 24 hrs (**Fig. 3.3.D**), supporting the notion that sufficient APP levels are required to enhance Aβ levels. Indeed, studies have shown a reduction in the rate

of APP turnover with increasing APP overexpression (Wu et al., 2015), and a decrease in α-secretase processing of APP in AD patients, i.e. the enzyme that cleaves APP inside the Aβ sequence, further augmenting Aβ production (Yan and Vassar, 2014). Therefore, strategies to either decrease β-secretase activity, or increase Aβ clearance prior to cell death onset, i.e. early disease stages, may be effective in AD treatment.

The combination of light microscopy with electron microscopy, i.e. CLEM, affords the dual advantages of fluorescent imaging with the high-resolution of electron microscopy. APP fluorescence intensity APP is increased upon 12, 24, and 48 hrs APP overexpression compared to control cells, and APP increasingly also localizes in extracellular regions (**Fig. 3.4**). CLEM analysis reveals, that indeed, membrane structures visible in the SEM micrograph, are APP positive, indicating active shedding of APP positive membrane structures which is further increased upon 24 hrs and 48 hrs BA exposure. In line with these observations, the cell membrane is thought to be the first site where the amyloidogenic cascade is initiated (Peters et al., 2009). Although the mechanism through which this cascade is initiated remains unclear, findings by Yanagisawa (2007) demonstrate that Aβ reduces membrane fluidity in PC12 cells and alters the localization of receptors within the plasma membrane. Peters and colleagues demonstrated that Aβ stimulates its own production through a positive feedback mechanism that enhances amyloidogenic processing of APP by complexing with GM-1 ganglioside to reduce membrane fluidity (Peters et al., 2009). Indeed, our western blot findings of elevated APP, and Aβ expression with time (**Fig. 3.3**) may support the notion of changing membrane dynamics since APP-positive membrane structures are being released into the extracellular space (**Fig. 3.4**). These findings provide new insights into the mechanism of APP release and subsequent Aβ generation.

3.8. Time-dependent effects of APP overexpression on the molecular markers MA and CMA over time – assessed by western blot and immunofluorescence analysis

Neurotoxic accumulation of Aβ in the brain is hypothesized to result from an imbalance in Aβ production and clearance (Musiek and Holtzman, 2015). Indeed, impaired Aβ clearance mechanisms, rather than its overproduction, have been shown to contribute to the pathological accumulation of cerebral Aβ as evidenced in sporadic AD cases (Mawuenyega et al., 2010), while increased β-secretase activity is reported to increase Aβ load in FAD patients (Holsinger et al., 2002; Li et al., 2004a), thereby impacting the capacity of Aβ clearance mechanisms. However, the interplay between MA activity in the process of APP overexpression is not clear. Our western blot analysis reveals a significant increase in LC3II protein expression upon 24, 36, and 48 hrs APP overexpression compared to control cells (**Fig. 3.5.B**), suggesting either an increase in autophagosome synthesis, or a decrease in autophagosome clearance. When assessing the MA cargo receptor p62, it becomes clear that MA activity may indeed be increased as p62 expression is comparable to control cells in the process of 36, and 48 hrs APP overexpression, suggesting p62 turnover is maintained even with late APP overexpression (**Fig. 3.5.D**). However, the expression of p62 is significantly increased upon 24 hrs APP overexpression compared to the control cells. This increase may be reflective of a temporary cargo increase, which is being cleared through the enhanced MA activity as evidenced by the significant decrease in p62 levels upon 48 hrs APP overexpression compared to 24 hrs APP overexpression. This pattern is not mirrored by the Aβ cargo (**Fig. 3.3.F**), which could be due to the continuous overexpression of APP (**Fig. 3.3.B**). Based on the p62 expression profile, our data suggest that even during the process of the late APP overexpression, there is no MA failure *per se*, but rather a mismatch between macroautophagic activity and toxic protein cargo aggregation. In line with these findings, MA has been shown to be the 'first-line of defence' in an orchestrated stress-induced response which allows cells to remove damaged organelles, misfolded proteins, and aggregate-prone proteins such as Aβ in AD (Kroemer et al., 2010; Ravanan et al., 2017). Further support by Li et al. (2012), following the incubation of mouse neuroblastoma N2a cells and primary

cortical neurons obtained from 17-day-old embryos of wild-type C57BL/6 mice in exogenous $A\beta_{42}$, reveals a concentration-dependent increase in the production of lysosomal system components is observed, while dysfunction of MA leads to the accumulation of Aβ. Although However, others suggest that protein variants shown to contribute to the pathogenesis of neurodegenerative disorders may fail to undergo degradation by MA and accumulate intracellularly resulting in cell toxicity and often cell death (Menzies et al., 2015; Nixon, 2013), consistent with our results, Nixon (2007) suggests that the combination of increased MA induction and defective clearance of Aβ-laden AVs may create conditions favourable for Aβ accumulation in AD. It is possible, that abnormal APP expression may constitute a cellular stress, the cell may therefore upregulate MA as a pro-survival stress response in an effort to mitigate the cytotoxic effects of increased Aβ production. Our model system allowed us to more finely dissect this relationship, by controlling the level of APP from non-toxic to toxic conditions, potentially better resolving the relationship between macroautophagic activity and toxicity onset with Aβ cargo generation. These findings provide rationale for the use of therapeutic strategies which enhance MA clearance, particularly with late disease progression, and may therefore have potential implications for clinical application.

Our immunofluorescence analysis reveals an increase in APP, Aβ, and LC3II localization in distinct protein clusters that increase in abundance over time (**Fig. 3.6**). These clusters are particularly abundant upon 24 hrs, and 48 hrs APP overexpression, which is consistent with our western blot data demonstrating a significant increase in APP (**Fig. 3.3.B**), Aβ (**Fig. 3.3.F**), and LC3II (**Fig. 3.5.B**) protein expression at these time points. In line with our findings, the link between aberrant APP processing, Aβ generation, and impaired MA in AD has been extensively documented by others using western blot analysis, and pulse chase experiments (Li et al., 2012; Nixon, 2007). These data also highlight the clear relationship between MA machinery and Aβ cargo.

Under stress conditions, the selective removal of proteins by CMA also contributes to protein degradation, and recycling of amino acids. Due to its cross talk with MA under selective stress conditions (Kaushik and Cuervo, 2009; Massey et al., 2006c), it is important to determine the status of CMA, as APP overexpression and increased Aβ production constitutes a cellular stress which may necessitate a switch between these pathways. Although it is known that CMA is usually a late response that follows MA induction under nutrient, ER, or oxidative stress conditions (Gan et al., 2017; Ravanan et al., 2017), to what extent the CMA pathway engages under APP overexpression, remains however unclear. Hence, we performed western blot analysis to assess the effects of APP overexpression on the molecular markers of CMA activity, i.e. LAMP2A and HSC70, the abundance of which correlates well with an increase in CMA activity (**Fig. 3.7**). To our surprise, the results indicate a significant increase in LAMP2A protein expression in the process of 36 hrs, and 48 hrs APP overexpression compared to control cells, and is further increased upon 48 hrs compared to 24 hrs APP overexpression (**Fig. 3.7.B**). Studies indicate that the levels of LAMP2A at the lysosomal membrane is limiting for CMA activity in lysosomal fractions isolated from mouse fibroblasts cells (NIH 3T3) (Bandyopadhyay et al., 2008), and dopaminergic neurons cells derived from the substantia nigra of transgenic mouse embryos (SN4741 cells) (Li et al., 2017c; Rodriguez-Losada et al., 2017). Here we demonstrate that CMA activity is increased in the process of late APP overexpression, possibly as a complementary pathway to MA as the cells attempt to accelerate APP clearance. In support of this notion, recent work by Park et al. (2016) discovered the presence of a KFERQ-like targeting sequence in APP, a characteristic that makes APP correct for degradation via CMA. However, most recent data by Tekirdag and Cuervo (2018) suggests that the presence of a KFERQ-like motif is necessary, but not sufficient to classify a protein as *bona fide* CMA substrate, as the same targeting sequence can also be used to target cytosolic proteins to late endosomes for degradation via the endosomal microautophagic pathway (Sahu et al., 2011). To our surprise, no difference in HSC70 protein expression is indicated with APP overexpression overtime (**Fig. 3.7.D**). It could be that a lysosomal fraction analysis is required, in order to finely interrogate the role of CMA in this context, since it has been shown that isolated

lysosomal fractions contain comparatively more CMA-active lysosomes than cellular lysates (Arias, 2017; Patel and Cuervo, 2015). It is plausible that additional pathways, such as endosomal microautophagy, may also play a role in this context. This notion may be addressed in the future. Our LAMP2A data suggest that a change in the CMA-specific lysosomal pool size may be induced indicating that CMA is indeed induced, particularly at later time points in APP overexpression (**Fig. 3.7.B**). In line with our finding, Xiao et al. (2014) demonstrated that the expression of transcription factor EB (TFEB), a master regulator of lysosomal pathways, enhanced Aβ uptake and its lysosomal degradation to reduce Aβ levels in astrocytes. More recently, the authors reported a reduction in APP and Aβ levels in the brain ISF of aged APP/PS1 mice following the induction of CMV promoter-driven TFEB. These findings were further validated *in vitro* where TFEB transfection in N2a cells stably expressing APP695, enhanced lysosome biogenesis, reduced APP levels, and attenuated Aβ generation (Xiao et al., 2015**).** Our findings thus raise the possibility that a change in the lysosomal pool, as evidenced by enhanced LAMP2A protein levels (**Fig. 3.7.B**), may impact lysosomal degradative pathways to promote APP/Aβ clearance.

Our western blot data are supported by the immunofluorescence analysis, where we show significant colocalization of LAMP2A with HSC70 following 12 hrs APP overexpression onwards (**Fig. 3.8**). This colocalization is further enhanced at 48 hrs compared to 24 hrs APP overexpression, suggesting that CMA activity is more pronounced at these later time points. These findings provide new insights into the mechanism of both MA and CMA recruitment. In line with our findings, cellular toxicity resulting from the accumulation of altered proteins (or proteotoxicity) has been shown to modulate CMA activity, as evidenced in mouse fibroblasts, PD, and HD-affected neuronal cells expressing mutant α-synuclein (Vogiatzi et al., 2008), huntingtin protein (htt) aggregates (Sarkar et al., 2009), ataxin-7, the protein bearing the polyQ stretch in spinocerebellar ataxia 7 (Duncan et al., 2010). Moreover, work by Bandyopadhyay et al. (2010) demonstrates that CMA is maximally activated under prolonged stress conditions, e.g. 48 hrs nutrient deprivation, as evidenced by increased colocalization of *bona fide* CMA substrates such as nuclear factor of kappa light polypeptide gene

enhancer in β-cells inhibitor, α (IκBα) and RNase with LAMP2A in isolated lysosomes from rat liver and mouse fibroblasts. In our study context, increased APP overexpression constitutes a cellular stress condition, these findings provide novel insights, that also upon APP–induced proteotoxicity, CMA activity is engaged, and highly active at later time points, even though neuronal toxicity is already detectable.

3.9. Time-dependent effects of APP overexpression on the molecular markers of cell death with time – assessed by Caspase-3/7 Glo Assay and western blot analysis

While Aβ has been shown to enhance endothelial cell survival in nanomolar concentrations, only becoming toxic in the micromolar range (Cantara et al., 2005), it remains unclear at what stage/time point in APP processing Aβ becomes toxic in neuronal cells. Accordingly, the Caspase-3/7 Glo assay was utilized to assess the time-dependent effects of APP overexpression on cell death, as evidenced by the activity levels of apoptotic executioner caspase proteins, caspase-3 and caspase-7, the activation of which is a consistent feature in AD brains (Smale et al., 1995; Su et al., 1994). The results indicate a time-dependent increase in caspase 3 and 7 activity following 24, 36 and 48 hrs APP overexpression compared to control cells, with the activity levels rising further significantly at 48 hrs compared to 24 hrs APP overexpression (**Fig. 3.9.A**). Of note, our data reveals that caspase activity becomes significant at the same time points where Aβ levels become significantly enhanced (**Fig. 3.3.F**). In line with our findings, previous reports indicate that APP overexpression may impact caspase activity, as APP has been shown to be a caspase substrate and caspase cleavage of APP has been shown to promote the production of C-terminal APP fragments in the brain of AD patients (Gervais et al., 1999; Lu et al., 2000). Caspase-3 is a key cell death protease involved in apoptotic cell death (Porter and Jänicke, 1999), and mediates the cleavage of several key proteins including DNA repair enzyme, poly (ADP-ribose) polymerase (PARP) (Brentnall et al., 2013). Under physiological conditions, the primary function of PARP repair DNA damage, while the 89 kD cleaved-PARP fragment reveals greatly reduced DNA

binding capacity (Soldani and Scovassi, 2002). Consistent with enhanced caspase activity at these time points, our results indicate a significant increase in cleaved-PARP protein expression following 24, 36 and 48 hrs APP overexpression compared to control cells, and PARP cleavage is further enhanced in during 36 hrs and 48 hrs APP overexpression compared to 24 hrs APP overexpression (**Fig. 3.9.B**). These data suggest that apoptosis is not only activated, but fact executed as early as 24 hrs APP overexpression. Moreover, the activation of executioner caspases 3 and 7, has been shown to result in the irreversible proteolysis of PARP, leading to inevitable cell death, as evidenced in multiple cell lines, including HeLa cells, 3T3 fibroblasts, and various *in vivo* systems, including neuronal cells of *C. elegans*, and mammalian cardiac myocytes and neurons (Brentnall et al., 2013; Tang et al., 2012, 2013). In line with these findings, others have echoed the sentiment that PARP cleavage is the 'point of no return' because it typically leads to cell death (Loos and Engelbrecht, 2009; Tait and Green, 2013). Thus, our findings indicate that the induction of apoptosis is inevitable as early as 24 hrs APP overexpression. In agreement, earlier work by Mattson et al. (2001) demonstrated that enhanced APP processing leads to decreased levels of neuroprotective sAPPα in the cellular microenvironment, making cells more susceptible to cell death onset. We further assessed Total Caspase-3 activity using western blot analysis, and the results indicate a significant increase in Total Caspase-3 protein expression upon 36 hrs, and 48 hrs APP overexpression compared to control cells (**Fig. 3.9.E**). Consistent with increased caspase activity in the process of enhanced APP expression, others have shown that APP is also a substrate for caspase-3 cleavage (LeBlanc et al., 1999; Lu et al., 2000), suggesting that increased caspase activity may exacerbate amyloidogenic processing. In line with this sentiment, Tesco et al. (2003) demonstrate that caspase-3 activation increases the production of total Aβ and $A\beta_{42}$ in Chinese hamster ovary (CHO) cell lines stably transfected with APP751. Similarly, *in vivo* work by Zhao et al. (2003) has demonstrates that caspase-mediated proteolysis of APP may contribute to neurodegeneration in AD. Conversely, western blotting and RT-PCR analysis reveals that caspase-3 inhibition decreases ischemia-induced Aβ production by reducing APP proteolysis and β-secretase mRNA and protein levels (Xiong et al., 2008). These findings provide new insights into the

potential link between apoptosis and amyloidogenic processing and may offer insights into the mechanisms involved in the cells life and death decisions. Importantly, our findings suggest N2aswe cells undergo apoptosis (**Fig. 3.9**), even with the upregulation of MA early in the process of APP overexpression (**Fig. 3.5**), and the induction of CMA later in the process (**Fig. 3.7-3.8**), suggesting that the cells are unable to counteract the sustained additional stress emanating from increased APP and Aβ levels (**Fig. 3.3**). Overall, these findings suggest that a delicate equilibrium in APP processing and Aβ production/clearance may exists within cells where sustained APP processing can induce cell death onset through increased Aβ production. They also point towards the interplay between caspase-mediated APP cleavage, apoptosis induction, and the time-dependent upregulation of both MA and CMA in the process of enhanced APP/Aβ levels. This interplay warrants further investigation to better exploit mechanisms of cell protection in the future.

3.10. Colocalization of APP with p62 and LAMP2A, and LAMP2A with HSC70 – assessed by immunofluorescence analysis

Studies by Nilsson and Saido have not only demonstrated a role for MA in Aβ metabolism (Nilsson and Saido, 2014), but have also indicated increased Aβ accumulation in MA-deficient mice (Nilsson and Saido, 2014; Nilsson et al., 2015), suggesting a duel role for MA in Aβ production and clearance. However, when APP becomes cargo in the process of APP overexpression is less understood. Hence, colocalization analysis was performed to assess the interaction of p62 with APP over time. p62 is a receptor protein involved in cargo recruitment to the autophagosome and is in part degraded through MA (Salminen et al., 2012), therefore, p62 serves as a critical marker protein to indicate cargo degradation. Our findings reveal significantly increased APP/p62 colocalization in the process of 24 hrs and 48 hrs APP overexpression compared to control cells **(Fig. 3.10)**. The increased colocalization observed during 24 hrs APP overexpression is consistent with our western blot data showing increased p62 (**Fig. 3.5.D**), and APP protein expression (**Fig. 3.3.B**), which

are both enhanced at the 48-hr time point. These findings suggest that APP could be sequestered as MA proteinaceous cargo. In line with our findings, previous work by Yu et al. (2004) in an AD mouse model of amyloidosis demonstrates that AVs are enriched in both APP and Aβ, and Pickford et al. (2008) revealed increased Aβ load in in affected brain regions of patients AD, and following the deletion of MA-induction protein, BECN1, in APP mice. More recently, Caccamo et al. (2017) showed that removing the LIR domain of p62, which facilitates p62-mediated selective MA, in 7PA2 cells, or blocking MA though 14 hrs 3MA treatment in p62 infected neuronal cells from APP/PS1 mice, was sufficient to prevent APP/Aβ clearance through MA. Further supporting the notion that APP is indeed being cleared, and not only engulfed into autophagosomes, our colocalization analysis of APP with LAMP2A, indicates that APP is indeed reaching the lysosome (**Fig. 3.11.A**). A time-dependent increase in APP/LAMP2A colocalization is observed compared to control cells, reaching significance already at 12 hrs APP overexpression, suggesting that APP cargo has been delivered to the lysosome already at this time point (**Fig. 3.11.B**). In line with our data, previous work by Park et al. (2016) reveals increased colocalization LAMP2A and APP in SH-SY5Y neuronal cells transfected with wild-type APP, while KFERQ-deficient cells did not. These results provide new insights, that also during increased APP, at a time where toxicity is already indicated, APP increasingly colocalizes with LAMP2A (**Fig. 3.11.B**). To our surprise, APP/LAMP2A colocalization is reduced at the 48-hr compared to the 24-hr time point, which may be explained, at least in part, by the fact that CMA activity was assessed in whole lysates instead of isolated lysosomes shown to be enriched in CMA-positive lysosomes (Arias, 2017). Significant colocalization late in APP overexpression suggests that the lysosomes at a late time point are composited of a higher percentage of CMA positive lysosomes, over the entire lysosome pool size. This may warrant further investigation, especially since novel techniques have been recently developed to isolate lysosomes (Abu-Remaileh et al., 2017).

3.11. APP proteome signature

Despite the prevalence of shared pathology, and overlap in molecular machinery, characterisation of the proteome network linking lysosomal systems, including MA, CMA, and endocytosis, with the UPS and apoptosis and the dynamics of these systems with AD progression are incompletely understood. Here we report a large-scale quantitative LC-MS proteomic dataset following APP overexpression in N2aswe cells. To this end, the global proteome signature of early (24 hrs) versus and late (48 hrs) APP overexpression was profiled. This is, to the best of our knowledge, the first global proteome analysis of APP overexpression in an *in vitro* model of AD. The major advantage of LC-MS ‐ based proteomics over western blot, or immunofluorescence analysis is the quantity of proteins identified and the specificity of algorithms utilized in the automated quantification of protein datasets (Chiva and Sabidó, 2017). Surprisingly, the Venn diagram analysis indicates that the largest quantity of shared and unique proteins is expressed in response to early APP overexpression compared to control cells (**Fig. 3.12.A**), while **Fig 3.12 B, C** reveal less unique proteins between early versus late APP overexpression, and late APP overexpression versus control conditions, respectively. These results could suggest the robust engagement of pathways early in APP overexpression, while this response gradually decreases with increasing APP overexpression. In line with this notion, Seyfried et al. (2017) demonstrate a transient, concerted upregulation of a protein network prior to symptom onset, with key upregulated proteins linked to inflammatory responses, activation of astrocytes and microglia prior to cognitive decline in glial cells of asymptomatic and AD patients. In addition, large-scale transcriptome studies in the CA1 field of the hippocampus of individuals with advanced AD and non-demented controls reveals the modulation of pathways consistent with early microglial activation, production of energy, cytoskeletal dynamics, synaptic transmission, and apoptosis early in disease progression (Miller et al., 2013). Using an isobaric tag for relative and absolute quantitation (iTRAQ)-based two-dimensional LC coupled with tandem mass spectrometry (2D-LC-MS/MS), Manavalan et al. (2013) identified 950 proteins in the

hippocampus, cortex, and cerebellum of AD brains, most of which were implicated in in molecular transport, nervous system development, synaptic plasticity and apoptosis. Following Ingenuity Pathway Analysis (IPA)-based network analysis, Manavalan et al. (2013) suggested reduced UPS activity as one of the causative factors of sporadic AD (early stage). While these studies have generated significant knowledge regarding proteomic changes early in AD pathogenesis, there is a clear lack of quantitative proteomic studies designed specifically to identify APP and/or autophagy-related proteomic changes throughout AD pathogenesis. Given suggestions of apoptosis induction early in disease progression (Manavalan et al., 2013; Miller et al., 2013; Wood, 2017), the APP early proteome response (**Fig. 3.12**) may indicate enhanced proteomic upregulation already early APP overexpression. Our volcano plot analysis reveals that APP expression is significantly higher during late APP expression compared to control cells (**Fig. 3.14**, 3.0 FC), and between 24 hrs and 48 hrs APP overexpression (**Fig. 3.15**, 2.3 FC), which is consistent with our western blot data of the cell lysates utilized for proteome analysis (**Fig. 3.19.B**). To our surprise**,** the volcano plots reveal that MA protein BECN1 is significantly expressed during both early (**Fig. 3.13**, 2.81 FC) and late (**Fig. 3.14**, 2.75) APP overexpression, suggesting that BECN1 expression is maintained during APP overexpression, even at the late time point. BECN1, is an important protein that regulates the initiation of autophagosome formation. Our findings are contrast to a previous study by Pickford et al. (2008) which demonstrates that BECN1 is significantly reduced in brain tissue from the midfrontal cortex grey matter of moderate (mean age, 85.1 ± 2.7 years) to severe AD patients (mean age, 81.6 ± 4.2 years). In addition, these findings were confirmed cortical cells from aged APP transgenic mice leading to Aβ accumulation and neurodegeneration (Pickford et al., 2008). These findings were further confirmed by Jaeger et al. (2010) who showed a significant decline of BECN1 expression in cortical neurons from the mid-frontal tissue of confirmed AD patients. These data shed particularly new light into the relationship between APP and BECN1, suggesting a role for MA in the regulation of APP processing, and more studies are needed in this regard. In further support of our volcano plot data (**Fig. 3.13-14**), our western blot data also indicates significantly increased LC3II and ATG5 protein levels in the cell lysates

utilized for proteome analysis (**Fig. 3.20)**, suggesting that MA activity is sustained early and late in APP overexpression. ATG5 forms part of the ATG12-ATG5-ATG16L complex, one of the two ubiquitin-like conjugation systems involved in the early stages of autophagosome formation. Studies by Kuma et al. (2004) highlight the importance of this protein, showing that ATG5-knockout mice die at the neonatal stage, while overexpression of ATG5 in mice has been shown to induce MA and extend lifespan (Pyo et al., 2013). In line with our findings, microarray-based proteomics analysis carried out in DU145, MCF7, HT29 cells exposed to different durations of hypoxia reveals enhanced LC3II and ATG5 levels (Rouschop et al., 2010). Further work by Jaeger et al., (2010) also reveals significantly increased LC3II levels in AD brain tissue, with reduced BECN1 levels thought to inhibit the degradation rate of autophagosomes in this context, while ATG5 levels were not significantly changed. Contrary to our findings, Qiu et al. (2016) demonstrate reduced LC3II levels in the frontal cortex of AD post-mortem tissues of various Braak stages (Braak stages III, IV, V, VI), indicating MA impairment may be an early event in AD. Moreover, microarray data of the hippocampus and entorhinal cortex tissue from late-onset AD patients (mean age, 79.9 ± 6.9 years) reveal that ATG5 is downregulated in AD progression, and at the transcriptional level during ageing in healthy humans [young (≤40 y old) and old (≥70 y old)] (Lipinski et al., 2010). Recent work by Cavieres et al. (2015) found that depletion of ATG5 enhanced the accumulation of APP even in the presence of tetrahydrohyperforin (IDN5706), a compound previously shown to promote the degradation of APP/Aβ via MA in an ATG5-dependent manner (Inestrosa et al., 2011). These findings suggest that ATG5-dependent MA induction may impact Aβ metabolism, however, further studies are needed. Our volcano plot analysis indicates that HSP7c (also called HSC70) protein expression is significantly indicated only upon early APP overexpression (**Fig. 3.13**), suggesting that CMA may be induced as early as 24 hrs. In line with these findings, Cuervo et al. (1995) demonstrate that CMA is unregulated as early as 12 hrs following starvation in rat liver cells and remains active as long as starvation persists. Others have also shown that CMA activity is promoted in response to increased proteotoxicity, as evidenced *in vivo* for mutant tau and α-synuclein (Chesser et al., 2013; Vogiatzi et al., 2008), however, it was not specified at

which time point in proteotoxicity CMA was induced. To our surprise, our western blot data reveals no significant difference in CMA activity at the 24-hr time point, instead, CMA activity is significantly induced only upon 48 hrs APP overexpression, i.e. enhanced LAMP2A, while HSC70 expression remains unchanged (**Fig. 3.21.B,C**). These findings are in contrast with previous data revealing that enhanced HSC70 and LAMP2A protein levels as early as 20 hrs in lysosomes isolated from the liver of rats starved for 20-88 hrs in the presence or absence of the protease inhibitor, leupeptin (Cuervo et al., 2000). These findings may be better aligned in the future using CMA-positive lysosomes isolated from APP overexpression N2aswe cells.

During early APP overexpression (**Fig. 3.13**), our volcano plot indicates increased caspase-3 (indicated as CASP3) levels, while no expression is revealed upon late APP overexpression (**Fig. 3.14**). Caspase-3 is a principal effector caspase that is critically involved in the progression of apoptosis and the appearance of hallmark morphological changes such as nuclear fragmentation (Brentnall et al., 2013). Our volcano plot finding is in contradiction with earlier caspase-3/7 Glo analysis which indicates a caspase 3/7 activation from 24 hrs onwards (**Fig. 3.9**). Similarly, others have demonstrated increased levels of caspase-3 immunoreactivity in AD hippocampal neurons of various Braak stages, where caspase-3 exhibits a high degree of colocalization with Aβ deposits and NFT (Louneva et al., 2008; Su et al., 2001). Moreover, *in situ* immunohistochemistry and western blot analysis demonstrates that both caspase-3 and APP are increased in AD hippocampal and frontal cortex tissue [Braak stage IV-VI] compared to aged-matched control cases (Zhao et al., 2003). The detection of increased caspase-3 activity with APP expression supports the hypothesis that caspases contribute to amyloidogenic processes, and my thus contribute to AD neurodegeneration. To further address the role of apoptosis, western blot analysis of cytochrome c expression was performed. Cytochrome c is a mitochondrial protein with a dual role in respiration and apoptosis. Under physiological conditions, cytochrome c functions as a ROS scavenger and participates in the mitochondrial electron transport chain, thus playing an essential role in efficient ATP generation process (Hüttemann et al., 2011). Robust cytochrome c expression is indicated upon 48 hrs APP overexpression, with no difference upon 24 hrs APP

overexpression (**Fig. 3.22.B**). In line with our findings, *in situ* hybridization, immunocytochemistry analysis reveals a significant increase in cytochrome c levels in hippocampal, cortex, and cerebellum tissues obtained from AD patients at autopsy (mean age, 85 ± 4.2 years) (Hirai et al., 2001). Others have shown rapid cell death associated with decreased ATP production and the release of several apoptotic proteins, including cytochrome c, which triggered the caspase cascade leading to apoptosis in Jurkat T cells treated with ATP-synthase inhibitor or mitochondrial uncoupler (Aronis et al., 2003). Increased cytochrome c release has been shown to exacerbate the bioenergetic defect observed in platelet mitochondria and hippocampi and cortex tissue sections from AD patients [Braak stage IV (mean age, 65.2 ± 8.5 years)] compared to age-matched control subjects (Bosetti et al., 2002). These data suggest a role of mitochondrial bioenergetics in the pathogenesis of AD, mitochondrial isolation from N2aswe cells may shed insight into oxidative phosphorylation (OXPHOS) function and ATP production in the process of APP overexpression. The volcano plot analysis representing protein expression between early and late APP overexpression reveals increased expression of APP, HSP7c, and anti-apoptotic protein BCL6 in addition to other proteins (**Fig. 3.15**). BCL6 has been called a “master regulator” of germinal centre formation and is thought to repress the transcription of hundreds of proteins, including those implicated in apoptosis (Basso et al., 2012). It is plausible that BCL6 may indicate a failed rescue attempt, as our data suggest a clear role for apoptosis machinery engagement after the 24-hr time point as evidenced by enhanced Aβ expression (**Fig. 3.3**) and caspase activation (**Fig. 3.9**). In fact, previous work by Kurosu et al. (2003) revealed that BCL6 overexpression significantly inhibited apoptosis and the increase in ROS levels in lymphoma cell lines following treatment with etoposide, a chemotherapeutic compound used for the treatments of various types of cancer, by enhancing the antioxidant defence systems. BCL6 has also been shown to be a repressor of the integral membrane 2B gene (*ITM2B*) (Del Campo et al., 2014). ITM2B is abundantly distributed in the hippocampus and cerebellum compared to the cortex . This protein has been found to bind to APP and inhibits its processing (Fotinopoulou et al., 2005; Matsuda et al., 2005, 2011), leading to a reduction Aβ production in N2a, HEK293, and HEK293T cells stably expressing APP-751(Fotinopoulou et al., 2005), with a 3-fold increase in ITM2B found in AD hippocampus in early pathologic stages (Braak-III) (Del Campo et al., 2014), suggesting that BCL6 may have a role in AD progression. Overall, our findings raise

the possibility that key proteins involved in cellular stress mechanisms are upregulated during early and late APP overexpression. These include enhanced expression of APP Binding Family A Member 1 (APBA1) a protein that facilitates APP accumulation in the trans-Golgi network, ras-related protein, Rab7, which has a role in the late endocytic pathway and lysosome biogenesis. Indeed, electron microscopy studies by Jäger et al. (2004) found that Rab7 participated in the final maturation of late AVs and was highly colocalised with LC3II and late endosomal and lysosomal markers in HeLa and MEF cells following 1-4 hrs starvation. More recently, Rab7 has been suggested to regulate MA activity through its interaction with ATG4B (Kjos et al., 2017). In U2OS cells co‐transfected with GFP‐ATG4B and mCherry‐Rab7 and starved for 2 hrs, live‐cell imaging of indicates increased ATG4B colocalization with Rab7. Furthermore, TEM analysis revealed that Rab7 knockdown increased the size of AVs, with western blot analysis showing a substantial increase in LC3II levels in Rab7b‐knockdown cells compared to control cells following macroautophagic flux assessment, i.e. cells were starved for 2 hrs in in the absence and presence of lysosomal acidification inhibitor bafilomycin A1 (Kjos et al., 2017). Overall, our findings suggest that MA activity is enhanced early in APP overexpression and remains enhanced as indicated by sustained BECN1 expression. Moreover, APP overexpression elicits transient and temporal engagement of CMA and the endolytic pathway machinery the in response to enhanced proteotoxicity, as evidenced by increased expression of oxidative stress and apoptosis markers (**ADDENDUM A Table A2-A4**).

To gain further understanding of the protein networks involved in the context of APP overexpression, STRING database analysis was employed. This open-source database contains information on protein–protein interactions derived from the analyses of co-expressed proteins, high-throughput experimental data, database mining, and computational predictions (Rezadoost et al., 2016). STRING network analysis employs a scoring framework based on benchmarks of the various types of associations against a common reference set to produce a single confidence score per prediction (Szklarczyk et al., 2015). The STRING network analysis reveals a time-

dependent increase in the complexity and abundance of APP-associated protein-protein interactions in response to early (**Fig. 3.16**) and late (**Fig. 3.17**) APP overexpression. Notably, direct protein-protein interactions are consistently indicated between APP, BACE1 (also known as β-secretase), CASP3, and GAPDH during both early and late APP overexpression. Although reports have shown the upregulation of APP, BACE1, CASP3, as well as BECN1, the role of GAPDH is less understood. GAPDH is an abundantly expressed enzyme known for its role in glucose metabolism. Additionally, GAPDH is also a CMA substrate (Cuervo et al., 2000), and has been found to interact with disease-associated proteins such as Aβ (Sunaga et al., 1995), implicating this protein in neurodegeneration. Our STRING protein-protein network between early and late APP overexpression indicates that APP is also strongly associated with GAPDH (**Fig. 3.18**). In line with our findings, a large-scale single-nucleotide polymorphism (SNP)-based association studies suggest that the GAPDH gene (*GAPD*) may be a risk factor for late-onset AD (Li et al., 2004b; Lin et al., 2006), showing increased colocalization with such as Aβ plaques extracted from AD cortical tissue (Sunaga et al., 1995). Hence, our data suggest that APP overexpression contributes to an enhanced glycolytic pathway activity, possibly as a cellular attempt to meet the increasing energetic demands following the upregulation of energy intensive proteolytic pathways such as MA, CMA, and the UPS during APP overexpression. In contrast with our findings, a three-year longitudinal study reveals that brain glucose metabolism was pathologically reduced in the temporal lobes of FAD patients before the clinical onset of symptoms became obvious (Wahlund et al., 1999), suggesting that glycolysis may be impaired early in AD development. In support of this data, brain imaging study by Rapoport (1999) indicates that glucose metabolism is significantly reduced in severe AD patients compared to mildly demented patients, as well as age-matched controls. These analyses, in addition to others, serve to emphasize the critical role GAPDH plays in AD, however, more studies are required to further unravel the role of GAPDH in Aβ pathology, and AD pathogenesis. Although not indicated when comparing early and late APP overexpression to control cells, strong interaction between APP and cathepsin D (CasD) is indicated between early and late APP overexpression (**Fig. 3.18**). Our data, suggest that CasD expression in

N2aswe cells may form part of the APP proteome signature of AD. CasD is a lysosomal enzyme whose primary function is to degrade proteins through lysosomal proteolysis. In line with our findings, other studies indicate that CasD mRNA levels and enzyme activity are upregulated in blood lymphocytes of AD patients (Bai et al., 2014), and this protease is present in Aβ plaques, and may have a role in APP processing and Aβ clearance *in vitro* (Leissring and Turner, 2013; Tian et al., 2014). Indeed, several studies have reported dysfunction in the MA-lysosomal system at several stages of AD pathology (Cataldo et al., 1991, 1996; Nixon and Cataldo, 2006). Therefore, lysosomal proteases may have a role in neurodegeneration, as they play a dual role in APP processing within autophagosomal/endosomal vesicles and their dysregulation has been shown to contribute to the overall lysosomal pathology in numerous diseases, including AD. In fact, studies by Nixon et al. (2000, 2005) reveals that both immature AVs and hydrolase-containing lysosomes accumulate in dystrophic neurites, suggesting that fusion between these structures is inefficient. Morphometric analyses of post-mortem AD brain tissue (62-78 years) by Cataldo et al. (1996), reveals a 2 to 8 increase in CasD-positive vacuolar structures in 80–93% of all hippocampal, and pyramidal cells compared to age-matched controls, suggesting that MA activity and/or endocytosis are robustly activated. Conversely, Koike et al. (2005) demonstrate that AVs structures accumulate in neurons and dystrophic neurites of CasD-deficient mice, while enhancing neuronal cathepsin activity significantly reduced Aβ levels, mitigated AV pathology, and improved cognitive function in APP mice (Gowrishankar et al., 2015; Wang et al., 2012; Yang et al., 2011a, 2011b). These reports all support our data, which suggest an interplay between MA, endocytosis and the APP system.

Notably our data also suggests an interplay between MA, and the UPS system, particularly late in APP overexpression (**Fig. 3.17**), as evidenced by the cluster of UPS-related proteins at this time point (**ADDENDUM A Table A3**). In line with our findings, studies have suggested that the UPS may contribute to AD pathogenesis (Hong et al., 2014; Upadhya and Hegde, 2007). In fact, recent studies reveal that de-ubiquitinating enzymes, play a pivotal role in Aβ clearance. For example, enhanced

proteasomal degradation of β-secretase and γ-secretase components has been shown to result in reduced Aβ accumulation in HEK-293T, and cortical neuronal cells (Hong et al., 2014; Williamson et al., 2017). In support of these findings, Keller and colleagues, demonstrated a significant decrease in UPS activity in the hippocampal gyrus (48%), superior and middle temporal gyri (38%), and inferior parietal lobule (28%) of AD patients (mean age 77.9 ± 3.3 years), while no significant changes in proteasome activity was observed in less vulnerable brain regions, such as the cerebellum (Keller et al., 2000). In line with our findings, these studies indicate a possible role for the UPS during APP overexpression. However, future studies are needed to investigate the mechanism underlying the interplay between macroautophagic activity, APP/Aβ and the UPS in AD pathology.

LC-MS proteomics is extensively used to facilitate the high-throughput detection and quantification of thousands of proteins in numerous AD clinical samples (Panis et al., 2014; Ping et al., 2018). Of the two prevalent strategies used for protein-based quantitation, either label-free or differential labelling-based approaches, the former is favoured for quantitative proteomic studies (Théron et al., 2014). Hence, we employed a label-free LC-MS approach to characterise the APP proteome signatures early and late in APP overexpression. However, this approach has several limitations, including dependence on accurate mass measurements and reproducible peptide retention times by liquid chromatography (LC), which if not tightly controlled can introduce bias in peptide ion intensities and ultimately contribute to a higher number of missing values and increased variance of lower abundant proteins (Di Luca et al., 2015; Karpievitch et al., 2012). Accordingly, the expression of key amyloidogenic (APP, Aβ), MA (LC3II, ATG5), CMA (LAMP2A, HSC70), and apoptotic (cytochrome c) molecular markers proteins was further assessed by western blot analysis using the remaining cell lysates utilized in LC-MS proteome analysis.

CHAPTER 4 RESULTS: APP AND MACROAUTOPHAGIC FLUX ASSESSMENT

4.1. Introduction to results

Autophagic/macroautophagic flux refers to the dynamic balance between AV formation and clearance with the term flux referring to the rate of flow along the MA pathway (Klionsky et al., 2016; Loos et al., 2014). Impaired macroautophagic flux, as evidenced by the abnormal accumulation of AV, including autophagosomes or autolysosomes, in affected neurons of the brain is prominently observed at several stages in AD progression (Nixon and Yang, 2012). However, it is unclear whether accumulated AV reflect an increase in macroautophagic flux, as an increased autophagosome number can indicate macroautophagy induction or failed autophagosome fusion (Lee et al., 2010, 2011b). While LC3 levels serve as a read-out of AV number at specific time points, they do not provide information about MA activity *per se*, as AV numbers can also be increased by blocking MA in later stages of the process (Klionsky et al., 2016). Macroautophagic flux is a more reliable indicator of MA activity and can be determined by comparing the numbers of AV in control conditions and after blocking the final steps of the process, e.g., after lysosomal inactivation. Hence, the aim of this chapter was to assess the effects of APP overexpression on flux, i.e. (i) MA and CMA activity, (ii) protein clearance, and (iii) neuronal protection. To this end, BA (5 mM) treated N2aswe cells were treated in the presence and absence of BafA1. Subsequently, western blot analysis for relevant protein levels, and TEM was conducted.

4.2. Results

In order to assess whether macroautophagic flux is still functional under APP overexpression, and whether flux may increase in time, N2aswe cells were treated with saturating concentrations of BafA1 (Loos et al., 2014). Briefly, western blot analysis was performed using 400 nM BafA1 for a treatment duration of 2 hrs (indicated as **+**), and 5 mM BA for a treatment duration of 24 hrs.

4.2.1. Effect of flux modulation on amyloidogenic processing

As shown in **Fig. 4.1.A**, APP protein expression is significantly increased in the 24 hrs BA treated group **(+)** [0.89 ± 0.02 ($p<0.05$)] compared to the 24 hrs BA treated group **(-)** [0.64 ± 0.06], and in the 48 hrs BA treated group **(+)** [1.09 ± 0.03 ($p<0.05$)] compared to the 48 hrs BA treated group **(-)** [0.85 ± 0.02]. More importantly, a significant increase in APP expression is indicated in the 24 hrs BA treated group **(+)** and the 48 hrs BA treated group **(+)** compared to the 12 hrs BA treated group **(+)**, and in the 48 hrs BA treated group **(+)** compared the 24 hrs BA treated group **(+)** (**Fig. 4.1.B**).

Figure 4.1.C reveals that β-secretase protein expression is significantly increased in the 24 hrs BA treated group **(+)** [0.77 ± 0.03 ($p<0.05$)] compared to the 24 hrs BA treated group **(-)** [0.47 ± 0.029], and in the 48 hrs BA treated group **(+)** [1.08 ± 0.12 ($p<0.05$)] compared to the 48 hrs BA treated group **(-)** [0.77 ± 0.08]. Moreover, β-secretase expression is significantly increased in the 24 hrs BA treated group **(+)** and the 48 hrs BA treated group **(+)** compared to the 12 hrs BA treated group **(+)**, and in the 48 hrs BA treated group **(+)** compared the 24 hrs BA treated group **(+)** (**Fig. 4.1.D**).

Similarly in **Fig. 4.1.E,** Aβ protein expression is significantly increased in the 24 hrs BA treated group **(+)** [0.77 ± 0.03 ($p<0.05$)] compared to the 24 hrs BA treated group **(-)** [0.57 ± 0.06], and in the 48 hrs BA **(+)** [1.0 ± 0.04 ($p<0.05$)] compared to the 48 hrs BA treated group **(-)** [0.84 ± 0.007]. Aβ expression is also significantly increased in the 24 hrs BA treated group **(+)** and the 48 hrs BA treated group **(+)** compared to the 12

hrs BA treated group **(+)**, and in the 24 hrs BA treated group **(+)** compared to the 48 hrs BA treated group **(+)** (**Fig. 4.1.F**).

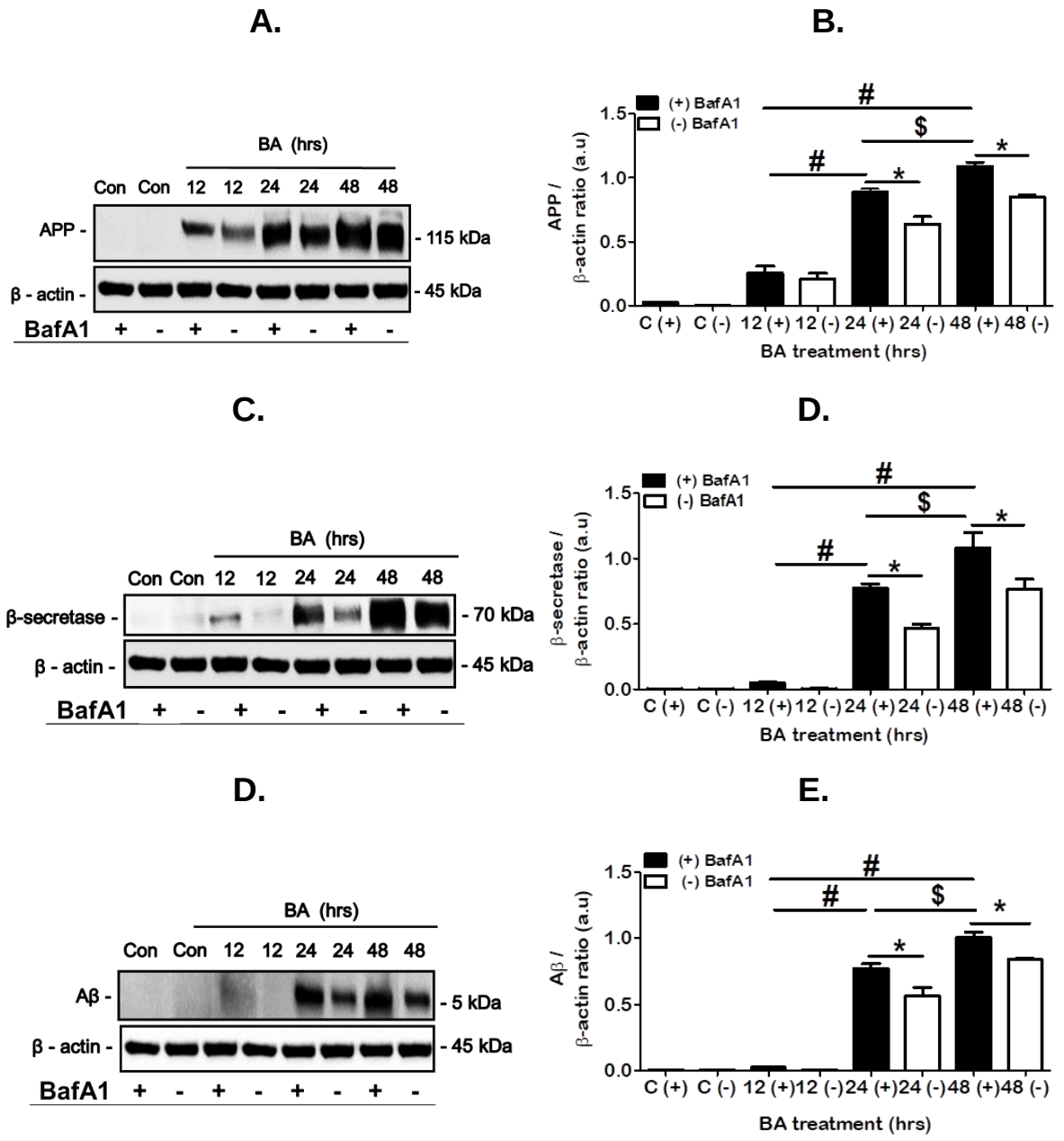

Figure 4.1: Effect of flux modulation on amyloidogenic processing in N2aswe cells. Representative western blot and densitometric analysis for (**A**, **B**) APP, (**C**, **D**) β-secretase, and (**E, F**) Aβ protein expression is shown. Data expressed as mean ± SEM, statistical analysis: ANOVA and Bonferroni correction, *p<0.05 vs. time-specific control **(-)**, #p<0.05 vs 12 hrs BA **(+)**, **$**p<0.05 vs 24 hrs BA **(+)**, n = 3, arbitrary units (a.u).

4.2.2. Effect of APP overexpression on macroautophagic flux

In order to assess the impact of APP overexpression on macroautophagic flux in time, western blot analysis of key MA proteins was performed.

As shown in **Fig. 4.2.A**, LC3II protein expression is significantly increased in control **(+)** [1.44 ± 0.17 ($p<0.05$)] compared to control **(-)** [0.28 ± 0.09], in the 12 hrs BA treated group **(+)** [2.38 ± 0.21 ($p<0.05$)] compared to the 12 hrs BA treated group **(-)** [1.09 ± 0.29], in the 24 hrs BA treated group **(+)** [3.58 ± 0.26 ($p<0.05$)] compared to the 24 hrs BA treated group **(-)** [2.19 ± 0.23], and in the 48 hrs BA treated group **(+)** [5.24 ± 0.31 ($p<0.05$)] compared to the 48 hrs BA treated group **(-)** [3.72 ± 0.32]. Moreover, a significant increase in LC3II expression is observed in the 24 hrs treated group **(+)** and the 48 hrs BA treated group **(+)** compared to the12 hrs BA treated group **(+)**, and in the 48 hrs BA treated group **(+)** compared the 24 hrs BA treated group **(+)** (**Fig. 4.2.B**), suggesting an increase in macroautophagic flux.

Figure 4.2.C reveals that p62 protein expression is significantly increased in the 24 hrs BA treated group **(+)** [4.47 ± 0.18 ($p<0.05$)] compared to the 24 hrs BA treated group **(-)** [2.96 ± 0.37], and in the 48 hrs BA treated group **(+)** [5.33 ± 0.4 ($p<0.05$)] compared to the 48 hrs BA treated groups **(-)** [3.46 ± 0.27]. Moreover, a significant increase in p62 expression is observed in the 24 hrs BA treated group **(+)** and the 48 hrs BA treated group **(+)** compared to the 12 hrs BA treated group **(+)** (**Fig. 4.2.D**), suggesting a decrease in cargo degradation with increasing flux, and APP overexpression.

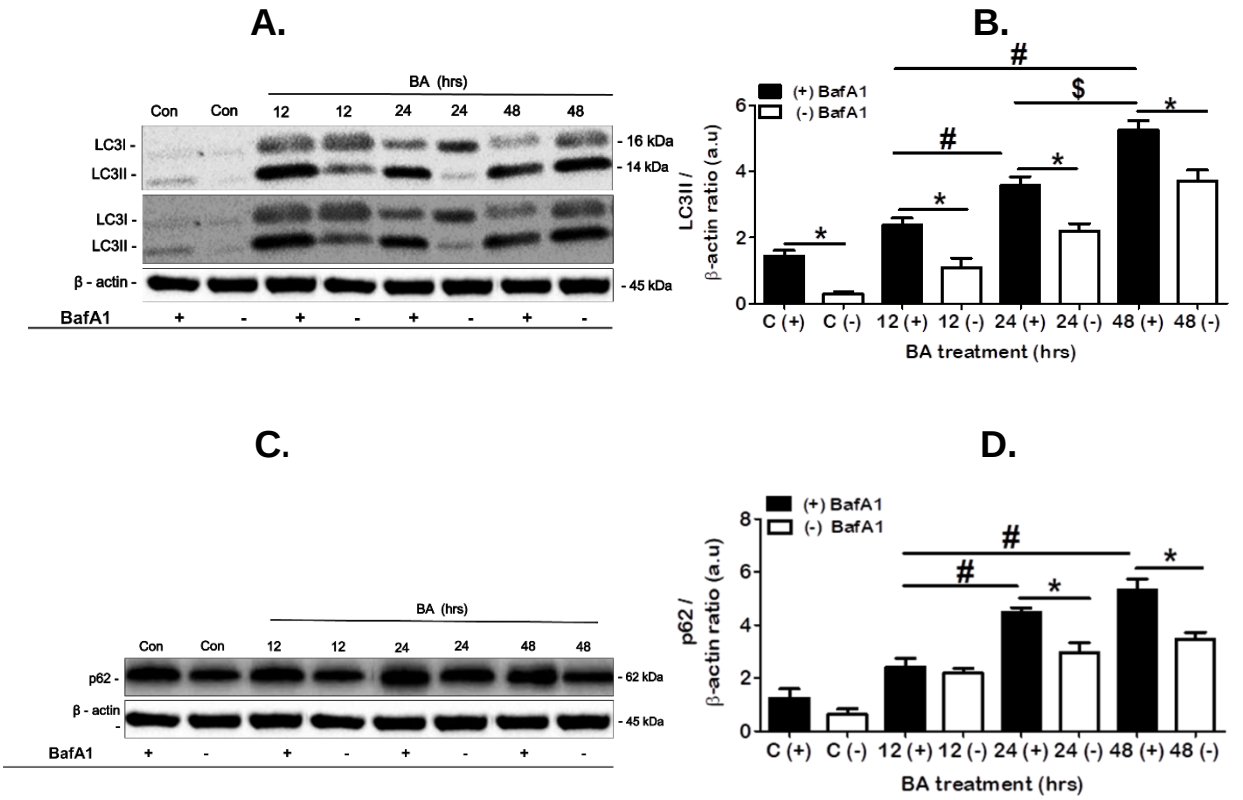

Figure 4.2: Assessment of macroautophagic flux in N2aswe cells in response to APP overexpression. Representative western blot and densitometric analysis for (**B**, **C**) LC3II (low and high exposure), and (**D**, **E**) p62 protein expression is shown. Data expressed as mean ± SEM, statistical analysis: ANOVA and Bonferroni correction, *****p<0.05 vs. time-specific control (-), #p<0.05 vs 12 hrs BA **(+)**, **$**p<0.05 vs 24 hrs BA **(+)**, n = 3, arbitrary units (a.u).

4.2.3. Effect of flux modulation in the context of APP overexpression on CMA activity

In order to assess whether inhibition of cargo degradation through MA affects CMA activity over time, western blot analysis of key CMA proteins was performed.

As shown in **Fig. 4.3.A**, LAMP2A protein expression is significantly increased in the 24 hrs BA treated group **(+)** [1.19 ± 0.07 (p<0.05)] compared to the 24 hrs BA treated group **(-)** [0.84 ± 0.09], and in the 48 hrs BA **(+)** treated group [1.31 ± 0.06 (p<0.05)] compared to the 48 hrs BA treated group **(-)** [0.95 ± 0.05]. Moreover, LAMP2A expression is significantly increased in the 24 hrs BA treated group **(+)** and the 48 hrs BA treated group **(+)** compared to the 12 hrs BA treated group **(+)** [0.59 ± 0.05] (**Fig. 4.3.B**), suggesting an increase in CMA activity.

Figure 4.3.C indicates that HSC70 expression is significantly increased in the 24 hrs BA treated group **(+)** [2.49 ± 0.12 ($p<0.05$)], and the 48 hrs BA treated group [2.72 ± 0.26 ($p<0.05$)] compared to the 12 hrs BA treated group **(+)** [0.26 ± 0.07] (**Fig. 4.3.D**).

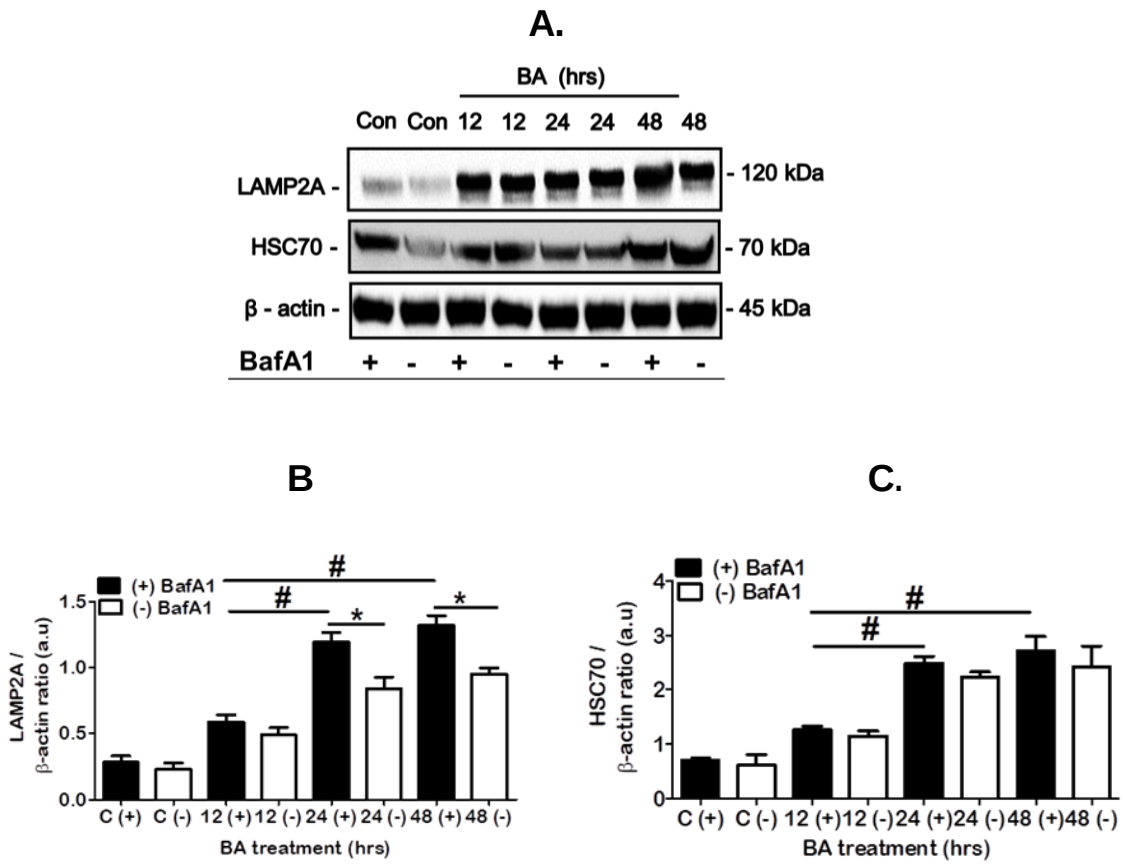

Figure 4.3: Effect of flux modulation in the context of APP overexpression on CMA activity in N2aswe cells. Representative western blot and densitometric analysis for (**A**, **B**) LAMP2A, and (**A**, **C**) HSC70 protein expression is shown. Data expressed as mean ± SEM, statistical analysis: ANOVA and Bonferroni correction, ***p<0.05 vs. time-specific control (-), #p<0.05 vs 12 hrs BA **(+)**, n = 3, arbitrary units (a.u).

4.2.4. Effect of flux modulation in the context of APP overexpression on apoptosis

In order to assess whether inhibition of MA cargo degradation in the context of APP overexpression impacts apoptosis in time, western blot analysis of key apoptotic proteins was performed.

As shown in **Fig. 4.4.A**, there is no significant difference in Total Caspase-3 protein expression under similar treatment conditions in the absence and presence of BafA1. In contrast, a significant increase in Total Caspase-3 is observed in the 24 hrs BA treated group **(+)** and the 48 hrs BA treated group **(+)** compared to the 12 hrs BA treated group **(+)** (**Fig. 4.4. B**).

Figure 4.4.C reveals that cleaved-PARP protein expression is significantly increased in the 24 hrs BA treated group **(+)** [2.48 ± 0.14 ($p<0.05$)] compared to the 24 hrs BA treated group **(-)** [1.71 ± 0.25], and in the 48 hrs BA treated group **(+)** [3.17 ± 0.13 ($p<0.05$)] compared to the 48 hrs BA treated group **(-)** [2.38 ± 0.22]. Additionally, a significant increase in cleaved-PARP expression is observed in the 24 hrs BA treated group **(+)** and the 48 hrs BA treated group **(+)** compared to the 12 hrs BA treated group **(+)** (**Fig. 4.4.D**).

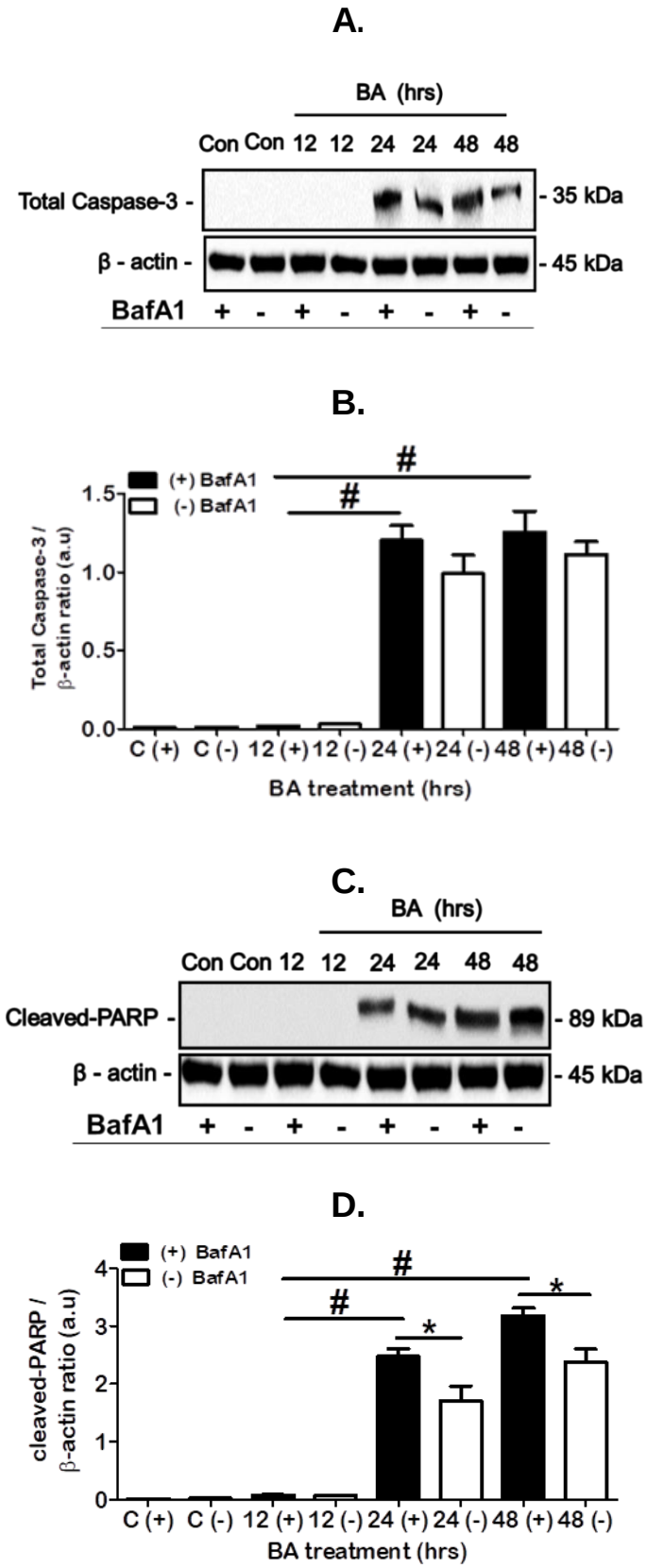

Figure 4.4: Effect of flux modulation in the context of APP overexpression on apoptosis in N2aswe cells. Representative western blot and densitometric analysis for (**A**, **B**) Total Caspase-3, and (**C**, **D**) cleaved-PARP protein expression is shown. Data expressed as mean ± SEM, statistical analysis: ANOVA and Bonferroni correction, *****$p<0.05$ vs. time-specific control **(-)**, #$p<0.05$ vs 12 hrs BA **(+)**, n = 3, arbitrary units (a.u).

4.2.5. Effect of APP overexpression on AV formation in N2aswe cells

TEM analysis reveals increased abundance of AVs in a time-dependent manner upon BA exposure (**Fig. 4.5 A, C, E, G**). Moreover, AV formation is further increased in abundance and complexity upon BafA1 treatment (**Fig. 4.5 B, D, F, H**). These observations suggest that AV clearance is increasingly impeded in response APP overexpression, and further exacerbated in response to BafA1 treatment.

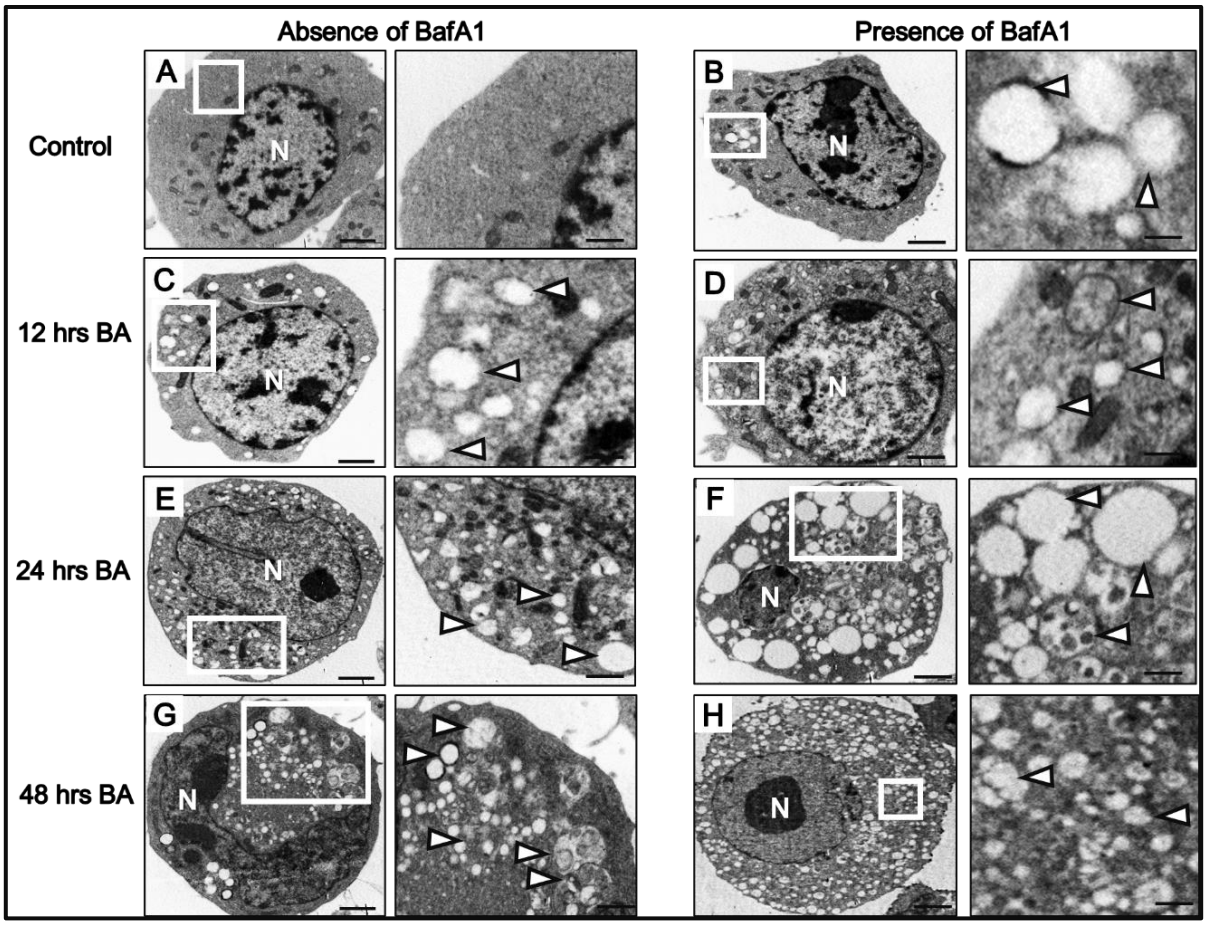

Figure 4.5: Autophagic vacuole (AV) formation in the absence (left panel), and presence (right panel) of BafA1 in response to APP overexpression. Lower magnification micrographs (**left of each panel**) indicate general cellular ultrastructure; higher magnification micrographs (**right of each panel**) reveal the presence of AV structures. Nucleus = N, scale bar **A-H** = 5000 nm, higher magnification micrographs = 2000 nm, arrowheads indicate AV structures.

4.2.6. Quantification of AVs in N2aswe cells

Image J automatic particle counting plug-in was used to quantify the number and area of AVs. The results indicate a significant increase in the number of AVs per cell in the control **(+)** [44.6 ± 4.08 ($p<0.05$)] compared to the control **(-)** [19.68 ± 0.99], in the 12 hrs BA treated group **(+)** [59.65 ± 5.17 ($p<0.05$)] compared to the 12 hrs BA treated group **(-)** [35.11 ± 4.2], in the 24 hrs BA treated group **(+)** [80.63 ± 2.85 ($p<0.05$)] compared to the 24 hrs BA treated group **(-)** [58.03 ± 4.78], and in the 48 hrs BA treated group **(+)** [122.4 ± 3.08 ($p<0.05$)] compared to the 48 hrs BA treated group **(-)** [95.13 ± 4.93]. Moreover, a significant increase in AVs is observed in both the 24 hrs BA treated group **(+)** and the 48 hrs BA **(+)** treated group compared to the 12 hrs BA treated group **(+)**, and in the 48 hrs BA treated group **(+)** compared to the 24 hrs BA treated group **(+)** (**Fig. 4.6.A**).

Automated analysis of each AV reveals a significant increase in AV surface area per cell in the control **(+)** [45.19 ± 4.35 ($p<0.05$)] compared to the control **(-)** [21.33 ± 3.46], in the 12 hrs BA treated group **(+)** [58.18 ± 4.49 ($p<0.05$)] compared to the 12 hrs BA **(-)** [32.76 ± 3.0], in the 24 hrs BA treated group **(+)** [79.84 ± 4.7 ($p<0.05$)] compared to 24 hrs BA treated group **(-)** [54.16 ± 7.47], with no significant difference between the 48 hrs BA treated group **(+)** and the 48 hrs BA treated group **(-)** (**Fig. 4.6.B**).

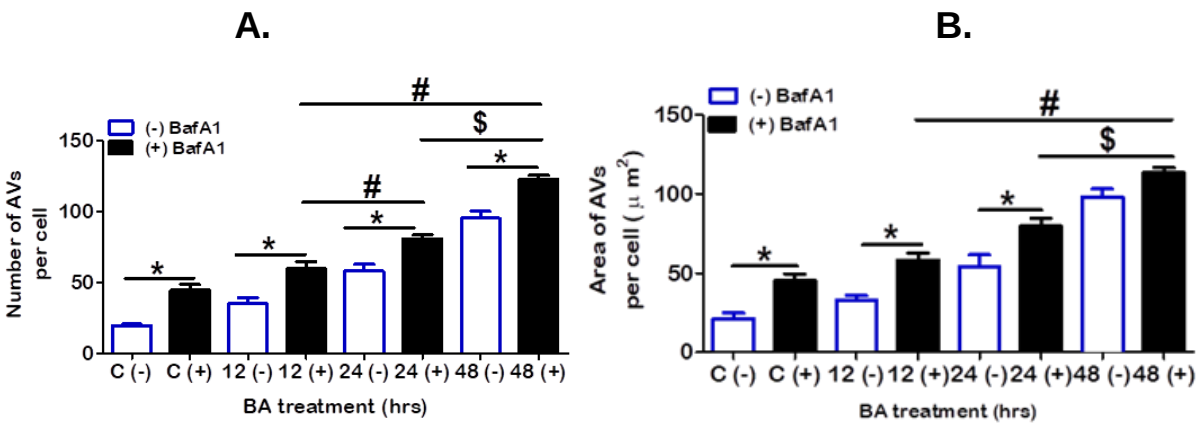

Figure 4.6: Quantification of the number and area of AVs in response to APP overexpression in N2aswe cells. A. Number of AVs per cell. **B**. Average area of AVs per cell. Data expressed as mean ± SEM, statistical analysis: ANOVA and Bonferroni correction, ***p<0.05 vs. time-specific control **(-)**, #p<0.05 vs 12 hrs BA **(+)**, **$**p<0.05 vs 24 hrs BA **(+)**. A total of 40 cells were analysed, n = 2.

4.2.7. Effect of APP overexpression on fibrillar ultrastructure in N2aswe cells

Figure 4.7 A, C, E, G reveals fibrillar protein ultrastructure formation which increases in size upon BA exposure, and the abundance and size of these electron dense structures is further increased upon BafA1 treatment (**Fig. 4.7 B, D, F, H**), suggesting that APP overexpression impacts the formation and length of these structures, while BafA1 treatment impacts the abundance and length.

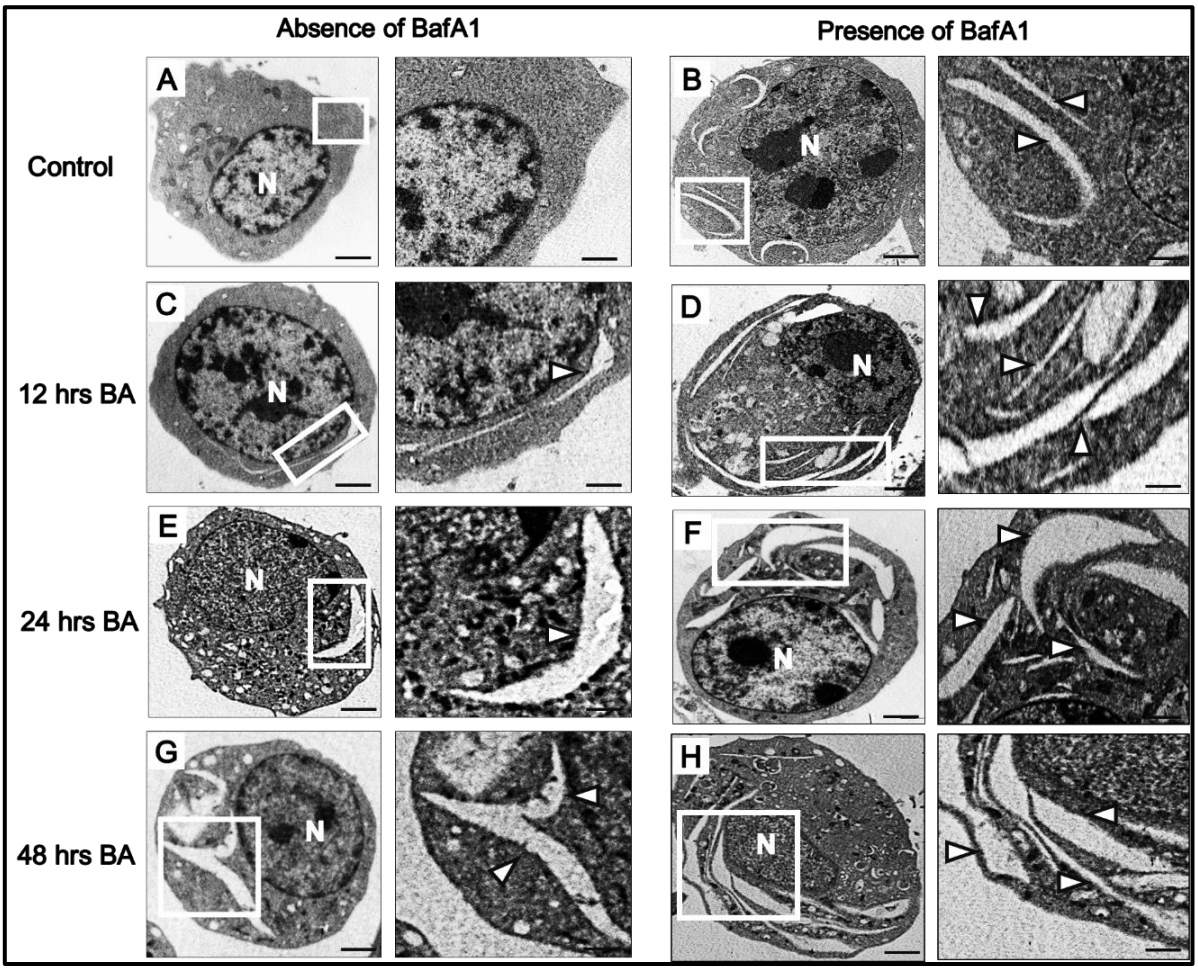

Figure 4.7: Fibrillar protein ultrastructure formation in the absence (left panel), and presence (right panel) of BafA1 in response to APP overexpression. Lower magnification micrographs (**left of each panel**) indicate general cellular ultrastructure; higher magnification micrographs (**right of each panel**) reveal the presence of fibrillar structures. Nucleus = N, scale bar **A-H** = 5000 nm, higher magnification micrographs = 2000 nm, arrowheads indicate fibrillar structures.

4.2.8. Effect of APP overexpression on mitochondrial ultrastructure

As revealed in **Fig. 4.8 A, C, E, G,** mitochondrial organelle accumulation is increased in abundance upon BA exposure, and is further increased in abundance upon BafA1 treatment (**Fig. 4.8 B, D, F, H**), suggesting that APP overexpression increasingly impedes mitophagy, and this condition is further impacted upon BafA1 treatment.

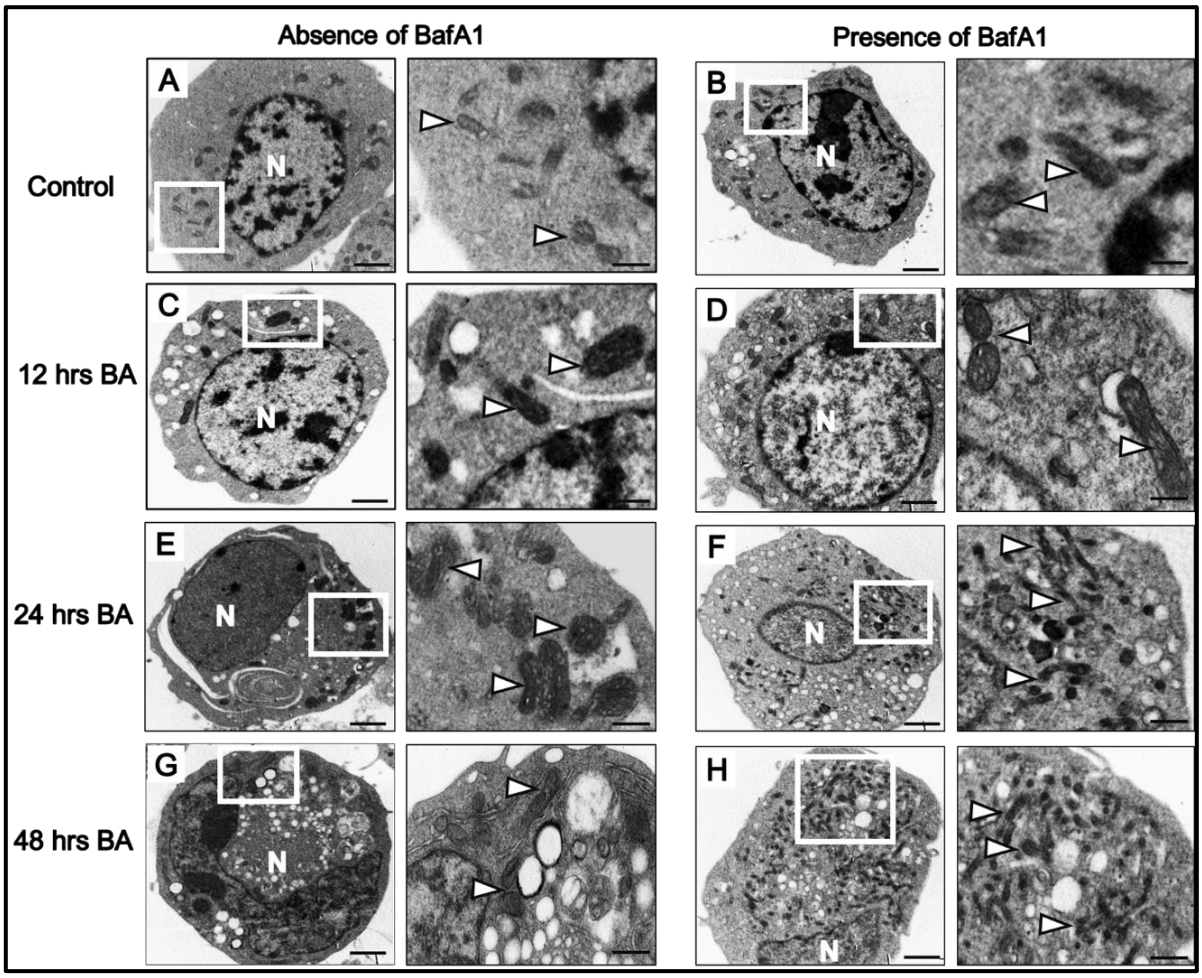

Figure 4.8: Mitochondrial ultrastructure in the absence (left panel), and presence (right panel) of BafA1 in response to APP overexpression. Lower magnification micrographs (**left of each panel**) indicate general cellular ultrastructure; higher magnification micrographs (**right of each panel**) reveal mitochondrial structures. Nucleus = N, scale bar **A-H** = 5000 nm, higher magnification micrographs = 2000 nm, arrowheads indicate mitochondrial structures.

4.2.9. Effect of APP overexpression on ferritin-like inclusions

TEM analysis reveals increased abundance of ferritin-like inclusions upon 24 hrs BA exposure and 48 hrs BA exposure (**Fig. 4.9 A, C, E, G**), and these inclusions are further increased in abundance upon BafA1 treatment (**Fig. 4.9 B, D, F, H**). Notably, these inclusions are absent in the control and 12 hrs BA exposed group, but are revealed in these groups upon BafA1 treatment, suggesting that clearance is impacted upon late APP overexpression and further impacted upon BafA1 treatment, even as early as 12 hrs BA exposure.

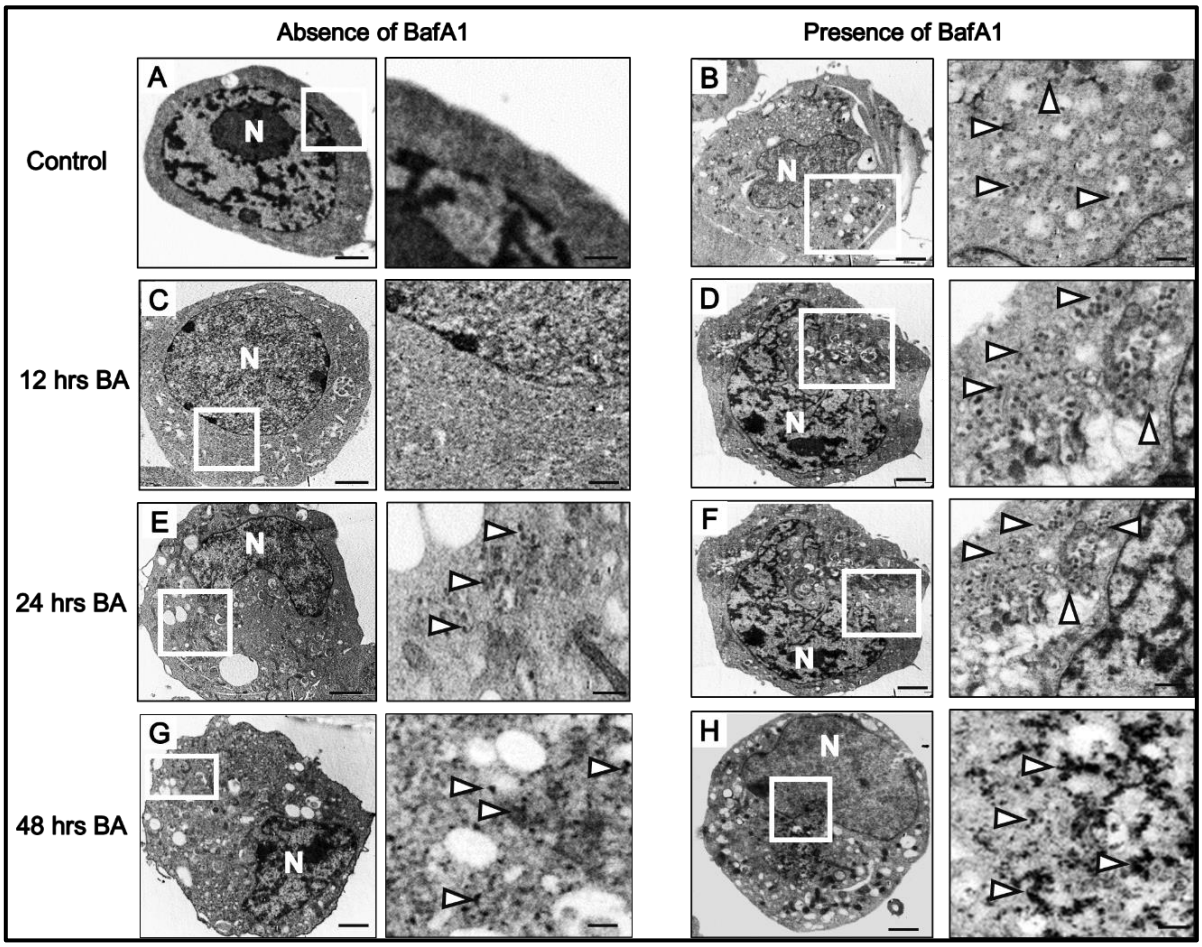

Figure 4.9: The presence of ferritin in the absence (left panel), and presence (right panel) of BafA1 in response to APP overexpression. Lower magnification micrographs (**left of each panel**) indicate general cellular ultrastructure; higher magnification micrographs (**right of each panel**) reveal a time-dependent accumulation black inclusion bodies, most likely ferritin. Nucleus = N, scale bar **A-H** = 5000 nm, higher magnification micrographs = 2000 nm, arrowheads indicate electron dense inclusion bodies.

CHAPTER 4 DISCUSSION: APP AND MACROAUTOPHAGIC FLUX

The role of MA dysfunction in neurodegeneration has received considerable attention in the last years. However, it remains largely unclear, whether MA dysfunction manifests with high macroautophagic activity or whether degradation of proteins completely fails. One of the challenges in this context is to accurately assess macroautophagic flux. To this end, macroautophagic flux was assessed in the context of APP overexpression by inhibiting autophagosome/lysosome fusion while observing the accumulation of autophagosomes or LC3II protein levels.

4.3. Effect of flux modulation on amyloidogenic processing with APP overexpression

To assess whether APP, β-secretase, and Aβ turnover is impacted by the blockade of MA's degradative capacity over time, western blot analysis was performed in the absence and presence of BafA1 treatment (**Fig. 4.1**). The results indicate a time-dependent increase in APP (**Fig. 4.1.B**), β-secretase (**Fig. 4.1.D**), and Aβ (**Fig. 4.1.F**) protein levels following 24 hrs and 48 hrs APP overexpression in the presence of BafA1 treatment compared to control cells. This data strongly suggests that (a), the macroautophagic pathway is still functional, since APP is increased in the presence of BafA1 at each time point, and (b) that the macroautophagic pathway is unable to clear the highly abundant APP protein, since it is continuously increasing. This result strongly suggests that the MA machinery, although dysfunctional in the context of coping with toxic protein aggregates, is, *per se* still functional and clears toxic protein. The line with our findings, others have shown that MA contributes to Aβ pathology. In a study by Nilsson et al. (2013), significantly decreased Aβ plaque load was reported in MA-deficient mice, and these findings were confirmed in MA-deficient cortical/hippocampal neurons in which Aβ was significantly reduced. Conversely, ATG7 lentivirus supplementation restored the level of Aβ released to that of MA-competent neurons (Nilsson and Saido, 2014; Nilsson et al., 2013). More recently,

confocal microscopy analysis by Barbero-Camps et al. (2018) revealed higher presence of Aβ and autophagosomes (LC3B puncta) in the hippocampus from 7-month-old APP mice. These data support our findings that MA influences APP/Aβ accumulation by regulating the clearance of these proteins. In line our findings of significantly enhanced β-secretase (**Fig. 4.1.D**), Cai et al. (2015) demonstrated that both MA inhibitor (24 hrs 3MA treatment) and inducer (24 hrs serum starvation) Aβ production and accumulation by enhancing the activity of β-, and γ-secretases in SH-SY5Y cells. Our data also suggests that MA activity effects β-secretase and turnover since BafA1 treatment enhances its abundance, suggesting that β-secretase itself is also targeted to the MA machinery. These findings are supported by previous data showing enhanced the retention of β-secretase with AVs of cortical neurons isolated from APP mice, thereby leading to enhanced β-secretase cleavage of APP within these vesicles (Feng et al., 2016). Moreover, studies by Fukumoto et al. (2002, 2004) reveal that the levels of Aβ, and β-secretase activity are elevated with age in AD patient brains, rhesus monkeys**,** and in APP transgenic mice.

Overall, our data reveals a time-dependent increase of APP, β-secretase, and toxic Aβ protein cargo, which is further enhanced following the blockage of autophagosome degradation (**Fig. 4.1**), raising the possibility that MA activity is not sufficient to meet the increased cargo. Therefore, MA enhancing drugs could promote the clearance of these proteins with disease progression and may represent a viable therapeutic strategy in the amelioration of Aβ neurotoxicity in AD. To our knowledge, this is novel and critical insights into the role of MA in Aβ induced toxicity.

4.4. Effect of APP overexpression on macroautophagic flux

To our surprise, our data reveals that autophagosome abundance is significantly increased (LC3II protein levels), however, macroautophagic flux remains unchanged, yet functional, even at the 48-hr time point (**Fig. 4.2.B**). However, despite a functional

macroautophagic activity, p62 levels increase, suggesting the mismatch between overall protein clearance and macroautophagic activity (**Fig. 4.2.D**). This data contrasts previous findings indicating that macroautophagic flux is reduced in brain tissue from AD patients, and *in vivo* AD models (Colacurcio and Nixon, 2016; Nixon and Yang, 2011). Our results clearly indicate that MA remains functional, albeit unable to clear APP, Aβ and β-secretase sufficiently. In line with our findings, a study by Bordi et al. (2016), which assessed the entire MA process in CA1 pyramidal neurons from early and late-stage AD patients, revealed that MA is upregulated early and progressively throughout the disease course. Consistent with our data, macroautophagy flux did not decrease, instead, becoming progressively impeded due to insufficient substrate clearance, as reflected by autolysosomal accumulation p62 and expansion of autolysosomal size and total area. It is reasonable to propose that the upregulation of MA activity may be an initial neuroprotective to increasing proteotoxicity, which is maintained with increasing APP, and Aβ expression, but is insufficient to maintain substrate turnover. In contrast with our findings, accumulation of Aβ-laden autophagosomes have been reported in AD brain tissue and *in vivo* models of AD with AD progression (Nilsson et al., 2013; Nixon, 2007; Yu et al., 2004, 2005). These findings not only suggest that the end stage of autophagosomal clearance is impaired, but also, that impaired MA may be implicated in the mechanism of Aβ toxicity as suggested by Nixon (2007). To our knowledge, our results indicate for the first time, that macroautophagic flux remains functional in APP overexpressing N2aswe cells, and in fact, is significantly upregulated even as the clearance of MA cargo is progressively reduced. This novel observation indicates that MA activity can still be modulated even at late time points, as macroautophagic flux is maintained with increasing Aβ neurotoxicity. However, further studies are needed to comprehensively evaluate the entire MA process, specifically in vulnerable neuronal cell populations, from early to late stages in AD progression compared to controls. In addition, a component of model system utilization may also contribute to the variability in findings.

4.5. Effect of flux modulation in the context of APP overexpression on CMA activity

Autophagic pathways are closely interconnected (Park and Cuervo, 2013), and although MA and CMA are preferentially activated in a time- and stimuli-specific manner, most cells activate MA in response to CMA blockage and *vice versa* (Kaushik and Cuervo, 2018). The interplay between MA and CMA activity during the progression of AD is not well understood. Hence, in order to determine whether CMA is induced as a compensatory response to the inhibition of autophagosome-degradation, western blot analysis was performed to assess LAMP2A and HSC70 protein levels in the context of APP overexpression in the presence and absence of BafA1 treatment (**Fig. 4.3.A**). While LAMP2A protein expression is significantly at the 24-hr and 48-hr time points compared to the time-specific control cells following BafA1 treatment (**Fig. 4.3.B**), no significant difference in HSC70 levels is observed at these time points (**Fig. 4.3.C**). However, HSC70 expression is significantly enhanced during 24 hrs and 48 hrs APP overexpression compared to 12-hrs APP overexpression following BafA1 treatment. These data indicate that CMA activity remains relatively unchanged early in APP overexpression, however, it is enhanced upon impairment of MA's degradative capacity, as revealed following BafA1 treatment during 24 hrs and 48 hrs APP overexpression. These findings are supported by previous reports that have shown that increased LAMP2A and HSC70 protein levels serve as preliminary indicators of increased CMA activity (Arias, 2017). Although there are discrepancies in HSC70 expression, it may be that the cell lysates utilized in this analysis contained a lower lysosomal fraction of HSC70, however, this does not infer a reduction in CMA capacity as LAMP2A levels at the lysosomal membrane have been shown to be rate-limiting step for CMA activity in lysosomes isolated from rat liver with age (Cuervo et al., 1995b, 1997). Moreover, a study by Xilouri et al. (2013) found that overexpression of LAMP2A alone was sufficient to enhance CMA activity and reduce the levels of mutant α-synuclein in rat cortical neurons *in vitro*, SH-SY5Y cells, and dopaminergic neurons *in vivo*, thereby mitigating α-synuclein-induced proteotoxicity. Our data indicates sequential activation in CMA activity at the later time points (**Fig. 4.3.B**), which is maintained with MA activity at these time points (**Fig. 4.2.B**), following

significantly APP and Aβ expression (**Fig. 4.1**). Our data suggests that the activity of both pathways remain functional but are not sufficient for Aβ clearance. In contrast with our findings, previous studies by Wang and colleagues in a cell model of tauopathy demonstrate that of mutated tau protein is incompletely digested by the CMA pathway, leading to tau aggregation (Wang et al., 2009). At the same time, MA activity was enhanced and able to clear these CMA-related tau aggregates, suggesting the functional interplay between MA and CMA in the context of mutant tau proteotoxicity (Wang et al., 2009, 2010). Our data therefore suggests that compensatory CMA induction, while beneficial in certain contexts such as tau (Wang et al., 2009) and mutant α-synuclein-mediated blockage of CMA function (Cuervo et al., 2004), is not sufficient to compensate for the MA activity in the context of APP overexpression over time. These data provide new insights into CMA activity following inhibition of autophagosome degradation in this context, however, further studies are warranted to determine whether Aβ toxicity is further augmented when both MA and CMA function is inhibited.

4.6. Effect of flux modulation in the context of APP overexpression on apoptosis

Massive neuronal cell death due to apoptosis is a common characteristic in neurodegeneration and has been extensively characterised in the brains of AD patients (Obulesu and Lakshmi, 2014; Shimohama, 2000). However, the role of MA in impacting apoptosis onset in the face of Aβ-induced toxicity in the context of APP overexpression remains unclear. Hence, western blot analysis of key apoptosis molecular markers was assessed in the absence and presence of BafA1 during APP overexpression (**Fig. 4.4**). Our results indicate a similar trend in Total Caspase-3 and cleaved-PARP expression, with the level of both proteins being significantly increased during 24 hrs, and 48 hrs APP overexpression in the presence of BafA1 compared to 12 hrs APP overexpression in the presence of BafA1 (**Fig. 4.4.B,D**). More importantly, the induction of apoptosis is only revealed in response to MA dysfunction, as indicated by the enhanced cleavage of PARP protein during 24 hrs and 48 hrs APP

overexpression in the presence of BafA1 compared to the time-specific control cells (**Fig. 4.4.D**). These results indicate that the blockage of autophagosome degradation impacts cell viability in favour of cell death onset during APP overexpression at later time points, and therefore highlight the protective role of MA in the context of Aβ-induced toxicity. In line with these findings, studies of MA-deficient mice reveal enhanced neuronal cell death and the accumulation of cytoplasmic proteins (Komatsu et al., 2006, 2007b; Liang et al., 2010). Others have shown that impaired autophagosome degradation augments the aggregation of Aβ oligomers and promotes cytochrome c release in APP mice with age, thereby triggering activation of the caspase cascade and favour cell death onset (Hashimoto et al., 2003; Sasaguri et al., 2017). Similarly, a study by Lustbader et al. (2004) suggests that APP overexpression may impact cell viability as evidenced by increased ROS levels, cell death onset, and impaired cognitive function in the brains of AD patients and AD mouse models in response to increased Aβ proteotoxicity. Our data reveals that the expression of Total Caspase-3 and cleaved-PARP is augmented following APP overexpression with impaired MA function at the same time points that Aβ protein levels are enhanced (**Fig. 4.1.F**). These results suggest a direct link between cell death onset, APP overexpression/Aβ toxicity and impaired macroautophagic activity. In accord, other studies have demonstrated that APP overexpression increases the susceptibility of APPswe transfected PC12 cells to oxidative stress, resulting in the rapid onset of caspase-3 dependent cell death (Eckert et al., 2001; Marques et al., 2003). Additionally, Eckert et al. (2001) also revealed that following treatment with caspase-3 inhibitors, cell death onset was significantly attenuated in these transfected PC12 cells, thereby reinforcing the important role of caspase-3 dependent apoptotic induction during APP overexpression. Others have also demonstrated the efficient cleavage APP by caspase-3 during apoptosis, as evidenced by elevated Aβ production following increased caspase activity. This finding suggests that APP may be a substrate for caspase-3 cleavage. In fact, caspase-3 has been found to be highly colocalised with Aβ in senile plaques of dying neurons in the brains AD patients (Gervais et al., 1999). Findings by Nilsson and colleagues also indicate a link between impaired MA function, Aβ accumulation, and apoptosis. Using MA-deficient APP mice,

the authors found enhanced cell death onset coupled to increased caspase-3 activation compared to MA-deficient mice without Aβ amyloidosis (Nilsson et al., 2013). In agreement with our data, these findings indicate that MA dysfunction may further augment Aβ accumulation, therefore demonstrating that MA acts as a pro-survival mechanism in the context of APP overexpression. However, further investigations are warranted to fully clarify the implications of such a connection.

4.7. Effect of APP overexpression on AV formation in N2aswe cells

Given the intense interest in the molecular and cellular underpinnings of the MA pathway, transmission electron microscopy (TEM) analysis continues to play a central role in the field of MA research since autophagosomes were first identified and described in 1950s by Christian de Duve using this technique (Deter et al., 1967). Owing to its capacity to generate high resolution cellular ultrastructural information, TEM facilitates the direct count of autophagosomes and autolysosomes (Klionsky et al., 2016; Shibutani and Yoshimori, 2014). In most scenarios, cell analysis using conventional TEM in the presence and absence of lysosomal inhibitors such as BafA1, is sufficient to discern whether there are changes in macroautophagic flux in response to various treatment conditions (Eskelinen et al., 2011). Upon MA induction, the accumulation of degradative structures increases, and the number of autolysosomes, lysosomes and amphisomes per cell section can thus be quantified to provide simple morphological read out of macroautophagic flux (Klionsky et al., 2016). However, given the difficulty that may arise when distinguishing between autolysosomes, lysosomes, and amphisomes, these structures are generally classified as AVs (Eskelinen, 2008).

In order to determine to what extent impaired autophagosome degradation contributes to the accumulation of AVs on an ultrastructural level, as well as other aspects of cellular injury, such as mitochondrial damage, N2aswe cells were incubated in the

presence and absence of BafA1 during APP overexpression over time. **Figure 4.5** (**left panel**) reveals that the clearance of AVs is increasingly reduced in response to APP overexpression, particularly at the 24-hr and 48-hr time point, suggesting that APP overexpressing may reduce MA's clearance capacity at later time points. Moreover, and most importantly, the abundance of AVs is further enhanced upon BafA1 treatment [**Fig. 4.5** (**right panel**)]. These observations reveal that MA is continuously induced as early as 12 hrs and as late as 48 hrs APP overexpression, consistent with our western blot data (**Fig. 4.2.B)**. Our findings are supported in an electron-microscopy based study by Nixon et al. (2005), which reveals the striking accumulation of AVs in neocortical biopsies from AD brains, while this pathology was reportedly uncommon in control patients. Studies by Boland et al. (2008) also confirm that MA is constitutively active and highly efficient in healthy neurons, while impaired macroautophagic clearance accounts for the extensive AVs pathology observed with AD progression. More recent studies demonstrate that not only is the retrograde transport and maturation of AVs to lysosomes impaired in AD, but most importantly, that the accumulation of Aβ oligomers within these AVs further augment macroautophagic stress and exacerbate disease progression in the brains of AD patient brains, and in APP mice with age (Sanchez-Varo et al., 2012; Tammineni et al., 2017).

Next, we quantified the abundance of AVs in response to APP overexpression and in the absence and presence of BafA1 treatment. A significant time-dependent increase in the total number of AVs counted per cell is indicated (**Fig. 4.6.A**). Notably, the increase in AVs is further enhanced in the 24-hr versus 12-hr BA treated group upon BafA1 treatment, and the 48-hr compared to the 24 hr BA treated group upon BafA1 treatment. These data suggest that the level of MA activity during APP overexpression at these time points is not sufficient to clear the accumulating AVs. Further analysis reveals a significant increase in AVs surface area in response to APP overexpression over time, with the exception of the 48-hr BA treated group in the presence of BafA1 (**Fig. 4.6.B**). The surface area is further enhanced in the 48-hr BA treated group compared to both the 12-hr and 24-hr BA treated group upon BafA1 treatment,

suggesting that amount/volume of cytoplasmic contents engulfed within these vesicles may be increased with increasing MA activity and APP overexpression. In line with our finding, Nixon et al. (2005) previously highlighted the massive accumulation of AVs in 'swollen' neurites as a unique feature of AD pathology, suggesting that the enhanced engulfment of cytoplasmic contents within these vesicles may account for their swollen morphology. These data support our findings which indicate that targeting late steps in the MA pathway may aid in the maturation Aβ-laden AVs to lysosomes, and the subsequent degradation of vesicles, thereby attenuating proteotoxicity. Moreover, our findings suggest that therapeutic intervention, by modulating MA activity, is possible throughout the disease progression.

4.8. Effect of APP overexpression on fibrillar ultrastructure in N2aswe cells

Other ultrastructural structures are also revealed in the N2aswe cells TEM micrographs. These include the formation of fibrillar protein structures, which we suspect may be Aβ fibrils (**Fig. 4.7**). A time-dependent increase in the extension/length of these structures is observed with APP overexpression [**Fig. 4.7** (**left panel**)]. Moreover, the abundance of these structures is further enhanced upon BafA1 treatment with APP overexpression over time [**Fig. 4.8.B** (**right panel**)]. These observations suggest that MA impacts the clearance of these fibrillar structures. In line with our observations, Gremer et al. (2017) described similar structures using cryo–electron microscopy (cryo-EM) to reconstruct the atomic model Aβ(1–42) fibril, as twisted filaments which became progressively intertwined with increasing abundance. Our TEM observations suggests that these fibrillar structures may be potential proteinaceous cargo for MA as a notable increase in the length and distribution of these structures is observed with impaired autophagosome degradation, particularly in response to 24 hrs and 48 hrs APP overexpression. However, we cannot conclusively identify the observed structures as Aβ fibrils using conventional TEM analyses. Hence, future work through CLEM can be suggested.

4.9. Effect of APP overexpression on mitochondrial ultrastructure

In addition to the accumulation of AVs, our TEM analysis revealed the sequestration of specific cargo, particularly upon BafA1 treatment. A distinct increase in mitochondrial organelle clusters is revealed in response to APP overexpression over time [**Fig. 4.8** (**left panel**)]. Mitochondrial abundance is further enhanced upon BafA1 treatment [(**Fig. 4.8** (**right panel**)]. Most notably, the accumulation of these organelles is more pronounced following 24 hrs and 48 hrs APP overexpression upon BafA1 treatment, suggesting that mitochondrial turnover is reduced at later time points, consistent with reduced mitophagy, i.e. selective mitochondrial degradation by MA. In line with our findings, impaired MA function has been shown to exacerbate mitochondrial dysfunction and accumulation of damaged mitochondria with age (Edens et al., 2016; Sebastián et al., 2016). A recent study by Song et al. (2018) suggests that impaired autophagosome degradation with concomitant mitophagy dysfunction may be the primary cause of neuronal cell damage during chronic hypoxia. Conversely, rapamycin treatment *in vivo* (García-Prat et al., 2016), and moderate exercise in the elderly (Moreira et al., 2017) has been shown to impact major cellular pathways involved in the mitochondrial quality and quantity control, such as MA. Accordingly, therapeutic strategies targeting MA induction with age holds great promise for delaying AD progression.

4.10. Effect of APP overexpression on ferritin-like inclusions

Interestingly, ferritin-like inclusion structures were observed upon closer inspection of the TEM micrographs (**Fig. 4.9**). Ferritin is a cytosolic protein that stores excess iron in a redox inactive form, thereby protecting cells from iron toxicity (Asano et al., 2011; Koperdanova and Cullis, 2015). In line with our findings, cconventional electron microscopy analysis by Kishi-Itakura et al. (2014) revealed similar structures, described as ferritin clusters, in the AVs of MA-deficient MEF cells under starvation

conditions. The accumulation of these inclusions is observed in response to 24 hrs and 48 hrs APP overexpression [**Fig. 4.9** (**left panel**)], and further increased in abundance upon BafA1 treatment with APP overexpression [**Fig. 4.9** (**left panel**)], suggesting that ferritin may proteinaceous cargo for MA. In line with our findings, studies indicate that ferritin degradation occurs by two routes, MA and the UPS (Domenico et al., 2010). In agreement, Ma et al. (2017) reported that ferritin is partially dependent upon MA degradation, and Asano et al. (2011) revealed that the acidic environment of the lysosome was crucial for iron extraction from ferritin and utilization by cells. Given that BafA1 treatment inhibits the acidification of lysosomes, it not only impairs autophagosome-lysosome fusion but also the degradation of ferritin within lysosomes. In line with our findings, Ott et al. (2016) reveal that CMA plays a negligible role in ferritin degradation, while this protein was found to colocalise with LC3 following inhibition autophagosome degradation, indicating that MA plays a pivotal role in ferritin clearance. Our findings also raise the possibility that ferritin aggregation may be implicated in APP overexpression [**Fig. 4.9** (**left panel**)]. In fact, MRI evaluation of brain iron in neocortical neurons revealed significantly higher iron stores in AD patients compared normal subjects (Bartzokis et al., 1994). Our findings are further supported by western blot analysis shown by Rogers et al. (2002) which reveals that when cellular iron levels are high, APP processing and ferritin levels are increased. Our findings provide new insights into the mechanism Aβ proteotoxicity, linking iron accumulation to enhanced APP overexpression. However, whether ferroptosis, APP and MA are linked is unclear in this context.

Overall, our data reveal that MA activity is not impaired during APP overexpression, but rather a mismatch between MA activity and protein aggregation. APP overexpression increased the APP cytosolic pool, which in turn induced a concomitant increase in β-secretase activity to favour Aβ production, and the interaction between APP/β-secretase was further enhanced upon BafA1 treatment, favouring Aβ generation/accumulation. In response to increased APP and Aβ protein cargo with time, macroautophagic flux was maintained, while LC3 abundance and autophagosome pool size increased. Although MA remained functional, CMA activity

was induced late in APP overexpression, but both pathways proved insufficient to clear Aβ load or prevent cell death onset. Future examination of brain tissue from of AD patients or APP overexpressing mice at various Braak stages may yield a better understanding of the modulation of autophagic pathways.

Our findings highlight that the modulation of MA throughout AD progression may be fundamental to the preservation of cell survival. However, multiple obstacles, including the lengthy period required for promising drugs to pass clinical trials, have hampered the implementation of disease-modifying treatment strategies targeting MA in the management of neurodegenerative disease on a clinical level. Recent systemic reviews highlight the urgent need for the implementation of lifestyle-based interventions which may be safely and immediately executed to halt disease progression (Metaxakis et al., 2018; O'Flanagan et al., 2017). To this end, recent translational studies have tested the therapeutic potential of CR, and CR mimetic drugs as adjuvant therapies in neurodegeneration.

CHAPTER 5 RESULTS: THE EFFECTS OF MA AND CMA MODULATION

5.1. Introduction to results

The imbalance between protein synthesis and degradation contributes to the accumulation of proteinaceous inclusions characteristic of several neurodegenerative diseases, as evidenced by the accumulation of Aβ in AD (Nixon, 2013). Compelling evidence demonstrates that increased Aβ-induced neurotoxicity, together with impaired protein degradation may be a key factor in AD pathogenesis (Hardy and Selkoe, 2002). Although the modulation of Aβ clearance following rapamycin treatment has been found to be neuroprotective, the side-effects of long-term rapamycin treatment make this compound unattractive for clinical use in pre-symptomatic patients who may require long-term therapy (Salmon, 2015). Hence, the use of non-pharmaceutical interventions that impact both MA and CMA activity may present a more practical approach for clinical use. One such example is CR, i.e. reduced intake of nutrients without causing malnutrition. CR is to date the most successful intervention shown to delay the onset of age associated pathologies, including AD (Balasubramanian et al., 2017). Several pharmaceutical drugs and naturally occurring compounds in food (nutraceuticals) have been found to mimic the beneficial effects of CR both *in vitro* and *in vivo* (Ito et al., 2016; Roth and Ingram, 2015), and these may be used as alternatives to a practically challenging CR dietary regime in humans.

The aims of this chapter were to assess (i) the effects of 2DG treatment on MA and CMA, and (ii) the contribution of MA and CMA modulation to protein clearance, and neuronal protection. To this end, the effects of 2DG, were assessed in BA (5 mM) treated N2aswe cells. To fully assess the contribution of each pathway to neuronal protection, N2aswe cells were treated with the most widely used MA inhibitor, 3-methyladenine (3MA).

5.2. Results

5.2.1. The modulation of MA and CMA using the CRM 2DG

In order to create an environment of caloric restriction, the caloric restriction mimetic 2DG was employed. Modulation of MA and CMA was assessed using 5 mM 2DG for a duration of 6 and 12 hrs, APP overexpression was induced for 24 hrs (BA, 5 mM).

5.2.1.1. Effect of 2DG on N2aswe cell viability during APP overexpression

WST-1 results indicate a significant increase in reductive capacity in the 6 hrs 2DG treated group [0.12 ± 0.004 ($p<0.05$)], and the 12 hrs 2DG treated group [0.14 ± 0.005 ($p<0.05$)] compared to control cells [0.1 ± 0.0] and the 24 hrs BA treated group [0.08 ± 0.008], with a significant decrease in the 24 hrs BA treated group [0.08 ± 0.008 ($p<0.05$)] compared to control cells. No significant difference is indicated in the 6 hrs 2DG + 24 hrs BA treated group [0.09 ± 0.004], and the 12 hrs 2DG + 24 hrs BA treated group [0.1 ± 0.014] compared to control cells, however, and most importantly, reductive capacity is significantly increased in the 12 hrs 2DG + 24 hrs BA treated group [0.1 ± 0.014 ($p<0.05$)] compared to the 24 hrs BA treated group [0.08 ± 0.008] (**Fig. 5.1**).

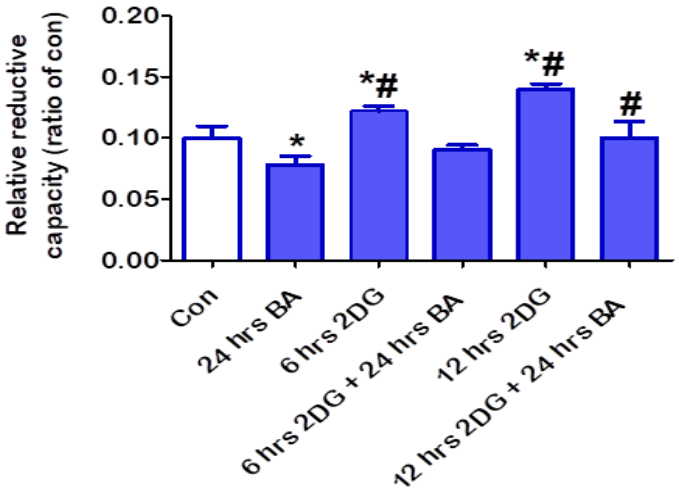

Figure 5.1: Effect of 2DG on reductive capacity in N2aswe cells in response to 24 hrs APP overexpression. Data expressed as mean ± SEM, statistical analysis: ANOVA and Bonferroni correction, *p<0.05 vs. control, #p<0.05 vs 24 hrs BA, n = 3.

5.2.1.2. Effect of 2DG on amyloidogenic processing in N2aswe cells during 24 hrs APP overexpression

The results indicate no reducing effect of 2DG on APP overexpression. In brief, APP protein expression is significantly increased in the 24 hrs BA treated group [0.98 ± 0.07 (p<0.05)], 6 hrs 2DG treated group [0.85 ± 0.08 (p<0.05)], 6 hrs 2DG + 24 hrs BA treated group [0.89 ± 0.08 (p<0.05)], and in the 12 hrs 2DG + 24 hrs BA treated group [0.93 ± 0.07 (p<0.05)] compared to control cells [0.39 ± 0.07], with no significant difference indicated in the 12 hrs 2DG treated group [0.7 ± 0.04] compared to control cells (**Fig. 5.2.B**).

Figure 5.2.A reveals that Aβ protein expression is significantly decreased in the 6 hrs 2DG + 24 hrs BA treated group [0.068 ± 0.012 (p<0.05)], and the 12 hrs 2DG + 24 hrs BA treated group [0.15 ± 0.027 (p<0.05)] compared to the 24 hrs BA treated group [0.28 ± 0.014], while Aβ expression is significantly increased in the 12 hrs 2DG + 24 hrs BA treated group compared to control cells [0.063 ± 0.014]. Similarly, Aβ expression is significantly increased in the 24 hrs BA treated group [0.28 ± 0.014 (p<0.05)], 6 hrs 2DG treated group [0.25 ± 0.014 (p<0.05)], and the 12 hrs 2DG treated group [0.235 ± 0.009 (p<0.05)] compared to control cells [0.063 ± 0.014] (**Fig. 5.2.C**).

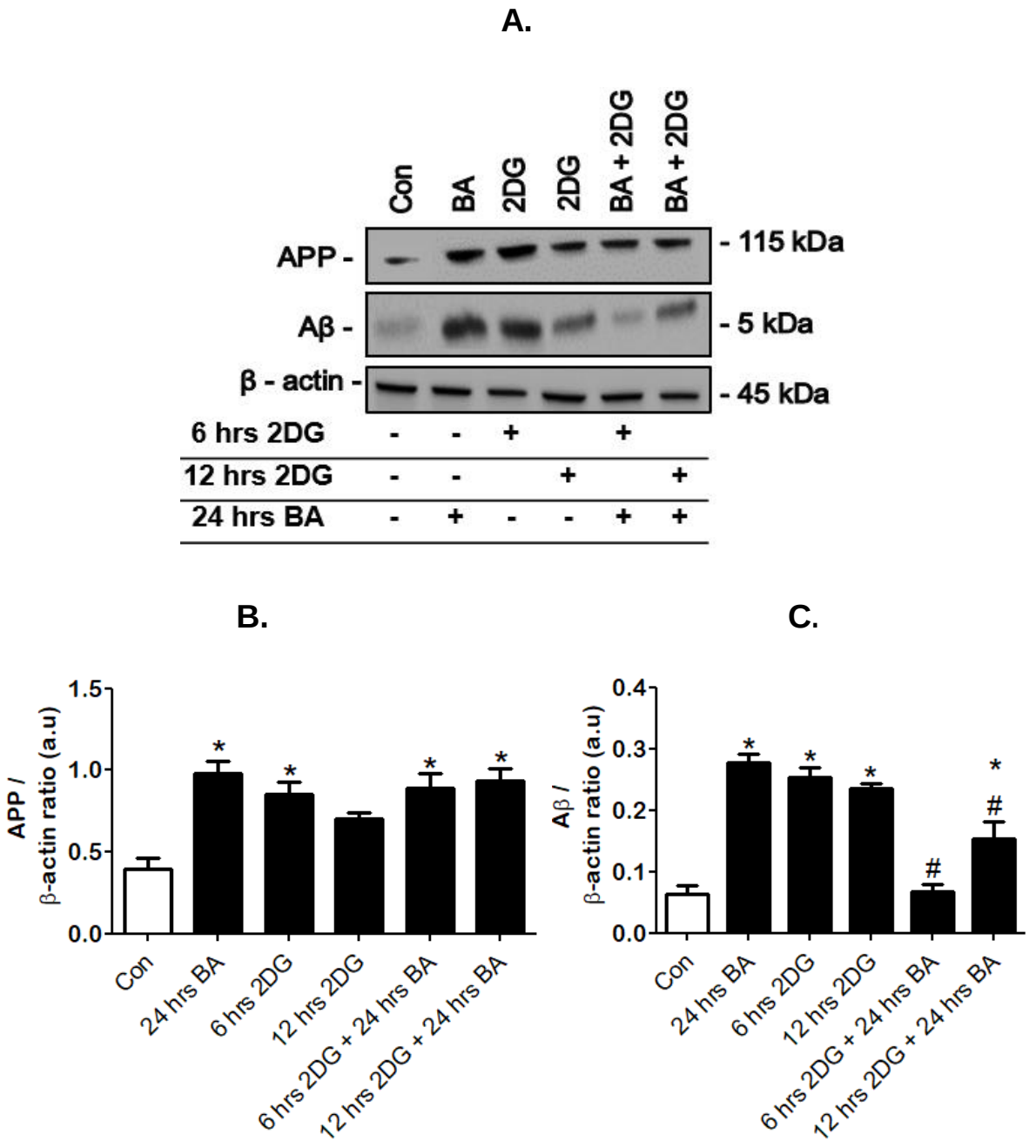

Figure 5.2: Effect of 2DG on amyloidogenic processing in N2aswe cells in response to 24 hrs APP overexpression. Representative western blot and densitometric analysis for **(A, B)** APP, and **(A, C)** Aβ protein expression is shown. Data expressed as mean ± SEM, statistical analysis: ANOVA and Bonferroni correction, *p<0.05 vs. control, # p<0.05 vs 24 hrs BA, n = 3, arbitrary units (a.u).

5.2.1.3. Effect of 2DG on MA in N2aswe cells during 24 hrs APP overexpression

LC3II protein expression is significantly increased in the 24 hrs BA treated group [1.57 ± 0.096 ($p<0.05$)], 6 hrs 2DG treated group [1.68 ± 0.083 ($p<0.05$)], 12 hrs 2DG treated group [1.73 ± 0.11 ($p<0.05$)], 6 hrs 2DG + 24 hrs BA treated group [1.64 ± 0.08 ($p<0.05$)], and in the 12 hrs 2DG + 24 hrs BA treated group [1.59 ± 0.17 ($p<0.05$)] compared to control cells [0.82 ± 0.1] (**Fig. 5.3.B**).

Figure 5.3.C reveals no significant difference in p62 protein expression for any of the BA, 2DG, or BA/2DG treated groups compared to control cells (**Fig. 5.3.D**).

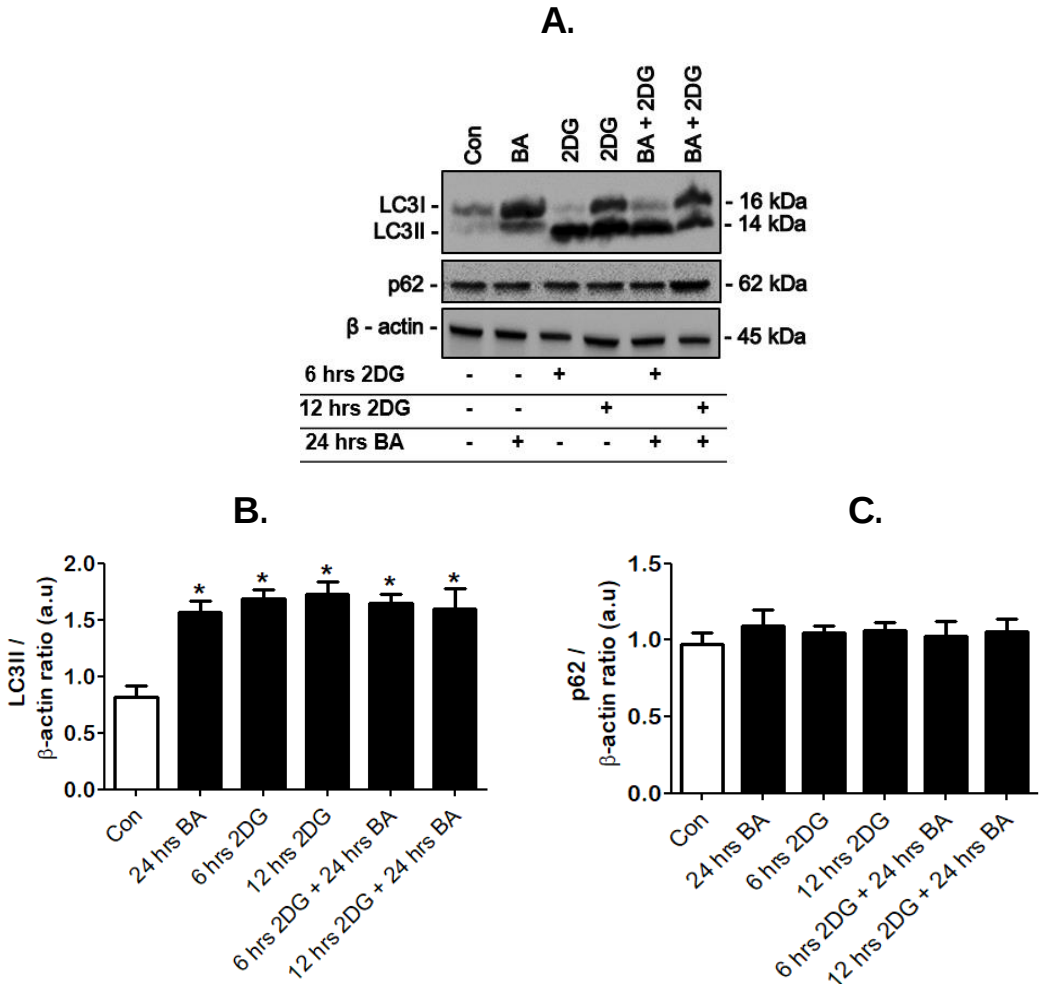

Figure 5.3: Effect of 2DG treatment on MA activity in N2aswe cells in response to 24 hrs APP overexpression. Representative western blot and densitometric analysis for **(A, B)** LC3II, and **(A, C)** p62 protein expression is shown. Data expressed as mean ± SEM, statistical analysis: ANOVA and Bonferroni correction, *$p<0.05$ vs. control, # $p<0.05$ vs 24 hrs BA, n = 3, arbitrary units (a.u).

5.2.1.4. Effect of 2DG on CMA in N2aswe cells during 24 hrs APP overexpression

Western blot analysis of key CMA proteins (**Fig. 5.4.A**) reveals that LAMP2A protein expression is significantly increased in the 24 hrs BA treated group [1.49 ± 0.15 ($p<0.05$)], 12 hrs 2DG treated group [1.57 ± 0.07 ($p<0.05$)], 6 hrs 2DG + 24 hrs BA treated group [1.57 ± 0.08 ($p<0.05$)], and in the 12 hrs 2DG + 24 hrs BA treated group [1.63 ± 0.06 ($p<0.05$)] compared to control cells [0.97 ± 0.09], with LAMP2A expression significantly decreased only in the 6 hrs 2DG treated group [1.201 ± 0.05 ($p<0.05$)] compared to the 24 hrs BA treated group [1.49 ± 0.15] (**Fig. 5.4.B**).

No significant difference in HSC70 protein expression is indicated for any of the BA, 2DG, or BA/2DG treated groups compared to control cells (**Fig. 5.4.C**).

The expression of CMA cargo Tau, is significantly decreased in the 6 hrs 2DG + 24 hrs BA treated group [0.84 ± 0.04 ($p<0.05$)], and in the 12 hrs 2DG + 24 hrs BA treated group [0.78 ± 0.06 ($p<0.05$)] compared to control cells [1.35 ± 0.09] and the 24 hrs BA treated group [1.32 ± 0.05], with no significant difference indicated in the 6 hrs 2DG treated group [1.08 ± 0.09] and the 12 hrs 2DG treated group [0.99 ± 0.12] (**Fig. 5.4.D**).

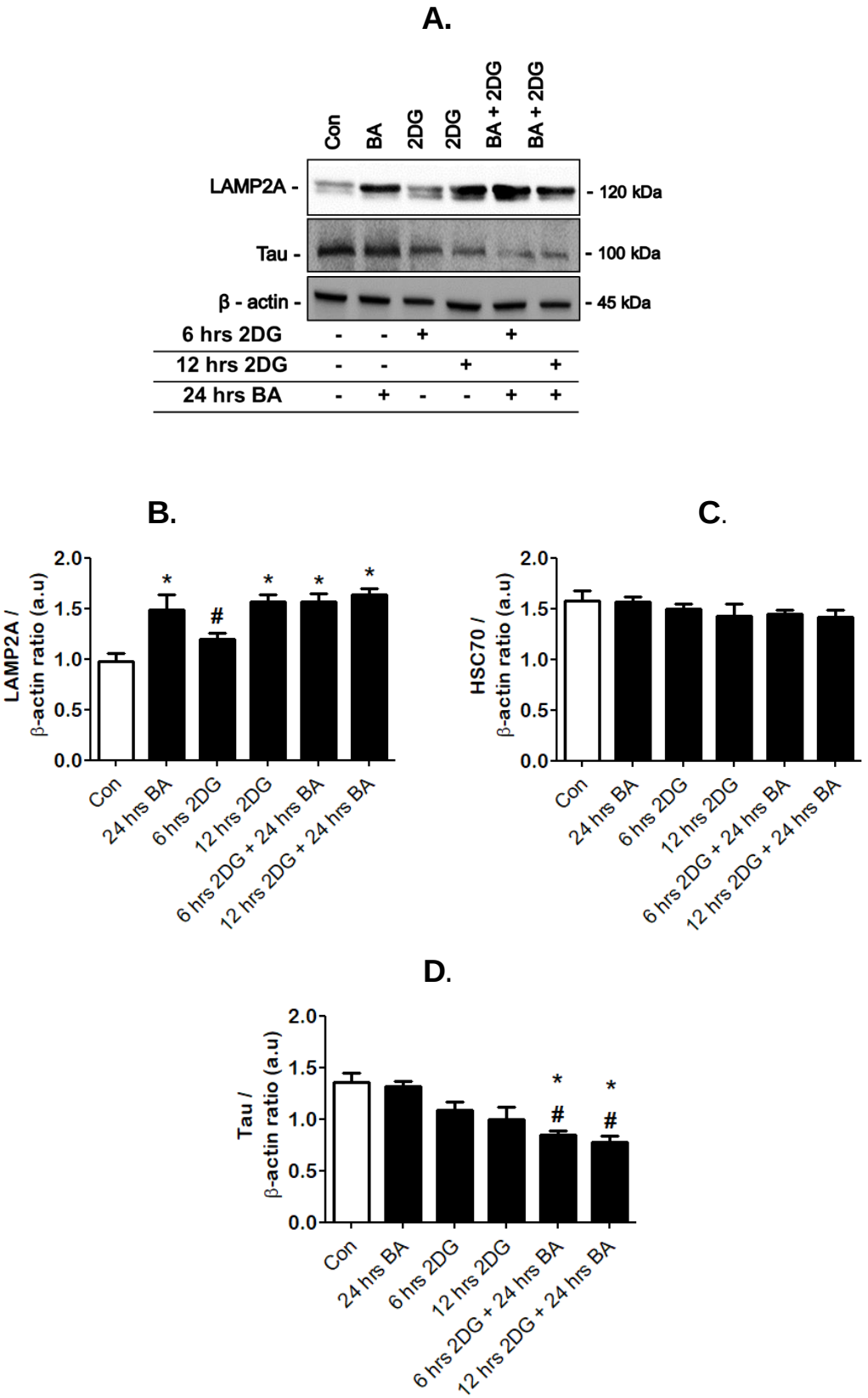

<u>Figure 5.4:</u> Effect of 2DG on CMA activity in N2aswe cells in response to 24 hrs APP overexpression. Representative western blot and densitometric analysis for **(A, B)** LAMP2A, **(A, C)** HSC70**,** and **(A, D)** Tau protein expression is shown. Data expressed as mean ± SEM, statistical analysis: ANOVA and Bonferroni correction, *p<0.05 vs. control, # p<0.05 vs 24 hrs BA, n = 3, arbitrary units (a.u).

5.2.1.5. Immunofluorescence tracking of CMA using the KFERQ-mCherry CMA-specific reporter

In order to assess the effect of 2DG on CMA activity during increasing APP overexpression, the KFERQ-mCherry CMA probe was used to monitor CMA activity. The probe binds to CMA-active lysosomes, and a change in the KFERQ-mCherry-lysosomal binding signal intensity, or number of fluorescent puncta per cell in response to incubation with the probe is indicative of CMA activation (Koga et al., 2011b). As shown in **Fig. 5.5**, the signal intensity of the KFERQ-mCherry reporter (**red**) becomes stronger, and less diffuse in the 24 hrs BA + 12 hrs 2DG treated group and the 48 hrs BA + 12 hrs 2DG treated group compared to the respective controls.

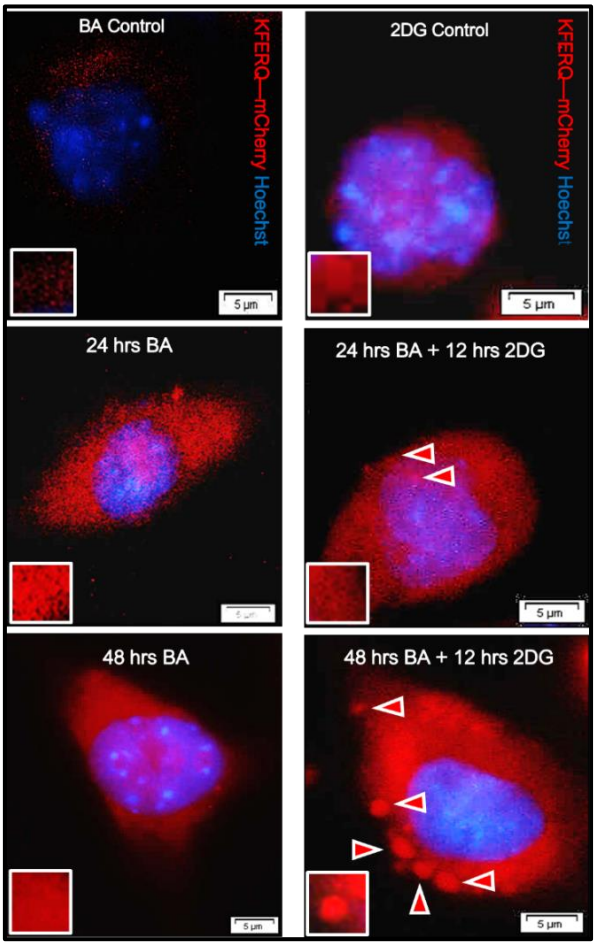

Figure 5.5: **Immunofluorescence micrographs indicating the localization of the CMA reporter KFERQ-mCherry (red) in N2aswe cells in response to 2DG treatment and APP overexpression**. Nuclei are counterstained with Hoechst 33342; scale bar indicates 5 µm.

5.2.1.6. Effect of 2DG on cell death in N2aswe cells during 24 hrs APP overexpression

As indicated in **Fig. 5.6.A,** Total Caspase-3 protein expression is significantly increased in the 24 hrs BA treated group [1.84 ± 0.14 ($p<0.05$)], 6 hrs 2DG treated group [1.48 ± 0.15 ($p<0.05$)], and the 12 hrs 2DG treated group [1.79 ± 0.05 ($p<0.05$)] compared to control cells [0.47± 0.08], but significantly decreased in the 6 hrs 2DG + 24 hrs BA treated group [0.97 ± 0.19 ($p<0.05$)], and the 12 hrs 2DG + 24 hrs BA treated group [0.7 ± 0.09 ($p<0.05$)] compared to the 24 hrs BA treated group [1.84 ± 0.14] (**Fig. 5.6.B**), suggesting protection upon 2DG exposure during APP overexpression.

Cleaved-PARP expression is significantly increased in the 24 hrs BA treated group [0.79 ± 0.03 ($p<0.05$)], 6 hrs 2DG treated group [0.72 ± 0.02 ($p<0.05$)], 12 hrs 2DG treated group [0.7 ± 0.04 ($p<0.05$)], and the 12 hrs 2DG + 24 hrs BA treated group [0.79 ± 0.05 ($p<0.05$)] compared to control cells [0.39 ± 0.07], but is significantly decreased only in the 6 hrs 2DG + 24 hrs BA treated group [0.5 ± 0.05 ($p<0.05$)] compared to the 24 hrs BA treated group [0.79 ± 0.03] (**Fig. 5.6.C**).

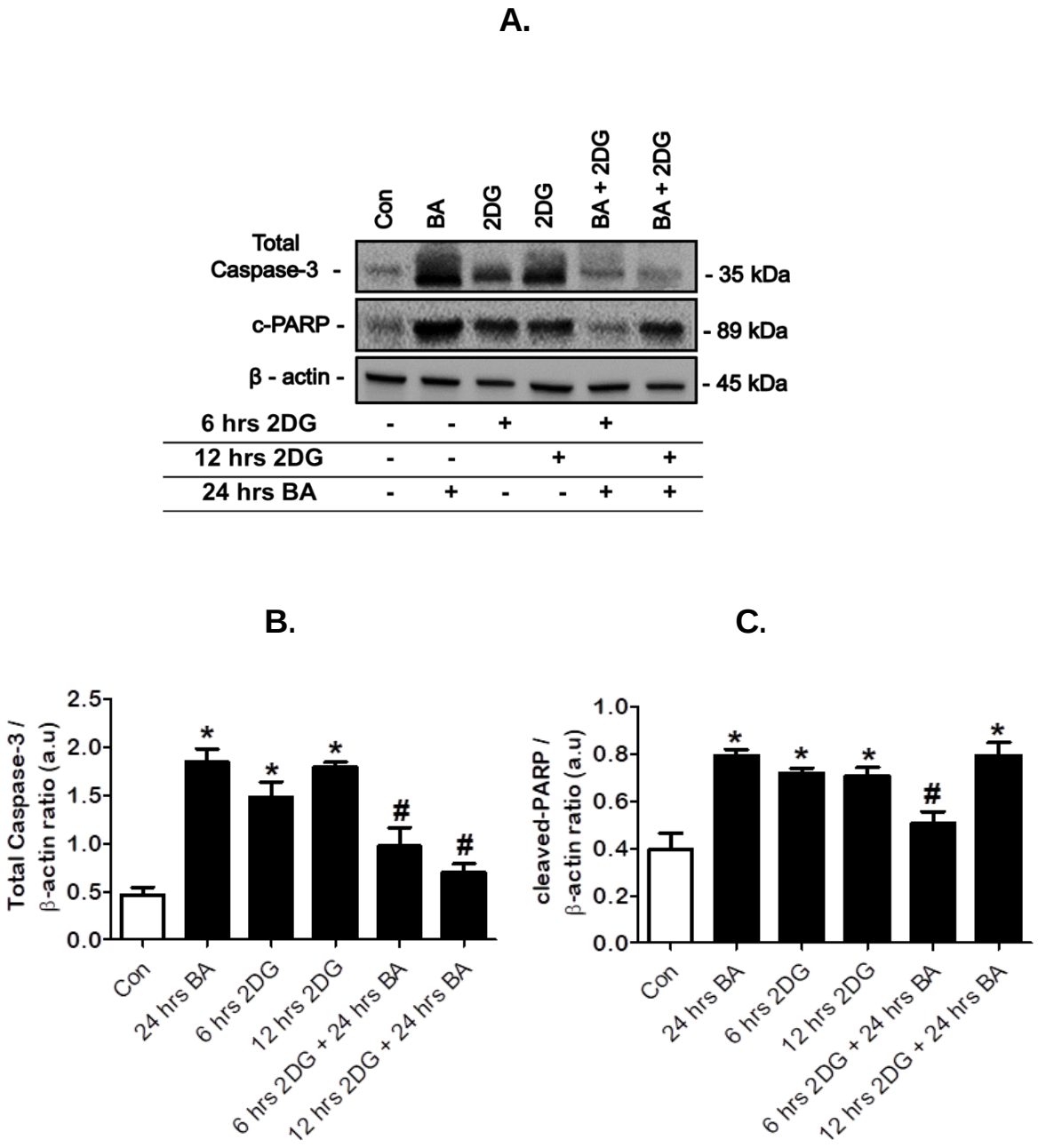

Figure 5.6: Effect of 2DG on key apoptosis proteins in N2aswe cells in response to 24 hrs APP overexpression. Representative western blot and densitometric analysis for **(A, B)** Total Caspase-3, and **(A, C)** cleaved-PARP protein expression is shown. Data expressed as mean ± SEM, statistical analysis: ANOVA and Bonferroni correction, *p<0.05 vs. control, # p<0.05 vs 24 hrs BA, n = 3, arbitrary units (a.u).

5.2.2. The modulation of MA and CMA activity using 3MA

In order to further interrogate the role of MA in the observed response, 3MA was utilized. 3MA is the most widely inhibitor of MA induction, which modulates autophagosome synthesis through inhibition of the class III phosphatidylinositol 3-kinase (PtdIns3K) (Wu et al., 2010). A 3MA concentration of 5 mM was utilized (Heckmann et al., 2013).

5.2.2.1. Effect of 3MA treatment on N2aswe cell viability

In order to determine the amount of time required to completely inhibit MA induction, five 3MA treatment time points were assessed. As shown in **Fig. 5.7**, reductive capacity is significantly decreased in the 6 hrs 3MA treated group [0.077 ± 0.002 ($p<0.05$)], 12 hrs 3MA treated group [0.046 ± 0.003 ($p<0.05$)], and the 18 hrs 3MA treated group [0.067 ± 0.003 ($p<0.05$)] compared to control cells [0.092 ± 0.007]. No significant difference is indicated in the 24 hrs 3MA treated group [0.097 ± 0.007], and the 48 hrs 3MA treated group [0.089 ± 0.005] compared to control cells.

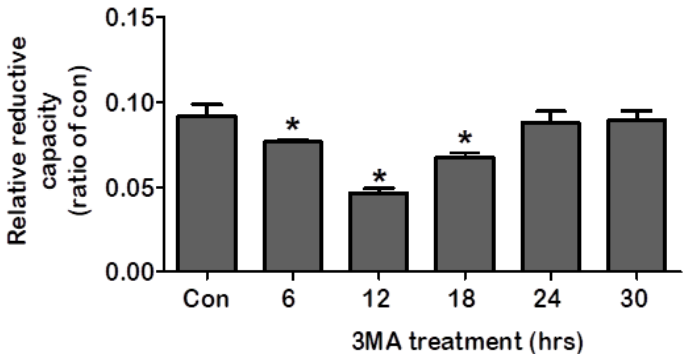

Figure 5.7: The time-dependent effect of 3MA treatment on the reductive capacity of N2aswe cells. Data expressed as mean ± SEM, statistical analysis: ANOVA and Bonferroni correction, *$p<0.05$ vs. control, n = 3.

5.2.2.2. Effect of 3MA on MA activity in response to APP overexpression

Western blot analysis assessing the effect of 3MA on LC3II, and p62 protein expression was performed (**Fig. 5.8.A**). A significant decrease in LC3II protein expression is indicated following 6 hrs 3MA exposure [0.018 ± 0.0 ($p<0.05$)], 12 hrs 3MA exposure [0.018 ± 0.0 ($p<0.05$)], and 18 hrs 3MA exposure [0.73 ± 0.07 ($p<0.05$)] compared to control cells [1.09 ± 0.04], with a significant increase following 30 hrs 3MA exposure [1.43 ± 0.08 ($p<0.05$)] compared to control cells (**Fig. 5.8.B**).

MA cargo protein p62, is significantly increased following 12 hrs 3MA exposure [2.11 ± 0.12 ($p<0.05$)] compared to control cells [1.26 ± 0.07], with no significant difference following 6 hrs 3MA exposure [1.77 ± 0.05], 18 hrs 3MA exposure [1.53 ± 0.13], 24 hrs 3MA exposure [1.34 ± 0.08)] and 30 hrs 3MA exposure [1.33 ± 0.14)] compared to control cells (**Fig. 5.8.C**). These data highlight the complete loss of protein clearance upon 12 hrs 3MA exposure.

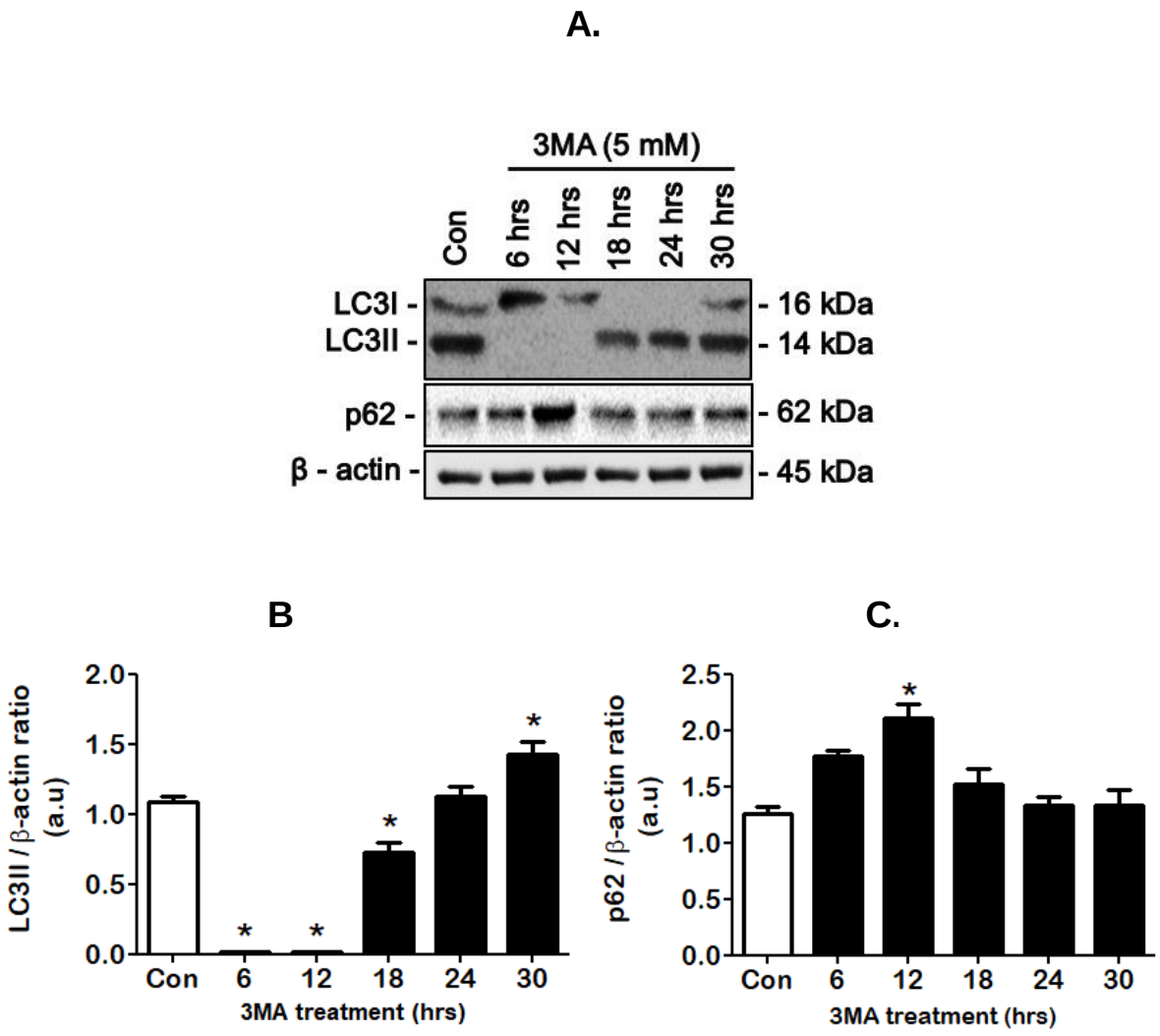

Figure 5.8: The time-dependent effect of 3MA treatment on MA activity in N2aswe cells. Representative western blot and densitometric analysis for **(A, B)** LCII, and **(A, C)** p62 protein expression is shown. Data expressed as mean ± SEM, statistical analysis: ANOVA and Bonferroni correction, *p<0.05 vs. control, n = 3, arbitrary units (a.u).

5.2.3. The modulation of MA and CMA activity using concomitant 2DG and 3MA treatment

In order to assess the contribution of MA in 2DG mediated cytoprotection (**Fig. 5.2**), concomitant 3MA treatment was performed. Modulation of MA and CMA activity was performed using 5 mM 2DG and 3MA both for a duration of 12 hrs, APP overexpression was induced for 24 hrs (BA, 5 mM).

5.2.3.1. Effect of 12 hrs [2DG and 3MA] treatment on N2aswe cell viability during 24 hrs APP overexpression

The results indicate that reductive capacity is significantly decreased in the 24 hrs BA treated group [0.06 ± 0.005 ($p<0.05$)], and the 12 hrs 3MA treated group [0.056 ± 0.003 ($p<0.05$)] compared to control cells [0.092 ± 0.001], while reductive capacity is significantly increased in the 12 hrs 2DG treated group [0.097 ± 0.006 ($p<0.05$)], 24 hrs BA + 12 hrs 2DG treated group [0.086 ± 0.003 ($p<0.05$)], and the 24 hrs BA + 12 hrs (3MA +2DG) treated group [0.098 ± 0.003 ($p<0.05$)] compared to the 24 hrs BA treated group [0.06 ± 0.005] (**Fig. 5.9**).

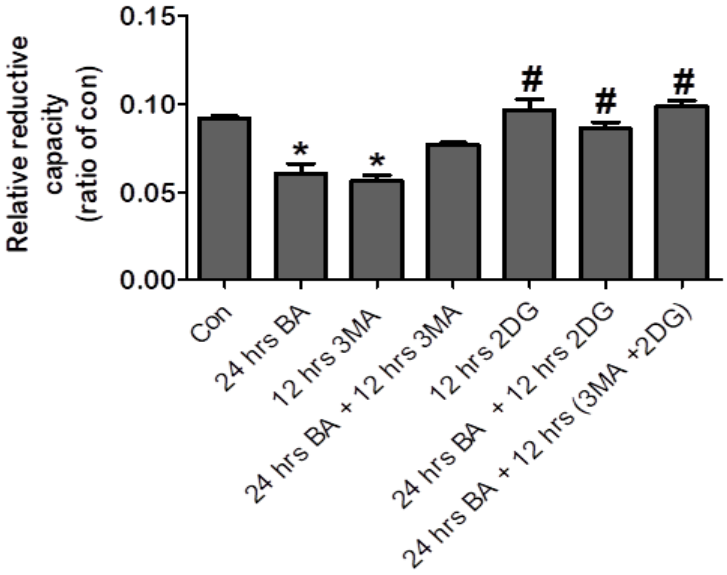

Figure 5.9: Effect of 12 hrs [3MA and 2DG] treatment on N2aswe cell viability during 24 hrs APP overexpression. Data expressed as mean ± SEM, statistical analysis: ANOVA and Bonferroni correction, *$p<0.05$ vs. control, #$p<0.05$ vs. 24 hrs BA, n = 3.

5.2.3.2. Effect of 12 hrs [2DG and 3MA] treatment on amyloidogenic processing in N2aswe cells during 24 hrs APP overexpression

APP protein expression is significantly increased in the 24 hrs BA treated group [1.52 ± 0.09 ($p<0.05$)], 12 hrs 3MA treated group [1.67 ± 0.09 ($p<0.05$)], 24 hrs BA + 12 hrs 3MA treated group [1.76 ± 0.07 ($p<0.05$)], and the 24 hrs BA + 12 hrs (3MA +2DG) treated group [1.62 ± 0.09 ($p<0.05$)] compared to control cells [0.7 ± 0.08], with APP expression significantly increased in the 24 hrs BA + 12 hrs (3MA +2DG) treated group compared to the 24 hrs BA + 12 hrs 2DG treated group [1.13 ± 0.08]. In contrast, APP expression is significantly decreased in the 12 hrs 2DG treated group [1.08 ± 0.04 ($p<0.05$)], and the 24 hrs BA + 12 hrs 2DG treated group [1.13 ± 0.08 ($p<0.05$)] compared to the 24 hrs BA treated group [1.52 ± 0.09] (**Fig. 5.10.B**).

Figure 5.10.C indicates that β-secretase protein expression is significantly increased in the 12 hrs 3MA treated group [2.51 ± 0.29 ($p<0.05$)], 24 hrs BA + 12 hrs 3MA treated group [2.24 ± 0.16 ($p<0.05$)], 12 hrs 2DG treated group [1.92 ± 0.14 ($p<0.05$)], 24 hrs BA + 12 hrs 2DG treated group [2.19 ± 0.17 ($p<0.05$)], and the 24 hrs BA + 12 hrs (3MA +2DG) treated group [2.75 ± 0.3 ($p<0.05$)] compared to control cells [0.79 ± 0.1], with β-secretase expression also significantly increased in the 12 hrs 3MA treated group, 24 hrs BA + 12 hrs 3MA treated group, and the 24 hrs BA + 12 hrs (3MA +2DG) treated group compared to the 24 hrs BA treated group [1.09 ± 0.13] (**Fig. 5.10.D**).

As revealed in **Fig. 5.10.E**, Aβ protein expression is significantly increased in the 12 hrs 3MA treated group [0.05 ± 0.006 ($p<0.05$)], 24 hrs BA + 12 hrs 3MA treated group [0.06 ± 0.004 ($p<0.05$)], and the 24 hrs BA + 12 hrs (3MA +2DG) treated group [0.05 ± 0.004 ($p<0.05$)] compared to control cells [0.02 ± 0.002], and the 24 hrs BA treated group [0.02 ± 0.003]. Moreover, Aβ expression is significantly increased in the 24 hrs BA + 12 hrs (3MA +2DG) treated group compared to the 24 hrs BA + 12 hrs 2DG treated group [0.03 ± 0.004] (**Fig. 5.10.F**).

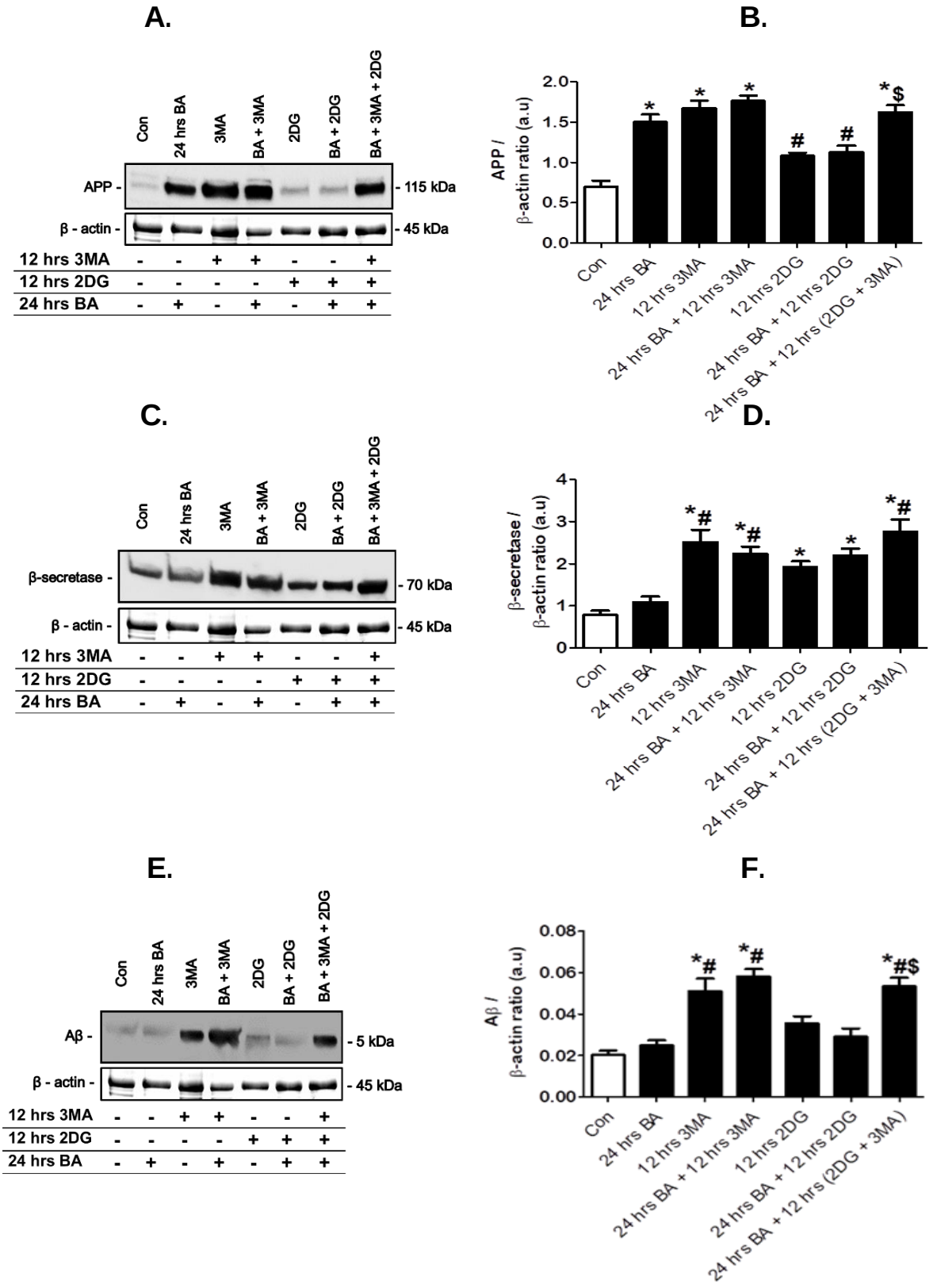

Figure 5.10: Effect of 12 hrs [3MA and 2DG] treatment on amyloidogenic processing in N2aswe cells during 24 hrs APP overexpression. Representative western blot and densitometric analysis for **(A, B)** APP, **(C, D)** β-secretase**,** and **(E, F)** Aβ protein expression is shown. Data expressed as mean ± SEM, statistical analysis: ANOVA and Bonferroni correction, *p<0.05 vs. control, #p<0.05 vs. 24 hrs BA, $p<0.05 vs. 24 hrs BA + 12 hrs 2DG, n = 3, arbitrary units (a.u).

5.2.3.3. Effect of 12 hrs [2DG and 3MA] treatment on MA activity in N2aswe cells during 24 hrs APP overexpression

Figure 5.11.A indicates that LC3II protein expression is significantly increased in the 24 hrs BA treated group [1.18 ± 0.12 ($p<0.05$)], 12 hrs 3MA treated group [0.7 ± 0.12 ($p<0.05$)], 24 hrs BA + 12 hrs 3MA treated group [0.94 ± 0.08 ($p<0.05$)], 12 hrs 2DG treated group [1.64 ± 0.06 ($p<0.05$)], 24 hrs BA + 12 hrs 2DG treated group [1.83 ± 0.08 ($p<0.05$)], and the 24 hrs BA + 12 hrs (3MA +2DG) treated group [1.52 ± 0.15 ($p<0.05$)] compared to control cells [0.05 ± 0.008]. Notably, LC3II expression is significantly increased only in the 24 hrs BA + 12 hrs 2DG treated group compared to the 24 hrs BA treated group (**Fig. 5.11.B**).

As shown in **Fig. 5.11.C**, p62 protein expression is significantly increased in the 12 hrs 3MA treated group [1.39 ± 0.04 ($p<0.05$)], 24 hrs BA + 12 hrs 3MA treated group [1.27 ± 0.04 ($p<0.05$)], 24 hrs BA + 12 hrs 2DG treated group [1.16 ± 0.09 ($p<0.05$)], and the 24 hrs BA + 12 hrs (3MA +2DG) treated group [1.46 ± 0.07 ($p<0.05$)] compared to the control cells [0.68 ± 0.1] and the 24 hrs BA treated group [0.75 ± 0.07] (**Fig. 5.11.D**).

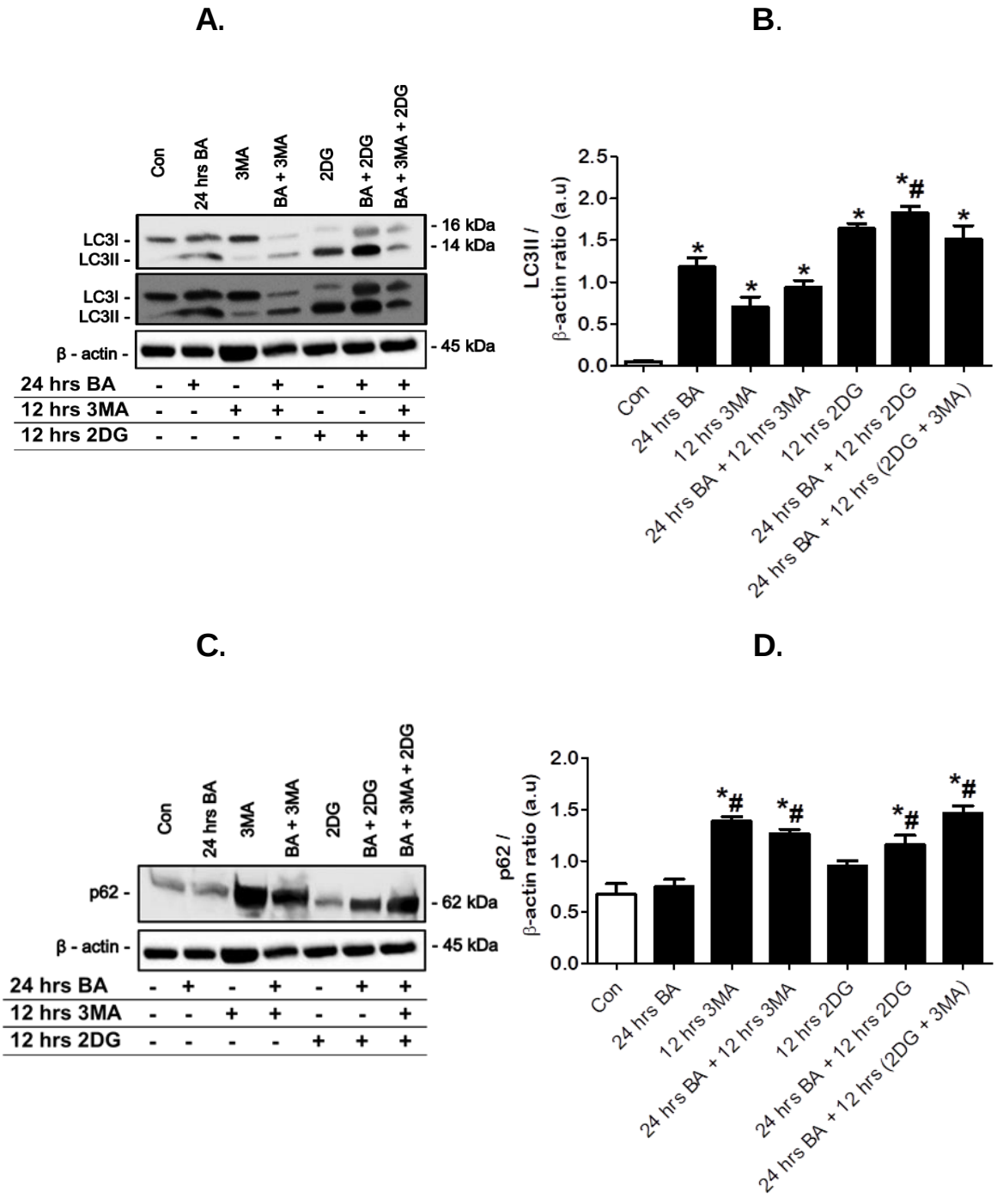

Figure 5.11: Effect of 12 hrs [3MA and 2D] treatment on key MA proteins in N2aswe cells during 24 hrs APP overexpression. Representative western blot and densitometric analysis for **(A, B)** LCII, and **(C, D)** p62 protein expression is shown. Data expressed as mean ± SEM, statistical analysis: ANOVA and Bonferroni correction, *p<0.05 vs. control, #p<0.05 vs. 24 hrs BA, n = 3, arbitrary units (a.u).

5.2.3.4. Effect of 12 hrs [2DG and 3MA] treatment on CMA activity in N2aswe cells during 24 hrs APP overexpression

No significant difference in LAMP2A protein expression is indicated in all the treatment groups (**Fig. 5.12.B**).

Similarly, no significant difference in HSC70 protein expression is revealed in all groups (**Fig. 5.12.D**), suggesting that 2DG may not have a role in CMA activity during APP overexpression.

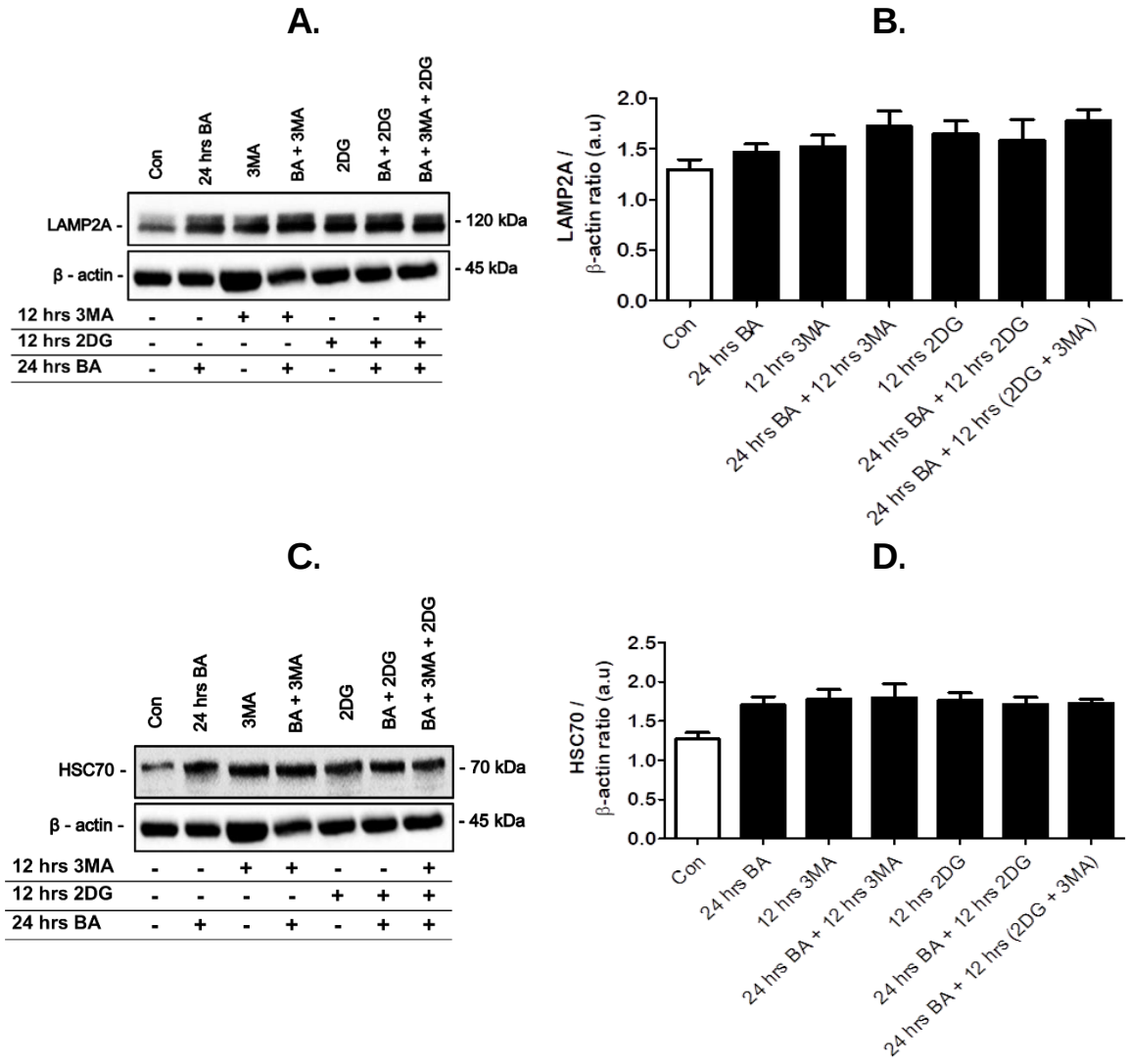

Figure 5.12: Effect of 12 hrs [3MA and 2DG] treatment on CMA activity in N2aswe cells during 24 hrs APP overexpression. Representative western blot and densitometric analysis for **(A, B)** LAMP2A, and **(C, D)** HSC70 protein expression is shown. Data expressed as mean ± SEM, statistical analysis: ANOVA and Bonferroni correction, n = 3, arbitrary units (a.u).

5.2.3.5. Effect of 12 hrs [2DG and 3MA] treatment on apoptosis in N2aswe cells during 24 hrs APP overexpression

As shown in **Fig. 5.14.A**, Total Caspase-3 protein expression is significantly increased in the 24 hrs BA treated group [0.21 ± 0.007 ($p<0.05$)], 12 hrs 3MA treated group [0.3 ± 0.009 ($p<0.05$)], 24 hrs BA + 12 hrs 3MA treated group [0.29 ± 0.009 ($p<0.05$)], 12 hrs 2DG treated group [0.24 ± 0.02 ($p<0.05$)], 24 hrs BA + 12 hrs 2DG treated group [0.22 ± 0.02 ($p<0.05$)], and in the 24 hrs BA + 12 hrs (3MA +2DG) treated group [0.22 ± 0.01 ($p<0.05$)] compared to control cells [0.045 ± 0.02]. Importantly, Total Caspase-3 expression is significantly increased only in the 12 hrs 3MA treated group compared to the 24 hrs BA treated group (**Fig. 5.13.B**), suggesting that complete inhibition of MA impacts apoptosis.

Similarly, **Fig. 5.13.C** reveals a significant increase in cleaved-PARP protein expression in all groups compared to the control. Briefly, a significant increase is indicated in the 24 hrs BA treated group [0.479 ± 0.02 ($p<0.05$)], 12 hrs 3MA treated group [0.51 ± 0.05 ($p<0.05$)], 24 hrs BA + 12 hrs 3MA treated group [0.56 ± 0.05 ($p<0.05$)], 12 hrs 2DG treated group [0.52 ± 0.02 ($p<0.05$)], 24 hrs BA + 12 hrs 2DG treated group [0.54 ± 0.02 ($p<0.05$)], and in the 24 hrs BA + 12 hrs (3MA +2DG) treated group [0.59 ± 0.06 ($p<0.05$)] compared to control cells [0.04 ± 0.003] (**Fig. 5.13.D**).

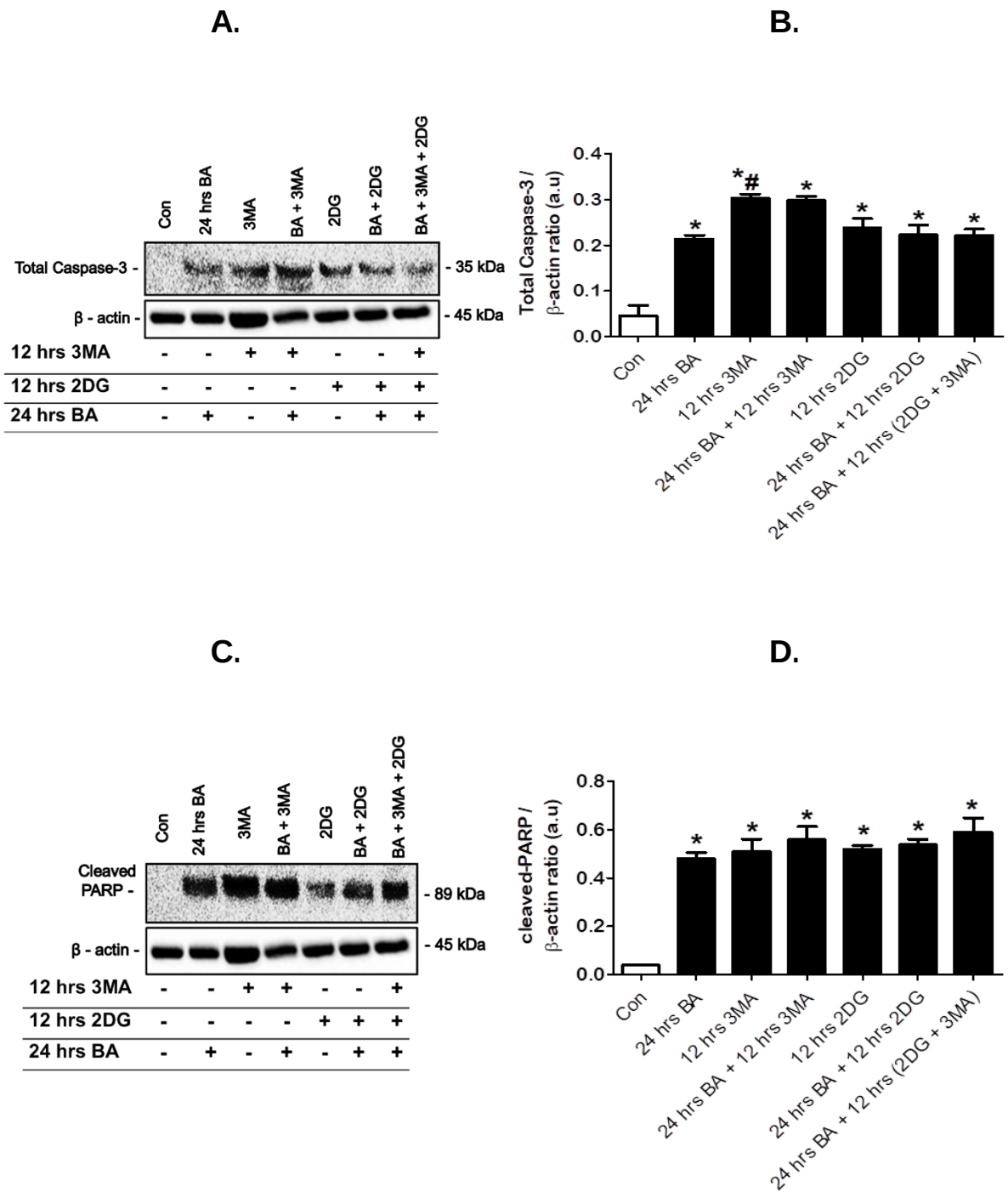

Figure 5.13: Effect of 12 hrs [3MA and 2DG] treatment on key apoptosis proteins in N2aswe cells during 24 hrs APP overexpression. Representative western blot and densitometric analysis for **(A, B)** Total Caspase-3, and **(C, D)** cleaved-PARP protein expression is shown. Data expressed as mean ± SEM, statistical analysis: ANOVA and Bonferroni correction, *p<0.05 vs. control, #p<0.05 vs. 24 hrs BA, n = 3, arbitrary units (a.u).

CHAPTER 5 DISCUSSION. THE EFFECTS OF MA AND CMA MODULATION

AD requires precise diagnosis and treatment, preferably before the first pathophysiological symptoms manifest. The accumulation of Aβ aggregates in the brain is thought to trigger neuronal damage and synaptic dysfunction. Hence, the removal and/or inhibition of the formation of these aggregates is proposed to be a potential therapeutic approach in the mitigation of AD progression. Efforts in aetiology-based treatment are currently underway in clinical trials, as well as adjuvant therapies such as physical activity, reduced caloric diets, and cognitive stimulation (Nelson and Tabet, 2015; Scheltens et al., 2016). The MA and CMA pathways are crucial mechanisms through which cells degrades aggregate-prone proteins, such as Aβ. However, the relationship between enhanced MA and/or CMA activity and ability to clear protein aggregates is not very clear. Hence, we assessed the role of glucose analogue 2-deoxy-D-glucose (2DG), a CR mimic (CRM), in the context of enhanced Aβ toxicity and its ability to control MA or CMA activity.

5.3. The modulation of MA and CMA using the CRM 2DG

CR is a dietary intervention shown to promote mammalian cell survival *in vitro* and *in vivo* (Liang et al., 2018; Mattison et al., 2017). The effects of CRM 2DG on cell viability, as measured by the WST-1 tetrazolium conversion assay, was assessed in response to 24 hrs APP overexpression. Our findings reveal a significant increase in the reductive capacity of N2aswe cells upon 6 hrs and 12 hrs 2DG treatment compared to control cells (**Fig. 5.1**). Moreover, and most importantly, the reductive capacity was significantly increased in the aforementioned treatment groups and the [24 hrs BA + 12 hrs 2DG] treated group compared to the 24 hrs BA treated group. These results indicate that while 24 hrs APP overexpression decreases cell viability, 12 hrs concomitant treatment with 2DG tips the balance in favour of cell survival. In line with our findings, 2DG treatment was found to protects neurons in co-culture with

astrocytes and microglia, by causing microglial loss through ATP depletion, thereby protecting neurons (Vilalta and Brown, 2014). 2DG treatment has also been shown to prevent neurodegeneration in the brains of triple-transgenic AD mouse model. Six-month-old mice fed a diet supplemented with 2DG for 7 weeks exhibited a significant reduction in both APP and Aβ oligomers, with a parallel decrease in γ-secretase expression, and a significant increase in α-secretase expression (Yao et al., 2011), suggesting that 2DG induced a shift towards the nonamyloidogenic pathway. Additionally, mitochondrial bioenergetic capacity was maintained with reduced oxidative stress levels in mice fed the 2DG diet compared to those fed a regular diet (Yao et al., 2011). In support of our findings of a neuroprotective role following 2DG treatment with concomitant APP overexpression (**Fig. 5.1**), these studies suggest that 2DG may be used as a disease-modifying intervention to mitigate Aβ load, neurodegeneration and delay the onset of bioenergetic deficits associated with AD progression.

Western blot analysis was performed to assess the effects of 2DG treatment on amyloidogenic pathway during 24 hrs APP (**Fig. 5.2.A**). Our results indicate that APP protein expression is comparable to control cells upon 12 hrs 2DG treatment, however, a significant increase in APP is observed upon [24 hrs BA + 12 hrs 2DG] treatment compared to control cells (**Fig. 5.2.B**). These data suggest that 2DG treatment attenuates APP overexpression. To our surprise, Aβ expression is significantly increased upon 12 hrs 2DG treatment (**Fig. 5.2.C**), suggesting that 2DG does not sufficient promote Aβ clearance. Moreover, Aβ is significantly decreased upon [24 hrs BA + 6 hrs 2DG] and [24 hrs BA + 12 hrs 2DG] treatment compared to the 24 hrs BA treated group (**Fig. 5.2.C**), which is contrast with the increased APP levels observed in these treatment groups (**Fig. 5.2.B**). Although these findings suggest that 2DG treatment may not impact APP expression in this context, they also suggest that 2DG treatment modulates Aβ levels in favour of enhanced clearance during 24 hrs APP overexpression. These data are supported in a recent study by Chakraborty (2017), which demonstrated that nutrient starvation significantly decreased the level of Aβ, and amyloid precursor protein intracellular domain (AICD) without affecting APP

transcription in SH-SY5Y neuroblastoma cells overexpressing the APP London mutation. In line with our findings (**Fig. 5.2.C)**, in a study by Yao et al. (2011) 2DG induced a shift towards the nonamyloidogenic pathway, reducing both APP and Aβ protein levels in AD mouse models. The neuroprotective effects of CR regimes have also been extended to *in vivo* settings where sustained CR in AD mice has been shown to reduce Aβ neuropathology compared to *ad libitum* fed mice (Mouton et al., 2009; Patel et al., 2005). In agreement, Wang et al. (2005) also demonstrated that CR reduced Aβ production and Aβ neuritic plaque deposition in AD mouse models. Overall, our findings of reduced Aβ production/accumulation suggests that 2DG treatment may confer a neuroprotective effect, in favour of the nonamyloidogenic pathway.

In order to assess effects of 2DG treatment on key of MA molecular markers during 24 hrs APP overexpression, western blot analysis was performed to examine LC3II and p62 protein levels (**Fig. 5.3.A**). Our results indicate a significant increase in LC3II levels following 6 hrs, and 12 hrs 2DG treatment only, and upon 6 hrs and 12 hrs 2DG treatment with 24 hrs APP overexpression compared to control cells (**Fig. 5.3.B**). These data suggest that 2DG increases LC3II levels and autophagosome abundance even during APP overexpression. In line with these findings, western blot analysis revealed LC3II levels in neuronal SK-N-SH cells treated with 2DG for 16 hrs (Nijholt et al., 2011). MacCallum and colleagues have also shown that LC3II levels are markedly increased in kidneys harvested from CR rates, while decreased those subjected to a high calorie diet (MacCallum et al., 2013).In a study by Ramírez-Peinado et al. (2013), alveolar Rh4 cells treated with 2DG for 3, 6, 18, and 24 hrs in the absence or presence of 20 nM BafA1 for 3 hrs, was found to induce macroautophagic flux. Similarly, Ferreira-Marques et al. (2016) reported a significant increase in LC3II expression in response to CR in the presence of chloroquine treatment compared to cells under CR treatment conditions in the absence of chloroquine treatment. Consistent with our data, these studies support the view that MA protects cells from glucose deprivation, and my attenuate proteotoxicity following 2DG treatment. To our surprise, no significant changes in p62 protein levels are

indicated (**Fig. 5.3.C**), despite the significant increase in MA induction. These findings are in contrast with previous studies that have shown a concomitant increase in LC3II levels with decreased p62 levels in rat cortical neurons, with the level of p62 being significantly higher under CR conditions in the presence of chloroquine, than under CR conditions in the absence of chloroquine (Ferreira-Marques et al., 2016). It was previously established in the current study that macroautophagic flux was maintained with increasing APP overexpression (**Fig. 4.2.B**), while the autophagosome pool size, as indicated by increased LC3II expression, increased in a time-dependent manner. It is therefore possible that lysosomal degradation of p62 may be affected by APP overexpression. However, this possibility can only be determined if autophagosome degradation is inhibited in this context.

In order to determine assess the effects of 2DG treatment CMA during APP overexpression, western blot analysis of LAMP2A, HSC70, and CMA cargo protein Tau was performed (**Fig. 5.4.A**). The results indicate that LAMP2A levels are significantly reduced in the 6 hrs 2DG treatment group compared to the 24 hrs BA, but still comparable to the control cells. For all the other treatment groups, LAMP2A levels are significantly increased compared to control cells (**Fig. 5.4.B**). Conversely, HSC70 levels are not significantly changed for all the treatment groups compared to control cells (**Fig. 5.4.C**). Assessment of Tau levels reveals a significant decrease in both the [6 hrs 2DG + 24 hrs BA] and [12 hrs 2DG + 24 hrs BA] treatment groups compared to the control cells and the 24 hrs BA treated group (**Fig. 5.4.D**). Although HSC70 remains relatively unchanged, the increased LAMP2A and decreased Tau protein levels suggests that under conditions of glucose deprivation and 24 hrs APP overexpression, CMA activity is increased to favour protein clearance since Tau protein is efficiently cleared following 2DG/BA combination treatment. In line with our findings, others have shown that CMA is induced in higher organisms following glucose or amino acid deprivation *in vitro* (Cuervo et al., 1995b, 1997). Indeed, a study by Finn and Dice (2005) indicate that isolated lysosomes from fibroblast cells maintained in serum-free media demonstrate an increased ability to degrade CMA substrates GAPDH, and RNaseA. In support of these findings, Li et al. (2014) showed

sequential activation of MA and CMA in response to serum deprivation and arsenic exposure in Raji cells.

We further confirmed the contribution of CMA to protein turnover following 2DG treatment during 24 hrs APP overexpression by transfecting N2aswe cells with the CMA-fluorescent reporter (KFERQ-mCherry), which allows for fluorescence microscopy-based visualization of CMA activity as a change in the distribution of the fluorescent reporter from the cytosol (diffuse fluorescent puncta pattern) to the lysosomal membrane (punctate fluorescent pattern). Our immunofluorescence analysis reveals that the KFERQ-mCherry reporter is increasingly localised to the lysosomal membrane following [24 hrs BA + 12 hrs 2DG] treatment, and further enhanced in the [12 hrs 2DG + 48hrs BA] treatment compared to their respective control groups (**Fig. 5.5**). These observations suggest that glucose deprivation further induces CMA activity in the presence of APP overexpression. In line with these findings, Koga et al. (2011) revealed that the fluorescence pattern of the KFERQ-PS-CFP2 reporter transfected in mouse fibroblasts cells changed with increasing CMA activity 16 hrs serum starvation. Mukherjee and colleagues confirmed that the change in the distribution of the CMA reporter was due to enhanced CMA induction and is temporally distinct from MA activity in which 1 hr CR was sufficient for induction, while no punctate structures were formed under fed conditions, and that 1 - 4 hrs of starvation was not sufficient to detect the CMA reporter (Mukherjee et al., 2016). Instead, puncta formation required at least 12 hrs starvation, with puncta formation being highly pronounced following 25 hrs starvation, suggesting that puncta formation associated with the KFERQ-mCherry reporter is kinetically distinct for CMA following prolonged starvation (Mukherjee et al., 2016). In accord, our data strongly indicates that the increased localization of the KFERQ-mCherry reporter with lysosomes is indicative of robust CMA induction, particularly following 48 hrs APP overexpression with 12 hrs 2DG treatment (**Fig. 5.5**). Taken together, our data clearly suggests that the enhancement of CMA activity may contribute to the preservation of the cellular energetic status following glucose deprivation.

The effects of 2DG modulation on cell death onset during 24 hrs APP overexpression were assessed using western blot analysis of apoptosis markers Total Caspase-3 and cPARP (**Fig. 5.6.A**). Our results indicate a significant increase in Total Caspase-3 expression in the 24 hrs BA, 6 hrs 2DG, and 12 hrs 2DG treatment groups (**Fig. 5.6.B**). More importantly, a significant decrease in Total Caspase-3 expression is indicated in the 6 hrs sand 24 hrs BA + 12 hrs 2DG treatment group, consistent with the reduced induction of apoptosis in these treatment groups. In support of our findings, Duan and Mattson (1999) revealed that 2DG treatment can mimic the beneficial effects of CR regimes on neurodegeneration. In this study, 2DG supplementation to *ad libitum* fed mice ameliorated the loss of dopaminergic neurons, improved deficits in cognitive function and preserved mitochondrial function following exposure to 1-methyl-4-phenyl-1,2,3,6-tetrahydropyridine (MPTP)-induced oxidative stress. Consistent Total Caspase-3 activation, our results indicate a significant increase in cPARP expression in the 24 hrs BA, 6 hrs 2DG, and 12 hrs 2DG treated group compared to control cells (**Fig.5.6.C**). To our surprise, cPARP expression is also significantly enhanced in the [12 hrs 2DG + 24 hrs BA] treatment group compared to control cells, while Total Caspase-3 activity in this group is comparable to the control cells (**Fig. 5.6.B**). This data suggests a mismatch between caspase activity and PARP cleavage in this context. It is possible that PARP may be cleaved by other proteases other than Total Caspase-3. In support of this notion, findings by Gobeil et al. (2001) reveal that cathepsins B and G can also cleaved PARP in an *in vitro*. Notably, PARP cleavage is significantly reduced in the [6 hrs 2DG + 24 hrs BA] treated group compared to the 24 hrs BA treated group, consistent with the reduced Total Caspase-3 levels in this group (**Fig. 5.6.B**). These findings suggest that 2DG confers neuronal protection during 24 hrs APP overexpression in this group. Indeed, we previously reported the amelioration of Aβ levels, with this protein being significantly reduced in the [6 hrs and 12 hrs + 24 hrs BA] treatment groups (**Fig. 5.2.C)**, the same groups in which apoptosis induction is significantly reduced, translating to cell protection. In line with our findings, others have reported the neuroprotective effects of CR and CRM in various pathologies (Guo et al., 2016). Indeed, 2DG has been found to neuroprotective in the brains of animals subjected to a variety of insults, including enhanced Aβ proteotoxicity in a triple

transgenic model of AD (Yao et al., 2011), excitotoxic and oxidative injury in hippocampal neurons (Lee et al., 1999), chemical or electrical induction of epileptic seizure-induced spatial memory deficits and hippocampal neuron loss (Garriga-Canut et al., 2006), neurotoxin exposure (3,3′-iminodipropionitrile-induced neurobehavioral toxicity in mice) (Tariq et al., 1999), and has been shown to improve brain radiotherapy in clinical studies (Dwarakanath et al., 2009), as well as increase the chemosensitivity of carcinoma cell lines to doxorubicin and sorafenib treatment (Wang et al., 2015). Others have also shown that administration of 2DG in rodents improved cardiovascular stress, and up-regulated genes associated with neurogenesis and increased stress resistance to cold shock, Aβ, iron exposure (Guo and Mattson, 2000; Wan et al., 2004). In support of our findings (**Fig. 5.6**), Ma et al. (2016) suggests that long-term CR may prevent age-related cognitive impairment via suppression of apoptosis, as evidenced by a significant reduction in Total Caspase-3, PARP, as well as proapoptotic protein Bax in mice. Although it is unknown if 2DG ameliorates proteotoxicity in humans, our data supports the role of 2DG supplementation as an effective treatment intervention that can be executed immediately and safely in the prevention of cell death onset, particularly in AD, as this CRM has been found to ameliorate Aβ load by enhancing autophagic function during APP overexpression. Although the mechanisms of CR/CRM-induced neuroprotection are complex and not fully understood, our findings suggest that CRM 2DG may confer neuroprotection via the induction of autophagic pathways and suppression of apoptosis during APP overexpression. These findings raise the possibility that 2DG may be utilized to harness the power of enhanced autophagic activity for therapeutic intervention in AD. However, further studies are needed to investigate the contribution of autophagic pathways, MA and CMA, in the mechanism of 2DG neuroprotection.

5.4. The modulation of MA and CMA activity using 3MA

To fully assess the contribution of both MA and CMA to neuronal protection following 2DG treatment with 24 hrs APP overexpression, we next assessed the time-

dependent effects of the MA inhibitor, 3MA, on cell viability. The WST-1 results indicate that the reductive capacity of N2aswe cells is significantly reduced following 6 hrs, 12 hrs, and 18 hrs 3MA treatment compared to control cells (**Fig. 5.7**). In line with our findings, studies have reported the time-dependent detrimental effects of inhibiting autophagosome synthesis on cell viability (Hou et al., 2012; Wu et al., 2010). 3MA inhibits the early stages of autophagosome biogenesis, hence, the drastic reduction in cell viability, particularly during 12 hrs 3MA treatment, supports the role of MA as a cytoprotective mechanism, which triggers cell death onset when suppressed. In agreement, a study by Boya et al. (2005). demonstrates that cell viability is severely compromised in response to the complete inhibition of MA, tipping the scales towards cell death onset. Furthermore, the significant increase in cell recovery, following prolonged 3MA treatment, as noted during 24 hrs and 30 hrs 3MA treatment, clearly indicates that MA induction may act as pro-survival mechanism.

Western blot analysis of autophagosome formation, i.e.LC3II, and p62 protein levels (**Fig. 5.8.A**) was performed to determine the most suitable time point at which complete MA inhibition may be achieved using 3MA treatment. Our results indicate a profound decrease in LC3II expression/autophagosome synthesis following 6 hrs, 12 hrs, and 18 hrs 3MA treatment compared to control cells, while LC3II levels are significantly increased upon 24 hrs, and 30 hrs 3MA treatment compared to control cells (**Fig. 5.8.B**). These findings suggest that 3MA's inhibitory effects on autophagosome synthesis are transient, and time dependent. When assessing the effects of 3MA treatment on p62 degradation, our results indicate a significant increase in p62 expression upon 12 hrs 3MA treatment compared to control cells (**Fig. 5.8.C**). Notably, this increase was further enhanced at the time point in which cell viability was previously found to be at its lowest (**Fig. 5.7**). In line with our findings, kinetic studies have reported the temporal effects of 3MA inhibition on autophagosome synthesis. In fact, 3MA has been shown to have short-lived inhibitory effects on VPS34 activity, whereas its effects on the class I PI3K is comparatively longer-lived, resulting in increased autophagosome synthesis following extended periods of 3MA treatment (Heckmann et al., 2013; Wu et al., 2010), as evidenced by the increased LC3II

expression at the 24 hrs, and 30 hrs 3MA treatment time points. In line with our data, studies have reported a self-limiting negative feedback mechanism through which nutrient availability regulates in MA activity (Avruch et al., 2009; Yu et al., 2010). Briefly, when intracellular amino acids are decreased due to inhibition of MA, mTORC1 signalling can in turn be inhibited, thereby inducing MA activity. Conversely, an increase in the amino acid pool size following MA-mediated protein degradation, can reactivate mTORC1 signalling, thereby inhibiting MA activity (Avruch et al., 2009; Yu et al., 2010). This negative feedback mechanism is thought to prevent the pathologic overactivation of MA.

5.5. The modulation of MA and CMA activity using concomitant 2DG and 3MA treatment

WST-1 analysis reveals increased reductive capacity in the 12 hrs 2DG, [24 hrs BA + 12 hrs 2DG], and [24 hrs BA + 12 hrs (2DG + 3MA)] treatment groups compared to the 24 hrs BA treatment group (**Fig. 5.9).** Conversely, cellular reductive capacity is significantly reduced following 24 hrs BA treatment and complete inhibition of autophagosome synthesis in the 12 hrs 3MA treatment group. This data indicates that cell viability is preserved and cytoprotection is conferred following 2DG treatment with and without 24 hrs APP overexpression. Moreover, our results suggest that neuroprotection may not only be dependent on MA induction alone, as enhanced cell viability is also indicated following concomitant 2DG and 3MA treatment with 24 hrs APP overexpression.

Western blot analysis of concomitant 2DG, and 3MA treatment with 24 hrs APP overexpression was performed to further unravel the role of MA in the regulation of 2DG mediated neuroprotection. Our results reveal a significant reduction in APP expression following 12 hrs 2DG, and [24 hrs BA + 12 hrs 2DG] compared to 24 hrs BA treatment, while a significant increase in APP expression is revealed in the 24 hrs

BA, 24 hrs 3MA, [24 hrs BA + 12 hrs 3MA], and [24 hrs BA + 12 hrs (2DG + 3MA)] compared to control cells (**Fig. 5.10.B**). Moreover, APP is further enhanced in the [24 hrs BA + 12 hrs (2DG + 3MA)] treatment group compared to the [24 hrs BA + 12 hrs 2DG] treatment group. This data suggests that (i) concomitant 2DG treatment during 24 hrs APP overexpression attenuates APP expression, while concomitant 2DG and 3MA treatment with 24 hrs APP overexpression is not neuroprotective in this context, additionally, (ii) that complete inhibition of autophagosome synthesis enhances APP expression, and this effect is further enhanced following concomitant 3MA treatment during 24 hrs APP overexpression. These findings suggest that (i) 2DG mitigates APP levels translating to cell protection, (ii) APP may be proteinaceous cargo for MA degradation, as APP levels are increased when MA induction is inhibited, and further augmented with increasing APP expression. In line with our findings, previous reports have shown increased APP levels following 24 hrs 3MA treatment in the neuroblastoma SH-SY5Y cell line, and APP expression was further enhanced following concomitant 24 hrs treatment with 3MA, and MA inducer (STF-62247) (Cai et al., 2015). It is reasonable to propose that inhibition of MA augments APP processing. Our data reveal that β-secretase activity is significantly increased in all the treatment groups compared to control cells, and further enhanced in the 12 hrs 3MA, [24 hrs BA + 12 hrs 3MA], and [24 hrs BA + 12 hrs (2DG + 3MA)] treatment groups compared to the 24 hrs BA treatment group (**Fig. 5.10.D**). This data suggests that amyloidogenic processing is enhanced following induction and complete inhibition of MA with and without 24 hrs APP overexpression. Moreover, our findings indicate that concomitant 2DG and 3MA treatment with 24 hrs APP overexpression also favours amyloidogenic processing as evidenced by the increased β-secretase activity in this treatment group. Indeed, we found that β-secretase activity is enhanced in the [24 hrs BA + 12 hrs (2DG + 3MA)] treatment group compared to the 24 hrs BA treatment group (**Fig. 5.10.D**), suggesting that simultaneous inhibition and induction of MA augments APP overexpression through increased β-secretase activity. Moreover, our results reveal that amyloidogenic processing is more pronounced following complete inhibition of MA. Indeed, Cai et al. (2015) reveal enhanced β-secretase activity following 24 hrs 3MA treatment in SH-SY5Y cells. These findings are further supported

in Zheng et al. (2011) SH-SY5Y cells transfected with APPwt and APPswe plasmids and exposed to hyperoxia or normoxia conditions for 7 days with or without 3MA treatment (1 mM). Consistent with enhanced APP, and β-secretase expression in these groups, Aβ levels are significantly increased in the 12 hrs 3MA, [24 hrs BA + 12 hrs 3MA], and the [24 hrs BA + 12 hrs (2DG + 3MA)] treatment groups compared to both the control cells, and the 24 hrs BA treatment group (**Fig. 5.10.F**). These findings suggest Aβ accumulation is increased due to complete MA inhibition. Consistent with our results, Cai et al. (2015) reveal that the level of $A\beta_{1–42}$ peptide SH-SY5Y cells was significantly increased by 3MA treatment compared to control cells. Our findings are further supported in a study by Fonseca et al. (2014)., which demonstrates an increase in Aβ levels of brain endothelial cells incubated with $A\beta_{1–40}$ for 6 hrs. Additionally, this study revealed that the aggregation state of Aβ peptide was further enhanced when cells were simultaneously incubated with 24 hrs 3MA treatment and extracellularly added $A\beta_{1–40}$ (Fonseca et al., 2014). Hence, it is reasonable to suggest that Aβ is degraded through the MA pathway, and inhibition of this pathway promotes Aβ accumulation. Our results also reveal that Aβ expression in the 12 hrs 2DG, and [24 hrs BA + 12 hrs 2DG] is comparable to the control cells (**Fig. 5.10.F**). This data indicates that while 2DG with and without 24 hrs APP overexpression limits Aβ production translating to protection, inhibition of the MA pathway following 3MA with and without 24 hrs APP overexpression favours enhanced Aβ accumulation/proteotoxicity. Indeed, work by Yu et al. (2004) has revealed that Aβ is produced in AVs within the AD brain, suggesting that induction and inhibition of MA does indeed impact APP processing/Aβ production within this pathway. Overall, our data suggests that 2DG treatment is protective as it mitigates APP processing in favour of cell protection as evidenced by decreased Aβ production. Moreover, this data suggests that MA is the primary cytoprotective mechanism, as evidenced by enhanced APP overexpression following inhibition of this pathway (**Fig. 5.10.B**). In accord, Nixon (2007) suggests that the defective clearance of Aβ-generating AVs creates conditions favourable for Aβ accumulation in AD, and this is supported by data indicating that MA induction following rapamycin treatment reduces Aβ levels both *in vivo* and *in vitro*

(Cho et al., 2014; Spilman et al., 2010). Our work dissects this further, by bringing together clearance and proteotoxicity in the context of MA pathway proficiency.

Western blot analysis of MA molecular markers was performed to assess the contribution of this pathway in 2DG-mediated preservation of cell viability (**Fig. 5.9**). Our results reveal a significant increase in LC3II expression for all the treatment groups compared to the control cells, and LC3II levels are further enhanced in the [24 hrs BA + 12 hrs 2DG] treatment group compared to the 24 hrs BA treatment group (**Fig. 5.11.B**). Although the level of LC3II observed provides a good index of MA induction, it is important to note that LC3II expression is increased in all the groups for different reasons. Briefly, in the 12 hrs 3MA and [24 hrs BA + 12 hrs 3MA] treatment group LC3II levels are enhanced due to complete inhibition of autophagosome synthesis, hence the observed LC3II levels may be indicative of the basal MA activity prior to inhibition of this process. Conversely, in the 12 hrs 2DG, [24 hrs BA + 12 hrs 2DG], and the [24 hrs BA + 12 hrs (2DG + 3MA)] treatment group, LC3II levels are enhanced due to enhanced MA activity above basal levels following 2DG treatment, while enhanced LC3II levels in the 3MA/2DG concomitant treatment group during APP overexpression may reflect impaired autophagosome clearance. In line with our findings, Chakraborty (2017) have also demonstrated that CR regimes upregulate MA activity above basal levels and mitigate APP expression both *in vitro* and *in vivo*. In support of these findings, a time-lapse imaging assessment by Chen et al. (2015) revealed that fasting upregulates MA activity above basal levels in neurons of AD mouse models. Similarly, Ni et al. (2010) also reported increased LC3II levels, with reduced BECN1 expression following 3MA treatment in rat cortical tissue, suggesting that the detected LC3II levels were due to the accumulation of autophagosomes formed prior to inhibition of autophagosome synthesis. Moreover**,** 3MA is known to have an MA stimulatory effect under nutrient-rich conditions based on its inhibitory effect on the class I PtdIns3K (Klionsky et al., 2016; Wu et al., 2010), which is consistent with our observations in the 12 hrs 3MA, and 24 hrs BA + 12 hrs 3MA treatment groups (**Fig. 5.11.B**).

Our results also reveal that p62 expression is significantly increased in the 12 hrs 3MA, [24 hrs BA + 12 hrs MA], [24 hrs BA + 12 hrs 2DG], and the [24 hrs BA + 12 hrs (2DG + 3MA)] treatment group compared to both the control cells and the 24 hrs BA treatment group (**Fig. 5.11.D**). This data suggests that MA-mediated cargo degradation is impaired in response to complete of autophagosome synthesis with and without 24 hrs APP overexpression, with 2DG treatment in the presence of 24 hrs APP overexpression, and with 3MA/2DG concomitant treatment with 24 hrs APP overexpression, while p62 clearance in the 12 hrs 2DG is comparable to control cells. A mismatch is revealed, whereby increased p62 levels (**Fig. 5.11.D)** are not consistent with the indication that MA activity is increased above basal levels (**Fig. 5.11.B**), indicating that other mechanisms/cellular response may impact p62 expression. Indeed, studies by Jamart et al. (2013) and Sanchez et al. (2014) reveal that p62 are affected by both increased transcription and decreased degradation.

The contribution of the CMA pathway to 2DG-mediated preservation of cell viability during 24 hrs APP expression (**Fig. 5.9**) was assessed with western blot analysis. To our surprise, our findings reveals no significant changes in LAMP2A (**Fig. 5.12.B**) and HSC70 (**Fig. 5.12.D**) protein expression for all the treatment groups compared to control cells. This data suggests that CMA activity is not activated above basal levels in the presence of complete MA pathway inhibition or induction of MA with and without 24 hrs APP overexpression. These finding suggest that CMA has little to no role in amyloidogenic processing in this context. In contrast with our findings, previous studies have demonstrated that CMA is activated above basal levels in response to amino acid or glucose deprivation in lysosomes isolated from rat liver, however, MA was not inhibited in this context (Cuervo et al., 1995, 1997). Moreover, the authors also revealed that CMA is induced following ‘prolonged’ nutrient starvation, indicating temporal differences in the activation of MA and CMA. Our findings suggest that 12 hrs 2DG treatment may not be sufficient to induce CMA above basal levels in this context. This findings LRP1 is contrast with a study by Schneider et al. (2014) which demonstrated an induction in MA activity in LAMP2A knockout/CMA-deficient mice. Similarly, Galan-Acosta et al. (2015) reported enhanced CMA activity in response to

nutrient-deprivation, and inhibition of the MA pathway using spautin-1 in cancer cells (Galan-Acosta et al., 2015). However, and most importantly, these experiments were performed in different experimental model systems, not under such controlled APP environment in the current study context. Overall, our findings suggest that inhibition of the MA pathway during 24 hrs APP overexpression does not promote compensatory CMA response. Moreover, despite suggestions of CMA's role in APP clearance, our results indicate that CMA has, at least in this *in vitro* scenario, no role in 2DG-medaited cytoprotection.

Finally, western blot was performed to assess the effects of 3MA/ 2DG concomitant treatment during 24 hrs APP overexpression on apoptosis (**Fig. 5.13**). Our results reveal significantly increased Total Caspase-3 (**Fig. 5.13.B**) and c-PARP (**Fig. 5.13.D**) expression for all the treatment groups compared to control cells, with Total Caspase-3 further enhanced in the 12 hrs 3MA treatment group compared to the 24 hrs BA treatment group. These results indicate that the apoptotic pathway is activated irrespective whether MA is induced or inhibited. Although MA has previously been shown to impact APP processing in favour of decreased Aβ production and/or increased clearance (**Fig. 5.10.B,F**), this response appears insufficient to mediate complete cytoprotection following 24 hrs APP overexpression. However, Total Caspase-3 expression is further enhanced in response to complete MA inhibition, suggesting the role of MA towards creating a more favourable environment for cell survival. These findings raise the possibility that inducing MA activity above basal levels should be performed earlier in APP overexpression, i.e. 12 hrs BA treatment, or that the duration of 2DG exposure should be prolonged, e.g. 24 hrs 2DG treatment, which may also create more favourable conditions for CMA to be fully induced. However, the induction of MA has been described as a 'double-edged sword'. On the one hand, MA is an essential neuroprotective response shown to regulate the clearance of cytotoxic Aβ oligomers (Nilsson and Saido, 2014; Nilsson et al., 2013, 2015), on the other hand, excessive MA induction has been shown to be pathogenic due to its sustained degradation of critical cellular constituents, ultimately leading to cell death onset as reviewed in Levine and Yuan (2005). While the decision to further

enhance MA can lead to adverse effects in cells under certain pathological conditions, our results clearly show that the upregulation of MA above basal levels may translate into neuronal protection in the context of APP overexpression. It is reasonable to propose that therapeutic interventions with dual-functionality in both enhanced MA activity, and Aβ clearance may ameliorate Aβ proteotoxicity in AD, translating to neuroprotection.

CHAPTER 6 RESULTS: *IN VIVO* ASSESSMENT OF THE ROLE OF MA AND CMA IN A PARAQUAT-INDUCED BRAIN INJURY MODEL

6.1. Introduction to results

Paraquat (PQ)-induced neurotoxicity is a well-established model system in the field of neurodegeneration and proteotoxicity (Huang et al., 2016; Wang et al., 2017). PQ is a commonly used pesticide shown to induce mitochondrial damage and increased ROS production, ultimately leading to neurodegeneration (Yan et al., 2016). Oxidative stress is associated with increased production of ROS and reactive nitrogen species, including hydrogen peroxide, which have been shown to contribute to the early stages of AD prior to the onset of clinical symptoms (Uttara et al., 2009). Oxidative stress markers including high levels of lipid peroxidation have been reported in post-mortem brain tissue from individuals with preclinical or early stage AD (Sultana et al., 2011). CR regimes have consistently been shown to ameliorate age-associated pathology in various organisms (Mattson, 2005). Intermittent fasting (IF), a dietary intervention analogous to CR and involving *ad libitum* to food access on alternate days, has also been shown to attenuate brain aging through the reduction of inflammatory processes, including the reduction of ROS and induction of cellular stress resistance mechanisms (Li et al., 2017; Parikh et al., 2016). However, the effect of CR regimes on particularly MA, and CMA activity, but also glial fibrillary acidic protein (GFAP), a marker of brain injury, cytochrome c, a marker of apoptosis, and 4-hydroxynonenal (4HNE), a marker of lipid peroxidation, in the PQ-induced brain injury model is largely unclear. Therefore, the aims of this chapter were to assess (i) the contribution of MA and CMA in this model system in protein clearance, and (ii) the effects of 48 hrs IF on oxidative stress in the hippocampus, cortex, and cerebellum region. These brain regions were selected based on pathological studies of AD patients, which indicate that the greatest neurodegenerative changes, including generalised cell loss, occur in these regions at varying degrees in response to increased oxidative stress (Schmahmann, 2016). Mice were subjected twice weekly to PQ treatment of 10 mg/kg followed by 48 hrs IF for 3 weeks.

6.2. Results

6.2.1. Effect of the treatment intervention on body weight

6.2. Results

6.2.1. Effect of the treatment intervention on body weight

As shown in **Fig. 6.1,** the results indicate a significant decrease in body weight in the 48 hrs IF group [21.11 ± 0.53 ($p<0.05$)], and [(48 hrs IF) + PQ] group [21.27 ± 0.53 ($p<0.05$)] compared to the control [25.22 ± 0.25] and PQ exposed group [26.26 ± 0.27] after the completion of the 21-day treatment intervention. Body weight loss reached significance on day 8, however, and most importantly, body weight was regained in response to the 24 hrs refeeding period. In Brief, body weight loss was significant: (i) on **day 8**, in the 48 hrs IF group [17.68 ± 0.47 ($p<0.05$)], and [(48 hrs IF) + PQ] group [18.38 ± 0.47 ($p<0.05$)] compared to the control [24.87 ± 0.47] and PQ exposed group [25.9 ± 0.47]; (ii) on **day 11**, in the 48 hrs IF group [17.45 ± 0.47 ($p<0.05$)], and [(48 hrs IF) + PQ] group [18.03 ± 0.47 ($p<0.05$)] compared to the control [25.47 ± 0.47] and PQ exposed group [26.47 ± 0.47]; (iv) on **day 14**, in the 48 hrs IF group [17.26 ± 0.47 ($p<0.05$)], and [(48 hrs IF) + PQ] group [17.79 ± 0.47 ($p<0.05$)] compared to the control [25.96 ± 0.47] and PQ exposed group [27.14 ± 0.47]; (vii) on **day 17**, in the 48 hrs IF group [18.0 ± 0.47 ($p<0.05$)], and [(48 hrs IF) + PQ] group [17.6 ± 0.47 ($p<0.05$)] compared to the control [26.6 ± 0.47] and PQ exposed group [27.73 ± 0.47]; and (ix) on **day 20**, in the 48 hrs IF group [18.26 ± 0.47 ($p<0.05$)], and [(48 hrs IF) + PQ] group [17.79 ± 0.47 ($p<0.05$)] compared to the control [26.89 ± 0.47] and PQ exposed group [28.05 ± 0.47] (**Fig. 6.1**), suggesting that the 24 hrs refeeding period was sufficient to counteract the loss in body weight.

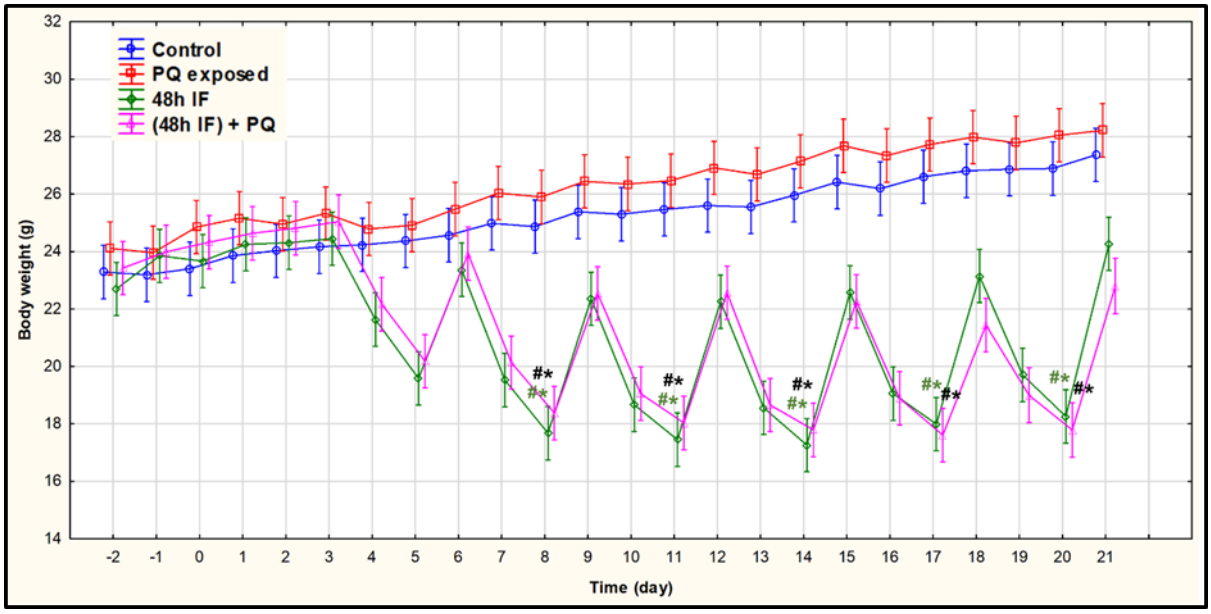

Figure 6.1: Body weight in response to the 21-day treatment intervention. Data expressed as mean ± SEM, statistical analysis: ANOVA and Bonferroni correction, *p<0.05 vs control, #p<0.05 vs. PQ, n = 12. Abbreviations: PQ, paraquat exposed group; 48h (IF), 48 hrs intermittent fasted group; [(48h IF) + PQ], 48 hrs intermittent fasted and paraquat group.

6.2.2. Effect of the 21-day treatment intervention on overall food consumption and *ex vivo* brain weight

As shown in **Fig. 6.2.A**, a significant increase in overall food consumption is indicated in the 48 hrs IF group [27.06 ± 0.3 (p<0.05)], and [(48 hrs IF) + PQ] group [25.77 ± 2.35 (p<0.05)] compared to control [18.78 ± 0.71] and the PQ exposed group [19.38 ± 0.77].

No significant difference in *ex vivo* brain weight is revealed for all groups (**Fig. 6.2.B**).

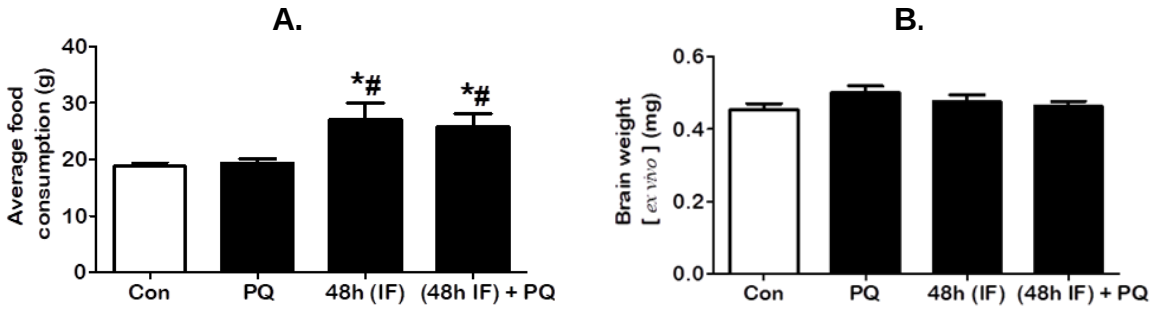

Figure 6.2: (A) food consumption and **(B)** *ex vivo* brain weight in response to treatment intervention. Data expressed as mean ± SEM, statistical analysis: ANOVA and Bonferroni correction, *p<0.05 vs control, #p<0.05 vs. PQ, n = 12.

6.2.3. Effect of the 21-day treatment intervention on survival

Figure 6.3 reveals no significant difference in survival following the 21-day treatment intervention. Three mice were censored in the [(48 hrs IF) + PQ] group, with no effect on survival when compared to the control, PQ exposed group, or the 48 hrs IF group.

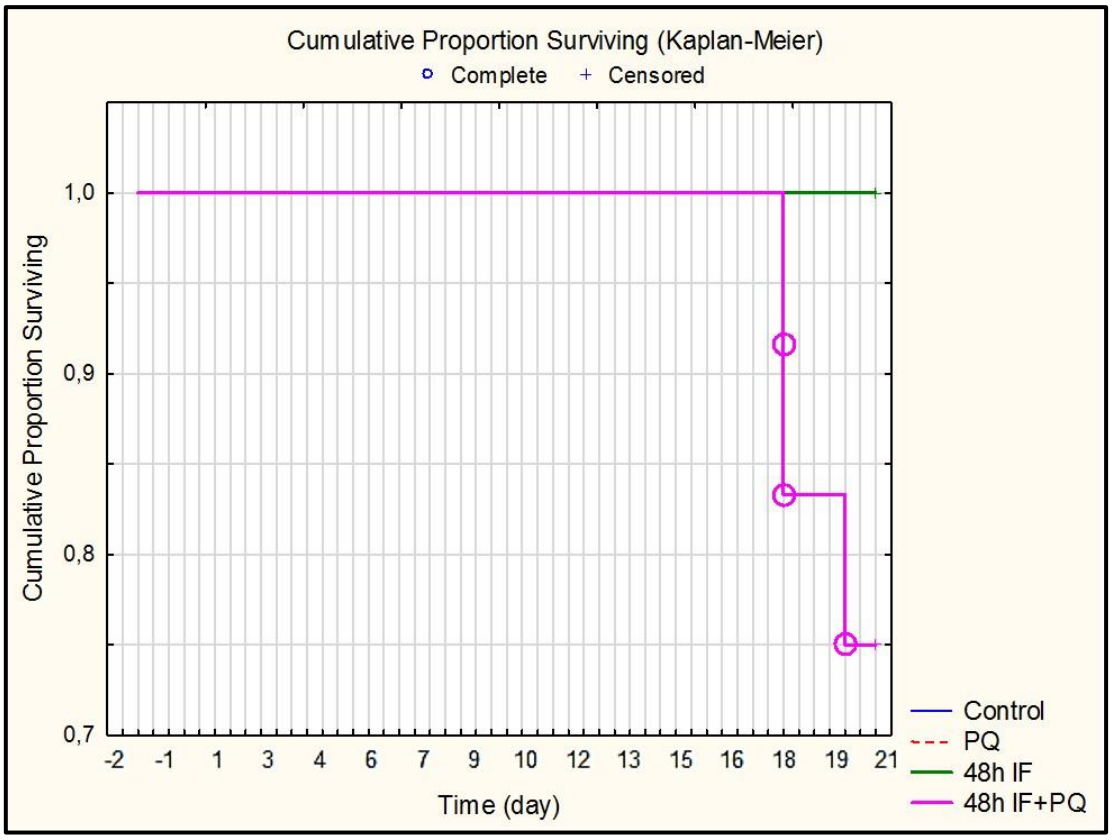

Figure 6.3: Kaplan–Meier survival curves of treatment groups. Overall survival was quantified using the log rank test, $p < 0.05$, $n = 12$. Abbreviations: PQ, paraquat exposed group; 48h (IF), 48 hrs intermittent fasted group; [(48h IF) + PQ], 48 hrs intermittent fasted and paraquat group.

6.2.4. Assessment of the hippocampus region

In order to assess the overall histology and cellular morphology of the hippocampus region following the 21-day treatment intervention period, Haematoxylin and Eosin (H & E) staining was performed. As shown in **Fig. 6.4**, no major abnormalities in individual nuclei distribution or density is observed in any of the treatment groups compared to the control.

6.2.4.1. Representative H & E micrographs of the hippocampus

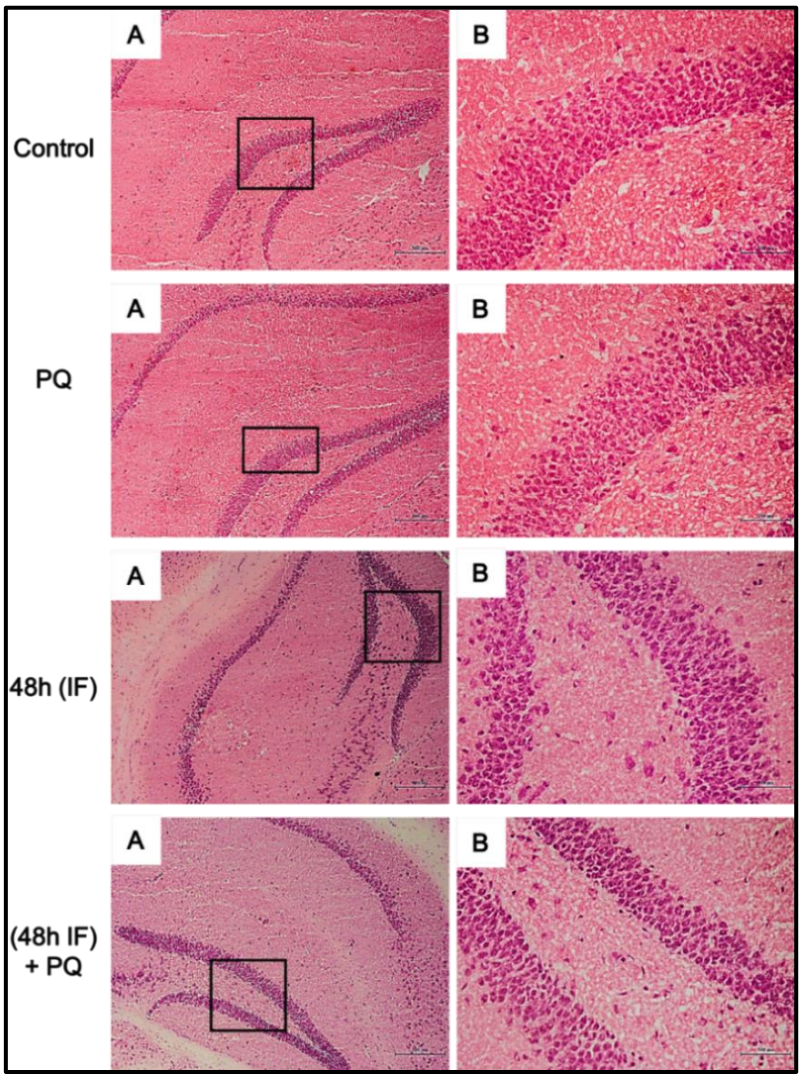

Figure 6.4: Representative H & E micrographs of the hippocampus in response to the 21-day treatment intervention. Representative micrographs indicate the control, paraquat exposed (PQ) group, 48 hrs intermittent fasting (IF) group, and [(48 hrs IF) + PQ)] group, n= 6. Scale bars indicate 500 µm. Images (**A**) = ×4 magnification, images (**B**) = ×10 magnification**.**

6.2.4.2. Effect of the 21-day treatment intervention on lipid peroxidation and apoptosis in the hippocampus

As shown in **Fig. 6.5.A**, 4HNE protein expression is significantly increased in the PQ exposed group [0.71 ± 0.02 ($p<0.05$)] compared to the control [0.58 ± 0.04], while 4HNE expression is significantly decreased in the 48 hrs IF group [0.17 ± 0.03 ($p<0.05$)], and importantly, the [(48 hrs IF) PQ] group [0.08 ± 0.02 ($p<0.05$)] compared to the PQ exposed group [0.71 ± 0.02] and control group (**Fig. 6.5.B**).

Figure 6.5.C indicates that cytochrome c expression follows the same pattern as 4HNE, i.e. cytochrome c is significantly increased in the PQ exposed group [0.56 ± 0.02 ($p<0.05$)] compared to the control [0.34 ± 0.05], while a significant decrease is indicated in the [(48 hrs IF) + PQ] group [0.19 ± 0.02 ($p<0.05$)] compared to the PQ exposed group [0.56 ± 0.02] and the control, with a similar decrease in the 48 hrs IF group [0.32 ± 0.02 ($p<0.05$)] compared to the PQ exposed group only (**Fig. 6.5.D**). These data indicate robust protection in response to the IF regime.

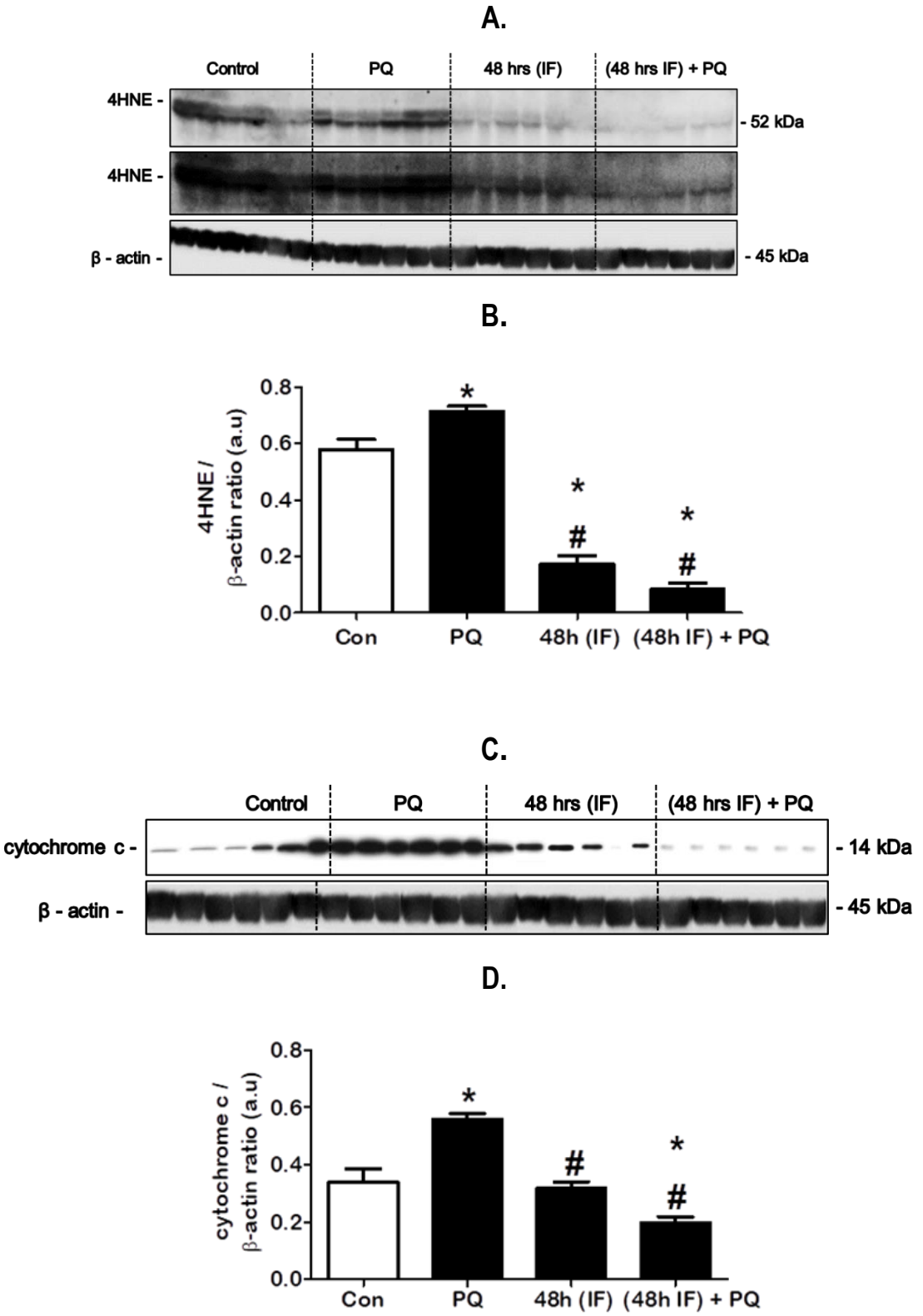

Figure 6.5: Effect of the 21-day treatment intervention on lipid peroxidation and apoptosis in the hippocampus. Representative western blot and densitometric analysis for **(A, B)** 4HNE (low and high exposure), and **(C, D)** cytochrome c protein expression is shown. Data expressed as mean ± SEM, statistical analysis: ANOVA and Bonferroni correction, * $p<0.05$ vs. control, #$p<0.05$ vs. PQ, n = 6, arbitrary units (a.u).

6.2.4.3. Representative 4HNE and cytochrome c fluorescence micrographs of the hippocampus

In order to assess the localization and signal intensity pattern of 4HNE, and cytochrome c protein in the hippocampus region, immunofluorescence analysis was performed. As shown in **Fig. 6.6**, 4HNE signal (**red, left panel**), and cytochrome c signal (**red, right panel**) are both strongly indicted in the PQ exposed group compared to the control, the 48 hrs IF group and the [(48 hrs IF) PQ] group.

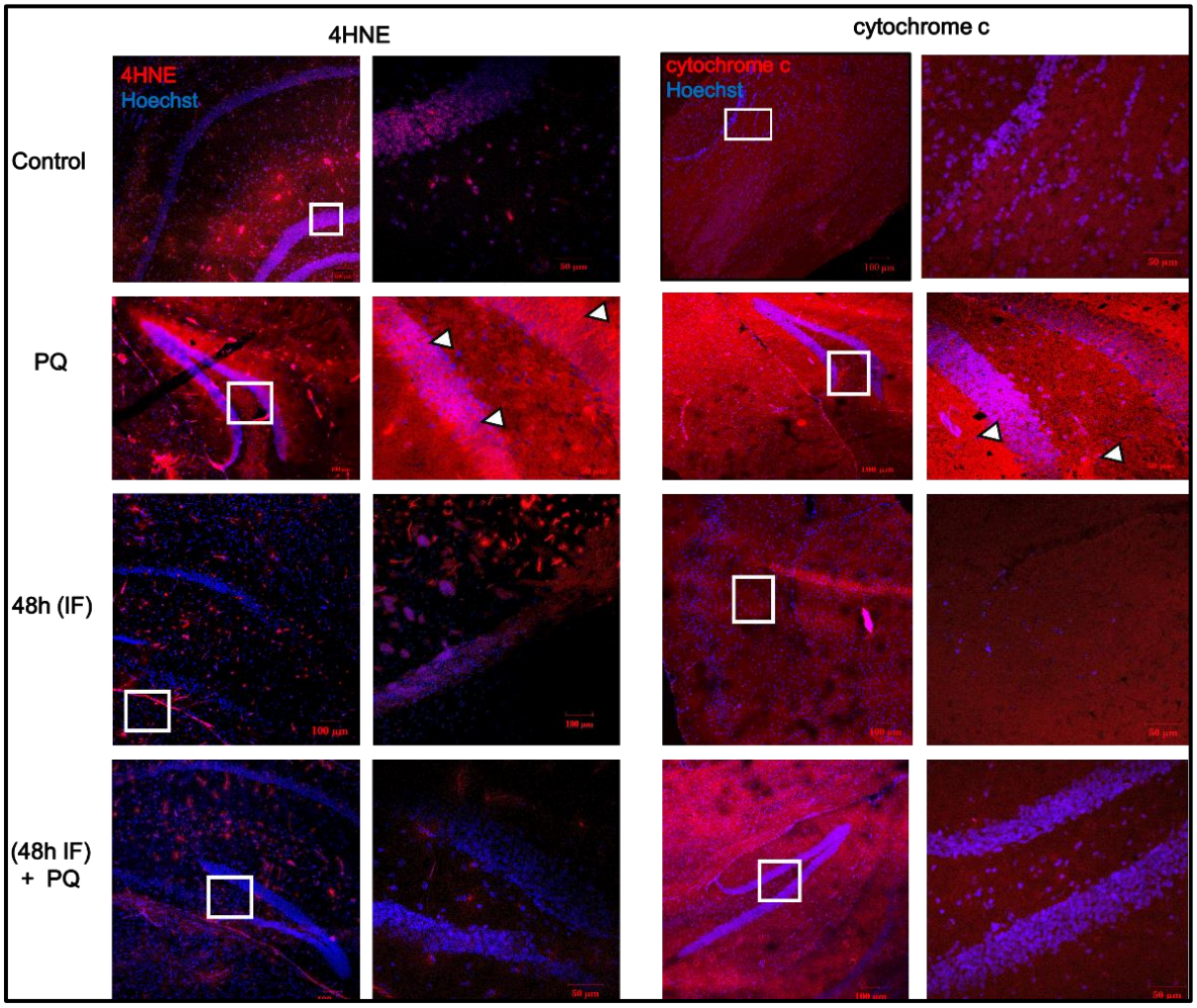

Figure 6.6: Immunofluorescence micrographs indicating 4HNE and cytochrome c protein expression in the hippocampus. **Left panel** indicates 4HNE (**red**). **Right panel** indicates cytochrome c (**red**). The treatment intervention groups are defined as the control, paraquat exposed (PQ) group, 48 hrs intermittent fasting (IF) group, and [(48 hrs IF) + PQ)] group, n = 6. Nuclei counterstained with Hoechst 33342 (**blue**), scale bars = 100 µm, higher magnification micrographs = 50 µm. Arrowheads indicate regions of strong 4HNE or cytochrome c protein signal.

6.2.4.4. Effect of the 21-day treatment intervention on MA activity in the hippocampus

Figure 6.7.A indicates a significant increase in LC3II protein expression in the 48 hrs IF group [1.39 ± 0.06 ($p<0.05$)], and the [(48 hrs IF) + PQ] group [0.19 ± 0.02 ($p<0.05$)] compared to the control [1.07 ± 0.01]. More importantly, LC3II expression is significantly increased in the [(48 hrs IF) + PQ] group [0.19 ± 0.02 ($p<0.05$)] compared to the PQ exposed group [1.17 ± 0.03] (**Fig. 6.7.B**).

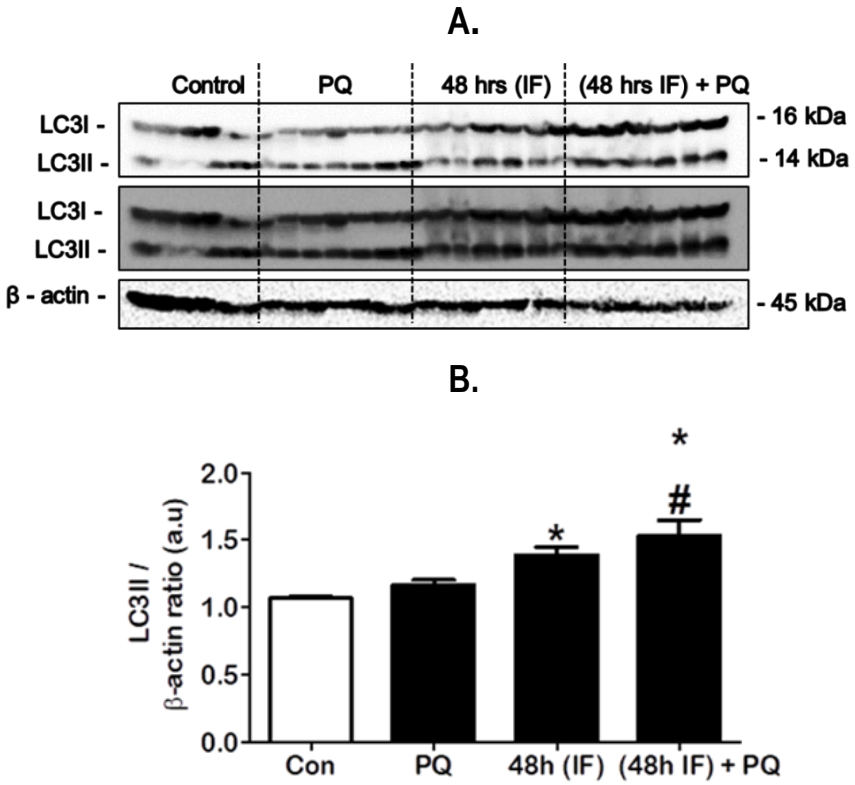

Figure 6.7: Effect of the 21-day treatment intervention on MA activity in the hippocampus. Representative western blot (low and high exposure) and densitometric analysis for **(A, B)** LC3II protein expression is shown. Data expressed as mean ± SEM, statistical analysis: ANOVA and Bonferroni correction, * $p<0.05$ vs. control, #$p<0.05$ vs. PQ, n = 6, arbitrary units (a.u).

6.2.4.5. Representative GFAP and LC3II fluorescence micrographs of the hippocampus

As shown in **Fig. 6.8**, GFAP (**red**), and LC3II (**green**) protein signal is strongly indicated in the PQ exposed group compared to the other treatment groups.

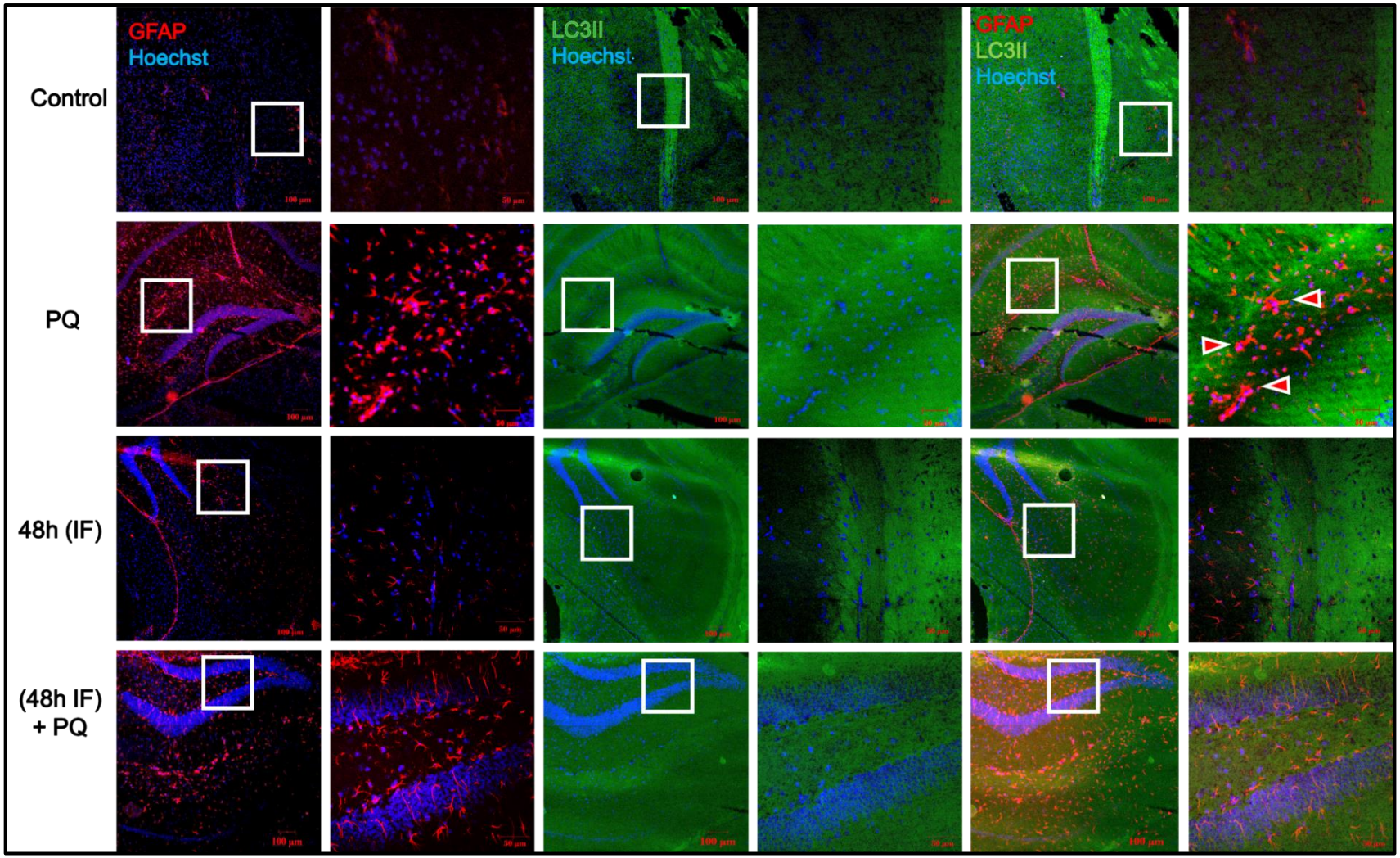

Figure 6.8: **Immunofluorescence micrographs indicating LC3II (green) and GFAP (red) expression in the hippocampus**. Representative micrographs indicate the control, paraquat exposed (PQ) group, 48 hrs intermittent fasting (IF) group, and [(48 hrs IF) + PQ) group. Nuclei counterstained with Hoechst 33342 (**blue**), scale bars = 100 µm, higher magnification micrographs = 50 µm. Arrowheads indicate regions of strong GFAP or LC3II protein signal.

6.2.4.6. Effect of the 21-day treatment intervention on MA cargo protein degradation in the hippocampus

As shown in **Fig. 6.9.A**, p62 protein expression is significantly decreased in the 48 hrs IF group [0.41 ± 0.06 ($p<0.05$)], and [(48 hrs IF) + PQ] group [0.27 ± 0.05 ($p<0.05$)] compared to the control [0.65 ± 0.02]. Importantly, a significant decrease is indicated in the [(48 hrs IF) + PQ] group [0.27 ± 0.05 ($p<0.05$)] compared to the PQ exposed group [0.56 ± 0.03] (**Fig. 6.9.B**).

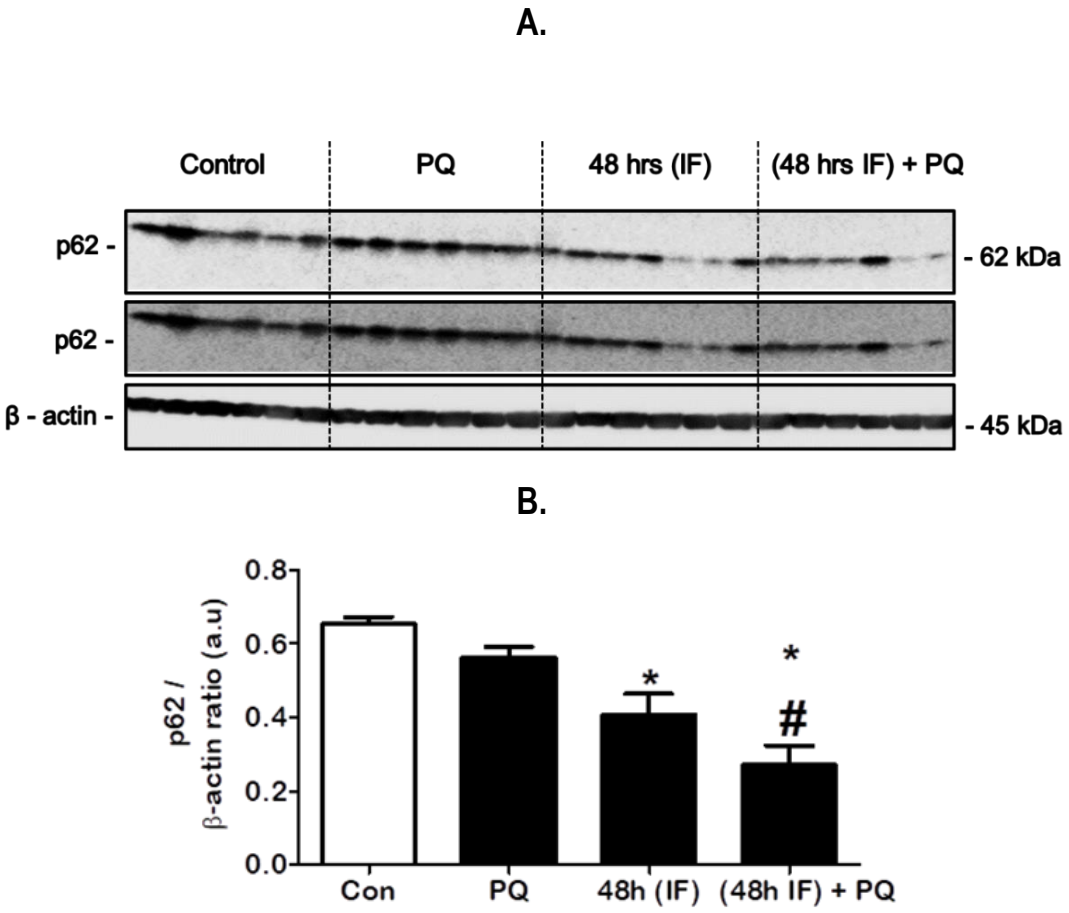

Figure 6.9: Effect of the 21-day treatment intervention on MA cargo protein degradation in the hippocampus. Representative western blot (low and high exposure) and densitometric analysis for **(A, B)** p62 protein expression is shown. Data expressed as mean ± SEM, statistical analysis: ANOVA and Bonferroni correction, *$p<0.05$ vs. control, #$p<0.05$ vs. PQ, n = 6, arbitrary units (a.u).

6.2.4.7. Representative p62 fluorescence micrographs of the hippocampus

Figure 6.10 reveals that p62 (magenta) protein signal is strongly indicated in the PQ exposed group compared to the control, the 48 hrs IF group, and the [(48 hrs IF) + PQ] group.

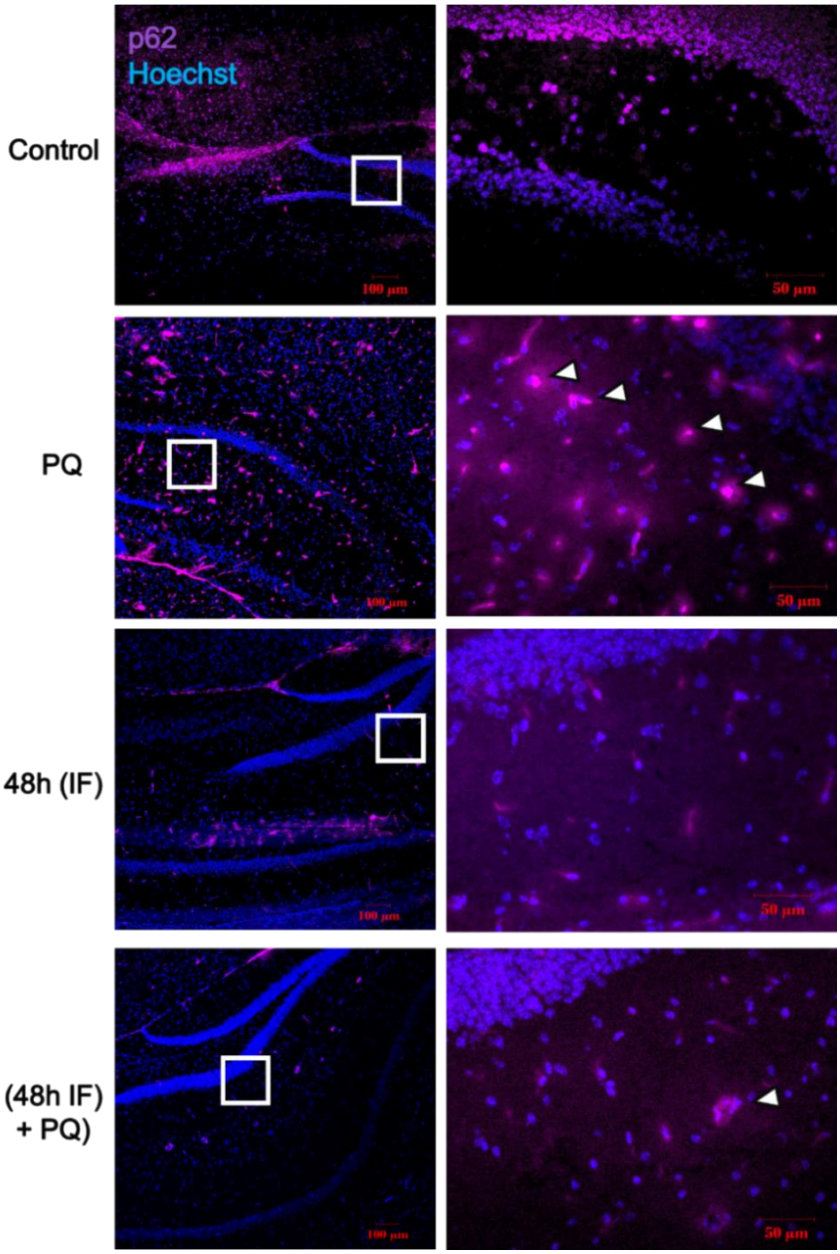

Figure 6.10: Immunofluorescence micrographs indicating p62 signal (magenta) in the hippocampus. Representative micrographs indicate the control, paraquat exposed (PQ) group, 48 hrs intermittent fasting (IF) group, and the [(48 hrs IF) + PQ)] group. Nuclei counterstained with Hoechst 33342 (**blue**), scale bars = 100 µm, higher magnification micrographs = 50 µm. Arrowheads indicate regions of strong p62 protein signal.

6.2.4.8. Effect of the 21-day treatment intervention on the expression of CMA exclusive protein in the hippocampus

As shown in **Fig. 6.11.A**, LAMP2A protein expression is significantly increased in the 48 hrs IF group [1.12 ± 0.07 ($p<0.05$)], and the [(48 hrs IF) + PQ] group [1.11 ± 0.03 ($p<0.05$)] compared to the control [0.75 ± 0.12]. Importantly, LAMP2A expression is significantly increased in the 48 hrs IF group, and the [(48 hrs IF) + PQ] group compared to the PQ exposed group [0.75 ± 0.05] (**Fig. 6.11.B**), suggesting that the IF regime may impact CMA activity in this region.

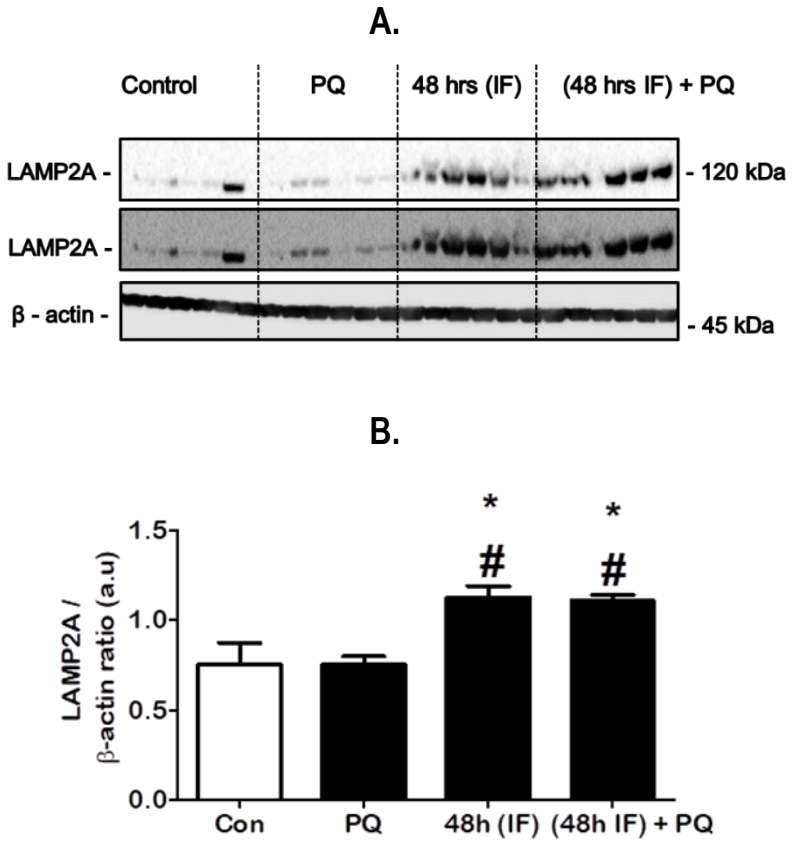

Figure 6.11: Effect of the 21-day treatment intervention on CMA activity in the hippocampus. Representative western blot (low and high exposure) and densitometric analysis for **(A, B)** LAMP2A protein expression is shown. Data expressed as mean ± SEM, statistical analysis: ANOVA and Bonferroni correction, *$p<0.05$ vs. control, #$p<0.05$ vs. PQ, n = 6, arbitrary units (a.u).

6.2.4.9. Effect of the 21-day treatment intervention on APP expression in the hippocampus

Figure 6.12.A reveals that APP expression is significantly increased in the PQ exposed group [1.86 ± 0.13 ($p<0.05$)] compared to the control [0.62 ± 0.1]. However, and most importantly, APP expression is significantly decreased in the 48 hrs IF group [0.18 ± 0.04 ($p<0.05$)] and [(48 hrs IF) + PQ] [0.78 ± 0.13 ($p<0.05$)] group compared to the PQ exposed group, while significantly increased APP expression is revealed in the [(48 hrs IF) + PQ] group compared to the 48 hrs IF group (**Fig. 6.12.B**).

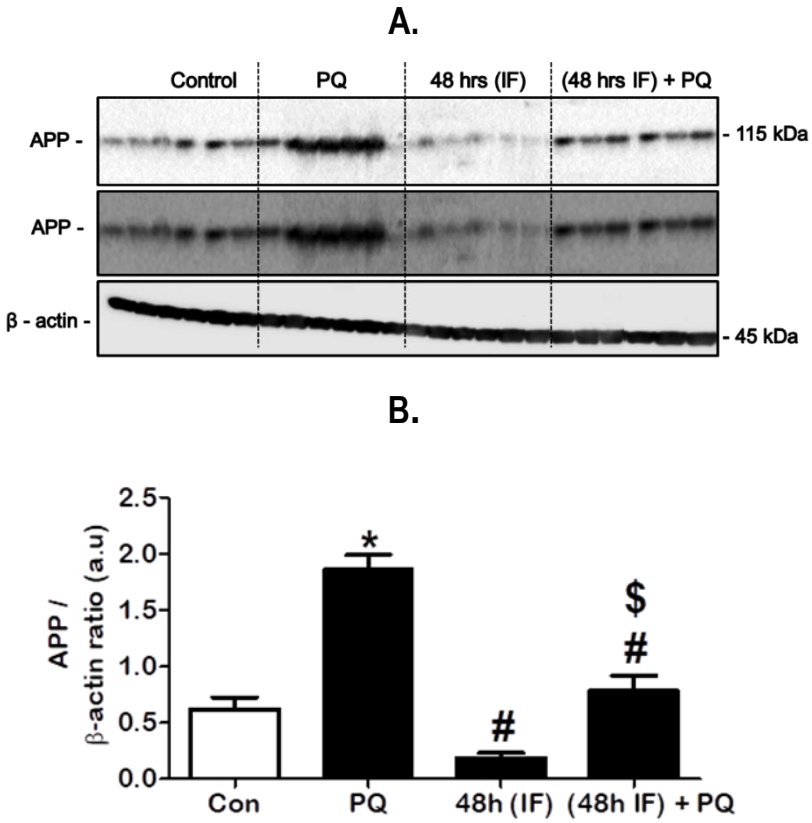

Figure 6.12: Effect of the 21-day treatment intervention on APP expression in the hippocampus. Representative western blot (low and high exposure) and densitometric analysis for **(A, B)** APP protein expression is shown. Data expressed as mean ± SEM, statistical analysis: ANOVA and Bonferroni correction, *$p<0.05$ vs. control, #$p<0.05$ vs. PQ, #$p<0.05$ vs. 48h IF, n = 6, arbitrary units (a.u).

6.2.5. Assessment of the cortex region

As shown in **Fig. 6.13**, H & E staining of the cortex reveals uniform distribution of individual nuclei for all the groups, with no indications of cell loss, or architectural abnormalities following the 21-day treatment intervention.

6.2.5.1. Representative H & E micrographs of the cortex

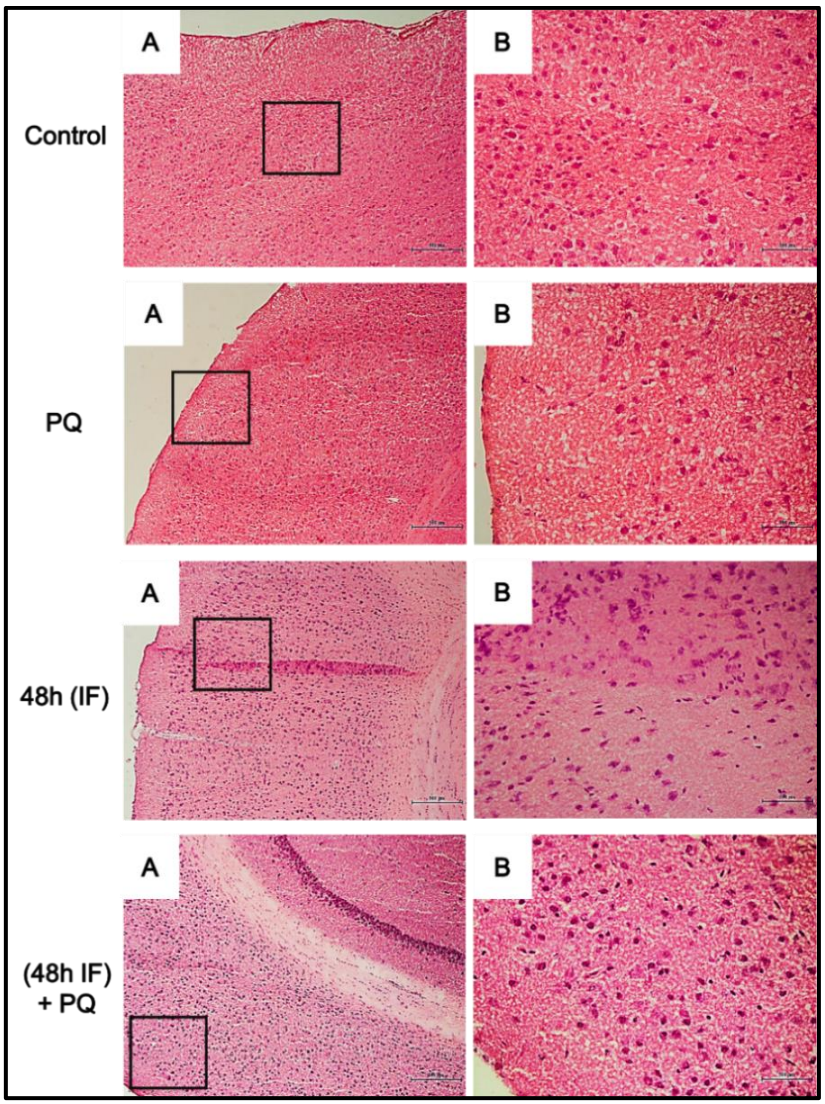

Figure 6.13: Representative H&E micrographs of the cortex in response to the 21-day treatment intervention. Representative micrographs indicate the control, paraquat exposed (PQ) group, 48 hrs intermittent fasting (IF) group, and [(48 hrs IF) + PQ] group, n= 6. Scale bars indicate 500 µm. Images (**A**) = ×4 magnification, images (**B**) = ×10 magnification**.**

6.2.5.2. Effect of the 21-day treatment intervention on lipid peroxidation and apoptosis in the cortex

Figure 6.14.A reveals a significant increase in 4HNE protein expression in the PQ exposed group [0.54 ± 0.01 ($p<0.05$)] compared to the control [0.31 ± 0.02], while 4HNE expression is significantly decreased in the 48 hrs IF group [0.04 ± 0.002 ($p<0.05$)], and the [(48 hrs IF) + PQ] group [0.02 ± 0.006 ($p<0.05$)] compared to the PQ exposed group and the control (**Fig. 6.14.B**).

As shown in **Fig. 6.14.C**, cytochrome c protein expression significantly increased in the PQ exposed group [0.068 ± 0.003 ($p<0.05$)] compared to the control [0.03 ± 0.0], while cytochrome c expression is significantly decreased in the 48 hrs IF group [0.03 ± 0.002 ($p<0.05$)], and the [(48 hrs IF) + PQ] group [0.03 ± 0.0 ($p<0.05$)] compared to the PQ exposed group (**Fig. 6.14.D**). These data suggest that the IF regime may be protective.

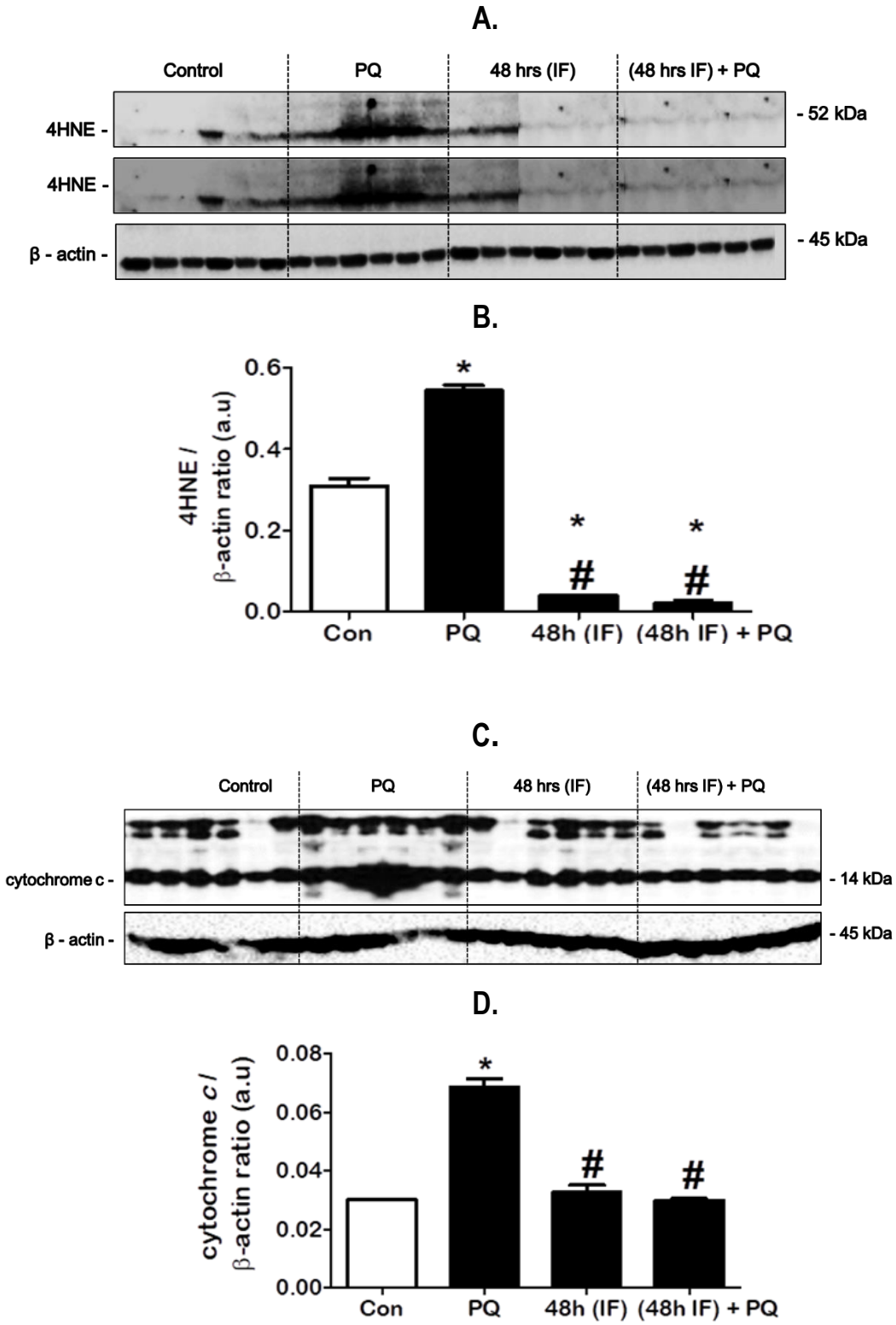

Figure 6.14: Effect of the 21-day treatment intervention on lipid peroxidation and apoptosis in the cortex. Representative western blot and densitometric analysis for **(A, B)** 4HNE (low and high exposure), and **(C, D)** cytochrome c protein expression is shown. Data expressed as mean ± SEM, statistical analysis: ANOVA and Bonferroni correction, * $p<0.05$ vs. control, #$p<0.05$ vs. PQ, n = 6, arbitrary units (a.u).

6.2.5.3. Representative 4HNE and cytochrome c fluorescence micrographs of the cortex

Figure 6.15 indicates that 4HNE (**red, left panel**), and cytochrome c (**red, right panel**) protein signal is strongly revealed in the PQ exposed group while the control, 48h IF group and the [(48 hrs IF) + PQ] group reveal diminished 4HNE and cytochrome c protein signal.

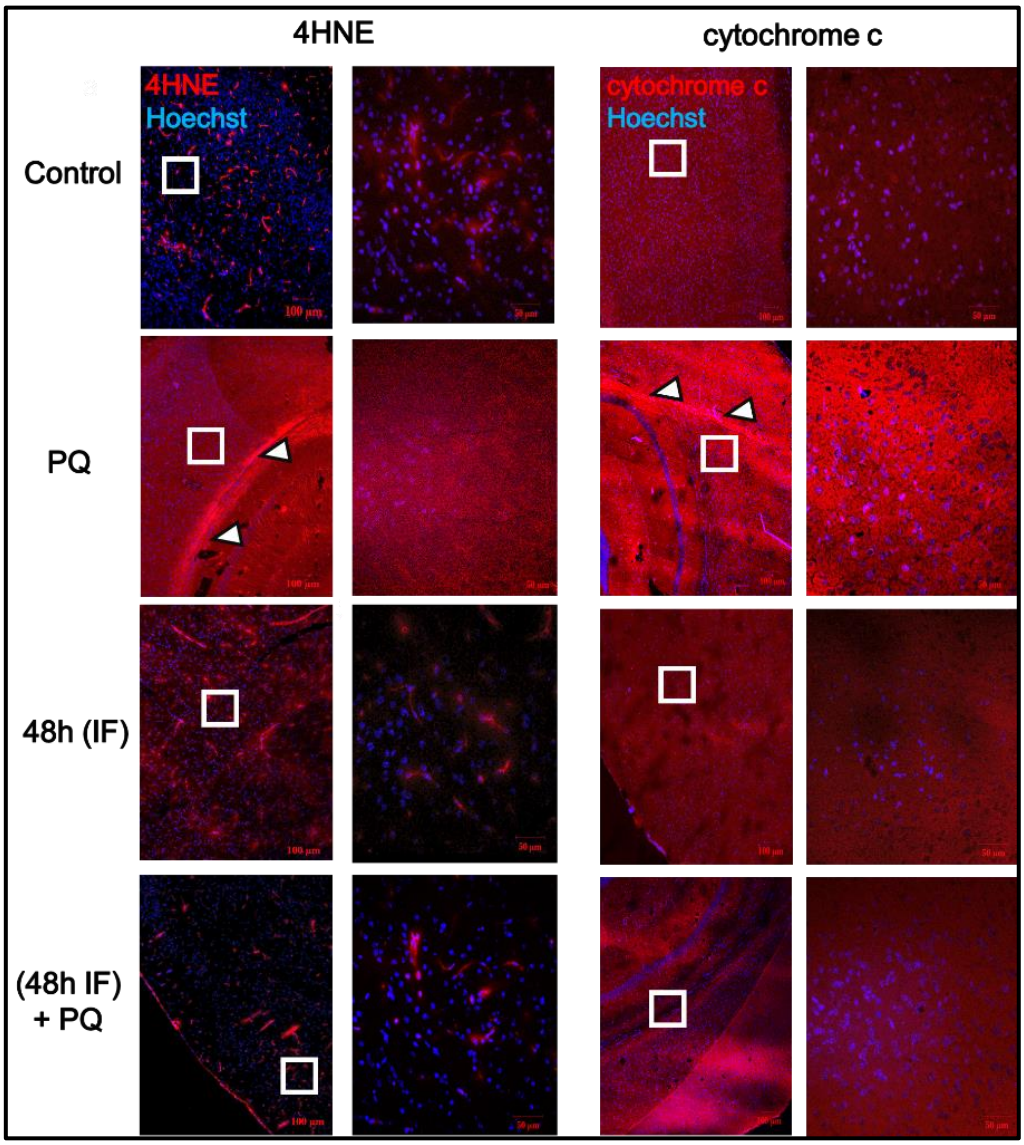

Figure 6.15: Immunofluorescence micrographs indicating 4HNE and cytochrome c signal in the cortex. Left panel indicates 4HNE (**red**). **Right panel** indicates cytochrome c (**red**). The treatment intervention is defined as the control, paraquat exposed (PQ) group, 48 hrs intermittent fasting (IF) group, and [(48 hrs IF) + PQ)] treatment group. Nuclei counterstained with Hoechst 33342 (**blue**), scale bars = 100 µm, higher magnification micrographs = 50 µm. Arrowheads indicate regions of strong 4HNE or cytochrome c protein signal.

6.2.5.4. Effect of the 21-day treatment intervention on MA activity in the cortex

As shown in **Fig. 6.16.A**, LC3II protein expression is significantly increased in the 48 hrs IF group [0.87 ± 0.06 ($p<0.05$)], and the [(48 hrs IF) + PQ] group [0.95 ± 0.03 ($p<0.05$)] compared to the control [0.65 ± 0.005], with no significant difference in LC3II expression indicated in the PQ exposed group [0.826 ± 0.03] (**Fig. 6.16.B**).

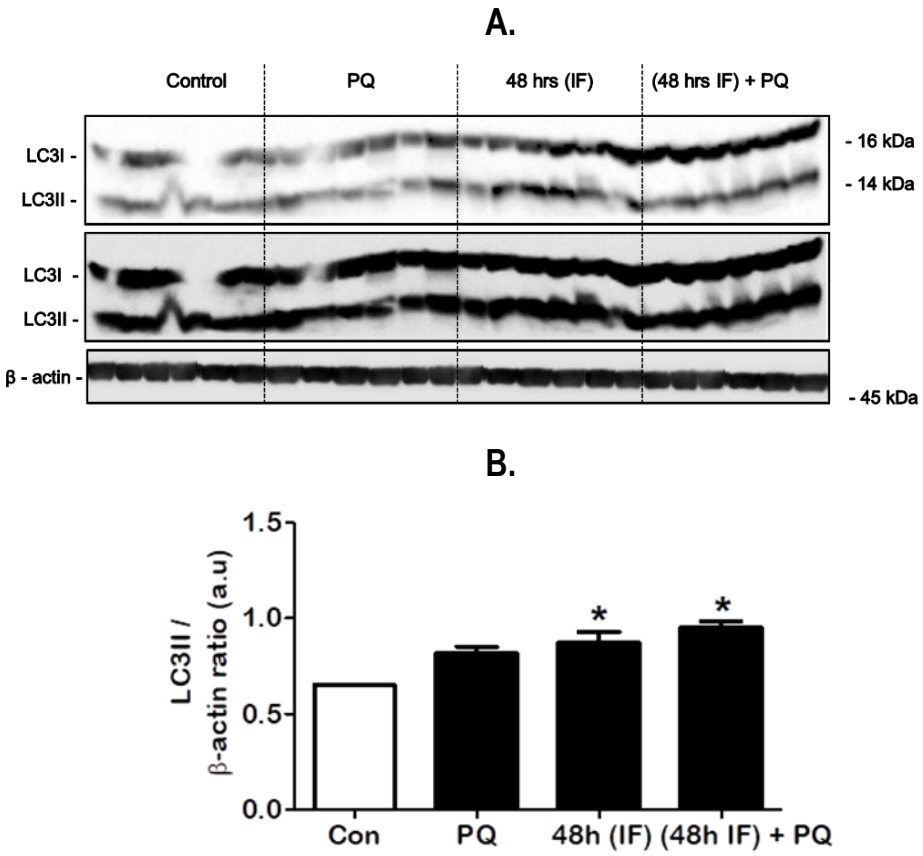

Figure 6.16: Effect of the 21-day treatment intervention on MA activity in the cortex. Representative western blot (low and high exposure) and densitometric analysis for **(A, B)** LC3II protein expression is shown. Data expressed as mean ± SEM, statistical analysis: ANOVA and Bonferroni correction, * $p<0.05$ vs. control, n = 6, arbitrary units (a.u).

6.2.5.5. Representative GFAP and LC3II fluorescence micrographs of the cortex

Figure 6.17 reveals relatively uniform GFAP (**red**) protein signal in all the groups, while LC3II (**green**) protein signal appears slightly increased in the 48h IF group and [(48 hrs IF) + PQ] group compared to the control.

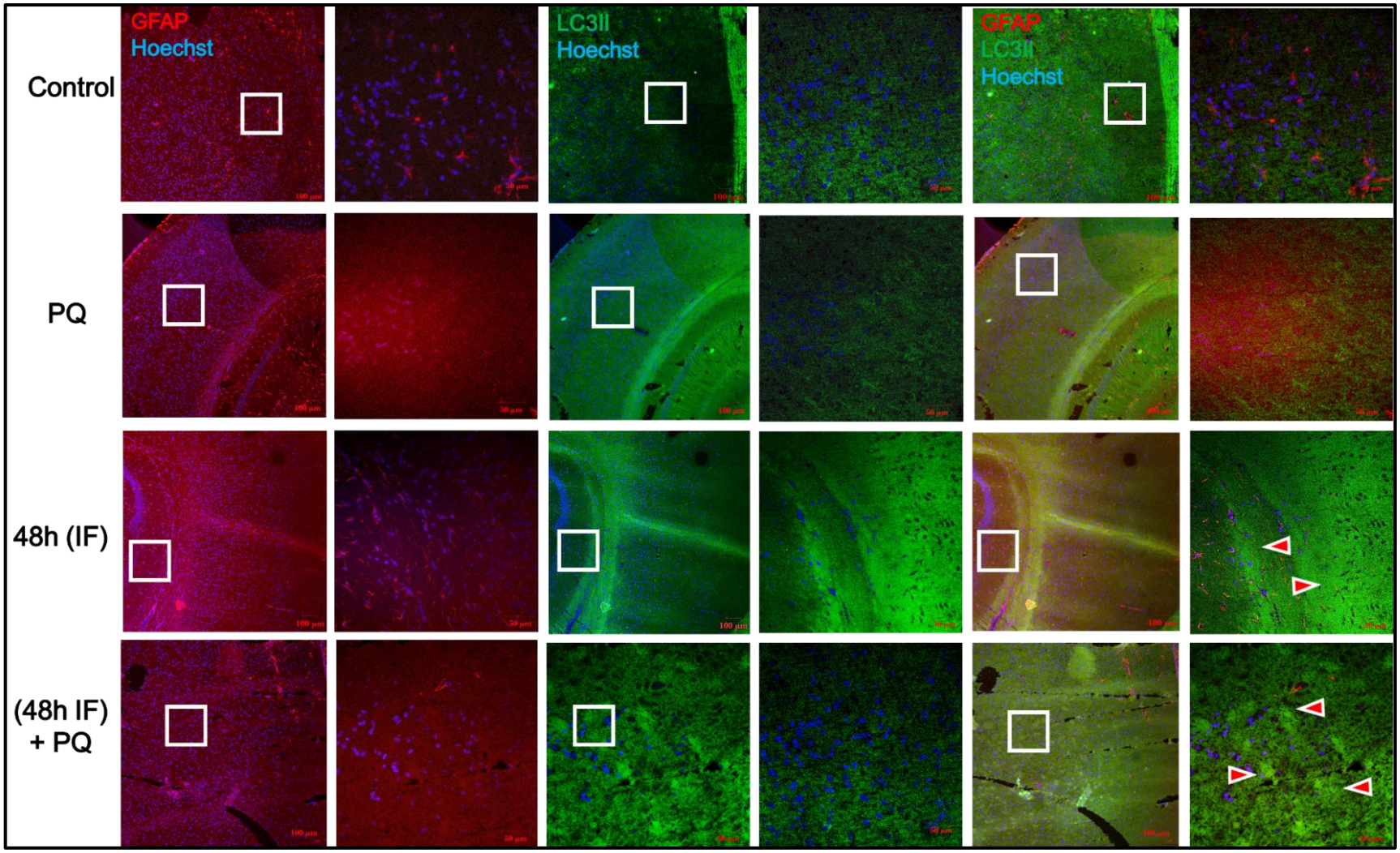

Figure 6.17: Immunofluorescence micrographs indicating LC3II (green) and GFAP (red) signal in the cortex. Representative micrographs indicate the control, paraquat exposed (PQ) group, 48 hrs intermittent fasting (IF) group, and [(48 hrs IF) + PQ)] group. Nuclei counterstained with Hoechst 33342 (**blue**), scale bars = 100 µm, higher magnification micrographs = 50 µm. Arrowheads indicate regions of strong LC3II protein signal.

6.2.5.6. Effect of the 21-day treatment intervention on MA cargo degradation in the cortex

Figure 6.18.A indicates that p62 protein expression is significantly decreased in the 48 hrs IF group [0.31 ± 0.03 ($p<0.05$)], and [(48 hrs IF) + PQ] group [0.24 ± 0.05 ($p<0.05$)] compared to the control [0.79 ± 0.03] and the PQ exposed group [0.89 ± 0.06] (**Fig. 6.18.B**), suggesting increased MA degradative activity in this region in response to the IF regime.

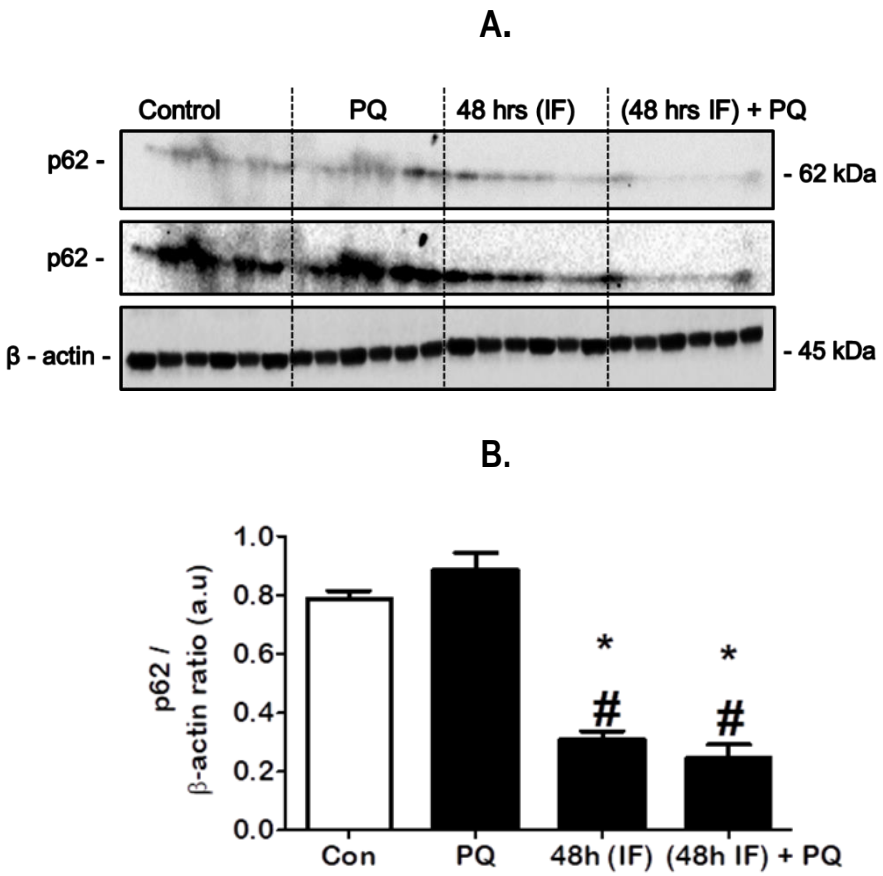

Figure 6.18: Effect of the 21-day treatment intervention on MA cargo protein degradation in the cortex. Representative western blot (low and high exposure) and densitometric analysis for **(A, B)** p62 protein expression is shown. Data expressed as mean ± SEM, statistical analysis: ANOVA and Bonferroni correction, *$p<0.05$ vs. control, #$p<0.05$ vs. PQ, n = 6, arbitrary units (a.u).

6.2.5.7. Representative p62 fluorescence micrographs of the cortex

As shown in **Fig. 6.19**, immunofluorescence analysis indicates that p62 protein signal (**magenta**) is diminished in the 48h IF group, and the [(48 hrs IF) + PQ] group compared to the PQ exposed group, where p62 signal is revealed more intensely.

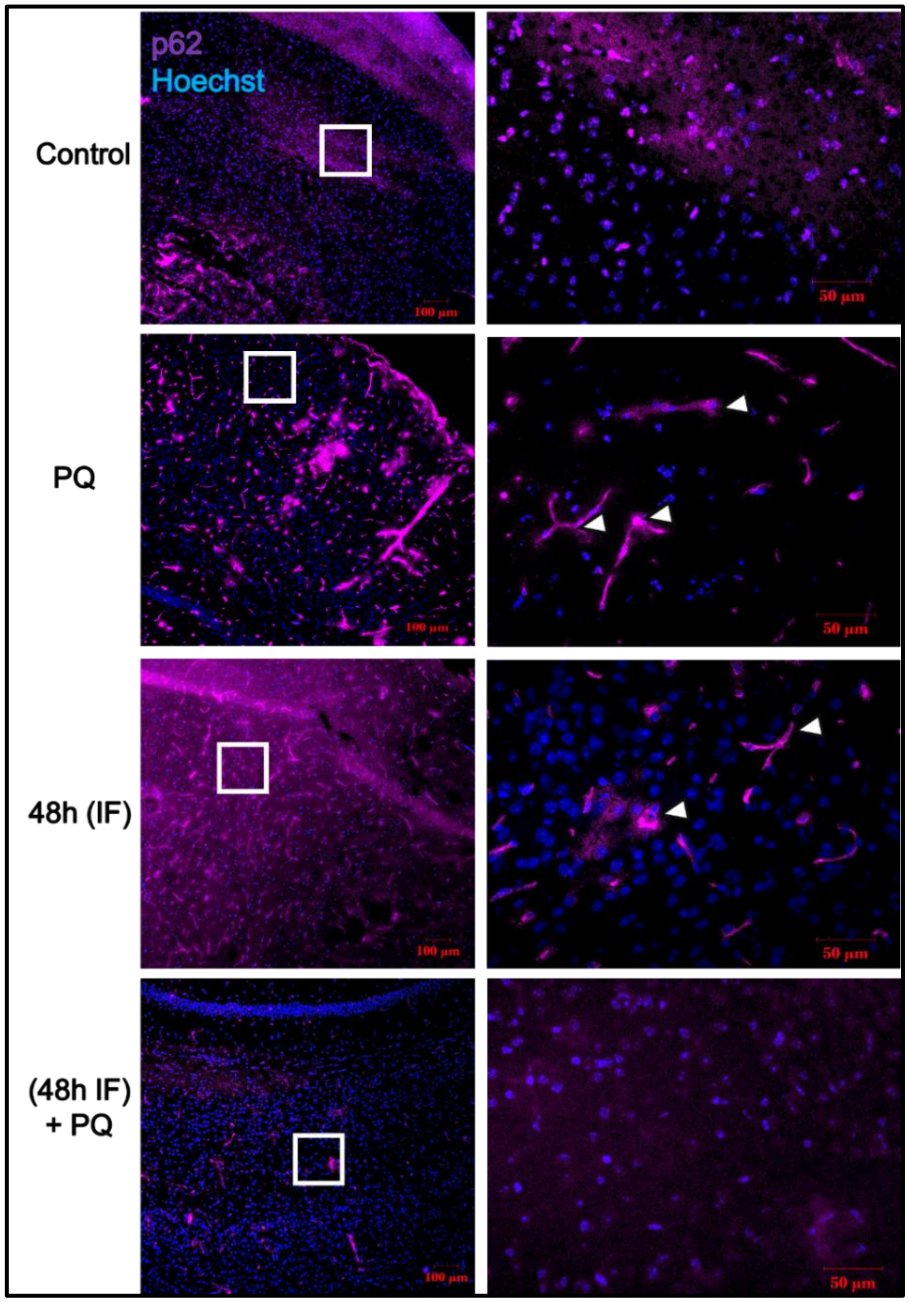

Figure 6.19: **Immunofluorescence micrographs indicating p62 signal (magenta) in the cortex.** Representative micrographs indicate the control, paraquat exposed (PQ) group, 48 hrs intermittent fasting (IF) group, and [(48 hrs IF) + PQ)] group. Nuclei counterstained with Hoechst 33342 (**blue**), scale bars = 100 µm, higher magnification micrographs = 50 µm. Arrowheads indicate regions of strong p62 protein signal.

6.2.5.8. Effect of the 21-day treatment intervention on the expression of CMA exclusive protein in the cortex

As shown in **Fig. 6.20.A,** LAMP2A protein expression is significantly increased in the 48 hrs IF group [1.57 ± 0.04 ($p<0.05$)], and [(48 hrs IF) + PQ] group [1.7 ± 0.04 ($p<0.05$)] compared to the control [1.05 ± 0.0] and the PQ exposed group [1.17 ± 0.07] (**Fig. 6.20.B**).

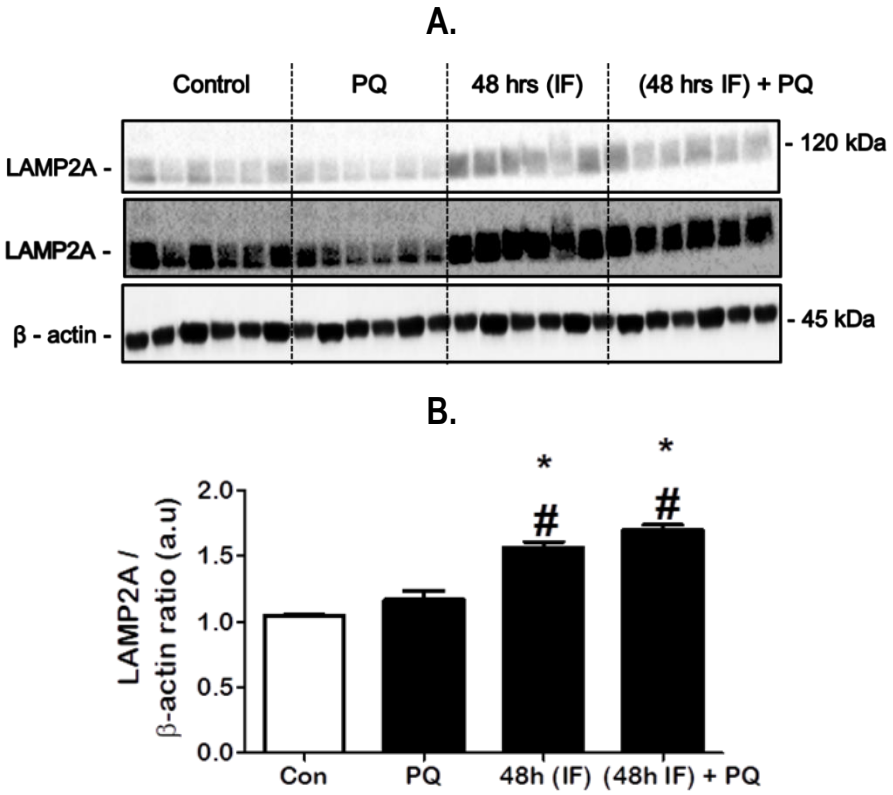

Figure 6.20: Effect of the 21-day treatment intervention on CMA activity in the cortex. Representative western blot (low and high exposure) and densitometric analysis for **(A, B)** LAMP2A protein expression is shown. Data expressed as mean ± SEM, statistical analysis: ANOVA and Bonferroni correction, *$p<0.05$ vs. control, #$p<0.05$ vs. PQ, n = 6, arbitrary units (a.u).

6.2.5.9. Effect of the 21-day treatment intervention on APP expression in the cortex

Figure 6.21.A indicates that APP protein expression is significantly increased in the PQ exposed group [0.88 ± 0.09 ($p<0.05$)] compared to control [0.51 ± 0.04]. Notably, APP expression is significantly decreased in the 48 hrs IF group [0.46 ± 0.03 ($p<0.05$)], and [(48 hrs IF) + PQ] group [0.43 ± 0.04 ($p<0.05$)] compared to the PQ exposed group (**Fig. 6.21.B**), suggesting that the IF regime may impact amyloidogenic processing.

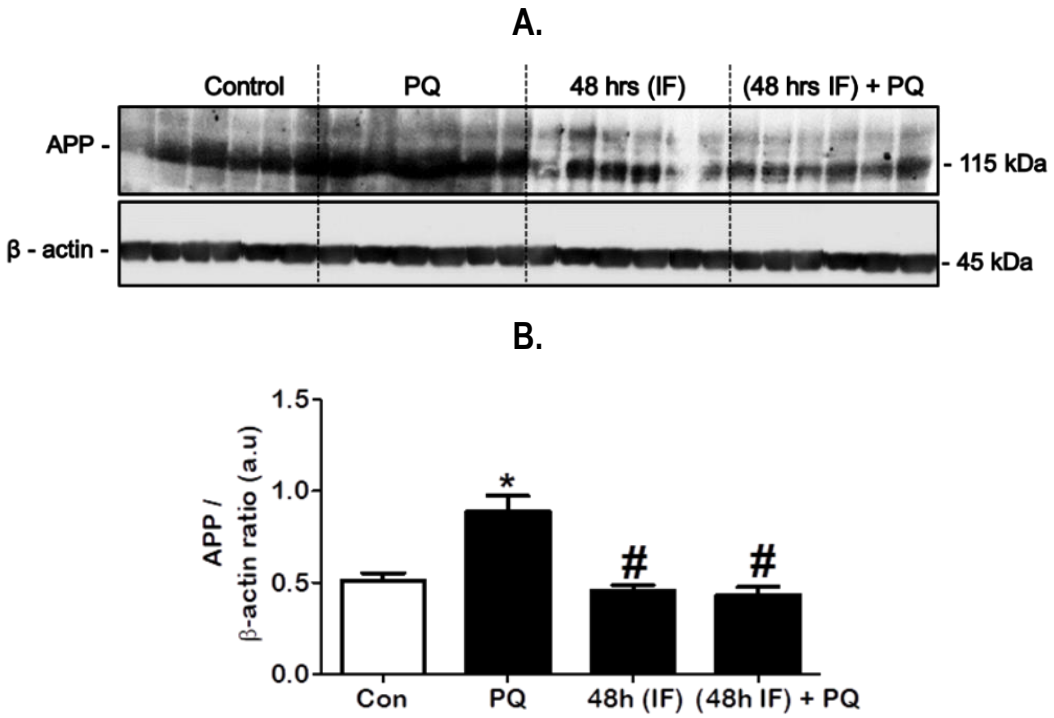

Figure 6.21: Effect of the 21-day treatment intervention on APP expression in the cortex. Representative western blot and densitometric analysis for **(A, B)** APP protein expression is shown. Data expressed as mean ± SEM, statistical analysis: ANOVA and Bonferroni correction, *$p<0.05$ vs. control, #$p<0.05$ vs. PQ, n = 6, arbitrary units (a.u).

6.2.6. Assessment of the cerebellum region

As shown in **Fig. 6.22**, H & E staining of the cerebellum reveals no structural architectural abnormalities in the density or nuclei distribution for all the groups in response to the 21-day treatment intervention.

6.2.6.1. Representative H & E staining of the cerebellum

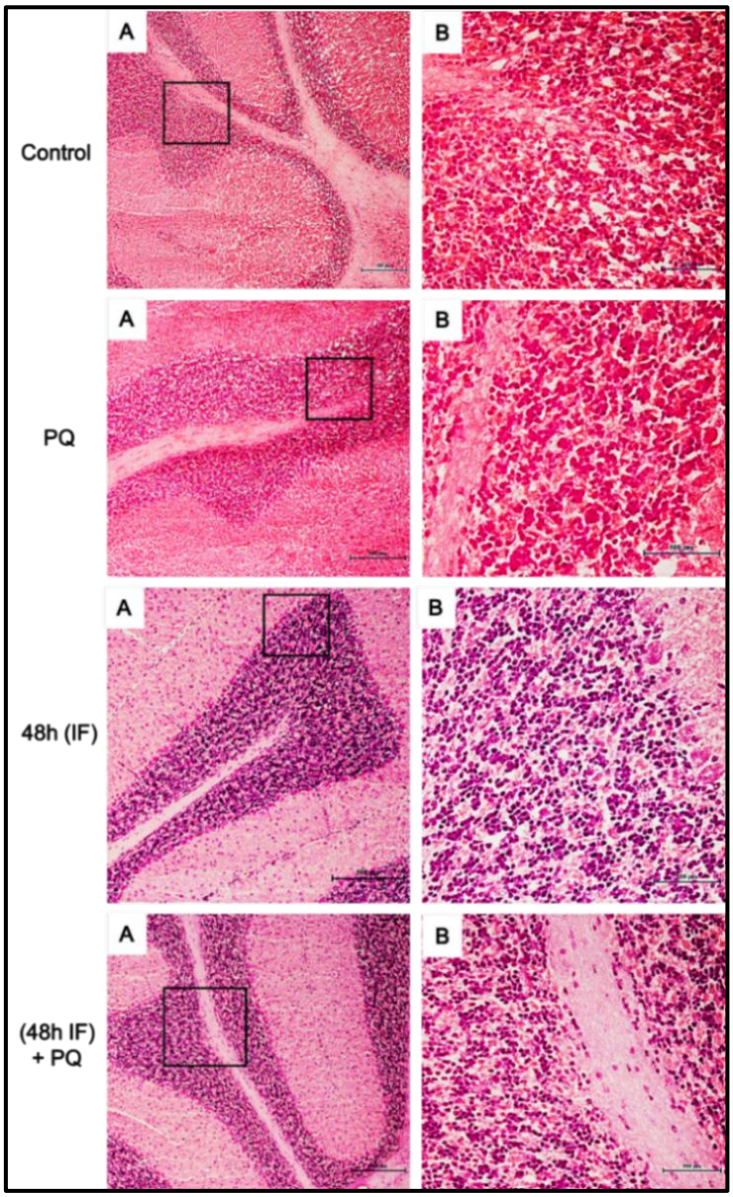

Figure 6.22: Representative H & E micrographs of the cerebellum in response to a 21-day treatment intervention. Representative micrographs indicate the control, paraquat exposed (PQ) group, 48 hrs intermittent fasting (IF) group, and [(48 hrs IF) + PQ] group. Scale bars indicate 500 µm. Images (**A**) = ×4 magnification, images (**B**) = ×10 magnification.

6.2.6.2. Effect of the 21-day treatment intervention on lipid peroxidation and apoptosis in the cerebellum

As shown in **Fig. 6.23.A**, no significant difference in 4HNE protein expression is indicated in the 48 hrs IF group [0.92 ± 0.0], [(48 hrs IF) + PQ] group [0.91 ± 0.02], and the PQ exposed group [0.95 ± 0.03] compared to the control [0.84 ± 0.0] (**Fig. 6.23.B**).

However, as shown in **Fig. 6.23.C,** cytochrome c protein expression is significantly increased in the PQ exposed group [1.1 ± 0.03 ($p<0.05$)] compared to the control [0.76 ± 0.05], more importantly, cytochrome c expression is significantly decreased in the 48 hrs IF group [0.69 ± 0.03 ($p<0.05$)], and [(48 hrs IF) + PQ] group [0.57 ± 0.07 ($p<0.05$)] compared to the PQ exposed group [1.1 ± 0.03]. No significant difference is indicated in the 48 hrs IF group, and [(48 hrs IF) + PQ] group compared to the control (**Fig. 6.23.D**).

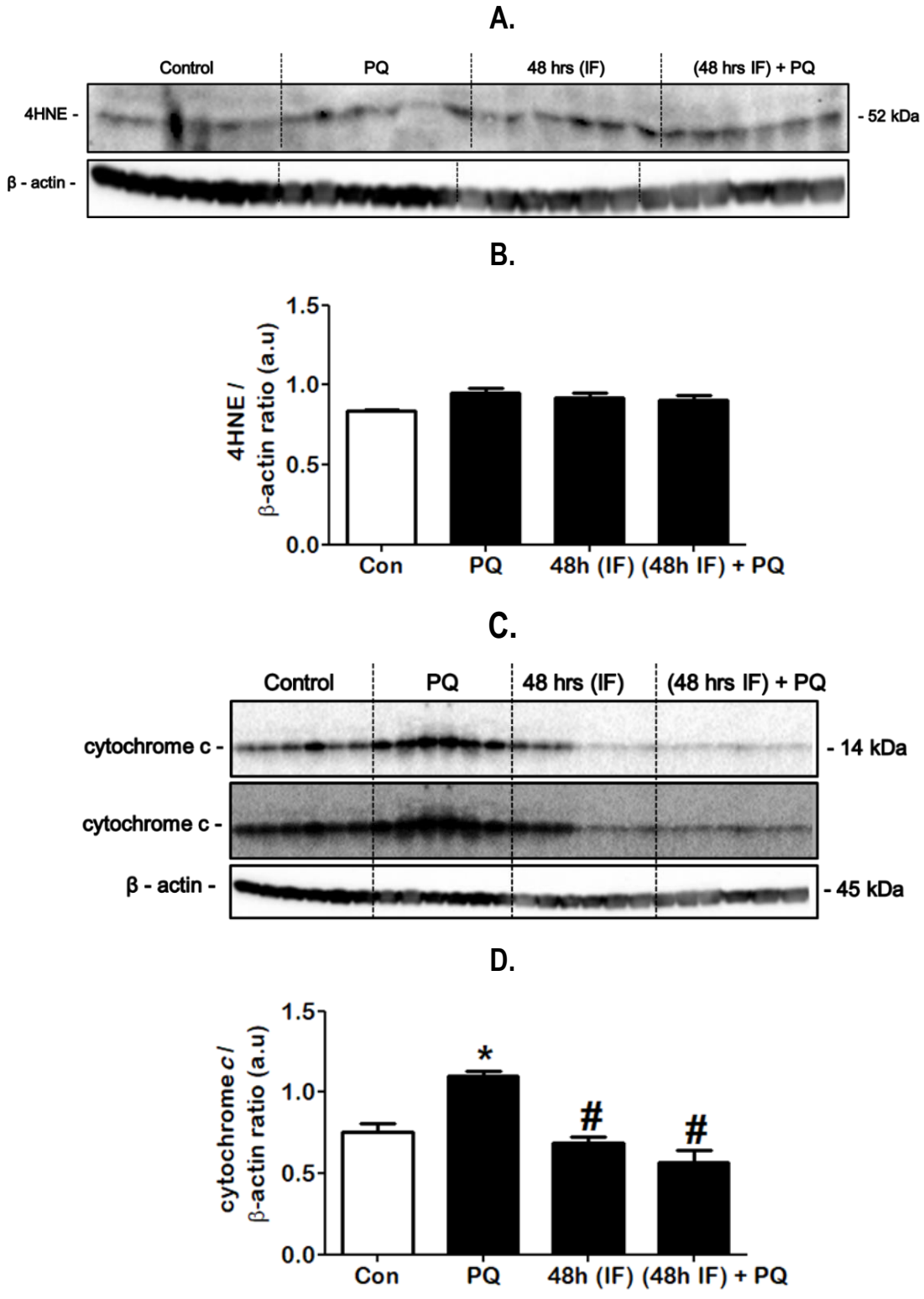

Figure 6.23: Effect of the 21-day treatment intervention on lipid peroxidation and apoptosis in the cerebellum. Representative western blot and densitometric analysis for **(A, B)** 4HNE, and **(C, D)** cytochrome c (low and high exposure) protein expression is shown. Data expressed as mean ± SEM, statistical analysis: ANOVA and Bonferroni correction, *p<0.05 vs. control, #p<0.05 vs. PQ, n = 6, arbitrary units (a.u).

6.2.6.3. Representative HNE and cytochrome c fluorescence micrographs of the cerebellum

As shown in **Fig. 6.24,** no major differences in 4HNE (**red, left panel**), and cytochrome c (**red, right panel**) protein signal is observed in all the groups. However, 4HNE protein signal is comparatively diminished in the control compared to the treatment groups.

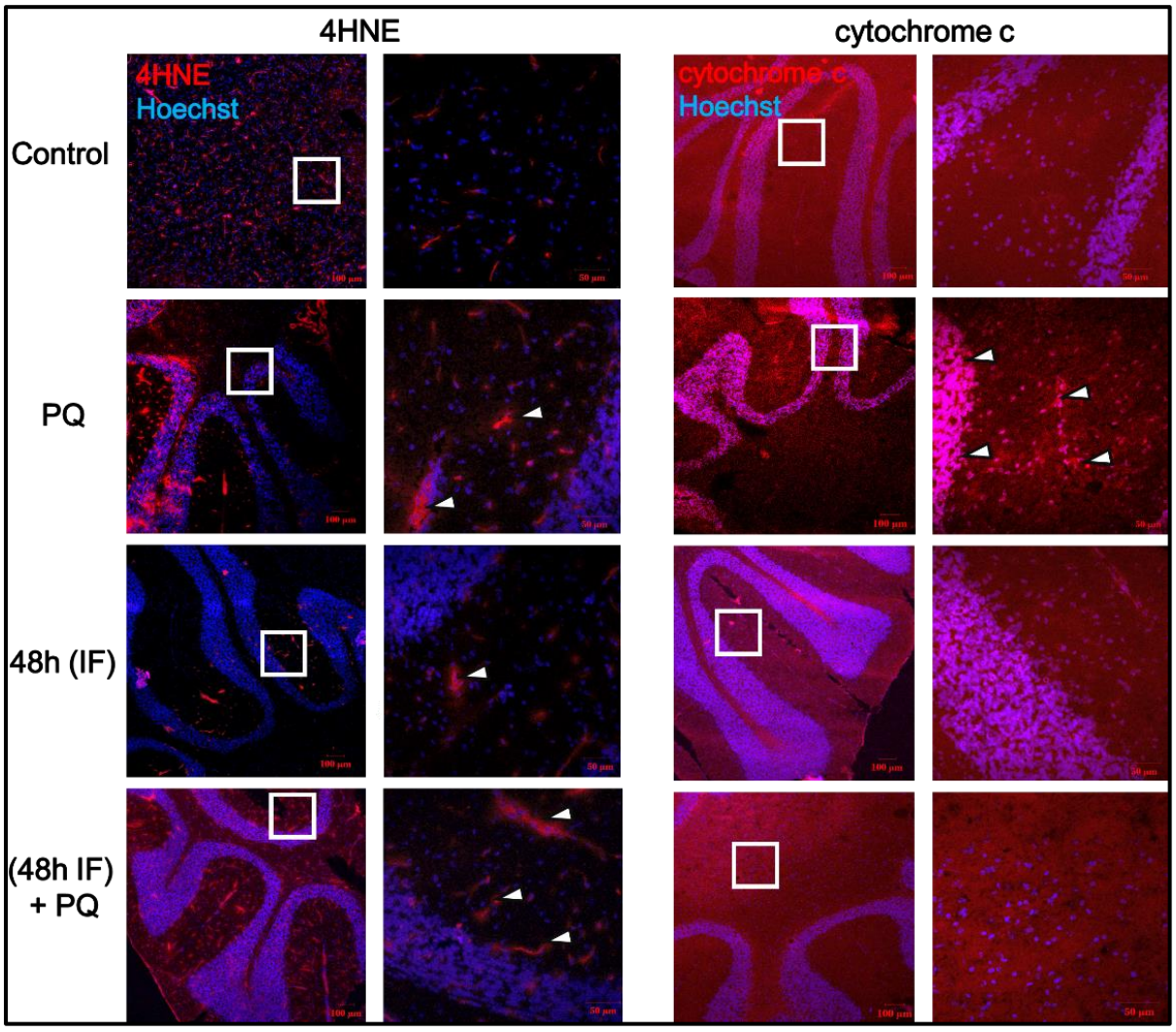

Figure 6.24: Immunofluorescence micrographs indicating 4HNE and cytochrome c signal in the cerebellum. Left panel indicates 4HNE (**red**). **Right panel** indicates cytochrome c (**red**). The treatment intervention is defined as the control, paraquat exposed (PQ) group, 48 hrs intermittent fasting (IF) group, and [(48 hrs IF) + PQ)] group. Nuclei counterstained with Hoechst 33342 (**blue**), scale bar**s** = 100 µm, higher magnification micrographs = 50 µm. Arrowheads indicate regions of strong 4HNE, or cytochrome c protein signal.

6.2.6.4. Effect of the 21-day treatment intervention on MA activity in the cerebellum

LC3II expression is significantly increased in the PQ exposed group [1.35 ± 0.06 ($p<0.05$)], 48 hrs IF group [1.32 ± 0.05 ($p<0.05$)], and [(48 hrs IF) + PQ] group [1.43 ± 0.06 ($p<0.05$)] compared to the control [1.07 ± 0.0] (**Fig. 6.25.A**), suggesting that MA activity is upregulated in the cerebellum region (**Fig. 6.25.B**).

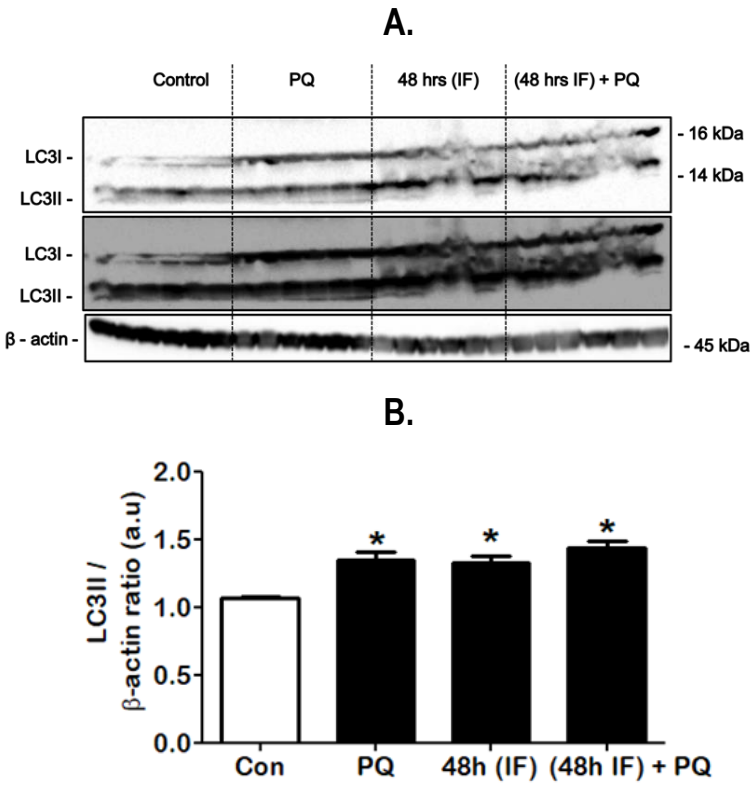

Figure 6.25: Effect of the 21-day treatment intervention on MA activity in the cerebellum. Representative western blot (low and high exposure) and densitometric analysis for **(A, B)** LC3II protein expression is shown. Data expressed as mean ± SEM, statistical analysis: ANOVA and Bonferroni correction, *$p<0.05$ vs. control, n = 6, arbitrary units (a.u).

6.2.6.5. Representative GFAP and LC3II fluorescence micrographs of the cerebellum

Figure 6.26 reveals uniform GFAP (**red**) protein signal in all the treatment groups, with strong signal in the PQ exposed group. Stronger LC3II (**green**) protein signal is indicated in the PQ exposed group, 48h IF group, and [(48 hrs IF) + PQ] group compared to the control, in accordance with increased MA activity in this region.

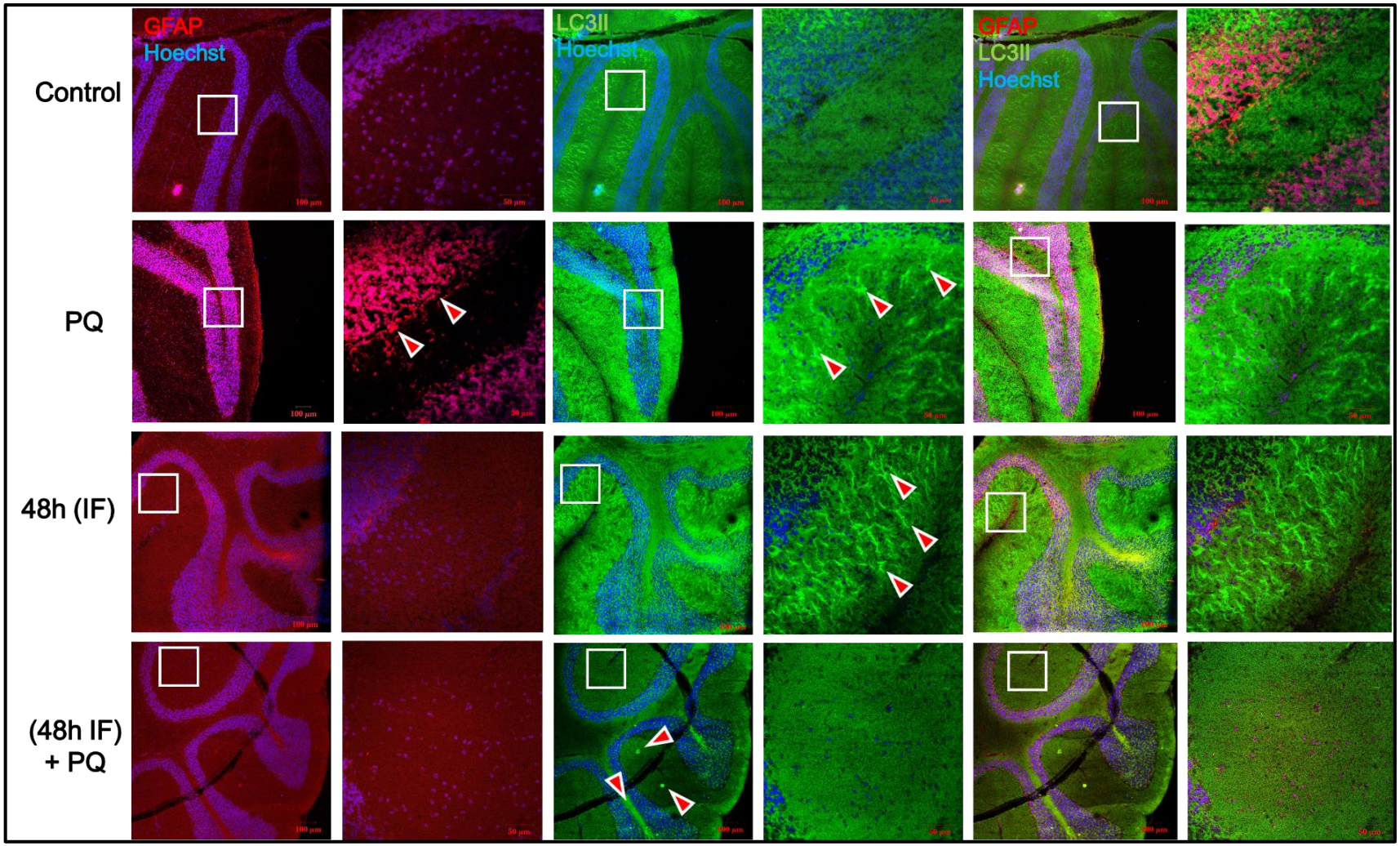

Figure 6.26: Immunofluorescence micrographs indicating LC3II (green) and GFAP (red) expression in the cerebellum. Representative micrographs indicate the control, paraquat exposed (PQ) group, 48 hrs intermittent fasting (IF) group, and [(48 hrs IF) + PQ)] group. Nuclei counterstained with Hoechst 33342 (**blue**), scale bars = 100 µm, higher magnification micrographs = 50 µm. Arrowheads indicate regions of strong GFAP or LC3II protein signal.

6.2.6.6. Effect of the 21-day treatment intervention on MA cargo degradation in the cerebellum

Figure 6.27.A reveals a significant increase in p62 protein expression in the 48 hrs IF group [0.74 ± 0.05 ($p<0.05$)], compared to the [(48 hrs IF) + PQ] group [0.19 ± 0.04]. Importantly, p62 expression is significantly decreased in the 48 hrs IF group, and [(48 hrs IF) + PQ] group compared to the control [1.29 ± 0.01] and the PQ exposed group [1.41 ± 0.07] (**Fig. 6.27.B**), suggesting that the IF regime impacts MA cargo protein degradation.

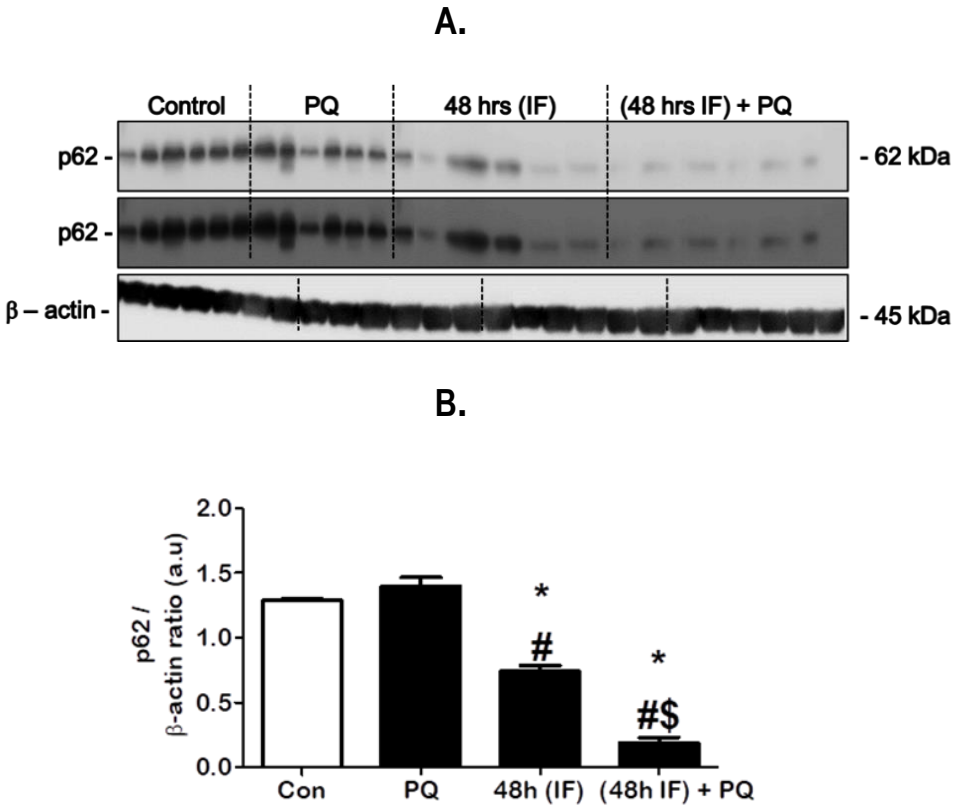

Figure 6.27: Effect of the 21-day treatment intervention on MA cargo protein degradation in the cerebellum. Representative western blot (low and high exposure) and densitometric analysis for **(A, B)** p62 protein expression is shown. Data expressed as mean ± SEM, statistical analysis: ANOVA and Bonferroni correction, *$p<0.05$ vs. control, #$p<0.05$ vs. PQ, \$$p<0.05$ vs. 48h IF, n = 6, arbitrary units (a.u).

6.2.6.7. Representative p62 fluorescence micrographs of the cerebellum

As shown in **Fig. 6.28**, p62 protein signal (**magenta**) appears diminished in the 48h IF group and the [(48 hrs IF) + PQ] group compared to the control, with increased p62 signal in the PQ exposed group compared to the 48h IF group, and the [(48 hrs IF) + PQ] group.

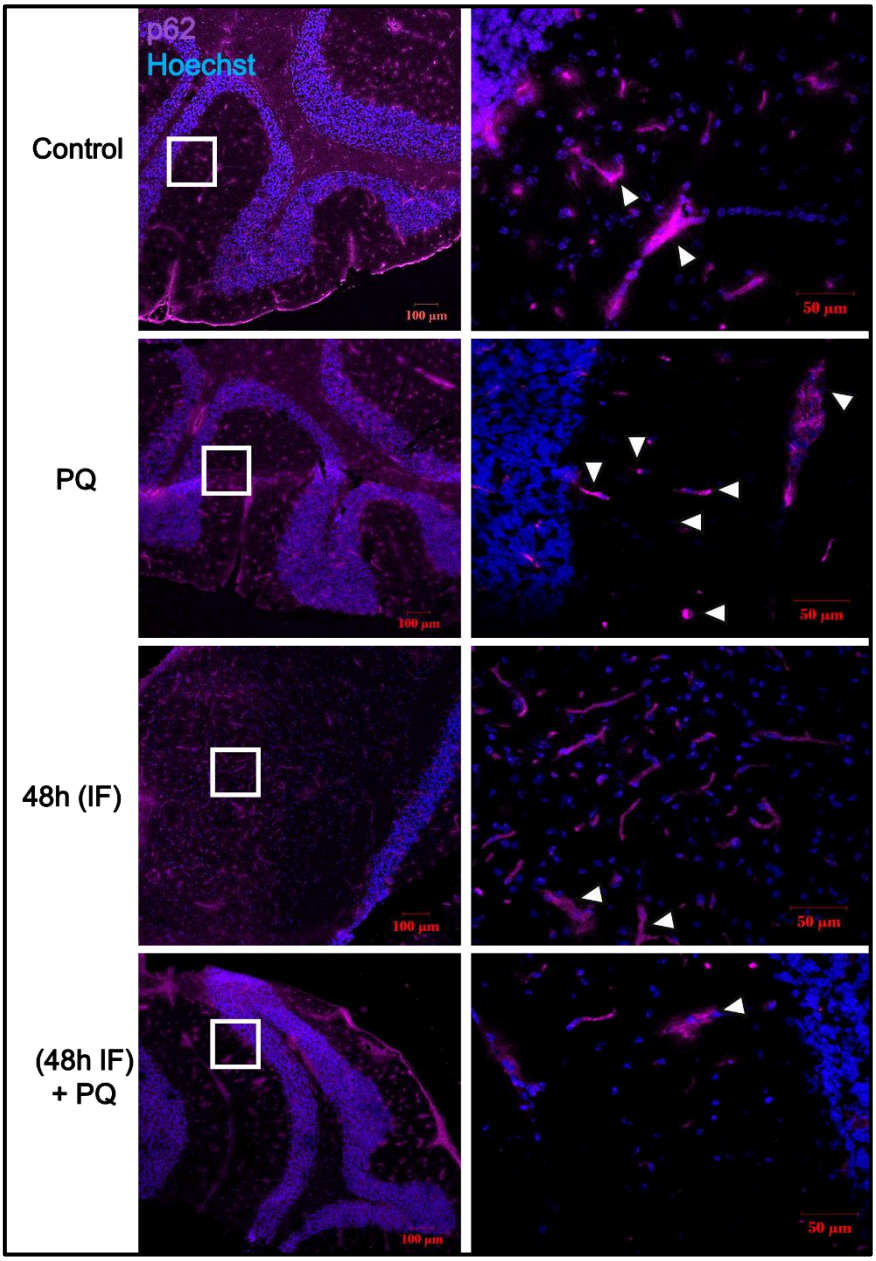

Figure 6.28: Immunofluorescence micrographs indicating p62 expression (magenta) in the cerebellum. Representative micrographs indicate the control, paraquat exposed (PQ) group, 48 hrs intermittent fasting (IF) group, and [(48 hrs IF) + PQ)] group. Nuclei counterstained with Hoechst 33342 (**blue**), scale bars = 100 µm, higher magnification micrographs = 50 µm. Arrowheads indicate regions of strong p62 protein signal.

6.2.6.8. Effect of the 21-day treatment intervention on CMA exclusive protein in the cerebellum

As indicated in **Fig. 6.29.A,** LAMP2A expression is significantly increased in the PQ exposed group [0.29 ± 0.04 ($p<0.05$)], 48 hrs IF group [1.02 ± 0.03 ($p<0.05$)], and [(48 hrs IF) + PQ] group [1.22 ± 0.06 ($p<0.05$)] compared to the control [0.04 ± 0.0]. Moreover, LAMP2A expression significantly increased in the 48 hrs IF group, and [(48 hrs IF) + PQ] group compared to the PQ exposed group and each other (**Fig. 6.29.B**).

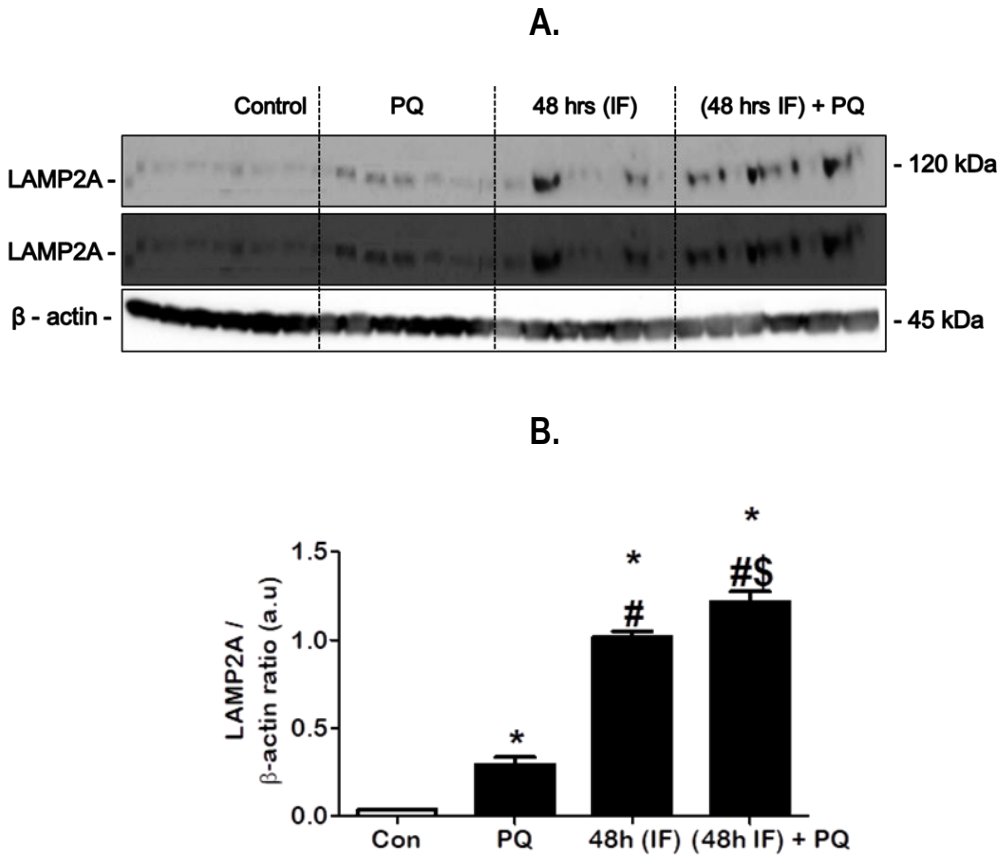

Figure 6.29: Effect of the 21-day treatment intervention on CMA activity in the cerebellum. Representative western blot (low and high exposure) and densitometric analysis for **(A, B)** LAMP2A protein expression is shown. Data expressed as mean ± SEM, statistical analysis: ANOVA and Bonferroni correction, *$p<0.05$ vs. control, #$p<0.05$ vs. PQ, \$$p<0.05$ vs. (48h IF) + PQ, n = 6, arbitrary units (a.u).

6.2.6.9. Effect of the 21-day treatment intervention on APP expression in the cerebellum

No significant difference in APP protein expression is indicated in all the treatment groups (**Fig. 6.30.B**).

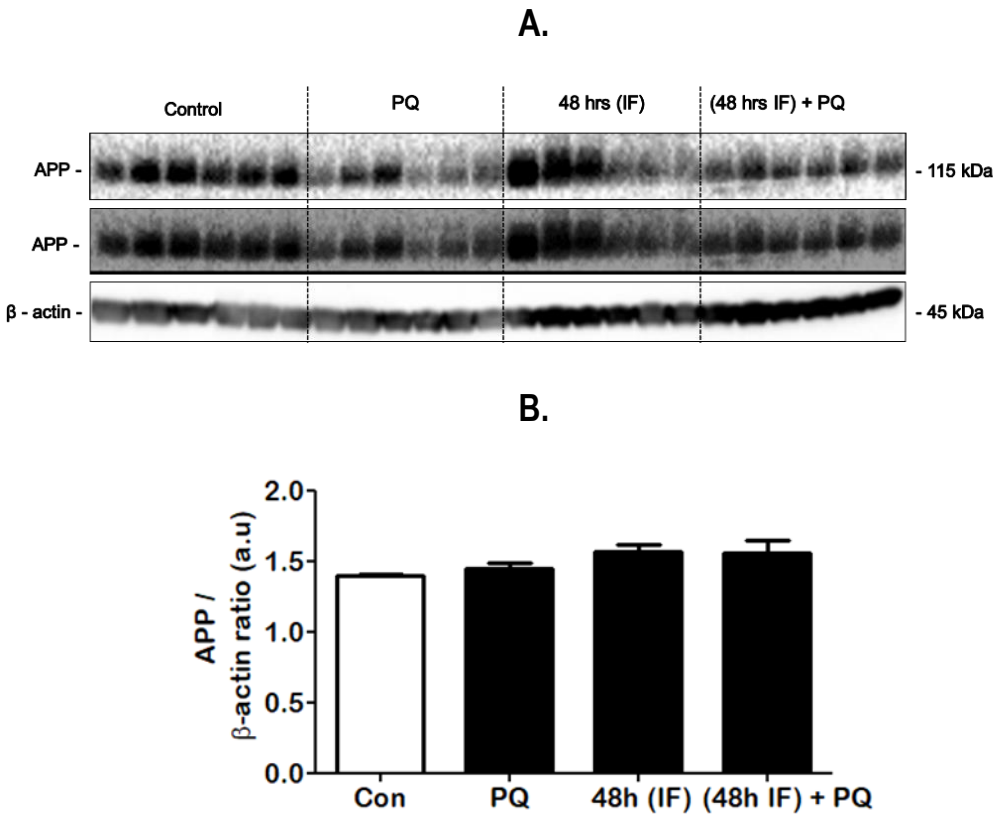

Figure 6.30: Effect of the 21-day treatment intervention on APP expression in the cerebellum. Representative western blot (low and high exposure) and densitometric analysis for **(A, B)** APP protein expression is shown. Data expressed as mean ± SEM, statistical analysis: ANOVA and Bonferroni correction, n = 6, arbitrary units (a.u).

CHAPTER 6 DISCUSSION: *IN VIVO* ASSESSMENT OF THE ROLE OF MA AND CMA IN A PARAQUAT-INDUCED BRAIN INJURY MODEL

To date, CR is the only intervention that has consistently been found to enhance physiological function with advancing age, and delay the onset of age-associated diseases, such as neurodegeneration, cancer and diabetes mellitus type 2, across multiple species including nonhuman primates (Balasubramanian et al., 2017; Colman et al., 2014). The beneficial physiological effects of CR are thought to be mediated through its modulation of the cellular nutrient-sensing pathways, including mTOR signalling, the insulin-like growth factor 1 (IGF-1) signalling, and Sirtuin 1 (SIRT1) (Fontana et al., 2010; Ravussin et al., 2015). Importantly, long term CR is known to counteract physiological effects of aging, and recent research has provided compelling evidence that CR slows down brain aging and protects from age-related neurodegenerative diseases (Balasubramanian et al., 2017; Colman et al., 2014). Indeed, CR has been shown to significantly delay the onset of neurodegeneration, by preventing synaptic loss and preserving cognitive capacities, as observed in a mouse model of neurodegeneration (Gräff et al., 2013). The oxidative stress hypothesis of aging ascribes increased oxidative stress as the major causal factor of cell death, given that the amount of oxidative damage increases as an organism ages (Harman, 1956; Stadtman, 1992, 2001). Moreover, experimental evidence suggests that overexpression of antioxidative enzymes may retard the age-related accumulation of oxidative damage and extend life-span in disease models of aging (Sun et al., 2002), and as shown by Stankovic et al. (2013), differences in life-span among different species may inversely correlate with the rate of mitochondrial generation of the superoxide anion radical and hydrogen peroxide. However, the potential contribution of nutrient signalling pathways, i.e. primarily MA and CMA, in mediating the beneficial physiological effects of CR on brain health remains unclear. In the previous chapters we assessed in great detail the relationship between MA and CMA in the context of APP induced neuronal toxicity. To what extent these two pathways play a role in an *in vivo* environment is largely unclear. Hence, here we investigated the potential role of these pathways in neuroprotection.

We therefore investigated the effects of IF, defined as 48 hrs followed by 24 hrs refeeding (Collier, 2013) in GFP–LC3 expressing transgenic mice subjected to a robust neuronal injury associated with neurodegeneration (Niveditha et al., 2017), induced by paraquat exposure. GFP-LC3 mice were uniquely chosen for our experimental purposes, which included the assessment of MA using immunofluorescence microscopy as previously described (Mizushima, 2004). Brain injury was simulated in these mice using a well-established paraquat PQ protocol, previously shown to result in neurodegeneration (Chen et al., 2012). PQ is used as a quaternary ammonium herbicide; one of the most widely used herbicides, which is quick-acting, non-selective, and has been shown to be toxic to various organisms (Bismuth et al., 1990). The oxidation of this agent by oxygen has been shown to generate superoxide radicals, which result from the transfer of a single electron from reduced PQ to oxygen (Litteljohn et al., 2011). Due to its structural similarity to N-methyl-4-phenyl pyridinium (MPP^+), PQ exposure has been shown to induce dopaminergic toxicity and selective nigrostriatal degeneration in the mouse brain (Litteljohn et al., 2011; McCormack et al., 2002). The PQ model of neurodegeneration was utilized in order to examine whether CR can protect against neuronal loss in the context of oxidative stress, and if so, whether MA and CMA pathways play a role in this context. Although paraquat preferentially affects the nigrostriatal system, HAS been shown to accumulate in the hippocampus and cortex regions (Prasad et al., 2009). Therefore, paraquat could potentially impair learning and memory and affect AD pathogenesis. The mechanism of PQ toxicity is defined as the induction oxidative stress and mitochondrial of oxidative damage (Drechsel and Patel, 2008). Here we determined the effects of PQ-induced oxidative stress in vulnerable neuronal populations of the hippocampus, cortex, and cerebellum brain regions using LC3II and p62 as markers for MA activity, LAMP2A as a marker for CMA activity, 4HNE as a marker for lipid peroxidation, cytochrome c as marker for mitochondrial injury and cell death onset, GFAP as a marker for inflammation, and APP expression as an indicator of amyloidogenic processing.

6.3. Physiological effects to the 21-day treatment intervention

After 21 days of the treatment intervention, there were no significant differences in body weight (**Fig. 6.1**). However, a significant reduction in body weight is observed only during the second day of the IF intervention, indicated as day 8, 11, 14, 17, and 20, in the 48 hrs IF, and [(48 hrs IF) + PQ) treatment groups compared to both the control and PQ exposed group. Notably, body weight in these treatment groups was comparable to the control and the PQ exposed group following the 24 hrs *ad libitum* refeeding, suggesting that *ad libitum* refeeding for this period was sufficient to counteract the loss of weight. The reduction in body weight was expected, and in line with our findings, others have shown that CR diets do not generally lead to lasting weight loss, instead resulting in muscle-mass reduction over time (Miller and Wolfe, 2008). In further support of these findings, *ad libitum* refeeding has been shown to restore body weight, and the level of most CR-induced biomarker changes to baseline levels following moderate CR in rodents (Greene et al., 2001; Keenan et al., 1999).

Our findings reveal that the average food intake of the 48 hrs IF, and [(48 hrs IF) + PQ] treatment groups was significantly higher than that of the control and PQ exposed group (**Fig. 6.2.A**). In line with our findings, Mahoney et al. (2006) have revealed that on the day of refeeding, CR mice typically 'binge ate', consuming approximately twice as much food as their unrestricted counterparts. Despite the increased food intake, the body weights of the 48 hrs IF, and [(48 hrs IF) + PQ) treatment groups was comparable to the control and PQ exposed group upon completion of the 21-day treatment intervention. Moreover, no differences in *ex vivo* brain weight were observed for all the groups (**Fig. 6.2.B**), suggesting that CR does not impact the brain structural integrity. In agreement, others have reported that CR also preserves structural brain integrity, synaptic plasticity and cognitive function in mouse models of neurodegeneration (Gräff et al., 2013; Guo et al., 2015).

Consistent with the life-prolonging effects of CR, our results indicate that the 21-day treatment intervention had no significant impact on survival for all the treatment groups (**Fig. 6.3**). Indeed, CR has been found to retard age-associated changes and extend maximum life-span by mitigation the effects of damage (Sohal and Weindruch, 1996).

6.4. Analysis of the hippocampal region

In order to assess the tissue for signs of injury, such as neuronal loss, inclusion body formation, apoptotic bodies or fibrotic lesions, Haematoxylin and Eosin (H & E) staining was performed. Our data reveals no major structural abnormalities or morphological indices for neuronal cell loss in the hippocampus region following the 21-day treatment intervention (**Fig. 6.4**). This observation suggests that neuronal injury is likely of a less severe nature in this context. Indeed, systemic exposure of PQ exposure has been shown to promote aggregate formation within neurons of the substantia nigra in in an *in vivo* model of PD (Manning-Bog et al., 2002). Immunohistochemistry staining of brain sections by (Chen et al., 2012) revealed pronounced inclusion body formation with associated Aβ plaque deposition following PQ exposure over a period of 3 weeks in APP transgenic mice, and these observations were further exacerbated following PQ exposure over a period of 5 months in the same mouse model (Chen et al., 2015a). These findings raise the possibility that PQ-induced oxidative stress was not sufficient to cause the expected neuronal loss reported in the above studies.

4HNE is one of the major end products of lipid peroxidation, the production of which is accelerated in response to increased oxidative stress, and it also serves as a source of further ROS generation, making 4HNE both an inducer and mediator of oxidative stress (Zhong and Yin, 2015). Under physiological conditions the cellular concentration of 4HNE ranges from 0.1-0.3 µM and considered to play an important role in stimulating the expression of antioxidative enzymes during the induction of oxidative stress adaptive responses (Ceaser et al., 2004; Chen et al., 2005). However,

under conditions of excessive oxidative stress, 4HNE has been found to accumulate up to concentrations of 10 µM to 5 mM in various pathological states including AD, PD, inflammation, atherosclerosis, and cancer (Ji et al., 2016; Uchida, 2003). In these pathological states, lipid peroxidation has been shown to mediate changes in the permeability and fluidity of the membrane lipid bilayer and can drastically alter the cell integrity, ultimately eliciting a decrease in cell proliferation and the induction of apoptosis (McCracken et al., 2000; Siegel et al., 2007). Enhanced 4HNE expression would hence indicate ROS damage. Hence, next, 4HNE levels were assessed. Our western blot data reveals a significant increase in 4HNE expression in the PQ exposed group compared to the control, 48 hrs IF, and [(48 hrs IF) + PQ] groups (**Fig. 6.5.B**). Moreover, a significant decrease in 4HNE expression is indicated in the 48 hrs IF, and [(48 hrs IF) + PQ] treatment groups compared to the control. In addition, we also observe that 4HNE is significantly decreased in CR compared to control. In line with our findings, SDS-PAGE data by Sharma et al. (2012) revealed a significant increase in 4HNE levels following nitric oxide exposure in 9-month-old rates subjected to CR (food intake adjusted weekly to 60 to 65% of *ad libitum* intake). In a study by Dobashi et al. (2018), simultaneously exercise training conducted simultaneously with CR was found to improve the redox status, and completely suppress the exercise-induced elevation in both hippocampal 4HNE and brain-derived neurotrophic factor (BDNF) levels. BDNF is pivotal neurotrophic factor which plays crucial roles in neuronal survival, brain development, and has been shown to contribute substantially to the prevention of AD and depression through maintaining cognitive function (Alomari et al., 2016; Yamada et al., 2002). In support of our data, these studies reveal that CR regimes mitigates lipid peroxidation through the activation of neuroprotective mechanisms to detoxify/remove 4HNE and thereby prevent its potentially damaging actions.

Cytochrome c plays a crucial role in apoptosis execution, at least in part, by complexing with other pro-apoptotic factors in the cytosol to induce apoptosis (Kagan et al., 2006, 2009). Indeed, cells lacking cytochrome c have been shown to have reduced caspase-3 activation and are resistant to the proapoptotic effects of UV

irradiation, nutrient starvation (Li et al., 2000). These studies confirm the role of cytochrome c in apoptotic signalling cascades, and hence underpin the severity of oxidative insult. Similar to our observations for 4HNE expression, our western blot data reveals a similar pattern in cytochrome c expression, which is significantly increased in the PQ exposed group compared to the control, 48 hrs IF, and [(48 hrs IF) + PQ] treatment groups, with a significant reduction also indicated in the [(48 hrs IF) + PQ] treatment group compared to the control (**Fig. 6.5.D**). These results indicate that the IF regime ameliorated the effects of increased oxidative stress, as evidenced by reduced cytochrome c expression in the IF treatment groups, in favour of protection.

In line with our findings, others have shown that resveratrol, a CRM, translates to protection by, at least in part, preventing cytochrome c release in the hippocampal CA1 neurons following global cerebral ischaemia (Endo et al., 2006; Matapurkar and Lazebnik, 2006; Sanderson et al., 2008). Similar findings in the hippocampal region have been replicated by others in different *in vivo* models of oxidative stress damage (Liang et al., 2000; Zheng et al., 2011). Excessive ROS production has been shown to induce cytochrome c release from the mitochondrial membrane into the cytosol where it binds with apoptotic protease-activating factor 1, promoting the formation of the apoptosome (a large quaternary protein structure formed in the process of apoptosis), and in turn stimulating the recruitment and activation of caspases for the initiation of apoptosis (Sun et al., 2010; Wang, 2001). Therefore, the modulation of ROS levels, particularly in the brain, may represent a promising treatment strategy in neurodegeneration. In line with our western blot data, our immunofluorescence analysis mirrors the increased localization and expression of 4HNE and cytochrome c protein in the hippocampus of the PQ exposed group compared to the control, 48 hrs IF, and [(48 hrs IF) + PQ] treatment groups, with selective hotspots revealed within the hippocampus (**Fig. 6.6**). Given that 4HNE is also significantly decreased in the IF only group, this observation could also indicate the overall benefit of IF on ROS handling. The immunofluorescence images also support the notion that the hippocampus is a particularly sensitive region of susceptibility, as surrounding tissue is less positive for 4HNE positive (Lumkwana et al., 2017).

Accumulating evidence suggests that CR plays a major role in longevity, and that the neuroprotective effects of this dietary regime can largely be attributed to increased MA activity above basal levels (Bergamini et al., 2007; Knuppertz et al., 2014). Hence, in order to assess the role of MA in the context of PQ-induced neuronal toxicity, LC3II protein levels were assessed. Our western blot analysis reveals a significant increase in LC3II levels in the [(48 hrs IF) + PQ] treatment group compared to the PQ exposed group, the 48 hrs IF treatment group, and control, with LC3II levels also significantly increased in the 48 hrs IF treatment group compared to the control (**Fig. 6.7.B**). This data suggests that MA activity in the hippocampus region is indeed increased above basal levels in response to IF in this model system, and further enhanced in combination with PQ-induced injury, while PQ exposure alone does not appear sufficient to robustly induce MA. Our data is supported previous findings that show that CR induces AMPK activation, this molecular energy sensor in turn induced MA activity above basal levels to provide essential amino acids under conditions of nutrient deprivation (Hursting et al., 2010, 2013). Others have also shown that established tumours utilize the MA pathways to reduce oxidative stress and preserve mitochondrial bioenergetics in order to overcome /adapt to stressors, such as nutrient deprivation (Guo and White, 2016; White et al., 2015). Our results shed light onto the mechanism of CR-induced neuroprotection in this model system. These data are supported by the immunofluorescence analysis which reveals distinct hotspots of LC3II localization strongly indicated in the hippocampus of the 48 hrs IF, and [(48 hrs IF) + PQ] treatment groups compared to the PQ exposed group and the control (**Fig. 6.7**). Additionally, GFAP localization is indicated in the PQ exposed group compared to the control, 48 hrs IF, and [(48 hrs IF) + PQ] treatment group, suggesting that increased oxidative stress elicits a strong inflammatory response in the PQ exposed group. More importantly, this inflammatory response is attenuated in the [(48 hrs IF) + PQ] treatment group, suggesting that the IF regime is protective in this context. These observations are supported by studies that have reported increased levels of GFAP in the CSF (Ishiki et al., 2016) and frontal cortices, and hippocampal tissues of AD patients (Kamphuis et al., 2014). Current literature suggests that inflammation, MA

and neurodegeneration are connected processes. Indeed, recent work by François et al. (2013, 2014) revealed evidence of a cross-talk between these processes. In these studies, increased $A\beta_{42}$ expression was found to enhance oxidative stress, modulate the expression of selective MA proteins (p62, p70S6K) (François et al., 2013), with the levels of inflammatory mediators correlating with expression of key MA regulators, such as mTOR and BECN1 (François et al., 2014). Furthermore, findings from preclinical studies suggests that CR reduces inflammation (Harvey et al., 2014; Harvie and Howell, 2012). Notably, IF dietary regimes (from 24 hrs to 6 days) have been found to promote similar metabolic and anti-inflammatory changes as observed with chronic CR regimes (Lee and Longo, 2011). Consistent with our immunofluorescence observations, these studies suggest that increased oxidative stress, may induce inflammation, while MA induction above basal levels mitigates this stress response. Thus, IF/CR-mediated induction of MA may play a protective role in the context of increased oxidative stress.

Consistent with enhanced MA activity in these groups (**Fig. 6.7.B**), our western blot data reveals a significant reduction in p62 levels in the 48 hrs IF, and [(48 hrs IF) + PQ)] treatment group compared to the control and PQ exposed group (**Fig. 6.9.B**). Moreover, p62 levels are significantly decreased in the [(48 hrs IF) + PQ] treatment group compared to the PQ exposed group. These data are supported by the immunofluorescence analysis which reveal that p62 protein signal is strongly indicated in the PQ exposed group, with minor signal in the control, 48 hrs IF, and [(48 hrs IF) + PQ)] treatment group (**Fig. 6.10**). Together, these findings suggest that cargo degradation is robustly induced above basal levels in the hippocampus of the 48 hrs IF, and [(48 hrs IF) + PQ)] treatment group, suggesting that oxidative stress, and IF strongly induce protein turnover. The significant decrease in p62 levels in the IF groups further reiterates the role of CR in MA pathway induction, which is generally associated with a concomitant decrease in p62 levels. In line with our findings, increased p62 levels have been reported *in vitro* under CR conditions in the presence of chloroquine than under CR conditions without chloroquine (Ferreira-Marques et al., 2016), suggesting that p62 levels are enhanced following inhibition of autophagosome

degradation. These data suggest that indeed CR enhances protein clearance, which in turn will contribute towards decreasing proteotoxicity, translating to protection.

Interestingly, western blot analysis CMA activity also reveals enhanced LAMP2A levels in the 48 hrs IF, and [(48 hrs IF) + PQ)] treatment group compared to the control and PQ exposed group (**Fig. 6.11.B**). This data suggests that prolonged IF induces CMA activity in addition to enhanced MA activity. These findings shed new light onto the interplay between MA and CMA *in vivo*. In the past, CMA activity has been primarily assessed in lysosomes isolated from rat liver (Cuervo et al., 1995b, 1998), however, its role in PQ-induced injury has not assessed. Findings by Wing et al. (1991) suggest that the CMA pathway is either not be active, or may function at constitutively low levels in brain, based on the absence of changes in the levels of KFERQ-containing proteins under starvation conditions. However, in line with our findings, studies indeed support the active role of the CMA pathway in lysosomes isolated from astrocytes, dopaminergic and cortical neurons, although these studies were not performed in the context of CR or oxidative stress (Cuervo, 2004; Martinez-Vicente et al., 2008). In line with our findings, studies by Cuervo and Dice (2000) reveal maximal activation of CMA activity above basal levels following 36 hrs amino acid deprivation, as evidenced by the increased recruitment of LAMP2A to the lysosomal membrane. In contrast with our findings (**Fig. 6.11.B**), previous findings reveal that oxidative stress exposure alone is sufficient to robustly induce CMA activity *in vitro* (Kiffin et al., 2004; Su et al., 2016). This discrepancy can perhaps be attributed to the model system assessed. Nevertheless, transgenic mice overexpressing LAMP2A have been shown to accumulate fewer 4HNE modified proteins compared to wild-type controls, at least in part, due to an enhanced CMA activity above basal levels (Zhang and Cuervo, 2008). Although, this finding was reported in a different tissue, it is possible that CMA induction may also contribute to the decreased 4HNE expression observed in the 48 hrs IF, and [(48 hrs IF) + PQ)] treatment groups (**Fig. 6.7 – 6.8**), but further studies are warranted in this regard.

Our western blot analysis indicates a significant decrease in APP levels in the 48 hrs IF treatment group compared to the [(48 hrs IF) + PQ] treatment group (**Fig. 6.12.B**). More importantly, APP levels are significantly increased in the PQ exposed group compared to the 48 hrs IF, and [(48 hrs IF) + PQ] treatment group. These data suggest that IF is indeed modulating amyloidogenic processing, in fact clearing the accumulating APP. This IF-mediated APP clearance contributes towards the protective effect observed (**Fig. 6.7 - 6.8**), by decreasing APP load. In support of these findings, CR has been shown to prevent Aβ generation and neuritic plaque deposition in the neocortical and hippocampal brain regions in a mouse model of amyloidosis (Wang et al., 2005). Findings by Wang et al. (2005) suggest that CR impacts APP processing by promoting α-secretase activity through mechanisms resulting in reduced Aβ neurotoxicity. Indeed, this possibility is supported by evidence of decreased α-secretase activity in the brain of CR transgenic mice compared to controls (Kawarabayashi et al., 2001; Postina et al., 2004). Given the critical role of particularly the hippocampus in neurodegeneration and memory formation, our findings are of significance.

6.5. Analysis of the cortex region

In order to contextualize the hippocampal data, the effects of the treatment intervention in the cortex region was assessed in a similar manner. The cortex is usually associated with degeneration at later stages, such as indicated by the 'Braak staging' (Braak and Braak, 1991). Our H & E analysis reveals no obvious indications of cell loss or architectural abnormalities following the 21-day treatment intervention (**Fig. 6.13**). This lack of subcellular alterations may suggest that similarly to the hippocampus, the ROS levels in this region may not have yet exceeded the antioxidant capacity of the tissue in this region, as described by Kannan and Jain (2000), whereby the cells are still able to sufficiently counteract the deleterious effects of excessive ROS in favour of cell survival.

Western blot analysis reveals a significant increase in 4HNE expression in the PQ exposed group compared to the control, 48 hrs IF, and [(48 hrs IF) + PQ] treatment group, while 4HNE is significantly reduced in the 48 hrs IF, and [(48 hrs IF) + PQ] treatment group compared to the control, and, more importantly, compared to the PQ exposed group (**Fig. 6.14.B**). Similarly, cytochrome c expression is significantly enhanced in the PQ exposed group compared to the control, 48 hrs IF, and [(48 hrs IF) + PQ] treatment group (**Fig. 6.14.D**). More importantly, cytochrome c expression is significantly reduced in the [(48 hrs IF) + PQ] treatment group compared to PQ only, suggesting that is protection from neuronal injury via IF intervention. Indeed, neuroprotection in the cortex region in response to the IF is echoed by the reduced levels of lipid peroxidation, and apoptosis. These results are supported by work conducted by Lohren et al. (2015), where it was revealed that the reported decrease in cortical cellular populations could be associated with induction of apoptosis in the motor cortex of adult rats following chronic oxidative stress exposure. Work by Teixeira et al. (2018) also suggests that lipid peroxidation plays a major role in necrosis and cell death detected in the cortical tissue of *in vivo* models of chronic oxidative stress exposure. Our results suggest apoptosis onset, however, no obvious decrease in cortical cells was indicated and it is possible that the extent and duration of oxidative stress was not sufficient to induce robust neuronal loss our model system. In line with our findings, work by Hyun et al. (2006) revealed that age-related increases in lipid peroxidation, and markers of oxidative stress were significantly reduced in rat cortical cells incubated in medium containing serum from animals subjected to CR, compared to cells treated with *ad libitum* serum. The neuroprotective effect of CR in the context of oxidative stress exposure in the cortex has also been replicated *in vivo*, where several studies reveal that cortical cells isolated from AD, PD, and HD mouse models maintained on CR regimens were relatively more resistant to oxidative and metabolic stress compared with animals fed *ad libitum* (Bruce-Keller et al., 1999; Duan and Mattson, 1999; Maswood et al., 2004). Consistent with our western blot data, our immunofluorescence analysis reveals that 4HNE and cytochrome c protein signal is strongly indicated in the PQ exposed group with no particular neuronal cell layer

showing a distinct response, compared to the control, 48 hrs IF, and [(48 hrs IF) + PQ] treatment group (**Fig. 6.15**).

Western blot analysis indicates a significant increase in LC3II expression in the 48 hrs IF, and [(48 hrs IF) + PQ] treatment group compared to the control (**Fig. 6.16.B**). This data suggests that MA is robustly induced in response to IF, with and without oxidative stress exposure, while oxidative stress alone appears to have no effect on LC3II protein levels compared to the control. In agreement, our western blot data indicates that MA cargo degradation, as evidenced by p62 expression, is significantly enhanced in the 48 hrs IF, and [(48 hrs IF) + PQ] treatment group compared to the control, and most importantly, compared to the PQ exposed group (**Fig. 6.18.B**). Our data suggests that MA activity in the cortex is increased above basal levels in the IF groups, with and without oxidative stress exposure, while MA activity in response to oxidative stress alone elicits a response comparable to that observed in the control. Indeed, previous studies reveal that CR mitigates the effects of oxidative damage via three major mechanisms: (1) increased protein turnover through MA induction above basal levels, (2) diminished production of mitochondrial ROS, and increased antioxidant defence responses (Bevilacqua et al., 2005; Gredilla and Barja, 2005). In line with our data, work by Arumugam et al. (2010) demonstrated that IF modulates neurotrophic and inflammatory pathways to protect neurons against brain injury, while this neuroprotection was severely compromised with age, partly, due to diminished proteolytic activity, resulting in progressively reduced cognitive capabilities and poorer functional outcome. In support of this data, others have suggested that CR may exert its beneficial effects on longevity through a 'hormetic' response that results in the activation of the MA above basal levels, recruitment of chaperon proteins, as well as the inhibition of inflammatory pathway responses in rodents (Lee and Notterpek, 2013; Mattson, 2008, 2010). While our immunofluorescence analysis reveals strong localization of LC3II protein signal in the 48 hrs IF and [(48 hrs IF) + PQ] treatment group compared to the PQ exposed group, and the control, the localization of GFAP appears uniformly diminished in all the groups, with strongest signal in the PQ group (**Fig. 6.17**). Our findings suggest that the PQ treatment did not induce such a strong

GFAP signal as was observed in the hippocampus (**Fig. 6.8**), indicating that potentially susceptibility to oxidative stress injury is generally lower in the cortex. Indeed, these findings are in line with Braak staging (Braak and Braak, 1991), and evidence from studies of neuronal number in the hippocampus, and cortex of species from rodents to primates using unbiased stereological measurements has determined that significant cell loss does not occur first, and most profoundly in the aging hippocampus (Christopher et al., 2017; Rapp and Gallagher, 1996; Vivar et al., 2013). In line with our findings, work by Manzanero et al. (2011) reveals that CR-mediated protection following stroke-induced cerebral cortex injury, in part, by through the upregulation anti-inflammatory cytokines, and cellular protective mechanisms such as MA. Our immunofluorescence analysis also reveals strong p62 protein signal in the PQ exposed group, consistent with reduced cargo turnover, with minor p62 signal observed in the 48 hrs IF treatment group, while increased cargo degradation is revealed in the [(48 hrs IF) + PQ] treatment group (**Fig. 6.19**), suggesting IF may confer neuroprotection through increased autophagosome degradation in this context.

Western blot analysis of CMA activity reveals a significant increase in LAMP2A expression in the 48 hrs IF, and [(48 hrs IF) + PQ] treatment group compared to the control, and most importantly, compared to the PQ exposed group (**Fig. 6.20.B**). This data suggests that IF induces CMA activity above basal levels, while oxidative stress alone does not elicit a significant response. A similar response was indicated in the hippocampus (**Fig. 6.11**), indicating that CMA activity and its response is not distinct in these two brain regions. Although, to our knowledge, the CMA pathway has not been specifically assessed in the cortex, upregulation of pathway has been extensively reported in the context of mild oxidative stress, serum starvation, and proteo- and lipotoxicity in fibroblasts (Massey et al., 2006c, 2008), hepatocytes (Schneider et al., 2015), lysosomes isolated from aging liver (Zhang and Cuervo, 2008). Nevertheless, long-term nutrient deprivation has been shown to enhance CMA activity, improve cellular viability in ST14A cells were transiently transfected with Htt25QP-HBH + CBP + IKK-βHD (overexpressing the HD protein) (Thompson et al., 2009), by preferentially targeting mutant huntingtin protein to the CMA pathway in HD mouse models (Bauer

et al., 2010). Additionally, exogenous overexpression LAMP2A has been shown to preserve CMA function until late in life, reducing intracellular levels of oxidized and aggregated proteins, and thereby enhancing the oxidative stress response of these mice (Zhang and Cuervo, 2008). In line with our data, these findings support the protective role of CR in the activation of CMA, particularly in the context of increased oxidative stress.

Our western blot data reveals significantly enhanced APP expression, most notably, in the PQ exposed group compared to the control, 48 hrs IF, and [(48 hrs IF) + PQ] treatment group (**Fig. 6.21.B**). These results suggest that IF may either enhance APP clearance, and/or decrease APP processing in the cortex. In line with our findings, Schafer et al. (2015) have demonstrated that compared to *ad libitum* fed Tg2576 mice (*in vivo* model of age-related neurodegeneration), significantly reduced APP levels and Aβ deposition was revealed within the hippocampal and the cortex of the mice subjected to CR, suggesting that CR mitigates APP/Aβ accumulation translating to neuroprotection with age. Consistent with our data, work by Muche et al. (2017) reveals that increased oxidative stress the cortical tissue of Tg2576 mice induces the amyloidogenic route of APP processing, suggesting that oxidative stress may represent a major risk factor for Aβ proteotoxicity. In agreement, earlier work by White et al. (1998) reported increased cell viability in primary cortical and cerebellar neuronal cultures established from APP knock-out mice compared to wild-type mice when exposed to oxidative stress, suggesting that oxidative stress is one of the mechanisms of Aβ-induced proteotoxicity. Although these studies were not performed in the context of CR conditions, our overall assessment of the cortex region indicates, to our knowledge, for the first time a protective role for both MA and CMA activity, which is increased above basal levels following IF-mediated induction.

6.6. Analysis of the cerebellum region

The cerebellum has often been described as least sensitive to neurodegenerative processes (Lumkwana et al., 2017), on the other hand, it has been elegantly shown that CR enables particularly an autophagy response in the cerebellum (Alirezaei et al., 2010). Representative H & E micrographs reveal no structural or archetypical abnormalities in cell distribution or density in all the groups in response to the 21-day treatment intervention (**Fig. 6.22**). In contradiction with these data, McFarland et al. (2007) presented evidence for sustained manganese super oxide dismutase activity (oxidative stress marker) with concomitant increase in Purkinje cell death in Lurcher transgenic mice (harbouring an autosomal dominant mutation in the d2 glutamate receptor (GluRd2), suggesting that oxidative stress may play a role in cerebellar cell death. It is possible that the dosage of PQ utilised in this context was not sufficient to impact the cerebellum on a cellular level. Notably, previous work using this same injury model was performed in APP transgenic APP mice or other AD-related pathology (Chen et al., 2012, 2015a), which may account for the discrepancy.

To our surprise, western blot analysis reveals no significant differences in 4HNE expression in all the treatment groups compared to the control (**Fig. 6.23.B**), supporting the notion of the cerebellum being least impacted in protein aggregation and toxicity (Lumkwana et al., 2017). These findings are in contrast with work by Wang et al. (2009), which revealed that cerebellar granule neurons are so sensitive to oxidative stress that even the oxygen tension in the ambient air induced cell death. However, our immunofluorescence analysis reveals strong 4HNE protein signal in all the treatment groups, with more intense 4HNE localization indicated in the PQ exposed group (**Fig. 6.24**). Interestingly, despite the lack of major changes in 4HNE, our findings indicate that the execution of apoptosis may be initiated, as evidenced by the enhanced cytochrome c expression in the PQ exposed group compared to the control, 48 hrs IF, and [(48 hrs IF) + PQ] treatment group (**Fig. 6.23.D**). It is however likely that these changes are not strong enough to result in significant changes in

4HNE protein levels. The 4HNE data can perhaps be attributed to the vulnerability of cerebellar neurons to selective oxidative stress-inducing agents (Niveditha et al., 2017). Consistent with our observations of robust cytochrome c expression in the PQ exposed group (**Fig. 6.23.D**), work by Anderson et al. (2009) found enhanced cell death onset in aged individuals with concomitant oxidative stress induction. It is therefore reasonable to propose that the reduced cytochrome c expression indicated in the IF groups (**Fig. 6.24**) may suggest that IF indeed confers neuronal protection in the cerebellum.

Western blot analysis of MA activity reveals a significant increase in LC3II expression in the PQ exposed group, 48 hrs IF, and [(48 hrs IF) + PQ] treatment group (**Fig. 6.25.B**). In support of this finding, a significant reduction in p62 expression is indicated in the 48 hrs IF, and [(48 hrs IF) + PQ] treatment group compared to the PQ exposed group and the control (**Fig. 6.27.B**). Although our immunofluorescence analysis reveals strong p62 hotspots in all the treatment groups, p62 localization appears comparatively more pronounced in the PQ exposed group, and overall weaker in the IF groups, further supporting neuronal protein clearance (**Fig. 6.28**). In support of these findings, work by Cunha-Santos et al. (2016) demonstrated that CR significantly reduced neuropathology, and neuroinflammation through robust activation of MA activity and SIRT1 protein expression in mice models of Machado–Joseph disease (MJD), a neurodegenerative disease characterised by the abnormal CAG triplet expansion of in the *ATXN3* gene particularly in the cerebellum region. Work by Lee et al. (2008) reveals that increased SIRT1 expression under CR conditions in turn induces MA activity, by deacetylating ATG5, ATG7 and ATG8, suggesting that SIRT1 deacetylase is an important regulator of MA during conditions of nutrient limitation. Indeed, Huang et al. (2015) recently demonstrated that SIRT1 plays a crucial role in MA induction under nutrient starvation conditions. In line with our findings, work by Cunha-Santos et al. (2016) reveals that MA activity is robustly induced, in turn mitigating Purkinje cell death onset in a CR MJD mouse model of following oxidative stress exposure compared with *ad libitum* fed MJD mice. Consistent with our western blot data, our immunofluorescence analysis reveals increased LC3II signal in the 48

hrs IF, and [(48 hrs IF) + PQ] treatment group, while strong GFAP protein signal is only indicated in the PQ exposed group (**Fig. 6.26**). This observation suggests that the IF may indeed attenuate inflammatory pathway responses in this region. In agreement, Cunha-Santos et al. (2016) reported a significant decrease of gliosis markers and mRNA levels of neuroinflammatory markers in the cerebellum of CR MJD mouse models following oxidative stress exposure.

Increased CMA activity is indicated by the significant increase in LAMP2A expression in the [(48 hrs IF) + PQ] treatment group compared to the PQ exposed group, the 48 hrs IF treatment group, and the control (**Fig. 6.28.B**). Moreover, LAMP2A expression is significantly increased in the 48 hrs IF treatment group compared to the PQ exposed group. This data suggests that both oxidative stress and IF induce CMA, in favour of increased proteostasis. As extensively described by Xilouri and Stefanis (2016), CMA operates at basal conditions in most mammalian cell models, and is generally activated in response to nutrient deprivation, or oxidative stress, as evidenced in the cerebellum region of our treatment groups.

To our surprise, following the 21-day treatment regime, western blot analysis revealed no significant changes in APP expression in all the treatment groups compared to the control (**Fig. 6.30**). This data suggests that, in contrast to the data observed in the hippocampus **(Fig. 6.12)** and cortex (**Fig. 6.21**) where indeed the hippocampus was shown to be most susceptible to APP expression profile changes in response to the intervention, APP processing may operate distinctively in the cerebellum. These findings are somewhat in contrast to reports indicating increased APP, and Aβ deposition in the cerebellum of APPswe/PSΔE9 double transgenic mice [i.e. expressing both APPswe and a mutant human presenilin 1 (PS1-dE9)] (Deng et al., 2014), and APPSwDI transgenic mice (harbouring human APP with Swedish, Dutch and Iowa mutations on a C57BL/6 background) (Dhurandhar et al., 2013). Recent work by Cheignon et al. (2018) suggests that oxidative stress and increased APP processing may represent a unifying mechanism of neurotoxicity in the pathogenesis

of a number of neurodegenerative diseases, such as AD. Our findings indeed reveal region specific stress responses, as revealed by Braak and Braak (1991), that may be of critical importance to understanding the differences in neurodegeneration susceptibility.

Taken together, our *in vivo* results strongly suggest a protective role for the IF regime in PQ-induced brain injury, through its induction of both MA, and CMA activity above basal levels, its reduction of lipid peroxidation, cytochrome c release from the mitochondrial membrane, and mitigation of neuroinflammation, particularly in the most vulnerable brain regions, the hippocampus and cortex. Our data further indicates that IF, is a safe and attractive intervention, to potentially harness the protective role of both MA and CMA activity. The experimental evidence summarized herein further supports the notion of regional and cellular heterogeneity. Even within subpopulations of hippocampal neuronal clusters, studies have shown selective vulnerability depending on the stressor, with the cellular response varying according to the cell type, stress duration and environmental factors (Cleveland and Rothstein, 2001; Floyd and Hensley, 2002). Therefore, in an attempt to exploit cellular mechanisms that play a causal or protective role in neurodegeneration, it is important to mechanistically understand the intrinsic characteristics of vulnerable neuronal populations and how they uniquely respond when challenged for example by the excessive oxidative stress, in neurodegenerative diseases. Our data has shed light on the role of both MA and CMA in this context, which deserves further study.

CHAPTER 7: SUMMARY AND CONCLUSIONS

Firstly, our findings clearly demonstrate that Aβ clearance is impaired following the pharmacological inhibition of autophagosomal lysosomal fusion using BafA1, suggesting that MA pathway dysfunction directly regulates the production and clearance of Aβ, as evidenced by increased Aβ levels following inhibition of autophagosomal lysosomal fusion. These findings suggest that disturbances in autophagosome turnover can further exacerbate Aβ proteotoxicity potentially worsening the cellular capacity to degrade APP and other proteotoxic metabolites. These findings are consistent with work by Nilsson and Saido (2014), which reveals that MA plays a role in both the production and clearance of Aβ. Moreover, previous studies have contributed to the clarification of the relationship between APP and MA, providing evidence that an essential component of the MA pathway, such as BECN1, is reduced in early AD progression, which in turn promotes Aβ accumulation and proteotoxicity in AD models (Lee and Gao, 2008; Pickford et al., 2008). Moreover, APP containing vesicles, have been found to build up within cells (Jaeger et al., 2010; Pickford et al., 2008), as evidenced in the present study following inhibition of autophagosome degradation using 3MA, which led to cell death onset. Secondly, our global proteome analysis revealed an increase in APP protein-protein interaction network in response to APP overexpression over time, suggesting that enhanced amyloidogenic processing progressively affects more cellular response pathways with disease progression. Thirdly, we revealed, to our knowledge for the first time, that macroautophagic flux remains fully functional with increasing APP overexpression but was insufficient to clear the Aβ load and prevent the induction of apoptosis. Modulation of both MA and CMA, using CRM 2DG reduced Aβ production, relatively decreased the level of apoptosis induction, and to our surprise, also decreased APP processing in favour of cell protection. These findings dissect the molecular relationship in a clear manner, due to the sequential APP overexpression and the rigorous modulation of the autophagic pathways, assessing both MA and CMA ‘s contribution to neuroprotection.

7.1. FINAL CONCLUSIONS

Both our *in vitro* and *in vivo* findings provide compelling evidence of the protective role of both MA and CMA modulation, using CRM in the *in vitro* AD model system, and the IF regime in the *in vivo* model of PQ-induced brain injury. While our findings suggest that the augmentation of MA above basal levels may be a promising therapeutic intervention, even with late disease progression, others have shown that MA induction in diseases like AD may exacerbate already impaired lysosomal clearance (Lee et al., 2010, 2011b). These studies indicate that the combination of excessive MA induction with faulty clearance of Aβ producing autophagosomes may further promote circumstances favourable to Aβ peptide aggregation and accumulation in AD brains. Therefore, it is important to consider the downstream effects of intervention strategies targeted at each stage of the MA pathway, and how the intervention strategy might affect the delicate balance between autophagosome formation and lysosomal degradation. We propose that a non-pharmaceutical intervention such as CR, or IF may be a promising therapeutic strategy for the augmentation of Aβ clearance through the MA pathway in AD and other neurodegenerative diseases. This strategy not only targets CMA induction, but also later steps in the MA pathway, thus improving macroautophagic flux, ROS handling, protein clearance, and thereby robustly contributing to proteostasis and neuronal protection. Given the nutritional concerns of CR and fasting in patients, CRM such as metformin and resveratrol, dietary regimens such as low carbohydrate/ketogenic and IF regimes, may serve as attractive, inexpensive therapeutic interventions that can be executed safely and rapidly to mimic the protective effects of CR both in the prevention neurodegeneration and as adjuvant therapies to current therapeutics. Future work may include a categoric characterization of such CRM's with regard to their potency to enhance both MA and CMA activity, the duration of their pathway upregulation, and the context of most efficient protein clearance.

CHAPTER 8: LIMITATIONS AND FUTURE OUTLOOK

7.2.1. *IN VITRO*

This study has shed crucial insights into the role of autophagic pathways, MA and CMA, in the degradation of APP and its proteotoxic metabolites and suggests that once autophagosomal flux and turnover is impaired, an escalating cycle of APP/Aβ accumulation and insufficient autophagic activity occurs. However, the contribution of MA modulation following 2DG treatment during APP overexpression in the absence or presence of BafA1 could further be evaluated to compliment the study. Macroautophagic flux assessment may be finer dissected as described by du Toit et al. (2018), using a single-cell fluorescence live-cell imaging-based approach that would allow for more robust assessment of autophagosome flux in the context of APP overexpression, and would allow to quantify the extent of flux enhancement based on MA pathway intermediates. This measurement of the complete autophagosomal pool size per cell would require the z-stack acquisition of all fluorescence images in order to achieve a complete measure of the intracellular autophagosome pool size, and the autophagosome count can then objectively be achieved using the 'particle count/analysis' function of an open source programme such as ImageJ as detailed in Loos et al. (2014). This assessment would enable one to better delineate the functional state of the macroautophagic system during APP overexpression, by providing a more sensitive quantitative read-out of autophagosome flux, pool sizes and transition time in N2aswe cells during APP overexpression. CMA assessment can also be further enhanced using purified CMA-positive lysosomal isolated from N2aswe cells during APP overexpression. To this end, a lysosome immunoprecipitation (LysoIP) technique has been described in recent work by Abu-Remaileh et al. (2017), who engineered cultured human embryonic kidney (HEK) 293T cells to produce a protein tag (transmembrane protein 192 (TMEM192) fused to three tandem hemagglutinin (HA) epitopes] on lysosomal membranes that can be used to rapidly precipitate purified

lysosomes on magnetic beads. These kinds of analyses would be extremely powerful to further contextualize the role of CMA and lysosomal function in models of AD.

7.2.2. *IN VIVO*

The *in vivo* brain-injury model may be improved, and better aligned with the *in vitro* model system, by assessing the role of MA and CMA during CR in the hippocampus, and the contribution of these pathways to neuroprotection following chronic oxidative stress exposure in an APP overexpressing mouse model. The functionality of the complete MA pathway could also be assessed in transgenic mice expressing the mRFP-GFP-LC3 (i.e. is a fusion protein of GFP-LC3 and RFP-LC3) probe in the whole organism (Castillo et al., 2013; Hariharan et al., 2011; Li et al., 2014b). These mice have been generated and successfully used to assess starvation-induced MA, and the dynamics of MA activity after ischemia–reperfusion injury in the proximal tubules (Castillo et al., 2013; Li et al., 2014b). In these mice, GFP/RFP ratio precisely quantifies the cumulative GFP-LC3 degradation by MA, with MA induction resulting in an increase in GFP-LC3 degradation and reduction in the GFP/RFP ratio. In a study by Castillo et al. (2013), the mRFP-GFP-LC3 MA probe was successfully introduced through intracerebroventricular injection of adeno-associated viruses in new-born mice, and its expression was observed throughout the nervous system; with an increased number of mCherry-positive and GFP-negative puncta being observed upon rapamycin or trehalose injection. Theoretically, an elaborate APP transgenic mouse model expressing the GFP-LC3-RFP-LC3ΔG (Kaizuka et al., 2016) MA probe could be generated in the future, as this would be a powerful tool to monitor both basal and induced MA in the context of APP overexpression. The study of CMA *in vivo* is still in its infancy, and additional studies, for example using CMA-positive lysosomes isolated from the hippocampal tissues of APP mice, are needed to fully dissect the role of CMA in both physiological and disease conditions. To this end, further investigations assessing long-term CR or 2DG dietary supplementation may better elucidate the precise role of CMA in the progression of AD-associated amyloidosis.

ADDENDUM A

Table A.1. Routinely used solutions.

Solution	Formulation
Ammonium persulphate (APS)	1 g APS, H_2O 10 ml. Stored at 4°C
10x Phosphate Buffered Saline (PBS)	In 800 ml dH_2O, dissolve: 80 g of NaCl, 2.0 g f KCl,14.4 g of Na_2HPO_4, and 2.4 g of KH_2PO_4. Volume adjusted to 1 L with additional dH_2O. pH adjusted 7.4. Sterilize by autoclaving.
1x PBS-T	100 ml 10x PBS, 900 ml dH_2O, 1 ml Tween-20
1% BSA in 1x PBS-T	0.1 g BSA in 10 ml 1x PBS-T.
RIPA lysis buffer	Tris-HCl 50 mM; NaCl 150 mM, EDTA 1 mM, NP-40 1%, Na-deoxycholate 0.25%. Stored at 4°C.
Protease and phosphatase inhibitor supplementation to 1 ml RIPA lysis buffer	1 mM Sodium Orthovanadate (Na_3VO_4), 1 mM Sodium Fluoride (NaF), 1mM PMSF (phenylmethylsulfonyl fluoride) and 1xcOmplete™ Protease Inhibitor Cocktail Tablets (#11873580001)
Stripping buffer for Western blotting	0.2 M Glycine, 1% SDS and pH adjusted to 2.5 using HCl
10x Tris-Buffered Saline (TBS)	4.2 g Tris, 80 g NaCl, dissolved in 600 ml dH2O (volume adjusted to 1 L with additional dH_2O, pH adjusted to 7.6 using HCl
1x TBST-T	100 ml 10x TBS, 1 ml Tween-20, 900 ml dH_2O
Freezing media (for cell lines)	FCS 90%, DMSO 10%
Laemmli's sample buffer	Solution A: 38 ml dH_2O, 10 ml 0.5 M Tris (pH 6.8), 8 ml glycerol, 16 ml 10% SDS, 4 ml 0.05% (w/v) Bromophenol blue. Solution B: β-mercaptoethanol. On day of use, 850 µl Solution A, was added to 150 µl Solution B
Tris-acetate-EDTA (TAE)	40 mM Tris, 0.1% glacial acetic acid, 1 mM EDTA

4% Paraformaldehyde (PFA) fixative solution	For 1 L of 4% PFA, 800 ml 1x PBS is added to a glass beaker on a stir plate in a ventilated hood and heated to ~60°C while stirring. 40 g PFA is added to the heated PBS solution. pH slowly raised by adding 1 N NaOH dropwise until the solution clears. Once the PFA is dissolved, the solution is cooled, filtered, and the volume of the solution is adjusted to 1 L with 1x PBS
Permeabilization solution (1x PBS/0.2% Triton X-100)	In 25 ml: 2.5 ml 10x PBS, and 22.5 ml dH_2O is added and mixed well. While stirring, 50 µl Triton X-100 is added
5 % BSA solution	2.5 g BSA in 50 ml of 1x TBS-T. Stored at 4°C for 10 min to dissolve (stirring causes foam, which is generally the denatured BSA)
1x Tris-glycine SDS running buffer	100 ml 10x Tris-glycine running buffer (#161- 0772) is added to 900 ml dH_2O, and mixed well
Western blotting blocking buffer	5% fat free milk is added in 1x TBS-T
Immunofluorescence blocking buffer	5% donkey serum is added in 1x PBS-T
Primary antibody dilution buffer:	5% BSA is added in 1x TBS-T
Harris haematoxylin	5 g Harris haematoxylin, 100 g Ammonium, 50 ml 100% ethanol, and 2.5 g mercuric acid is added to 1 L dH_2O
Eosin stock solution	2.0 g of water-soluble eosin Y is added to 40 ml of dH_2O, and mixed until dissolved. Then 160 ml of 95% ethanol is added, and mixed. Store at RT. <u>Working solution</u> 200 ml of eosin Y stock solution is added to 600 ml 80% ethanol and mixed well. In a fume hood, 4 ml of glacial acetic acid is added and mixed well. Store covered at RT
Scott's tap water	20 g $MgSO_4$, 3.5 g $NaHCO_3$, and 10 ml 37% formalin is added to 1 L dH_2O
0.85% Saline solution	For 1 L: 8.5 g NaCl is dissolved in dH_2O. Autoclaved for 25 min at 121°C and cooled at RT. Solution stored at -20°C

Table A.2: List of proteins with significantly increased expression during 24 hrs APP overexpression relative to control.

	Protein	Gene	Accession ID.	*P* value	Fold change
1	Amyloid precursor protein	**APP**	P05067	1.4E-02	1.59
2	60S ribosomal protein L26	**Rpl26**	P61255	9.8E-03	2.01
3	Caspase-3	**CASP3**	P70677	9.7E-03	2.02
4	55 kDa erythrocyte membrane protein	**Mpp1**	P70290	9.3E-03	2.03
5	Dihydroorotate dehydrogenase (quinone)	**Dhodh**	O35435	9.3E-03	2.03
6	Tryptophan-tRNA ligase. cytoplasmic	**Wars**	P32921	8.7E-03	2.06
7	Lamin-B1	**Lmnb1**	P14733	8.6E-03	2.07
8	Ribosomal protein L8	**RPL8**	Q9Z237	8.1E-03	2.09
9	Inositol polyphosphate 4-phosphatase type II alpha	**Inpp4b**	Q1A6V1	7.1E-03	2.15
10	Integrin beta-4	**Itgb4**	A2A863	7.0E-03	2.15
11	CD97 antigen	**Cd97**	Q9Z0M6	6.7E-03	2.18
12	Nuclear factor NF-kappa-B p105 subunit	**Nfkb1**	P25799	6.5E-03	2.19
13	Histidine-tRNA ligase. cytoplasmic	**Hars**	Q61035	6.1E-03	2.21
14	Paired box protein Pax-8	**Pax8**	Q00288	5.8E-03	2.24
15	Pyruvate dehydrogenase E1 component subunit beta. mitochondrial	**Pdhb**	Q9D051	5.4E-03	2.26
16	Lysosome-associated membrane glycoprotein 1	**Lamp1**	P11438	5.1E-03	2.29
17	Tripeptidyl-peptidase 2	**Tpp2**	Q64514	4.9E-03	2.31
18	Disintegrin and metalloproteinase domain-	**Adam15**	O88839	4.9E-03	2.31

	containing protein 15				
19	Synaptotagmin-1	**Syt1**	P46096	4.9E-03	2.31
20	Transcriptional repressor NF-X1	**Nfx1**	B1AY10	4.6E-03	2.34
21	Tyrosine-protein kinase ZAP-70	**Zap70**	P43404	4.2E-03	2.37
22	Voltage-dependent calcium channel subunit beta-4	**Cacnb4**	Q8R0S4	4.2E-03	2.37
23	Acyl-CoA-binding protein	**Dbi**	M0QWU8	4.0E-03	2.41
24	Proteasome subunit beta type-9	**Psmb9**	P28076	3.8E-03	2.42
25	Fatty acid-binding protein. epidermal	**Fabp5**	Q05816	3.7E-03	2.43
26	Serine/threonine-protein kinase Nek4	**Nek4**	Q9Z1J2	3.6E-03	2.44
27	Homeobox protein Hox-D4	**Hoxd4**	P10628	3.2E-03	2.50
28	Calmodulin	**Calm1**	P62204	3.2E-03	2.50
29	Probable allantoicase	**Allc**	Q9JHX6	3.1E-03	2.50
30	Band 3 anion transport protein	**Slc4a1**	P04919	3.1E-03	2.50
31	Activated CDC42 kinase 1	**Tnk2**	O54967	3.1E-03	2.50
32	Heat shock cognate 71 kDa protein	**Hspa8**	P63017	3.1E-03	2.51
33	Mitochondrial carnitine/acylcarnitine carrier protein	**Slc25a20**	Q9Z2Z6	2.7E-03	2.57
34	ATP-citrate synthase	**Acly**	Q3V117	2.5E-03	2.60
35	Glyceraldehyde-3-phosphate dehydrogenase	**Gapdh**	P16858	2.1E-03	2.68
36	Proteasome subunit alpha type-5	**Psma5**	Q9Z2U1	2.0E-03	2.69
37	Tenascin-W	**Tnn**	Q70HX0	1.8E-03	2.75

38	Catalase	**Cat**	P24270	1.6E-03	2.80
39	Histone H3.1	**Hist1h3a**	P68433	1.6E-03	2.80
40	Beclin 1-	**BECN1**	O88597	1.6E-03	2.81
41	Retinol dehydrogenase 11	**Rdh11**	Q9QYF1	1.4E-03	2.84
42	N-acetylglutamate synthase. mitochondrial	**Nags**	Q8R4H7	1.2E-03	2.93
43	Zinc finger protein 185	**Znf185**	Q62394	1.2E-03	2.93
44	Neuromodulin	**Gap43**	P06837	7.2E-04	3.14
45	Beta-2-microglobulin	**B2m**	P01887	5.7E-04	3.24
46	Integrin alpha-E	**Itgae**	Q60677	5.7E-04	3.25
47	Ubiquitin-conjugating enzyme E2 C	**Ube2c**	UBE2C	5.5E-04	3.26
48	LIM domain kinase 1	**Limk1**	P53668	4.1E-04	3.39
49	Acetoacetyl-CoA synthetase	**Aacs**	Q9D2R0	2.6E-04	3.58
50	Histone H3.3	**H3f3a**	P84244	2.0E-04	3.71
51	Probable ATP-dependent RNA helicase	**Ddx5**	Q61656	1.9E-04	3.72
52	Protein disulphide-isomerase A3	**Pdia3**	P27773	1.8E-04	3.74
53	Nectin-1	**Nectin-1**	Q9JKF6	9.6E-05	4.02
54	26S proteasome non-ATPase regulatory subunit 12	**Psmd12**	Q9D8W5	5.6E-05	4.25
55	Alpha-mannosidase 2	**Man2a1**	P27046	5.1E-05	4.29
56	Eukaryotic initiation factor 4A-I	**Eif4a1**	P60843	4.8E-06	5.31

Table A.3: List of proteins with significantly increased expression during 48 hrs APP overexpression relative to control.

	Protein Description	Gene Name	Accession ID	*P* value	Fold change
1	Nuclear migration protein nudC	**Nudc**	O35685	9.9E-03	2.01
2	Myosin-9	**Myh9**	Q8VDD5	9.8E-03	2.01
3	T-box protein 22	**Tbx22**	Q811Z5	9.4E-03	2.02
4	Homogentisate 1.2-dioxygenase	**Hgd**	O09173	8.6E-03	2.07
5	Thrombopoietin receptor	**Mpl**	Q08351	2.1E-03	2.07
6	Class I MHC receptor KLRA5	**Klra5**	Q548A2	4.3E-03	2.07
7	Aspartate aminotransferase. cytoplasmic	**Got1**	F7ALS6	8.1E-03	2.07
8	Proteasome subunit alpha type-7	**Psma7**	Q9Z2U0	8.3E-03	2.08
9	BAG family molecular chaperone regulator 3	**Bag3**	Q9JLV1|	8.1E-03	2.09
10	Proteasome subunit beta type-2	**Psmb2**	Q9R1P3	7.9E-03	2.10
11	Prefoldin subunit 3	**Vbp1**	P61759	7.3E-03	2.13
12	Heat shock protein HSP 90-beta	**Hsp90ab1**	P11499	7.2E-03	2.15
13	CPN10-like protein	**Cpn10-rs1**	Q9JI95	7.1E-03	2.15
14	H-2 class I histocompatibility antigen. Q7 alpha chain	**H2-Q7**	P14429	7.4E-03	2.16
15	Glyceraldehyde-3-phosphate dehydrogenase	**Gapdh**	P16858	6.4E-03	2.17
16	Amyloid beta A4 precursor protein-binding family A member 1	**Apba1**	B2RUJ5	6.2E-03	2.20

17	Phospholipase D1	**Pld1**	Q9Z280	5.9E-03	2.20
18	ATP-dependent RNA helicase A	**Dhx9**	O70133	6.0E-03	2.23
19	LIM and SH3 domain protein 1	**Lasp1**	Q61792	4.8E-03	2.23
20	Tenascin-W	**Tnn**	Q70HX0	5.5E-03	2.26
21	Chloride channel accessory 3A2	**Clca3a2**	Q9EQR4	4.4E-03	2.26
22	Serum albumin	**Alb**	P02768	5.4E-03	2.27
23	Pyruvate dehydrogenase E1 component subunit beta	**Pdhb**	Q9D051	Pdhb	2.31
24	D-3-phosphoglycerate dehydrogenase	**Phgdh**	Q61753	4.7E-03	2.33
25	Msx2-interacting protein	**Spen**	Q62504	4.5E-03	2.35
26	Pyruvate kinase PKM	**Pkm**	P52480	4.4E-03	2.35
27	RWD domain-containing protein 1	**Rwdd1**	Q9CQK7	2.6E-03	2.41
28	Adenosine deaminase	**Ada**	P03958	3.5E-03	2.43
29	Gelsolin	**Gsn**	P13020	3.8E-03	2.43
30	Retinoic acid receptor gamma	**Rarg**	P18911	1.0E-03	2.48
31	Multiple PDZ domain protein	**Mpdz**	Q8VBX6	3.3E-03	2.49
32	Caspase-3	**Casp3**	P70677	3.2E-03	2.49
33	Desmocollin-1	**Dsc1**	P55849	3.0E-03	2.53

34	Talin-2	**Tln2**	Q71LX4	2.9E-03	2.54
35	Tyrosine-protein kinase JAK1	**Jak1**	P52332	2.6E-03	2.59
36	Acyl-CoA-binding protein	**Dbi**	M0QWU8	2.4E-03	2.63
37	Proteasome subunit alpha type-1	**Psma1**	Q9R1P4	2.1E-03	2.68
38	Catenin delta-2	**Ctnnd2**	E9QKH8	2.0E-03	2.69
39	Polycomb protein EED	**Eed**	Q921E6	2.0E-03	2.69
40	Extracellular matrix protein 1	**Ecm1**	Q61508	1.9E-03	2.71
41	Beclin1	**BECN1**	O88597	1.9E-03	2.75
42	Valyl-tRNA synthetase 2	**Vars**	Q790I0	1.9E-03	2.73
43	Ras-related protein Rab-7a	**Rab7a**	P51150	1.8E-03	2.73
44	Eukaryotic initiation factor 4A-I	**Eif4a1**	P60843	1.2E-03	2.80
45	Acetoacetyl-CoA synthetase	**Aacs**	Q9D2R0	1.4E-03	2.82
46	Proteasome subunit alpha type-4	**Psma4**	Q9R1P0	1.4E-03	2.85
47	ANK repeat and PH domain-containing protein 2	**Arap2**	E9QP44	1.3E-03	2.89
48	Proteasome subunit alpha type-5	**Psma5**	Q9Z2U1	1.2E-03	2.92
49	Neural Wiskott-Aldrich syndrome protein	**Wasl**	Q91YD9	9.0E-04	2.92
50	Apoptosis regulator BAX	**Bax**	Q91YD9	1.0E-03	2.92
51	Proteasome subunit alpha type-3	**Psma3**	O70435	1.1E-03	2.96

52	Amyloid beta A4 protein	**APP**	P05067	6.3E-04	2.99
53	H-2 class I histocompatibility antigen. D-B alpha chain	**H2-D1**	P01899	9.8E-04	3.02
54	T-cell surface glycoprotein	**Cd4**	P06332	5.0E-04	3.03
55	Dynactin subunit 2	**Dctn2**	Q99KJ8	5.7E-04	3.04
56	N-acyl-aromatic-L-amino acid amidohydrolase	**Acy3**	Q91XE4	9.0E-04	3.07
57	Creatine kinase B-type	**Ckb**	Q04447	8.3E-04	3.08
58	DbpA murine homologue	**Ybx3**	Q61478	7.8E-04	3.11
59	26S protease regulatory subunit 8	**Psmc5**	P62196	7.4E-04	3.13
60	Dihydrolipoyllysine-residue acetyltransferase	**Dlat**	Q8BMF4	7.1E-04	3.15
61	DNA replication licensing factor MCM3	**Mcm3**	P25206	6.4E-04	3.20
62	Probable ATP-dependent RNA helicase DDX5	**Ddx5**	Q61656	6.3E-04	3.20
63	Threonine-tRNA ligase. cytoplasmic	**Tars**	Q9D0R2	5.4E-04	3.27
64	Bifunctional methylenetetrahydrofolate dehydrogenase	**Mthfd2**	P18155	4.7E-04	3.33
65	Plakophilin-4	**Pkp4**	A2AS45	3.6E-04	3.40
66	Serum amyloid A-3 protein	**Saa3**	P04918	3.1E-04	3.45
67	Eukaryotic peptide chain release factor subunit 1	**Etf1**	Q8BWY3	2.0E-04	3.69
68	Dihydropyrimidinase-related protein 2	**Dpysl2**	O08553	2.0E-04	3.70

69	Bifunctional glutamate/proline-tRNA ligase	**Eprs**	Q8CGC7	1.0E-04	3.98
70	Integrin beta-1	**Itgb1**	P09055	9.6E-05	4.02
71	ATP-citrate synthase	**Acly**	Q91V92	6.0E-05	4.22
72	Superoxide dismutase [Mn]. mitochondrial	**Sod2**	P09671	3.5E-04	4.46
73	Tripeptidyl-peptidase 2	**Tpp2**	Q64514	7.7E-06	4.97
74	mouse NK cell activating receptor Ly49H	**Ly49H**	Q49U25	1.0E-05	5.00
75	H-2 class I histocompatibility antigen. K-K alpha chain	**H2-K1**	P04223	1.2E-06	5.93

Table A.4: List of proteins with significantly increased expression levels between 24 hrs and 48 hrs APP overexpression.

	Protein	Gene	Accession ID	*P* value	Fold change
1	Multiple PDZ domain protein	**Mpdz**	Q8VBX6	9.1E-03	2.04
2	Homogentisate 1.2-dioxygenase	**Hgd**	O09173	9.0E-03	2.05
3	Proteasome subunit alpha type-6	**Psma6**	Q9QUM9	8.9E-03	2.05
4	Serine/threonine-protein kinase MAK	**Mak**	Q04859	8.3E-03	2.08
5	4F2 cell-surface antigen heavy chain	**Slc3a2**	P10852	8.2E-03	2.08
6	Cathepsin D	**CasD**	P18242	7.7E-03	2.11
7	Methylcytosine dioxygenase TET2	**Tet2**	Q4JK59	7.5E-03	2.12
8	Plasminogen activator inhibitor 2. macrophage	**Serpinb2**	P12388	7.4E-03	2.13
9	Adenosine deaminase	**Ada**	P03958	7.0E-03	2.15
10	MHC class Ib antigen	**H2-M2**	Q6W9J8	6.8E-03	2.17
11	Tyrosine-protein phosphatase non-receptor type 4	**Ptpn4**	Q9WU22	6.2E-03	2.21
12	Mitochondrial carnitine/acylcarnitine carrier protein	**SLC25A20**	Q9Z2Z6	5.9E-03	2.23
13	Amyloid beta A4 protein	**APP**	P05067	5.8E-03	2.28
14	Citron Rho-interacting kinase	**Cit**	P49025	5.4E-03	2.27
15	T-cell surface antigen CD2	**Cd2**	P08920	5.1E-03	2.29

16	Dihydropyrimidinase-related protein 2	**Dpysl2**	O08553	4.9E-03	2.31
17	Serum albumin	**Alb**	P02768	4.4E-03	2.36
18	Adhesion G protein-coupled receptor B2	**Adgrb2**	H7BWZ2	3.8E-03	2.42
19	Testin	**Tes**	P47226	3.0E-03	2.52
20	ABCG4	**Abcg4**	Q8K4E1	3.0E-03	2.52
21	RNA/DNA-binding protein	**Rnps1**	Q62150	2.9E-03	2.53
22	Extracellular matrix protein 1	**Ecm1**	Q61508	2.9E-03	2.59
23	Nuclear factor 1	**Nfib**	Q6GSP7	2.3E-03	2.63
24	B-cell lymphoma 6 protein homolog	**Bcl6**	P41183	2.3E-03	2.63
25	Neural Wiskott-Aldrich syndrome protein	**Wasl**	Q91YD9	2.3E-03	2.64
26	Heat shock protein HSC70t	**HSC70t**	Q91ZU4	1.8E-03	2.20
27	Polyhomeotic-like protein 1	**Phc1**	Q64028	1.6E-03	2.80
28	Tyrosine-protein kinase	**Btk**	P35991	1.5E-03	2.82
29	Integrin beta-1	**Itgb1**	P09055	1.5E-03	2.83
30	T-cell surface glycoprotein CD4	**Cd4**	P06332	1.3E-03	2.87
31	EC2-V2R pheromone receptor protein	**Vmn2r43**	Q80Z08	1.1E-03	2.96

32	Macrophage colony-stimulating factor 1	**Csf1**	P07141	1.0E-03	2.99
33	Homeobox protein Hox-A6	**Hoxa6**	P09092	1.0E-03	2.99
34	Bifunctional glutamate/proline-tRNA ligase	**Eprs**	Q8CGC7	4.8E-04	3.32
35	Dynactin subunit 2	**Dctn2**	Q99KJ8	3.8E-04	3.42
36	Valyl-tRNA synthetase 2	**Vars**	Q790I0	3.6E-04	3.45
37	Zinc finger 202 m1	**Zfp202**	Q99PG9	1.8E-04	3.74
38	Calcium/calmodulin-dependent protein kinase type II subunit	**Camk2b**	Q5SVI3	1.5E-04	3.81
39	Klra21 protein	**Klra21**	Q49U25	6.4E-05	4.20

ADDENDUM B:

Table B.1: Animal welfare monitoring sheet (6 mice housed per cage with a total of 12 mice per group).

Experimental group									
Monitoring frequency	Daily								
Date									
Weight measurements for:	**Baseline (g)**	**Day 1**	**Day 2**	**Day 3**	**Day 4**	**Day 5**	**Day 6**	**Day 7**	**Body weight % compared to baseline**
Mouse 1									
Mouse 2									
Mouse 3									
Mouse 4									
Mouse 5									
Mouse 6									
Mouse 7									
Mouse 8									
Mouse 9									
Mouse 10									
Mouse 11									
Mouse 12									

* Mouse grimace scale: assessment of visible discomfort									
Comfort scores for:	**Baseline score**	**score**	**score**	**score**	**score**	**score**	**score**	**score**	**Average score per week**
Mouse 1									
Mouse 2									
Mouse 3									
Mouse 4									

Table B.2: Description of behavioural or visible symptoms.

Symptom	Mild symptoms	Severe symptoms
Inactivity	Fully mobile, active as usual	Occasional movement, but largely unresponsive to prompting
Hunched posture	Small change in normal posture	Noticeably hunched over without regaining normal posture
Ruffled fur	Some isolated ruffling of fur	Obvious ruffling of fur
Rate of breathing	Slightly above, or below normal	Excessive panting, or markedly diminished rate of breathing
Crusty eyes	Slight build-up of excretion in eyes	Significant excretion in eyes, vision likely to be impaired
Shivering	Occasional shivering	Constant prominent shivering with normal temperature
Diarrhea	Loose stools	Stools have completely loose stools
Inquisitive/alertness	Slightly reduced response to stimuli	Largely unresponsive to stimuli

Action taken:

0 = normal: no action

1 = moderate changes: should be monitored daily

2 = significant changes: monitor twice daily

3 = euthanise

[Welfare monitoring sheets adapted from (Animals, 2009; Langford et al., 2010; Leach et al., 2012)]

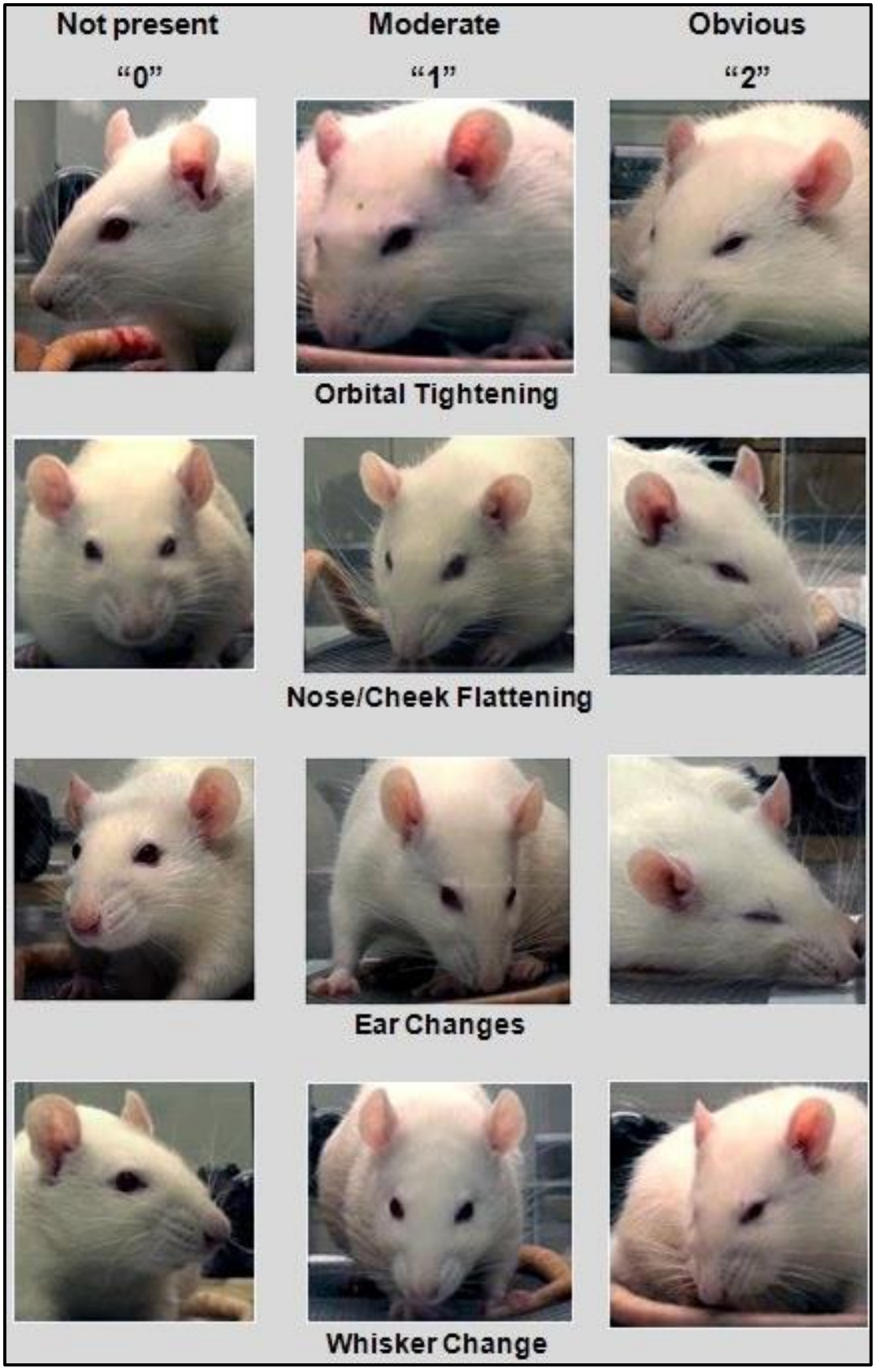

Figure B.1. Grimace scale: evaluating mouse well post-and pre-treatment monitoring. Coding system for assessing mouse facial expressions of pain (Langford et al., 2010).

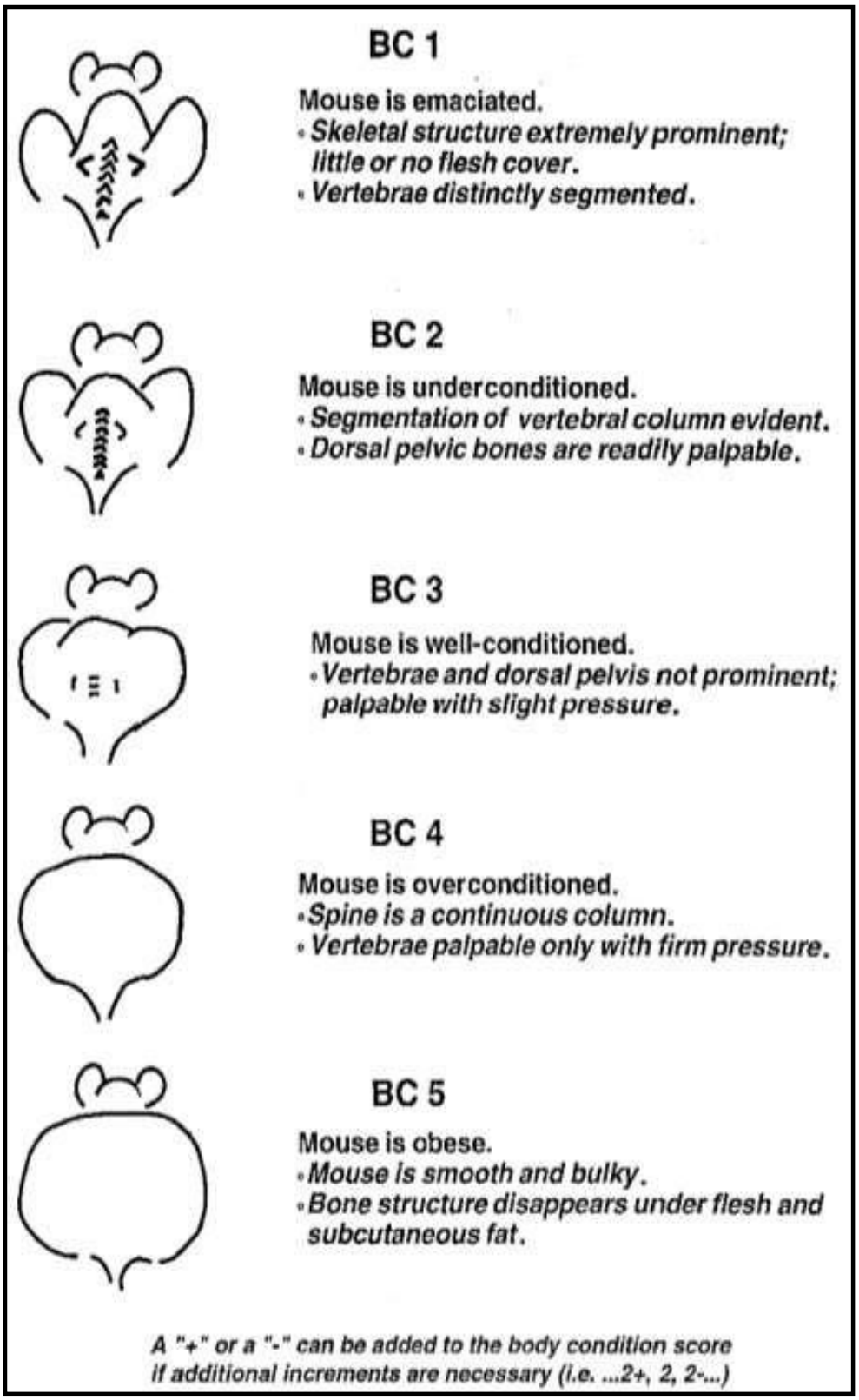

Figure B.2: Mouse body condition assessment scoring chart. Mandatory euthanasia is suggested provided there is no improvement after consecutive daily monitoring and if an animal is chronically emaciated (>20%) weight loss (Ullman-Culleré and Foltz, 1999).

References:

Abu-Remaileh, M., Wyant, G.A., Kim, C., Laqtom, N.N., Abbasi, M., Chan, S.H., Freinkman, E., and Sabatini, D.M. (2017). Lysosomal metabolomics reveals V-ATPase- and mTOR-dependent regulation of amino acid efflux from lysosomes. Science *358*, 807–813.

Adler, J., and Parmryd, I. (2010). Quantifying colocalization by correlation: The Pearson correlation coefficient is superior to the Mander's overlap coefficient. Cytometry A *77A*, 733–742.

Adler, J., Pagakis, S.N., and Parmryd, I. (2008). Replicate-based noise corrected correlation for accurate measurements of colocalization. J. Microsc. *230*, 121–133.

Agarraberes, F.A., Terlecky, S.R., and Dice, J.F. (1997). An intralysosomal hsp70 is required for a selective pathway of lysosomal protein degradation. J. Cell Biol. *137*, 825–834.

Aisen, P.S., Vellas, B., and Hampel, H. (2013). Moving towards early clinical trials for amyloid-targeted therapy in Alzheimer's disease. Nat. Rev. Drug Discov. *12*, 324–324.

Alers, S., Löffler, A.S., Wesselborg, S., and Stork, B. (2012). Role of AMPK-mTOR-Ulk1/2 in the Regulation of Autophagy: Cross Talk, Shortcuts, and Feedbacks. Mol. Cell. Biol. *32*, 2–11.

Ali, S., Jain, S.K., Abdulla, M., and Athar, M. (1996). Paraquat induced DNA damage by reactive oxygen species. Biochem. Mol. Biol. Int. *39*, 63–67.

Alirezaei, M., Kemball, C.C., Flynn, C.T., Wood, M.R., Whitton, J.L., and Kiosses, W.B. (2010). Short-term fasting induces profound neuronal autophagy. Autophagy *6*, 702–710.

Alomari, M.A., Khabour, O.F., Alzoubi, K.H., and Alzubi, M.A. (2016). Combining restricted diet with forced or voluntary exercises improves hippocampal BDNF and cognitive function in rats. Int. J. Neurosci. *126*, 366–373.

Alzheimer's Association (2016). 2016 Alzheimer's disease facts and figures. Alzheimer's Dement. J. Alzheimer's Assoc. *12*, 459–509.

Anderson, R.M., Shanmuganayagam, D., and Weindruch, R. (2009). Caloric restriction and aging: studies in mice and monkeys. Toxicol. Pathol. *37*, 47–51.

Animals, N.R.C. (US) C. on R. and A. of P. in L. (2009). Humane Endpoints for Animals in Pain (National Academies Press (US)).

Anisimov, V.N., and Bartke, A. (2013). The key role of growth hormone — insulin — IGF-1 signalling in aging and cancer. Crit. Rev. Oncol. Hematol. *87*, 201–223.

Arias, E. (2017). Methods to Study Chaperone-Mediated Autophagy. Methods Enzymol. *588*, 283–305.

Arias, E., Koga, H., Diaz, A., Mocholi, E., Patel, B., and Cuervo, A.M. (2015). Lysosomal mTORC2/PHLPP1/Akt Regulate Chaperone-Mediated Autophagy. Mol. Cell *59*, 270–284.

Aronis, A., Melendez, J.A., Golan, O., Shilo, S., Dicter, N., and Tirosh, O. (2003). Potentiation of Fas-mediated apoptosis by attenuated production of mitochondria-derived reactive oxygen species. Cell Death Differ. *10*, 335–344.

Arumugam, T.V., Phillips, T.M., Cheng, A., Morrell, C.H., Mattson, M.P., and Wan, R. (2010). Age and energy intake interact to modify cell stress pathways and stroke outcome. Ann. Neurol. *67*, 41–52.

Asano, T., Komatsu, M., Yamaguchi-Iwai, Y., Ishikawa, F., Mizushima, N., and Iwai, K. (2011). Distinct Mechanisms of Ferritin Delivery to Lysosomes in Iron-Depleted and Iron-Replete Cells. Mol. Cell. Biol. *31*, 2040–2052.

Audrain, M., Fol, R., Dutar, P., Potier, B., Billard, J.-M., Flament, J., Alves, S., Burlot, M.-A., Dufayet-Chaffaud, G., Bemelmans, A.-P., et al. (2016). Alzheimer's disease-like APP processing in wild-type mice identifies synaptic defects as initial steps of disease progression. Mol. Neurodegener. *11*, 5.

Avruch, J., Long, X., Ortiz-Vega, S., Rapley, J., Papageorgiou, A., and Dai, N. (2009). Amino acid regulation of TOR complex 1. Am. J. Physiol. Endocrinol. Metab. *296*, E592-602.

Axe, E.L., Walker, S.A., Manifava, M., Chandra, P., Roderick, H.L., Habermann, A., Griffiths, G., and Ktistakis, N.T. (2008). Autophagosome formation from membrane compartments enriched in phosphatidylinositol 3-phosphate and dynamically connected to the endoplasmic reticulum. J. Cell Biol. *182*, 685–701.

Backer, J.M., and Dice, J.F. (1986). Covalent linkage of ribonuclease S-peptide to microinjected proteins causes their intracellular degradation to be enhanced during serum withdrawal. Proc. Natl. Acad. Sci. U. S. A. *83*, 5830–5834.

Bahr, B.A., Abai, B., Gall, C.M., Vanderklish, P.W., Hoffman, K.B., and Lynch, G. (1994). Induction of beta-amyloid-containing polypeptides in hippocampus: evidence for a concomitant loss of synaptic proteins and interactions with an excitotoxin. Exp. Neurol. *129*, 81–94.

Bai, Z., Stamova, B., Xu, H., Ander, B.P., Wang, J., Jickling, G.C., Zhan, X., Liu, D., Han, G., Jin, L.-W., et al. (2014). Distinctive RNA expression profiles in blood associated with Alzheimer disease after accounting for white matter hyperintensities. Alzheimer Dis. Assoc. Disord. *28*, 226–233.

Balasubramanian, P., Howell, P.R., and Anderson, R.M. (2017). Aging and Caloric Restriction Research: A Biological Perspective with Translational Potential. EBioMedicine *21*, 37–44.

Bales, C.W., and Kraus, W.E. (2013). Caloric Restriction. J. Cardiopulm. Rehabil. Prev. *33*, 201–208.

Bandyopadhyay, U., and Cuervo, A.M. (2008). Entering the lysosome through a transient gate by chaperone-mediated autophagy. Autophagy *4*, 1101–1103.

Bandyopadhyay, U., Kaushik, S., Varticovski, L., and Cuervo, A.M. (2008). The chaperone-mediated autophagy receptor organizes in dynamic protein complexes at the lysosomal membrane. Mol. Cell. Biol. *28*, 5747–5763.

Bandyopadhyay, U., Sridhar, S., Kaushik, S., Kiffin, R., and Cuervo, A.M. (2010). Identification of regulators of chaperone-mediated autophagy. Mol. Cell *39*, 535–547.

Bánréti, Á., Sass, M., and Graba, Y. (2013). The emerging role of acetylation in the regulation of autophagy. Autophagy *9*, 819–829.

Baranello, R.J., Bharani, K.L., Padmaraju, V., Chopra, N., Lahiri, D.K., Greig, N.H., Pappolla, M.A., and Sambamurti, K. (2015). Amyloid-beta protein clearance and degradation (ABCD) pathways and their role in Alzheimer's disease. Curr. Alzheimer Res. *12*, 32–46.

Barbero-Camps, E., Roca-Agujetas, V., Bartolessis, I., Dios, C. de, Fernández-Checa, J.C., Marí, M., Morales, A., Hartmann, T., and Colell, A. (2018). Cholesterol impairs autophagy-mediated clearance of amyloid beta while promoting its secretion. Autophagy *0*, 1–26.

Barth, S., Glick, D., and Macleod, K.F. (2010). Autophagy: assays and artefacts. J. Pathol. *221*, 117–124.

Bartzokis, G., Mintz, J., Sultzer, D., Marx, P., Herzberg, J.S., Phelan, C.K., and Marder, S.R. (1994). *In vivo* MR evaluation of age-related increases in brain iron. AJNR Am. J. Neuroradiol. *15*, 1129–1138.

Basso, K., Schneider, C., Shen, Q., Holmes, A.B., Setty, M., Leslie, C., and Dalla-Favera, R. (2012). BCL6 positively regulates AID and germinal centre gene expression via repression of miR-155. J. Exp. Med. *209*, 2455–2465.

Bateman, R.J., Munsell, L.Y., Morris, J.C., Swarm, R., Yarasheski, K.E., and Holtzman, D.M. (2006). Human amyloid-beta synthesis and clearance rates as measured in cerebrospinal fluid in vivo. Nat. Med. *12*, 856–861.

Bateman, R.J., Xiong, C., Benzinger, T.L.S., Fagan, A.M., Goate, A., Fox, N.C., Marcus, D.S., Cairns, N.J., Xie, X., Blazey, T.M., et al. (2012). Clinical and biomarker changes in dominantly inherited Alzheimer's disease. N. Engl. J. Med. *367*, 795–804.

Bauer, P.O., Goswami, A., Wong, H.K., Okuno, M., Kurosawa, M., Yamada, M., Miyazaki, H., Matsumoto, G., Kino, Y., Nagai, Y., et al. (2010). Harnessing chaperone-mediated autophagy for the selective degradation of mutant huntingtin protein. Nat. Biotechnol. *28*, 256–263.

Bejarano, E., and Cuervo, A.M. (2010). Chaperone-Mediated Autophagy. Proc. Am. Thorac. Soc. *7*, 29–39.

Bergamini, E., and Gori, Z. (2013). Towards an understanding of the anti-aging mechanism of dietary restriction: A signal transduction theory of aging. Aging Clin. Exp. Res. *7*, 473–475.

Bergamini, C.M., Gambetti, S., Dondi, A., and Cervellati, C. (2004). Oxygen, reactive oxygen species and tissue damage. Curr. Pharm. Des. *10*, 1611–1626.

Bergamini, E., Cavallini, G., Donati, A., and Gori, Z. (2007). The role of autophagy in aging: its essential part in the anti-aging mechanism of caloric restriction. Ann. N. Y. Acad. Sci. *1114*, 69–78.

Berk, C., and Sabbagh, M.N. (2013). Successes and failures for drugs in late-stage development for Alzheimer's disease. Drugs Aging *30*, 783–792.

den Besten, G., van Eunen, K., Groen, A.K., Venema, K., Reijngoud, D.-J., and Bakker, B.M. (2013). The role of short-chain fatty acids in the interplay between diet, gut microbiota, and host energy metabolism. J. Lipid Res. *54*, 2325–2340.

Bevilacqua, L., Ramsey, J.J., Hagopian, K., Weindruch, R., and Harper, M.-E. (2005). Long-term caloric restriction increases UCP3 content but decreases proton leak and reactive oxygen species production in rat skeletal muscle mitochondria. Am. J. Physiol. Endocrinol. Metab. *289*, E429-438.

Bhutani, S., Klempel, M.C., Berger, R.A., and Varady, K.A. (2010). Improvements in coronary heart disease risk indicators by alternate-day fasting involve adipose tissue modulations. Obes. Silver Spring Md *18*, 2152–2159.

Birgisdottir, Å.B., Lamark, T., and Johansen, T. (2013). The LIR motif - crucial for selective autophagy. J. Cell Sci. *126*, 3237–3247.

Bismuth, C., Garnier, R., Baud, F.J., Muszynski, J., and Keyes, C. (1990). Paraquat poisoning. An overview of the current status. Drug Saf. *5*, 243–251.

Blanc, S., Schoeller, D., Kemnitz, J., Weindruch, R., Colman, R., Newton, W., Wink, K., Baum, S., and Ramsey, J. (2003). Energy expenditure of rhesus monkeys subjected to 11 years of dietary restriction. J. Clin. Endocrinol. Metab. *88*, 16–23.

Bodkin, N.L., Alexander, T.M., Ortmeyer, H.K., Johnson, E., and Hansen, B.C. (2003). Mortality and morbidity in laboratory-maintained Rhesus monkeys and effects of long-term dietary restriction. J. Gerontol. A. Biol. Sci. Med. Sci. *58*, 212–219.

Boland, B., Kumar, A., Lee, S., Platt, F.M., Wegiel, J., Yu, W.H., and Nixon, R.A. (2008). Autophagy induction and autophagosome clearance in neurons: relationship to autophagic pathology in Alzheimer's disease. J. Neurosci. Off. J. Soc. Neurosci. *28*, 6926–6937.

Bordi, M., Berg, M.J., Mohan, P.S., Peterhoff, C.M., Alldred, M.J., Che, S., Ginsberg, S.D., and Nixon, R.A. (2016). Autophagy flux in CA1 neurons of Alzheimer hippocampus: Increased induction overburdens failing lysosomes to propel neuritic dystrophy. Autophagy *12*, 2467–2483.

Bosetti, F., Brizzi, F., Barogi, S., Mancuso, M., Siciliano, G., Tendi, E.A., Murri, L., Rapoport, S.I., and Solaini, G. (2002). Cytochrome c oxidase and mitochondrial F1F0-ATPase (ATP synthase) activities in platelets and brain from patients with Alzheimer's disease. Neurobiol. Aging *23*, 371–376.

Boya, P., González-Polo, R.-A., Casares, N., Perfettini, J.-L., Dessen, P., Larochette, N., Métivier, D., Meley, D., Souquere, S., Yoshimori, T., et al. (2005). Inhibition of Macroautophagy Triggers Apoptosis. Mol. Cell. Biol. *25*, 1025–1040.

Boya, P., Reggiori, F., and Codogno, P. (2013). Emerging regulation and functions of autophagy. Nat. Cell Biol. *15*, 713–720.

Braak, H., and Braak, E. (1991). Neuropathological stageing of Alzheimer-related changes. Acta Neuropathol. (Berl.) *82*, 239–259.

Brenmoehl, J., and Hoeflich, A. (2013). Dual control of mitochondrial biogenesis by sirtuin 1 and sirtuin 3. Mitochondrion *13*, 755–761.

Brentnall, M., Rodriguez-Menocal, L., De Guevara, R.L., Cepero, E., and Boise, L.H. (2013). Caspase-9, caspase-3 and caspase-7 have distinct roles during intrinsic apoptosis. BMC Cell Biol. *14*, 32.

Bruce-Keller, A.J., Umberger, G., McFall, R., and Mattson, M.P. (1999). Food restriction reduces brain damage and improves behavioral outcome following excitotoxic and metabolic insults. Ann. Neurol. *45*, 8–15.

Brunk, U.T., and Terman, A. (2002). The mitochondrial-lysosomal axis theory of aging: accumulation of damaged mitochondria as a result of imperfect autophagocytosis. Eur. J. Biochem. FEBS *269*, 1996–2002.

Burdick, D., Soreghan, B., Kwon, M., Kosmoski, J., Knauer, M., Henschen, A., Yates, J., Cotman, C., and Glabe, C. (1992). Assembly and aggregation properties of synthetic Alzheimer's A4/beta amyloid peptide analogs. J. Biol. Chem. *267*, 546–554.

Butler, D., Hwang, J., Estick, C., Nishiyama, A., Kumar, S.S., Baveghems, C., Young-Oxendine, H.B., Wisniewski, M.L., Charalambides, A., and Bahr, B.A. (2011). Protective effects of positive lysosomal modulation in Alzheimer's disease transgenic mouse models. PloS One *6*, e20501.

Butterfield, D.A. (2002). Amyloid beta-peptide (1-42)-induced oxidative stress and neurotoxicity: implications for neurodegeneration in Alzheimer's disease brain. A review. Free Radic. Res. *36*, 1307–1313.

Caballero, B., and Coto-Montes, A. (2012). An insight into the role of autophagy in cell responses in the aging and neurodegenerative brain. Histol. Histopathol. *27*, 263–275.

Caccamo, A., Majumder, S., Richardson, A., Strong, R., and Oddo, S. (2010). Molecular Interplay between Mammalian Target of Rapamycin (mTOR), Amyloid-β, and Tau. J. Biol. Chem. *285*, 13107–13120.

Caccamo, A., Maldonado, M.A., Majumder, S., Medina, D.X., Holbein, W., Magrí, A., and Oddo, S. (2011). Naturally Secreted Amyloid-β Increases Mammalian Target of Rapamycin (mTOR) Activity via a PRAS40-mediated Mechanism. J. Biol. Chem. *286*, 8924–8932.

Caccamo, A., Ferreira, E., Branca, C., and Oddo, S. (2017). p62 improves AD-like pathology by increasing autophagy. Mol. Psychiatry *22*, 865–873.

Cai, H., Wang, Y., McCarthy, D., Wen, H., Borchelt, D.R., Price, D.L., and Wong, P.C. (2001). BACE1 is the major beta-secretase for generation of Abeta peptides by neurons. Nat. Neurosci. *4*, 233–234.

Cai, Z., Zhou, Y., Liu, Z., Ke, Z., and Zhao, B. (2015). Autophagy dysfunction upregulates beta-amyloid peptides via enhancing the activity of γ-secretase complex. Neuropsychiatr. Dis. Treat. *11*, 2091–2099.

Cantara, S., Ziche, M., and Donnini, S. (2005). Opposite effects of beta amyloid on endothelial cell survival: role of fibroblast growth factor-2 (FGF-2). Pharmacol. Rep. PR *57 Suppl*, 138–143.

Castello, M.A., and Soriano, S. (2014). On the origin of Alzheimer's disease. Trials and tribulations of the amyloid hypothesis. Ageing Res. Rev. *13*, 10–12.

Castillo, K., Valenzuela, V., Matus, S., Nassif, M., Oñate, M., Fuentealba, Y., Encina, G., Irrazabal, T., Parsons, G., Court, F.A., et al. (2013). Measurement of autophagy flux in the nervous system *in vivo*. Cell Death Dis. *4*, e917.

Cataldo, A.M., Paskevich, P.A., Kominami, E., and Nixon, R.A. (1991). Lysosomal hydrolases of different classes are abnormally distributed in brains of patients with Alzheimer disease. Proc. Natl. Acad. Sci. U. S. A. *88*, 10998–11002.

Cataldo, A.M., Hamilton, D.J., Barnett, J.L., Paskevich, P.A., and Nixon, R.A. (1996). Properties of the endosomal-lysosomal system in the human central nervous system: disturbances mark most neurons in populations at risk to degenerate in Alzheimer's disease. J. Neurosci. Off. J. Soc. Neurosci. *16*, 186–199.

Cava, E., and Fontana, L. (2013). Will calorie restriction work in humans? Aging *5*, 507–514.

Cavieres, V.A., González, A., Muñoz, V.C., Yefi, C.P., Bustamante, H.A., Barraza, R.R., Tapia-Rojas, C., Otth, C., Barrera, M.J., González, C., et al. (2015). Tetrahydrohyperforin Inhibits the Proteolytic Processing of Amyloid Precursor Protein and Enhances Its Degradation by Atg5-Dependent Autophagy. PLoS ONE *10*.

Ceaser, E.K., Moellering, D.R., Shiva, S., Ramachandran, A., Landar, A., Venkartraman, A., Crawford, J., Patel, R., Dickinson, D.A., Ulasova, E., et al. (2004). Mechanisms of signal transduction mediated by oxidized lipids: the role of the electrophile-responsive proteome. Biochem. Soc. Trans. *32*, 151–155.

Cervenka, M.C., Henry, B., Nathan, J., Wood, S., and Volek, J.S. (2013). Worldwide dietary therapies for adults with epilepsy and other disorders. J. Child Neurol. *28*, 1034–1040.

Chakraborty, R. (2017). Caloric restriction and SirT1 modulate APP metabolism *in vitro* and *in vivo*.

Chatfield, D.A., and Fitzgerald, R.L. (2004). Liquid Chromatography-Mass Spectrometry: An Introduction. Robert E. Ardrey. Huddersfield, UK: Wiley, 2003, 276 pp., $110.00, hardcover. ISBN 0-471-49799-1. Clin. Chem. *50*, 261–262.

Cheignon, C., Tomas, M., Bonnefont-Rousselot, D., Faller, P., Hureau, C., and Collin, F. (2018). Oxidative stress and the amyloid beta peptide in Alzheimer's disease. Redox Biol. *14*, 450–464.

Chen, C., and Okayama, H. (1987). High-efficiency transformation of mammalian cells by plasmid DNA. Mol. Cell. Biol. *7*, 2745–2752.

Chen, Y., and Yu, L. (2017). Recent progress in autophagic lysosome reformation. Traffic *18*, 358–361.

Chen, G., Chen, K.S., Knox, J., Inglis, J., Bernard, A., Martin, S.J., Justice, A., McConlogue, L., Games, D., Freedman, S.B., et al. (2000). A learning deficit related to age and beta-amyloid plaques in a mouse model of Alzheimer's disease. Nature *408*, 975–979.

Chen, L., Yoo, S.-E., Na, R., Liu, Y., and Ran, Q. (2012). Cognitive impairment and increased Aβ levels induced by paraquat exposure are attenuated by enhanced removal of mitochondrial H2O2. Neurobiol. Aging *33*, 432.e15-432.e26.

Chen, L., Na, R., Boldt, E., and Ran, Q. (2015a). NLRP3 inflammasome activation by mitochondrial reactive oxygen species plays a key role in long-term cognitive impairment induced by paraquat exposure. Neurobiol. Aging *36*, 2533–2543.

Chen, X., Kondo, K., Motoki, K., Homma, H., and Okazawa, H. (2015b). Fasting activates macroautophagy in neurons of Alzheimer's disease mouse model but is insufficient to degrade amyloid-beta. Sci. Rep. *5*, 12115.

Chen, Z.-H., Saito, Y., Yoshida, Y., Sekine, A., Noguchi, N., and Niki, E. (2005). 4-Hydroxynonenal induces adaptive response and enhances PC12 cell tolerance primarily

through induction of thioredoxin reductase 1 via activation of Nrf2. J. Biol. Chem. *280*, 41921–41927.

Cherra, S.J., and Chu, C.T. (2008). Autophagy in neuroprotection and neurodegeneration: A question of balance. Future Neurol. *3*, 309–323.

Chesser, A.S., Pritchard, S.M., and Johnson, G.V.W. (2013). Tau clearance mechanisms and their possible role in the pathogenesis of Alzheimer disease. Front. Neurol. *4*, 122.

Chiva, C., and Sabidó, E. (2017). Peptide Selection for Targeted Protein Quantitation. J. Proteome Res. *16*, 1376–1380.

Cho, M.-H., Cho, K., Kang, H.-J., Jeon, E.-Y., Kim, H.-S., Kwon, H.-J., Kim, H.-M., Kim, D.-H., and Yoon, S.-Y. (2014). Autophagy in microglia degrades extracellular β-amyloid fibrils and regulates the NLRP3 inflammasome. Autophagy *10*, 1761–1775.

Christopher, M.A., Myrick, D.A., Barwick, B.G., Engstrom, A.K., Porter-Stransky, K.A., Boss, J.M., Weinshenker, D., Levey, A.I., and Katz, D.J. (2017). LSD1 protects against hippocampal and cortical neurodegeneration. Nat. Commun. *8*, 805.

Churchman, L.S., and Spudich, J.A. (2012). Colocalization of Fluorescent Probes: Accurate and Precise Registration with Nanometer Resolution. Cold Spring Harb. Protoc. *2012*, 141–149.

Cirrito, J.R., May, P.C., O'Dell, M.A., Taylor, J.W., Parsadanian, M., Cramer, J.W., Audia, J.E., Nissen, J.S., Bales, K.R., Paul, S.M., et al. (2003). *In vivo* assessment of brain interstitial fluid with microdialysis reveals plaque-associated changes in amyloid-beta metabolism and half-life. J. Neurosci. Off. J. Soc. Neurosci. *23*, 8844–8853.

Cleveland, D.W., and Rothstein, J.D. (2001). From Charcot to Lou Gehrig: deciphering selective motor neuron death in ALS. Nat. Rev. Neurosci. *2*, 806–819.

Colacurcio, D.J., and Nixon, R.A. (2016). Disorders of lysosomal acidification—The emerging role of v-ATPase in aging and neurodegenerative disease. Ageing Res. Rev. *32*, 75–88.

Collier, R. (2013). Intermittent fasting: the science of going without. CMAJ Can. Med. Assoc. J. *185*, E363–E364.

Colman, R.J., Anderson, R.M., Johnson, S.C., Kastman, E.K., Kosmatka, K.J., Beasley, T.M., Allison, D.B., Cruzen, C., Simmons, H.A., Kemnitz, J.W., et al. (2009). Caloric restriction delays disease onset and mortality in rhesus monkeys. Science *325*, 201–204.

Colman, R.J., Beasley, T.M., Allison, D.B., and Weindruch, R. (2012). Skeletal effects of long-term caloric restriction in rhesus monkeys. Age Dordr. Neth. *34*, 1133–1143.

Colman, R.J., Beasley, T.M., Kemnitz, J.W., Johnson, S.C., Weindruch, R., and Anderson, R.M. (2014). Caloric restriction reduces age-related and all-cause mortality in rhesus monkeys. Nat. Commun. *5*, 3557.

Colquhoun, D. (2014). An investigation of the false discovery rate and the misinterpretation of *p*-values. Open Sci. *1*, 140216.

Cuervo, A.M. (2004). Autophagy: in sickness and in health. Trends Cell Biol. *14*, 70–77.

Cuervo, A.M., and Dice, J.F. (1996). A receptor for the selective uptake and degradation of proteins by lysosomes. Science *273*, 501–503.

Cuervo, A.M., and Dice, J.F. (2000a). Age-related decline in chaperone-mediated autophagy. J. Biol. Chem. *275*, 31505–31513.

Cuervo, A.M., and Dice, J.F. (2000b). Regulation of lamp2a levels in the lysosomal membrane. Traffic Cph. Den. *1*, 570–583.

Cuervo, A.M., Knecht, E., Terlecky, S.R., and Dice, J.F. (1995a). Activation of a selective pathway of lysosomal proteolysis in rat liver by prolonged starvation. Am. J. Physiol. *269*, C1200-1208.

Cuervo, A.M., Palmer, A., Rivett, A.J., and Knecht, E. (1995b). Degradation of proteasomes by lysosomes in rat liver. Eur. J. Biochem. FEBS *227*, 792–800.

Cuervo, A.M., Dice, J.F., and Knecht, E. (1997). A Population of Rat Liver Lysosomes Responsible for the Selective Uptake and Degradation of Cytosolic Proteins. J. Biol. Chem. *272*, 5606–5615.

Cuervo, A.M., Hu, W., Lim, B., and Dice, J.F. (1998). IκB Is a Substrate for a Selective Pathway of Lysosomal Proteolysis. Mol. Biol. Cell *9*, 1995–2010.

Cuervo, A.M., Gomes, A.V., Barnes, J.A., and Dice, J.F. (2000). Selective degradation of annexins by chaperone-mediated autophagy. J. Biol. Chem. *275*, 33329–33335.

Cuervo, A.M., Stefanis, L., Fredenburg, R., Lansbury, P.T., and Sulzer, D. (2004). Impaired degradation of mutant alpha-synuclein by chaperone-mediated autophagy. Science *305*, 1292–1295.

Cummings, J., and Fox, N. (2017). Defining Disease Modifying Therapy for Alzheimer's Disease. J. Prev. Alzheimers Dis. *4*, 109–115.

Cunha-Santos, J., Duarte-Neves, J., Carmona, V., Guarente, L., Pereira de Almeida, L., and Cavadas, C. (2016). Caloric restriction blocks neuropathology and motor deficits in Machado–Joseph disease mouse models through SIRT1 pathway. Nat. Commun. *7*.

Deane, R., Du Yan, S., Submamaryan, R.K., LaRue, B., Jovanovic, S., Hogg, E., Welch, D., Manness, L., Lin, C., Yu, J., et al. (2003). RAGE mediates amyloid-beta peptide transport across the blood-brain barrier and accumulation in brain. Nat. Med. *9*, 907–913.

Deane, R., Bell, R., Sagare, A., and Zlokovic, B. (2009). Clearance of amyloid-β peptide across the blood-brain barrier: Implication for therapies in Alzheimer's disease. CNS Neurol. Disord. Drug Targets *8*, 16–30.

DeKosky, S.T., and Scheff, S.W. (1990). Synapse loss in frontal cortex biopsies in Alzheimer's disease: correlation with cognitive severity. Ann. Neurol. *27*, 457–464.

Del Campo, M., Hoozemans, J.J.M., Dekkers, L.-L., Rozemuller, A.J., Korth, C., Müller-Schiffmann, A., Scheltens, P., Blankenstein, M.A., Jimenez, C.R., Veerhuis, R., et al. (2014). BRI2-BRICHOS is increased in human amyloid plaques in early stages of Alzheimer's disease. Neurobiol. Aging *35*, 1596–1604.

Delgado, M.E., Dyck, L., Laussmann, M.A., and Rehm, M. (2014). Modulation of apoptosis sensitivity through the interplay with autophagic and proteasomal degradation pathways. Cell Death Dis. *5*, e1011.

Deng, Y., Hou, D., Tian, M., Li, W., and Feng, X. (2014). [β-amyloid peptide deposition and expression of related miRNAs in the cerebellum of a mouse model of Alzheimer's disease]. Nan Fang Yi Ke Da Xue Xue Bao *34*, 323–328.

Deter, R.L., and de Duve, C. (1967). INFLUENCE OF GLUCAGON, AN INDUCER OF CELLULAR AUTOPHAGY, ON SOME PHYSICAL PROPERTIES OF RAT LIVER LYSOSOMES. J. Cell Biol. *33*, 437–449.

Deter, R.L., Baudhuin, P., and de Duve, C. (1967). PARTICIPATION OF LYSOSOMES IN CELLULAR AUTOPHAGY INDUCED IN RAT LIVER BY GLUCAGON. J. Cell Biol. *35*, C11–C16.

Dhurandhar, E.J., Allison, D.B., Groen, T. van, and Kadish, I. (2013). Hunger in the Absence of Caloric Restriction Improves Cognition and Attenuates Alzheimer's Disease Pathology in a Mouse Model. PLOS ONE *8*, e60437.

Di Fede, G., Catania, M., Morbin, M., Rossi, G., Suardi, S., Mazzoleni, G., Merlin, M., Giovagnoli, A.R., Prioni, S., Erbetta, A., et al. (2009). A recessive mutation in the APP gene with dominant-negative effect on amyloidogenesis. Science *323*, 1473–1477.

Di Luca, A., Henry, M., Meleady, P., and O'Connor, R. (2015). Label-free LC-MS analysis of HER2+ breast cancer cell line response to HER2 inhibitor treatment. Daru J. Fac. Pharm. Tehran Univ. Med. Sci. *23*, 40.

Dice, J.F. (1987). Molecular determinants of protein half-lives in eukaryotic cells. FASEB J. Off. Publ. Fed. Am. Soc. Exp. Biol. *1*, 349–357.

Dice, J.F. (1990). Peptide sequences that target cytosolic proteins for lysosomal proteolysis. Trends Biochem. Sci. *15*, 305–309.

Dice, J.F. (2007). Chaperone-mediated autophagy. Autophagy *3*, 295–299.

Dickerson, B.C., Brickhouse, M., McGinnis, S., and Wolk, D.A. (2016). Alzheimer's disease: The influence of age on clinical heterogeneity through the human brain connectome. Alzheimers Dement. Diagn. Assess. Dis. Monit. *6*, 122–135.

Dickerson, B.C., McGinnis, S.M., Xia, C., Price, B.H., Atri, A., Murray, M.E., Mendez, M.F., and Wolk, D.A. (2017). Approach to atypical Alzheimer's disease and case studies of the major subtypes. CNS Spectr. 1–11.

Dobashi, S., Aiba, C., Ando, D., Kiuchi, M., Yamakita, M., and Koyama, K. (2018). Caloric restriction suppresses exercise-induced hippocampal BDNF expression in young male rats. J. Phys. Fit. Sports Med. *7*, 239–245.

Dobrowolska, J.A., Michener, M.S., Wu, G., Patterson, B.W., Chott, R., Ovod, V., Pyatkivskyy, Y., Wildsmith, K.R., Kasten, T., Mathers, P., et al. (2014). CNS amyloid-β, soluble APP-α and -β kinetics during BACE inhibition. J. Neurosci. Off. J. Soc. Neurosci. *34*, 8336–8346.

Domenico, I.D., Ward, D.M., and Kaplan, J. (2010). Autophagy, ferritin and iron chelation. Autophagy *6*, 157–157.

Donati, A. (2006). The involvement of macroautophagy in aging and anti-aging interventions. Mol. Aspects Med. *27*, 455–470.

Donati, A., Cavallini, G., and Bergamini, E. (2013). Effects of aging, antiaging calorie restriction and *in vivo* stimulation of autophagy on the urinary excretion of 8OHdG in male Sprague–Dawley rats. Age *35*, 261–270.

Dorszewska, J., Prendecki, M., Oczkowska, A., Dezor, M., and Kozubski, W. (2016). Molecular Basis of Familial and Sporadic Alzheimer's Disease. Curr. Alzheimer Res. *13*, 952–963.

Douglas, P.M., and Dillin, A. (2010). Protein homeostasis and aging in neurodegeneration. J. Cell Biol. *190*, 719–729.

Drechsel, D.A., and Patel, M. (2008). Role of reactive oxygen species in the neurotoxicity of environmental agents implicated in Parkinson's disease. Free Radic. Biol. Med. *44*, 1873–1886.

Du, J., Liang, Y., Xu, F., Sun, B., and Wang, Z. (2013). Trehalose rescues Alzheimer's disease phenotypes in APP/PS1 transgenic mice. J. Pharm. Pharmacol. *65*, 1753–1756.

Duan, W., and Mattson, M.P. (1999). Dietary restriction and 2-deoxyglucose administration improve behavioral outcome and reduce degeneration of dopaminergic neurons in models of Parkinson's disease. J. Neurosci. Res. *57*, 195–206.

Duncan, C., Papanikolaou, T., and Ellerby, L.M. (2010). Autophagy: polyQ toxic fragment turnover. Autophagy *6*, 312–314.

Dutta, M., Subramani, E., Taunk, K., Gajbhiye, A., Seal, S., Pendharkar, N., Dhali, S., Ray, C.D., Lodh, I., Chakravarty, B., et al. (2015). Mass spectrometry and bioinformatics analysis data. Data Brief *2*, 21.

Dwarakanath, B.S., Singh, D., Banerji, A.K., Sarin, R., Venkataramana, N.K., Jalali, R., Vishwanath, P.N., Mohanti, B.K., Tripathi, R.P., Kalia, V.K., et al. (2009). Clinical studies for improving radiotherapy with 2-deoxy-D-glucose: present status and future prospects. J. Cancer Res. Ther. *5 Suppl 1*, S21-26.

Ebner, M., Sinkovics, B., Szczygieł, M., Ribeiro, D.W., and Yudushkin, I. (2017). Localization of mTORC2 activity inside cells. J Cell Biol jcb.201610060.

Eckert, A., Steiner, B., Marques, C., Leutz, S., Romig, H., Haass, C., and Müller, W.E. (2001). Elevated vulnerability to oxidative stress-induced cell death and activation of caspase-3 by the Swedish amyloid precursor protein mutation. J. Neurosci. Res. *64*, 183–192.

Edens, B.M., Miller, N., and Ma, Y.-C. (2016). Impaired Autophagy and Defective Mitochondrial Function: Converging Paths on the Road to Motor Neuron Degeneration. Front. Cell. Neurosci. *10*.

Eisenberg, T., Knauer, H., Schauer, A., Büttner, S., Ruckenstuhl, C., Carmona-Gutierrez, D., Ring, J., Schroeder, S., Magnes, C., Antonacci, L., et al. (2009). Induction of autophagy by spermidine promotes longevity. Nat. Cell Biol. *11*, 1305–1314.

Endo, H., Saito, A., and Chan, P.H. (2006). Mitochondrial translocation of p53 underlies the selective death of hippocampal CA1 neurons after global cerebral ischaemia. Biochem. Soc. Trans. *34*, 1283–1286.

Eskelinen, E.-L. (2005). Maturation of autophagic vacuoles in Mammalian cells. Autophagy *1*, 1–10.

Eskelinen, E.-L. (2008). To be or not to be? Examples of incorrect identification of autophagic compartments in conventional transmission electron microscopy of mammalian cells. Autophagy *4*, 257–260.

Eskelinen, E.-L., and Kovács, A.L. (2011). Double membranes vs. lipid bilayers, and their significance for correct identification of macroautophagic structures. Autophagy *7*, 931–932.

Eskelinen, E.-L., Reggiori, F., Baba, M., Kovács, A.L., and Seglen, P.O. (2011). Seeing is believing: the impact of electron microscopy on autophagy research. Autophagy *7*, 935–956.

Feng, Z. (2010). p53 Regulation of the IGF-1/AKT/mTOR Pathways and the Endosomal Compartment. Cold Spring Harb. Perspect. Biol. *2*.

Feng, T., Tammineni, P., Agrawal, C., Jeong, Y.Y., and Cai, Q. (2016). Autophagy-Mediated Regulation of BACE1 Trafficking and Degradation. J. Biol. Chem. jbc.M116.766584.

Ferreira-Marques, M., Aveleira, C.A., Carmo-Silva, S., Botelho, M., de Almeida, L.P., and Cavadas, C. (2016). Caloric restriction stimulates autophagy in rat cortical neurons through neuropeptide Y and ghrelin receptors activation. Aging *8*, 1470–1484.

Ferri, C.P., and Jacob, K.S. (2017). Dementia in low-income and middle-income countries: Different realities mandate tailored solutions. PLOS Med. *14*, e1002271.

Filimonenko, M., Isakson, P., Finley, K.D., Anderson, M., Jeong, H., Melia, T.J., Bartlett, B.J., Myers, K.M., Birkeland, H.C.G., Lamark, T., et al. (2010). The selective macroautophagic degradation of aggregated proteins requires the PI3P-binding protein Alfy. Mol. Cell *38*, 265–279.

Finn, P.F., and Dice, J.F. (2005). Ketone bodies stimulate chaperone-mediated autophagy. J. Biol. Chem. *280*, 25864–25870.

Fischer, K.E., Gelfond, J.A.L., Soto, V.Y., Han, C., Someya, S., Richardson, A., and Austad, S.N. (2015). Health Effects of Long-Term Rapamycin Treatment: The Impact on Mouse Health of Enteric Rapamycin Treatment from Four Months of Age throughout Life. PLOS ONE *10*, e0126644.

Flora, S.J.S. (2007). Role of free radicals and antioxidants in health and disease. Cell. Mol. Biol. Noisy--Gd. Fr. *53*, 1–2.

Floyd, R.A., and Hensley, K. (2002). Oxidative stress in brain aging. Implications for therapeutics of neurodegenerative diseases. Neurobiol. Aging *23*, 795–807.

Folch, J., Petrov, D., Ettcheto, M., Abad, S., S&#xe1, nchez-L&#xf3, Pez, E., Garc&#xed, A, M.L., Olloquequi, J., et al. (2016). Current Research Therapeutic Strategies for Alzheimer’s Disease Treatment.

Folch, J., Ettcheto, M., Petrov, D., Abad, S., Pedrós, I., Marin, M., Olloquequi, J., and Camins, A. (2017). Review of the advances in treatment for Alzheimer disease: strategies for combating β-amyloid protein. Neurol. Engl. Ed.

Fonseca, A.C., Oliveira, C.R., Pereira, C.F., and Cardoso, S.M. (2014). Loss of proteostasis induced by amyloid beta peptide in brain endothelial cells. Biochim. Biophys. Acta BBA - Mol. Cell Res. *1843*, 1150–1161.

Fontana, L., Partridge, L., and Longo, V.D. (2010). Extending healthy life span--from yeast to humans. Science *328*, 321–326.

Forster, M.J., Sohal, B.H., and Sohal, R.S. (2000). Reversible Effects of Long-Term Caloric Restriction on Protein Oxidative Damage. J. Gerontol. Ser. A *55*, B522–B529.

Fotinopoulou, A., Tsachaki, M., Vlavaki, M., Poulopoulos, A., Rostagno, A., Frangione, B., Ghiso, J., and Efthimiopoulos, S. (2005). BRI2 interacts with amyloid precursor protein (APP) and regulates amyloid beta (Abeta) production. J. Biol. Chem. *280*, 30768–30772.

François, A., Terro, F., Janet, T., Bilan, A.R., Paccalin, M., and Page, G. (2013). Involvement of interleukin-1β in the autophagic process of microglia: relevance to Alzheimer's disease. J. Neuroinflammation *10*, 915.

François, A., Rioux Bilan, A., Quellard, N., Fernandez, B., Janet, T., Chassaing, D., Paccalin, M., Terro, F., and Page, G. (2014). Longitudinal follow-up of autophagy and inflammation in brain of APPswePS1dE9 transgenic mice. J. Neuroinflammation *11*, 139.

Fukumoto, H., Cheung, B.S., Hyman, B.T., and Irizarry, M.C. (2002). Beta-secretase protein and activity are increased in the neocortex in Alzheimer disease. Arch. Neurol. *59*, 1381–1389.

Fukumoto, H., Rosene, D.L., Moss, M.B., Raju, S., Hyman, B.T., and Irizarry, M.C. (2004). Beta-secretase activity increases with aging in human, monkey, and mouse brain. Am. J. Pathol. *164*, 719–725.

Galan-Acosta, L., Xia, H., Yuan, J., and Vakifahmetoglu-Norberg, H. (2015). Activation of chaperone-mediated autophagy as a potential anticancer therapy. Autophagy *11*, 2370–2371.

Galluzzi, L., Bravo-San Pedro, J.M., Levine, B., Green, D.R., and Kroemer, G. (2017). Pharmacological modulation of autophagy: therapeutic potential and persisting obstacles. Nat. Rev. Drug Discov. *16*, 487–511.

Gan, L., Liu, Z., Luo, D., Ren, Q., Wu, H., Li, C., and Sun, C. (2017). Reduced Endoplasmic Reticulum Stress-Mediated Autophagy Is Required for Leptin Alleviating Inflammation in Adipose Tissue. Front. Immunol. *8*.

Ganley, I.G., Lam, D.H., Wang, J., Ding, X., Chen, S., and Jiang, X. (2009). ULK1.ATG13.FIP200 complex mediates mTOR signaling and is essential for autophagy. J. Biol. Chem. *284*, 12297–12305.

Gao, L.-B., Yu, X.-F., Chen, Q., and Zhou, D. (2016). Alzheimer's Disease therapeutics: current and future therapies. Minerva Med. *107*, 108–113.

García-Prat, L., Martínez-Vicente, M., Perdiguero, E., Ortet, L., Rodríguez-Ubreva, J., Rebollo, E., Ruiz-Bonilla, V., Gutarra, S., Ballestar, E., Serrano, A.L., et al. (2016). Autophagy maintains stemness by preventing senescence. Nature *529*, nature16187.

Garriga-Canut, M., Schoenike, B., Qazi, R., Bergendahl, K., Daley, T.J., Pfender, R.M., Morrison, J.F., Ockuly, J., Stafstrom, C., Sutula, T., et al. (2006). 2-Deoxy-D-glucose reduces epilepsy progression by NRSF-CtBP-dependent metabolic regulation of chromatin structure. Nat. Neurosci. *9*, 1382–1387.

Gelino, S., and Hansen, M. (2012). Autophagy - An Emerging Anti-Aging Mechanism. J. Clin. Exp. Pathol. *Suppl 4*.

Gervais, F.G., Xu, D., Robertson, G.S., Vaillancourt, J.P., Zhu, Y., Huang, J., LeBlanc, A., Smith, D., Rigby, M., Shearman, M.S., et al. (1999). Involvement of caspases in proteolytic cleavage of Alzheimer's amyloid-beta precursor protein and amyloidogenic A beta peptide formation. Cell *97*, 395–406.

Giasson, B.I., Lee, V.M.Y., and Trojanowski, J.Q. (2003). Interactions of amyloidogenic proteins. NeuroMolecular Med. *4*, 49–58.

Giller, K., Huebbe, P., Hennig, S., Dose, J., Pallauf, K., Doering, F., and Rimbach, G. (2013). Beneficial effects of a 6-month dietary restriction are time-dependently abolished within 2 weeks or 6 months of refeeding-genome-wide transcriptome analysis in mouse liver. Free Radic. Biol. Med. *61*, 170–178.

Glenner, G.G., and Wong, C.W. (1984). Alzheimer's disease and Down's syndrome: Sharing of a unique cerebrovascular amyloid fibril protein. Biochem. Biophys. Res. Commun. *122*, 1131–1135.

Goate, A., Chartier-Harlin, M.C., Mullan, M., Brown, J., Crawford, F., Fidani, L., Giuffra, L., Haynes, A., Irving, N., and James, L. (1991). Segregation of a missense mutation in the amyloid precursor protein gene with familial Alzheimer's disease. Nature *349*, 704–706.

Gobeil, S., Boucher, C.C., Nadeau, D., and Poirier, G.G. (2001). Characterization of the necrotic cleavage of poly(ADP-ribose) polymerase (PARP-1): implication of lysosomal proteases. Cell Death Differ. *8*, 588–594.

Gomes, A.P., Price, N.L., Ling, A.J.Y., Moslehi, J.J., Montgomery, M.K., Rajman, L., White, J.P., Teodoro, J.S., Wrann, C.D., Hubbard, B.P., et al. (2013). Declining NAD(+) induces a pseudohypoxic state disrupting nuclear-mitochondrial communication during aging. Cell *155*, 1624–1638.

Goodrick, C.L., Ingram, D.K., Reynolds, M.A., Freeman, J.R., and Cider, N. (1990). Effects of intermittent feeding upon body weight and lifespan in inbred mice: interaction of genotype and age. Mech. Ageing Dev. *55*, 69–87.

Gouras, G.K., Tsai, J., Naslund, J., Vincent, B., Edgar, M., Checler, F., Greenfield, J.P., Haroutunian, V., Buxbaum, J.D., Xu, H., et al. (2000). Intraneuronal Abeta42 accumulation in human brain. Am. J. Pathol. *156*, 15–20.

Gowrishankar, S., Yuan, P., Wu, Y., Schrag, M., Paradise, S., Grutzendler, J., De Camilli, P., and Ferguson, S.M. (2015). Massive accumulation of luminal protease-deficient axonal lysosomes at Alzheimer's disease amyloid plaques. Proc. Natl. Acad. Sci. U. S. A. *112*, E3699–E3708.

Gradnigo, J.S., Majumdar, A., Jr, R.B.N., and Moriyama, E.N. (2016). Advantages of an Improved Rhesus Macaque Genome for Evolutionary Analyses. PLOS ONE *11*, e0167376.

Gräff, J., Kahn, M., Samiei, A., Gao, J., Ota, K.T., Rei, D., and Tsai, L.-H. (2013). A dietary regimen of caloric restriction or pharmacological activation of SIRT1 to delay the onset of neurodegeneration. J. Neurosci. Off. J. Soc. Neurosci. *33*, 8951–8960.

Gravina, S.A., Ho, L., Eckman, C.B., Long, K.E., Otvos, L., Younkin, L.H., Suzuki, N., and Younkin, S.G. (1995). Amyloid beta protein (A beta) in Alzheimer's disease brain. Biochemical

and immunocytochemical analysis with antibodies specific for forms ending at A beta 40 or A beta 42(43). J. Biol. Chem. *270*, 7013–7016.

Gredilla, R., and Barja, G. (2005). Minireview: The Role of Oxidative Stress in Relation to Caloric Restriction and Longevity. Endocrinology *146*, 3713–3717.

Greene, A.E., Todorova, M.T., McGowan, R., and Seyfried, T.N. (2001). Caloric restriction inhibits seizure susceptibility in epileptic EL mice by reducing blood glucose. Epilepsia *42*, 1371–1378.

Greener, M. (2014). The link between laughing death and Alzheimer's disease. Prog. Neurol. Psychiatry *18*, 9–12.

Greer, E.L., Dowlatshahi, D., Banko, M.R., Villen, J., Hoang, K., Blanchard, D., Gygi, S.P., and Brunet, A. (2007). An AMPK-FOXO pathway mediates longevity induced by a novel method of dietary restriction in C. elegans. Curr. Biol. CB *17*, 1646–1656.

Gremer, L., Schölzel, D., Schenk, C., Reinartz, E., Labahn, J., Ravelli, R.B.G., Tusche, M., Lopez-Iglesias, C., Hoyer, W., Heise, H., et al. (2017). Fibril structure of amyloid-β(1-42) by cryo-electron microscopy. Science *358*, 116–119.

Guertin, D.A., and Sabatini, D.M. (2007). Defining the role of mTOR in cancer. Cancer Cell *12*, 9–22.

Guo, J.Y., and White, E. (2016). Autophagy, Metabolism, and Cancer. Cold Spring Harb. Symp. Quant. Biol. *81*, 73–78.

Guo, Z.H., and Mattson, M.P. (2000). *In vivo* 2-deoxyglucose administration preserves glucose and glutamate transport and mitochondrial function in cortical synaptic terminals after exposure to amyloid beta-peptide and iron: evidence for a stress response. Exp. Neurol. *166*, 173–179.

Guo, J., Bakshi, V., and Lin, A.-L. (2015). Early Shifts of Brain Metabolism by Caloric Restriction Preserve White Matter Integrity and Long-Term Memory in Aging Mice. Front. Aging Neurosci. *7*.

Guo, X., Kimura, A., Azuchi, Y., Akiyama, G., Noro, T., Harada, C., Namekata, K., and Harada, T. (2016). Caloric restriction promotes cell survival in a mouse model of normal tension glaucoma. Sci. Rep. *6*, srep33950.

Gutierrez, M.G., Munafó, D.B., Berón, W., and Colombo, M.I. (2004). Rab7 is required for the normal progression of the autophagic pathway in mammalian cells. J. Cell Sci. *117*, 2687–2697.

Haass, C., Schlossmacher, M.G., Hung, A.Y., Vigo-Pelfrey, C., Mellon, A., Ostaszewski, B.L., Lieberburg, I., Koo, E.H., Schenk, D., and Teplow, D.B. (1992). Amyloid beta-peptide is produced by cultured cells during normal metabolism. Nature *359*, 322–325.

Haass, C., Kaether, C., Thinakaran, G., and Sisodia, S. (2012). Trafficking and Proteolytic Processing of APP. Cold Spring Harb. Perspect. Med. *2*.

Hara, T., Nakamura, K., Matsui, M., Yamamoto, A., Nakahara, Y., Suzuki-Migishima, R., Yokoyama, M., Mishima, K., Saito, I., Okano, H., et al. (2006). Suppression of basal autophagy in neural cells causes neurodegenerative disease in mice. Nature *441*, 885–889.

Hardy, J., and Selkoe, D.J. (2002). The amyloid hypothesis of Alzheimer's disease: progress and problems on the road to therapeutics. Science *297*, 353–356.

Hardy, J.A., and Higgins, G.A. (1992). Alzheimer's disease: the amyloid cascade hypothesis. Science *256*, 184–185.

Hariharan, N., Zhai, P., and Sadoshima, J. (2011). Oxidative stress stimulates autophagic flux during ischemia/reperfusion. Antioxid. Redox Signal. *14*, 2179–2190.

Harman, D. (1956). Aging: a theory based on free radical and radiation chemistry. J. Gerontol. *11*, 298–300.

Harvey, A.E., Lashinger, L.M., Hays, D., Harrison, L.M., Lewis, K., Fischer, S.M., and Hursting, S.D. (2014). Calorie Restriction Decreases Murine and Human Pancreatic Tumor Cell Growth, Nuclear Factor-κB Activation, and Inflammation-Related Gene Expression in an Insulin-like Growth Factor-1−Dependent Manner. PLOS ONE *9*, e94151.

Harvie, M., and Howell, A. (2012). Energy restriction and the prevention of breast cancer. Proc. Nutr. Soc. *71*, 263–275.

Hashimoto, M., Rockenstein, E., Crews, L., and Masliah, E. (2003). Role of protein aggregation in mitochondrial dysfunction and neurodegeneration in Alzheimer's and Parkinson's diseases. Neuromolecular Med. *4*, 21–36.

Hayashi, S., Sato, N., Yamamoto, A., Ikegame, Y., Nakashima, S., Ogihara, T., and Morishita, R. (2009). Alzheimer Disease–Associated Peptide, Amyloid β40, Inhibits Vascular Regeneration with Induction of Endothelial Autophagy. Arterioscler. Thromb. Vasc. Biol. *29*, 1909–1915.

Hayashi-Nishino, M., Fujita, N., Noda, T., Yamaguchi, A., Yoshimori, T., and Yamamoto, A. (2009). A subdomain of the endoplasmic reticulum forms a cradle for autophagosome formation. Nat. Cell Biol. *11*, 1433–1437.

He, K., Fu, Y., Zeng, W.-F., Luo, L., Chi, H., Liu, C., Qing, L.-Y., Sun, R.-X., and He, S.-M. (2015). A theoretical foundation of the target-decoy search strategy for false discovery rate control in proteomics. ArXiv150100537 Math Stat.

Head, D., Bugg, J.M., Goate, A.M., Fagan, A.M., Mintun, M.A., Benzinger, T., Holtzman, D.M., and Morris, J.C. (2012). Exercise Engagement as a Moderator of the Effects of APOE Genotype on Amyloid Deposition. Arch. Neurol. *69*, 636–643.

Heckmann, B.L., Yang, X., Zhang, X., and Liu, J. (2013). The autophagic inhibitor 3-methyladenine potently stimulates PKA-dependent lipolysis in adipocytes. Br. J. Pharmacol. *168*, 163–171.

Heilbronn, L.K., de Jonge, L., Frisard, M.I., DeLany, J.P., Larson-Meyer, D.E., Rood, J., Nguyen, T., Martin, C.K., Volaufova, J., Most, M.M., et al. (2006). Effect of 6-month calorie restriction on biomarkers of longevity, metabolic adaptation, and oxidative stress in overweight individuals: a randomized controlled trial. JAMA *295*, 1539–1548.

Heras-Sandoval, D., Pérez-Rojas, J.M., Hernández-Damián, J., and Pedraza-Chaverri, J. (2014). The role of PI3K/AKT/mTOR pathway in the modulation of autophagy and the clearance of protein aggregates in neurodegeneration. Cell. Signal. *26*, 2694–2701.

Hirai, K., Aliev, G., Nunomura, A., Fujioka, H., Russell, R.L., Atwood, C.S., Johnson, A.B., Kress, Y., Vinters, H.V., Tabaton, M., et al. (2001). Mitochondrial abnormalities in Alzheimer's disease. J. Neurosci. Off. J. Soc. Neurosci. *21*, 3017–3023.

Holsinger, R.M.D., McLean, C.A., Beyreuther, K., Masters, C.L., and Evin, G. (2002). Increased expression of the amyloid precursor beta-secretase in Alzheimer's disease. Ann. Neurol. *51*, 783–786.

Holtzman, D.M., Goate, A., Kelly, J., and Sperling, R. (2011). Mapping the road forward in Alzheimer's disease. Sci. Transl. Med. *3*, 114ps48.

Hondius, D.C., Nierop, P. van, Li, K.W., Hoozemans, J.J.M., Schors, R.C. van der, Haastert, E.S. van, Vies, S.M. van der, Rozemuller, A.J.M., and Smit, A.B. (2016). Profiling the human hippocampal proteome at all pathologic stages of Alzheimer's disease. Alzheimers Dement. J. Alzheimers Assoc. *0*.

Hong, L., Huang, H.-C., and Jiang, Z.-F. (2014). Relationship between amyloid-beta and the ubiquitin-proteasome system in Alzheimer's disease. Neurol. Res. *36*, 276–282.

Hong, S., Quintero-Monzon, O., Ostaszewski, B.L., Podlisny, D.R., Cavanaugh, W.T., Yang, T., Holtzman, D.M., Cirrito, J.R., and Selkoe, D.J. (2011). Dynamic analysis of amyloid β-protein in behaving mice reveals opposing changes in ISF versus parenchymal Aβ during age-related plaque formation. J. Neurosci. Off. J. Soc. Neurosci. *31*, 15861–15869.

Hosokawa, N., Hara, T., Kaizuka, T., Kishi, C., Takamura, A., Miura, Y., Iemura, S., Natsume, T., Takehana, K., Yamada, N., et al. (2009). Nutrient-dependent mTORC1 association with the ULK1-Atg13-FIP200 complex required for autophagy. Mol. Biol. Cell *20*, 1981–1991.

Hosp, F., and Mann, M. (2017). A Primer on Concepts and Applications of Proteomics in Neuroscience. Neuron *96*, 558–571.

Hou, H., Zhang, Y., Huang, Y., Yi, Q., Lv, L., Zhang, T., Chen, D., Hao, Q., and Shi, Q. (2012). Inhibitors of Phosphatidylinositol 3′-Kinases Promote Mitotic Cell Death in HeLa Cells. PLOS ONE *7*, e35665.

Hu, X., He, W., Luo, X., Tsubota, K.E., and Yan, R. (2013). BACE1 regulates hippocampal astrogenesis via the Jagged1-Notch pathway. Cell Rep. *4*, 40–49.

Huang, C.-L., Chao, C.-C., Lee, Y.-C., Lu, M.-K., Cheng, J.-J., Yang, Y.-C., Wang, V.-C., Chang, W.-C., and Huang, N.-K. (2016). Paraquat Induces Cell Death Through Impairing Mitochondrial Membrane Permeability. Mol. Neurobiol. *53*, 2169–2188.

Huang, R., Xu, Y., Wan, W., Shou, X., Qian, J., You, Z., Liu, B., Chang, C., Zhou, T., Lippincott-Schwartz, J., et al. (2015). Deacetylation of nuclear LC3 drives autophagy initiation under starvation. Mol. Cell *57*, 456–466.

Hunt, N.D., Li, G.D., Zhu, M., Miller, M., Levette, A., Chachich, M.E., Spangler, E.L., Allard, J.S., Hyun, D.-H., Ingram, D.K., et al. (2012). Effect of calorie restriction and refeeding on skin wound healing in the rat. Age Dordr. Neth. *34*, 1453–1458.

Hursting, S.D., Smith, S.M., Lashinger, L.M., Harvey, A.E., and Perkins, S.N. (2010). Calories and carcinogenesis: lessons learned from 30 years of calorie restriction research. Carcinogenesis *31*, 83–89.

Hursting, S.D., Dunlap, S.M., Ford, N.A., Hursting, M.J., and Lashinger, L.M. (2013). Calorie restriction and cancer prevention: a mechanistic perspective. Cancer Metab. *1*, 10.

Hüttemann, M., Pecina, P., Rainbolt, M., Sanderson, T.H., Kagan, V.E., Samavati, L., Doan, J.W., and Lee, I. (2011). The multiple functions of cytochrome c and their regulation in life and death decisions of the mammalian cell: from respiration to apoptosis. Mitochondrion *11*, 369–381.

Huynh, R.A., and Mohan, C. (2017). Alzheimer's Disease: Biomarkers in the Genome, Blood, and Cerebrospinal Fluid. Front. Neurol. *8*.

Hyun, D.-H., Emerson, S.S., Jo, D.-G., Mattson, M.P., and Cabo, R. de (2006). Calorie restriction up-regulates the plasma membrane redox system in brain cells and suppresses oxidative stress during aging. Proc. Natl. Acad. Sci. *103*, 19908–19912.

Inestrosa, N.C., Tapia-Rojas, C., Griffith, T.N., Carvajal, F.J., Benito, M.J., Rivera-Dictter, A., Alvarez, A.R., Serrano, F.G., Hancke, J.L., Burgos, P.V., et al. (2011). Tetrahydrohyperforin prevents cognitive deficit, Aβ deposition, tau phosphorylation and synaptotoxicity in the APPswe/PSEN1ΔE9 model of Alzheimer's disease: a possible effect on APP processing. Transl. Psychiatry *1*, e20.

Ingegni, T., Nocentini, G., Mariani, E., Spazzafumo, L., Polidori, M.C., Cherubini, A., Catani, M., Cadini, D., Senin, U., and Mecocci, P. (2003). Cathepsin D Polymorphism in Italian Elderly Subjects with Sporadic Late-Onset Alzheimer's Disease. Dement. Geriatr. Cogn. Disord. *16*, 151–155.

Inoki, K., Li, Y., Zhu, T., Wu, J., and Guan, K.-L. (2002). TSC2 is phosphorylated and inhibited by Akt and suppresses mTOR signalling. Nat. Cell Biol. *4*, 648–657.

Inoki, K., Zhu, T., and Guan, K.-L. (2003). TSC2 mediates cellular energy response to control cell growth and survival. Cell *115*, 577–590.

Ishiki, A., Kamada, M., Kawamura, Y., Terao, C., Shimoda, F., Tomita, N., Arai, H., and Furukawa, K. (2016). Glial fibrillar acidic protein in the cerebrospinal fluid of Alzheimer's disease, dementia with Lewy bodies, and frontotemporal lobar degeneration. J. Neurochem. *136*, 258–261.

Itakura, E., Kishi-Itakura, C., Koyama-Honda, I., and Mizushima, N. (2012). Structures containing Atg9A and the ULK1 complex independently target depolarized mitochondria at initial stages of Parkin-mediated mitophagy. J. Cell Sci. *125*, 1488–1499.

Ito, H., Kamei, J., Aizawa, N., Fujita, Y., Suzuki, M., Fukuhara, H., Fujimura, T., Kojima, T., Homma, Y., Kubota, Y., et al. (2016). Preventive Effects of Long-Term Caloric Restriction on Aging Related *In vivo* Bladder Dysfunction and Molecular Biological Changes in the Bladder and Dorsal Root Ganglia in Rats. J. Urol. *196*, 1575–1583.

Jaeger, P.A., Pickford, F., Sun, C.-H., Lucin, K.M., Masliah, E., and Wyss-Coray, T. (2010). Regulation of amyloid precursor protein processing by the Beclin 1 complex. PloS One *5*, e11102.

Jäger, S., Bucci, C., Tanida, I., Ueno, T., Kominami, E., Saftig, P., and Eskelinen, E.-L. (2004). Role for Rab7 in maturation of late autophagic vacuoles. J. Cell Sci. *117*, 4837–4848.

de Jager, C.A., Msemburi, W., Pepper, K., and Combrinck, M.I. (2017). Dementia Prevalence in a Rural Region of South Africa: A Cross-Sectional Community Study. J. Alzheimers Dis. JAD *60*, 1087–1096.

Jamart, C., Naslain, D., Gilson, H., and Francaux, M. (2013). Higher activation of autophagy in skeletal muscle of mice during endurance exercise in the fasted state. Am. J. Physiol. Endocrinol. Metab. *305*, E964-974.

Jarrett, J.T., Berger, E.P., and Lansbury, P.T. (1993). The carboxy terminus of the beta amyloid protein is critical for the seeding of amyloid formation: implications for the pathogenesis of Alzheimer's disease. Biochemistry (Mosc.) *32*, 4693–4697.

Ji, Y., Dai, Z., Wu, G., and Wu, Z. (2016). 4-Hydroxy-2-nonenal induces apoptosis by activating ERK1/2 signaling and depleting intracellular glutathione in intestinal epithelial cells. Sci. Rep. *6*, 32929.

Jia, K., and Levine, B. (2007). Autophagy is required for dietary restriction-mediated life span extension in C. elegans. Autophagy *3*, 597–599.

Jin, J. (2015). Alzheimer Disease. JAMA *313*, 1488–1488.

Jung, C.H., Ro, S.-H., Cao, J., Otto, N.M., and Kim, D.-H. (2010). mTOR regulation of autophagy. FEBS Lett. *584*, 1287–1295.

Kaeberlein, M., Powers, R.W., Steffen, K.K., Westman, E.A., Hu, D., Dang, N., Kerr, E.O., Kirkland, K.T., Fields, S., and Kennedy, B.K. (2005). Regulation of yeast replicative life span by TOR and Sch9 in response to nutrients. Science *310*, 1193–1196.

Kagan, V.E., Tyurina, Y.Y., Bayir, H., Chu, C.T., Kapralov, A.A., Vlasova, I.I., Belikova, N.A., Tyurin, V.A., Amoscato, A., Epperly, M., et al. (2006). The "pro-apoptotic genies" get out of mitochondria: oxidative lipidomics and redox activity of cytochrome c/cardiolipin complexes. Chem. Biol. Interact. *163*, 15–28.

Kagan, V.E., Bayir, A., Bayir, H., Stoyanovsky, D., Borisenko, G.G., Tyurina, Y.Y., Wipf, P., Atkinson, J., Greenberger, J.S., Chapkin, R.S., et al. (2009). Mitochondria-targeted disruptors and inhibitors of cytochrome c/cardiolipin peroxidase complexes: a new strategy in anti-apoptotic drug discovery. Mol. Nutr. Food Res. *53*, 104–114.

Kahn, B.B., Alquier, T., Carling, D., and Hardie, D.G. (2005). AMP-activated protein kinase: ancient energy gauge provides clues to modern understanding of metabolism. Cell Metab. *1*, 15–25.

Kaizuka, T., Morishita, H., Hama, Y., Tsukamoto, S., Matsui, T., Toyota, Y., Kodama, A., Ishihara, T., Mizushima, T., and Mizushima, N. (2016). An Autophagic Flux Probe that Releases an Internal Control. Mol. Cell *64*, 835–849.

Kamphuis, W., Mamber, C., Moeton, M., Kooijman, L., Sluijs, J.A., Jansen, A.H.P., Verveer, M., Groot, L.R. de, Smith, V.D., Rangarajan, S., et al. (2012). GFAP Isoforms in Adult Mouse Brain with a Focus on Neurogenic Astrocytes and Reactive Astrogliosis in Mouse Models of Alzheimer Disease. PLOS ONE *7*, e42823.

Kamphuis, W., Middeldorp, J., Kooijman, L., Sluijs, J.A., Kooi, E.-J., Moeton, M., Freriks, M., Mizee, M.R., and Hol, E.M. (2014). Glial fibrillary acidic protein isoform expression in plaque related astrogliosis in Alzheimer's disease. Neurobiol. Aging *35*, 492–510.

Kang, D.E., Pietrzik, C.U., Baum, L., Chevallier, N., Merriam, D.E., Kounnas, M.Z., Wagner, S.L., Troncoso, J.C., Kawas, C.H., Katzman, R., et al. (2000). Modulation of amyloid beta-protein clearance and Alzheimer's disease susceptibility by the LDL receptor-related protein pathway. J. Clin. Invest. *106*, 1159–1166.

Kannan, null, and Jain, null (2000). Oxidative stress and apoptosis. Pathophysiol. Off. J. Int. Soc. Pathophysiol. *7*, 153–163.

Kapahi, P., and Zid, B. (2004). TOR Pathway: Linking Nutrient Sensing to Life Span. Sci. Aging Knowl. Environ. SAGE KE *2004*, PE34.

Karch, C.M., and Goate, A.M. (2015). Alzheimer's disease risk genes and mechanisms of disease pathogenesis. Biol. Psychiatry *77*, 43–51.

Karpievitch, Y.V., Dabney, A.R., and Smith, R.D. (2012). Normalization and missing value imputation for label-free LC-MS analysis. BMC Bioinformatics *13 Suppl 16*, S5.

Kaushik, S., and Cuervo, A.M. (2009). Methods to monitor chaperone-mediated autophagy. Methods Enzymol. *452*, 297–324.

Kaushik, S., and Cuervo, A.M. (2012). Chaperone-mediated autophagy: a unique way to enter the lysosome world. Trends Cell Biol. *22*, 407–417.

Kaushik, S., and Cuervo, A.M. (2015). Proteostasis and aging. Nat. Med. *21*, 1406–1415.

Kaushik, S., and Cuervo, A.M. (2018). The coming of age of chaperone-mediated autophagy. Nat. Rev. Mol. Cell Biol. *19*, 365–381.

Kaushik, S., Massey, A.C., Mizushima, N., and Cuervo, A.M. (2008). Constitutive Activation of Chaperone-mediated Autophagy in Cells with Impaired Macroautophagy. Mol. Biol. Cell *19*, 2179–2192.

Kawarabayashi, T., Younkin, L.H., Saido, T.C., Shoji, M., Ashe, K.H., and Younkin, S.G. (2001). Age-dependent changes in brain, CSF, and plasma amyloid (beta) protein in the Tg2576 transgenic mouse model of Alzheimer's disease. J. Neurosci. Off. J. Soc. Neurosci. *21*, 372–381.

Kayed, R., Head, E., Thompson, J.L., McIntire, T.M., Milton, S.C., Cotman, C.W., and Glabe, C.G. (2003). Common structure of soluble amyloid oligomers implies common mechanism of pathogenesis. Science *300*, 486–489.

Keenan, K.P., Ballam, G.C., Soper, K.A., Laroque, P., Coleman, J.B., and Dixit, R. (1999). Diet, caloric restriction, and the rodent bioassay. Toxicol. Sci. Off. J. Soc. Toxicol. *52*, 24–34.

Keller, J.N., Hanni, K.B., and Markesbery, W.R. (2000). Impaired proteasome function in Alzheimer's disease. J. Neurochem. *75*, 436–439.

Kiffin, R., Christian, C., Knecht, E., and Cuervo, A.M. (2004). Activation of Chaperone-mediated Autophagy during Oxidative Stress. Mol. Biol. Cell *15*, 4829–4840.

Kiffin, R., Kaushik, S., Zeng, M., Bandyopadhyay, U., Zhang, C., Massey, A.C., Martinez-Vicente, M., and Cuervo, A.M. (2007). Altered dynamics of the lysosomal receptor for chaperone-mediated autophagy with age. J. Cell Sci. *120*, 782–791.

Kim, Y.C., and Guan, K.-L. (2015). mTOR: a pharmacologic target for autophagy regulation. J. Clin. Invest. *125*, 25–32.

Kim, J., Kundu, M., Viollet, B., and Guan, K.-L. (2011). AMPK and mTOR regulate autophagy through direct phosphorylation of Ulk1. Nat. Cell Biol. *13*, 132–141.

Kishi-Itakura, C., Koyama-Honda, I., Itakura, E., and Mizushima, N. (2014). Ultrastructural analysis of autophagosome organization using mammalian autophagy-deficient cells. J Cell Sci *127*, 4089–4102.

Kjos, I., Distefano, M.B., Sætre, F., Repnik, U., Holland, P., Jones, A.T., Engedal, N., Simonsen, A., Bakke, O., and Progida, C. (2017). Rab7b modulates autophagic flux by interacting with Atg4B. EMBO Rep. e201744069.

Klionsky, D.J., Abdelmohsen, K., Abe, A., Abedin, M.J., Abeliovich, H., Acevedo Arozena, A., Adachi, H., Adams, C.M., Adams, P.D., Adeli, K., et al. (2016). Guidelines for the use and interpretation of assays for monitoring autophagy (3rd edition). Autophagy *12*, 1–222.

Knuppertz, L., Hamann, A., Pampaloni, F., Stelzer, E., and Osiewacz, H.D. (2014). Identification of autophagy as a longevity-assurance mechanism in the aging model Podospora anserina. Autophagy *10*, 822–834.

Koga, H., and Cuervo, A.M. (2011). Chaperone-mediated autophagy dysfunction in the pathogenesis of neurodegeneration. Neurobiol. Dis. *43*, 29–37.

Koga, H., Martinez-Vicente, M., Arias, E., Kaushik, S., Sulzer, D., and Cuervo, A.M. (2011a). Constitutive upregulation of chaperone-mediated autophagy in Huntington's disease. J. Neurosci. Off. J. Soc. Neurosci. *31*, 18492–18505.

Koga, H., Martinez-Vicente, M., Macian, F., Verkhusha, V.V., and Cuervo, A.M. (2011b). A photoconvertible fluorescent reporter to track chaperone-mediated autophagy. Nat. Commun. *2*, 386.

Koike, M., Shibata, M., Waguri, S., Yoshimura, K., Tanida, I., Kominami, E., Gotow, T., Peters, C., von Figura, K., Mizushima, N., et al. (2005). Participation of autophagy in storage of lysosomes in neurons from mouse models of neuronal ceroid-lipofuscinoses (Batten disease). Am. J. Pathol. *167*, 1713–1728.

Komatsu, M., Waguri, S., Chiba, T., Murata, S., Iwata, J., Tanida, I., Ueno, T., Koike, M., Uchiyama, Y., Kominami, E., et al. (2006). Loss of autophagy in the central nervous system causes neurodegeneration in mice. Nature *441*, 880–884.

Komatsu, M., Waguri, S., Koike, M., Sou, Y.-S., Ueno, T., Hara, T., Mizushima, N., Iwata, J.-I., Ezaki, J., Murata, S., et al. (2007a). Homeostatic levels of p62 control cytoplasmic inclusion body formation in autophagy-deficient mice. Cell *131*, 1149–1163.

Komatsu, M., Wang, Q.J., Holstein, G.R., Friedrich, V.L., Iwata, J., Kominami, E., Chait, B.T., Tanaka, K., and Yue, Z. (2007b). Essential role for autophagy protein Atg7 in the maintenance of axonal homeostasis and the prevention of axonal degeneration. Proc. Natl. Acad. Sci. U. S. A. *104*, 14489–14494.

Koperdanova, M., and Cullis, J.O. (2015). Interpreting raised serum ferritin levels. BMJ *351*, h3692.

Kroemer, G., and Levine, B. (2008). Autophagic cell death: the story of a misnomer. Nat. Rev. Mol. Cell Biol. *9*, 1004–1010.

Kroemer, G., Mariño, G., and Levine, B. (2010). Autophagy and the integrated stress response. Mol. Cell *40*, 280–293.

Kuhn, P.-H., Wang, H., Dislich, B., Colombo, A., Zeitschel, U., Ellwart, J.W., Kremmer, E., Rossner, S., and Lichtenthaler, S.F. (2010). ADAM10 is the physiologically relevant, constitutive alpha-secretase of the amyloid precursor protein in primary neurons. EMBO J. *29*, 3020–3032.

Kuma, A., Hatano, M., Matsui, M., Yamamoto, A., Nakaya, H., Yoshimori, T., Ohsumi, Y., Tokuhisa, T., and Mizushima, N. (2004). The role of autophagy during the early neonatal starvation period. Nature *432*, 1032–1036.

Kuma, A., Matsui, M., and Mizushima, N. (2007). LC3, an autophagosome marker, can be incorporated into protein aggregates independent of autophagy: caution in the interpretation of LC3 localization. Autophagy *3*, 323–328.

Kumar-Singh, S. (2009). Hereditary and Sporadic Forms of Aβ-Cerebrovascular Amyloidosis and Relevant Transgenic Mouse Models. Int. J. Mol. Sci. *10*, 1872–1895.

Kuo, Y.M., Emmerling, M.R., Vigo-Pelfrey, C., Kasunic, T.C., Kirkpatrick, J.B., Murdoch, G.H., Ball, M.J., and Roher, A.E. (1996). Water-soluble Abeta (N-40, N-42) oligomers in normal and Alzheimer disease brains. J. Biol. Chem. *271*, 4077–4081.

Kurosu, T., Fukuda, T., Miki, T., and Miura, O. (2003). BCL6 overexpression prevents increase in reactive oxygen species and inhibits apoptosis induced by chemotherapeutic reagents in B-cell lymphoma cells. Oncogene *22*, 4459–4468.

Langford, D.J., Bailey, A.L., Chanda, M.L., Clarke, S.E., Drummond, T.E., Echols, S., Glick, S., Ingrao, J., Klassen-Ross, T., Lacroix-Fralish, M.L., et al. (2010). Coding of facial expressions of pain in the laboratory mouse. Nat. Methods *7*, 447–449.

Leach, M.C., Klaus, K., Miller, A.L., Scotto di Perrotolo, M., Sotocinal, S.G., and Flecknell, P.A. (2012). The assessment of post-vasectomy pain in mice using behaviour and the Mouse Grimace Scale. PloS One *7*, e35656.

LeBlanc, A., Liu, H., Goodyer, C., Bergeron, C., and Hammond, J. (1999). Caspase-6 role in apoptosis of human neurons, amyloidogenesis, and Alzheimer's disease. J. Biol. Chem. *274*, 23426–23436.

Lee, C., and Longo, V. (2016). Dietary restriction with and without caloric restriction for healthy aging. F1000Research *5*.

Lee, C., and Longo, V.D. (2011). Fasting vs dietary restriction in cellular protection and cancer treatment: from model organisms to patients. Oncogene *30*, 3305–3316.

Lee, J.-A., and Gao, F.-B. (2008). Regulation of Abeta pathology by beclin 1: a protective role for autophagy? J. Clin. Invest. *118*, 2015–2018.

Lee, S., and Notterpek, L. (2013). Dietary restriction supports peripheral nerve health by enhancing endogenous protein quality control mechanisms. Exp. Gerontol. *48*, 1085–1090.

Lee, S.-H., and Min, K.-J. (2013). Caloric restriction and its mimetics. BMB Rep. *46*, 181–187.

Lee, H.R., Shin, H.K., Park, S.Y., Kim, H.Y., Bae, S.S., Lee, W.S., Rhim, B.Y., Hong, K.W., and Kim, C.D. (2015). Cilostazol Upregulates Autophagy via SIRT1 Activation: Reducing Amyloid-β Peptide and APP-CTFβ Levels in Neuronal Cells. PLOS ONE *10*, e0134486.

Lee, I.H., Cao, L., Mostoslavsky, R., Lombard, D.B., Liu, J., Bruns, N.E., Tsokos, M., Alt, F.W., and Finkel, T. (2008a). A role for the NAD-dependent deacetylase Sirt1 in the regulation of autophagy. Proc. Natl. Acad. Sci. U. S. A. *105*, 3374–3379.

Lee, J., Bruce-Keller, A.J., Kruman, Y., Chan, S.L., and Mattson, M.P. (1999). 2-Deoxy-D-glucose protects hippocampal neurons against excitotoxic and oxidative injury: evidence for the involvement of stress proteins. J. Neurosci. Res. *57*, 48–61.

Lee, J., Retamal, C., Cuitiño, L., Caruano-Yzermans, A., Shin, J.-E., van Kerkhof, P., Marzolo, M.-P., and Bu, G. (2008b). Adaptor protein sorting nexin 17 regulates amyloid precursor protein trafficking and processing in the early endosomes. J. Biol. Chem. *283*, 11501–11508.

Lee, J.-H., Yu, W.H., Kumar, A., Lee, S., Mohan, P.S., Peterhoff, C.M., Wolfe, D.M., Martinez-Vicente, M., Massey, A.C., Sovak, G., et al. (2010). Lysosomal proteolysis and autophagy require presenilin 1 and are disrupted by Alzheimer-related PS1 mutations. Cell *141*, 1146–1158.

Lee, S., Sato, Y., and Nixon, R.A. (2011a). Primary lysosomal dysfunction causes cargo-specific deficits of axonal transport leading to Alzheimer-like neuritic dystrophy. Autophagy *7*, 1562–1563.

Lee, S., Sato, Y., and Nixon, R.A. (2011b). Lysosomal proteolysis inhibition selectively disrupts axonal transport of degradative organelles and causes an Alzheimer's-like axonal dystrophy. J. Neurosci. Off. J. Soc. Neurosci. *31*, 7817–7830.

Lefevre, M., Redman, L.M., Heilbronn, L.K., Smith, J.V., Martin, C.K., Rood, J.C., Greenway, F.L., Williamson, D.A., Smith, S.R., and Ravussin, E. (2009). CALORIC RESTRICTION ALONE AND WITH EXERCISE IMPROVES CVD RISK IN HEALTHY NON-OBESE INDIVIDUALS. Atherosclerosis *203*, 206–213.

Leissring, M.A. (2014). Aβ degradation—the inside story. Front. Aging Neurosci. *6*.

Leissring, M.A., and Turner, A.J. (2013). Regulation of distinct pools of amyloid β-protein by multiple cellular proteases. Alzheimers Res. Ther. *5*, 37.

Levine, B., and Yuan, J. (2005). Autophagy in cell death: an innocent convict? J. Clin. Invest. *115*, 2679–2688.

Li, C.-L., Wei, H.-L., Chen, J., Wang, B., Xie, B., Fan, L.-L., and Li, L.-J. (2014a). Ebb-and-flow of macroautophagy and chaperone-mediated autophagy in Raji cells induced by starvation and arsenic trioxide. Asian Pac. J. Cancer Prev. APJCP *15*, 5715–5719.

Li, J., Kanekiyo, T., Shinohara, M., Zhang, Y., LaDu, M.J., Xu, H., and Bu, G. (2012). Differential regulation of amyloid-β endocytic trafficking and lysosomal degradation by apolipoprotein E isoforms. J. Biol. Chem. *287*, 44593–44601.

Li, J., Zhang, C.-X., Liu, Y.-M., Chen, K.-L., Chen, G., Li, J., Zhang, C.-X., Liu, Y.-M., Chen, K.-L., and Chen, G. (2017a). A comparative study of anti-aging properties and mechanism: resveratrol and caloric restriction. Oncotarget *8*, 65717–65729.

Li, K., Li, Y., Shelton, J.M., Richardson, J.A., Spencer, E., Chen, Z.J., Wang, X., and Williams, R.S. (2000). Cytochrome c deficiency causes embryonic lethality and attenuates stress-induced apoptosis. Cell *101*, 389–399.

Li, L., Wang, Z.V., Hill, J.A., and Lin, F. (2014b). New autophagy reporter mice reveal dynamics of proximal tubular autophagy. J. Am. Soc. Nephrol. JASN *25*, 305–315.

Li, M., Li, Z., Yao, Y., Jin, W.-N., Wood, K., Liu, Q., Shi, F.-D., and Hao, J. (2017b). Astrocyte-derived interleukin-15 exacerbates ischemic brain injury via propagation of cellular immunity. Proc. Natl. Acad. Sci. U. S. A. *114*, E396–E405.

Li, R., Lindholm, K., Yang, L.-B., Yue, X., Citron, M., Yan, R., Beach, T., Sue, L., Sabbagh, M., Cai, H., et al. (2004a). Amyloid β peptide load is correlated with increased β-secretase activity in sporadic Alzheimer's disease patients. Proc. Natl. Acad. Sci. U. S. A. *101*, 3632–3637.

Li, W., Tang, Y., Fan, Z., Meng, Y., Yang, G., Luo, J., and Ke, Z.-J. (2013). Autophagy is involved in oligodendroglial precursor-mediated clearance of amyloid peptide. Mol. Neurodegener. *8*, 27.

Li, W., Zhu, J., Dou, J., She, H., Tao, K., Xu, H., Yang, Q., and Mao, Z. (2017c). Phosphorylation of LAMP2A by p38 MAPK couple's ER stress to chaperone-mediated autophagy. Nat. Commun. *8*, 1763.

Li, Y., Nowotny, P., Holmans, P., Smemo, S., Kauwe, J.S.K., Hinrichs, A.L., Tacey, K., Doil, L., van Luchene, R., Garcia, V., et al. (2004b). Association of late-onset Alzheimer's disease with genetic variation in multiple members of the GAPD gene family. Proc. Natl. Acad. Sci. U. S. A. *101*, 15688–15693.

Liang, C.-C., Wang, C., Peng, X., Gan, B., and Guan, J.-L. (2010). Neural-specific deletion of FIP200 leads to cerebellar degeneration caused by increased neuronal death and axon degeneration. J. Biol. Chem. *285*, 3499–3509.

Liang, L.P., Ho, Y.S., and Patel, M. (2000). Mitochondrial superoxide production in kainate-induced hippocampal damage. Neuroscience *101*, 563–570.

Liang, Y., Liu, C., Lu, M., Dong, Q., Wang, Z., Wang, Z., Xiong, W., Zhang, N., Zhou, J., Liu, Q., et al. (2018). Calorie restriction is the most reasonable anti-ageing intervention: a meta-analysis of survival curves. Sci. Rep. *8*, 5779.

Lin, C.-L., Cheng, Y.-S., Li, H.-H., Chiu, P.-Y., Chang, Y.-T., Ho, Y.-J., and Lai, T.-J. (2016). Amyloid-β suppresses AMP-activated protein kinase (AMPK) signaling and contributes to α-synuclein-induced cytotoxicity. Exp. Neurol. *275 Pt 1*, 84–98.

Lin, P.I., Martin, E.R., Bronson, P.G., Browning-Large, C., Small, G.W., Schmechel, D.E., Welsh-Bohmer, K.A., Haines, J.L., Gilbert, J.R., and Pericak-Vance, M.A. (2006). Exploring the association of glyceraldehyde-3-phosphate dehydrogenase gene and Alzheimer disease. Neurology *67*, 64–68.

Lipinski, M.M., Zheng, B., Lu, T., Yan, Z., Py, B.F., Ng, A., Xavier, R.J., Li, C., Yankner, B.A., Scherzer, C.R., et al. (2010). Genome-wide analysis reveals mechanisms modulating autophagy in normal brain aging and in Alzheimer's disease. Proc. Natl. Acad. Sci. U. S. A. *107*, 14164–14169.

Lippa, C.F., Saunders, A.M., Smith, T.W., Swearer, J.M., Drachman, D.A., Ghetti, B., Nee, L., Pulaski-Salo, D., Dickson, D., Robitaille, Y., et al. (1996). Familial and sporadic Alzheimer's disease: neuropathology cannot exclude a final common pathway. Neurology *46*, 406–412.

Lista, S., O'Bryant, S.E., Blennow, K., Dubois, B., Hugon, J., Zetterberg, H., and Hampel, H. (2015). Biomarkers in Sporadic and Familial Alzheimer's Disease. J. Alzheimers Dis. JAD *47*, 291–317.

Litteljohn, D., Nelson, E., Bethune, C., and Hayley, S. (2011). The effects of paraquat on regional brain neurotransmitter activity, hippocampal BDNF and behavioural function in female mice. Neurosci. Lett. *502*, 186–191.

Liu, Y., and Levine, B. (2015). Autosis and autophagic cell death: the dark side of autophagy. Cell Death Differ. *22*, 367–376.

Lo, A.C., Haass, C., Wagner, S.L., Teplow, D.B., and Sisodia, S.S. (1994). Metabolism of the "Swedish" amyloid precursor protein variant in Madin-Darby canine kidney cells. J. Biol. Chem. *269*, 30966–30973.

Lo, A.C.Y., Thinakaran, G., Slunt, H.H., and Sisodia, S.S. (1995). Metabolism of the Amyloid Precursor-like Protein 2 in MDCK Cells. POLARIZED TRAFFICKING OCCURS INDEPENDENT OF THE CHONDROITIN SULFATE GLYCOSAMINOGLYCAN CHAIN. J. Biol. Chem. *270*, 12641–12645.

Lodish, H., Berk, A., Zipursky, S.L., Matsudaira, P., Baltimore, D., and Darnell, J. (2000). Overview of the Secretory Pathway.

Lohren, H., Blagojevic, L., Fitkau, R., Ebert, F., Schildknecht, S., Leist, M., and Schwerdtle, T. (2015). Toxicity of organic and inorganic mercury species in differentiated human neurons and human astrocytes. J. Trace Elem. Med. Biol. Organ Soc. Miner. Trace Elem. GMS *32*, 200–208.

Loos, B., and Engelbrecht, A.-M. (2009). Cell death: a dynamic response concept. Autophagy *5*, 590–603.

Loos, B., du Toit, A., and Hofmeyr, J.-H.S. (2014). Defining and measuring autophagosome flux—concept and reality. Autophagy *10*, 2087–2096.

López-Lluch, G., and Navas, P. (2016). Calorie restriction as an intervention in ageing. J. Physiol. *594*, 2043–2060.

Louneva, N., Cohen, J.W., Han, L.-Y., Talbot, K., Wilson, R.S., Bennett, D.A., Trojanowski, J.Q., and Arnold, S.E. (2008). Caspase-3 Is Enriched in Postsynaptic Densities and Increased in Alzheimer's Disease. Am. J. Pathol. *173*, 1488–1495.

Lu, D.C., Rabizadeh, S., Chandra, S., Shayya, R.F., Ellerby, L.M., Ye, X., Salvesen, G.S., Koo, E.H., and Bredesen, D.E. (2000). A second cytotoxic proteolytic peptide derived from amyloid beta-protein precursor. Nat. Med. *6*, 397–404.

Lue, L.F., Kuo, Y.M., Roher, A.E., Brachova, L., Shen, Y., Sue, L., Beach, T., Kurth, J.H., Rydel, R.E., and Rogers, J. (1999). Soluble amyloid beta peptide concentration as a predictor of synaptic change in Alzheimer's disease. Am. J. Pathol. *155*, 853–862.

Lumkwana, D., du Toit, A., Kinnear, C., and Loos, B. (2017). Autophagic flux control in neurodegeneration: Progress and precision targeting-Where do we stand? Prog. Neurobiol. *153*, 64–85.

Lundgren, D.H., Hwang, S.-I., Wu, L., and Han, D.K. (2010). Role of spectral counting in quantitative proteomics. Expert Rev. Proteomics *7*, 39–53.

Luo, Y., Bolon, B., Damore, M.A., Fitzpatrick, D., Liu, H., Zhang, J., Yan, Q., Vassar, R., and Citron, M. (2003). BACE1 (beta-secretase) knockout mice do not acquire compensatory gene expression changes or develop neural lesions over time. Neurobiol. Dis. *14*, 81–88.

Lustbader, J.W., Cirilli, M., Lin, C., Xu, H.W., Takuma, K., Wang, N., Caspersen, C., Chen, X., Pollak, S., Chaney, M., et al. (2004). ABAD directly links Abeta to mitochondrial toxicity in Alzheimer's disease. Science *304*, 448–452.

Ma, L., Wang, R., Dong, W., Li, Y., Xu, B., Zhang, J., and Zhao, Z. (2016). Long-term caloric restriction in mice may prevent age-related learning impairment via suppression of apoptosis. Behav. Brain Res. *315*, 45–50.

Ma, M.W., Wang, J., Dhandapani, K.M., and Brann, D.W. (2018). Deletion of NADPH oxidase 4 reduces severity of traumatic brain injury. Free Radic. Biol. Med. *117*, 66–75.

Ma, S., Dielschneider, R.F., Henson, E.S., Xiao, W., Choquette, T.R., Blankstein, A.R., Chen, Y., and Gibson, S.B. (2017). Ferroptosis and autophagy induced cell death occur independently after siramesine and lapatinib treatment in breast cancer cells. PLoS ONE *12*.

MacCallum, S.F., Groves, M.J., James, J., Murray, K., Appleyard, V., Prescott, A.R., Drbal, A.A., Nicolaou, A., Cunningham, J., Haydock, S., et al. (2013). Dysregulation of autophagy in chronic lymphocytic leukemia with the small-molecule Sirtuin inhibitor Tenovin-6. Sci. Rep. *3*, srep01275.

Mahoney, L.B., Denny, C.A., and Seyfried, T.N. (2006). Caloric restriction in C57BL/6J mice mimics therapeutic fasting in humans. Lipids Health Dis. *5*, 13.

Majima, H., Nakanishi-Ueda, T., and Ozawa, T. (2002). 4-Hydroxy-2-Nonenal (4-HNE) Staining by Anti-HNE Antibody. In Oxidants and Antioxidants, D. Armstrong, ed. (Humana Press), pp. 31–34.

Majumder, S., Richardson, A., Strong, R., and Oddo, S. (2011). Inducing Autophagy by Rapamycin Before, but Not After, the Formation of Plaques and Tangles Ameliorates Cognitive Deficits. PLoS ONE *6*, e25416.

Makioka, K., Yamazaki, T., Kakuda, S., and Okamoto, K. (2009). Variations in the effects on synthesis of amyloid beta protein in modulated autophagic conditions. Neurol. Res. *31*, 959–968.

Manavalan, A., Mishra, M., Feng, L., Sze, S.K., Akatsu, H., and Heese, K. (2013). Brain site-specific proteome changes in aging-related dementia. Exp. Mol. Med. *45*, e39.

Manders, E.M.M., Verbeek, F.J., and Aten, J.A. (1993). Measurement of co-localization of objects in dual-colour confocal images. J. Microsc. *169*, 375–382.

Maniti, O., François-Moutal, L., Lecompte, M.-F., Vial, C., Lagarde, M., Guichardant, M., Marcillat, O., and Granjon, T. (2015). Protein "amyloid-like" networks at the phospholipid

membrane formed by 4-hydroxy-2-nonenal-modified mitochondrial creatine kinase. Mol. Membr. Biol. *32*, 1–10.

Manning-Bog, A.B., McCormack, A.L., Li, J., Uversky, V.N., Fink, A.L., and Monte, D.A.D. (2002). The Herbicide Paraquat Causes Up-regulation and Aggregation of α-Synuclein in Mice PARAQUAT AND α-SYNUCLEIN. J. Biol. Chem. *277*, 1641–1644.

Manzanero, S., Gelderblom, M., Magnus, T., and Arumugam, T.V. (2011). Calorie restriction and stroke. Exp. Transl. Stroke Med. *3*, 8.

Marambaud, P., Zhao, H., and Davies, P. (2005). Resveratrol promotes clearance of Alzheimer's disease amyloid-beta peptides. J. Biol. Chem. *280*, 37377–37382.

Mariño, G., Pietrocola, F., Madeo, F., and Kroemer, G. (2014). Caloric restriction mimetics: natural/physiological pharmacological autophagy inducers. Autophagy *10*, 1879–1882.

Markesbery, W.R., and Lovell, M.A. (1998). Four-hydroxynonenal, a product of lipid peroxidation, is increased in the brain in Alzheimer's disease. Neurobiol. Aging *19*, 33–36.

Marques, C.A., Keil, U., Bonert, A., Steiner, B., Haass, C., Müller, W.E., and Eckert, A. (2003). Neurotoxic Mechanisms Caused by the Alzheimer's Disease-linked Swedish Amyloid Precursor Protein Mutation OXIDATIVE STRESS, CASPASES, AND THE JNK PATHWAY. J. Biol. Chem. *278*, 28294–28302.

Marr, R., and Masliah, E. (2015). Amyloid-beta clearance in Alzheimer's disease (Frontiers Media SA).

Martinez-Vicente, M., Sovak, G., and Cuervo, A.M. (2005). Protein degradation and aging. Exp. Gerontol. *40*, 622–633.

Martinez-Vicente, M., Talloczy, Z., Kaushik, S., Massey, A.C., Mazzulli, J., Mosharov, E.V., Hodara, R., Fredenburg, R., Wu, D.-C., Follenzi, A., et al. (2008). Dopamine-modified alpha-synuclein blocks chaperone-mediated autophagy. J. Clin. Invest. *118*, 777–788.

Masoro, E.J. (2006). Dietary restriction-induced life extension: a broadly based biological phenomenon. Biogerontology *7*, 153–155.

Masoro, E.J. (2009). Caloric restriction-induced life extension of rats and mice: a critique of proposed mechanisms. Biochim. Biophys. Acta *1790*, 1040–1048.

Massey, A.C., Kaushik, S., and Cuervo, A.M. (2006a). Lysosomal chat maintains the balance. Autophagy *2*, 325–327.

Massey, A.C., Zhang, C., and Cuervo, A.M. (2006b). Chaperone-mediated autophagy in aging and disease. Curr. Top. Dev. Biol. *73*, 205–235.

Massey, A.C., Kaushik, S., Sovak, G., Kiffin, R., and Cuervo, A.M. (2006c). Consequences of the selective blockage of chaperone-mediated autophagy. Proc. Natl. Acad. Sci. U. S. A. *103*, 5805–5810.

Massey, A.C., Follenzi, A., Kiffin, R., Zhang, C., and Cuervo, A.M. (2008). Early cellular changes after blockage of chaperone-mediated autophagy. Autophagy *4*, 442–456.

Maswood, N., Young, J., Tilmont, E., Zhang, Z., Gash, D.M., Gerhardt, G.A., Grondin, R., Roth, G.S., Mattison, J., Lane, M.A., et al. (2004). Caloric restriction increases neurotrophic

factor levels and attenuates neurochemical and behavioral deficits in a primate model of Parkinson's disease. Proc. Natl. Acad. Sci. U. S. A. *101*, 18171–18176.

Matapurkar, A., and Lazebnik, Y. (2006). Requirement of cytochrome c for apoptosis in human cells. Cell Death Differ. *13*, 2062–2067.

Matsuda, S., Giliberto, L., Matsuda, Y., Davies, P., McGowan, E., Pickford, F., Ghiso, J., Frangione, B., and D'Adamio, L. (2005). The familial dementia BRI2 gene binds the Alzheimer gene amyloid-beta precursor protein and inhibits amyloid-beta production. J. Biol. Chem. *280*, 28912–28916.

Matsuda, S., Matsuda, Y., Snapp, E.L., and D'Adamio, L. (2011). Maturation of BRI2 generates a specific inhibitor that reduces APP processing at the plasma membrane and in endocytic vesicles. Neurobiol. Aging *32*, 1400–1408.

Matsui, T., Ingelsson, M., Fukumoto, H., Ramasamy, K., Kowa, H., Frosch, M.P., Irizarry, M.C., and Hyman, B.T. (2007). Expression of APP pathway mRNAs and proteins in Alzheimer's disease. Brain Res. *1161*, 116–123.

Matsunaga, K., Morita, E., Saitoh, T., Akira, S., Ktistakis, N.T., Izumi, T., Noda, T., and Yoshimori, T. (2010). Autophagy requires endoplasmic reticulum targeting of the PI3-kinase complex via Atg14L. J. Cell Biol. *190*, 511–521.

Mattison, J.A., Colman, R.J., Beasley, T.M., Allison, D.B., Kemnitz, J.W., Roth, G.S., Ingram, D.K., Weindruch, R., Cabo, R. de, and Anderson, R.M. (2017). Caloric restriction improves health and survival of rhesus monkeys. Nat. Commun. *8*, ncomms14063.

Mattson, M.P. (2005). Energy intake, meal frequency, and health: a neurobiological perspective. Annu. Rev. Nutr. *25*, 237–260.

Mattson, M.P. (2008). Dietary factors, hormesis and health. Ageing Res. Rev. *7*, 43–48.

Mattson, M.P. (2010). The Impact of Dietary Energy Intake on Cognitive Aging. Front. Aging Neurosci. *2*.

Mattson, M.P., Gary, D.S., Chan, S.L., and Duan, W. (2001). Perturbed endoplasmic reticulum function, synaptic apoptosis and the pathogenesis of Alzheimer's disease. Biochem. Soc. Symp. 151–162.

Matus, S., Valenzuela, V., and Hetz, C. (2014). A new method to measure autophagy flux in the nervous system. Autophagy *10*, 710–714.

Mawuenyega, K.G., Sigurdson, W., Ovod, V., Munsell, L., Kasten, T., Morris, J.C., Yarasheski, K.E., and Bateman, R.J. (2010). Decreased clearance of CNS beta-amyloid in Alzheimer's disease. Science *330*, 1774.

McCay, C.M., Crowell, M.F., and Maynard, L.A. (1989). The effect of retarded growth upon the length of life span and upon the ultimate body size. 1935. Nutr. Burbank Los Angel. Cty. Calif *5*, 155–171; discussion 172.

McCormack, A.L., Thiruchelvam, M., Manning-Bog, A.B., Thiffault, C., Langston, J.W., Cory-Slechta, D.A., and Di Monte, D.A. (2002). Environmental risk factors and Parkinson's disease: selective degeneration of nigral dopaminergic neurons caused by the herbicide paraquat. Neurobiol. Dis. *10*, 119–127.

McCracken, E., Valeriani, V., Simpson, C., Jover, T., McCulloch, J., and Dewar, D. (2000). The lipid peroxidation by-product 4-hydroxynonenal is toxic to axons and oligodendrocytes. J. Cereb. Blood Flow Metab. Off. J. Int. Soc. Cereb. Blood Flow Metab. *20*, 1529–1536.

McDermott, J.R., and Gibson, A.M. (1997). Degradation of Alzheimer's beta-amyloid protein by human and rat brain peptidases: involvement of insulin-degrading enzyme. Neurochem. Res. *22*, 49–56.

McFarland, R., Blokhin, A., Sydnor, J., Mariani, J., and Vogel, M.W. (2007). Oxidative stress, nitric oxide, and the mechanisms of cell death in Lurcher Purkinje cells. Dev. Neurobiol. *67*, 1032–1046.

McLean, C.A., Cherny, R.A., Fraser, F.W., Fuller, S.J., Smith, M.J., Beyreuther, K., Bush, A.I., and Masters, C.L. (1999). Soluble pool of Abeta amyloid as a determinant of severity of neurodegeneration in Alzheimer's disease. Ann. Neurol. *46*, 860–866.

Mei, S. (2018). In Silico Enhancing M. Tuberculosis Protein Interaction Networks in STRING To Predict Drug-Resistance Pathways and Pharmacological Risks. J. Proteome Res. *17*, 1749–1760.

Meléndez, A., Tallóczy, Z., Seaman, M., Eskelinen, E.-L., Hall, D.H., and Levine, B. (2003). Autophagy genes are essential for dauer development and life-span extension in C. elegans. Science *301*, 1387–1391.

Menting, K.W., and Claassen, J.A.H.R. (2014). β-secretase inhibitor; a promising novel therapeutic drug in Alzheimer's disease. Front. Aging Neurosci. *6*.

Menzies, F.M., Fleming, A., and Rubinsztein, D.C. (2015). Compromised autophagy and neurodegenerative diseases. Nat. Rev. Neurosci. *16*, 345–357.

Mercer, C.A., Kaliappan, A., and Dennis, P.B. (2009). A novel, human Atg13 binding protein, Atg101, interacts with ULK1 and is essential for macroautophagy. Autophagy *5*, 649–662.

Mercken, E.M., Crosby, S.D., Lamming, D.W., JeBailey, L., Krzysik-Walker, S., Villareal, D.T., Capri, M., Franceschi, C., Zhang, Y., Becker, K., et al. (2013). Calorie restriction in humans inhibits the PI3K/AKT pathway and induces a younger transcription profile. Aging Cell *12*, 645–651.

Mesaros, C., and Blair, I.A. (2016). Mass spectrometry-based approaches to targeted quantitative proteomics in cardiovascular disease. Clin. Proteomics *13*, 20.

Metaxakis, A., Ploumi, C., and Tavernarakis, N. (2018). Autophagy in Age-Associated Neurodegeneration. Cells *7*.

Michaëlsson, K., Bergström, R., Mallmin, H., Holmberg, L., Wolk, A., and Ljunghall, S. (1996). Screening for osteopenia and osteoporosis: selection by body composition. Osteoporos. Int. J. Establ. Result Coop. Eur. Found. Osteoporos. Natl. Osteoporos. Found. USA *6*, 120–126.

Milac, T.I., Randolph, T.W., and Wang, P. (2012). Analyzing LC-MS/MS data by spectral count and ion abundance: two case studies. Stat. Interface *5*, 75–87.

Miller, S.L., and Wolfe, R.R. (2008). The danger of weight loss in the elderly. J. Nutr. Health Aging *12*, 487–491.

Miller, J.A., Woltjer, R.L., Goodenbour, J.M., Horvath, S., and Geschwind, D.H. (2013). Genes and pathways underlying regional and cell type changes in Alzheimer's disease. Genome Med. *5*, 48.

Miller, M.C., Tavares, R., Johanson, C.E., Hovanesian, V., Donahue, J.E., Gonzalez, L., Silverberg, G.D., and Stopa, E.G. (2008). Hippocampal RAGE immunoreactivity in early and advanced Alzheimer's disease. Brain Res. *1230*, 273–280.

Miller, R.A., Harrison, D.E., Astle, C.M., Fernandez, E., Flurkey, K., Han, M., Javors, M.A., Li, X., Nadon, N.L., Nelson, J.F., et al. (2014). Rapamycin-mediated lifespan increase in mice is dose and sex dependent and metabolically distinct from dietary restriction. Aging Cell *13*, 468–477.

Mindell, J.A. (2012). Lysosomal acidification mechanisms. Annu. Rev. Physiol. *74*, 69–86.

Mitra, S., Tsvetkov, A.S., and Finkbeiner, S. (2009). Single neuron ubiquitin-proteasome dynamics accompanying inclusion body formation in huntington disease. J. Biol. Chem. *284*, 4398–4403.

Mizushima, N. (2004). Methods for monitoring autophagy. Int. J. Biochem. Cell Biol. *36*, 2491–2502.

Mizushima, N. (2007). Autophagy: process and function. Genes Dev. *21*, 2861–2873.

Mizushima, N. (2009a). Chapter 2 Methods for Monitoring Autophagy Using GFP-LC3 Transgenic Mice. B.-M. in Enzymology, ed. (Academic Press), pp. 13–23.

Mizushima, N. (2009b). Methods for monitoring autophagy using GFP-LC3 transgenic mice. Methods Enzymol. *452*, 13–23.

Mizushima, N. (2010). The role of the Atg1/ULK1 complex in autophagy regulation. Curr. Opin. Cell Biol. *22*, 132–139.

Mizushima, N., and Komatsu, M. (2011). Autophagy: renovation of cells and tissues. Cell *147*, 728–741.

Mizushima, N., and Yoshimori, T. (2007). How to interpret LC3 immunoblotting. Autophagy *3*, 542–545.

Mizushima, N., Kuma, A., Kobayashi, Y., Yamamoto, A., Matsubae, M., Takao, T., Natsume, T., Ohsumi, Y., and Yoshimori, T. (2003). Mouse Apg16L, a novel WD-repeat protein, targets to the autophagic isolation membrane with the Apg12-Apg5 conjugate. J. Cell Sci. *116*, 1679–1688.

Mizushima, N., Levine, B., Cuervo, A.M., and Klionsky, D.J. (2008). Autophagy fights disease through cellular self-digestion. Nature *451*, 1069–1075.

Mizushima, N., Yoshimori, T., and Ohsumi, Y. (2011). The role of Atg proteins in autophagosome formation. Annu. Rev. Cell Dev. Biol. *27*, 107–132.

Mo, C., Peng, Q., Sui, J., Wang, J., Deng, Y., Xie, L., Li, T., He, Y., Qin, X., and Li, S. (2014). Lack of association between cathepsin D C224T polymorphism and Alzheimer's disease risk: an update meta-analysis. BMC Neurol. *14*, 13.

Mohamed, A., and Posse de Chaves, E. (2011). Aβ Internalization by Neurons and Glia.

Moreira, O.C., Estébanez, B., Martínez-Florez, S., Paz, J.A. de, Cuevas, M.J., and González-Gallego, J. (2017). Mitochondrial Function and Mitophagy in the Elderly: Effects of Exercise.

Moulis, M., and Vindis, C. (2017). Methods for Measuring Autophagy in Mice. Cells *6*, 14.

Mouton, P.R., Chachich, M.E., Quigley, C., Spangler, E., and Ingram, D.K. (2009). Caloric restriction attenuates amyloid deposition in middle-aged dtg APP/PS1 mice. Neurosci. Lett. *464*, 184–187.

Muche, A., Arendt, T., and Schliebs, R. (2017). Oxidative stress affects processing of amyloid precursor protein in vascular endothelial cells. PLoS ONE *12*.

Mueller-Steiner, S., Zhou, Y., Arai, H., Roberson, E.D., Sun, B., Chen, J., Wang, X., Yu, G., Esposito, L., Mucke, L., et al. (2006). Antiamyloidogenic and neuroprotective functions of cathepsin B: implications for Alzheimer's disease. Neuron *51*, 703–714.

Mukherjee, A., Patel, B., Koga, H., Cuervo, A.M., and Jenny, A. (2016). Selective endosomal microautophagy is starvation-inducible in Drosophila. Autophagy *12*, 1984–1999.

Mullan, M., Crawford, F., Axelman, K., Houlden, H., Lilius, L., Winblad, B., and Lannfelt, L. (1992). A pathogenic mutation for probable Alzheimer's disease in the APP gene at the N-terminus of beta-amyloid. Nat. Genet. *1*, 345–347.

Murphy, M.P., and LeVine, H. (2010). Alzheimer's Disease and the β-Amyloid Peptide. J. Alzheimers Dis. JAD *19*, 311.

Murray, K.K., Boyd, R.K., Eberlin, M.N., Langley, G.J., Li, L., and Naito, Y. (2013). Definitions of terms relating to mass spectrometry (IUPAC Recommendations 2013). Pure Appl. Chem. *85*, 1515–1609.

Murrow, L., and Debnath, J. (2013). Autophagy as a stress-response and quality-control mechanism: implications for cell injury and human disease. Annu. Rev. Pathol. *8*, 105–137.

Musiek, E.S., and Holtzman, D.M. (2015). Three dimensions of the amyloid hypothesis: time, space and "wingmen." Nat. Neurosci. *18*, 800–806.

Nakai, A., Yamaguchi, O., Takeda, T., Higuchi, Y., Hikoso, S., Taniike, M., Omiya, S., Mizote, I., Matsumura, Y., Asahi, M., et al. (2007). The role of autophagy in cardiomyocytes in the basal state and in response to hemodynamic stress. Nat. Med. *13*, 619–624.

Neer, E.J., Schmidt, C.J., Nambudripad, R., and Smith, T.F. (1994). The ancient regulatory-protein family of WD-repeat proteins. Nature *371*, 297–300.

Nelson, L., and Tabet, N. (2015). Slowing the progression of Alzheimer's disease; what works? Ageing Res. Rev. *23*, 193–209.

Netzer, W.J., Bettayeb, K., Sinha, S.C., Flajolet, M., Greengard, P., and Bustos, V. (2017). Gleevec shifts APP processing from a β-cleavage to a nonamyloidogenic cleavage. Proc. Natl. Acad. Sci. *114*, 1389–1394.

Ni, H., Gong, Y., Yan, J., and Zhang, L. (2010). Autophagy inhibitor 3-methyladenine regulates the expression of LC3, Beclin-1 and ZnTs in rat cerebral cortex following recurrent neonatal seizures. World J. Emerg. Med. *1*, 216–223.

Nijholt, D. a. T., Graaf, T.R. de, Haastert, E.S. van, Oliveira, A.O., Berkers, C.R., Zwart, R., Ovaa, H., Baas, F., Hoozemans, J.J.M., and Scheper, W. (2011). Endoplasmic reticulum stress activates autophagy but not the proteasome in neuronal cells: implications for Alzheimer's disease. Cell Death Differ. *18*, 1071–1081.

Nikolai, S., Pallauf, K., Huebbe, P., and Rimbach, G. (2015). Energy restriction and potential energy restriction mimetics. Nutr. Res. Rev. *28*, 100–120.

Nikoletopoulou, V., Papandreou, M.-E., and Tavernarakis, N. (2015). Autophagy in the physiology and pathology of the central nervous system. Cell Death Differ. *22*, 398–407.

Nilsson, P., and Saido, T.C. (2014). Dual roles for autophagy: degradation and secretion of Alzheimer's disease Aβ peptide. BioEssays News Rev. Mol. Cell. Dev. Biol. *36*, 570–578.

Nilsson, P., Loganathan, K., Sekiguchi, M., Matsuba, Y., Hui, K., Tsubuki, S., Tanaka, M., Iwata, N., Saito, T., and Saido, T.C. (2013). Aβ secretion and plaque formation depend on autophagy. Cell Rep. *5*, 61–69.

Nilsson, P., Sekiguchi, M., Akagi, T., Izumi, S., Komori, T., Hui, K., Sörgjerd, K., Tanaka, M., Saito, T., Iwata, N., et al. (2015). Autophagy-Related Protein 7 Deficiency in Amyloid β (Aβ) Precursor Protein Transgenic Mice Decreases Aβ in the Multivesicular Bodies and Induces Aβ Accumulation in the Golgi. Am. J. Pathol. *185*, 305–313.

Nishiyama, J., Miura, E., Mizushima, N., Watanabe, M., and Yuzaki, M. (2007). Aberrant membranes and double-membrane structures accumulate in the axons of Atg5-null Purkinje cells before neuronal death. Autophagy *3*, 591–596.

Nisoli, E., Tonello, C., Cardile, A., Cozzi, V., Bracale, R., Tedesco, L., Falcone, S., Valerio, A., Cantoni, O., Clementi, E., et al. (2005). Calorie restriction promotes mitochondrial biogenesis by inducing the expression of eNOS. Science *310*, 314–317.

Niveditha, S., Ramesh, S.R., and Shivanandappa, T. (2017). Paraquat-Induced Movement Disorder in Relation to Oxidative Stress-Mediated Neurodegeneration in the Brain of Drosophila melanogaster. Neurochem. Res. *42*, 3310–3320.

Nixon, R.A. (2007). Autophagy, amyloidogenesis and Alzheimer disease. J. Cell Sci. *120*, 4081–4091.

Nixon, R.A. (2013). The role of autophagy in neurodegenerative disease. Nat. Med. *19*, 983–997.

Nixon, R.A., and Cataldo, A.M. (2006). Lysosomal system pathways: genes to neurodegeneration in Alzheimer's disease. J. Alzheimers Dis. JAD *9*, 277–289.

Nixon, R.A., and Yang, D.-S. (2011). Autophagy failure in Alzheimer's disease--locating the primary defect. Neurobiol. Dis. *43*, 38–45.

Nixon, R.A., and Yang, D.-S. (2012). Autophagy and Neuronal Cell Death in Neurological Disorders. Cold Spring Harb. Perspect. Biol. *4*.

Nixon, R.A., Cataldo, A.M., and Mathews, P.M. (2000). The endosomal-lysosomal system of neurons in Alzheimer's disease pathogenesis: a review. Neurochem. Res. *25*, 1161–1172.

Nixon, R.A., Wegiel, J., Kumar, A., Yu, W.H., Peterhoff, C., Cataldo, A., and Cuervo, A.M. (2005). Extensive involvement of autophagy in Alzheimer disease: an immuno-electron microscopy study. J. Neuropathol. Exp. Neurol. *64*, 113–122.

Nixon, R.A., Yang, D.-S., and Lee, J.-H. (2008). Neurodegenerative lysosomal disorders: a continuum from development to late age. Autophagy *4*, 590–599.

Noda, T., and Ohsumi, Y. (1998). Tor, a phosphatidylinositol kinase homologue, controls autophagy in yeast. J. Biol. Chem. *273*, 3963–3966.

Ntsapi, C., and Loos, B. (2016). Caloric restriction and the precision-control of autophagy: A strategy for delaying neurodegenerative disease progression. Exp. Gerontol. *83*, 97–111.

Ntsapi, C., Swart, C., Lumkwana, D., and Loos, B. (2016). Autophagic Flux Failure in Neurodegeneration: Identifying the Defect and Compensating Flux Offset.

Ntsapi, C., Lumkwana, D., Swart, C., du Toit, A., and Loos, B. (2018). New Insights into Autophagy Dysfunction Related to Amyloid Beta Toxicity and Neuropathology in Alzheimer's Disease. Int. Rev. Cell Mol. Biol. *336*, 321–361.

O'Brien, R.J., and Wong, P.C. (2011). Amyloid Precursor Protein Processing and Alzheimer's Disease. Annu. Rev. Neurosci. *34*, 185–204.

Obulesu, M., and Lakshmi, M.J. (2014). Apoptosis in Alzheimer's disease: an understanding of the physiology, pathology and therapeutic avenues. Neurochem. Res. *39*, 2301–2312.

O'Flanagan, C.H., Smith, L.A., McDonell, S.B., and Hursting, S.D. (2017). When less may be more: calorie restriction and response to cancer therapy. BMC Med. *15*, 106.

Ohsumi, Y. (1997). [Autophagy in yeast, bulk protein degradation in the vacuole]. Seikagaku *69*, 39–44.

Ohsumi, Y. (2014). Historical landmarks of autophagy research. Cell Res. *24*, 9–23.

Osborne, T.B., Mendel, L.B., and Ferry, E.L. (1917). THE EFFECT OF RETARDATION OF GROWTH UPON THE BREEDING PERIOD AND DURATION OF LIFE OF RATS. Science *45*, 294–295.

Ott, C., König, J., Höhn, A., Jung, T., and Grune, T. (2016). Reduced autophagy leads to an impaired ferritin turnover in senescent fibroblasts. Free Radic. Biol. Med. *101*, 325–333.

Panis, C., Pizzatti, L., Herrera, A.C., Corrêa, S., Binato, R., and Abdelhay, E. (2014). Label-Free Proteomic Analysis of Breast Cancer Molecular Subtypes. J. Proteome Res. *13*, 4752–4772.

Pankiv, S., Clausen, T.H., Lamark, T., Brech, A., Bruun, J.-A., Outzen, H., Øvervatn, A., Bjørkøy, G., and Johansen, T. (2007). p62/SQSTM1 binds directly to Atg8/LC3 to facilitate degradation of ubiquitinated protein aggregates by autophagy. J. Biol. Chem. *282*, 24131–24145.

Park, C., and Cuervo, A.M. (2013). Selective autophagy: talking with the UPS. Cell Biochem. Biophys. *67*, 3–13.

Park, J.-S., Kim, D.-H., and Yoon, S.-Y. (2016). Regulation of amyloid precursor protein processing by its KFERQ motif. BMB Rep. *49*, 337–342.

Pasquier, B. (2016). Autophagy inhibitors. Cell. Mol. Life Sci. CMLS *73*, 985–1001.

Patel, B., and Cuervo, A.M. (2015). Methods to study chaperone-mediated autophagy. Methods San Diego Calif *75*, 133–140.

Patel, N.V., Gordon, M.N., Connor, K.E., Good, R.A., Engelman, R.W., Mason, J., Morgan, D.G., Morgan, T.E., and Finch, C.E. (2005). Caloric restriction attenuates Abeta-deposition in Alzheimer transgenic models. Neurobiol. Aging *26*, 995–1000.

Peters, I., Igbavboa, U., Schütt, T., Haidari, S., Hartig, U., Böttner, S., Copanaki, E., Deller, T., Kögel, D., Wood, W.G., et al. (2009). The interaction of beta-amyloid protein with cellular membranes stimulates its own production. Biochim. Biophys. Acta *1788*, 964–972.

Pickford, F., Masliah, E., Britschgi, M., Lucin, K., Narasimhan, R., Jaeger, P.A., Small, S., Spencer, B., Rockenstein, E., Levine, B., et al. (2008). The autophagy-related protein beclin 1 shows reduced expression in early Alzheimer disease and regulates amyloid beta accumulation in mice. J. Clin. Invest. *118*, 2190–2199.

Ping, L., Duong, D.M., Yin, L., Gearing, M., Lah, J.J., Levey, A.I., and Seyfried, N.T. (2018). Global quantitative analysis of the human brain proteome in Alzheimer's and Parkinson's Disease. Sci. Data *5*, 180036.

Poli, G., Biasi, F., and Leonarduzzi, G. (2008). 4-Hydroxynonenal-protein adducts: A reliable biomarker of lipid oxidation in liver diseases. Mol. Aspects Med. *29*, 67–71.

Porter, A.G., and Jänicke, R.U. (1999). Emerging roles of caspase-3 in apoptosis. Cell Death Differ. *6*, 99–104.

Postina, R. (2008). A closer look at alpha-secretase. Curr. Alzheimer Res. *5*, 179–186.

Postina, R., Schroeder, A., Dewachter, I., Bohl, J., Schmitt, U., Kojro, E., Prinzen, C., Endres, K., Hiemke, C., Blessing, M., et al. (2004). A disintegrin-metalloproteinase prevents amyloid plaque formation and hippocampal defects in an Alzheimer disease mouse model. J. Clin. Invest. *113*, 1456–1464.

Prasad, K., Tarasewicz, E., Mathew, J., Ohman Strickland, P.A., Buckley, B., Richardson, J.R., and Richfield, E.K. (2009). Toxicokinetics and toxicodynamics of paraquat accumulation in mouse brain. Exp. Neurol. *215*, 358–367.

Pyo, J.-O., Yoo, S.-M., Ahn, H.-H., Nah, J., Hong, S.-H., Kam, T.-I., Jung, S., and Jung, Y.-K. (2013). Overexpression of Atg5 in mice activates autophagy and extends lifespan. Nat. Commun. *4*, 2300.

Qiu, L., Ng, G., Tan, E.K., Liao, P., Kandiah, N., and Zeng, L. (2016). Chronic cerebral hypoperfusion enhances Tau hyperphosphorylation and reduces autophagy in Alzheimer's disease mice. Sci. Rep. *6*, 23964.

Quiroz-Baez, R., Rojas, E., and Arias, C. (2009). Oxidative stress promotes JNK-dependent amyloidogenic processing of normally expressed human APP by differential modification of α-, β- and γ-secretase expression. Neurochem. Int. *55*, 662–670.

Rabinowitz, J.D., and White, E. (2010). Autophagy and metabolism. Science *330*, 1344–1348.

Rajawat, Y.S., Hilioti, Z., and Bossis, I. (2009). Aging: central role for autophagy and the lysosomal degradative system. Ageing Res. Rev. *8*, 199–213.

Rajendran, L., and Annaert, W. (2012). Membrane trafficking pathways in Alzheimer's disease. Traffic Cph. Den. *13*, 759–770.

Ramalho, R.M., Borralho, P.M., Castro, R.E., Solá, S., Steer, C.J., and Rodrigues, C.M.P. (2006). Tauroursodeoxycholic acid modulates p53-mediated apoptosis in Alzheimer's disease mutant neuroblastoma cells. J. Neurochem. *98*, 1610–1618.

Ramanathan, A., Nelson, A.R., Sagare, A.P., and Zlokovic, B.V. (2015). Impaired vascular-mediated clearance of brain amyloid beta in Alzheimer's disease: the role, regulation and restoration of LRP1. Front. Aging Neurosci. *7*.

Ramírez-Peinado, S., León-Annicchiarico, C.L., Galindo-Moreno, J., Iurlaro, R., Caro-Maldonado, A., Prehn, J.H.M., Ryan, K.M., and Muñoz-Pinedo, C. (2013). Glucose-starved Cells Do Not Engage in Prosurvival Autophagy. J. Biol. Chem. *288*, 30387–30398.

Rapoport, S.I. (1999). *In vivo* PET imaging and postmortem studies suggest potentially reversible and irreversible stages of brain metabolic failure in Alzheimer's disease. Eur. Arch. Psychiatry Clin. Neurosci. *249 Suppl 3*, 46–55.

Rapp, P.R., and Gallagher, M. (1996). Preserved neuron number in the hippocampus of aged rats with spatial learning deficits. Proc. Natl. Acad. Sci. U. S. A. *93*, 9926–9930.

Ravanan, P., Srikumar, I.F., and Talwar, P. (2017). Autophagy: The spotlight for cellular stress responses. Life Sci. *188*, 53–67.

Ravikumar, B., Vacher, C., Berger, Z., Davies, J.E., Luo, S., Oroz, L.G., Scaravilli, F., Easton, D.F., Duden, R., O'Kane, C.J., et al. (2004). Inhibition of mTOR induces autophagy and reduces toxicity of polyglutamine expansions in fly and mouse models of Huntington disease. Nat. Genet. *36*, 585–595.

Ravussin, E., Redman, L.M., Rochon, J., Das, S.K., Fontana, L., Kraus, W.E., Romashkan, S., Williamson, D.A., Meydani, S.N., Villareal, D.T., et al. (2015). A 2-Year Randomized Controlled Trial of Human Caloric Restriction: Feasibility and Effects on Predictors of Health Span and Longevity. J. Gerontol. A. Biol. Sci. Med. Sci. *70*, 1097–1104.

Redman, L.M., and Ravussin, E. (2009). ENDOCRINE ALTERATIONS IN RESPONSE TO CALORIE RESTRICTION IN HUMANS. Mol. Cell. Endocrinol. *299*.

Redman, L.M., and Ravussin, E. (2011). Caloric Restriction in Humans: Impact on Physiological, Psychological, and Behavioral Outcomes. Antioxid. Redox Signal. *14*, 275–287.

Reiman, E.M., Chen, K., Liu, X., Bandy, D., Yu, M., Lee, W., Ayutyanont, N., Keppler, J., Reeder, S.A., Langbaum, J.B.S., et al. (2009). Fibrillar amyloid-beta burden in cognitively normal people at 3 levels of genetic risk for Alzheimer's disease. Proc. Natl. Acad. Sci. U. S. A. *106*, 6820–6825.

Rezadoost, H., Karimi, M., and Jafari, M. (2016). Proteomics of hot-wet and cold-dry temperaments proposed in Iranian traditional medicine: a Network-based Study. Sci. Rep. *6*, srep30133.

Ringman, J.M. (2017). Dementia, An Issue of Neurologic Clinics, E-Book (Elsevier Health Sciences).

Robinson, J.L., Molina-Porcel, L., Corrada, M.M., Raible, K., Lee, E.B., Lee, V.M.-Y., Kawas, C.H., and Trojanowski, J.Q. (2014). Perforant path synaptic loss correlates with cognitive impairment and Alzheimer's disease in the oldest-old. Brain *137*, 2578–2587.

Rodriguez-Losada, N., Romero, P., Estivill-Torrús, G., Guzmán de Villoria, R., and Aguirre, J.A. (2017). Cell survival and differentiation with nanocrystalline glass-like carbon using substantia nigra dopaminergic cells derived from transgenic mouse embryos. PloS One *12*, e0173978.

Rodriguez-Navarro, J.A., Kaushik, S., Koga, H., Dall'Armi, C., Shui, G., Wenk, M.R., Di Paolo, G., and Cuervo, A.M. (2012). Inhibitory effect of dietary lipids on chaperone-mediated autophagy. Proc. Natl. Acad. Sci. U. S. A. *109*, E705-714.

Rogers, J.T., Randall, J.D., Cahill, C.M., Eder, P.S., Huang, X., Gunshin, H., Leiter, L., McPhee, J., Sarang, S.S., Utsuki, T., et al. (2002). An iron-responsive element type II in the 5'-untranslated region of the Alzheimer's amyloid precursor protein transcript. J. Biol. Chem. *277*, 45518–45528.

Rogina, B., and Helfand, S.L. (2004). Sir2 mediates longevity in the fly through a pathway related to calorie restriction. Proc. Natl. Acad. Sci. U. S. A. *101*, 15998–16003.

Rosenbaum, M.W., Willcox, B.J., Willcox, D.C., and Suzuki, M. (2010). Okinawa: A Naturally Calorie Restricted Population. In Calorie Restriction, Aging and Longevity, A.V. Everitt, S.I.S. Rattan, D.G. le Couteur, and R. de Cabo, eds. (Springer Netherlands), pp. 43–53.

Ross, C., Salmon, A., Strong, R., Fernandez, E., Javors, M., Richardson, A., and Tardif, S. (2015). Metabolic consequences of long-term rapamycin exposure on common marmoset monkeys (Callithrix jacchus). Aging *7*, 964–973.

Roth, G.S., and Ingram, D.K. (2015). Calorie Restriction Mimetics: Progress and Potential. In Nutrition, Exercise and Epigenetics: Ageing Interventions, B.P. Yu, ed. (Springer International Publishing), pp. 211–243.

Rouschop, K.M.A., van den Beucken, T., Dubois, L., Niessen, H., Bussink, J., Savelkouls, K., Keulers, T., Mujcic, H., Landuyt, W., Voncken, J.W., et al. (2010). The unfolded protein response protects human tumor cells during hypoxia through regulation of the autophagy genes MAP1LC3B and ATG5. J. Clin. Invest. *120*, 127–141.

Rubinsztein, D.C. (2006). The roles of intracellular protein-degradation pathways in neurodegeneration. Nature *443*, 780–786.

Rubinsztein, D.C., Mariño, G., and Kroemer, G. (2011). Autophagy and aging. Cell *146*, 682–695.

Rubinsztein, D.C., Bento, C.F., and Deretic, V. (2015). Therapeutic targeting of autophagy in neurodegenerative and infectious diseases. J. Exp. Med. *212*, 979–990.

Russell, M.R.G., Lerner, T.R., Burden, J.J., Nkwe, D.O., Pelchen-Matthews, A., Domart, M.-C., Durgan, J., Weston, A., Jones, M.L., Peddie, C.J., et al. (2017). 3D correlative light and electron microscopy of cultured cells using serial blockface scanning electron microscopy. J Cell Sci *130*, 278–291.

Sabbagh, J.J., Kinney, J.W., and Cummings, J.L. (2013). Animal systems in the development of treatments for Alzheimer's disease: challenges, methods, and implications. Neurobiol. Aging *34*, 169–183.

Saftig, P., Beertsen, W., and Eskelinen, E.-L. (2008). LAMP-2: a control step for phagosome and autophagosome maturation. Autophagy *4*, 510–512.

Sahu, R., Kaushik, S., Clement, C.C., Cannizzo, E.S., Scharf, B., Follenzi, A., Potolicchio, I., Nieves, E., Cuervo, A.M., and Santambrogio, L. (2011). Microautophagy of cytosolic proteins by late endosomes. Dev. Cell *20*, 131–139.

Saido, T., and Leissring, M.A. (2012). Proteolytic degradation of amyloid β-protein. Cold Spring Harb. Perspect. Med. *2*, a006379.

Salminen, A., Kaarniranta, K., Haapasalo, A., Hiltunen, M., Soininen, H., and Alafuzoff, I. (2012). Emerging role of p62/sequestosome-1 in the pathogenesis of Alzheimer's disease. Prog. Neurobiol. *96*, 87–95.

Salmon, A.B. (2015). About-face on the metabolic side effects of rapamycin. Oncotarget *6*, 2585–2586.

Salto, R., Vílchez, J.D., Girón, M.D., Cabrera, E., Campos, N., Manzano, M., Rueda, R., and López-Pedrosa, J.M. (2015). β-Hydroxy-β-Methylbutyrate (HMB) Promotes Neurite Outgrowth in Neuro2a Cells. PLoS ONE *10*.

Sanabria-Castro, A., Alvarado-Echeverría, I., and Monge-Bonilla, C. (2017). Molecular Pathogenesis of Alzheimer's Disease: An Update. Ann. Neurosci. *24*, 46–54.

Sanchez, A.M.J., Bernardi, H., Py, G., and Candau, R.B. (2014). Autophagy is essential to support skeletal muscle plasticity in response to endurance exercise. Am. J. Physiol. Regul. Integr. Comp. Physiol. *307*, R956-969.

Sanchez-Varo, R., Trujillo-Estrada, L., Sanchez-Mejias, E., Torres, M., Baglietto-Vargas, D., Moreno-Gonzalez, I., De Castro, V., Jimenez, S., Ruano, D., Vizuete, M., et al. (2012). Abnormal accumulation of autophagic vesicles correlates with axonal and synaptic pathology in young Alzheimer's mice hippocampus. Acta Neuropathol. (Berl.) *123*, 53–70.

Sanderson, T.H., Kumar, R., Sullivan, J.M., and Krause, G.S. (2008). Insulin blocks cytochrome c release in the reperfused brain through PI3-K signaling and by promoting Bax/Bcl-XL binding. J. Neurochem. *106*, 1248–1258.

Sannerud, R., Declerck, I., Peric, A., Raemaekers, T., Menendez, G., Zhou, L., Veerle, B., Coen, K., Munck, S., Strooper, B.D., et al. (2011). ADP ribosylation factor 6 (ARF6) controls amyloid precursor protein (APP) processing by mediating the endosomal sorting of BACE1. Proc. Natl. Acad. Sci. *108*, E559–E568.

Sarkar, S. (2013). Regulation of autophagy by mTOR-dependent and mTOR-independent pathways: autophagy dysfunction in neurodegenerative diseases and therapeutic application of autophagy enhancers. Biochem. Soc. Trans. *41*, 1103–1130.

Sarkar, S., Ravikumar, B., Floto, R.A., and Rubinsztein, D.C. (2009). Rapamycin and mTOR-independent autophagy inducers ameliorate toxicity of polyglutamine-expanded huntingtin and related proteinopathies. Cell Death Differ. *16*, 46–56.

Sasaguri, H., Nilsson, P., Hashimoto, S., Nagata, K., Saito, T., Strooper, B.D., Hardy, J., Vassar, R., Winblad, B., and Saido, T.C. (2017). APP mouse models for Alzheimer's disease preclinical studies. EMBO J. e201797397.

Schafer, M.J., Dolgalev, I., Alldred, M.J., Heguy, A., and Ginsberg, S.D. (2015). Calorie Restriction Suppresses Age-Dependent Hippocampal Transcriptional Signatures. PLOS ONE *10*, e0133923.

Scheltens, P., Blennow, K., Breteler, M.M.B., de Strooper, B., Frisoni, G.B., Salloway, S., and Van der Flier, W.M. (2016). Alzheimer's disease. Lancet Lond. Engl. *388*, 505–517.

Scheuner, D., Eckman, C., Jensen, M., Song, X., Citron, M., Suzuki, N., Bird, T.D., Hardy, J., Hutton, M., Kukull, W., et al. (1996). Secreted amyloid beta-protein similar to that in the senile plaques of Alzheimer's disease is increased *in vivo* by the presenilin 1 and 2 and APP mutations linked to familial Alzheimer's disease. Nat. Med. *2*, 864–870.

Schlachetzki, J.C.M., Saliba, S.W., Oliveira, A.C.P. de, Schlachetzki, J.C.M., Saliba, S.W., and Oliveira, A.C.P. de (2013). Studying neurodegenerative diseases in culture models. Rev. Bras. Psiquiatr. *35*, S92–S100.

Schneider, J.L., Suh, Y., and Cuervo, A.M. (2014). Deficient chaperone-mediated autophagy in liver leads to metabolic dysregulation. Cell Metab. *20*, 417–432.

Schneider, J.L., Villarroya, J., Diaz-Carretero, A., Patel, B., Urbanska, A.M., Thi, M.M., Villarroya, F., Santambrogio, L., and Cuervo, A.M. (2015). Loss of hepatic chaperone-mediated autophagy accelerates proteostasis failure in aging. Aging Cell *14*, 249–264.

Schultz, M.B., and Sinclair, D.A. (2016). When stem cells grow old: phenotypes and mechanisms of stem cell aging. Development *143*, 3–14.

Schulz, T.J., Zarse, K., Voigt, A., Urban, N., Birringer, M., and Ristow, M. (2007). Glucose restriction extends Caenorhabditis elegans life span by inducing mitochondrial respiration and increasing oxidative stress. Cell Metab. *6*, 280–293.

Sebastián, D., Sorianello, E., Segalés, J., Irazoki, A., Ruiz-Bonilla, V., Sala, D., Planet, E., Berenguer-Llergo, A., Muñoz, J.P., Sánchez-Feutrie, M., et al. (2016). Mfn2 deficiency links age-related sarcopenia and impaired autophagy to activation of an adaptive mitophagy pathway. EMBO J. *35*, 1677–1693.

Selkoe, D.J., and Hardy, J. (2016). The amyloid hypothesis of Alzheimer's disease at 25 years. EMBO Mol. Med. *8*, 595–608.

Selman, C. (2014). Dietary restriction and the pursuit of effective mimetics. Proc. Nutr. Soc. *73*, 260–270.

Serang, O., and Noble, W. (2012). A review of statistical methods for protein identification using tandem mass spectrometry. Stat. Interface *5*, 3–20.

Seyfried, N.T., Dammer, E.B., Swarup, V., Nandakumar, D., Duong, D.M., Yin, L., Deng, Q., Nguyen, T., Hales, C.M., Wingo, T., et al. (2017). A Multi-network Approach Identifies Protein-Specific Co-expression in Asymptomatic and Symptomatic Alzheimer's Disease. Cell Syst. *4*, 60-72.e4.

Sharifi, M.N., Mowers, E.E., Drake, L.E., and Macleod, K.F. (2015). Measuring Autophagy in Stressed Cells. Methods Mol. Biol. Clifton NJ *1292*, 129–150.

Sharma, N., Bhat, A.D., Kassa, A.D., Xiao, Y., Arias, E.B., and Cartee, G.D. (2012). Improved insulin sensitivity with calorie restriction does not require reduced JNK1/2, p38, or ERK1/2

phosphorylation in skeletal muscle of 9-month-old rats. Am. J. Physiol. - Regul. Integr. Comp. Physiol. *302*, R126–R136.

Shepherd, C., McCann, H., and Halliday, G.M. (2009). Variations in the neuropathology of familial Alzheimer's disease. Acta Neuropathol. (Berl.) *118*, 37–52.

Shibutani, S.T., and Yoshimori, T. (2014). A current perspective of autophagosome biogenesis. Cell Res. *24*, 58–68.

Shimohama, S. (2000). Apoptosis in Alzheimer's disease--an update. Apoptosis Int. J. Program. Cell Death *5*, 9–16.

Siegel, S.J., Bieschke, J., Powers, E.T., and Kelly, J.W. (2007). The Oxidative Stress Metabolite 4-Hydroxynonenal Promotes Alzheimer Protofibril Formation. Biochemistry (Mosc.) *46*, 1503.

Silva, D.F.F., Esteves, A.R., Arduino, D.M., Oliveira, C.R., and Cardoso, S.M. (2011). Amyloid-β-induced mitochondrial dysfunction impairs the autophagic lysosomal pathway in a tubulin dependent pathway. J. Alzheimers Dis. JAD *26*, 565–581.

Simonsen, A., Cumming, R.C., Brech, A., Isakson, P., Schubert, D.R., and Finley, K.D. (2008). Promoting basal levels of autophagy in the nervous system enhances longevity and oxidant resistance in adult Drosophila. Autophagy *4*, 176–184.

Sinclair, A.J., Barnett, A.H., and Lunec, J. (1990). Free radicals and antioxidant systems in health and disease. Br. J. Hosp. Med. *43*, 334–344.

Sinha, S., Anderson, J.P., Barbour, R., Basi, G.S., Caccavello, R., Davis, D., Doan, M., Dovey, H.F., Frigon, N., Hong, J., et al. (1999). Purification and cloning of amyloid precursor protein β-secretase from human brain. Nature *402*, 537–540.

Sisodia, S.S. (1992). Beta-amyloid precursor protein cleavage by a membrane-bound protease. Proc. Natl. Acad. Sci. U. S. A. *89*, 6075–6079.

Sisodia, S.S., and St George-Hyslop, P.H. (2002). gamma-Secretase, Notch, Abeta and Alzheimer's disease: where do the presenilins fit in? Nat. Rev. Neurosci. *3*, 281–290.

Sisodia, S.S., Koo, E.H., Beyreuther, K., Unterbeck, A., and Price, D.L. (1990). Evidence that beta-amyloid protein in Alzheimer's disease is not derived by normal processing. Science *248*, 492–495.

Smale, G., Nichols, N.R., Brady, D.R., Finch, C.E., and Horton, W.E. (1995). Evidence for apoptotic cell death in Alzheimer's disease. Exp. Neurol. *133*, 225–230.

Soare, A., Cangemi, R., Omodei, D., Holloszy, J.O., and Fontana, L. (2011). Long-term calorie restriction, but not endurance exercise, lowers core body temperature in humans. Aging *3*, 374–379.

Sohal, R.S., and Forster, M.J. (2014). Caloric restriction and the aging process: a critique. Free Radic. Biol. Med. *73*, 366–382.

Sohal, R.S., and Weindruch, R. (1996). Oxidative stress, caloric restriction, and aging. Science *273*, 59–63.

Sohal, R.S., Agarwal, S., Candas, M., Forster, M.J., and Lal, H. (1994). Effect of age and caloric restriction on DNA oxidative damage in different tissues of C57BL/6 mice. Mech. Ageing Dev. *76*, 215–224.

Soldani, C., and Scovassi, A.I. (2002). Poly(ADP-ribose) polymerase-1 cleavage during apoptosis: An update. Apoptosis *7*, 321–328.

Song, Y., Du, Y., Zou, W., Luo, Y., Zhang, X., and Fu, J. (2018). Involvement of impaired autophagy and mitophagy in Neuro-2a cell damage under hypoxic and/or high-glucose conditions. Sci. Rep. *8*, 3301.

Sooparb, S., Price, S.R., Shaoguang, J., and Franch, H.A. (2004). Suppression of chaperone-mediated autophagy in the renal cortex during acute diabetes mellitus. Kidney Int. *65*, 2135–2144.

Spilman, P., Podlutskaya, N., Hart, M.J., Debnath, J., Gorostiza, O., Bredesen, D., Richardson, A., Strong, R., and Galvan, V. (2010). Inhibition of mTOR by rapamycin abolishes cognitive deficits and reduces amyloid-beta levels in a mouse model of Alzheimer's disease. PloS One *5*, e9979.

Stadtman, E.R. (1992). Protein oxidation and aging. Science *257*, 1220–1224.

Stadtman, E.R. (2001). Protein oxidation in aging and age-related diseases. Ann. N. Y. Acad. Sci. *928*, 22–38.

Stankovic, M., Mladenovic, D., Ninkovic, M., Vucevic, D., Tomasevic, T., and Radosavljevic, T. (2013). Effects of caloric restriction on oxidative stress parameters. Gen. Physiol. Biophys. *32*, 277–283.

Stolz, A., Ernst, A., and Dikic, I. (2014). Cargo recognition and trafficking in selective autophagy. Nat. Cell Biol. *16*, 495–501.

Su, J.H., Anderson, A.J., Cummings, B.J., and Cotman, C.W. (1994). Immunohistochemical evidence for apoptosis in Alzheimer's disease. Neuroreport *5*, 2529–2533.

Su, J.H., Zhao, M., Anderson, A.J., Srinivasan, A., and Cotman, C.W. (2001). Activated caspase-3 expression in Alzheimer's and aged control brain: correlation with Alzheimer pathology. Brain Res. *898*, 350–357.

Su, M., Guan, H., Zhang, F., Gao, Y., Teng, X., and Yang, W. (2016). HDAC6 Regulates the Chaperone-Mediated Autophagy to Prevent Oxidative Damage in Injured Neurons after Experimental Spinal Cord Injury.

Sun, J., Folk, D., Bradley, T.J., and Tower, J. (2002). Induced overexpression of mitochondrial Mn-superoxide dismutase extends the life span of adult Drosophila melanogaster. Genetics *161*, 661–672.

Sun, L., Xiao, L., Nie, J., Liu, F.-Y., Ling, G.-H., Zhu, X.-J., Tang, W.-B., Chen, W.-C., Xia, Y.-C., Zhan, M., et al. (2010). p66Shc mediates high-glucose and angiotensin II-induced oxidative stress renal tubular injury via mitochondrial-dependent apoptotic pathway. Am. J. Physiol. Renal Physiol. *299*, F1014-1025.

Sun, X., Chen, W.-D., and Wang, Y.-D. (2015). β-Amyloid: the key peptide in the pathogenesis of Alzheimer's disease. Front. Pharmacol. *6*.

Sunaga, K., Takahashi, H., Chuang, D.M., and Ishitani, R. (1995). Glyceraldehyde-3-phosphate dehydrogenase is over-expressed during apoptotic death of neuronal cultures and is recognized by a monoclonal antibody against amyloid plaques from Alzheimer's brain. Neurosci. Lett. *200*, 133–136.

Suzuki, M., Wilcox, B.J., and Wilcox, C.D. (2001). Implications from and for food cultures for cardiovascular disease: longevity. Asia Pac. J. Clin. Nutr. *10*, 165–171.

Szklarczyk, D., Franceschini, A., Wyder, S., Forslund, K., Heller, D., Huerta-Cepas, J., Simonovic, M., Roth, A., Santos, A., Tsafou, K.P., et al. (2015). STRING v10: protein–protein interaction networks, integrated over the tree of life. Nucleic Acids Res. *43*, D447–D452.

Tait, S.W.G., and Green, D.R. (2013). Mitochondrial Regulation of Cell Death. Cold Spring Harb. Perspect. Biol. *5*, a008706.

Tammineni, P., Ye, X., Feng, T., Aikal, D., and Cai, Q. (2017). Impaired retrograde transport of axonal autophagosomes contributes to autophagic stress in Alzheimer's disease neurons. ELife *6*, e21776.

Taneike, M., Yamaguchi, O., Nakai, A., Hikoso, S., Takeda, T., Mizote, I., Oka, T., Tamai, T., Oyabu, J., Murakawa, T., et al. (2010). Inhibition of autophagy in the heart induces age-related cardiomyopathy. Autophagy *6*, 600–606.

Tang, H.L., Tang, H.M., Mak, K.H., Hu, S., Wang, S.S., Wong, K.M., Wong, C.S.T., Wu, H.Y., Law, H.T., Liu, K., et al. (2012). Cell survival, DNA damage, and oncogenic transformation after a transient and reversible apoptotic response. Mol. Biol. Cell *23*, 2240–2252.

Tang, H.L., Tang, H.M., and Montell, D.J. (2013). Stress induced mutagenesis, genetic diversification, and cell survival via anastasis, the reversal of late stage apoptosis. Stress-Induc. Mutagen. 223–241.

Tanida, I., Nishitani, T., Nemoto, T., Ueno, T., and Kominami, E. (2002). Mammalian Apg12p, but not the Apg12p.Apg5p conjugate, facilitates LC3 processing. Biochem. Biophys. Res. Commun. *296*, 1164–1170.

Tanida, I., Ueno, T., and Kominami, E. (2004). LC3 conjugation system in mammalian autophagy. Int. J. Biochem. Cell Biol. *36*, 2503–2518.

Tanida, I., Minematsu-Ikeguchi, N., Ueno, T., and Kominami, E. (2005). Lysosomal turnover, but not a cellular level, of endogenous LC3 is a marker for autophagy. Autophagy *1*, 84–91.

Tarasoff-Conway, J.M., Carare, R.O., Osorio, R.S., Glodzik, L., Butler, T., Fieremans, E., Axel, L., Rusinek, H., Nicholson, C., Zlokovic, B.V., et al. (2015). Clearance systems in the brain—implications for Alzheimer disease. Nat. Rev. Neurol. *11*, 457–470.

Tariq, M., Khan, H.A., al Moutaery, K., and al Deeb, S. (1999). Protection by 2-deoxy-D-glucose against beta,beta'-iminodipropionitrile-induced neurobehavioral toxicity in mice. Exp. Neurol. *158*, 229–233.

Teixeira, F.B., de Oliveira, A.C.A., Leão, L.K.R., Fagundes, N.C.F., Fernandes, R.M., Fernandes, L.M.P., da Silva, M.C.F., Amado, L.L., Sagica, F.E.S., de Oliveira, E.H.C., et al. (2018). Exposure to Inorganic Mercury Causes Oxidative Stress, Cell Death, and Functional Deficits in the Motor Cortex. Front. Mol. Neurosci. *11*.

Tekirdag, K., and Cuervo, A.M. (2018). Chaperone-mediated autophagy and endosomal microautophagy: Joint by a chaperone. J. Biol. Chem. *293*, 5414–5424.

Terlecky, S.R., and Dice, J.F. (1993). Polypeptide import and degradation by isolated lysosomes. J. Biol. Chem. *268*, 23490–23495.

Terlecky, S.R., Chiang, H.L., Olson, T.S., and Dice, J.F. (1992). Protein and peptide binding and stimulation of *in vitro* lysosomal proteolysis by the 73-kDa heat shock cognate protein. J. Biol. Chem. *267*, 9202–9209.

Terman, A. (1995). The effect of age on formation and elimination of autophagic vacuoles in mouse hepatocytes. Gerontology *41 Suppl 2*, 319–326.

Tesco, G., Koh, Y.H., and Tanzi, R.E. (2003). Caspase Activation Increases β-Amyloid Generation Independently of Caspase Cleavage of the β-Amyloid Precursor Protein (APP). J. Biol. Chem. *278*, 46074–46080.

Théron, L., Gueugneau, M., Coudy, C., Viala, D., Bijlsma, A., Butler-Browne, G., Maier, A., Béchet, D., and Chambon, C. (2014). Label-free quantitative protein profiling of vastus lateralis muscle during human aging. Mol. Cell. Proteomics MCP *13*, 283–294.

Thinakaran, G., Teplow, D.B., Siman, R., Greenberg, B., and Sisodia, S.S. (1996). Metabolism of the Swedish Amyloid Precursor Protein Variant in Neuro2a (N2a) Cells EVIDENCE THAT CLEAVAGE AT THE “β-SECRETASE” SITE OCCURS IN THE GOLGI APPARATUS. J. Biol. Chem. *271*, 9390–9397.

Thompson, L.M., Aiken, C.T., Kaltenbach, L.S., Agrawal, N., Illes, K., Khoshnan, A., Martinez-Vincente, M., Arrasate, M., O’Rourke, J.G., Khashwji, H., et al. (2009). IKK phosphorylates Huntingtin and targets it for degradation by the proteasome and lysosome. J. Cell Biol. *187*, 1083–1099.

Tian, L., Zhang, K., Tian, Z.-Y., Wang, T., Shang, D.-S., Li, B., Liu, D.-X., Fang, W.-G., Wang, Z.-Y., and Chen, Y.-H. (2014a). Decreased expression of cathepsin D in monocytes is related to the defective degradation of amyloid-β in Alzheimer’s disease. J. Alzheimers Dis. JAD *42*, 511–520.

Tian, Y., Chang, J.C., Greengard, P., and Flajolet, M. (2014b). The convergence of endosomal and autophagosomal pathways. Autophagy *10*, 694–696.

du Toit, A., Hofmeyr, J.-H.S., Gniadek, T.J., and Loos, B. (2018). Measuring autophagosome flux. Autophagy 1–12.

Tong, Y., Zhou, W., Fung, V., Christensen, M.A., Qing, H., Sun, X., and Song, W. (2005). Oxidative stress potentiates BACE1 gene expression and Aβ generation. J. Neural Transm. *112*, 455–469.

Towers, C.G., and Thorburn, A. (2016). Therapeutic Targeting of Autophagy. EBioMedicine *14*, 15–23.

Uchida, K. (2003). 4-Hydroxy-2-nonenal: a product and mediator of oxidative stress. Prog. Lipid Res. *42*, 318–343.

Uemura, T., Yamamoto, M., Kametaka, A., Sou, Y., Yabashi, A., Yamada, A., Annoh, H., Kametaka, S., Komatsu, M., and Waguri, S. (2014). A Cluster of Thin Tubular Structures

Mediates Transformation of the Endoplasmic Reticulum to Autophagic Isolation Membrane. Mol. Cell. Biol. *34*, 1695–1706.

Ullman-Culleré, M.H., and Foltz, C.J. (1999). Body condition scoring: a rapid and accurate method for assessing health status in mice. Lab. Anim. Sci. *49*, 319–323.

Upadhya, S.C., and Hegde, A.N. (2007). Role of the ubiquitin proteasome system in Alzheimer's disease. BMC Biochem. *8 Suppl 1*, S12.

Van Uden, E., Mallory, M., Veinbergs, I., Alford, M., Rockenstein, E., and Masliah, E. (2002). Increased extracellular amyloid deposition and neurodegeneration in human amyloid precursor protein transgenic mice deficient in receptor-associated protein. J. Neurosci. Off. J. Soc. Neurosci. *22*, 9298–9304.

Varady, K.A., and Hellerstein, M.K. (2007). Alternate-day fasting and chronic disease prevention: a review of human and animal trials. Am. J. Clin. Nutr. *86*, 7–13.

Vassar, R. (2014). BACE1 inhibitor drugs in clinical trials for Alzheimer's disease. Alzheimers Res. Ther. *6*.

Vellai, T. (2009). Autophagy genes and ageing. Cell Death Differ. *16*, 94–102.

Vellai, T., Takacs-Vellai, K., Zhang, Y., Kovacs, A.L., Orosz, L., and Müller, F. (2003). Genetics: influence of TOR kinase on lifespan in C. elegans. Nature *426*, 620.

Vellas, B., Hampel, H., Rougé-Bugat, M.E., Grundman, M., Andrieu, S., Abu-Shakra, S., Bateman, R., Berman, R., Black, R., Carrillo, M., et al. (2012). Alzheimer's disease therapeutic trials: EU/US Task Force report on recruitment, retention, and methodology. J. Nutr. Health Aging *16*, 339–345.

Vemuri, P., and Jack, C.R. (2010). Role of structural MRI in Alzheimer's disease. Alzheimers Res. Ther. *2*, 23.

Vilalta, A., and Brown, G.C. (2014). Deoxyglucose prevents neurodegeneration in culture by eliminating microglia. J. Neuroinflammation *11*, 58.

Vittorini, S., Paradiso, C., Donati, A., Cavallini, G., Masini, M., Gori, Z., Pollera, M., and Bergamini, E. (1999). The age-related accumulation of protein carbonyl in rat liver correlates with the age-related decline in liver proteolytic activities. J. Gerontol. A. Biol. Sci. Med. Sci. *54*, B318-323.

Vivar, C., Potter, M.C., and van Praag, H. (2013). All about running: synaptic plasticity, growth factors and adult hippocampal neurogenesis. Curr. Top. Behav. Neurosci. *15*, 189–210.

Vogiatzi, T., Xilouri, M., Vekrellis, K., and Stefanis, L. (2008). Wild type alpha-synuclein is degraded by chaperone-mediated autophagy and macroautophagy in neuronal cells. J. Biol. Chem. *283*, 23542–23556.

Wahlund, L.-O., Basun, H., Almkvist, O., Julin, P., Axelman, K., Shigeta, M., Jelic, V., Nordberg, A., and Lannfelt, L. (1999). A Follow-Up Study of the Family with the Swedish APP 670/671 Alzheimer's Disease Mutation. Dement. Geriatr. Cogn. Disord. *10*, 526–533.

Walsh, D.M., and Selkoe, D.J. (2007). A beta oligomers - a decade of discovery. J. Neurochem. *101*, 1172–1184.

Walsh, D.M., Klyubin, I., Shankar, G.M., Townsend, M., Fadeeva, J.V., Betts, V., Podlisny, M.B., Cleary, J.P., Ashe, K.H., Rowan, M.J., et al. (2005). The role of cell-derived oligomers of Abeta in Alzheimer's disease and avenues for therapeutic intervention. Biochem. Soc. Trans. *33*, 1087–1090.

Wan, R., Camandola, S., and Mattson, M.P. (2004). Dietary supplementation with 2-deoxy-D-glucose improves cardiovascular and neuroendocrine stress adaptation in rats. Am. J. Physiol. Heart Circ. Physiol. *287*, H1186-1193.

Wang, X. (2001). The expanding role of mitochondria in apoptosis. Genes Dev. *15*, 2922–2933.

Wang, Y., and Mandelkow, E. (2012). Degradation of tau protein by autophagy and proteasomal pathways. Biochem. Soc. Trans. *40*, 644–652.

Wang, C., Sun, B., Zhou, Y., Grubb, A., and Gan, L. (2012). Cathepsin B Degrades Amyloid-β in Mice Expressing Wild-type Human Amyloid Precursor Protein. J. Biol. Chem. *287*, 39834–39841.

Wang, J., Ho, L., Qin, W., Rocher, A.B., Seror, I., Humala, N., Maniar, K., Dolios, G., Wang, R., Hof, P.R., et al. (2005). Caloric restriction attenuates beta-amyloid neuropathology in a mouse model of Alzheimer's disease. FASEB J. Off. Publ. Fed. Am. Soc. Exp. Biol. *19*, 659–661.

Wang, Q., Ren, N., Cai, Z., Lin, Q., Wang, Z., Zhang, Q., Wu, S., and Li, H. (2017). Paraquat and MPTP induce neurodegeneration and alteration in the expression profile of microRNAs: the role of transcription factor Nrf2. NPJ Park. Dis. *3*.

Wang, S.-Y., Wei, Y.-H., Shieh, D.-B., Lin, L.-L., Cheng, S.-P., Wang, P.-W., and Chuang, J.-H. (2015). 2-Deoxy-d-Glucose Can Complement Doxorubicin and Sorafenib to Suppress the Growth of Papillary Thyroid Carcinoma Cells. PLOS ONE *10*, e0130959.

Wang, Y., Martinez-Vicente, M., Krüger, U., Kaushik, S., Wong, E., Mandelkow, E.-M., Cuervo, A.M., and Mandelkow, E. (2009). Tau fragmentation, aggregation and clearance: the dual role of lysosomal processing. Hum. Mol. Genet. *18*, 4153–4170.

Wang, Y., Martinez-Vicente, M., Krüger, U., Kaushik, S., Wong, E., Mandelkow, E.-M., Cuervo, A.M., and Mandelkow, E. (2010). Synergy and antagonism of macroautophagy and chaperone-mediated autophagy in a cell model of pathological tau aggregation. Autophagy *6*, 182–183.

Ward, W.F. (2002). Protein degradation in the aging organism. Prog. Mol. Subcell. Biol. *29*, 35–42.

Webb, J.L., Ravikumar, B., Atkins, J., Skepper, J.N., and Rubinsztein, D.C. (2003). Alpha-Synuclein is degraded by both autophagy and the proteasome. J. Biol. Chem. *278*, 25009–25013.

Weidberg, H., Shvets, E., and Elazar, Z. (2011). Biogenesis and cargo selectivity of autophagosomes. Annu. Rev. Biochem. *80*, 125–156.

White, A.R., Zheng, H., Galatis, D., Maher, F., Hesse, L., Multhaup, G., Beyreuther, K., Masters, C.L., and Cappai, R. (1998). Survival of cultured neurons from amyloid precursor protein knock-out mice against Alzheimer's amyloid-beta toxicity and oxidative stress. J. Neurosci. Off. J. Soc. Neurosci. *18*, 6207–6217.

White, E., Mehnert, J.M., and Chan, C.S. (2015). Autophagy, Metabolism, and Cancer. Clin. Cancer Res. Off. J. Am. Assoc. Cancer Res. *21*, 5037–5046.

Wildsmith, K.R., Holley, M., Savage, J.C., Skerrett, R., and Landreth, G.E. (2013). Evidence for impaired amyloid β clearance in Alzheimer's disease. Alzheimers Res. Ther. *5*, 33.

Willcox, B.J., Willcox, D.C., Todoriki, H., Fujiyoshi, A., Yano, K., He, Q., Curb, J.D., and Suzuki, M. (2007). Caloric restriction, the traditional Okinawan diet, and healthy aging: the diet of the world's longest-lived people and its potential impact on morbidity and life span. Ann. N. Y. Acad. Sci. *1114*, 434–455.

Willcox, D.C., Willcox, B.J., Todoriki, H., and Suzuki, M. (2009). The Okinawan diet: health implications of a low-calorie, nutrient-dense, antioxidant-rich dietary pattern low in glycemic load. J. Am. Coll. Nutr. *28 Suppl*, 500S-516S.

Williamson, R.L., Laulagnier, K., Miranda, A.M., Fernandez, M.A., Wolfe, M.S., Sadoul, R., and Paolo, G.D. (2017). Disruption of amyloid precursor protein ubiquitination selectively increases amyloid beta (Aβ) 40 levels via presenilin 2-mediated cleavage. J. Biol. Chem. jbc.M117.818138.

Wimo, A., Guerchet, M., Ali, G.-C., Wu, Y.-T., Prina, A.M., Winblad, B., Jönsson, L., Liu, Z., and Prince, M. (2017). The worldwide costs of dementia 2015 and comparisons with 2010. Alzheimers Dement. *13*, 1–7.

Wing, S.S., Chiang, H.L., Goldberg, A.L., and Dice, J.F. (1991). Proteins containing peptide sequences related to Lys-Phe-Glu-Arg-Gln are selectively depleted in liver and heart, but not skeletal muscle, of fasted rats. Biochem. J. *275 (Pt 1)*, 165–169.

Wolfe, D.M., Lee, J.-H., Kumar, A., Lee, S., Orenstein, S.J., and Nixon, R.A. (2013). Autophagy failure in Alzheimer's disease and the role of defective lysosomal acidification. Eur. J. Neurosci. *37*, 1949–1961.

Wood, H. (2017). Alzheimer disease: Localized proteomics distinguishes AD subtypes.

Wu, H., Chen, S., Ammar, A.-B., Xu, J., Wu, Q., Pan, K., Zhang, J., and Hong, Y. (2015a). Crosstalk Between Macroautophagy and Chaperone-Mediated Autophagy: Implications for the Treatment of Neurological Diseases. Mol. Neurobiol. *52*, 1284–1296.

Wu, L., Feng, Z., Cui, S., Hou, K., Tang, L., Zhou, J., Cai, G., Xie, Y., Hong, Q., Fu, B., et al. (2013a). Rapamycin Upregulates Autophagy by Inhibiting the mTOR-ULK1 Pathway, Resulting in Reduced Podocyte Injury. PLOS ONE *8*, e63799.

Wu, Y., Wang, X., Guo, H., Zhang, B., Zhang, X.-B., Shi, Z.-J., and Yu, L. (2013b). Synthesis and screening of 3-MA derivatives for autophagy inhibitors. Autophagy *9*, 595–603.

Wu, Y., Deng, Y., Zhang, S., Luo, Y., Cai, F., Zhang, Z., Zhou, W., Li, T., and Song, W. (2015b). Amyloid-β precursor protein facilitates the regulator of calcineurin 1-mediated apoptosis by downregulating proteasome subunit α type-5 and proteasome subunit β type-7. Neurobiol. Aging *36*, 169–177.

Wu, Y., Zhang, S., Xu, Q., Zou, H., Zhou, W., Cai, F., Li, T., and Song, W. (2016). Regulation of global gene expression and cell proliferation by APP. Sci. Rep. *6*.

Wu, Y.-T., Tan, H.-L., Shui, G., Bauvy, C., Huang, Q., Wenk, M.R., Ong, C.-N., Codogno, P., and Shen, H.-M. (2010). Dual role of 3-methyladenine in modulation of autophagy via different

temporal patterns of inhibition on class I and III phosphoinositide 3-kinase. J. Biol. Chem. *285*, 10850–10861.

Xiao, Q., Yan, P., Ma, X., Liu, H., Perez, R., Zhu, A., Gonzales, E., Burchett, J.M., Schuler, D.R., Cirrito, J.R., et al. (2014). Enhancing astrocytic lysosome biogenesis facilitates Aβ clearance and attenuates amyloid plaque pathogenesis. J. Neurosci. Off. J. Soc. Neurosci. *34*, 9607–9620.

Xiao, Q., Yan, P., Ma, X., Liu, H., Perez, R., Zhu, A., Gonzales, E., Tripoli, D.L., Czerniewski, L., Ballabio, A., et al. (2015). Neuronal-Targeted TFEB Accelerates Lysosomal Degradation of APP, Reducing Aβ Generation and Amyloid Plaque Pathogenesis. J. Neurosci. *35*, 12137–12151.

Xilouri, M., and Stefanis, L. (2016). Chaperone mediated autophagy in aging: Starve to prosper. Ageing Res. Rev. *32*, 13–21.

Xilouri, M., Vogiatzi, T., Vekrellis, K., Park, D., and Stefanis, L. (2009). Abberant alpha-synuclein confers toxicity to neurons in part through inhibition of chaperone-mediated autophagy. PloS One *4*, e5515.

Xilouri, M., Brekk, O.R., Landeck, N., Pitychoutis, P.M., Papasilekas, T., Papadopoulou-Daifoti, Z., Kirik, D., and Stefanis, L. (2013). Boosting chaperone-mediated autophagy *in vivo* mitigates α-synuclein-induced neurodegeneration. Brain J. Neurol. *136*, 2130–2146.

Xiong, M., Zhang, T., Zhang, L.-M., Lu, S.-D., Huang, Y.-L., and Sun, F.-Y. (2008). Caspase inhibition attenuates accumulation of beta-amyloid by reducing beta-secretase production and activity in rat brains after stroke. Neurobiol. Dis. *32*, 433–441.

Yamada, K., Mizuno, M., and Nabeshima, T. (2002). Role for brain-derived neurotrophic factor in learning and memory. Life Sci. *70*, 735–744.

Yan, R., and Vassar, R. (2014). Targeting the β secretase BACE1 for Alzheimer's disease therapy. Lancet Neurol. *13*, 319–329.

Yan, P., Bero, A.W., Cirrito, J.R., Xiao, Q., Hu, X., Wang, Y., Gonzales, E., Holtzman, D.M., and Lee, J.-M. (2009). Characterizing the appearance and growth of amyloid plaques in APP/PS1 mice. J. Neurosci. Off. J. Soc. Neurosci. *29*, 10706–10714.

Yan, Y., Gong, K., Ma, T., Zhang, L., Zhao, N., Zhang, X., Tang, P., and Gong, Y. (2012). Protective effect of edaravone against Alzheimer's disease-relevant insults in neuroblastoma N2a cells. Neurosci. Lett. *531*, 160–165.

Yanagisawa, K. (2007). Role of gangliosides in Alzheimer's disease. Biochim. Biophys. Acta *1768*, 1943–1951.

Yang, A.J., Chandswangbhuvana, D., Margol, L., and Glabe, C.G. (1998). Loss of endosomal/lysosomal membrane impermeability is an early event in amyloid Abeta1-42 pathogenesis. J. Neurosci. Res. *52*, 691–698.

Yang, D.-S., Stavrides, P., Mohan, P.S., Kaushik, S., Kumar, A., Ohno, M., Schmidt, S.D., Wesson, D., Bandyopadhyay, U., Jiang, Y., et al. (2011a). Reversal of autophagy dysfunction in the TgCRND8 mouse model of Alzheimer's disease ameliorates amyloid pathologies and memory deficits. Brain J. Neurol. *134*, 258–277.

Yang, D.-S., Stavrides, P., Mohan, P.S., Kaushik, S., Kumar, A., Ohno, M., Schmidt, S.D., Wesson, D.W., Bandyopadhyay, U., Jiang, Y., et al. (2011b). Therapeutic effects of remediating autophagy failure in a mouse model of Alzheimer disease by enhancing lysosomal proteolysis. Autophagy *7*, 788–789.

Yang, J., Carra, S., Zhu, W.-G., and Kampinga, H.H. (2013). The Regulation of the Autophagic Network and Its Implications for Human Disease. Int. J. Biol. Sci. *9*, 1121–1133.

Yang, Y.-H., Lin, W.-Y., and Lee, W.-C. (2016). A Fuzzy Permutation Method for False Discovery Rate Control. Sci. Rep. *6*, srep28507.

Yankner, B.A., Dawes, L.R., Fisher, S., Villa-Komaroff, L., Oster-Granite, M.L., and Neve, R.L. (1989). Neurotoxicity of a fragment of the amyloid precursor associated with Alzheimer's disease. Science *245*, 417–420.

Yao, J., Chen, S., Mao, Z., Cadenas, E., and Brinton, R.D. (2011). 2-Deoxy-D-Glucose Treatment Induces Ketogenesis, Sustains Mitochondrial Function, and Reduces Pathology in Female Mouse Model of Alzheimer's Disease. PLOS ONE *6*, e21788.

Yonekawa, T., and Thorburn, A. (2013). Autophagy and Cell Death. Essays Biochem. *55*, 105–117.

Yoshii, S.R., and Mizushima, N. (2017). Monitoring and Measuring Autophagy. Int. J. Mol. Sci. *18*.

Yu, L., McPhee, C.K., Zheng, L., Mardones, G.A., Rong, Y., Peng, J., Mi, N., Zhao, Y., Liu, Z., Wan, F., et al. (2010). Termination of autophagy and reformation of lysosomes regulated by mTOR. Nature *465*, 942–946.

Yu, W.H., Kumar, A., Peterhoff, C., Shapiro Kulnane, L., Uchiyama, Y., Lamb, B.T., Cuervo, A.M., and Nixon, R.A. (2004). Autophagic vacuoles are enriched in amyloid precursor protein-secretase activities: implications for beta-amyloid peptide over-production and localization in Alzheimer's disease. Int. J. Biochem. Cell Biol. *36*, 2531–2540.

Yu, W.H., Cuervo, A.M., Kumar, A., Peterhoff, C.M., Schmidt, S.D., Lee, J.-H., Mohan, P.S., Mercken, M., Farmery, M.R., Tjernberg, L.O., et al. (2005). Macroautophagy--a novel Beta-amyloid peptide-generating pathway activated in Alzheimer's disease. J. Cell Biol. *171*, 87–98.

Zaffagnini, G., and Martens, S. (2016). Mechanisms of Selective Autophagy. J. Mol. Biol. *428*, 1714–1724.

Zare-shahabadi, A., Masliah, E., Johnson, G.V.W., and Rezaei, N. (2015). Autophagy in Alzheimer's Disease. Rev. Neurosci. *26*, 385–395.

Zhan, J., He, J., Zhou, Y., Wu, M., Liu, Y., Shang, F., and Zhang, X. (2016). Crosstalk Between the Autophagy-Lysosome Pathway and the Ubiquitin-Proteasome Pathway in Retinal Pigment Epithelial Cells. Curr. Mol. Med. *16*, 487–495.

Zhang, C., and Cuervo, A.M. (2008). Restoration of chaperone-mediated autophagy in aging liver improves cellular maintenance and hepatic function. Nat. Med. *14*, 959–965.

Zhang, X., Chen, S., Huang, K., and Le, W. (2013). Why should autophagic flux be assessed? Acta Pharmacol. Sin. *34*, 595–599.

Zhao, M., Su, J., Head, E., and Cotman, C.W. (2003). Accumulation of caspase cleaved amyloid precursor protein represents an early neurodegenerative event in aging and in Alzheimer's disease. Neurobiol. Dis. *14*, 391–403.

Zheng, L., Roberg, K., Jerhammar, F., Marcusson, J., and Terman, A. (2006). Autophagy of amyloid beta-protein in differentiated neuroblastoma cells exposed to oxidative stress. Neurosci. Lett. *394*, 184–189.

Zheng, L., Terman, A., Hallbeck, M., Dehvari, N., Cowburn, R.F., Benedikz, E., Kågedal, K., Cedazo-Minguez, A., and Marcusson, J. (2011). Macroautophagy-generated increase of lysosomal amyloid β-protein mediates oxidant-induced apoptosis of cultured neuroblastoma cells. Autophagy *7*, 1528–1545.

Zhong, H., and Yin, H. (2015). Role of lipid peroxidation derived 4-hydroxynonenal (4-HNE) in cancer: Focusing on mitochondria. Redox Biol. *4*, 193–199.

Zhou, F., van Laar, T., Huang, H., and Zhang, L. (2011a). APP and APLP1 are degraded through autophagy in response to proteasome inhibition in neuronal cells. Protein Cell *2*, 377–383.

Zhou, Z., Chan, C.H., Ma, Q., Xu, X., Xiao, Z., and Tan, E.-K. (2011b). The roles of amyloid precursor protein (APP) in neurogenesis, implications to pathogenesis and therapy of Alzheimer disease (AD). Cell Adhes. Migr. *5*, 280–292.

Zimin, A.V., Cornish, A.S., Maudhoo, M.D., Gibbs, R.M., Zhang, X., Pandey, S., Meehan, D.T., Wipfler, K., Bosinger, S.E., Johnson, Z.P., et al. (2014). A new rhesus macaque assembly and annotation for next-generation sequencing analyses. Biol. Direct *9*, 20.

Zinchuk, V., and Grossenbacher-Zinchuk, O. (2009). Recent advances in quantitative colocalization analysis: focus on neuroscience. Prog. Histochem. Cytochem. *44*, 125–172.

Zoncu, R., Efeyan, A., and Sabatini, D.M. (2011). mTOR: from growth signal integration to cancer, diabetes and ageing. Nat. Rev. Mol. Cell Biol. *12*, 21–35.